TECHNISCHE UNIVERSITÄT MÜNCHEN
TUM School of Engineering and Design

Harmonic and transient three-dimensional Structure-Soil-Structure-Interaction applying a coupled ITM-FEM approach

Julian Maria Freisinger

Vollständiger Abdruck der von der TUM School of Engineering and Design der Technischen Universität München zur Erlangung eines

Doktors der Ingenieurwissenschaften (Dr.-Ing.)

genehmigten Dissertation.

Vorsitz: Prof. Dr.-Ing. Roberto Cudmani

Prüfer*innen der Dissertation:

1. Prof. Dr.-Ing. Gerhard Müller
2. Prof. Dr. ir. Geert Degrande

Die Dissertation wurde am 18.08.2022 bei der Technischen Universität München eingereicht und durch die TUM School of Engineering and Design am 06.02.2023 angenommen.

Abstract

The dynamic interaction of surface and underground structures with each other and the surrounding soil can have a significant impact on the structural responses and the wave propagation patterns within the ground. Therefore, the integration of the dynamic Structure-Soil-Structure-Interaction (SSSI) is essential for an accurate prediction of the structure and ground borne vibrations.

In this thesis an efficient coupled Integral Transform Method (ITM) – Finite Element Method (FEM) approach is presented, based on a domain decomposition technique, subdividing the total system into substructures with different characteristics. The infinite extent of homogenous or layered soils including a cylindrical or spherical cavity or indentation is accounted for by the semi-analytical solutions of the ITM, whereas structures exhibiting sophisticated geometries and, if needed, a part of the surrounding soil are modelled by the FEM. Both substructures are coupled at the each matching interaction surfaces, enforcing the compatibility conditions. For length invariant structures, a 2.5D approach is used and the coupling is performed at the cylindrical interface, whereas for finite bounded structures, a 3D approach is applied and the coupling is carried out at the spherical boundary. Furthermore, to investigate the interaction of one or several surface structures with a possibly inhomogeneous soil, a methodology is developed that permits the determination of the soil stiffness at discrete points on the surface of any system that can be modelled with a coupled ITM-FEM approach. In all cases this leads to a description of the overall system by a complex dynamic stiffness matrix, enabling the computation of the system response to an arbitrary load applied on the discretized degrees of freedom.

The proposed approach is validated by comparison with literature results and semi-analytical solutions for multiple benchmark systems. It is further applied to assess the efficiency of different vibration mitigation measures in terms of insertion losses, thereby enabling the identification of the underlying physical mechanisms and relevant design parameters by numerical computations. Compliance functions of single and multiple adjacent surface foundations are presented and the influence of their mass and stiffness, the load distribution and different subsoil conditions on the system response as well as on the power transmission at the soil

foundation interface is studied. The distribution and wavenumber spectra of the stresses and displacements on the ground surface and within the soil, resulting from the Soil-Structure-Interaction (SSI), are computed by means of a postprocessing procedure and used together with a power flow analysis to deduce frequency dependent and site specific wave propagation characteristics like radiation directivity, predominant wave types and attenuation behaviour. Furthermore, the impact of vibration impeding or amplifying effects linked with layer resonance phenomena or the reflection, diffraction or scattering of waves at embedded structures or inhomogeneities on the foundation impedances and the free field response is illustrated.

In addition to the frequency domain analysis, the proposed approach facilitates also the investigation of the dynamic interaction of surface and underground structures subjected to transient loading. The time histories of the system response are either obtained by a Fourier synthesis of the complex frequency transfer functions or by a discrete convolution of the transient load with the impulse response functions of the system. An interpolation procedure is implemented for the transfer functions in order to ensure a sufficient time discretization. The influence of the hysteretic material damping on the causality of the response is studied and a confidence measure introduced to quantify the effect of the frequency band limitation. Time dependent compliance functions for rigid surface foundations are given and compared with existing solutions for verification. Moreover, an application of the coupled 2.5D ITM-FEM approach for the computation of the transient response of a twin tunnel system to a Gaussian modulated sine pulse is shown.

Eventually, a methodology for the incorporation of moving loads into the coupled ITM-FEM approach is introduced and validated by comparison of the moving load effects with those of existing analytical solutions for fundamental systems. The formation of shock waves and the confinement of all disturbances to a region limited by the corresponding Mach lines for a constant load moving with a velocity exceeding the wave speeds of the soil is illustrated as well as the Doppler effect in case of a moving oscillating load. Furthermore, these effects are correlated with the differing solution characteristics in the wavenumber frequency domain, before lastly the time dependent response of a twin tunnel system with a moving load inside one of the tunnel tubes is presented.

Kurzfassung

Die dynamische Wechselwirkung von ober- und unterirdischen Bauwerken untereinander und mit dem umgebenden Boden kann einen erheblichen Einfluss auf die Strukturreaktionen und die Wellenausbreitungseigenschaften im Boden haben. Daher ist die Integration der dynamischen Bauwerk-Boden-Bauwerk-Interaktion (SSSI) für eine genaue Vorhersage der Struktur- und Bodenschwingungen unerlässlich.

In dieser Arbeit wird ein effizienter gekoppelter Ansatz aus Integral-Transform-Methode (ITM) und Finite-Elemente-Methode (FEM) vorgestellt, der auf einer Gebietszerlegungsmethode basiert, bei der das Gesamtsystem in Teilstrukturen mit unterschiedlichen Eigenschaften unterteilt wird. Die unendliche Ausdehnung homogener oder geschichteter Böden einschließlich eines zylindrischen oder kugelförmigen Hohlraums oder einer Einsenkung wird durch die semi-analytischen Lösungen der ITM berücksichtigt, während Strukturen mit anspruchsvollen Geometrien und, falls erforderlich, ein Teil des umgebenden Bodens durch die FEM modelliert werden. Beide Teilstrukturen werden an den jeweils passenden Interaktionsflächen unter Anwendung der Kompatibilitätsbedingungen gekoppelt. Für längeninvariante Strukturen wird ein 2,5D-Ansatz verwendet und die Kopplung erfolgt an der zylindrischen Grenzfläche, während für endlich begrenzte Strukturen ein 3D-Ansatz angewandt wird und die Kopplung an der kugelförmigen Grenzfläche durchgeführt wird. Um die Interaktion einer oder mehrerer Oberflächenstrukturen mit einem möglicherweise inhomogenen Boden zu untersuchen, wird außerdem eine Methodik entwickelt, die die Bestimmung der Bodensteifigkeit an diskreten Punkten auf der Oberfläche eines beliebigen Systems ermöglicht, das mit einem gekoppelten ITM-FEM-Ansatz modelliert werden kann. In allen Fällen führt dies zu einer Beschreibung des Gesamtsystems durch eine komplexe dynamische Steifigkeitsmatrix, die die Berechnung der Systemreaktion auf eine beliebige, auf die diskretisierten Freiheitsgrade aufgebrachte Last ermöglicht.

Der vorgeschlagene Ansatz wird durch den Vergleich mit Literaturergebnissen und semi-analytischen Lösungen für mehrere Benchmark-Systeme validiert. Darüber hinaus wird er angewandt, um die Effizienz verschiedener schwingungsdämpfender Maßnahmen im Hinblick auf Einfügungsdämpfungen zu bewerten, wobei die zugrundeliegenden physikalischen Mechanismen und relevanten Designparameter durch numerische Berechnungen identifiziert

werden können. Es werden die Flexibilitäten von einzelnen und mehreren benachbarten Oberflächenfundamenten dargestellt und der Einfluss der Plattenmasse und -steifigkeit, der Lastverteilung und der verschiedenen Untergrundbedingungen auf die Systemantwort sowie auf die Kraftübertragung an der Schnittstelle zwischen Boden und Fundament untersucht. Die aus der Boden-Bauwerk-Interaktion (BBI) resultierenden Verteilungen und Wellenzahlspektren der Spannungen und Verschiebungen an der Bodenoberfläche und im Boden werden mit Hilfe eines Postprocessing-Verfahrens berechnet und zusammen mit einer Leistungsflussanalyse zur Ableitung von frequenzabhängigen und standortspezifischen Wellenausbreitungseigenschaften wie Abstrahlcharakteristik, vorherrschende Wellentypen und Dämpfungsverhalten verwendet. Darüber hinaus wird der Einfluss von schwingungshemmenden oder -verstärkenden Effekten im Zusammenhang mit Schichtresonanzphänomenen oder der Reflexion, Beugung oder Streuung von Wellen an eingebetteten Strukturen oder Inhomogenitäten auf die Fundamentimpedanzen und die Freifeldantwort dargestellt.

Neben der Analyse im Frequenzbereich ermöglicht der vorgeschlagene Ansatz auch die Untersuchung der dynamischen Interaktion von ober- und unterirdischen Strukturen, die einer transienten Belastung ausgesetzt sind. Die Zeitverläufe der Systemantwort werden entweder durch eine Fourier-Synthese der komplexen Frequenzübertragungsfunktionen oder durch eine diskrete Faltung der transienten Belastung mit den Impulsantwortfunktionen des Systems erhalten. Für die Übertragungsfunktionen wird ein Interpolationsverfahren eingesetzt, um eine ausreichende zeitliche Diskretisierung zu gewährleisten. Der Einfluss der hysteretischen Materialdämpfung auf die Kausalität der Antwort wird untersucht und ein Gütemaß zur Quantifizierung der Wirkung der Frequenzbandbegrenzung eingeführt. Es werden zeitabhängige Nachgiebigkeitsfunktionen für starre Oberflächenfundamente angegeben und zur Verifizierung mit bestehenden Lösungen verglichen. Darüber hinaus wird eine Anwendung des gekoppelten 2,5D ITM-FEM-Ansatzes für die Berechnung der transienten Antwort eines Zwillingstunnelsystems auf einen Gauß-modulierten Sinusimpuls gezeigt.

Schließlich wird eine Methodik für die Einbeziehung beweglicher Lasten in den gekoppelten ITM-FEM-Ansatz vorgestellt und durch den Vergleich der Auswirkungen beweglicher Lasten mit denen bestehender analytischer Lösungen für grundlegende Systeme validiert. Die Bildung von Stoßwellen und die Begrenzung aller Störungen auf einen durch die entsprechenden Mach-Linien begrenzten Bereich für eine konstante Last, die sich mit einer Geschwindigkeit bewegt, die die Wellengeschwindigkeiten des Bodens übersteigt, wird ebenso veranschaulicht wie der Dopplereffekt im Falle einer sich bewegenden oszillierenden Last. Darüber hinaus werden diese Effekte mit den unterschiedlichen Lösungseigenschaften im Wellenzahl-Frequenzbereich korreliert, bevor schließlich das zeitabhängige Verhalten eines Doppeltunnelsystems mit einer sich bewegenden Last in einer der Tunnelröhren dargestellt wird.

Acknowledgments

First of all, I would like to express my deep gratitude to my supervisor Prof. Gerhard Müller for giving me the opportunity to write this thesis at the Chair of Structural Mechanics and for providing me with guidance, constant support and scientific freedom throughout this work. Through your ability to comprehend complex issues extremely fast, you have contributed to the success of this work with your ideas and suggestions in every discussion. Moreover, the meetings with you had a value for me beyond the actual scientific matter and contributed to my personal development.

I would also like to thank Prof. Geert Degrande for taking part in examining the dissertation and Prof. Roberto Cudmani for chairing the board of examiners.

Special thanks go to my mentor Dr. Manuela Hackenberg, who accompanied, motivated and supported me from my first semester in mechanics through my Bachelor's and Master's theses to the completion of my dissertation. Thank you for all the time and commitment, without your support I wouldn't stand where I am now.

Another big thanks goes to all my colleagues and especially to Francesa, Axel, Moritz, Hannes, Quirin and of course Christoph and Felix, with whom I shared my office, for all the great discussions, helpful advice, support with any problem as well as the smooth cooperation in organizational and teaching issues. I will remember the time at the chair with great pleasure, because I know that it was an exciting and intensive time with a lot of work, but also a lot of fun, which I was allowed to share with colleagues who became and will remain friends beyond the time at TUM.

Finally, I would like to thank my family and my wife Corinna, who made all this possible in the first place and who have supported me unconditionally in every situation in life. Your listening, the bearing of my bad mood in difficult phases, your encouragement and motivation as well as the ability to bring one to other thoughts have significantly contributed to the creation and successful completion of this work.

Contents

List of Tables

List of Symbols

Latin Symbols

a_0	Dimensionless frequency
$a_l(\vartheta)$	Fourier series member along latitude
$a_{l,m}$	Coefficient of spherical harmonic series expansion
$\bar{\mathbf{a}}_{\mathbf{i}}^{\mathbf{F_n}}$	Matrix containing kinematic relation from rigid foundation DOFs to DOFs at node i on Λ_{f_n} of foundation F_n
A	Cross sectional area
A_{cv}	Total area of a control volume
A_1, A_2	Coefficients of P-wave for homog. halfspace
A_{01}, A_{02}	Coefficients of P-wave for homog. halfspace for $\omega = 0$
$\underline{A}_{1,L_l}$	Modified coefficients of P-wave for layered halfspace
A_r	Amplitude reduction factor
$\mathbf{A}^{\mathbf{F_n}}$	Matrix containing the load influence areas around the discretization points of a foundation F_n
b	Basic quantity width
b_x, b_y	Widths of the load in x- and y-direction
B_f, L_f, H_f	Foundation dimensions
B_{i1}, B_{i2}	Coefficients of S-wave in Cartesian coordinates
B_{0i1}, B_{0i2}	Coefficients of S-wave in Cartesian coordinates for $\omega = 0$
$\underline{B}_{\alpha 1,L_l}$	Modified coefficients of S-wave for layered halfspace
B_x, B_y, B_z	Repetition lengths in x-,y- and z-direction
$\bar{\mathbf{B}}$	Matrix containing the derivatives of the form functions
c_p, c_s, c_r	Velocities of the compressional, shear and Rayleigh wave
c_n	Complex Fourier series coefficient
conf	Confidence measure for frequency band limitation
C_{mn}^{ij}	Dimensionless foundation compliances
$\mathbf{C}$	Element and system FEM damping matrix

$\hat{\mathbf{C}}^{\mathbf{hs}}_{\mathbf{ITM}}$	Vector of unknowns for homog. halfspace
$\hat{\mathbf{C}}^{\mathbf{hs}}_{\mathbf{0_{ITM}}}$	Vector of unknowns for homog. halfspace for $\omega = 0$
$\hat{\mathbf{C}}^{\mathbf{hs\ L}_l}_{\mathbf{ITM}}$	Vector of unknowns for layered halfspace
$\hat{\mathbf{C}}^{\mathbf{hs\ L}_l}_{\mathbf{0_{ITM}}}$	Vector of unknowns for layered halfspace for $\omega = 0$
$\hat{\mathbf{C}}^{\mathbf{L}}_{\mathbf{ITM}}$	Vector of unknowns for discrete soil stratification
$\hat{\mathbf{C}}^{\mathbf{fs\ cyl}}_{\mathbf{ITM}}$	Vector of unknowns for fullspace with cyl. cavity
$\hat{\mathbf{C}}^{\mathbf{fs\ sph}}_{\mathbf{ITM}}$	Vector of unknowns for fullspace with sph. cavity
$\hat{\mathbf{C}}^{\mathbf{hs\ cph}}_{\mathbf{ITM}}$	Vector of unknowns for halfspace with cyl. cavity
$\hat{\mathbf{C}}^{\mathbf{hs\ sph}}_{\mathbf{ITM}}$	Vector of unknowns for halfspace with sph. cavity
$\hat{\mathbf{C}}^{\mathbf{hs\ cyl\ tw}}_{\mathbf{ITM}}$	Vector of unknowns for halfspace with two cyl. cavities
$\mathrm{d}s$	Finite element length along circumference
$\mathrm{d}x$,$\mathrm{d}y$,$\mathrm{d}z$	Spatial increments
$\mathrm{d}t$,$\mathrm{d}f$,$\mathrm{d}\omega$	Time and frequency increments
$\mathrm{d}_{\mathrm{x,f}_i\mathrm{f}_j}$, $\mathrm{d}_{\mathrm{y,f}_i\mathrm{f}_j}$	Distance between adjacent foundation i and j
d_{tr}, l_{tr}, w_{tr}	Depth, length and width of open or infilled trench
$d_{\mathrm{T}_{1-2}}$	Distance between boundaries of twin tunnels
$\mathrm{d}s_\vartheta$, $\mathrm{d}s_\varphi$	Finite element length along longitudes and latitudes
$\mathbf{D}$	Elasticity matrix
D	Lehr's Damping ratio
$D_{\mathrm{tr}}, L_{\mathrm{tr}}, W_{\mathrm{tr}}$	Dimensionless depth,length and width of open or infilled trench
E	Young's modulus
E_r	Energy decay due to mitigation measure
E_{sig}	Energy content of a discrete signal
$\mathrm{err}_{\mathrm{rel}}$	Relative error
$\mathrm{err}_{\mathrm{max}}$	Maximum error
f	Frequency
F_n	Foundation n
$\bar{F}^{ij}_{mn}$	Components of $\bar{\mathbf{F}}^{ij}_{\mathbf{s}}$
$\bar{\mathbf{F}}^{ij}_{\mathbf{s}}$	Dyn. soil flexibility matrix for a pair of discretization point i, j
$\bar{\mathbf{F}}_{\mathbf{s}}$	Dyn. soil flexibility matrix at all nodes of soil-foundation contact surface
$\bar{\mathbf{F}}^{\mathbf{F_{ij}}}_{\mathbf{s}}$	Flexibilities on nodes of foundation F_i due to a load on nodes of F_j
$\bar{\mathbf{F}}_{\mathbf{f,r}}$	Dyn. flexibility matrix of several rigid foundations coupled to the soil
$\bar{\mathbf{F}}^{\mathbf{F_n}}_{\mathbf{f,r}}$	Dyn. flexibility matrix of rigid massless foundation F_n coupled to the soil
$\bar{\mathbf{F}}^{\mathbf{F_n}}_{\mathbf{f,rm}}$	Dyn. flexibility matrix of rigid massive foundation F_n coupled to the soil
$\bar{\mathbf{F}}_{\mathrm{sys}}$	Dyn. flexibility matrix of total ITM-FEM soil-structure system
$\mathbf{g}_i$, $\mathbf{g}^i$	Co- and contravariant base vectors

G	Shear modulus
$\bar{\mathbf{G}}$	Matrix of constraint modes for CMS
h	Basic quantity height
h_l	Thickness of a spatially limited layer
h_{cyl}	Depth of the covering of a cyl. inclusion
h_{sph}	Depth of the covering of a sph. inclusion
H	Distance of center of cylinder/sphere from halfspace surface
H_{tot}	Distance of center of cylinder/sphere from surface of a layered halfspace
H_{lat}	Distance of first latitude below equator from the halfspace surface
I_x, I_y, I_z	Moments of inertia
I_T, I_{0,φ_i}	Torsional- and rocking moment of inertia
$\mathcal{I}$	Intensity flow through a defined surface
$\overline{\mathrm{IG}}_i$	Insertion gain of displacements u_i
$\overline{\mathrm{IL}}_i$	Insertion loss of displacements u_i
$\bar{\mathbf{I}}$	Intensity vector field
$\mathbf{J}$	Jacobian matrix
k_1, k_2	Coefficients in Hankel functions
k_b	Wavenumber of bending wave
k_p, k_s, k_r	Wavenumbers of the compressional, shear and Rayleigh wave
k_r	Radial wavenumber for static case
k_x, k_y	Wavenumbers in x- and y-direction
k_{zz}, c_{zz}	Stiffness and damping coefficients for equivalent dyn. soil stiffness
K, M	Dimensionless stiffness and mass ratio
$K_{0,zz}$	Equivalent static soil stiffness
$\bar{\mathbf{K}}$	Element and system FEM stiffness matrix
$\bar{\mathbf{K}}_{\mathbf{s}}$	Dyn. soil stiffness matrix at all nodes of soil-foundation contact area
$\bar{\mathbf{K}}_{\mathbf{s}}^{\mathbf{F_n}}$	Dyn. soil stiffness matrix at all nodes of contact area of foundation F_n to the soil
$\mathbf{K}_{\mathbf{f}}^{\mathbf{F_n}}$	Stiffness matrix of FEM model of foundation F_n
$\bar{\mathbf{K}}_{\mathbf{f}}^{\mathbf{F_n}}$	Dyn. stiffness matrix of FEM model of foundation F_n
$\bar{\mathbf{K}}_{\mathbf{f,r}}$	Dyn. stiffness matrix of several rigid foundations coupled to the soil
$\bar{\mathbf{K}}_{\mathbf{f,r}}^{\mathbf{F_n}}$	Dyn. stiffness matrix of rigid massless foundation F_n coupled to the soil
$\bar{\mathbf{K}}_{\mathbf{f,rm}}^{\mathbf{F_n}}$	Dyn. stiffness matrix of rigid massive foundation F_n coupled to the soil
$\bar{\mathbf{K}}_{\mathrm{sys}}$	Dyn. stiffness matrix of total ITM-FEM soil-structure system
$\hat{\mathbf{K}}_{\mathbf{ITM}}^{\mathbf{hs}}$	Dyn. stiffness matrix of homog. halfspace
$\hat{\mathbf{K}}_{\mathbf{ITM}}^{\mathbf{hs}}$	Dyn. stiffness matrix of homog. halfspace

$\hat{\mathbf{K}}^{\mathbf{hs}}_{\mathbf{0_{ITM}}}$	Dyn. stiffness matrix of homog. halfspace for $\omega = 0$
$\hat{\mathbf{K}}^{\mathbf{L}}_{\mathbf{ITM}}$	Dyn. stiffness matrix of discrete soil stratification
$\hat{\mathbf{K}}^{\mathbf{hs\,cyl}}_{\mathbf{ITM}}$	Dyn. stiffness matrix of halfspace with cyl. cavity/indentation
$\hat{\mathbf{K}}^{\mathbf{hs\,cyl\,L}}_{\mathbf{ITM}}$	Dyn. stiffness matrix of layered halfspace with cyl. cavity
$\hat{\mathbf{K}}^{\mathbf{hs\,cyl\,tw}}_{\mathbf{ITM}}$	Dyn. stiffness matrix of halfspace with two cyl. cavities/indentations
$\hat{\mathbf{K}}^{\mathbf{hs\,sph}}_{\mathbf{ITM}}$	Dyn. stiffness matrix of halfspace with sph. cavity/indentation
$\hat{\mathbf{K}}^{\mathbf{hs\,sph\,L}}_{\mathbf{ITM}}$	Dyn. stiffness matrix of layered halfspace with sph. cavity
$\tilde{\mathbf{K}}^{\mathbf{hs\,cyl}}_{\mathbf{FE}}$	Dyn. stiffness matrix of 2.5D FEM structure with cyl. boundary
$\bar{\mathbf{K}}^{\mathbf{hs\,sph}}_{\mathbf{FE}}$	Dyn. stiffness matrix of 3D FEM structure with sph. boundary
$\hat{\mathbf{K}}^{\mathbf{hs\,cyl}}_{\mathbf{ITM\,FE}}$	Dyn. stiffness matrix of halfspace with cyl. FEM inclusion
$\hat{\mathbf{K}}^{\mathbf{hs\,cyl\,L\,tw}}_{\mathbf{ITM\,FE}}$	Dyn. stiffness matrix of layered halfspace with two cyl. FEM inclusions
$\hat{\mathbf{K}}^{\mathbf{hs\,sph}}_{\mathbf{ITM\,FE}}$	Dyn. stiffness matrix of halfspace with sph. FEM inclusion/indentation
$\hat{\mathbf{K}}^{\mathbf{hs\,sph\,L}}_{\mathbf{ITM\,FE}}$	Dyn. stiffness matrix of layered halfspace with sph. FEM inclusion
l,L	Basic quantity length
L_l	Indicator for layer l
$\bar{\mathbf{L}}^{\mathbf{F_n}}_{\mathbf{f,r}}$	Transformation matrix from rigid foundation displ. to nodal displ. of foundation F_n
$\bar{\mathbf{L}}^{\mathbf{F_n}}_{\mathbf{f,r}}$	Transformation matrix from rigid foundation displ. to nodal displ. of several foundations
m, l	Degree and order of the sph. harmonics
m_i, l_i	Counter for degree and order of the sph. harmonics
m	Basic quantity mass
M	Maximum degree of the sph. harmonics
M_i	Mach numbers of elastic waves with $i = p$,s,r
$\bar{\mathbf{M}}$	Element and system FEM mass matrix
$\mathbf{M}^{\mathbf{hs\,cyl}}_{\mathbf{FE}}$	Global mass matrix of FEM structure with cyl. boundary
$\mathbf{M}^{\mathbf{F_n}}_{\mathbf{f}}$	Mass matrix of FEM model of foundation F_n
n	Fourier series member in circumferential direction
n_f	Number of nodes per foundation
$n_{\mathrm{f_x}}, n_{\mathrm{f_y}}$	Number of discretization points of a foundation in $x-$ resp. y-direction
n_tot	Number of nodes of all foundations
n_p	Number of processing units
n_cv	Number of control volume
n_GP	Number of Gauss points
n_Δ	Scaling factor for transition from coarse to fine discretization
N	Number of samples of one period of a discrete signal

N_f	Number of foundations
N_t, N_f	Number of samples in the time and frequency domain
N_x, N_y	Number of samples on the halfspace surface in x- and y-direction
N_ϑ	Maximum number of points on the longitude of a sphere
N_φ	Maximum number of points on the latitude of a sphere
N_φ	Max. number of points/Fourier members along circumference of cylinder
$\mathbf{N}$	Matrix containing the form functions
o,s	Fourier series members on Λ_l
$\bar{P}_n^j$	Harmonic unit concentrated load in direction n at point j
$\mathcal{P}_s$	Power flow through a defined surface s
$\mathcal{P}_{c_p}$	Power input for uniform P-wave radiation
$\mathcal{P}_\mathrm{in}$	Power input at soil foundation interface
$\mathcal{P}_\mathrm{tot,CV}$	Total power flow through a control volume
$\mathcal{P}_\mathrm{sides}$	Total power flow through side areas of control volume
$\mathcal{P}_\mathrm{bottom}$	Total power flow through bottom area of control volume
$\tilde{\mathbf{p}}_\mathbf{n}$	Nodal load vector of finite element
$\bar{\mathbf{P}}_\mathbf{c}$	Vector of nodal contact forces at soil foundation-interface
$\bar{\mathbf{P}}_\mathbf{s}^j$	Load vector of harmonic unit concentrated load at point j
$\bar{\mathbf{P}}_\mathbf{s}$	Load vector for all nodes of soil-foundation contact surface
$\bar{\mathbf{P}}_\mathbf{s}^{\mathbf{F_j}}$	Load vector for all nodes on foundation F_j
$\bar{\mathbf{P}}_\mathbf{f}^{\mathbf{F_n}}$	Load vector for FEM model of foundation F_n
$\bar{\mathbf{P}}_\mathbf{f,r}^{\mathbf{F_n}}$	Load vector of rigid massless foundation F_n coupled to the soil
$\bar{\mathbf{P}}_\mathbf{f,r}$	Load vector of several rigid foundations coupled to the soil
$\bar{\mathbf{P}}_\mathrm{sys}$	Load vector for total ITM-FEM soil-structure system
$\bar{\mathbf{P}}_\mathbf{mov}$	Load vector for moving load
$\hat{\mathbf{P}}_{\mathbf{\Lambda_{ITM}}}^{\mathbf{hs}}$	Load vector for homog. halfspace
$\hat{\mathbf{P}}_{\mathbf{\Lambda_{ITM}}}^{\mathbf{hs\ L}}$	Load vector for layered halfspace
$\hat{\mathbf{P}}_\mathbf{ITM}^\mathbf{L}$	Load vector for discrete soil stratification
$\hat{\mathbf{P}}_\mathbf{ITM}^\mathbf{fs\ cyl}$	Load vector for fullspace with cyl. cavity
$\hat{\mathbf{P}}_\mathbf{ITM}^\mathbf{fs\ sph}$	Load vector for fullspace with sph. cavity
$\hat{\mathbf{P}}_\mathbf{ITM}^\mathbf{hs\ cyl}$	Load vector for halfspace with cyl. cavity
$\hat{\mathbf{P}}_\mathbf{ITM}^\mathbf{hs\ cyl\ L}$	Load vector for layered halfspace with cyl. cavity
$\hat{\mathbf{P}}_\mathbf{ITM}^\mathbf{hs\ cyl\ tw}$	Load vector for halfspace with two cyl. cavities/indentations
$\hat{\mathbf{P}}_\mathbf{ITM}^\mathbf{hs\ sph}$	Load vector for halfspace with sph. cavity
$\hat{\mathbf{P}}_\mathbf{ITM}^\mathbf{hs\ sph\ L}$	Load vector for layered halfspace with sph. cavity
$\tilde{\mathbf{P}}_\mathbf{FE}^\mathbf{hs\ cyl}$	Load vector for 2.5D FEM structure with cyl. boundary

$\bar{\mathbf{P}}^{\mathbf{hs\ sph}}_{\mathbf{FE}}$	Load vector for 3D FEM structure with sph. boundary
$\hat{\mathbf{P}}^{\mathbf{hs\ cyl}}_{\mathbf{ITM\,FE}}$	Load. vector for halfspace with cyl. FEM inclusion
$\hat{\mathbf{P}}^{\mathbf{hs\ cyl\,L\,tw}}_{\mathbf{ITM\,FE}}$	Load. vector for layered halfspace with two cyl. FEM inclusions
$\hat{\mathbf{P}}^{\mathbf{hs\ sph}}_{\mathbf{ITM\,FE}}$	Load. vector for halfspace with sph. FEM inclusion/indentation
$\hat{\mathbf{P}}^{\mathbf{hs\ sph\,L}}_{\mathbf{ITM\,FE}}$	Load. vector for layered halfspace with sph. FEM inclusion
r, ϑ, φ	Spherical coordinates
R	Radius of the cylinder or the sphere
$\bar{S}_{zz}$	Equivalent dyn. soil stiffness for SDOF model
$\hat{\mathbf{S}}^{\mathbf{hs}}_{\mathbf{ITM}}$	Stress matrix due to unit loads for homog. halfspace
$\hat{\mathbf{S}}^{\mathbf{hs}}_{\mathbf{0_{ITM}}}$	Stress matrix due to unit loads for homog. halfspace for $\omega = 0$
$\hat{\mathbf{S}}^{\mathbf{hs\ L}_l}_{\mathbf{ITM}}$	Stress matrix due to unit loads for layered halfspace
$\hat{\mathbf{S}}^{\mathbf{hs\ L}_l}_{\mathbf{0_{ITM}}}$	Stress matrix due to unit loads for layered halfspace for $\omega = 0$
$\hat{\mathbf{S}}^{\mathbf{L}}_{\mathbf{ITM}}$	Stress matrix due to unit loads for discrete soil stratification
$\hat{\mathbf{S}}^{\mathbf{fs\ cyl}}_{\mathbf{ITM}}$	Stress matrix due to unit loads for fullspace with cyl. cavity
$\hat{\mathbf{S}}^{\mathbf{fs\ sph}}_{\mathbf{ITM}}$	Stress matrix due to unit loads for fullspace with sph. cavity
$\hat{\mathbf{S}}^{\mathbf{hs\ cyl}}_{\mathbf{ITM}}$	Stress matrix due to unit loads for halfspace with cyl. cavity
$\hat{\mathbf{S}}^{\mathbf{hs\ cyl\ tw}}_{\mathbf{ITM}}$	Stress matrix due to unit loads for halfspace with two cyl. cavities
$\hat{\mathbf{S}}^{\mathbf{hs\ sph}}_{\mathbf{ITM}}$	Stress matrix due to unit loads for halfspace with sph. cavity
t	Time coordinate
t_s, t_p	Serial- and parallel computation time
$t_{\max}$	Time of the maximum displacement
T	Time period of a signal
T	Total computation time
Tan	Tanimoto coefficient
$\mathbf{T_c}$	Transformation matrix for halfspace with cyl. cavity
$\mathbf{T_{c1}}$	Transformation matrix from polar into Cartesian coordinates
$\mathbf{T_{c2}}$	Transformation matrix for Fourier series expansion along cyl. boundary
$\mathbf{T_s}$	Transformation matrix for halfspace with sph. cavity
$\mathbf{T_{s1}}$	Transformation matrix from sph. into Cartesian coordinates
$\mathbf{T_{s2}}$	Transformation matrix for development into sph. harmonics
u_i, u^i	Co- and contravariant displacement components
$\bar{u}^i_m$	Displ. at point i in direction m due to harmonic unit concentrated load
$\bar{\mathbf{u}}_m, \bar{\mathbf{u}}_s$	Master- and slave DOFs for Guyan reduction
$\tilde{\mathbf{u}}$	Approx. displ. field of finite element
$\bar{\mathbf{u}}_\mathbf{c}$	Vector of nodal contact displ. at soil foundation-interface
$\tilde{\mathbf{u}}_\mathbf{n}$	Nodal displacements of finite element

$\bar{\mathbf{u}}_{\mathbf{s}}^{i}$	Displ. vector of point i due to harmonic unit concentrated load
$\bar{\mathbf{u}}_{\mathbf{s}}$	Displ. vector of all nodes of soil-foundation contact surface
$\bar{\mathbf{u}}_{\mathbf{s}}^{\mathbf{F_i}}$	Displ. vector of all nodes on foundation F_i
$\bar{\mathbf{u}}_{\mathbf{f}}^{\mathbf{F_n}}$	Displ. vector of FEM model of foundation F_n
$\bar{\mathbf{u}}_{\mathbf{f,r}}$	Displ. vector of several rigid foundations coupled to the soil
$\bar{\mathbf{u}}_{\mathbf{f,r}}^{\mathbf{F_n}}$	Displ. vector of rigid massless foundation F_n coupled to the soil
$\bar{\mathbf{u}}_{\mathrm{sys}}$	Displ. vector of total ITM-FEM soil-structure system
$\hat{\mathbf{u}}_{\mathbf{ITM}}^{\mathbf{hs}}$	Displ. vector of homog. halfspace
$\hat{\mathbf{u}}_{\mathbf{0_{ITM}}}^{\mathbf{hs}}$	Displ. vector of homog. halfspace for $\omega = 0$
$\hat{\mathbf{u}}_{\mathbf{ITM}}^{\mathbf{hs\ L}_l}$	Displ. vector of layered halfspace
$\hat{\mathbf{u}}_{\mathbf{0_{ITM}}}^{\mathbf{hs\ L}_l}$	Displ. vector of layered halfspace for $\omega = 0$
$\hat{\mathbf{u}}_{\mathbf{ITM}}^{\mathbf{L}}$	Displ. vector of discrete soil stratification
$\hat{\mathbf{u}}_{\mathbf{ITM}}^{\mathbf{fs\ cyl}}$	Displ. vector of fullspace with cyl. cavity
$\hat{\mathbf{u}}_{\mathbf{ITM}}^{\mathbf{fs\ sph}}$	Displ. vector of fullspace with sph. cavity
$\hat{\mathbf{u}}_{\mathbf{ITM}}^{\mathbf{hs\ cyl}}$	Displ. vector of halfspace with cyl. cavity
$\hat{\mathbf{u}}_{\mathbf{ITM}}^{\mathbf{hs\ cyl\ L}}$	Displ. vector of layered halfspace with cyl. cavity
$\hat{\mathbf{u}}_{\mathbf{ITM}}^{\mathbf{hs\ cyl\ tw}}$	Displ. vector of halfspace with two cyl. cavities
$\hat{\mathbf{u}}_{\mathbf{ITM}}^{\mathbf{hs\ sph}}$	Displ. vector of halfspace with sph. cavity
$\hat{\mathbf{u}}_{\mathbf{ITM}}^{\mathbf{hs\ sph\ L}}$	Displ. vector of layered halfspace with sph. cavity
$\tilde{\mathbf{u}}_{\mathbf{FE}}^{\mathbf{hs\ cyl}}$	Displ. vector of 2.5D FEM structure with cyl. boundary
$\bar{\mathbf{u}}_{\mathbf{FE}}^{\mathbf{hs\ sph}}$	Displ. vector of 3D FEM structure with sph. boundary
$\hat{\mathbf{u}}_{\mathbf{ITM\,FE}}^{\mathbf{hs\ cyl}}$	Displ. vector of halfspace with cyl. FEM inclusion
$\hat{\mathbf{u}}_{\mathbf{ITM\,FE}}^{\mathbf{hs\ cyl\ L\ tw}}$	Displ. vector of layered halfspace with two cyl. FEM inclusions
$\hat{\mathbf{u}}_{\mathbf{ITM\,FE}}^{\mathbf{hs\ sph}}$	Displ. vector of halfspace with sph. FEM inclusion/indentation
$\hat{\mathbf{u}}_{\mathbf{ITM\,FE}}^{\mathbf{hs\ sph\ L}}$	Displ. vector of layered halfspace with sph. FEM inclusion
$\hat{\mathbf{U}}_{\mathbf{ITM}}^{\mathbf{hs}}$	Displ. matrix due to unit loads for homog. halfspace
$\hat{\mathbf{U}}_{\mathbf{0_{ITM}}}^{\mathbf{hs}}$	Displ. matrix due to unit loads for homog. halfspace for $\omega = 0$
$\hat{\mathbf{U}}_{\mathbf{ITM}}^{\mathbf{hs\ L}_l}$	Displ. matrix due to unit loads for layered halfspace
$\hat{\mathbf{U}}_{\mathbf{0_{ITM}}}^{\mathbf{hs\ L}_l}$	Displ. matrix due to unit loads for layered halfspace for $\omega = 0$
$\hat{\mathbf{U}}_{\mathbf{ITM}}^{\mathbf{L}}$	Displ. matrix due to unit loads for soil stratification
$\hat{\mathbf{U}}_{\mathbf{ITM}}^{\mathbf{fs\ cyl}}$	Displ. matrix due to unit loads for fullspace with cyl. cavity
$\hat{\mathbf{U}}_{\mathbf{ITM}}^{\mathbf{fs\ sph}}$	Displ. matrix due to unit loads for fullspace with sph. cavity
$\hat{\mathbf{U}}_{\mathbf{ITM}}^{\mathbf{hs\ cyl}}$	Displ. matrix due to unit loads for halfspace with cyl. cavity
$\hat{\mathbf{U}}_{\mathbf{ITM}}^{\mathbf{hs\ cyl\ tw}}$	Displ. matrix due to unit loads for halfspace with two cyl. cavities
$\hat{\mathbf{U}}_{\mathbf{ITM}}^{\mathbf{hs\ sph}}$	Displ. matrix due to unit loads for halfspace with sph. cavity
v	Velocity of a moving load

v_j^e	Nodal element velocities
$\bar{\mathbf{v}}$	Nodal velocity vector
$\bar{\mathbf{v}}_\mathbf{c}$	Nodal velocity vector at soil foundation contact surface
V	Volume
w_k, w_l	Weighting factors of the Gauss points
$\tilde{x}[n]$, $\tilde{X}[k]$	Discrete Fourier transform pair
x, r, φ	Cylindrical coordinates
x, y, z	Cartesian coordinates
x_j^e, y_j^e	Nodal element coordinates
$(x_i^{F_n}, y_i^{F_n})$	Discretization points of foundation F_n
$y_{\mathrm{T_{c_i}}}$	Horizontal center distance of cyl. cavity i
$\bar{Z}_{zz}$	Equivalent dyn. soil impedance

Greek Symbols

α_i	Radiation angle of elastic waves in $x-z$ plane
α, β	Counter for different indices
α, β	Rayleigh damping coefficients
ϵ	Threshold for truncation criterion
Γ_c	Cyl. coupling surface
Γ_s	Sph. coupling surface
δW	Total virtual work
δW_e	Virtual work of the external forces
δW_i	Virtual work of the internal forces
δW_I	Virtual work of the inertia forces
Δ_{mn}^{ij}	Dimensionless foundation displacements
$\boldsymbol{\varepsilon}$	Strain vector for 2.5D FEM
η, ζ	Local element coordinates
η	Loss factor
ζ	Hysteretic damping ratio
ζ_k, η_k	Coordinates of the Gauß points
κ	Shear coefficient
λ	Lamé constant
$\Lambda_{\mathrm{f_n}}$	Contact area of foundation n
Λ_l	Horizontal surfaces of homog. and a layered halfspace

λ_1, λ_2	Exponents of the solution of homog. halfspace
λ_p, λ_s, λ_r	Wavelengths of the compressional, shear and Rayleigh wave
$\boldsymbol{\lambda}$	Eigenvector
μ	Lamé constant
ν	Poisson ratio
π	Mathematical constant
ρ	Density
$\boldsymbol{\rho}$	Density matrix
σ_j^e	Nodal element stresses
$\boldsymbol{\sigma}$	Stress vector for 2.5D FEM
$\bar{\boldsymbol{\sigma}}_{\mathbf{c}}$	Contact stress vector at soil foundation interface
$\hat{\boldsymbol{\sigma}}^{\mathbf{hs}}_{\mathbf{ITM}}$	Stress vector of homog. halfspace
$\hat{\boldsymbol{\sigma}}^{\mathbf{hs}}_{\mathbf{0_{ITM}}}$	Stress vector of homog. halfspace for $\omega = 0$
$\hat{\boldsymbol{\sigma}}^{\mathbf{hs\ L}_l}_{\mathbf{ITM}}$	Stress vector of layered halfspace
$\hat{\boldsymbol{\sigma}}^{\mathbf{hs\ L}_l}_{\mathbf{0_{ITM}}}$	Stress vector of layered halfspace for $\omega = 0$
$\hat{\boldsymbol{\sigma}}^{\mathbf{fs\ cyl}}_{\mathbf{ITM}}$	Stress vector of fullspace with cyl. cavity
$\hat{\boldsymbol{\sigma}}^{\mathbf{fs\ sph}}_{\mathbf{ITM}}$	Stress vector of fullspace with sph. cavity
$\tilde{\boldsymbol{\sigma}}_{\mathbf{k}}$	Stress vector of 2.5D FEM structure at Gauss points
$\tilde{\boldsymbol{\sigma}}_{\mathbf{n}}$	Stress vector of 2.5D FEM structure at element nodes
π	Pi
ϕ	Angle of Mach line in $x-y-$plane
Φ	Scalar Helmholtz potential
$\boldsymbol{\Psi}$	Vector Helmholtz potential
Ψ_i	Components of the vector Helmholtz potential
ψ, χ	Scalar potentials in the cyl. and sph. coordinate systems
τ	Dimensionless time
θ	Propagation angle of elastic waves w.r.t. $x-y$ plane
θ_c	Critical angle for wave impediment
ω	Angular frequency
Ω	Angular excitation frequency
Ω_{c}	Interior of cyl. FEM domain
Ω_{s}	Interior of sph. FEM domain
$\Omega_{\mathrm{f_n}}$	Interior of FEM domain of foundation F_n

Mathematical Symbols

$\circ\!\!-\!\!\bullet$	Fourier transform
$\bullet\!\!-\!\!\circ$	Inverse Fourier transform
δ	Delta-Dirac distribution
$\delta\square$	Virtual quantity
Δ	Incremental quantity
$\det(\square)$	Determinant of a parameter
$\mathrm{diag}(\square)$	Diagonal matrix
e	Eulerian number
i	Imaginary unit
$\lvert\ \rvert$	Absolute value of a parameter
$\lvert\lvert\square\rvert\rvert_2$	L_2 norm of a quantity
$\mathbf{I}$	Identity matrix
$[A]^T$	Transpose of a matrix
$[A]^H$	Complex conjugate transpose of a matrix
sign	Signum function
Γ	Gamma function
$h_n^{(1)}(x)$, $h_n^{(2)}(x)$	Sph. Hankel functions of first and second kind
$H_n^{(1)}(x)$, $H_n^{(2)}(x)$	Hankel functions of first and second kind
$\mathbf{H}(t), \bar{\mathbf{H}}(\omega)$	Heaviside function and its Fourier transform
$j_n(z)$	Sph. Bessel function
$J_n(z)$	Bessel function
$P_m^l(x)$	Associated Legendre polynomial
$\check{P}_m^l(x)$	Normalized associated Legendre polynomial
Re, Im	Real and imaginary part of complex number
$y_n(z)$	Sph. Neumann function
$Y_n(z)$	Neumann function
$Y_m^l(\vartheta, \varphi)$	Sph. harmonic of degree m and order l
$\in^{ikl}$	Permutation symbol
$\dot{\square}$	First partial derivative w.r.t. time
$\frac{\partial}{\partial x}$	Partial derivative w.r.t. coordinate x
$\square\vert_x$	Covariant derivative w.r.t. coordinate x
$\square_{,x}$	Partial derivative w.r.t. coordinate x
$\mathbf{a} * \mathbf{b}$	Convolution
$\mathbf{a} \cdot \mathbf{b}$	Dot product

Diacritical Signs

$\bar{\square}$	Value in the single Fourier transformed domain
$\tilde{\square}$	Value in the twofold Fourier transformed domain
$\hat{\square}$	Value in the threefold transformed domain
$\check{\square}$	Value in moving coordinate system
$\square^*$	Conjugate complex to a value

Acronyms

ABC	Absorbing Boundary Conditions
BEM	Boundary Element Method
CFS	Complex Frequency Shifted
CMS	Component Mode Synthesis
CPU	Central Processing Unit
CV	Control Volume
DFS	Discrete Fourier Series
DFT	Discrete Fourier Transform
DKQ	Discrete Kirchhoff Quadrilateral
DOF	Degree of Freedom
FEM	Finite Element Method
FFT	Fast Fourier Transform
FRF	Frequency Response Function
FSFI	Foundation-Soil-Foundation Interaction
GPU	Graphics Processing Unit
IFFT	Inverse Fast Fourier Transform
ITM	Integral Transform Method
IRF	Impulse Response Function
MEX	Matlab executable
MFS	Method of Fundamental Solutions
PiP	Pipe in Pipe Method
PIM	Precise Integration Method
PML	Perfectly Matched Layers
QTFLS	Quadrilateral Thin Flat Layered Shell Element
RSS	Root Sum Square

SBFEM	Scaled Boundary Finite Element Method
SDOF	Single Degree of Freedom
SEM	Spectral Element Method
SSI	Soil-Structure Interaction
SSSI	Structure-Soil-Structure Interaction
TF	Transfer Function
TLM	Thin Layer Method
WBM	Wave base method
WIB	Wave Impeding Block

Abbreviations

Alg.	Algorithm
Appx.	Appendix
Approx.	Approximately
Ch.	Chapter
Corr.	Corresponding
Cp.	Compare
Cyl.	Cylindrical
Displ.	Displacements
Dyn.	Dynamic
E.g.	For example
Eq.	Equation
Fig.	Figure
Fs	Fullspace
Homog.	Homogeneous
Hs	Halfspace
L	System of Layers
Max.	Maximum
Min.	Minimum
Ref.	Reference
Resp.	Respective
Sec.	Section
Sph.	Spherical
Tw	Twin
w.r.t.	With respect to

Units

In general, throughout this thesis, the units of the following quantities unless explicitly stated otherwise are chosen as follows:

Displacements	u_i	m
Forces	P_i	N
Frequency	f	Hz
Radial frequency	ω	$\mathrm{rad\,s^{-1}}$
Stresses	σ	$\mathrm{N\,m^{-2}}$
Velocities	c_i,v_i	$\mathrm{m\,s^{-1}}$

1 Introduction

1.1 Motivation

Since the middle of the 20th century, continuous urbanisation due to the steady demographic growth, which has led to a strong aggregation of the inner cities as well as a massive increase in construction measures and traffic volume has been observed worldwide. Consequently, in the modern urban environment, there has also been a massive increase in the occurrence and intensity of ground vibrations caused by a variety of different sources on the ground surface or within the soil. Earthquakes, the passage of vehicles on uneven roads or tracks, as well as the operation of heavy machinery or wind induced building vibrations, generate elastodynamic waves that are transmitted through the ground and cause disturbances in adjacent structures, leading amongst others to malfunction of sensitive equipment, annoyance of residents by structure borne vibrations and re-radiated sound or even fatigue problems.

In many existing models for the investigation of the dynamic Soil-Structure-Interaction (SSI), only the response of individual isolated structures on or embedded in the soil is considered, and the soil is idealised as an infinite homogeneous medium. However, it has been shown that the soil composition as well as the presence of local geological inhomogeneities has a significant influence on the dynamic system response, as they can lead to amplification effects due to reflection, refraction and scattering phenomena at the material transition surfaces. Furthermore, the interference of the introduced elastic waves with other surface or underground structures located in the immediate vicinity, such as a group of adjacent buildings, an underground tunnel beneath a building or a twin tunnel system, can lead to a considerable gain in the resulting structural and ground vibrations. Considering the dynamic behaviour of a high-speed railway line, the interaction of the track with the underlying soil can lead to very large soil displacements and track deformations if travel speeds are in the range of the propagation velocity of the surface waves of a soft upper layer. In all these cases, the inclusion of the dynamic Structure-Soil-Structure-Interaction (SSSI) is indispensable, as neglecting these effects leads to an estimation of the displacement and stress amplitudes on the unsafe side. Nonetheless, it is important to notice that the SSSI can also have a beneficial effect on the soil vibrations and the oscillations of the involved structures and

a general deduction of the effect of the dynamic interaction is only possible for idealized cases.

Therefore, adequate approaches for the prediction of the environmental and structural vibrations are required which allow on the one hand the detailed modelling of the complex geometries and material properties of the considered structures and on the other hand the infinite extension of the surrounding soil exhibiting different compositions and satisfying the radiation condition. In addition, the approaches need to be able to capture different types of loading w.r.t. to their distribution and time dependence. Often, the occurring loads can be represented by means of stationary harmonic loads that exhibit a certain frequency or a limited frequency spectrum, as it is e.g. the case in the context of machine foundations. Here, a frequency domain analysis provides a very good insight into the response characteristics of the system and allows to compute the design relevant quantities. However, in case of transient processes such as suddenly applied, impact and pulse loads or random time varying loads as e.g. wind or earthquake, an analysis in the time domain allows a better understanding of the emerging effects. The same applies to moving loads which are mainly encountered in rail or road traffic applications.

Since analytical methods are generally only applicable for highly idealized systems, different coupled approaches are mostly used in the literature. Thereby, the system is divided into substructures with different characteristics allowing to take advantage of the individual strengths of the different methods in order to achieve the best conceivable approximation of the real system behaviour. Therewith, the SSSI can be modelled on a high level of complexity, simultaneously allowing to perform a large spectrum of investigations and thus to gain insight into the physical behaviour of the systems, their wave propagation characteristics and the corresponding energy distribution. It is possible to identify important system parameters already at an early stage and the sensitivity of the system response to a change in these can be evaluated numerically, permitting an optimisation of the final design. Moreover, the effect of the insertion of additional structures on already existing buildings can be assessed in advance and, if necessary, the effectiveness of different vibration mitigation measures can be evaluated.

1.2 Literature review

Before the contents of this thesis are described in detail in Sec. 1.3, an overview of the different analytical and numerical frequency and time domain methods proposed in the literature is given. Contributions dealing with elastodynamic wave propagation, dynamic soil-structure

interaction or cross-interaction between several structures through the common linear-elastic environment, ground vibrations originating from traffic systems, diffraction and scattering by obstacles in the soil, etc. are considered. Thereby, a distinction is made not by the applied methods, considered systems or load scenarios, but by the different types of interfaces where the load is applied or the structures are coupled to the unbounded linear-elastic environment, as this reconciles very well with the different systems and problem types investigated later in this thesis.

Sec. 1.2.1 covers analytical solutions for fundamental elastodynamic systems with finite harmonic and transient loads applied directly on or inside the soil. Furthermore, methods to investigate the interaction of single or multiple surface or embedded structures, coupled through the underlying soil, are presented together with approaches treating the effect of spatially embedded inclusions on the elastic wave propagation. In contrast, Sec. 1.2.2 deals with the interaction of structures with unbounded interface to the surrounding soil and the resulting vibrations. Both, 2D and 2.5D approaches, capable of representing length-invariant structures, are considered. The focus is on methods for the investigation of ground borne vibrations and oscillations in adjacent structures resulting from rail and road traffic on the ground surface or in tunnels, as well as on vibration mitigation measures at the source or in the transmission path. Eventually in Sec. 1.2.3, some closed form solutions addressing the physical phenomena due to moving loads on infinite elastic media are presented. Moreover, methods analysing the interaction of moving vehicles with the supporting infrastructure and the underlying or surrounding soil as well as the resulting track and ground vibrations are pointed out.

1.2.1 Interaction on single or multiple bounded interfaces

Fundamental solutions in elastodynamics

"A fundamental solution is an analytical expression for the response anywhere in a solid elicited by a static or dynamic point source at some arbitrary location. Such expressions can be thought of as influence functions and can be used as tools to construct other more complex solutions" [1]. Thus they form the basis of a large part of the today available sophisticated methods, dealing with complex SSI and SSSI problems.

The problem of loads on or within an infinite or semi-infinite elastic medium was firstly addressed by Lamé, Clapeyron and Lord Kelvin, who presented a fundamental solution for the static point load inside an infinite solid. Subsequently, Boussinesq [2] gave a solution for a vertical point load on the surface of an elastic halfspace and Cerruti [3] deduced an

approach to treat the response of an elastic solid due to prescribed tractions or displacements on a defined surface and thus formed the basis for modern boundary value problems. The first fundamental solution for a time harmonic concentrated load within an infinite elastic medium was given by Stokes [4]. Thereafter, an analytical solution for the response of an elastic halfspace due to a suddenly applied load on the ground surface was presented in Lamb [5], which gave rise to a series of papers [6–8] dealing with normal, tangential or torsional dynamic loads on the halfspace surface, applying integral transform methods and the Cagniard-de Hoop technique [9, 10] for the inverse transform. Closed form solutions for the transient response of an elastic halfspace due to an uniformly distributed strip load and a rectangular block load were presented in Mitra [11] and Guan and Novak [12]. Semi-analytical approaches for distributed loads on homogeneous and layered soils were introduced in [13–16]. A detailed overview of various other fundamental solutions or Green's functions for two- and three-dimensional elastodynamic problems is given in [1] and a comprehensive compendium of these is published in Kausel [17]. Furthermore, collections of analytical solutions for different canonical problems are gathered e.g. in Eringen and Suhubi [18] and Achenbach [19].

Soil structure interaction (SSI)

The origin for the development of a variety of methods treating the dynamic Soil-Structure-Interaction is the publication of Reissner [20], who dealt with the time harmonic response of a circular plate with frictionless contact to the halfspace surface assuming an uniform stress distribution at the interface. Bycroft [21] presented an approximate solution for the frequency dependent impedances of a rigid circular plate attached to the surface of a semi-infinite elastic solid or stratum, while compliance functions for rectangular foundations were derived in Thomson and Kobori [22]. The first closed form solutions solving the mixed boundary value problem were provided by Veletsos and Wei [23], Luco and Westmann [24] for rigid circular plates and Luco and Westmann [25] for rigid strip footings resting on an elastic halfspace. Impedance functions for this kind of foundations located on the surface of a layered soil or an elastic stratum were given by Luco [26] and Gazetas [27].

With increasing computational capacities, numerical methods moved more and more into the centre of research, as they made it possible to treat also foundations with arbitrary shapes and limited flexural rigidity, that may be located on or embedded in a possibly inhomogeneous soil, in contrast to the purely analytical methods which were usually afflicted with strong simplifications and assumptions.

One widely used tool in this context is the Finite-Element-Method (FEM) which allows a detailed modelling of complicated geometries and loads as well as different material properties.

However, in order to sufficiently consider the radiation damping of an infinite soil, rather large domains need to be discretized leading to a significant computational effort. Therefore, a couple of computational methods have been developed in order to minimize spurious reflections of waves at the artificial boundaries of the FEM domain and thus allowing the radiation of the elastodynamic waves to infinity.

One possibility is the coupling of infinite elements to the FEM domain, using decaying shape functions to model the attenuation of the waves travelling to infinity. Bettess [28] developed infinite elements with exponentially decaying Lagrange polynomials as shape functions, whereas Kazakov [29] used modified Bessel functions. An infinite element based on the mapping of a semi-infinite strip onto the finite element domain was presented by Zienkiewicz et al. [30], whereas Yang et al. [31] introduced a frequency independent infinite element for semi infinite problems. Alternatively different Absorbing Boundary Conditions (ABC), only allowing a wave propagation out of the modelled region, could be applied [32, 33]. Higher order ABCs were presented by Collino et al. [34] and Rabinovich et al. [35], enhanced for long time stability in [36]. Furthermore, Perfectly Matched Layers (PML), adjoint as additional surrounding layer which avoid any reflection at the interface and attenuates all waves within the layer exponentially by means of a complex coordinate stretching [37–39], are often used. Kausel and de Oliveira Barbosa [40] developed a PML formulation based on the application of the weighted residual method, in which the stretching functions are directly applied in the mass and stiffness matrices of a conventional FEM approach. Fathi et al. [41] derived a three dimensional time domain PML formulation, used in Papadopoulos et al. [42] to investigate the influence of uncertain local subsoil conditions on the response of buildings to ground vibration. In Fontara et al. [43] recommendations for a proper selection of the PML parameters were given and a FEM-PML approach, implemented as macro element in a commercial FEM software, was used to determine the dynamic flexibility functions of a rigid foundation embedded in a layered halfspace. In addition, the Thin Layer Method (TLM), can be used in combination with the FEM to model the infinite extension of the soil in horizontal direction. It was firstly introduced by Lysmer and Kuhlemeyer [44] and Waas [45] who discretized the soil layers with linear shape functions in vertical direction and applied analytical frequency domain solutions for the horizontal direction. Later on TLM formulations were derived in [46, 47], to obtain Green's functions for harmonic and impulsive sources in laminated media. Park [48] enhanced the TLM formulation for application to semi-infinite and infinite multilayered media and expanded it to cylindrical and spherical coordinate systems. Schepers and Kausel [49] showed a method to increase the accuracy of the Green's functions for layered media, obtained with the TLM, and de Oliveira Barbosa et al. [50] combined the TLM with the PML to achieve more accurate results for a layered halfspace subjected to arbitrary dynamic sources.

Alternatively, rigorous methods with non-local boundary conditions can be applied using analytical solutions that implicitly fulfill the radiation condition. They allow to treat the infinite extent with high accuracy and at the same time minimal modelling and computational effort [51]. The 3D dynamic SSI of harmonically loaded rigid, massless foundations of arbitrary shape, was firstly investigated in [52–55]. They obtained the frequency dependent foundation compliances by imposing the rigid body kinematic conditions on the dynamic soil stiffness, determined by discretizing the soil foundation contact area into a number of subregions assuming uniform contact tractions and applying the Green's functions for the homogenous or layered halfspace. A frequency domain Boundary Element Method (BEM), limiting the discretization to the soil foundation interface and thus reducing the size of the problem by one, was used in [56–58] to investigate the SSI of rigid rectangular foundations at the surface or embedded in a halfspace and to compute the corresponding dynamic impedance functions.

However, the most common approach to account for SSI problems is to couple different methods, using analytical solutions obtained e.g. with the BEM to represent the unbounded soil and model the structure by means of the FEM. Coupled frequency domain FEM-BEM approaches were used in [59–62] to investigate the SSI of arbitrarily shaped finite plates with limited flexural rigidity, providing compliance functions at characteristic points of the foundation and highlighting the influence of the mass and stiffness ratios of the structure and the soil on the dynamic system response. Following, a whole series of different coupled 3D FEM-BEM formulations in the time domain was published, dealing with the dynamic interaction of three dimensional structures and different underlying soils due to transient external loads or seismic motions. Thereby, the direct time domain solutions constitute the basis for an extension to non-linear soil-structure interaction problems, which is not feasible with frequency domain methods. Karabalis [63, 64] investigated the response of flexible surface foundations to vertical and horizontal impulse loads, applying a step-by-step integration in time assuming the tractions and displacements to be constant over a time interval as well as each boundary element. In contrast Ahmad and Banerjee [65] used higher order shape functions w.r.t. space and time to approximate the stresses and displacements and applied a time stepping in conjunction with a time domain BEM formulation based on Stoke's fundamental solution. The transient SSI of 3D structures on a homogeneous halfspace was addressed in [66–69], employing halfspace Green's functions for surface point loads with Heaviside time dependence. This allows to limit the spatial discretization only to the contact area between the foundation and the ground, since the zero stress boundary condition on the soil surface is inherently satisfied. Rizos and Wang [70] utilized the B-spline impulse response function of a homogeneous halfspace, obtained by an adapted BEM formulation in combination with a Newmark-β time integration, to account for the transient SSI response of

structures on the soil surface. A FEM-BEM formulation based on halfspace Green's functions was also used in Galvín and Romero [71] to analyse the transient response of multi-storey buildings due to earthquake loading.

Another approach, used together with the FEM to analyse SSI problems and satisfying the radiation condition exactly, is the Scaled Boundary Finite Element Method (SBFEM). The approach was firstly derived by Wolf and Song [72–74] in the frequency domain. Thereby only the boundary of the infinite medium is discretized with doubly-curved finite surface elements, resulting in an ordinary differential equation w.r.t. radial direction, originating in a scaling center that can be solved analytically. Thus no fundamental solution is necessary and no singular integrals need to be evaluated [72]. Later on it was expanded also to the time domain, wherefore a discretization of the SBFEM equations in unit-impulse response matrices is required and the transient solution is finally computed by a convolution integral [75]. In Yann et al. [76] a coupled 3D FEM-SBFEM approach in the time domain was used to analyse the three dimensional SSI of a massless square plate on a homogeneous halfspace. Schauer et al. [77] presented a parallelized algorithm to tackle large scale SSI problems and introduced a technique for the coupling of non-matching meshes at the near-field far-field interface, allowing different discretizations for the subdomains and thus an optimized meshing with lower computational costs. Birk and Behnke [78] presented a modified FEM-SBFEM formulation using a scaling line instead of a scaling center and applied it to study the SSI of rigid surface and embedded foundations with a horizontally layered soil. Han et al. [79] expanded the formulation by a mixed variable algorithm to investigate transient SSI processes. In contrast, Aslmand et al. [80] adapted it, introducing an axisymmetric geometry of the far field using cylindrical coordinates and expressing the quantities on the circumferential direction by means of a Fourier series. The resulting coupled FEM-SBFEM approach was then applied to analyse the transient response of arbitrarily shaped flexible surface foundations.

Another possibility for the exact description of the infinite extension of the soil is provided by the Integral Transform Method (ITM). It can be used to derive analytical solutions for different fundamental systems, which can then be coupled with other methods suitable for the detailed description of structures in order to investigate the dynamic soil structure interaction. Müller [81] presented a solution for a homogeneous or layered halfspace coupled with a beam, using a mixed boundary value formulation. A coupling of the ITM and the FEM is introduced in Zirwas [82] for a 2D case and expanded by Rastandi [83] for a 3D system. However, loads could only be applied inside the FEM domain which is restricted to a limited embedment depth from the halfspace surface [84]. In Freisinger et al. [84] a coupled ITM-FEM approach to investigate the 3D SSI of a rigid or flexible plate at the ground surface

or embedded in the homogeneous soil due to time harmonic loads was presented. In contrast Radišić [85–87] coupled the Spectral Element Method (SEM) to the ITM to analyse the interaction of a single or multiple foundations on the halfspace or a soil layer over bedrock.

Furthermore, some methods dealing with the dynamic SSI on inhomogeneous or anisotropic soils were published. Vrettos [88] derived analytical influence functions for a soil considering a varying soil stiffness with increasing depth and determined frequency-dependent stiffness and damping coefficients for rigid surface foundations on the latter. In Chen [89], this method was extended to flexible foundations modelled with the FEM and used to determine the harmonic and transient foundation responses. An energy method was used in Katebi and Selvadurai [90] to analyse the SSI of a flexible circular plate on an incompressible elastic halfspace with an elastic shear modulus varying exponentially with depth. Lin et al. [91] proposed a hybrid approach based on a precise integration algorithm and a mixed variable formulation to cope with the dynamic SSI of a rigid square footing on anisotropic stratified soil. Impedance functions for rigid massless foundations, embedded in an arbitrarily heterogeneous halfspace, computed by means of a coupled FEM-PML approach were presented in Esmaeilzadeh Seylabi et al. [92]. Moreover, a FEM-PML approach was applied in [93, 94] to investigate the modal characteristics of structures considering the dynamic SSI of 2D and 3D frame structures on and within the soil.

Structure Soil Structure Interaction (SSSI)

Since structures in practical issues are often not well separated from each other, also their mutual interaction has a significant effect on their dynamic behaviour and needs to be taken into account. In literature, various approaches have been employed to investigate the interaction of foundations located on or embedded in a homogeneous or layered halfspace. Warburton et al. [95] were the first to study the dynamic Foundation-Soil-Foundation Interaction (FSFI) of two neighbouring massive foundations, resting on a homogeneous halfspace, applying an approximate analytical method based on the Bycroft model. The cross interaction of multi-foundation systems, located on a viscoelastic stratum, due to different excitation types has been investigated by Kobori et al. [96]. Wong and Luco [97] analysed the effect of a layered halfspace on the interaction of two rigid, square surface foundations subjected to external forces by the boundary integral equation technique. Kausel et al. [98] and Lin et al. [99] used the FEM together with consistent boundaries to examine the FSFI of rigid foundations resting on or embedded in a stratum over bedrock for a harmonic force and moment excitation in all degrees of freedom [100]. An analytical method addressing the dynamic subsoil coupling between a finite number of rigid, rectangular foundations solving

the mixed boundary value problem by the Bubnov-Galerkin method has been presented by Triantafyllidis and Prange [101].

A frequency domain BEM based on quadratic elements and halfspace Green's functions to investigate the 3D FSFI of two adjacent, massless rigid foundations on homogeneous soil due to harmonic external and seismic loads was presented in [64, 102] and [103], while Karabalis and Mohammadi [104] considered the FSFI on a layered halfspace and gave compliance functions depending on the dimensionless frequency. Karabalis and Huang [105] and Huang [106] employed a time domain BEM to investigate the cross interaction of several massive foundations on a homogeneous soil. A coupled FEM-BEM approach for the 3D dynamic interaction of two surface foundations was presented by Mohammadi and Karabalis [107] in the frequency domain and in Rizos and Wang [70] and Aji et al. [108] in the time domain. Sbartai [109] coupled the BEM to the TLM to account for the interaction of two embedded, rigid 3D foundations within a layered soil over bedrock. A Precise Integration Method (PIM) was used by Han et al. [110] to analyse the FSFI of a group of adjacent massless and massive 3D foundations on multilayered ground. Radisic [85] used the ITM together with kinematic conditions for the deformation of a rigid foundation to investigate the mutual influence of adjacent foundations. In Bybordiani and Arici [111] a FEM-PML approach was used to account for the interaction of adjacent buildings subjected to seismic loading.

In addition to the interaction of buildings or their foundations, the mutual influence of structures on the surface with spatially limited inclusions in the soil is also part of the SSSI's scope of application. Initially Chouw et al. [112] investigated the vibration propagation in a soil layer over bedrock and found that no wave propagation occurs in there, if the excitation frequency is below the first eigenfrequency of the layer. This effect was used in Chouw and Schmid [113] where a spatially limited Wave Impeding Block (WIB) was implemented into the soil in order to mitigate the low frequency vibration transmission, induced by the active of two foundations and thus to reduce the dynamic response of the passive foundation. A 3D BEM frequency domain approach was used by Antes and von Estorff [114] to study the influence of the stiffness of a finite block shaped elastic inclusion within a homogenous halfspace on the dynamic response of an elastic surface foundation. The effectivity of a buried honeycomb structure, acting as an wave impeding barrier, was investigated in Takemiya [115] by means of a 3D FEM simulation. Gao et al. [116] derived a 3D BEM, based on Green's functions derived with the TLM, which allows to analyse the SSSI of a surface foundation with a WIB in a saturated stratified soil and to assess the screening efficiency of the WIB.[100]

1.2.2 Interaction on unbounded interface

Besides three dimensional structures with a bounded interaction surface to the infinite surrounding medium, also a large amount of papers has been published dealing with the SSI resp. SSSI of length invariant structures like tunnels, rail or road tracks, strip foundations, vibration isolation screens, pipelines or dams. Thereby, firstly 2D approaches assuming a plane strain condition were used which, apart from the structure, also only allowed the inclusion of longitudinally invariant loads or incident wave fields [117]. Thus later on 2.5D models, enabling a modelling of spatially bounded loads in conjunction with length invariant structural geometries as well as periodic approaches, were developed.

SSI and SSSI of strip footings

One of the first papers dealing with the two dimensional dynamic SSI of rigid strip foundations on homogeneous and layered soil were published by Luco and Westmann [25] and Gazetas and Roesset [118], providing semi-analytical expressions for the frequency dependent foundation compliances. Spyrakos and Beskos [119] and Antes and von Estorff [120] applied pure BEM formulations in the time and frequency domain to compute the response of a rigid massless strip foundation, while in [121, 122] a coupled time domain FEM-BEM approach is used. A comprehensive overview of the compliance functions for different foundation shapes and system setups is given in [123, 124]. The cross interaction of several flexible strip foundations on or embedded in a homogeneous halfspace was addressed in [125] by means of BEM whereas [126] uses a 2D coupled FEM-BEM approach for the same problem. A FEM-SBFEM method was utilized in [75, 127] studying the transient response of two strip foundation subjected to a triangular pulse. Genes [128] applied a coupled FEM-BEM-SBFEM approach to determine the compliances of a rigid strip foundation on a layered halfspace. A coupled ITM-SEM method was used in [129] to compute the dynamic response of rigid and flexible strip foundations on a viscoelastic soil.

Ground borne vibrations

Firstly, the SSI of large underground structures and the resulting ground borne vibrations was investigated by means of 2D [121] and 3D [130, 131] coupled FEM-BEM approaches or pure 3D BEM [132]. To reduce the computational effort linked with full three dimensional models, for periodic structures a Floquet transform of the longitudinal coordinate can be applied, allowing to represent the 3D response on a single bounded reference mesh [133]. Within the unit cell, the tunnel cross section is modelled by the FEM whereas the surrounding soil is accounted for by the BEM. These periodic models were used in [134–139]

to compute the ground-borne vibrations due to a dynamic loading of underground railway tunnels embedded in homogeneous or stratified media and to identify the influence of tunnel and soil parameters on the system response. Germonpré et al. [140] employed a periodic model for the prediction of the soil vibrations due to a parametric excitation on a surface railway track.

In case of arbitrary length invariant structures, usually 2.5D models are applied which allow to reduce the originally 3D computations to a series of 2D calculations for each wavenumber in longitudinal direction. Sheng et al. [141, 142] used a 2.5D FEM-BEM approach to predict the surface vibrations due to a track located on an embankment as well as a dynamic load within an underground tunnel in a homogeneous soil. The interaction between different longitudinally invariant structures and a stratified soil was investigated in François et al. [143] and Galvín et al. [144] who use a regularized 2.5D boundary integral equation, avoiding the evaluation of singular traction integrals, in conjunction with 2.5D Green's functions for the layered halfspace. Coulier et al. [145] applied a spatial windowing technique within the latter, enabling to consider finite lengths of the structures, thereby maintaining the computational efficiency of the 2.5D model. A validation of the numerical results of different 2.5D FEM-BEM approaches by measurement data has been published in Jin et al. [146] and Kuo et al. [147]. Coulier et al. [145] applied a 2.5D FEM-BEM approach for the investigation of the dynamic interaction between a four storey building and a railway tunnel as well as a railway track on the ground surface which is used in [148] to derive coupling loss factors for buildings subjected to railway induced vibrations. The SSI of a tunnel embedded in a poroelastic halfspace was investigated in [149].

Lombaert et al. [150] presented a model employing a boundary element method for the soil and an analytical beam model for the road to model the traffic induced free field vibrations, which was validated by in situ experiments in [151]. Galvín et al. [152] presented a methodology to determine the free field vibrations due to railway traffic by modulating the soil Green's function by a correction factor for the track soil interaction, obtained using a neural network, and combining them with the loads resulting from the train track interaction. An analytical model for the ground borne vibrations due to the dynamic loading of a tunnel embedded in a layered halfspace was deduced in [153] while a 2.5D FEM-BEM approach in combination with the Method of Fundamental Solutions (MFS) is used in [154].

The invariance of the soil structure system is also used in the Pipe-in-Pipe Method (PiP). Forrest and Hunt [155, 156] presented this semi-analytical method where the tunnel is modelled in the transformed domain with a circular shell while the soil is described by the analytical solution of the fullspace with circular cavity. In Gupta et al. [137] the results

of the PiP calculation were used for the validation of a coupled FEM-BEM approach, as it leads to the exact solution of the problem. Hussein et al. [157] introduced a horizontal plane, representing a halfspace surface in the system and in [158] extended it also for the computation of ground borne vibrations from a tunnel in a multilayered soil. For the introduction of the halfspace surface, they assumed that the near-field displacements of the tunnel surface are not influenced by the existence of the halfspace surface. [84]

Also the ITM provides exact solutions for fundamental soil systems which are superposed to derive a semi-analytical solution for a halfspace with cylindrical cavity in [159, 160] and were coupled with the FEM by Müller et al. [161]. The resulting 2.5D ITM-FEM approach was used to investigate the soil vibrations induced by traffic loads in an underground tunnel, while Hackenberg [162] applied the approach to compute the insertion loss for the surface vibrations due to a floating slab track inside the tunnel in case of a harmonic load.

Twin tunnels

The dynamic interaction of two parallel tunnels with circular cross-section embedded in a homogeneous fullspace was investigated by Kuo et al. [163]. In the model the SSSI is accounted for by superposing the solution for a single-tunnel model, originally derived in [155, 164], and used to calculate the ground borne vibrations due to dynamic train forces. A similar approach was presented in [165], addressing the interaction of neighbouring tunnels in a homogenous halfspace. The tunnel was modelled with a thick shell theory while the surrounding soil was modelled by the BEM. He et al. [133] provided an analytical model to predict the ground vibrations from two parallel tunnels embedded in a fullspace wherein the tunnels are modelled by length invariant cylindrical shells and are coupled to a fullspace including two cylindrical cavities. A 2.5D FEM-BEM model was used by Romero et al. [166] to investigate the scattered wave field due to the SSSI of two adjacent tunnels while He et al. [167] proposed a semi-analytical 2.5D model to account for the interaction of twin tunnels in a multilayered halfspace.

Vibration mitigation measures

Furthermore, a comprehensive amount of studies on vibration mitigation measures can be found in literature. First field tests on the screening effect of rectangular open and bentonite filled trenches were conducted by Dolling [168] and further measurements were performed by Woods [169]. Numerical studies, investigating the amplitude reduction of Rayleigh waves by open or concrete filled trenches using a 2D FEM in the frequency domain, were presented by Segol et al. [170] and Haupt [171]. Later, the BEM was employed in [172, 173] to investigate

the efficiency of open and infilled length invariant trenches within a homogeneous halfspace, while in [174] a layered halfspace was considered. Ahmad and Al-Hussaini [175] performed an extensive parametric study on the effects of the dimensions and the filling material of trenches and barriers, situated in a homogeneous as well as a layered soil [176].

To be able to include more complex barrier and source compositions, still satisfying the radiation condition, different FEM-BEM formulations were developed. In [177, 178] a 2D FEM-BEM approach was used to analyse mitigation measures aiming on the reduction of ground vibrations induced by moving loads. A coupled 2.5D FEM-BEM approach was applied by Coulier et al. [179] to investigate the effect of subgrade stiffening next to the track, in François et al. [143] and Thompson et al. [180] for open and soft filled trenches and in Coulier et al. [181] for stiff wave barriers. Furthermore, François et al. [182] used the same approach to analyse the efficiency of a composite vibration isolating screen and validated the results by in situ tests. The mitigation of railway induced ground vibrations by heavy masses next to the track was studied in [183] using a 2.5D FEM-BEM approach and in [184] by a 3D FEM with absorbing viscous boundaries. The efficiency of continuous floating slabs to reduce ground borne vibrations from railway traffic was assessed in [185], applying the 3D numerical model presented in [150]. Dijckmans et al. [186] investigated the vibration isolation efficiency of a sheet pile wall by means of numerical simulations with a 2.5D FEM-BEM approach and compare their results with measurement data. The efficiency of finite and infinite open trenches and infilled barriers was investigated in Freisinger and Müller [176] by means of a 2.5D ITM-FEM approach. In contrast, a 2.5D displacement based FEM-PML model was used in François et al. [187] to determine the efficiency of a vibration isolating screen. François et al. [188] derived a Complex Frequency Shifted (CFS)-PML formulation accounting for transient elastic wave propagation, thereby avoiding a convolutional formulation and allowing an easy incorporation into existing FEM code due to its description by mass, damping, and stiffness element matrices. A comprehensive overview on the excitation mechanisms, different prediction methods and mitigation measures can be found in Coulier et al. [189], Lombaert et al. [190] and Thompson et al. [191].

Earthquake engineering and geophysics

Moreover, the effect of buried structures on the propagation of elastic waves is of great importance, as due to diffraction and scattering of these at the structures additional waves arise, possibly leading to an amplification of the initial vibrations and thus significantly influencing both the distribution and the amplitude of the stresses and displacements near the surface and in adjacent structures [51]. Datta et al. [192] showed an exact three dimensional analysis for a long continuous pipeline in a halfspace by coupling the governing equations for the elastic medium with a shell model. Wong and Luco [193] analysed a tunnel with a

non circular cross section by using the FEM to model the tunnel and the soil in its immediate vicinity, combined with an analytical solution for the infinite soil deploying cylindrical eigenfunctions. The seismic response of a cylindrical shell embedded in a layered halfspace, subjected to plane waves striking at slanting angle was studied in [194, 195]. They combined an indirect integral representation, using moving Green's functions, for the exterior domain with the Donnell shell theory for the pipeline. Lin et al. [196] presented a formulation of the boundary value problem for a tunnel with circular cross section in an elastic halfspace, in which the scattered cylindrical waves are represented by Hankel functions in integral form in Cartesian coordinates, such that the zero stress boundary condition at the halfspace surface is satisfied exactly. Both, primary and secondary reflected waves at the ground surface were considered in the solution. The scattering of harmonic P, SV and Rayleigh waves by a shallow lined, circular tunnel using the image technique and complex variables, was studied by Liu et al. [197]. In Zhao et al. [198] a semi-analytical method, treating the three dimensional scattering of elastic waves by a infinitely long tunnel in a halfspace, was proposed. Furthermore, the contributions of the directly scattered field (at the tunnel) and the secondary scattered field (at the ground surface) on the dynamic response of the system at the halfspace surface and the interface between tunnel and soil were evaluated.

1.2.3 Interaction on moving interface

The modelling of ground borne vibration due to moving loads is essential for the understanding of the physical phenomena linked with it, especially if the propagation velocity approaches or exceeds the wave velocities of the underlying soil. A wide range of articles was published between 1950 and 1970 presenting closed form solutions for loads with constant amplitude moving along the surface of a semi-infinite elastic medium [199–203]. Therein especially the change in the dynamic response for transonic and supersonic load speeds was highlighted, leading to the formation of a shock wave and propagating waves behind the current position of the load. A load moving with constant velocity after a sudden application was treated in [204, 205]. Frýba [206] studied the response of moving loads with constant and harmonically oscillating amplitude on beam structures as well as on an elastic halfspace for different load distributions. A closed form solution for a moving point load on a hysteretically damped elastic halfspace was presented in Verruijt and Córdova [207]. Kaplunov et al. [208] deduced an approximate solution in terms of elementary functions which, however, is only valid in the near-field of a point force moving approximately with the Rayleigh wave velocity.

Numerical methods were required to determine also the dynamic response of more complex systems subjected to arbitrarily distributed moving loads. Various wavenumber frequency

domain methods were developed together with a numerical inverse Fourier transform and used, e.g. in de Barros and Luco [209] to calculate the response of a homogeneous halfspace due to a moving point load and in [210] due to a moving harmonic rectangular load. The ground vibrations in a layered soil due to a moving line load were analysed in de Barros and Luco [211]. Grundmann et al. [212] used a similar technique to predict the response of a homogeneous halfspace subjected to traffic loads. Bian and Chen [213] developed an explicit time domain solution, based on the TLM to compute the response of a soil stratum due to a harmonic moving load, while Galvín and Domínguez [214] applied a 3D time domain BEM for the analysis of the soil vibrations induced by high-speed moving loads.

The dynamic interaction between train, track and the elastic underground has been addressed by Dieterman et al. [215] who introduced the concept of replacing the halfspace by an equivalent stiffness combined with the differential equation of the beam to determine the critical velocities of a constant load moving along it. The same approach was used in [216, 217], applying the ITM for the computation of the equivalent halfspace stiffness. In Grundmann and Lenz [218], the interaction of a vehicle, modelled as a 5 DOF system, moving over the randomly uneven surface of a slab track on elastic subsoil was investigated while Metrikine et al. [219] studied the stability of a two-mass oscillator moving along a beam supported by a halfspace. Madshus and Kaynia [220] described the dynamic behaviour of a high-speed railway line on soft ground at critical speed and developed a numerical approach based on Green's functions for the layered halfspace, coupled with a beam modelled by the FEM. Sheng et al. [221, 222] derived a dynamic flexibility matrix for the layered halfspace in the wavenumber frequency domain and coupled it with the Fourier transformed equations for a layered beam system representing the track to compute the total system response to moving loads. A 3D periodic model for the simulation of vibrations induced by high-speed trains based on the Floquet transform was presented in [223], whereas the SSI of a periodically supported beam under a moving load was treated in Lu et al. [224], applying springs with frequency dependent equivalent stiffness at the sleepers taking into account the phase shift of the vibrations of neighbouring supports.

Also the ground borne vibrations due to railway traffic and moving loads in underground tunnels attained a lot of attention within the last decades. Gupta et al. [225] presented a numerical periodic FEM-BEM model to predict the free field vibrations due to dynamic moving loads in a subway tunnel together with an experimental validation. A 2.5D finite/infinite element approach was introduced in Yang and Hung [226] to simulate the soil vibrations due to moving trains in an underground tunnel, whereas Bian et al. [227] employed a 2.5D FEM with a gradually damped artificial boundary. Yuan et al. [228] showed a closed form semi-analytical solution for a moving point source in a tunnel embedded in a halfspace,

wherein the tunnel is modelled as hollow cylinder surrounded by an elastic continuum. The total wave field is decomposed in cylindrical outgoing waves and downwards travelling plane waves, which are forced to satisfy the boundary conditions at the ground surface and the tunnel soil interface, quite similar to the methodology used in the 2.5D ITM-FEM approach presented in [84] which also allows to determine the response to moving loads within a tunnel embedded in the halfspace. A curved 2.5D FEM was proposed in Ma et al. [229] to model the tunnel-soil system including an appropriate artificial boundary and combined with a 2.5D analytical method considering the motions of the rail in order to account for the vibrations of a track-tunnel-soil system in a curved section subjected to moving loads.

1.3 Outline of the thesis

In this thesis the coupled ITM-FEM approach, originally developed in [162, 230], is significantly extended as well as optimized with regard to computational efficiency in order to allow the treatment of a wide range of the issues and demands related to the dynamic SSSI of different surface and subsurface structures resting on or embedded in a homogeneous, layered or inhomogeneous soil, addressed in Sec. 1.1. Applying a domain decomposition approach, the overall system is divided into suitable ITM and FEM substructures and complex stiffness matrices, completely describing the dynamic behaviour of the respective substructures, are derived separately before they are coupled at the common interaction surfaces.

For this purpose in Ch. 2, firstly the ITM is applied to obtain analytical solutions for various fundamental systems from the basic elastodynamic equations (Sec. 2.1), such as a homogeneous (Sec. 2.2) or layered halfspace (Sec. 2.3), a discrete soil stratification (Sec. 2.4) as well as a fullspace with cylindrical (Sec. 2.5) or spherical cavity (Sec. 2.6). The solutions of the resulting wave equations are each described w.r.t. the most suitable reference system and the unknown wave amplitudes can be solved, imposing the respective boundary conditions of the system. Subsequently in Ch. 3, these fundamental solutions are superposed and coupled in order to deduce semi-analytical solutions for more complex systems like a halfspace with one (Sec. 3.1) or two (Sec. 3.2) cylindrical cavities or indentations, a halfspace with spherical cavity (Sec. 3.3) or a layered halfspace with cylindrical or spherical cavity (Sec. 3.4). Thereby, dynamic stiffness representations are deduced for each of the ITM substructures, providing a direct relation between the stresses applied at the boundaries of the overall system and the resulting displacements. Lastly, some notes on computational and numerical aspects within the implementation as well as truncation criteria for the discrete Fourier series and

error measures for the similarity assessment of the results with literature solutions are given (Sec. 3.5).

In Ch. 4, element stiffness formulations for a quadrilateral 2.5D finite element (Sec. 4.1), used to model length invariant structures or geometries, as well as different 3D elements (Sec. 4.2) for the description of finite structures on the ground surface or within a spherical boundary, are presented and global dynamic stiffness matrices for the FEM substructures, separated for the degrees of freedom (DOFs) on the interaction surfaces and inside the structure are given.

The coupling of ITM and FEM, applying the compatibility conditions at the common interfaces, is addressed in Ch. 5, whereby the 2.5D substructures are coupled at the cylindrical interface (Sec. 5.1) and the 3D substructures at the spherical interaction surface (Sec. 5.2) or the horizontal soil foundation interface (Sec. 5.3). The latter is used in case the SSI or SSSI of one or several surface structures with the underlying soil that may comprise finite structures or inhomogeneities shall be investigated. To this end, a methodology for the determination of the dynamic stiffness at discrete points on the ground surface of any ITM fundamental or coupled ITM-FEM subsystem is introduced. Furthermore, a postprocessing procedure (Sec. 5.4) is illustrated, allowing the prediction of the displacement and stress distributions on the ground surface and within the soil resulting from the dynamic interaction and thus also the power input at the soil foundation interface and the power flow through a defined control volume.

In the last part of the thesis, numerical results obtained with the previously introduced methodologies are presented for different types of loading. Thereby, the frequency domain response of different fundamental and coupled systems due to stationary harmonic loads is initially considered in Ch. 6. After verifying the proposed approaches by comparison of the results for different benchmark cases with literature solutions (Sec. 6.1), the coupled ITM-FEM approach is applied for the investigation of finite and length invariant vibration mitigation measures at the source or in the transmission path (Sec. 6.2), providing insight into the physical mechanisms and wave propagation characteristics. Subsequently, the dynamic SSI of a single rigid/flexible, massless/massive surface foundation with the underlying homogeneous or layered soil is investigated (Sec. 6.3) and the procedure for determining the dynamic soil stiffness is verified by comparing the resulting foundation flexibilities with the results of other methods. Conclusions on the radiation characteristics of the foundations are drawn from the power input at the soil foundation contact area as well as the wavenumber spectra of the resulting displacements and the behaviour of a foundation on more complex soil subsystems with local inhomogeneities is discussed. Moreover, the effects of the SSSI of

several adjacent surface foundations (Sec. 6.4) and the response of spatial frame structures with different footing conditions is analysed (Sec. 6.5), before finally the dynamic interaction of two parallel tunnels is investigated (Sec. 6.6).

Ch. 7 deals with the calculation of the dynamic response of different ITM-FEM systems due to transient loads. For this purpose, the procedure for the determination of the complex transfer functions is explained first (Sec. 7.1). The latter are then used to determine the time histories of the system responses using either a Fourier synthesis approach or a discrete convolution of the impulse response functions, obtained from the IFFT of the transfer functions, with the transient loads (Sec. 7.2). Following, the transient response of a homogenous soil due to a load on the ground surface (Sec. 7.3) as well as the frequency dependent flexibilities of a rigid foundation and the resulting time histories of the foundation compliances (Sec. 7.4) due to a suddenly applied load are investigated and compared with literature. In addition, some comments on the effects of frequency band limitation and hysteric material damping on both, the causality and the quality of the results are made. Finally, the 2.5D ITM-FEM approach is applied to determine the response of a twin tunnel system due to a Gaussian-modulated sinusoidal pulse within one tunnel tube.

Eventually, the dynamic response of fundamental and coupled ITM-FEM systems due to moving loads is treated in Ch. 8. Therefore, firstly a methodology to include moving loads within the proposed approach is derived in the wavenumber frequency domain (Sec. 8.1). Subsequently, numerical results for the displacement fields on the surface of a homogeneous halfspace subjected to a constant (Sec. 8.2) or harmonically oscillating (Sec. 8.3) moving load are presented and the effects, occurring for different load velocities, are explained by considerations in original as well as Fourier transformed domain. The validity of the implementation for coupled systems is verified by comparison with the previously validated homogeneous halfspace, before the response of a twin tunnel system with moving load inside one tunnel is computed by means of the 2.5D ITM-FEM approach (Sec. 8.4).

Ch. 9 concludes the thesis with a summary of the main findings and gives recommendations for further research.

2 Fundamental solutions in elastodynamics

Disturbances introduced into the soil by dynamic loads cause stress and deformation states, propagating in form of waves. The propagation characteristics and the frequency content of the waves depend strongly on the local soil composition and geological conditions as well as the magnitude of the disturbance. For ground borne vibrations, in general, only small strains occur, such that the soil can be described in good approximation as a linear elastic, homogeneous and isotropic medium [231].

In order to be able to describe also complex soil systems, such as a layered soil with local cylindrical or spherical cavities, in this chapter firstly solutions for the basic fundamental systems such as a halfspace, a layered halfspace, a soil layer over bedrock or a separated block of soil layers, a fullspace with cylindrical cavity and a fullspace with spherical cavity are presented in Secs. 2.2 - 2.6. These solutions are based on the fundamental elastodynamic differential equations introduced in Sec. 2.1. However, in this chapter, which is mainly predicated on Refs. [84] and [51], only the essential equations and correlations will be discussed. For a more detailed derivation of the fundamental solutions and its characteristics, the reader is referred to the Ref. [81, 160, 162, 232]. Furthermore, the superposition of the fundamental systems to the more complex soil systems is illustrated in the subsequent Ch. 3.

2.1 Fundamentals of linear elastodynamics

The dynamic equilibrium in a linear elastic, isotropic continuum is described by the Lamé differential equation

$$\mu u^i|^j_j + (\lambda + \mu)\, u^j|^i_j - \rho \ddot{u}^i = 0 \tag{2.1}$$

with the displacement field u^i (with $i, j = x, y, z$), the Lamé constants λ and μ, the density ρ and the vertical bar indicating the partial derivatives w.r.t. i and j. The Lamé constants can

be expressed by the elastic parameters Young's modulus E, shear modulus G and Poisson ratio ν as

$$\mu = G = \frac{E}{2\,(1+\nu)} \tag{2.2}$$

$$\lambda = \frac{E\nu}{(1+\nu)\,(1-2\nu)} \tag{2.3}$$

In order to solve the system of coupled, partial differential equations (2.1), firstly the equations are decoupled using the Helmholtz approach. Thus, the displacement field $\mathbf{u}$ is replaced by the sum of the rotation free gradient of a scalar field Φ and the source free rotation of a vector field $\mathbf{\Psi}$, with $\in^{ikl}$ as the permutation symbol [18].

$$u^i = \Phi|^i + \Psi_l|_k \; \in^{ikl} \tag{2.4}$$

Inserting Eq. (2.4) into the Lamé equation leads to the following decoupled wave equations

$$\Phi|^j_j - \frac{1}{{c_p}^2}\ddot{\Phi} \quad = 0 \tag{2.5}$$

$$\Psi_i|^j_j - \frac{1}{{c_s}^2}\ddot{\Psi}_i = 0 \tag{2.6}$$

with the compressional and the shear wave velocity

$$c_p = \sqrt{\frac{\lambda + 2\mu}{\rho}} \qquad \text{and} \qquad c_s = \sqrt{\frac{\mu}{\rho}} \tag{2.7}$$

The material damping in the ground is included in this work via a frequency-independent hysteretic damping. This damping model has shown in experimental investigations to reproduce the energy dissipation within the soil sufficiently well [81]. It can be introduced applying the correspondence principle, which states that the response including material damping, can be obtained from the pure elastic one, just by replacing the elastic constants by their complex counterparts [233, 234].

$$\hat{\mu} = \mu\,(1 + \mathrm{i}\ \mathrm{sign}\,(\omega)\ \eta) \tag{2.8}$$

$$\hat{\lambda} = \lambda\,(1 + \mathrm{i}\ \mathrm{sign}\,(\omega)\ \eta) \tag{2.9}$$

where $\omega = 2\pi f$ is the angular frequency and η represents the loss factor, which is related to the Lehr's damping ratio by $\eta = 2D$ resp. the hysteretic damping ratio by $\eta = 2\zeta$. Therefore, in case of material damping both, the material constants and the wave velocities are complex quantities. For the sake of simplicity, these complex quantities are not marked separately hereinafter.

2.2 Fundamental system halfspace

The resulting partial differential Eq. (2.5) and (2.6) can be described in Cartesian coordinates (x, y, z) to derive the solution of the halfspace depicted in Fig. 2.1, with x and y parallel to the halfspace surface and z as the depth coordinate [84]. Except the area under the external load $\bar{\mathbf{P}}^{\mathbf{hs}}_{\mathbf{\Lambda_{ITM}}}(x,y,z,\omega)$, the halfspace surface is free of tractions and no body forces occur within the infinite halfspace [51].

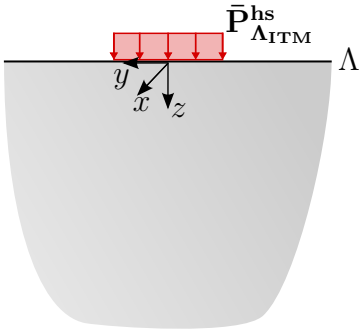

Figure 2.1: Homogeneous halfspace.

After a threefold Fourier transform into the wavenumber frequency domain, defined as

$$\hat{f}(k_x,k_y,z,\omega) = \int_{-\infty}^{\infty}\int_{-\infty}^{\infty}\int_{-\infty}^{\infty} f(x,y,z,t)\, \mathrm{e}^{-\mathrm{i}k_x x}\, \mathrm{e}^{-\mathrm{i}k_y y}\, \mathrm{e}^{-\mathrm{i}\omega t}\, \mathrm{d}x\, \mathrm{d}y\, \mathrm{d}t \tag{2.10}$$

four ordinary differential equations for the scalar potential Φ and the components Ψ_α (with $\alpha = x,y,z$) of the vector potential are obtained.

$$\left[-{k_x}^2 - {k_y}^2 + {k_p}^2 + \frac{\partial^2}{\partial z^2}\right] \hat{\Phi}\left(k_x, k_y, z, \omega\right) \quad = 0 \tag{2.11}$$

$$\left[-{k_x}^2 - {k_y}^2 + {k_s}^2 + \frac{\partial^2}{\partial z^2}\right] \hat{\Psi}_\alpha\left(k_x, k_y, z, \omega\right) = 0 \tag{2.12}$$

Therein the wavenumbers of the compressional and the shear waves are defined as

$$k_p = \omega/c_p \qquad \text{and} \qquad k_s = \omega/c_s \tag{2.13}$$

The component $\hat{\Psi}_z$ can be set to zero without any loss of information [235]. Furthermore, in Eqs. (2.11) and (2.12) the z-coordinate stays untransformed in order to be able to introduce horizontal soil layers later on. The $\hat{}$ symbol indicates parameters in the threefold transformed domain, whereas $\bar{}$ indicates those only transformed w.r.t. one dimension.

Solution for dynamic loading

In the dynamic case Eqs. (2.11) and (2.12) can be solved using the following exponential approach for the potentials

$$\hat{\Phi} \;\; = A_1 \, \mathrm{e}^{\lambda_1 z} + A_2 \, \mathrm{e}^{-\lambda_1 z} \tag{2.14a}$$

$$\hat{\Psi}_\alpha = B_{\alpha 1} \, \mathrm{e}^{\lambda_2 z} + B_{\alpha 2} \, \mathrm{e}^{-\lambda_2 z} \tag{2.14b}$$

with the exponents

$$\lambda_1 = \sqrt{{k_x}^2 + {k_y}^2 - {k_p}^2} \qquad \text{and} \qquad \lambda_2 = \sqrt{{k_x}^2 + {k_y}^2 - {k_s}^2} \tag{2.15}$$

Due to the external harmonic load $\hat{\mathbf{P}}^{\mathbf{hs}}_{\mathbf{\Lambda_{ITM}}}(k_x,k_y,z,\omega)$ spatially propagating and evanescent waves are introduced into the soil. These are described by Eqs. (2.14) depending on the relation of k_x, k_y and ω, which goes into the wavenumbers k_p reps. k_s. In case of real exponents λ_1 and λ_2, which holds for $k_x^2 + k_y^2 > k_p^2$ resp. k_s^2, the potentials $\hat{\Phi}$ and $\hat{\Psi}_\alpha$ represent exponentially increasing or decreasing surface waves. In contrast they describe spatially propagating compressional or shear waves for imaginary exponents, which holds for $k_x^2 + k_y^2 < k_p^2$ resp. k_s^2. For negative frequencies, the coefficients relating to non-physical waves according to the Sommerfeld radiation condition can be uniquely identified and thus excluded for further analysis ($A_1 = B_{x1} = B_{y1} = 0$). Therefore, in this work all dynamic calculations are performed for $\omega < 0$ and the results for $\omega > 0$ are completed as conjugate complex counterparts in the Fourier transformed domain. [81, 162]

The corresponding stresses and displacements inside the soil can be expressed in dependency of the wave amplitudes $\hat{\mathbf{C}}^{\mathbf{hs}}_{\mathbf{ITM}}$. With the matrices of Appx. A.1.1 they yield

$$\hat{\boldsymbol{\sigma}}^{\mathbf{hs}}_{\mathbf{ITM}} = \hat{\mathbf{S}}^{\mathbf{hs}}_{\mathbf{ITM}} \hat{\mathbf{C}}^{\mathbf{hs}}_{\mathbf{ITM}} \tag{2.16a}$$

$$\hat{\mathbf{u}}^{\mathbf{hs}}_{\mathbf{ITM}} = \hat{\mathbf{U}}^{\mathbf{hs}}_{\mathbf{ITM}} \hat{\mathbf{C}}^{\mathbf{hs}}_{\mathbf{ITM}} \tag{2.16b}$$

Thereby, $\hat{\mathbf{S}}^{\mathbf{hs}}_{\mathbf{ITM}}$ and $\hat{\mathbf{U}}^{\mathbf{hs}}_{\mathbf{ITM}}$ contain the stresses resp. the displacements inside the soil due to an unit stress state $\hat{\boldsymbol{\sigma}}^{\mathbf{hs}}_{\mathbf{ITM}}$ for each combination (k_x, k_y, ω) at a specific depth z. Applying the local boundary conditions on the halfspace surface $\hat{\sigma}^{\mathrm{hs}}_{iz,\Lambda}(k_x,k_y,z,\omega) = -\hat{p}^{\mathrm{hs}}_{iz,\Lambda}(k_x,k_y,z,\omega)$ with $i = x, y, z$ and the Sommerfeld radiation condition [236], the system of equations for the determination of $\hat{\mathbf{C}}^{\mathbf{hs}}_{\mathbf{ITM}}$ in the halfspace results as

$$\hat{\mathbf{S}}^{\mathbf{hs}}_{\mathbf{\Lambda_{ITM}}} \hat{\mathbf{C}}^{\mathbf{hs}}_{\mathbf{ITM}} = \hat{\mathbf{P}}^{\mathbf{hs}}_{\mathbf{\Lambda_{ITM}}} \tag{2.17}$$

With the wave amplitudes, all stresses and displacements at every position in the halfspace can be determined in dependency of (k_x, k_y, z, ω) in a postprocessing step applying Eqs. (2.16). The results in the original domain (x,y,z,t) are obtained by a threefold inverse Fourier transform [51]

$$f(x,y,z,t) = \frac{1}{(2\pi)^3} \int_{-\infty}^{\infty} \int_{-\infty}^{\infty} \int_{-\infty}^{\infty} \hat{f}(k_x,k_y,z,\omega)\, \mathrm{e}^{\mathrm{i}k_x x}\, \mathrm{e}^{\mathrm{i}k_y y}\, \mathrm{e}^{\mathrm{i}\omega t}\, \mathrm{d}k_x\, \mathrm{d}k_y\, \mathrm{d}\omega \tag{2.18}$$

If one is only interested in the displacements on the ground surface Λ due to an external load acting there, it is advantageous to introduce a direct stiffness formulation. By combining Eqs. (2.16a) and (2.16b) and evaluating them at $z = 0$, the stiffness matrix for the halfspace $\hat{\mathbf{K}}^{\mathbf{hs}}_{\mathbf{ITM}} = \hat{\mathbf{S}}^{\mathbf{hs}}_{\mathbf{\Lambda_{ITM}}} \hat{\mathbf{U}}^{\mathbf{hs}\,-\mathbf{1}}_{\mathbf{\Lambda_{ITM}}}$ in the (k_x, k_y, z, ω) domain can be derived. This leads to the following system of equations for the unknown surface displacements $\hat{\mathbf{u}}^{\mathbf{hs}}_{\mathbf{\Lambda_{ITM}}}$.

$$\hat{\mathbf{K}}^{\mathbf{hs}}_{\mathbf{ITM}} \hat{\mathbf{u}}^{\mathbf{hs}}_{\mathbf{\Lambda_{ITM}}} = \hat{\mathbf{P}}^{\mathbf{hs}}_{\mathbf{\Lambda_{ITM}}} \tag{2.19}$$

For the simple system of the homogeneous halfspace this is not essential, however the stiffness concept in general becomes very important for the coupling of fundamental or superposed ITM systems to the FEM (cp. Ch. 5).

Solution for static loading

In this work there are two occasions, where it is necessary to determine the static response of the halfspace in the Fourier transformed domain. Firstly, for the calculation of the Impulse Response Function (IRF) of the soil in Ch. 7 and secondly for the determination of the response to moving static or harmonic loads in Ch. 8.

In the static case ($\omega = 0$) the wavenumbers k_p and k_s become zero, the exponents λ_1 and λ_2 get identical and the determinant of $\hat{\mathbf{K}}^{\mathbf{hs}}_{\mathbf{\Lambda_{ITM}}}$ becomes zero. Thus, the solution approaches in Eqs. (2.14) are no longer complete and a solution for the static displacements is not possible [162]. Lenz [217], in contrast, used an exponential approach instead of the Helmholtz potentials to solve the Lamé equation in the wavenumber frequency domain. Therewith, after some sorting and substitutions, it is possible to express the stresses and displacements for $\omega = 0$ in terms of the unknowns $\hat{\mathbf{C}}^{\mathbf{hs}}_{\mathbf{0_{ITM}}}$ analogously to the dynamic case. With the matrices of Appx. A.1.2 they yield

$$\hat{\boldsymbol{\sigma}}^{\mathbf{hs}}_{\mathbf{0_{ITM}}} = \hat{\mathbf{S}}^{\mathbf{hs}}_{\mathbf{0_{ITM}}} \hat{\mathbf{C}}^{\mathbf{hs}}_{\mathbf{0_{ITM}}} \tag{2.20a}$$

$$\hat{\mathbf{u}}^{\mathbf{hs}}_{\mathbf{0_{ITM}}} = \hat{\mathbf{U}}^{\mathbf{hs}}_{\mathbf{0_{ITM}}} \hat{\mathbf{C}}^{\mathbf{hs}}_{\mathbf{0_{ITM}}} \tag{2.20b}$$

As the stresses and the displacements have to decay with increasing depth z also for $\omega = 0$, the contributions of the coefficients with positive exponents can be excluded [217]. Thus the system of equations can directly be solved in dependency of the boundary conditions at the halfspace surface Λ.

2.3 Fundamental system layered halfspace

In a horizontally stratified soil, with N elastic layers overlying a homogeneous halfspace, each layer can be described by the Lamé equation (2.1). Perfect adhesion is assumed at each interface between the different media and no body forces occur within a layer or the halfspace. External loads can only be applied on the layer boundaries Λ_l. [51]

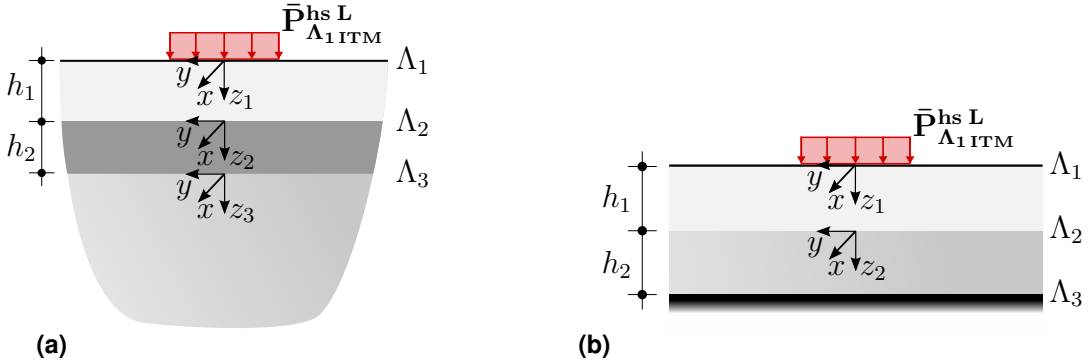

Figure 2.2: (a) Layered halfspace and (b) layered soil over bedrock.

Solution for dynamic loading

As for the homogeneous halfspace, an exponential approach w.r.t. the vertical coordinate z_l in each layer with the height h_l is applied in the wavenumber frequency domain. However, within a layer all kinds of propagating and evanescent waves can occur. To include also the waves reflected at the material transition surface as well as the surface waves exponentially increasing with z_l, none of the coefficients in Eqs. (2.14) can be set to zero, but all six need to be considered in the analysis.

To avoid the occurrence of numerical instabilities due to big arguments of the exponential functions associated with A_{1,L_l} and $B_{\alpha 1,L_l}$, decaying instead of increasing exponents are used [237] and thus these coefficients are substituted by

$$A_{1,L_l} \mathrm{e}^{\lambda_{1_l} z_l} = \underline{A}_{1,L_l} \mathrm{e}^{\lambda_{1_l}(z_l - h_l)} \tag{2.21a}$$

$$B_{\alpha 1,L_l} \mathrm{e}^{\lambda_{2_l} z_l} = \underline{B}_{\alpha 1,L_l} \mathrm{e}^{\lambda_{2_l}(z_l - h_l)} \tag{2.21b}$$

The stresses and displacements in the (k_x, k_y, z, ω) domain within one layer l can be expressed in dependency of the wave amplitudes $\hat{\mathbf{C}}^{\mathbf{hs\ L}_l}_{\mathbf{ITM}}$. Including the substitutions of Eqs. (2.21), and using the matrices from Appx. A.2.1, they yield [51]

$$\hat{\boldsymbol{\sigma}}^{\mathbf{hs\ L}_l}_{\mathbf{ITM}} = \hat{\mathbf{S}}^{\mathbf{hs\ L}_l}_{\mathbf{ITM}}\, \hat{\mathbf{C}}^{\mathbf{hs\ L}_l}_{\mathbf{ITM}} \tag{2.22a}$$

$$\hat{\mathbf{u}}^{\mathbf{hs\ L}_l}_{\mathbf{ITM}} = \hat{\mathbf{U}}^{\mathbf{hs\ L}_l}_{\mathbf{ITM}}\, \hat{\mathbf{C}}^{\mathbf{hs\ L}_l}_{\mathbf{ITM}} \tag{2.22b}$$

The total system of equations, exemplary shown for the halfspace with two top layers depicted in Fig. 2.2a, can be derived applying the local boundary conditions at the ground surface $\hat{\sigma}^{\mathrm{hs\ L}_1}_{iz,\Lambda_1}(k_x,k_y,z,\omega) = -\hat{p}^{\mathrm{hs\ L}_1}_{iz,\Lambda_1}(k_x,k_y,z,\omega)$, the continuity conditions at the layer interfaces Λ_2 and Λ_3 $\hat{u}^{\mathrm{hs\ L}_{l+1}}_{i,\Lambda_{l+1}}(k_x,k_y,z,\omega) = \hat{u}^{\mathrm{hs\ L}_l}_{i,\Lambda_{l+1}}(k_x,k_y,z,\omega)$ and $\hat{\sigma}^{\mathrm{hs\ L}_{l+1}}_{iz,\Lambda_{l+1}}(k_x,k_y,z,\omega) = \hat{\sigma}^{\mathrm{hs\ L}_l}_{iz,\Lambda_{l+1}}(k_x,k_y,z,\omega)$ all with $(i = x, y, z)$ as well as the radiation condition for the halfspace as [51]

$$\begin{bmatrix} \hat{\mathbf{S}}^{\mathbf{hs\ L}_1}_{\mathbf{\Lambda_1\,ITM}} & \mathbf{0} & \mathbf{0} \\ \hat{\mathbf{S}}^{\mathbf{hs\ L}_1}_{\mathbf{\Lambda_2\,ITM}} & -\hat{\mathbf{S}}^{\mathbf{hs\ L}_2}_{\mathbf{\Lambda_2\,ITM}} & \mathbf{0} \\ \hat{\mathbf{U}}^{\mathbf{hs\ L}_1}_{\mathbf{\Lambda_2\,ITM}} & -\hat{\mathbf{U}}^{\mathbf{hs\ L}_2}_{\mathbf{\Lambda_2\,ITM}} & \mathbf{0} \\ \mathbf{0} & \hat{\mathbf{S}}^{\mathbf{hs\ L}_2}_{\mathbf{\Lambda_3\,ITM}} & -\hat{\mathbf{S}}^{\mathbf{hs}}_{\mathbf{\Lambda_3\,ITM}} \\ \mathbf{0} & \hat{\mathbf{U}}^{\mathbf{hs\ L}_2}_{\mathbf{\Lambda_3\,ITM}} & -\hat{\mathbf{U}}^{\mathbf{hs}}_{\mathbf{\Lambda_3\,ITM}} \end{bmatrix} \begin{pmatrix} \hat{\mathbf{C}}^{\mathbf{hs\ L}_1}_{\mathbf{ITM}} \\ \hat{\mathbf{C}}^{\mathbf{hs\ L}_2}_{\mathbf{ITM}} \\ \hat{\mathbf{C}}^{\mathbf{hs}}_{\mathbf{ITM}} \end{pmatrix} = \begin{pmatrix} \hat{\mathbf{P}}^{\mathbf{hs\ L}}_{\mathbf{\Lambda_1\,ITM}} \\ \hat{\mathbf{P}}^{\mathbf{hs\ L}}_{\mathbf{\Lambda_2\,ITM}} \\ \mathbf{0} \\ \hat{\mathbf{P}}^{\mathbf{hs}}_{\mathbf{\Lambda_3\,ITM}} \\ \mathbf{0} \end{pmatrix} \tag{2.23}$$

In case of a stratified ground over bedrock, as depicted in Fig. 2.2b the local boundary conditions on the ground surface Λ_1, the continuity conditions at the layer interface Λ_2 and the zero displacement condition at the bedrock Λ_3 need to be considered, leading to the following system of equations

$$\begin{bmatrix} \hat{\mathbf{S}}^{\mathbf{hs\ L}_1}_{\mathbf{\Lambda_1\,ITM}} & \mathbf{0} \\ \hat{\mathbf{S}}^{\mathbf{hs\ L}_1}_{\mathbf{\Lambda_2\,ITM}} & -\hat{\mathbf{S}}^{\mathbf{hs\ L}_2}_{\mathbf{\Lambda_2\,ITM}} \\ \hat{\mathbf{U}}^{\mathbf{hs\ L}_1}_{\mathbf{\Lambda_2\,ITM}} & -\hat{\mathbf{U}}^{\mathbf{hs\ L}_2}_{\mathbf{\Lambda_2\,ITM}} \\ \mathbf{0} & \hat{\mathbf{U}}^{\mathbf{hs\ L}_2}_{\mathbf{\Lambda_3\,ITM}} \end{bmatrix} \begin{pmatrix} \hat{\mathbf{C}}^{\mathbf{hs\ L}_1}_{\mathbf{ITM}} \\ \hat{\mathbf{C}}^{\mathbf{hs\ L}_2}_{\mathbf{ITM}} \end{pmatrix} = \begin{pmatrix} \hat{\mathbf{P}}^{\mathbf{hs\ L}}_{\mathbf{\Lambda_1\,ITM}} \\ \hat{\mathbf{P}}^{\mathbf{hs\ L}}_{\mathbf{\Lambda_2\,ITM}} \\ \mathbf{0} \\ \mathbf{0} \end{pmatrix} \tag{2.24}$$

From Eqs. (2.23) or (2.24) it is possible to calculate the unknown wave amplitudes and in a postprocessing step, applying Eqs. (2.16) resp. (2.22), all stresses and displacements at every position inside the layered halfspace [51]. The same methodology is also applicable for an arbitrary number of different soil layers. For this purpose, just the matrices $\hat{\mathbf{S}}^{\mathbf{hs\ L}_l}_{\mathbf{ITM}}$ and $\hat{\mathbf{U}}^{\mathbf{hs\ L}_l}_{\mathbf{ITM}}$ for the desired number of layers need be included into the total system of equations under consideration of the corresponding transition conditions at the layer boundaries Λ_l.

In contrast to the homogeneous halfspace, for the layered halfspace and the layered soil over bedrock, stress and displacement continuity conditions at the layer interfaces are included in the total system of equations (2.23) or (2.24), leading to non quadratic matrices. Therefore, it is not straightforward to construct a stiffness matrix for these systems directly from $\hat{\mathbf{S}}^{\mathbf{hs\,L}_l}_{\mathbf{ITM}}$ and $\hat{\mathbf{U}}^{\mathbf{hs\,L}_l}_{\mathbf{ITM}}$. Nevertheless, the derivation of a stiffness matrix for the stratified halfspace, giving a relation between loads and displacements at its surface Λ_1, would be possible using the unit load concept, introduced for the block of discrete layers in Sec. 2.4. This is, however, omitted here, since the discrete soil stratification can be coupled to any system which is also described by a wavenumber and frequency-dependent stiffness matrix and is thus much more universally applicable.

Solution for static loading

To derive the static stresses and displacements within one layer l of a stratified soil, the same approach as for the homogeneous halfspace is applied. Using the matrices from Appx. A.2.2, they yield [51]

$$\hat{\boldsymbol{\sigma}}^{\mathbf{hs\,L}_l}_{\mathbf{0_{ITM}}} = \hat{\mathbf{S}}^{\mathbf{hs\,L}_l}_{\mathbf{0_{ITM}}}\,\hat{\mathbf{C}}^{\mathbf{hs\,L}_l}_{\mathbf{0_{ITM}}} \tag{2.25}$$

$$\hat{\mathbf{u}}^{\mathbf{hs\,L}_l}_{\mathbf{0_{ITM}}} = \hat{\mathbf{U}}^{\mathbf{hs\,L}_l}_{\mathbf{0_{ITM}}}\,\hat{\mathbf{C}}^{\mathbf{hs\,L}_l}_{\mathbf{0_{ITM}}} \tag{2.26}$$

The total system of equations to determine the static response of the layered halfspace is set up analogously to the dynamic case by applying the boundary conditions on the ground surface, the continuity conditions at the layer interfaces and the condition of decreasing amplitudes of stresses and displacements with increasing depth in the underlying halfspace.

2.4 Fundamental system discrete soil stratification

In this section, the stiffness matrix for one or more layers with parallel surfaces and a total upper and lower boundary Λ_1 resp. Λ_3, as depicted in Fig. 2.3, is derived as presented in [51]. With Eqs. (2.22) it is possible to determine the stresses and displacements in the (k_x, k_y, z, ω) domain at every position within one layer l. [51]

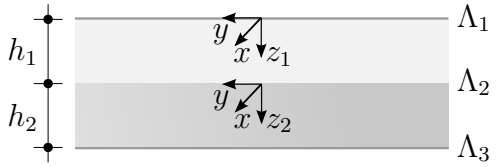

Figure 2.3: Separated block of soil layers.

As the calculations are carried out numerically, only a limited number of Fourier series members can be considered and all parameters are evaluated for the discrete wavenumbers

$$k_x = o\Delta k_x \quad \text{with} \quad o = -N_x/2,...,(N_x/2-1) \tag{2.27}$$

$$k_y = s\Delta k_y \quad \text{with} \quad s = -N_y/2,..., (N_y/2-1) \tag{2.28}$$

where N_x, N_y is the number of series members or sample points in the original domain respectively. [51]

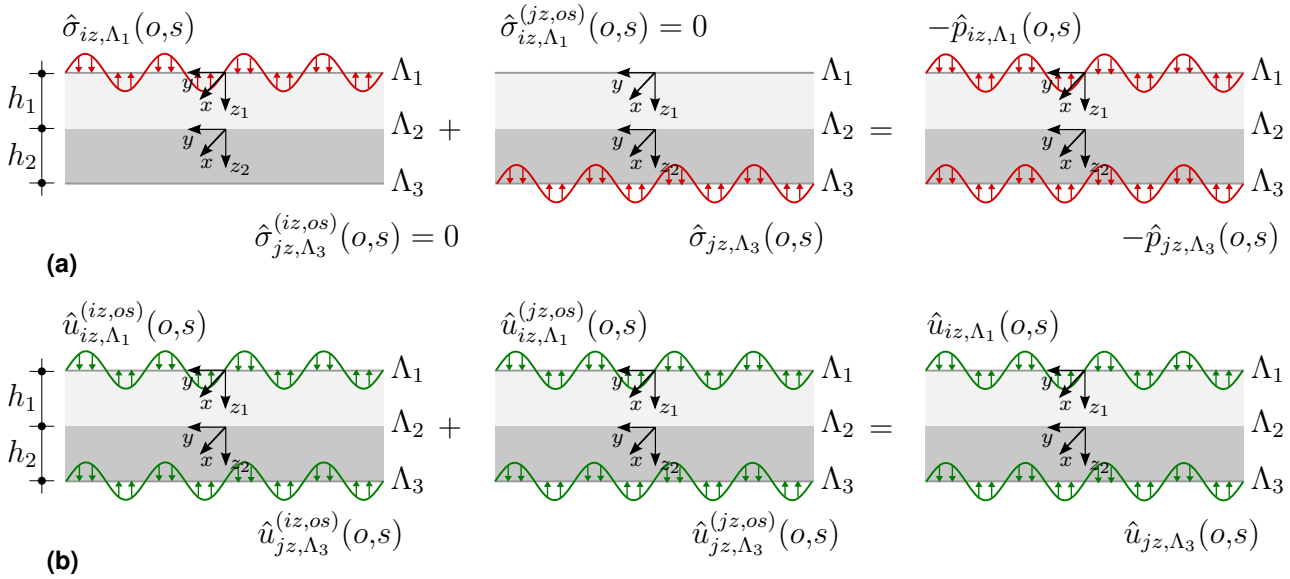

Figure 2.4: Superposition of (a) stresses and (b) displacements for separated block of layers [51].

If a perfect bond is assumed and therefore continuity conditions can be enforced at the horizontal transition surfaces between the different materials, it is possible to establish a system of equations that describes the system of layers only in dependence of the boundary conditions at Λ_1 and Λ_3. Subsequently, for each frequency ω, unit stress states $\hat{\sigma}_{iz,\Lambda_1}(o,s)$ with $i = z, y, x$ are applied at the upper boundary Λ_1 for each combination of the wavenumbers (k_x, k_y), whereas the stresses $\hat{\sigma}^{(iz,os)}_{jz,\Lambda_3}(o,s)$ at Λ_3 are set to zero, so that an unconstrained development of the displacements is possible. Finally, the displacements $\hat{u}^{(iz,os)}_{iz,\Lambda_1}(o,s)$ at Λ_1 and $\hat{u}^{(iz,os)}_{jz,\Lambda_3}(o,s)$ at Λ_3 are determined for this set of boundary conditions. Analogously, unit stress states $\hat{\sigma}_{jz,\Lambda_3}(o,s)$ with $j = z, y, x$ are applied at Λ_3, a stress free boundary is assumed at Λ_1 and the resulting displacements $\hat{u}^{(jz,os)}_{jz,\Lambda_3}(o,s)$ on Λ_3 and $\hat{u}^{(jz,os)}_{iz,\Lambda_1}(o,s)$ on Λ_1 are determined. The superposition of the unit stresses scaled with the amplitudes $\hat{C}_{iz,\Lambda_1}(o,s)$ on Λ_1 and $\hat{C}_{jz,\Lambda_3}(o,s)$ on Λ_3 have to be equal to the there applied external loads $\hat{p}_{iz,\Lambda_1}(o,s)$ and $\hat{p}_{jz,\Lambda_3}(o,s)$.[51] Thus the amplitudes can directly be calculated from:

$$\hat{C}_{iz,\Lambda_1}(o,s)\,\hat{\sigma}_{iz,\Lambda_1}(o,s) = -\hat{p}_{iz,\Lambda_1}(o,s) \tag{2.29a}$$

$$\hat{C}_{jz,\Lambda_3}(o,s)\,\hat{\sigma}_{jz,\Lambda_3}(o,s) = -\hat{p}_{jz,\Lambda_3}(o,s) \tag{2.29b}$$

Eqs. (2.29) can be summarized in matrix notation as

$$\underbrace{\begin{bmatrix} \hat{\mathbf{S}}^{\mathbf{L}}_{\mathbf{\Lambda_1\Lambda_1\,ITM}} & \mathbf{0} \\ \mathbf{0} & \hat{\mathbf{S}}^{\mathbf{L}}_{\mathbf{\Lambda_3\Lambda_3\,ITM}} \end{bmatrix}}_{\hat{\mathbf{S}}^{\mathbf{L}}_{\mathbf{ITM}}} \underbrace{\begin{pmatrix} \hat{\mathbf{C}}^{\mathbf{L}}_{\mathbf{\Lambda_1\,ITM}} \\ \hat{\mathbf{C}}^{\mathbf{L}}_{\mathbf{\Lambda_3\,ITM}} \end{pmatrix}}_{\hat{\mathbf{C}}^{\mathbf{L}}_{\mathbf{ITM}}} = \underbrace{\begin{pmatrix} \hat{\mathbf{P}}^{\mathbf{L}}_{\mathbf{\Lambda_1\,ITM}} \\ \hat{\mathbf{P}}^{\mathbf{L}}_{\mathbf{\Lambda_3\,ITM}} \end{pmatrix}}_{\hat{\mathbf{P}}^{\mathbf{L}}_{\mathbf{ITM}}} \tag{2.30}$$

The matrices $\hat{\mathbf{S}}^{\mathbf{L}}_{\alpha\beta_{\mathbf{ITM}}}$ with $\alpha,\beta = \Lambda_1,\Lambda_3$ contain the stresses on the surface α for a unit load $\hat{\mathbf{P}}^{\mathbf{L}}_{\beta_{\mathbf{ITM}}}$ on the surface β as a function of the amplitudes $\hat{\mathbf{C}}^{\mathbf{L}}_{\beta_{\mathbf{ITM}}}$. For the system of separated layers, the off diagonal terms of $\hat{\mathbf{S}}^{\mathbf{L}}_{\mathbf{ITM}}$ get zero and the amplitudes $\hat{\mathbf{C}}^{\mathbf{L}}_{\mathbf{\Lambda_1\,ITM}}$ and $\hat{\mathbf{C}}^{\mathbf{L}}_{\mathbf{\Lambda_3\,ITM}}$ for a given external load $\hat{\mathbf{P}}^{\mathbf{L}}_{\mathbf{ITM}}$ can be calculated independently. The corresponding displacements on the two boundaries Λ_1 and Λ_3 result as [51]

$$\hat{u}_{iz,\Lambda_1}(o,s) = \hat{C}_{iz,\Lambda_1}(o,s)\,\hat{u}^{(iz,os)}_{iz,\Lambda_1}(o,s) + \sum_j \hat{C}_{jz}\,\hat{u}^{(jz,os)}_{iz,\Lambda_1}(o,s) \tag{2.31a}$$

$$\hat{u}_{jz,\Lambda_3}(o,s) = \hat{C}_{jz,\Lambda_3}(o,s)\,\hat{u}^{(jz,os)}_{jz,\Lambda_3}(o,s) + \sum_i \hat{C}_{iz}\,\hat{u}^{(iz,os)}_{jz,\Lambda_3}(o,s) \tag{2.31b}$$

Again Eqs. (2.31) can be written in matrix notation

$$\underbrace{\begin{pmatrix} \hat{\mathbf{u}}^{\mathbf{L}}_{\mathbf{\Lambda_1\,ITM}} \\ \hat{\mathbf{u}}^{\mathbf{L}}_{\mathbf{\Lambda_3\,ITM}} \end{pmatrix}}_{\hat{\mathbf{u}}^{\mathbf{L}}_{\mathbf{ITM}}} = \underbrace{\begin{bmatrix} \hat{\mathbf{U}}^{\mathbf{L}}_{\mathbf{\Lambda_1\Lambda_1\,ITM}} & \hat{\mathbf{U}}^{\mathbf{L}}_{\mathbf{\Lambda_1\Lambda_3\,ITM}} \\ \hat{\mathbf{U}}^{\mathbf{L}}_{\mathbf{\Lambda_3\Lambda_1\,ITM}} & \hat{\mathbf{U}}^{\mathbf{L}}_{\mathbf{\Lambda_3\Lambda_3\,ITM}} \end{bmatrix}}_{\hat{\mathbf{U}}^{\mathbf{L}}_{\mathbf{ITM}}} \underbrace{\begin{pmatrix} \hat{\mathbf{C}}^{\mathbf{L}}_{\mathbf{\Lambda_1\,ITM}} \\ \hat{\mathbf{C}}^{\mathbf{L}}_{\mathbf{\Lambda_3\,ITM}} \end{pmatrix}}_{\hat{\mathbf{C}}^{\mathbf{L}}_{\mathbf{ITM}}} \tag{2.32}$$

The matrices $\hat{\mathbf{U}}^{\mathbf{L}}_{\alpha\beta_{\mathbf{ITM}}}$ contain the displacements due to the unit stress states and are scaled with the amplitudes $\hat{\mathbf{C}}^{\mathbf{L}}_{\beta_{\mathbf{ITM}}}$ to gain the actual displacements of the system $\hat{\mathbf{u}}^{\mathbf{L}}_{\mathbf{ITM}}$. [51] Combining equations (2.30) and (2.32), the dynamic stiffness matrix $\hat{\mathbf{K}}^{\mathbf{L}}_{\mathbf{ITM}} = \hat{\mathbf{S}}^{\mathbf{L}}_{\mathbf{ITM}}\hat{\mathbf{U}}^{\mathbf{L}\,-1}_{\mathbf{ITM}}$ of the block of separated layers can be derived, stating a direct relation between external loads and resulting displacements on Λ_1 and Λ_3 [51]

$$\underbrace{\begin{bmatrix} \hat{\mathbf{K}}^{\mathbf{L}}_{\mathbf{\Lambda_1\Lambda_1\,ITM}} & \hat{\mathbf{K}}^{\mathbf{L}}_{\mathbf{\Lambda_1\Lambda_3\,ITM}} \\ \hat{\mathbf{K}}^{\mathbf{L}}_{\mathbf{\Lambda_3\Lambda_1\,ITM}} & \hat{\mathbf{K}}^{\mathbf{L}}_{\mathbf{\Lambda_3\Lambda_3\,ITM}} \end{bmatrix}}_{\hat{\mathbf{K}}^{\mathbf{L}}_{\mathbf{ITM}}} \underbrace{\begin{pmatrix} \hat{\mathbf{u}}^{\mathbf{L}}_{\mathbf{\Lambda_1\,ITM}} \\ \hat{\mathbf{u}}^{\mathbf{L}}_{\mathbf{\Lambda_3\,ITM}} \end{pmatrix}}_{\hat{\mathbf{u}}^{\mathbf{L}}_{\mathbf{ITM}}} = \underbrace{\begin{pmatrix} \hat{\mathbf{P}}^{\mathbf{L}}_{\mathbf{\Lambda_1\,ITM}} \\ \hat{\mathbf{P}}^{\mathbf{L}}_{\mathbf{\Lambda_3\,ITM}} \end{pmatrix}}_{\hat{\mathbf{P}}^{\mathbf{L}}_{\mathbf{ITM}}} \tag{2.33}$$

2.5 Fundamental system fullspace with cylindrical cavity

The solution of the fullspace with cylindrical cavity, as depicted in Fig. 2.5, is derived in cylindrical coordinates (x, r, φ). Here, x denotes the longitudinal coordinate of the cylinder, r the radial and φ the circumferential coordinate. [84]

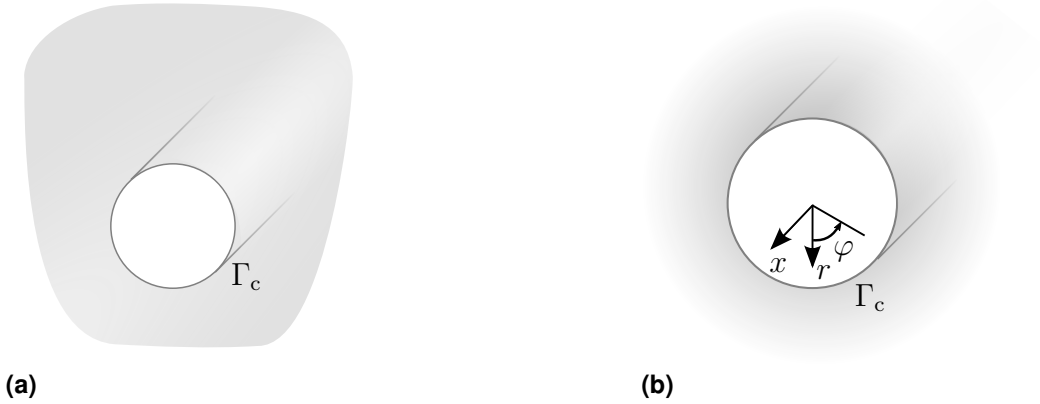

Figure 2.5: (a) Fullspace with cylindrical cavity and (b) cylindrical coordinates.

As the components of the vector potential are not decoupled in the cylindrical coordinate system, an additional step is necessary to decouple the equations after the Helmholtz decomposition. Therefore, the vector potential $\mathbf{\Psi}$ is replaced by two scalar functions ψ and χ. As presented by Eringen and Suhubi [18], $\mathbf{\Psi}$ is expressed by [84]

$$\mathbf{\Psi} = \psi \mathbf{g}^1 + \chi|^j \in_{ij1} \mathbf{g}^i \tag{2.34}$$

with $\in_{ij1}$ as the permutation symbol of the cylindrical coordinate system.

After the decoupling, the equations are transformed into the wavenumber frequency domain $(k_x,\ \omega)$ and a Fourier series expansion $\varphi \rightarrow n$ regarding the circumferential direction of the cylinder is carried out [84]. The $\tilde{}$ symbol denotes parameters in the twofold Fourier transformed domain, depending on k_x and ω.

$$\tilde{\Phi}\left(k_x, r, \varphi, \omega\right) = \sum_{n=-\infty}^{\infty} \hat{\Phi}\left(k_x, r, n, \omega\right) \mathrm{e}^{\mathrm{i}n\varphi} \tag{2.35a}$$

$$\tilde{\psi}\left(k_x, r, \varphi, \omega\right) = \sum_{n=-\infty}^{\infty} \hat{\psi}\left(k_x, r, n, \omega\right) \mathrm{e}^{\mathrm{i}n\varphi} \tag{2.35b}$$

$$\tilde{\chi}\left(k_x, r, \varphi, \omega\right) = \sum_{n=-\infty}^{\infty} \hat{\chi}\left(k_x, r, n, \omega\right) \mathrm{e}^{\mathrm{i}n\varphi} \tag{2.35c}$$

This finally leads to the following system of ordinary differential equations

$$\left[-{k_x}^2+\frac{\partial^2}{\partial r^2}+\frac{1}{r}\frac{\partial}{\partial r}-\frac{n^2}{r^2}+{k_p}^2\right]\hat{\Phi}\left(k_x,r,n,\omega\right)=0 \tag{2.36a}$$

$$\left[-{k_x}^2+\frac{\partial^2}{\partial r^2}+\frac{1}{r}\frac{\partial}{\partial r}-\frac{n^2}{r^2}+{k_s}^2\right]\hat{\psi}\left(k_x,r,n,\omega\right)=0 \tag{2.36b}$$

$$\left[-{k_x}^2+\frac{\partial^2}{\partial r^2}+\frac{1}{r}\frac{\partial}{\partial r}-\frac{n^2}{r^2}+{k_s}^2\right]\hat{\chi}\left(k_x,r,n,\omega\right)=0 \tag{2.36c}$$

The Eqs. (2.36) are differential equations of Bessel type and can be solved with Hankel functions of first $H_n^{(1)}$ and second kind $H_n^{(2)}$ given in Appx. A.5.1 [84]

$$\hat{\Phi}\left(k_x,r,n,\omega\right)=\hat{C}_{1n}\,H_n^{(1)}\left(k_1 r\right)+\hat{C}_{4n}\,H_n^{(2)}\left(k_1 r\right) \tag{2.37a}$$

$$\hat{\psi}\left(k_x,r,n,\omega\right)=\hat{C}_{2n}\,H_n^{(1)}\left(k_2 r\right)+\hat{C}_{5n}\,H_n^{(2)}\left(k_2 r\right) \tag{2.37b}$$

$$\hat{\chi}\left(k_x,r,n,\omega\right)=\hat{C}_{3n}\,H_n^{(1)}\left(k_2 r\right)+\hat{C}_{6n}\,H_n^{(2)}\left(k_2 r\right) \tag{2.37c}$$

in dependency of r and ${k_1}^2={k_p}^2-{k_x}^2$ resp. ${k_2}^2={k_s}^2-{k_x}^2$. In case of $k_1=k_2=0$, a different solution approach needs to be applied. However, this case is only possible for an undamped soil and is thus not further considered [160].

If an external load $\hat{\mathbf{P}}^{\mathbf{fs\,cyl}}_{\mathbf{\Gamma_c\,ITM}}$is applied at the surface of the cylindrical cavity Γ_c, spatially propagating and evanescent waves, w.r.t. the cylindrical coordinate system, are introduced into the soil. The corresponding stresses and displacements inside the soil can be expressed in dependency of the wave amplitudes $\hat{\mathbf{C}}^{\mathbf{fs\,cyl}}_{\mathbf{ITM}}$. With the matrices of Appx. A.3 they yield

$$\hat{\boldsymbol{\sigma}}^{\mathbf{fs\,cyl}}_{\mathbf{ITM}}=\hat{\mathbf{S}}^{\mathbf{fs\,cyl}}_{\mathbf{ITM}}\,\hat{\mathbf{C}}^{\mathbf{fs\,cyl}}_{\mathbf{ITM}} \tag{2.38a}$$

$$\hat{\mathbf{u}}^{\mathbf{fs\,cyl}}_{\mathbf{ITM}}=\hat{\mathbf{U}}^{\mathbf{fs\,cyl}}_{\mathbf{ITM}}\,\hat{\mathbf{C}}^{\mathbf{fs\,cyl}}_{\mathbf{ITM}} \tag{2.38b}$$

For negative frequencies, the Hankel functions $H_n^{(2)}(k_2 r)$ in Eqs. (2.38) are related to waves increasing with growing distance r or propagating against the radial coordinate back to the source. Since, for a soil with infinite extension in radial direction this is, according to the Sommerfeld radiation condition, physically not possible, the coefficients $\hat{C}_{4n}$ to $\hat{C}_{6n}$ can be set to zero [160]. Therefore, the remaining unknowns $\hat{C}_{1n}$ to $\hat{C}_{3n}$ can be determined applying the local boundary conditions on the cylindrical surface $\hat{\sigma}^{\mathrm{fs\,cyl}}_{jr,\Gamma_\mathrm{c}}(k_x,r,n,\omega)=-\hat{p}^{\mathrm{fs\,cyl}}_{jr,\Gamma_\mathrm{c}}(k_x,r,n,\omega)$ with $j=r,x,\varphi$. Given the wave amplitudes $\hat{\mathbf{C}}^{\mathbf{fs\,cyl}}_{\mathbf{ITM}}$, all stresses and displacements at every position in the halfspace can be determined in dependency on (k_x,r,n,ω) in a postprocessing step applying Eqs. (2.38). The results for positive frequencies are completed as conjugate complex counterparts in the transformed domain. The system response in the original do-

main (x, r, φ, t) is obtained by a Fourier series synthesis $n \rightarrow \varphi$ and a twofold inverse Fourier transform $(k_x, \omega) \rightarrow (x, t)$.

However, the solutions for the fullspace with cylindrical cavity derived above are only valid for the dynamic case, as for a static load the solution approach is not complete. In Konrad [232], a solution for this case is presented on the basis of the displacement approach introduced by Papkovich [238] and Neuber [239].

2.6 Fundamental system fullspace with spherical cavity

Using spherical coordinates (r, ϑ, φ) with the radial coordinate r, the elevation angle ϑ and the azimuth angle φ, the solution of a fullspace with spherical cavity, depicted in Fig. 2.6, can be derived. [84]

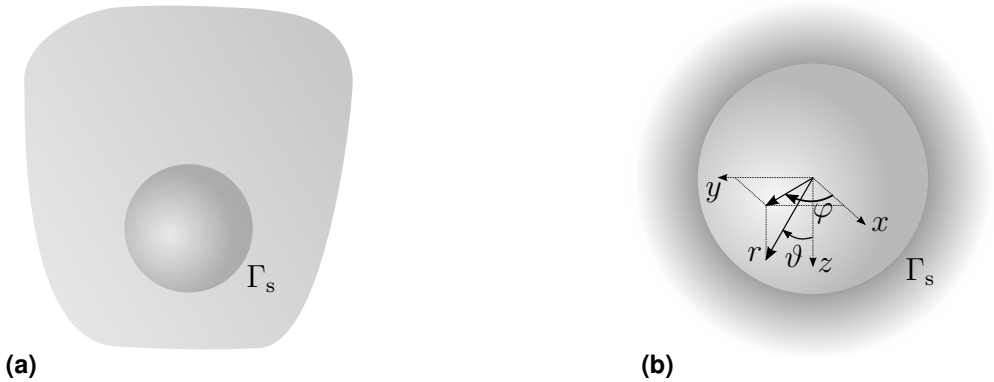

Figure 2.6: (a) Fullspace with spherical cavity and (b) spherical coordinates.

Analogously to the cylindrical coordinate system, the vector potential $\mathbf{\Psi}$ is replaced by two scalar potentials ψ and χ with [17, 18]

$$\mathbf{\Psi} = r\psi\mathbf{g}^1 + (r\chi)\,|^j \in_{ij1} \mathbf{g}^i \tag{2.39}$$

Following the decoupling, the equations are transformed into the frequency domain $(r, \vartheta, \varphi, \omega)$ and the corr. parameters are denoted by the $\bar{}$ symbol. [84]

$$\left[\frac{\partial^2}{\partial r^2} + \frac{2}{r}\frac{\partial}{\partial r} + \frac{1}{r^2}\left(\frac{\partial^2}{\partial \vartheta^2} + \frac{\cos(\vartheta)}{\sin(\vartheta)}\frac{\partial}{\partial \vartheta} + \frac{1}{\sin^2(\vartheta)}\frac{\partial^2}{\partial \varphi^2}\right) + {k_p}^2\right]\bar{\Phi}\,(r, \vartheta, \varphi, \omega) = 0 \tag{2.40a}$$

$$\left[\frac{\partial^2}{\partial r^2} + \frac{2}{r}\frac{\partial}{\partial r} + \frac{1}{r^2}\left(\frac{\partial^2}{\partial \vartheta^2} + \frac{\cos(\vartheta)}{\sin(\vartheta)}\frac{\partial}{\partial \vartheta} + \frac{1}{\sin^2(\vartheta)}\frac{\partial^2}{\partial \varphi^2}\right) + {k_s}^2\right]\bar{\psi}\,(r, \vartheta, \varphi, \omega) = 0 \tag{2.40b}$$

$$\left[\frac{\partial^2}{\partial r^2} + \frac{2}{r}\frac{\partial}{\partial r} + \frac{1}{r^2}\left(\frac{\partial^2}{\partial \vartheta^2} + \frac{\cos(\vartheta)}{\sin(\vartheta)}\frac{\partial}{\partial \vartheta} + \frac{1}{\sin^2(\vartheta)}\frac{\partial^2}{\partial \varphi^2}\right) + {k_s}^2\right]\bar{\chi}\,(r, \vartheta, \varphi, \omega) = 0 \tag{2.40c}$$

The term in round brackets is associated with the angular part of the Laplace operator and can be solved using spherical harmonics Y_m^l for each combination of the degree m and the order l [160]

$$\left(\frac{\partial^2}{\partial\vartheta^2}+\frac{\cos(\vartheta)}{\sin(\vartheta)}\frac{\partial}{\partial\vartheta}+\frac{1}{\sin^2(\vartheta)}\frac{\partial^2}{\partial\varphi^2}\right)Y_m^l(\vartheta,\varphi)=-m(m+1)Y_m^l(\vartheta,\varphi) \tag{2.41}$$

Thereby the spherical harmonics are defined as [84]

$$Y_m^l(\vartheta,\varphi)=\sqrt{\frac{2m+1}{2}\frac{(m-l)!}{(m+l)!}}\,P_m^l\left(\cos\left(\vartheta\right)\right)\,\mathrm{e}^{\mathrm{i}l\varphi}=\check{P}_m^l\left(\cos\left(\vartheta\right)\right)\,\mathrm{e}^{\mathrm{i}l\varphi} \tag{2.42}$$

with the associated Legendre polynomials defined for $l\neq 0$ by

$$P_m^l\left(x\right)=\frac{(-1)^l}{2^m m!}\left(1-x^2\right)^{l/2}\frac{\mathrm{d}^{l+m}}{\mathrm{d}x^{l+m}}\left(x^2-1\right)^m \tag{2.43}$$

The spherical harmonics form an orthogonal system on the unit sphere [240, 241]. Therefore, they generate a complete basis and each continuous function on a spherical surface can be expressed by a series of spherical harmonics [242]. In order to apply Eq. (2.41) for the solution of the partial differential Eqs. (2.40), the scalar potentials $\bar{\Phi}$, $\bar{\psi}$ and $\bar{\chi}$ are further developed into series of spherical harmonics. [84]

$$\bar{\Phi}\left(r,\vartheta,\varphi,\omega\right) = \sum_{m=0}^{\infty}\sum_{l=-m}^{m}\hat{\Phi}\left(r,m,l,\omega\right)Y_m^l(\vartheta,\varphi) \tag{2.44a}$$

$$\bar{\psi}\left(r,\vartheta,\varphi,\omega\right) = \sum_{m=0}^{\infty}\sum_{l=-m}^{m}\hat{\psi}\left(r,m,l,\omega\right)Y_m^l(\vartheta,\varphi) \tag{2.44b}$$

$$\bar{\chi}\left(r,\vartheta,\varphi,\omega\right) = \sum_{m=0}^{\infty}\sum_{l=-m}^{m}\hat{\chi}\left(r,m,l,\omega\right)Y_m^l(\vartheta,\varphi) \tag{2.44c}$$

Substituting the series expansions of the Eqs. (2.44) into the Eqs. (2.40) together with a comparison of the coefficients with Eq. (2.41), this finally leads to the following system of ordinary differential equations for each combination of the series members (m,l)

$$\left[\frac{\partial^2}{\partial r^2}+\frac{2}{r}\frac{\partial}{\partial r}+\left({k_p}^2-\frac{m\left(m+1\right)}{r^2}\right)\right]\hat{\Phi}\left(r,m,l,\omega\right)=0 \tag{2.45a}$$

$$\left[\frac{\partial^2}{\partial r^2}+\frac{2}{r}\frac{\partial}{\partial r}+\left({k_s}^2-\frac{m\left(m+1\right)}{r^2}\right)\right]\hat{\psi}\left(r,m,l,\omega\right)=0 \tag{2.45b}$$

$$\left[\frac{\partial^2}{\partial r^2}+\frac{2}{r}\frac{\partial}{\partial r}+\left({k_s}^2-\frac{m\left(m+1\right)}{r^2}\right)\right]\hat{\chi}\left(r,m,l,\omega\right)=0 \tag{2.45c}$$

Eqs. (2.45) are also Bessel differential equations and can be solved using spherical Hankel functions of first $h_m^{(1)}$ and second kind $h_m^{(2)}$ given in Appx. A.5.1 [84, 162, 243].

$$\hat{\Phi}\left(r,m,l,\omega\right) = \hat{C}_{1lm}\, h_m^{(1)}\left(|k_p|r\right) + \hat{C}_{4lm}\, h_m^{(2)}\left(|k_p|r\right) \tag{2.46a}$$

$$\hat{\psi}\left(r,m,l,\omega\right) = \hat{C}_{2lm}\, h_m^{(1)}\left(|k_s|r\right) + \hat{C}_{5lm}\, h_m^{(2)}\left(|k_s|r\right) \tag{2.46b}$$

$$\hat{\chi}\left(r,m,l,\omega\right) = \hat{C}_{3lm}\, h_m^{(1)}\left(|k_s|r\right) + \hat{C}_{6lm}\, h_m^{(2)}\left(|k_s|r\right) \tag{2.46c}$$

If an external load $\hat{\mathbf{P}}^{\mathbf{fs\,sph}}_{\mathbf{\Gamma_s\,ITM}}$ is applied at the surface of the spherical cavity Γ_s, spatially propagating and evanescent waves, w.r.t. the spherical coordinate system, are introduced into the soil. The corresponding stresses and displacements inside the soil can be expressed in dependency of the wave amplitudes $\hat{\mathbf{C}}^{\mathbf{fs\,sph}}_{\mathbf{ITM}}$. With the matrices of Appx. A.4 they yield

$$\hat{\boldsymbol{\sigma}}^{\mathbf{fs\,sph}}_{\mathbf{ITM}} = \hat{\mathbf{S}}^{\mathbf{fs\,sph}}_{\mathbf{ITM}}\, \hat{\mathbf{C}}^{\mathbf{fs\,sph}}_{\mathbf{ITM}} \tag{2.47a}$$

$$\hat{\mathbf{u}}^{\mathbf{fs\,sph}}_{\mathbf{ITM}} = \hat{\mathbf{U}}^{\mathbf{fs\,sph}}_{\mathbf{ITM}}\, \hat{\mathbf{C}}^{\mathbf{fs\,sph}}_{\mathbf{ITM}} \tag{2.47b}$$

Analogously to the fullspace with cylindrical cavity, for negative frequencies the spherical Hankel functions $h_m^{(2)}\left(|k_s|r\right)$ in Eqs. (2.46) are related to waves increasing with growing distance r or propagating against the radial coordinate back to the source. For a fullspace with spherical cavity exhibiting an infinite extension in radial direction, this type of waves disobeys the Sommerfeld radiation condition. Therefore, the coefficients $\hat{C}_{4lm}$ to $\hat{C}_{6lm}$ are set to zero [160]. The remaining unknowns $\hat{C}_{1lm}$ to $\hat{C}_{3lm}$ can be determined applying the local boundary conditions on the spherical surface $\hat{\sigma}^{\mathrm{fs\,sph}}_{rj,\Gamma_\mathrm{s}}(r,m,l,\omega) = -\hat{p}^{\mathrm{fs\,sph}}_{rj,\Gamma_\mathrm{s}}(r,m,l,\omega)$ with $j = r,\vartheta,\varphi$. With the wave amplitudes $\hat{\mathbf{C}}^{\mathbf{fs\,sph}}_{\mathbf{ITM}}$, all stresses and displacements at every position in the halfspace can be determined in dependency on (r,m,l,ω) in a postprocessing step applying Eqs. (2.47). The results for positive frequencies are completed as conjugate complex counterparts in the transformed domain. The system response in the original domain (r,ϑ,φ,t) is obtained by a spherical harmonic series synthesize $m,l \rightarrow \vartheta,\varphi$ and an inverse Fourier transform $\omega \rightarrow t$.

However, the solutions for the fullspace with spherical cavity derived above are only valid for the dynamic case, as for a static load the used solution approaches are not complete [160].

3 Integral Transform Method substructures

In the previous chapter, fundamental solutions of the Lamé equation for systems with either one or several horizontal, a cylindrical or a spherical boundary were presented. The obtained fundamental systems are now superposed and coupled in order to derive solutions for more complex systems. In Sec. 3.1 and 3.2 the halfspace and the fullspace with cylindrical cavity are used to deduce a stiffness formulation for a halfspace with one or two cylindrical cavities resp. indentations. The dynamic stiffness matrix for a halfspace with spherical cavity or indentation is presented in Sec. 3.3. Subsequently the stiffness of the discrete soil stratification from Sec. 2.4 is coupled with the above established systems, applying the compatibility conditions at the common interface, allowing also a representation of multilayered soils with local cylindrical or spherical excavations. Finally, in Sec. 3.5 some computational and numerical aspects are highlighted, which are important for the interpretation of the results later on. Furthermore, similarity measures for the assessment of the quality of the obtained results are introduced and an insight into the parallelized implementation is given.

3.1 Halfspace with one cylindrical cavity

3.1.1 Superposition procedure and dynamic stiffness matrix

In this section, the solution for a halfspace with cylindrical cavity, as depicted in Fig. 3.1c, is deduced from the superposition of the fundamental systems halfspace and fullspace with cylindrical cavity. The final system has two boundaries, namely the halfspace surface Λ and the cylindrical surface Γ_c. The superposition of the stresses and displacements of the two fundamental systems on Λ and Γ_c has to satisfy the boundary conditions $\hat{\sigma}_{iz,\Lambda}(k_x,k_y,z,\omega) = -\hat{p}_{iz,\Lambda}(k_x,k_y,z,\omega)$ and $\hat{\sigma}_{jr,\Gamma_c}(k_x,r,n,\omega) = -\hat{p}_{jr,\Gamma_c}(k_x,r,n,\omega)$ present at the resulting system halfspace with cylindrical cavity. Thus, it is necessary to be able to evaluate both fundamental systems on Λ and Γ_c.

The solution for the fundamental system halfspace is given in the (k_x,k_y,z,ω) domain, whereas the solution for the fullspace with cylindrical cavity is defined w.r.t. (k_x,r,n,ω). However,

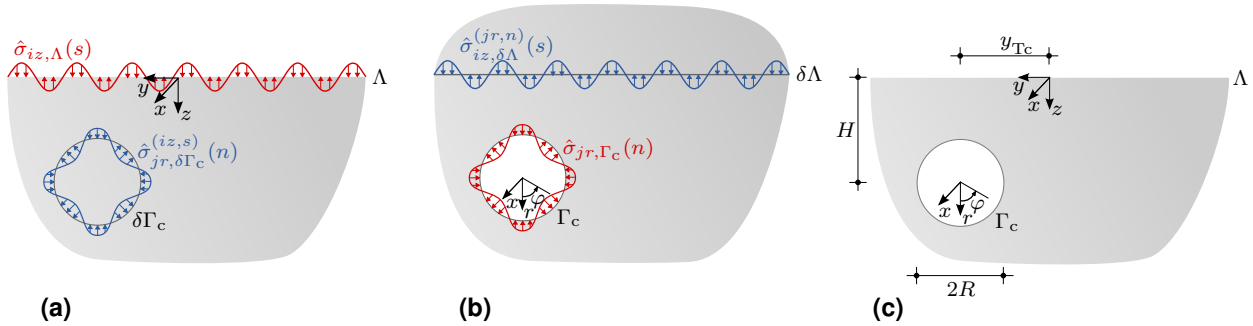

Figure 3.1: Fundamental systems (a) halfspace and (b) fullspace with cylindrical cavity for the superposition to the (c) halfspace with cylindrical cavity.

for both subsystems the response and thus also the superposition can be determined in dependency of (k_x,ω). With that and due to the length invariance of the system, it is possible to reduce the originally three dimensional computations to a series of independent two dimensional calculations for each combination of k_x and ω. The information of the third dimension is stored in the wavenumber k_x and the 3D results in the original domain are obtained after an inverse Fourier transform. This leads to an extremely efficient 2.5D approach, allowing a parallelized implementation that considerably reduces the computation times. [100, 162]

For the evaluation of the stress and displacement states on the two boundaries for both fundamental systems, a virtual cylindrical surface $\delta\Gamma_c$ is introduced into the halfspace (Fig. 3.1a) as well as a virtual halfspace surface $\delta\Lambda$ into the fullspace with cylindrical cavity (Fig. 3.1b). Thereby, the position of the cavity itself within the halfspace has no influence on the superposition procedure. For a pure translation of the Cartesian reference frame, the stress and displacement components remain unchanged, since the transformation matrices are equal to the identity matrix in this case. As the horizontal shift of the cavity can always be performed within the Cartesian reference frame, the transformation matrices from Cartesian to polar and vice versa (given in Frühe and Müller [160]) do not have to be modified. After the transformation into a common basis, the stresses and displacements on the boundaries Λ and Γ_c can thus be superposed directly.

Fundamental system halfspace

Firstly, unit stress states $\hat{\sigma}_{iz,\Lambda}(s)$ with $i = x,y,z$ in dependency of the discrete wavenumbers $k_y = s\Delta k_y$ with $s = -N_y/2,...,(N_y/2-1)$ are applied on the halfspace surface Λ. These lead to resulting stresses $\hat{\sigma}^{(iz,s)}_{iz,\delta\Gamma_c}(s)$ on the virtual surface $\delta\Gamma_c$ w.r.t. (k_x,k_y,z,ω), determined according to Sec. 2.2. To enable the superposition of these stresses with those of the fullspace with cylindrical cavity, they are transformed into the basis corresponding to the latter

(k_x,r,n,ω). Therefore, initially a Fourier series synthesis $k_y \rightarrow y$ is applied, followed by a transformation into polar coordinates $y,z \rightarrow r,\varphi$ and a Fourier series expansion in the circumferential direction $\varphi \rightarrow n$. Hence, each unit load $\hat{\sigma}_{iz,\Lambda}(s)$ on Λ for a defined wavenumber s leads to stresses $\hat{\sigma}^{(iz,s)}_{jr,\delta\Gamma_c}(n)$ with $j = r,x,\varphi$ on $\delta\Gamma_c$ for each series member n described in the (k_x,r,n,ω) domain. [84, 162]

Fundamental system fullspace with cylindrical cavity

Analogously, unit stress states $\hat{\sigma}_{jr,\Gamma_c}(n)$ with $j = r,x,\varphi$ in dependency of the discrete Fourier series members $n = 1,...,N_\varphi$ are applied on the cylindrical surface Γ_c. These lead to resulting stresses $\hat{\sigma}^{(jr,n)}_{jr,\delta\Lambda}(n)$ on the virtual halfspace surface $\delta\Lambda$ w.r.t. (k_x,r,n,ω) determined according to Sec. 2.5. To enable the superposition of these stresses with those of the halfspace, they are transformed into the basis corresponding to the latter (k_x,k_y,z,ω). Therefore, initially a Fourier series synthesis $n \rightarrow \varphi$ is applied, followed by a transformation into Cartesian coordinates $r,\varphi \rightarrow y,z$ and a Fourier series expansion w.r.t. the $y-$coordinate $y \rightarrow k_y$. Hence, each unit load $\hat{\sigma}_{jr,\Gamma_c}(n)$ on Γ_c for a defined Fourier series member n leads to stresses $\hat{\sigma}^{(jr,n)}_{iz,\delta\Lambda}(s)$ with $i = x,y,z$ on $\delta\Lambda$ for each wavenumber s described in the (k_x,k_y,z,ω) domain. [84, 162]

Superposition of fundamental systems

The superposition of the stresses on the two surfaces Λ and Γ_c has to fulfill the external boundary conditions applied on the halfspace with cylindrical cavity. Thus, the amplitudes of the unit stresses $\hat{C}_{iz,\Lambda}(s)$ on Λ and $\hat{C}_{jr,\Gamma_c}(n)$ on Γ_c can be determined solving the following system of equations

$$\hat{C}_{iz,\Lambda}(s)\,\hat{\sigma}_{iz,\Lambda}(s) + \sum_{n=1}^{N_\varphi} \sum_{j=r,x,\varphi} \hat{C}_{jr,\Gamma_c}(n)\,\hat{\sigma}^{(jr,n)}_{iz,\delta\Lambda}(s) \qquad = -\hat{p}_{iz,\Lambda}(s) \tag{3.1}$$

$$\sum_{s=-N_y/2}^{N_y/2-1} \sum_{i=x,y,z} \hat{C}_{iz,\Lambda}(s)\,\hat{\sigma}^{(iz,s)}_{jr,\delta\Gamma_c}(n) + \hat{C}_{jr,\Gamma_c}(n)\,\hat{\sigma}_{jr,\Gamma_c}(n) = -\hat{p}_{jr,\Gamma_c}(n) \tag{3.2}$$

Eqs. (3.1) and (3.2) can be written in matrix notation as

$$\underbrace{\begin{bmatrix} \hat{\mathbf{S}}^{\mathbf{hs\ cyl}}_{\mathbf{\Lambda\Lambda_{ITM}}} & \hat{\mathbf{S}}^{\mathbf{hs\ cyl}}_{\mathbf{\Lambda\Gamma_{c}ITM}} \\ \hat{\mathbf{S}}^{\mathbf{hs\ cyl}}_{\mathbf{\Gamma_c\Lambda_{ITM}}} & \hat{\mathbf{S}}^{\mathbf{hs\ cyl}}_{\mathbf{\Gamma_c\Gamma_{c}\,ITM}} \end{bmatrix}}_{\hat{\mathbf{S}}^{\mathbf{hs\ cyl}}_{\mathbf{ITM}}} \underbrace{\begin{pmatrix} \hat{\mathbf{C}}^{\mathbf{hs\ cyl}}_{\mathbf{\Lambda_{ITM}}} \\ \hat{\mathbf{C}}^{\mathbf{hs\ cyl}}_{\mathbf{\Gamma_{c}ITM}} \end{pmatrix}}_{\hat{\mathbf{C}}^{\mathbf{hs\ cyl}}_{\mathbf{ITM}}} = \underbrace{\begin{pmatrix} \hat{\mathbf{P}}^{\mathbf{hs\ cyl}}_{\mathbf{\Lambda_{ITM}}} \\ \hat{\mathbf{P}}^{\mathbf{hs\ cyl}}_{\mathbf{\Gamma_{c}ITM}} \end{pmatrix}}_{\hat{\mathbf{P}}^{\mathbf{hs\ cyl}}_{\mathbf{ITM}}} \tag{3.3}$$

The matrices $\hat{\mathbf{S}}^{\mathbf{hs\ cyl}}_{\alpha\beta_{\mathbf{ITM}}}$ with $\alpha = \Lambda,\Gamma_c$ and $\beta = \Lambda,\Gamma_c$ contain the results for the stresses on the surface α for a unit load $\hat{\mathbf{P}}^{\mathbf{hs\ cyl}}_{\beta_{\mathbf{ITM}}}$ on surface β in dependency of the unknown amplitudes $\hat{\mathbf{C}}^{\mathbf{hs\ cyl}}_{\alpha_{\mathbf{ITM}}}$ on surface β. [84]

With Eqs. (3.3) it is possible to determine the coefficients $\hat{\mathbf{C}}^{\mathbf{hs\ cyl}}_{\mathbf{ITM}}$. Thus the displacements on the halfspace surface $\hat{u}_{i,\Lambda}$ with $i = x,y,z$ and the cylindrical surface $\hat{u}_{j,\Gamma_c}$ with $j = r,x,\varphi$ of the superposed system can be calculated by the following system of equations

$$\hat{u}_{i,\Lambda}(s) = \sum_{k=x,y,z} \hat{C}_{kz,\Lambda}(s)\ \hat{u}^{(kz,s)}_{i,\Lambda}(s) + \sum_{n=1}^{N_\varphi} \sum_{l=r,x,\varphi} \hat{C}_{lr,\Gamma_c}(n)\ \hat{u}^{(lr,n)}_{i,\delta\Lambda}(s) \tag{3.4}$$

$$\hat{u}_{j,\Gamma_c}(n) = \sum_{s=-N_y/2}^{N_y/2-1} \sum_{k=x,y,z} \hat{C}_{kz,\Lambda}(s)\ u^{(kz,s)}_{j,\delta\Gamma_c}(n) + \sum_{l=r,x,\varphi} \hat{C}_{lr,\Gamma_c}(n)\ u^{(lr,n)}_{j,\Gamma_c}(n) \tag{3.5}$$

In matrix notation, the Eqs. (3.4) and (3.5) can be written as

$$\underbrace{\begin{pmatrix} \hat{\mathbf{u}}^{\mathbf{hs\ cyl}}_{\mathbf{\Lambda\,ITM}} \\ \hat{\mathbf{u}}^{\mathbf{hs\ cyl}}_{\mathbf{\Gamma_c\,ITM}} \end{pmatrix}}_{\hat{\mathbf{u}}^{\mathbf{hs\ cyl}}_{\mathbf{ITM}}} = \underbrace{\begin{bmatrix} \hat{\mathbf{U}}^{\mathbf{hs\ cyl}}_{\mathbf{\Lambda\Lambda\,ITM}} & \hat{\mathbf{U}}^{\mathbf{hs\ cyl}}_{\mathbf{\Lambda\Gamma_c\,ITM}} \\ \hat{\mathbf{U}}^{\mathbf{hs\ cyl}}_{\mathbf{\Gamma_c\Lambda\,ITM}} & \hat{\mathbf{U}}^{\mathbf{hs\ cyl}}_{\mathbf{\Gamma_c\Gamma_c\,ITM}} \end{bmatrix}}_{\hat{\mathbf{U}}^{\mathbf{hs\ cyl}}_{\mathbf{ITM}}} \underbrace{\begin{pmatrix} \hat{\mathbf{C}}^{\mathbf{hs\ cyl}}_{\mathbf{\Lambda\,ITM}} \\ \hat{\mathbf{C}}^{\mathbf{hs\ cyl}}_{\mathbf{\Gamma_c\,ITM}} \end{pmatrix}}_{\hat{\mathbf{C}}^{\mathbf{hs\ cyl}}_{\mathbf{ITM}}} \tag{3.6}$$

The matrices $\hat{\mathbf{U}}^{\mathbf{hs\ cyl}}_{\alpha\beta\mathbf{ITM}}$ contain the displacements due to the unit stress states and are scaled with the amplitudes $\hat{\mathbf{C}}^{\mathbf{hs\ cyl}}_{\beta\mathbf{ITM}}$ to gain the actual displacements of the system $\hat{\mathbf{u}}^{\mathbf{hs\ cyl}}_{\mathbf{ITM}}$.

Dynamic stiffness matrix

Combining Eqs. (3.3) and (3.6), the complex dynamic stiffness matrix

$$\hat{\mathbf{K}}^{\mathbf{hs\ cyl}}_{\mathbf{ITM}} = \hat{\mathbf{S}}^{\mathbf{hs\ cyl}}_{\mathbf{ITM}}\, \hat{\mathbf{U}}^{\mathbf{hs\ cyl}\ -1}_{\mathbf{ITM}} \tag{3.7}$$

of the ITM substructure halfspace with cylindrical cavity can be derived, separated for the parameters on the two surfaces Λ and Γ_c.

$$\underbrace{\begin{bmatrix} \hat{\mathbf{K}}^{\mathbf{hs\ cyl}}_{\mathbf{\Lambda\Lambda_{ITM}}} & \hat{\mathbf{K}}^{\mathbf{hs\ cyl}}_{\mathbf{\Lambda\Gamma_c\,ITM}} \\ \hat{\mathbf{K}}^{\mathbf{hs\ cyl}}_{\mathbf{\Gamma_c\Lambda_{ITM}}} & \hat{\mathbf{K}}^{\mathbf{hs\ cyl}}_{\mathbf{\Gamma_c\Gamma_c\,ITM}} \end{bmatrix}}_{\hat{\mathbf{K}}^{\mathbf{hs\ cyl}}_{\mathbf{ITM}}} \underbrace{\begin{pmatrix} \hat{\mathbf{u}}^{\mathbf{hs\ cyl}}_{\mathbf{\Lambda_{ITM}}} \\ \hat{\mathbf{u}}^{\mathbf{hs\ cyl}}_{\mathbf{\Gamma_c\,ITM}} \end{pmatrix}}_{\hat{\mathbf{u}}^{\mathbf{hs\ cyl}}_{\mathbf{ITM}}} = \underbrace{\begin{pmatrix} \hat{\mathbf{P}}^{\mathbf{hs\ cyl}}_{\mathbf{\Lambda_{ITM}}} \\ \hat{\mathbf{P}}^{\mathbf{hs\ cyl}}_{\mathbf{\Gamma_c\,ITM}} \end{pmatrix}}_{\hat{\mathbf{P}}^{\mathbf{hs\ cyl}}_{\mathbf{ITM}}} \tag{3.8}$$

3.1.2 Cylindrical indentation at the soil surface

The stiffness matrix for the halfspace with cylindrical indentation can also be derived by the superposition of the fundamental systems halfspace and fullspace with cylindrical cavity. In contrast to the case of the fully embedded cavity, for the indentation the virtual cylindrical

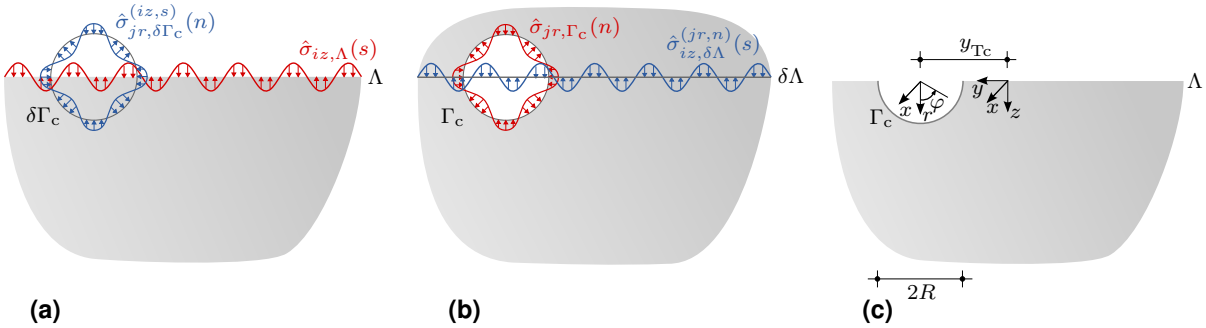

Figure 3.2: Fundamental systems (a) halfspace and (b) fullspace with cylindrical cavity for the superposition to the (c) halfspace with cylindrical indentation.

surface $\delta\Gamma_c$ is now partly located above the ground surface Λ and the virtual halfspace surface $\delta\Lambda$ is partly located within the boundary Γ_c of the cylindrical cavity inside the fullspace (Fig. 3.2).

Therefore, the resulting stresses $\hat{\sigma}^{(iz,s)}_{iz,\delta\Gamma_c}(s)$ on the virtual surface $\delta\Gamma_c$ due to the unit stress states $\hat{\sigma}_{iz,\Lambda}(s)$ can only be evaluated below the ground surface $z \geq 0$. Analogously, it is only possible to evaluate the stresses $\hat{\sigma}^{(jr,n)}_{jr,\delta\Lambda}(n)$, induced by the unit stress states $\hat{\sigma}_{jr,\Gamma_c}(n)$, outside of the cylindrical cavity $r \geq R$. The stresses above the ground surface Λ and inside the cavity boundary Γ_c are set to zero, since the superposition of the stresses only needs to be in equilibrium with the external loads acting on the boundaries of the resulting system halfspace with cylindrical indentation. As the superposition is carried out in the transformed domain (k_x,k_y,z,ω) on Λ and (k_x,r,n,ω) on Γ_c, a Fourier series expansion of the stresses of both fundamental systems is carried out w.r.t. the $y-$coordinate on the ground surface and w.r.t. the circumferential direction on the cylindrical boundary. For this reason, the resulting stresses $\hat{\sigma}^{(jr,n)}_{iz,\delta\Lambda}(s)$ and $\hat{\sigma}^{(iz,s)}_{jr,\delta\Gamma_c}(n)$ are not superposed with the unit stress states $\hat{\sigma}_{iz,\Lambda}(s)$ and $\hat{\sigma}_{jr,\Gamma_c}(n)$ directly on discrete points, but the corresponding series members are summed up (cp. Eqs. (3.1) and (3.2)) to fulfill the boundary conditions of the total system, thereby satisfying the equilibrium of external and internal stresses approximately in sense of the series expansion.

In case of a discrete Fourier series expansion, the number of discrete points in the original domain must always coincide with number of series members in the transformed domain. Therefore, within the numerical implementation of the superposition procedure, it is necessary to introduce nodes also on the physically not existent parts of the boundaries above the ground surface and inside the cavity, in order to allow a series expansion of $\hat{\sigma}^{(jr,n)}_{iz,\delta\Lambda}(s)$ over Λ and $\hat{\sigma}^{(iz,s)}_{jr,\delta\Gamma_c}(n)$ over Γ_c with the same number of series members s resp. n, as used for the unit stress states. Since the amplitude of the stresses on the nodes for $z \leq 0$ and $r \leq R$ were set to zero, a discontinuity at the transition point can occur prior the series expansion. Hence, to accurately represent the discontinuity in the transformed domain and thus to ensure a good

quality of the solution, a larger number of series members is needed for the halfspace with indentation compared to the halfspace with the cavity (i.e. $N_{\varphi,\mathrm{ind}} \approx 2N_{\varphi,\mathrm{cav}}$ for a constant geometry and discretization).

Also, the displacements due to the unit stress states are only evaluated below the halfspace surface and outside the cavity. For the superposition on the halfspace surface Λ and the cylindrical surface Γ they are transformed into the resp. basis and developed into Fourier series w.r.t. the $y-$coordinate resp. the circumferential direction φ, with the same number of series members for both fundamental systems. Thus, in Eqs. (3.4) and (3.5) also the corresponding series members of the displacements are summed up to fulfill the boundary conditions of the total system. Finally, with Eqs. (3.3) and (3.6) the dynamic stiffness matrix for the halfspace with indentation results analogously to the halfspace with cylindrical cavity as given in Eq. (3.8).

3.2 Halfspace with two cylindrical cavities

In this section, the stiffness matrix for a halfspace with two cylindrical cavities or indentations, depicted in Fig. 3.3 shall be derived. The final system contains three boundaries, namely the halfspace surface Λ and the two cylindrical surfaces Γ_{c_1} and Γ_{c_2}. The solution is deduced from the superposition of the fundamental systems halfspace and two fullspaces with each one cylindrical cavity [245]. The superposition of the stresses and displacements of all involved fundamental systems must satisfy the boundary conditions acting on the overall system. Therefore, each of the fundamental systems needs to be evaluated on the halfspace surface and the two cylindrical surfaces.

For the evaluation of the stresses and displacements, two virtual cylindrical surfaces $\delta\Gamma_{\mathrm{c}_1}$ and $\delta\Gamma_{\mathrm{c}_2}$ are introduced into the halfspace. Furthermore, a virtual horizontal surface $\delta\Lambda$ and a second virtual cylindrical surface $\delta\Gamma_{\mathrm{c}_1}$ resp. $\delta\Gamma_{\mathrm{c}_2}$ are inserted into the corresponding fullspaces with cylindrical cavity. Analogous to Sec. 3.1, unit stress states are applied on

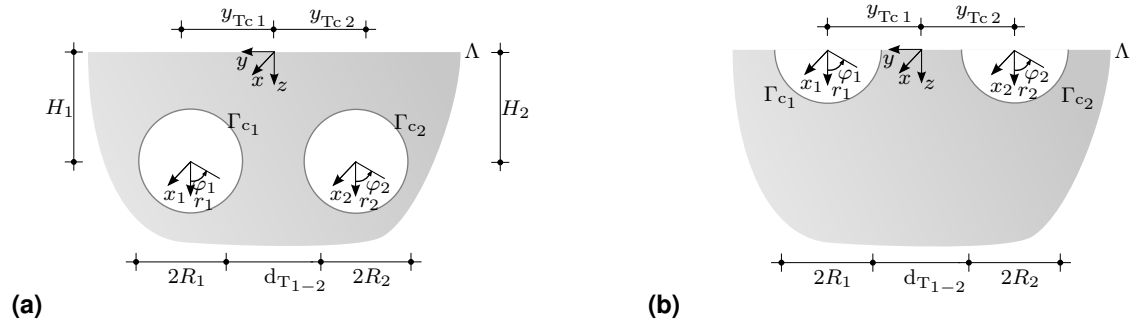

Figure 3.3: Halfspace with (a) two cylindrical cavities cp. [244] and (b) two cylindrical indentations.

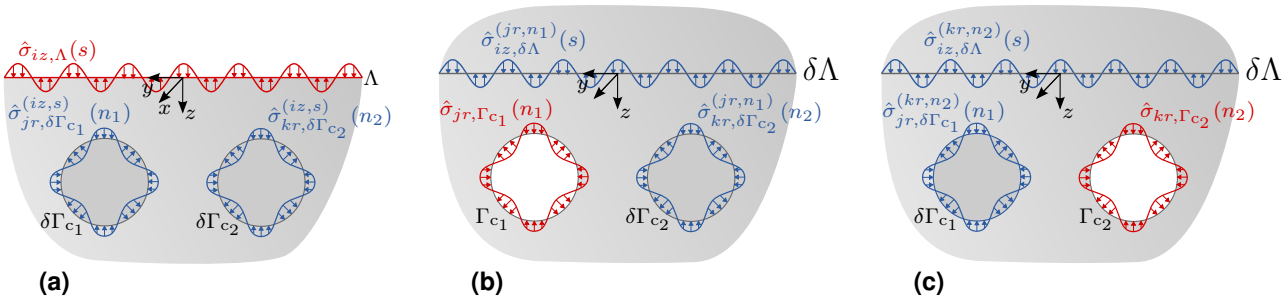

Figure 3.4: Fundamental systems (a) halfspace and (b),(c) fullspace with cylindrical cavity for the superposition to the system halfspace with two cylindrical cavities cp. [244].

the real surfaces Λ, Γ_{c_1} and Γ_{c_2} within each of the fundamental systems and the resulting stresses are evaluated on the respective virtual surfaces as illustrated in Fig. 3.4.

Fundamental system halfspace

Due to the unit stress states $\hat{\sigma}_{iz,\Lambda}(s)$ with $i = x,y,z$ on Λ, resulting stresses occur on $\delta\Gamma_{c_1}$ and $\delta\Gamma_{c_2}$, which are firstly determined in the (k_x,k_y,z,ω) domain according to Sec. 2.2. For the superposition with the stresses of the two fullspace systems and to comply with the external boundary conditions on Γ_{c_1} and Γ_{c_2}, they are firstly transformed into the respective cylindrical basis and then expanded into Fourier series along the circumference of the cylinders. Hence, each unit stress state $\hat{\sigma}_{iz,\Lambda}(s)$ leads to the stresses $\hat{\sigma}^{(iz,s)}_{jr,\delta\Gamma_{c_1}}(n_1)$ on $\delta\Gamma_{c_1}$ with $j = x,r,\varphi$ and $n_1 = 1,...,N_{\varphi_1}$ as well as $\hat{\sigma}^{(iz,s)}_{kr,\delta\Gamma_{c_2}}(n_2)$ on $\delta\Gamma_{c_2}$ with $k = x,r,\varphi$ and $n_2 = 1,...,N_{\varphi_2}$ defined in the (k_x,r,n,ω) domain. [244]

Fundamental system fullspace with cylindrical cavity Γ_{c_1}

Due to the unit stress states $\hat{\sigma}_{jr,\Gamma_{c_1}}(n_1)$ on Γ_{c_1}, resulting stresses occur on $\delta\Lambda$ and $\delta\Gamma_{c_2}$, which are firstly determined w.r.t. the cylindrical basis of the cavity Γ_{c_1} in the (k_x,r,n,ω) domain according to Sec. 2.5. For the superposition with the other fundamental systems and to comply with the external boundary conditions on Λ, the resulting stresses on the virtual halfspace surface $\delta\Lambda$ are firstly transformed into a Cartesian basis and then expanded into a Fourier series w.r.t. the $y-$coordinate. Thus each unit load $\hat{\sigma}_{jr,\Gamma_{c_1}}(n_1)$ with $j = r,x,\varphi$ leads to the stresses $\hat{\sigma}^{(jr,n_1)}_{iz,\delta\Lambda}(s)$ with $i = x,y,z$ on $\delta\Lambda$. [244]

The resulting stresses on $\delta\Gamma_{c_2}$ have to be transformed into the cylindrical coordinate system of the cavity Γ_{c_2} in order enable the superposition. Hereby, a transformation of the stresses from one cylindrical to another cylindrical coordinate system needs to be performed. Although the base vectors of both cylindrical reference systems are normalized w.r.t. the radial coordinate r, different base vectors are obtained at the same discretization point depending on the chosen coordinate system and thus also different components of the stress tensor in dependency on

the angles φ_1 and φ_2 result. Thereby the reason for the different base vectors is that the cylindrical basis in contrast to a Cartesian basis is not stationary. After this transformation and a Fourier series expansion along the circumferential direction, the stresses $\hat{\sigma}^{(jr,n_1)}_{kr,\delta\Gamma_{c_2}}(n_2)$ on $\delta\Gamma_{c_2}$ with $k = r,x,\varphi$ and $n_2 = 1,...,N_{\varphi_2}$ result from each unit stress state $\hat{\sigma}_{jr,\Gamma_{c_1}}(n_1)$ on Γ_{c_1}. [244]

Fundamental system fullspace with cylindrical cavity Γ_{c_2}

Analogously, unit stress states $\hat{\sigma}_{kr,\Gamma_{c_2}}(n_2)$ are applied on Γ_{c_2} and the resulting stresses on $\delta\Lambda$ and $\delta\Gamma_{c_1}$ are determined firstly w.r.t. the cylindrical basis of the cavity Γ_{c_2} in the (k_x,r,n,ω) domain. The stresses on $\delta\Lambda$ are transformed into a Cartesian reference system and expanded into a Fourier series w.r.t. the $y-$coordinate finally leading to $\hat{\sigma}^{(kr,n_2)}_{iz,\delta\Lambda}(s)$ with $i = x,y,z$ on $\delta\Lambda$. The stresses on $\delta\Gamma_{c_1}$ are firstly transformed into the cylindrical basis of the cavity Γ_{c_1} and expanded into a Fourier series along the circumferential direction finally leading to the stresses $\hat{\sigma}^{(kr,n_2)}_{jr,\delta\Gamma_{c_1}}(n_1)$ with $j = x,r,\varphi$ and $n_1 = 1,...,N_{\varphi_1}$ on $\delta\Gamma_{c_1}$. [244]

Superposition of fundamental systems

The superposition of the stresses on the three surfaces Λ, Γ_{c_1} and Γ_{c_2} has to fulfill the external boundary conditions applied on the halfspace with two cylindrical cavities. Thus, the amplitudes of the unit stresses $\hat{C}_{iz,\Lambda}(s)$ on Λ, $\hat{C}_{jr,\Gamma_{c_1}}(n_1)$ on Γ_{c_1} and $\hat{C}_{kr,\Gamma_{c_2}}(n_2)$ on Γ_{c_2} can be determined solving the following system of equations

$$\begin{aligned}\hat{C}_{iz,\Lambda}(s)\,\hat{\sigma}_{iz,\Lambda}(s) &+ \sum_{n_1=1}^{N_{\varphi_1}}\sum_{j=r,x,\varphi}\hat{C}_{jr,\Gamma_{c_1}}(n_1)\,\hat{\sigma}^{(jr,n_1)}_{iz,\delta\Lambda}(s)\\ &+ \sum_{n_2=1}^{N_{\varphi_2}}\sum_{k=r,x,\varphi}\hat{C}_{kr,\Gamma_{c_2}}(n_2)\,\hat{\sigma}^{(kr,n_2)}_{iz,\delta\Lambda}(s) = -\hat{p}_{iz,\Lambda}(s)\end{aligned} \tag{3.9}$$

$$\begin{aligned}\hat{C}_{jr,\Gamma_{c_1}}(n_1)\,\hat{\sigma}_{jr,\Gamma_{c_1}}(n_1) + &\sum_{s=-N_y/2}^{N_y/2-1}\sum_{i=x,y,z}\hat{C}_{iz,\Lambda}(s)\,\hat{\sigma}^{(iz,s)}_{jr,\delta\Gamma_{c_1}}(n_1)\\ &+ \sum_{n_2=1}^{N_{\varphi_2}}\sum_{k=r,x,\varphi}\hat{C}_{kr,\Gamma_{c_2}}(n_2)\,\hat{\sigma}^{(kr,n_2)}_{jr,\delta\Gamma_{c_1}}(n_1) = -\hat{p}_{jr,\Gamma_{c_1}}(n_1)\end{aligned} \tag{3.10}$$

$$\begin{aligned}\hat{C}_{kr,\Gamma_{c_2}}(n_2)\,\hat{\sigma}_{kr,\Gamma_{c_2}}(n_2) + &\sum_{s=-N_y/2}^{N_y/2-1}\sum_{i=x,y,z}\hat{C}_{iz,\Lambda}(s)\,\hat{\sigma}^{(iz,s)}_{kr,\delta\Gamma_{c_2}}(n_2)\\ &+ \sum_{n_1=1}^{N_{\varphi_1}}\sum_{j=r,x,\varphi}\hat{C}_{jr,\Gamma_{c_1}}(n_1)\,\hat{\sigma}^{(jr,n_1)}_{kr,\delta\Gamma_{c_2}}(n_2) = -\hat{p}_{kr,\Gamma_{c_2}}(n_2)\end{aligned} \tag{3.11}$$

Eqs. (3.9) to (3.11) can be written in matrix notation as

$$\underbrace{\begin{bmatrix} \hat{\mathbf{S}}^{\mathbf{hs\,cyl\,tw}}_{\mathbf{\Lambda\Lambda_{ITM}}} & \hat{\mathbf{S}}^{\mathbf{hs\,cyl\,tw}}_{\mathbf{\Lambda\Gamma_{c_1\,ITM}}} & \hat{\mathbf{S}}^{\mathbf{hs\,cyl\,tw}}_{\mathbf{\Lambda\Gamma_{c_2\,ITM}}} \\ \hat{\mathbf{S}}^{\mathbf{hs\,cyl\,tw}}_{\mathbf{\Gamma_{c_1}\Lambda_{ITM}}} & \hat{\mathbf{S}}^{\mathbf{hs\,cyl\,tw}}_{\mathbf{\Gamma_{c_1}\Gamma_{c_1\,ITM}}} & \hat{\mathbf{S}}^{\mathbf{hs\,cyl\,tw}}_{\mathbf{\Gamma_{c_1}\Gamma_{c_2\,ITM}}} \\ \hat{\mathbf{S}}^{\mathbf{hs\,cyl\,tw}}_{\mathbf{\Gamma_{c_2}\Lambda_{ITM}}} & \hat{\mathbf{S}}^{\mathbf{hs\,cyl\,tw}}_{\mathbf{\Gamma_{c_2}\Gamma_{c_1\,ITM}}} & \hat{\mathbf{S}}^{\mathbf{hs\,cyl\,tw}}_{\mathbf{\Gamma_{c_2}\Gamma_{c_2\,ITM}}} \end{bmatrix}}_{\hat{\mathbf{S}}^{\mathbf{hs\,cyl\,tw}}_{\mathbf{ITM}}} \underbrace{\begin{pmatrix} \hat{\mathbf{C}}^{\mathbf{hs\,cyl\,tw}}_{\mathbf{\Lambda_{ITM}}} \\ \hat{\mathbf{C}}^{\mathbf{hs\,cyl\,tw}}_{\mathbf{\Gamma_{c_1\,ITM}}} \\ \hat{\mathbf{C}}^{\mathbf{hs\,cyl\,tw}}_{\mathbf{\Gamma_{c_2\,ITM}}} \end{pmatrix}}_{\hat{\mathbf{C}}^{\mathbf{hs\,cyl\,tw}}_{\mathbf{ITM}}} = \underbrace{\begin{pmatrix} \hat{\mathbf{P}}^{\mathbf{hs\,cyl\,tw}}_{\mathbf{\Lambda_{ITM}}} \\ \hat{\mathbf{P}}^{\mathbf{hs\,cyl\,tw}}_{\mathbf{\Gamma_{c_1\,ITM}}} \\ \hat{\mathbf{P}}^{\mathbf{hs\,cyl\,tw}}_{\mathbf{\Gamma_{c_2\,ITM}}} \end{pmatrix}}_{\hat{\mathbf{P}}^{\mathbf{hs\,cyl\,tw}}_{\mathbf{ITM}}} \tag{3.12}$$

whereby the "tw" in the superscript indicates the twin cavities or indentations.

With Eqs. (3.12) it is possible to determine the coefficients $\hat{\mathbf{C}}^{\mathbf{hs\,cyl\,tw}}_{\mathbf{ITM}}$. Thus the displacements on the halfspace surface $\hat{u}_{i,\Lambda}$ with $i = x,y,z$ as well as the cylindrical surfaces $\hat{u}_{j,\Gamma_{c_1}}$ with $j = r,x,\varphi$ and $\hat{u}_{k,\Gamma_{c_2}}$ with $k = r,x,\varphi$ of the superposed system can be calculated by the following system of equations

$$\begin{aligned} \hat{u}_{i,\Lambda}(s) &= \sum_{k=x,y,z} \hat{C}_{kz,\Lambda}(s)\, \hat{u}^{(kz,s)}_{i,\Lambda}(s) + \sum_{n_1=1}^{N_{\varphi_1}} \sum_{l=r,x,\varphi} \hat{C}_{lr,\Gamma_{c_1}}(n_1)\; \hat{u}^{(lr,n_1)}_{i,\delta\Lambda}(s) \\ &\quad + \sum_{n_2=1}^{N_{\varphi_2}} \sum_{m=r,x,\varphi} \hat{C}_{mr,\Gamma_{c_2}}(n_2)\; \hat{u}^{(mr,n_2)}_{i,\delta\Lambda}(s) \end{aligned} \tag{3.13}$$

$$\begin{aligned} \hat{u}_{j,\Gamma_{c_1}}(n_1) &= \sum_{s=-N_y/2}^{N_y/2-1} \sum_{i=x,y,z} \hat{C}_{iz,\Lambda}(s)\, u^{(iz,s)}_{j,\delta\Gamma_{c_1}}(n_1) + \sum_{l=r,x,\varphi} \hat{C}_{lr,\Gamma_{c_1}}(n_1)\, u^{(lr,n_1)}_{j,\Gamma_{c_1}}(n_1) \\ &\quad + \sum_{n_2=1}^{N_{\varphi_2}} \sum_{m=r,x,\varphi} \hat{C}_{mr,\Gamma_{c_2}}(n_2)\; \hat{u}^{(mr,n_2)}_{j,\delta\Gamma_{c_1}}(n_1) \end{aligned} \tag{3.14}$$

$$\begin{aligned} \hat{u}_{k,\Gamma_{c_2}}(n_2) &= \sum_{s=-N_y/2}^{N_y/2-1} \sum_{i=x,y,z} \hat{C}_{iz,\Lambda}(s)\, u^{(iz,s)}_{k,\delta\Gamma_{c_2}}(n_2) + \sum_{n_1=1}^{N_{\varphi_1}} \sum_{m=r,x,\varphi} \hat{C}_{mr,\Gamma_{c_1}}(n_1)\; \hat{u}^{(mr,n_1)}_{k,\delta\Gamma_{c_2}}(n_2) \\ &\quad + \sum_{l=r,x,\varphi} \hat{C}_{lr,\Gamma_{c_2}}(n_2)\, u^{(lr,n_2)}_{k,\Gamma_{c_2}}(n_2) \end{aligned} \tag{3.15}$$

In matrix notation, the Eqs. (3.13) to (3.15) can be written as

$$\underbrace{\begin{pmatrix} \hat{\mathbf{u}}^{\mathbf{hs\,cyl\,tw}}_{\mathbf{\Lambda_{ITM}}} \\ \hat{\mathbf{u}}^{\mathbf{hs\,cyl\,tw}}_{\mathbf{\Gamma_{c_1\,ITM}}} \\ \hat{\mathbf{u}}^{\mathbf{hs\,cyl\,tw}}_{\mathbf{\Gamma_{c_2\,ITM}}} \end{pmatrix}}_{\hat{\mathbf{u}}^{\mathbf{hs\,cyl\,tw}}_{\mathbf{ITM}}} = \underbrace{\begin{bmatrix} \hat{\mathbf{U}}^{\mathbf{hs\,cyl\,tw}}_{\mathbf{\Lambda\Lambda_{ITM}}} & \hat{\mathbf{U}}^{\mathbf{hs\,cyl\,tw}}_{\mathbf{\Lambda\Gamma_{c_1\,ITM}}} & \hat{\mathbf{U}}^{\mathbf{hs\,cyl\,tw}}_{\mathbf{\Lambda\Gamma_{c_2\,ITM}}} \\ \hat{\mathbf{U}}^{\mathbf{hs\,cyl\,tw}}_{\mathbf{\Gamma_{c_1}\Lambda_{ITM}}} & \hat{\mathbf{U}}^{\mathbf{hs\,cyl\,tw}}_{\mathbf{\Gamma_{c_1}\Gamma_{c_1\,ITM}}} & \hat{\mathbf{U}}^{\mathbf{hs\,cyl\,tw}}_{\mathbf{\Gamma_{c_1}\Gamma_{c_2\,ITM}}} \\ \hat{\mathbf{U}}^{\mathbf{hs\,cyl\,tw}}_{\mathbf{\Gamma_{c_2}\Lambda_{ITM}}} & \hat{\mathbf{U}}^{\mathbf{hs\,cyl\,tw}}_{\mathbf{\Gamma_{c_2}\Gamma_{c_1\,ITM}}} & \hat{\mathbf{U}}^{\mathbf{hs\,cyl\,tw}}_{\mathbf{\Gamma_{c_2}\Gamma_{c_2\,ITM}}} \end{bmatrix}}_{\hat{\mathbf{U}}^{\mathbf{hs\,cyl\,tw}}_{\mathbf{ITM}}} \underbrace{\begin{pmatrix} \hat{\mathbf{C}}^{\mathbf{hs\,cyl\,tw}}_{\mathbf{\Lambda_{ITM}}} \\ \hat{\mathbf{C}}^{\mathbf{hs\,cyl\,tw}}_{\mathbf{\Gamma_{c_1\,ITM}}} \\ \hat{\mathbf{C}}^{\mathbf{hs\,cyl\,tw}}_{\mathbf{\Gamma_{c_2\,ITM}}} \end{pmatrix}}_{\hat{\mathbf{C}}^{\mathbf{hs\,cyl\,tw}}_{\mathbf{ITM}}} \tag{3.16}$$

Dynamic stiffness matrix

Combining Eqs. (3.12) and (3.16), the complex dynamic stiffness matrix

$$\hat{\mathbf{K}}_{\mathrm{ITM}}^{\mathbf{hs\,cyl\,tw}} = \hat{\mathbf{S}}_{\mathrm{ITM}}^{\mathbf{hs\,cyl\,tw}}\,\hat{\mathbf{U}}_{\mathrm{ITM}}^{\mathbf{hs\,cyl\,tw}\,-1} \tag{3.17}$$

of the ITM substructure halfspace with two cylindrical cavities or indentations can be derived separated for the parameters on the three surfaces Λ, Γ_{c_1} and Γ_{c_2}.

$$\underbrace{\begin{bmatrix} \hat{\mathbf{K}}_{\mathbf{\Lambda\Lambda}_{\mathrm{ITM}}}^{\mathbf{hs\,cyl\,tw}} & \hat{\mathbf{K}}_{\mathbf{\Lambda\Gamma_{c_1}}_{\mathrm{ITM}}}^{\mathbf{hs\,cyl\,tw}} & \hat{\mathbf{K}}_{\mathbf{\Lambda\Gamma_{c_2}}_{\mathrm{ITM}}}^{\mathbf{hs\,cyl\,tw}} \\ \hat{\mathbf{K}}_{\mathbf{\Gamma_{c_1}\Lambda}_{\mathrm{ITM}}}^{\mathbf{hs\,cyl\,tw}} & \hat{\mathbf{K}}_{\mathbf{\Gamma_{c_1}\Gamma_{c_1}}_{\mathrm{ITM}}}^{\mathbf{hs\,cyl\,tw}} & \hat{\mathbf{K}}_{\mathbf{\Gamma_{c_1}\Gamma_{c_2}}_{\mathrm{ITM}}}^{\mathbf{hs\,cyl\,tw}} \\ \hat{\mathbf{K}}_{\mathbf{\Gamma_{c_2}\Lambda}_{\mathrm{ITM}}}^{\mathbf{hs\,cyl\,tw}} & \hat{\mathbf{K}}_{\mathbf{\Gamma_{c_2}\Gamma_{c_1}}_{\mathrm{ITM}}}^{\mathbf{hs\,cyl\,tw}} & \hat{\mathbf{K}}_{\mathbf{\Gamma_{c_2}\Gamma_{c_2}}_{\mathrm{ITM}}}^{\mathbf{hs\,cyl\,tw}} \end{bmatrix}}_{\hat{\mathbf{K}}_{\mathrm{ITM}}^{\mathbf{hs\,cyl\,tw}}} \underbrace{\begin{pmatrix} \hat{\mathbf{u}}_{\mathbf{\Lambda}_{\mathrm{ITM}}}^{\mathbf{hs\,cyl\,tw}} \\ \hat{\mathbf{u}}_{\mathbf{\Gamma_{c_1}}_{\mathrm{ITM}}}^{\mathbf{hs\,cyl\,tw}} \\ \hat{\mathbf{u}}_{\mathbf{\Gamma_{c_2}}_{\mathrm{ITM}}}^{\mathbf{hs\,cyl\,tw}} \end{pmatrix}}_{\hat{\mathbf{u}}_{\mathrm{ITM}}^{\mathbf{hs\,cyl\,tw}}} = \underbrace{\begin{pmatrix} \hat{\mathbf{P}}_{\mathbf{\Lambda}_{\mathrm{ITM}}}^{\mathbf{hs\,cyl\,tw}} \\ \hat{\mathbf{P}}_{\mathbf{\Gamma_{c_1}}_{\mathrm{ITM}}}^{\mathbf{hs\,cyl\,tw}} \\ \hat{\mathbf{P}}_{\mathbf{\Gamma_{c_2}}_{\mathrm{ITM}}}^{\mathbf{hs\,cyl\,tw}} \end{pmatrix}}_{\hat{\mathbf{P}}_{\mathrm{ITM}}^{\mathbf{hs\,cyl\,tw}}} \tag{3.18}$$

3.3 Halfspace with spherical cavity

3.3.1 Superposition procedure and dynamic stiffness matrix

In this section the solution for a halfspace with spherical cavity or indentation, as depicted in Fig. 3.5c, is deduced from the superposition of the fundamental systems halfspace and fullspace with spherical cavity. The final system has two boundaries, namely the halfspace surface Λ and the spherical surface Γ_{s}. The superposition of the stresses and displacements of the two fundamental systems on Λ and Γ_{s} has to satisfy the boundary conditions $\hat{\sigma}_{iz,\Lambda}(k_x,k_y,z,\omega) = -\hat{p}_{iz,\Lambda}(k_x,k_y,z,\omega)$ with $i = x,y,z$ and $\hat{\sigma}_{rj,\Gamma_{\mathrm{s}}}(r,m,l,\omega) = -\hat{p}_{rj,\Gamma_{\mathrm{s}}}(r,m,l,\omega)$ with $j = r,\vartheta,\varphi$ present at the resulting system halfspace with spherical cavity. Thus, it is necessary to be able to evaluate the both fundamental systems on Λ and Γ_{s}.

The solution for the fundamental system halfspace is given in the (k_x,k_y,z,ω) domain, whereas the solution for the fullspace with spherical cavity is defined w.r.t. (r,m,l,ω). Since there is no common spatial wavenumber coordinate, the full three dimensional system must be solved and no reduction to a 2.5D calculation is possible [162]. Therewith, no parallel computation of independent two dimensional problems is possible leading to an increased computational effort compared to the halfspace with cylindrical cavity.

For the evaluation of the stress and displacement states on the two boundaries for both fundamental systems, a virtual spherical surface $\delta\Gamma_{\mathrm{s}}$ is introduced into the halfspace (Fig. 3.5a) as well as a virtual halfspace surface $\delta\Lambda$ into the fullspace with spherical cavity (Fig. 3.5b).

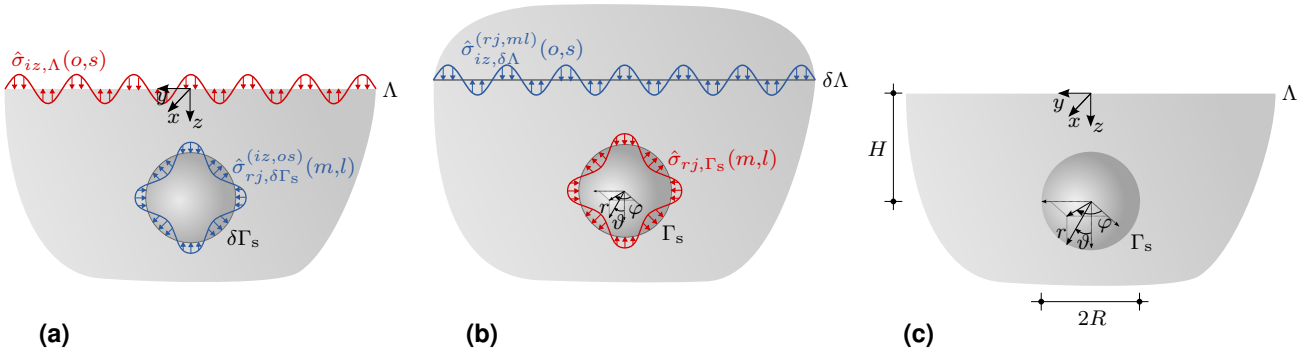

Figure 3.5: Fundamental systems (a) halfspace and (b) fullspace with spherical cavity for the superposition to the system (c) halfspace with spherical cavity.

Fundamental system halfspace

Unit stresses $\hat{\sigma}_{iz}\,(o,s)$ with $i = x,y,z$ in dependency of the discrete wavenumbers $k_x = o\,\Delta k_x$ with $o = -N_x/2, ..., (N_x/2-1)$ and $k_y = s\,\Delta k_y$ with $s = -N_y/2, ..., (N_y/2-1)$ are applied at the halfspace surface Λ. These lead to resulting stresses $\hat{\sigma}^{(iz,os)}_{iz,\delta\Gamma_s}\,(o,s)$ on the virtual surface $\delta\Gamma_s$. To enable the superposition and to comply with the boundary conditions, they are transformed into the basis of the fullspace with spherical cavity (r,m,l,ω). Hence, each unit load on Λ for a defined combination of k_x and k_y in the frequency domain leads to stresses $\hat{\sigma}^{(iz,os)}_{rj,\delta\Gamma_s}\,(m,l)$ with $j = r,\vartheta,\varphi$ on $\delta\Gamma_s$. [84]

Fundamental system fullspace with spherical cavity

Unit loads $\hat{\sigma}_{rj,\Gamma_s}\,(m,l)$ with $j = r,\vartheta,\varphi$ are applied on the spherical surface Γ_s for the different spherical harmonics with degree m and order l. The resulting stresses $\hat{\sigma}^{(rj,ml)}_{rj,\delta\Lambda}\,(m,l)$ on the virtual halfspace surface $\delta\Lambda$ are calculated and transformed into the coordinate system of the halfspace (k_x,k_y,z,ω). Thus, for each spherical harmonic unit load $\hat{\sigma}_{rj,\Gamma_s}\,(m,l)$ on Γ_s, stresses $\hat{\sigma}^{(rj,ml)}_{iz,\delta\Lambda}\,(o,s)$ with $i = x,y,z$ on $\delta\Lambda$ are obtained. [84]

Superposition of fundamental systems

The superposition of the stresses on the two surfaces Λ and Γ_s has to fulfill the boundary conditions present at the resulting system. Thus, the amplitudes of the unit stresses $\hat{C}_{iz,\Lambda}(o,s)$ on Λ and $\hat{C}_{rj,\Gamma_s}(m,l)$ on Γ_s have to be determined such, that they are equal to the there applied external loads. [84]

$$\hat{C}_{iz,\Lambda}(o,s)\;\hat{\sigma}_{iz,\Lambda}\,(o,s) + \sum_{m=0}^{M}\sum_{l=-m}^{m}\sum_{j=r,\vartheta,\varphi}\hat{C}_{rj,\Gamma_s}\,(m,l)\;\hat{\sigma}^{(rj,ml)}_{iz,\delta\Lambda}\,(o,s) \quad = -\hat{p}_{iz,\Lambda}\,(o,s) \tag{3.19}$$

$$\sum_{o=-N_x/2}^{N_x/2-1}\sum_{s=-N_y/2}^{N_y/2-1}\sum_{i=z,y,x}\hat{C}_{iz,\Lambda}(o,s)\;\hat{\sigma}^{(iz,os)}_{rj,\delta\Gamma_s}\,(m,l) + \hat{C}_{rj,\Gamma_s}(m,l)\;\hat{\sigma}_{rj,\Gamma_s}\,(m,l) \quad = -\hat{p}_{rj,\Gamma_s}\,(m,l) \tag{3.20}$$

Thereby, M is the maximum degree of the Legendre polynomials. Illustratively, this maximum degree M corresponds to the number of latitudes $M+1$ on the spherical surface that are taken into account for the development into spherical harmonics. Eqs. (3.19) and (3.20) can be written in matrix notation as [84]

$$\underbrace{\begin{bmatrix} \hat{\mathbf{S}}^{\mathbf{hs\,sph}}_{\mathbf{\Lambda\Lambda_{ITM}}} & \hat{\mathbf{S}}^{\mathbf{hs\,sph}}_{\mathbf{\Lambda\Gamma_{s}ITM}} \\ \hat{\mathbf{S}}^{\mathbf{hs\,sph}}_{\mathbf{\Gamma_{s}\Lambda_{ITM}}} & \hat{\mathbf{S}}^{\mathbf{hs\,sph}}_{\mathbf{\Gamma_{s}\Gamma_{s}\,ITM}} \end{bmatrix}}_{\hat{\mathbf{S}}^{\mathbf{hs\,sph}}_{\mathbf{ITM}}} \underbrace{\begin{pmatrix} \hat{\mathbf{C}}^{\mathbf{hs\,sph}}_{\mathbf{\Lambda_{ITM}}} \\ \hat{\mathbf{C}}^{\mathbf{hs\,sph}}_{\mathbf{\Gamma_{s}\,ITM}} \end{pmatrix}}_{\hat{\mathbf{C}}^{\mathbf{hs\,sph}}_{\mathbf{ITM}}} = \underbrace{\begin{pmatrix} \hat{\mathbf{P}}^{\mathbf{hs\,sph}}_{\mathbf{\Lambda_{ITM}}} \\ \hat{\mathbf{P}}^{\mathbf{hs\,sph}}_{\mathbf{\Gamma_{s}\,ITM}} \end{pmatrix}}_{\hat{\mathbf{P}}^{\mathbf{hs\,sph}}_{\mathbf{ITM}}} \tag{3.21}$$

With the boundary conditions (3.21), the vector of the unknowns $\hat{\mathbf{C}}^{\mathbf{hs\,sph}}_{\mathbf{ITM}}$ can be determined and thus the displacements on the halfspace surface $\hat{u}_{i,\Lambda}$ with $i = x,y,z$ and on the spherical surface $\hat{u}_{j,\Gamma_s}$ with $j = r,\vartheta,\varphi$ can be calculated as [84]

$$\begin{aligned} \hat{u}_{i,\Lambda}\,(o,s) \;&=\; \sum_{k=x,y,z} C_{kz,\Lambda}(o,s)\;\hat{u}^{(kz,os)}_{i,\Lambda}\,(o,s) \\ &+ \sum_{m=0}^{M}\;\sum_{l=-m}^{m}\;\sum_{l_s=r,\vartheta,\varphi} C_{l_s r,\Gamma_s}\,(m,l)\;\;\hat{u}^{(l_s r,ml)}_{i,\delta\Lambda}\,(o,s) \end{aligned} \tag{3.22}$$

$$\begin{aligned} \hat{u}_{j,\Gamma_s}\,(m,l) = &\sum_{o=-N_x/2}^{N_x/2-1}\;\sum_{s=-N_y/2}^{N_y/2-1}\;\sum_{k=x,y,z} C_{kz,\Lambda}(o,s)\;\hat{u}^{(kz,os)}_{j,\delta\Gamma_s}\,(m,l) \\ &+ \sum_{l_s=r,\vartheta,\varphi} C_{l_s r,\Gamma_s}(m,l)\;\hat{u}^{(l_s r,ml)}_{j,\Gamma_s}\,(m,l) \end{aligned} \tag{3.23}$$

Eqs. (3.22) and (3.23) can be summarized in matrix notation

$$\underbrace{\begin{pmatrix} \hat{\mathbf{u}}^{\mathbf{hs\,sph}}_{\mathbf{\Lambda_{ITM}}} \\ \hat{\mathbf{u}}^{\mathbf{hs\,sph}}_{\mathbf{\Gamma_{s}\,ITM}} \end{pmatrix}}_{\hat{\mathbf{u}}^{\mathbf{hs\,sph}}_{\mathbf{ITM}}} = \underbrace{\begin{bmatrix} \hat{\mathbf{U}}^{\mathbf{hs\,sph}}_{\mathbf{\Lambda\Lambda_{ITM}}} & \hat{\mathbf{U}}^{\mathbf{hs\,sph}}_{\mathbf{\Lambda\Gamma_{s}\,ITM}} \\ \hat{\mathbf{U}}^{\mathbf{hs\,sph}}_{\mathbf{\Gamma_{s}\Lambda_{ITM}}} & \hat{\mathbf{U}}^{\mathbf{hs\,sph}}_{\mathbf{\Gamma_{s}\Gamma_{s}\,ITM}} \end{bmatrix}}_{\hat{\mathbf{U}}^{\mathbf{hs\,sph}}_{\mathbf{ITM}}} \underbrace{\begin{pmatrix} \hat{\mathbf{C}}^{\mathbf{hs\,sph}}_{\mathbf{\Lambda_{ITM}}} \\ \hat{\mathbf{C}}^{\mathbf{hs\,sph}}_{\mathbf{\Gamma_{s}\,ITM}} \end{pmatrix}}_{\hat{\mathbf{C}}^{\mathbf{hs\,sph}}_{\mathbf{ITM}}} \tag{3.24}$$

Dynamic stiffness matrix

Combining Eqs. (3.21) and (3.24), the complex dynamic stiffness matrix

$$\hat{\mathbf{K}}^{\mathbf{hs\,sph}}_{\mathbf{ITM}} = \hat{\mathbf{S}}^{\mathbf{hs\,sph}}_{\mathbf{ITM}}\;\hat{\mathbf{U}}^{\mathbf{hs\,sph}\;-1}_{\mathbf{ITM}} \tag{3.25}$$

of the ITM substructure halfspace with spherical cavity can be derived, separated for the parameters on the two surfaces Λ and Γ_s. To ensure the robustness of the results computed with $\hat{\mathbf{K}}^{\mathbf{hs\,sph}}_{\mathbf{ITM}}$, the condition numbers of the matrices in Eq. (3.25) should always be monitored carefully, especially since the inverse of $\hat{\mathbf{U}}^{\mathbf{hs\,sph}}_{\mathbf{ITM}}$ is involved in the computation of the dynamic stiffness matrix.

$$\underbrace{\begin{bmatrix} \hat{\mathbf{K}}^{\mathbf{hs\ sph}}_{\mathbf{\Lambda\Lambda_{ITM}}} & \hat{\mathbf{K}}^{\mathbf{hs\ sph}}_{\mathbf{\Lambda\Gamma_{s\ ITM}}} \\ \hat{\mathbf{K}}^{\mathbf{hs\ sph}}_{\mathbf{\Gamma_s\Lambda_{ITM}}} & \hat{\mathbf{K}}^{\mathbf{hs\ sph}}_{\mathbf{\Gamma_s\Gamma_{s\ ITM}}} \end{bmatrix}}_{\hat{\mathbf{K}}^{\mathbf{hs\ sph}}_{\mathbf{ITM}}} \underbrace{\begin{pmatrix} \hat{\mathbf{u}}^{\mathbf{hs\ sph}}_{\mathbf{\Lambda_{ITM}}} \\ \hat{\mathbf{u}}^{\mathbf{hs\ sph}}_{\mathbf{\Gamma_{s\ ITM}}} \end{pmatrix}}_{\hat{\mathbf{u}}^{\mathbf{hs\ sph}}_{\mathbf{ITM}}} = \underbrace{\begin{pmatrix} \hat{\mathbf{P}}^{\mathbf{hs\ sph}}_{\mathbf{\Lambda_{ITM}}} \\ \hat{\mathbf{P}}^{\mathbf{hs\ sph}}_{\mathbf{\Gamma_{s\ ITM}}} \end{pmatrix}}_{\hat{\mathbf{P}}^{\mathbf{hs\ sph}}_{\mathbf{ITM}}} \tag{3.26}$$

3.3.2 Spherical indentation at the soil surface

The stiffness matrix of the system halfspace with spherical indentation can be derived applying the same superposition procedure as illustrated in the previous section. However, in this case the stresses and displacements on the virtual spherical surface $\delta\Gamma_s$, due to the unit stress states $\hat{\sigma}_{iz}(o,s)$ in the fundamental system halfspace, can only be evaluated below the halfspace surface. Analogously, in the fundamental system fullspace with spherical cavity the stresses and displacements on $\delta\Lambda$, due to the unit stress states $\hat{\sigma}_{rj}(m,l)$, can only be evaluated outside the cavity. Both, the stresses and displacements above the ground surface Λ and inside the cavity boundary Γ_s are set to zero, since the superposition only needs to satisfy the external boundary conditions on the physically existing surface of the overall system.

Also here the superposition is not performed point by point, but the quantities are transformed into the (k_x,k_y,z,ω) domain on the ground surface $z = 0$ and into the (r,m,l,ω) domain on the spherical surface $r = R$. Thereby the stresses and displacements are expanded into a Fourier series along the $x-$ and $y-$coordinate on Λ and into spherical harmonics on Γ_s. Since the amplitude of the stresses and displacements on the nodes for $z \leq 0$ and $r \leq R$ were set to zero, a discontinuity can occur at the transition point prior the series expansion. Hence, to represent this sufficiently in the transformed domain and thus to ensure a good quality of the solution, a larger number of series members resp. spherical harmonics is needed for the halfspace with spherical indentation compared to the halfspace with the spherical cavity. Finally, the amplitudes of the stresses and displacements are determined for the corresponding series members, such that the boundary conditions are satisfied (Eqs. (3.21) and (3.24)) and the stiffness matrix can be deduced analogously to Eqs. (3.25) and (3.26).

3.4 Layered halfspace with cylindrical or spherical cavity

In this section, the fundamental system of the discrete soil stratification, introduced in Sec. 2.4, will be coupled with the halfspace including a cylindrical or spherical cavity, derived

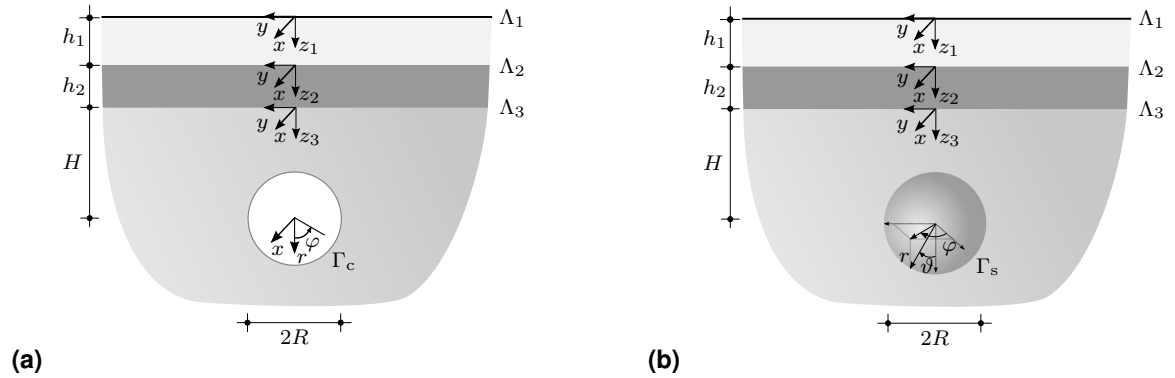

Figure 3.6: Multilayered halfspace with (a) cylindrical cavity and (b) spherical cavity.

in the previous chapters, in order to deduce a solution for a multilayered halfspace with either cylindrical or spherical cavity, as depicted in Fig. 3.6.

Preceding, stiffness formulations for all substructures have been derived, linking the displacements at the boundaries of the respective system with the there applied loads. For this purpose, the degrees of freedom (DOFs) in the matrices are arranged separately according to the two surfaces at hand. In case of the distinct soil stratification (Eq. (2.33)), it is distinguished between the DOFs on the upper surface Λ_1 and the lower surface Λ_3 of the layering. For the halfspace with cylindrical cavity (Eq. (3.8)) or the halfspace with spherical cavity (Eq. (3.26)), one differentiates between the DOFs on the halfspace surface Λ_3 and the corresponding cavity surface Γ_c resp. Γ_s.

The different substructures are then coupled using the continuity of the displacements

$$\hat{\mathbf{u}}^{\mathbf{L}}_{\mathbf{\Lambda_3\,ITM}} = \hat{\mathbf{u}}^{\mathbf{hs\ cyl}}_{\mathbf{\Lambda_3\,ITM}} \qquad \text{resp.} \qquad \hat{\mathbf{u}}^{\mathbf{L}}_{\mathbf{\Lambda_3\,ITM}} = \hat{\mathbf{u}}^{\mathbf{hs\ sph}}_{\mathbf{\Lambda_3\,ITM}} \tag{3.27a}$$

and the equilibrium of stresses

$$\hat{\mathbf{P}}^{\mathbf{L}}_{\mathbf{\Lambda_3\,ITM}} + \hat{\mathbf{P}}^{\mathbf{hs\ cyl}}_{\mathbf{\Lambda_3\,ITM}} = \hat{\mathbf{P}}^{\mathbf{hs\ cyl\,L}}_{\mathbf{\Lambda_3\,ITM}} \qquad \text{resp.} \qquad \hat{\mathbf{P}}^{\mathbf{L}}_{\mathbf{\Lambda_3\,ITM}} + \hat{\mathbf{P}}^{\mathbf{hs\ sph}}_{\mathbf{\Lambda_3\,ITM}} = \hat{\mathbf{P}}^{\mathbf{hs\ sph\,L}}_{\mathbf{\Lambda_3\,ITM}} \tag{3.28}$$

at the common interface Λ_3. Thereby, the sum of the stresses of the two substructures on the coupling surface has to be equal to the given external stresses $\hat{\mathbf{P}}^{\mathbf{hs\ cyl\,L}}_{\mathbf{\Lambda_3\,ITM}}$ resp. $\hat{\mathbf{P}}^{\mathbf{hs\ sph\,L}}_{\mathbf{\Lambda_3\,ITM}}$ applied at the coupling surface. Since the displacements and the stresses on the lower boundary of the soil stratification as well as the surface of the halfspace with inclusion are defined with respect to the same basis (k_x,k_y,z,ω), no transformations are necessary. However, the size of the total discretized domain as well as number and spacing of the discretization points on Λ_3 needs to be equal for both substructures, so that the same Fourier series members for the stresses and displacements are coupled.

Combining the corresponding transition conditions in Eqs. (3.27) and (3.4), the assembled

total stiffness matrix for the layered halfspace with cylindrical cavity yields

$$\underbrace{\begin{bmatrix} \hat{\mathbf{K}}^{\mathbf{L}}_{\mathbf{\Lambda_1\Lambda_1}\,\mathbf{ITM}} & \hat{\mathbf{K}}^{\mathbf{L}}_{\mathbf{\Lambda_1\Lambda_3}\,\mathbf{ITM}} & \mathbf{0} \\ \hat{\mathbf{K}}^{\mathbf{L}}_{\mathbf{\Lambda_3\Lambda_1}\,\mathbf{ITM}} & \hat{\mathbf{K}}^{\mathbf{L}}_{\mathbf{\Lambda_3\Lambda_3}\,\mathbf{ITM}} + \hat{\mathbf{K}}^{\mathbf{hs\ cyl}}_{\mathbf{\Lambda_3\Lambda_3}\,\mathbf{ITM}} & \hat{\mathbf{K}}^{\mathbf{hs\ cyl}}_{\mathbf{\Lambda_3\Gamma_c}\,\mathbf{ITM}} \\ \mathbf{0} & \hat{\mathbf{K}}^{\mathbf{hs\ cyl}}_{\mathbf{\Gamma_c\Lambda_3}\,\mathbf{ITM}} & \hat{\mathbf{K}}^{\mathbf{hs\ cyl}}_{\mathbf{\Gamma_c\Gamma_c}\,\mathbf{ITM}} \end{bmatrix}}_{\hat{\mathbf{K}}^{\mathbf{hs\ cyl\,L}}_{\mathbf{ITM}}} \underbrace{\begin{pmatrix} \hat{\mathbf{u}}^{\mathbf{hs\ cyl\,L}}_{\mathbf{\Lambda_1}\,\mathbf{ITM}} \\ \hat{\mathbf{u}}^{\mathbf{hs\ cyl\,L}}_{\mathbf{\Lambda_3}\,\mathbf{ITM}} \\ \hat{\mathbf{u}}^{\mathbf{hs\ cyl\,L}}_{\mathbf{\Gamma_c}\,\mathbf{ITM}} \end{pmatrix}}_{\hat{\mathbf{u}}^{\mathbf{hs\ cyl\,L}}_{\mathbf{ITM}}} = \underbrace{\begin{pmatrix} \hat{\mathbf{P}}^{\mathbf{hs\ cyl\,L}}_{\mathbf{\Lambda_1}\,\mathbf{ITM}} \\ \hat{\mathbf{P}}^{\mathbf{hs\ cyl\,L}}_{\mathbf{\Lambda_3}\,\mathbf{ITM}} \\ \hat{\mathbf{P}}^{\mathbf{hs\ cyl\,L}}_{\mathbf{\Gamma_c}\,\mathbf{ITM}} \end{pmatrix}}_{\hat{\mathbf{P}}^{\mathbf{hs\ cyl\,L}}_{\mathbf{ITM}}} \tag{3.29}$$

Analogously, the total stiffness matrix for the layered halfspace with spherical cavity yields

$$\underbrace{\begin{bmatrix} \hat{\mathbf{K}}^{\mathbf{L}}_{\mathbf{\Lambda_1\Lambda_1}\,\mathbf{ITM}} & \hat{\mathbf{K}}^{\mathbf{L}}_{\mathbf{\Lambda_1\Lambda_3}\,\mathbf{ITM}} & \mathbf{0} \\ \hat{\mathbf{K}}^{\mathbf{L}}_{\mathbf{\Lambda_3\Lambda_1}\,\mathbf{ITM}} & \hat{\mathbf{K}}^{\mathbf{L}}_{\mathbf{\Lambda_3\Lambda_3}\,\mathbf{ITM}} + \hat{\mathbf{K}}^{\mathbf{hs\ sph}}_{\mathbf{\Lambda_3\Lambda_3}\,\mathbf{ITM}} & \hat{\mathbf{K}}^{\mathbf{hs\ sph}}_{\mathbf{\Lambda_3\Gamma_s}\,\mathbf{ITM}} \\ \mathbf{0} & \hat{\mathbf{K}}^{\mathbf{hs\ sph}}_{\mathbf{\Gamma_s\Lambda_3}\,\mathbf{ITM}} & \hat{\mathbf{K}}^{\mathbf{hs\ sph}}_{\mathbf{\Gamma_s\Gamma_s}\,\mathbf{ITM}} \end{bmatrix}}_{\hat{\mathbf{K}}^{\mathbf{hs\ sph\,L}}_{\mathbf{ITM}}} \underbrace{\begin{pmatrix} \hat{\mathbf{u}}^{\mathbf{hs\ sph\,L}}_{\mathbf{\Lambda_1}\,\mathbf{ITM}} \\ \hat{\mathbf{u}}^{\mathbf{hs\ sph\,L}}_{\mathbf{\Lambda_3}\,\mathbf{ITM}} \\ \hat{\mathbf{u}}^{\mathbf{hs\ sph\,L}}_{\mathbf{\Gamma_s}\,\mathbf{ITM}} \end{pmatrix}}_{\hat{\mathbf{u}}^{\mathbf{hs\ sph\,L}}_{\mathbf{ITM}}} = \underbrace{\begin{pmatrix} \hat{\mathbf{P}}^{\mathbf{hs\ sph\,L}}_{\mathbf{\Lambda_1}\,\mathbf{ITM}} \\ \hat{\mathbf{P}}^{\mathbf{hs\ sph\,L}}_{\mathbf{\Lambda_3}\,\mathbf{ITM}} \\ \hat{\mathbf{P}}^{\mathbf{hs\ sph\,L}}_{\mathbf{\Gamma_s}\,\mathbf{ITM}} \end{pmatrix}}_{\hat{\mathbf{P}}^{\mathbf{hs\ sph\,L}}_{\mathbf{ITM}}} \tag{3.30}$$

3.5 Computational and numerical aspects

3.5.1 Numerical Fourier decomposition

In Ch. 2, continuous Fourier transforms were applied to the Lamé equation (2.3) in order to derive analytical solutions for selected fundamental systems in the transformed domain. For the superposition of these fundamental systems to more complex systems in Secs. 3.1 to 3.3, a discretization of the solutions in terms of Fourier series expansions was introduced, such that it can be performed numerically. In this section, the numerical implementation of the discrete series expansions along the plane horizontal, cylindrical and spherical surfaces, is presented. Furthermore, the accompanying effects, due to the domain truncation and the consideration of only a finite number of sample points resp. series members, are illustrated and linked to the corresponding numerical errors.

Numerical Fourier series expansion

A continuous periodic signal $f(x)$ with period B_x can be represented by a Fourier series as

$$f_n(x) = \sum_{n=-\infty}^{\infty} c_n \mathrm{e}^{\mathrm{i}\frac{2\pi}{B_x}nx} \qquad \text{with} \qquad c_n = \frac{1}{B_x} \int_{-B_x/2}^{B_x/2} f_n(x) \mathrm{e}^{-\mathrm{i}\frac{2\pi}{B_x}nx} \mathrm{d}x \tag{3.31}$$

thereby approximating $f(x)$ best in the sense of the quadratic mean.

In order to enable a numerical computation of the Fourier series for a given set of data within a finite interval, a discrete realization of the continuous signal is used. Each discrete signal in space or time can mathematically be represented by a sequence of numbers $x = x[n]$, where n is a integer and denotes the n^{th} sample in the sequence. If $\tilde{x}[n]$ is a periodic signal with period N (whereby the $\tilde{}$ indicates the periodicity) so that $\tilde{x}[n] = \tilde{x}[n + rN]$ holds for integer values of r and n, it is possible to represent it by a Fourier series corresponding to a sum of harmonically related complex exponentials [246]

$$\tilde{x}[n] = \frac{1}{N} \sum_{k=0}^{N-1} \tilde{X}[k] \, \mathrm{e}^{\mathrm{i} \frac{2\pi}{N} nk} \tag{3.32}$$

The sequence of Fourier series coefficients $\tilde{X}[k]$ can then be obtained by

$$\tilde{X}[k] = \sum_{n=0}^{N-1} \tilde{x}[n] \, \mathrm{e}^{-\mathrm{i} \frac{2\pi}{N} nk} \tag{3.33}$$

whereby Eqs. (3.32) and (3.33) are the discrete Fourier series (DFS) representation of a periodic sequence $\tilde{x}[n]$.

Next, a signal of finite length $x[n]$, chosen such that its samples correspond to the N samples of one period of $\tilde{x}[n]$, is considered. The corresponding samples of the finite length sequence $X[k]$ can be extracted from the discrete Fourier series $\tilde{X}[k]$ of the periodic expansion $\tilde{x}[n]$ of $x[n]$, whereby it holds

$$x[n] = \begin{cases} \tilde{x}[n] & \text{with} \quad 0 \leq n \leq N-1 \\ 0 & \text{otherwise} \end{cases} \tag{3.34a}$$

$$X[k] = \begin{cases} \tilde{X}[k] & \text{with} \quad 0 \leq k \leq N-1 \\ 0 & \text{otherwise} \end{cases} \tag{3.34b}$$

The sequence $X[k]$ is referred to as the discrete Fourier transform (DFT) of $x[n]$. Hence, the DFS representation of a periodic sequence $\tilde{x}[n]$ for $n, k = 0,...,N-1$ concurs with the DFT of the signal and the coefficients of the discrete Fourier series are equal to the sample values of the discrete Fourier transform [246]. Vice versa, if the DFT is applied to a discrete signal with N samples, a periodic repetition of the signal in the original and the transformed domain is inherently introduced [247], as in principle the DFT sample values are only a cutout of the DFS of a periodic signal $\tilde{x}[n] = x[n] * \sum_{-\infty}^{\infty} \delta[n - rN]$ formed by adding together a infinite number of shifted replicas of $x[n]$.

The DFT analysis and synthesis equations thus result as

$$X[k] = \sum_{n=0}^{N-1} x[n]\, \mathrm{e}^{-\mathrm{i}\frac{2\pi}{N}nk} \tag{3.35}$$

$$x[n] = \frac{1}{N} \sum_{k=0}^{N-1} X[k]\, \mathrm{e}^{\mathrm{i}\frac{2\pi}{N}nk} \tag{3.36}$$

According to the above stated equality between the coefficients of the DFS and the sample values of the DFT, the Fourier series expansion along the horizontal and cylindrical surfaces within the superposition procedure can be computed via the DFT. In this thesis, the Fast Fourier Transform (FFT) algorithm is used to determine the DFT efficiently. However, the DFT in general is only an approximation of the continuous Fourier transform. Depending on the properties of the analysed signal, the DFT can either correspond directly to the samples of the continuous Fourier transform of the corr. continuous signal at uniformly distributed evaluation points or be affected by numerical errors, that lead to deviations between the continuous and the discrete transform. Thereby the size of the error varies strongly depending on the selected period length and the number of samples resp. the resulting sampling intervals in the original and the transformed domain.

Subsequently, the most important effects, occurring due to the DFT, are illustrated exemplarily for the solution of the homogenous halfspace, which is determined in the threefold transformed (k_x,k_y,z,ω) domain. Fig. 3.7a depicts the theoretically obtained continuous response $f(x)$ of a homogeneous halfspace at $z = 0$ and its Fourier transform $F(k_x)$ for a specific combination (k_y, ω) due to a harmonic, spatial impulse load. To determine the Fourier transform pair $f(x) \circ\!\!-\!\!\bullet F(k_x)$ numerically, it is necessary to introduce a sampling in the space domain (Fig. 3.7b) and in the wavenumber domain (Fig. 3.7f), as well as to truncate the signal (Fig. 3.7d) to reduce it to a finite number of samples N_x within a spatial window of length B_x.

The discretization in the space domain, implemented by a multiplication with a Dirac comb $\Delta_0(x)$, leads to a convolution of $F(k_x)$ with its Fourier transform $\Delta_0(k_x)$ in the wavenumber domain. If the sampling interval $\mathrm{d}x = B_x/N_x$ is chosen too large, the spacing of the impulses $\Delta_0(k_x)$ becomes so small, that their convolution with $F(k_x)$ leads to an overlap of the periodically repeated functions. This effect, known as aliasing and depicted in Fig. 3.7c, can be avoided for band limited functions, if the sampling interval of $\Delta_0(k_x)$ is twice as large as the maximum wavenumber $k_{x_{\max}}$ included in $F(k_x)$ or resp., if $f(x)$ is sampled with $\mathrm{d}x \leq 2\pi/(2k_{x_{\max}})$, according to the Nyquist criterion [248]. However, if $F(k_x)$ doesn't converge to zero sufficiently fast, aliasing occurs always, but can nevertheless be reduced by decreasing the sampling interval $\mathrm{d}x$.

In case of the homogeneous halfspace the short wave components, linked to large k_x, attenuate much faster as the long wave components linked to small k_x, resulting in a low pass filter effect. Moreover, material damping is included in the model by means of a frequency independent hysteretic damping. Therefore, the spatial impulse response function $F(k_x)$ decays relatively fast with increasing k_x, so that aliasing can be reduced considerably by choosing a sufficiently fine spatial discretization.

The truncation of the signal to a finite length with N_x samples results in a convolution of the aliased wavenumber transform $F_{\Delta_0}(k_x)$ with the Fourier transform of the truncation function [247]. This leads to certain ripples in the progression of the resulting function and thus an artificial change in the magnitude of the wavenumber components of the signal. This effect, also known as leakage, can be reduced by choosing a larger window B_x as then the sinc function gets narrower and thus less ripples occur resp. a smaller numerical error is introduced. Another possibility would be to select a different window function which exhibits less side lobes in the wavenumber domain, responsible for the additional wavenumber contributions.

Summing up, to reduce the effects of the discrete Fourier transform resp. the numerical errors introduced by the discrete computation, it is favourable to choose a large observation interval B_x to reduce leakage and simultaneously a small sampling interval $\mathrm{d}x$ and thus a large number of samples N_x. Both measures together result in a significant computational effort. Therefore, the DFT parameters have to be chosen such, that the numerical errors are sufficiently small, the dominant waves are adequately represented in both domains and the necessary computational costs are acceptable. Of course the above illustrated effects and the related remedies apply also for the series expansions in the second spatial dimension as well as the circumferential direction of the cylinder.

As far as the discrete Fourier transform with respect to the Fourier pair $t \circ\!\!-\!\!\bullet f$ is concerned, it is evident from the above, that both the leakage and aliasing effects can be eliminated in the system response due to time-harmonic loads if the window length corresponds to one period of the signal and the sampling frequency is chosen according to the Nyquist criterion. If it comes to transient loads, the same effects as outlined for the spatial domain can occur and are also prevented or reduced in the same manner. Further details on the numerical computation of the transient soil or soil structure interaction response due to transient loads are illustrated in Ch. 7.

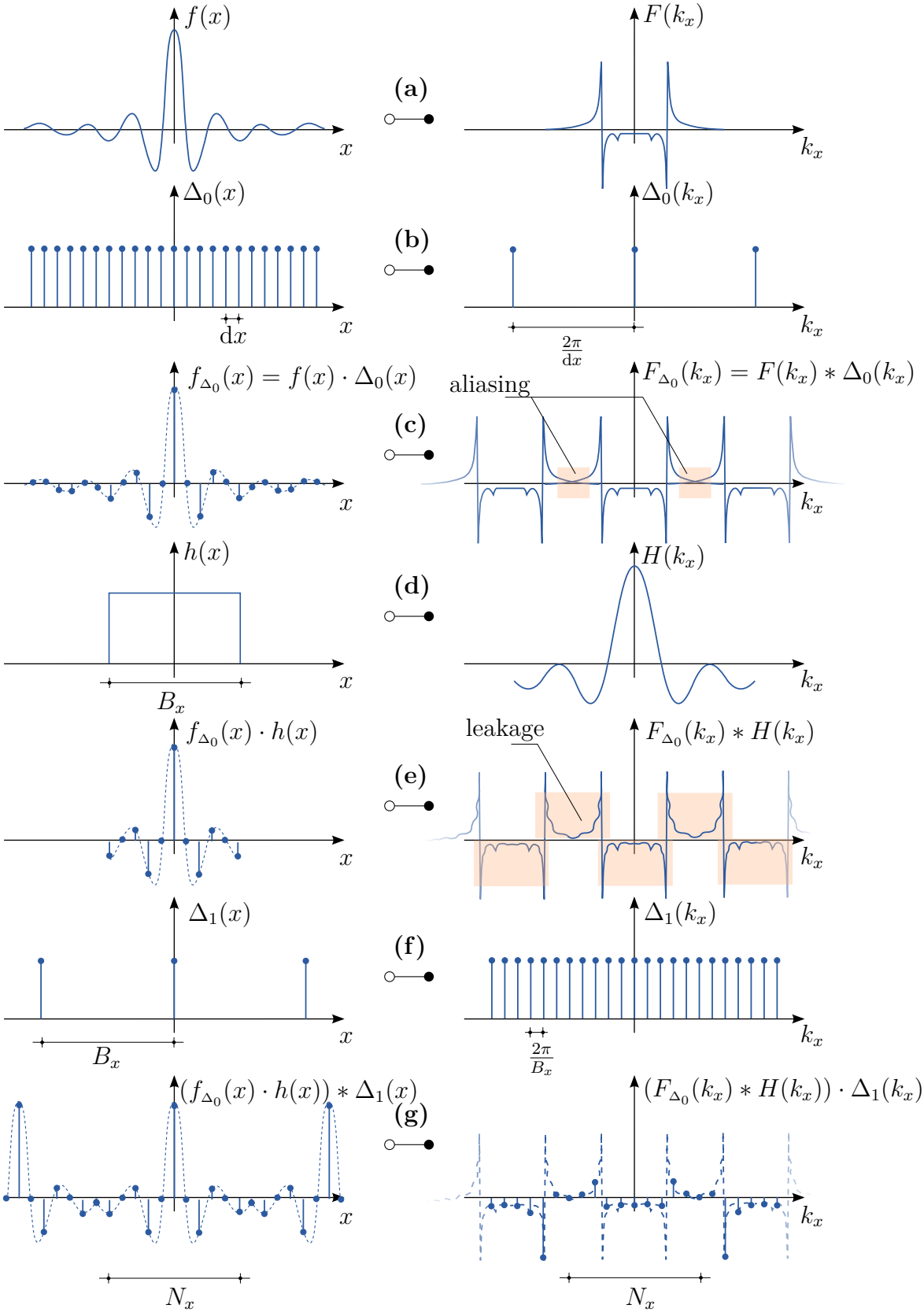

Figure 3.7: Schematic sketch of discrete Fourier transform and the associated numerical errors [247].

Numerical spherical Fourier series expansion

The spherical Fourier transform has applications in many different fields such as geophysics, meteorology or seismology. It is also used in spectral methods in order to solve partial differential equations within a spherical reference frame [249]. In this context, an expansion into a series of spherical harmonics was introduced in the solution of the elastodynamic problem of a fullspace with spherical cavity in Sec. 2.6. To reduce the computational time and the effort for the discrete evaluation of the numerical spherical Fourier series expansion, different algorithms were derived in literature [249–254]. The numerical implementation applied in this thesis is based on [160, 252] and briefly explained hereinafter.

A function $f(\vartheta,\varphi)$ can be expanded into a series of spherical harmonics on the surface of the sphere by

$$f(\vartheta,\varphi) = \sum_{m=0}^{M} \sum_{l=-m}^{m} a_{l,m} Y_m^l(\theta,\varphi) = \sum_{m=0}^{M} \sum_{l=-m}^{m} a_{l,m} \check{P}_m^l l\left(\cos\left(\vartheta\right)\right) \mathrm{e}^{\mathrm{i}l\varphi} \tag{3.37}$$

with the normalized associated Legendre functions defined in Sec. 2.6.

The determination of the coefficients $a_{l,m}$ is performed in two steps: Firstly, the function is developed into a Fourier series along the latitudes

$$a_l(\vartheta) = \int_0^{2\pi} f(\theta,\varphi)\, \mathrm{e}^{-\mathrm{i}l\varphi} \mathrm{d}\varphi \tag{3.38}$$

The numerical computation of this series expansion is implemented via the FFT as outlined previously in this section. Therefore, the function $f(\theta,\varphi)$ is discretized with N_φ equidistant samples along the latitude. [160]

Subsequently, a associated Legendre transform along the longitude is carried out

$$a_{l,m} = \int_0^{\pi} a_l(\vartheta) \check{P}_m^l l\left(\cos\left(\vartheta\right)\right) \sin(\vartheta) \mathrm{d}\vartheta \tag{3.39}$$

For the numerical computation of this integral the Gauß-Legendre-Quadrature is used. Thus, the function $f(\theta,\varphi)$ needs to be evaluated on N_ϑ discrete positions along a longitude of the sphere. The position of these discretization points $\vartheta_i = \mathrm{acos}(x_i) \in [0,\pi]$ is determined from the location of the Gauß quadrature nodes $x_i \in [-1,1]$, which are defined as the roots of the Legendre polynomial of degree n. Consequently, the number of Gauß points n is chosen equal to the number of latitudes N_ϑ. By means of the of the weights w_i of the Gauß-Legendre

integration, one obtains the following equation for the determination of the coefficients $a_{l,m}$

$$a_{l,m} = \sum_{i=1}^{N_\vartheta} a_l(\vartheta_i) \check{P}_m^l \left(\cos\left(\vartheta_i\right)\right) w_i \tag{3.40}$$

In matrix notation this Eq. (3.40) yields for each series member l

$$\begin{bmatrix} a_{l,l} \\ a_{l,l+1} \\ \vdots \\ a_{l,M} \end{bmatrix} = \begin{bmatrix} \check{P}_l^l\left(\cos\left(\vartheta_1\right)\right) & \check{P}_l^l\left(\cos\left(\vartheta_2\right)\right) & \dots & \check{P}_l^l\left(\cos\left(\vartheta_{N_\vartheta}\right)\right) \\ \check{P}_{l+1}^l\left(\cos\left(\vartheta_1\right)\right) & \check{P}_{l+1}^l\left(\cos\left(\vartheta_2\right)\right) & \dots & \check{P}_{l+1}^l\left(\cos\left(\vartheta_{N_\vartheta}\right)\right) \\ \vdots & \vdots & \ddots & \vdots \\ \check{P}_M^l\left(\cos\left(\vartheta_1\right)\right) & \check{P}_M^l\left(\cos\left(\vartheta_2\right)\right) & \dots & \check{P}_M^l\left(\cos\left(\vartheta_{N_\vartheta}\right)\right) \end{bmatrix} \operatorname{diag}(w_i) \begin{bmatrix} a_l(\vartheta_1) \\ a_l(\vartheta_2) \\ \vdots \\ a_l(\vartheta_{N_\vartheta}) \end{bmatrix} \tag{3.41}$$

The maximum number of series members depends on the total number of sample points $N_\varphi \cdot N_\vartheta$ on the spherical surface, which is given by the intersections of the latitudes and longitudes. However, to achieve a uniform resolution of waves on the sphere, the maximum degree of the spherical harmonics M must be chosen as $M < \min(N_\varphi/2, N_\vartheta)$ [252]. Thus the amount of sample points is not equal to that of the spherical harmonics, leading to a different number of unknowns in the system of equations in the (r,ϑ,φ,ω) domain compared to the (r,m,l,ω) domain. In case of $M = N_\vartheta - 1$ and $N_\vartheta = N_\varphi/2$, a total number of $(M+1)^2$ spherical harmonics results, leading to non square transformation matrices. Further details on the treatment of the latter for the coupling of two substructures on the common spherical surface are given in Sec. 5.2.

The backward transform, as given in Eq. (3.37), is performed numerically also in two phases [252]. Firstly, the coefficients $a_l(\vartheta)$ are computed from $a_{l,m}$ as

$$a_l(\vartheta) = \sum_{m=l}^{M} a_{l,m} \check{P}_m^l \left(\cos\left(\vartheta\right)\right) \tag{3.42}$$

followed by

$$f(\vartheta,\varphi) = \sum_{l=0}^{M} a_l(\vartheta)\, \mathrm{e}^{-\mathrm{i}l\varphi} \tag{3.43}$$

which is carried out numerically via the IFFT.

3.5.2 Truncation criteria due to radiation characteristics

In the superposition procedure presented in Secs. 3.1 to 3.3, all discrete wavenumbers on the halfspace, cylindrical and spherical surfaces were coupled respectively. As the amount of wavenumbers considered increases, this leads to a significantly higher computational effort

which can, however, be reduced by exploiting the solution properties of the fundamental systems. Depending on the combination of the wavenumbers resp. the series members on the cylindrical or spherical boundary and the frequency ω, the solutions describe either slowly decaying spatially propagating waves (far fields) or strongly attenuating evanescent waves (near fields). By only considering those combinations that lead to a significant contribution on the respective virtual surfaces within the halfspace or fullspace, the number of necessary computation as well as the size of the system of equations to be solved can be reduced seriously, without affecting the accuracy of the results [160].

In the following, the solution properties for the different fundamental systems are presented together with the corresponding truncation criteria for the ideal undamped soil, as this allows easier access to the basic behaviour of the solutions. However, due to the introduced hysteretic damping, the material constants and thus also the wave velocities and the wavenumbers are actually complex. Therefore, no pure real or imaginary exponents or arguments occur in the analytical solutions of the systems and thus no perfect near or far fields. Nevertheless, either the real or the imaginary part dominates substantially and the wave propagation characteristics are dominated either by propagating or decaying waves.

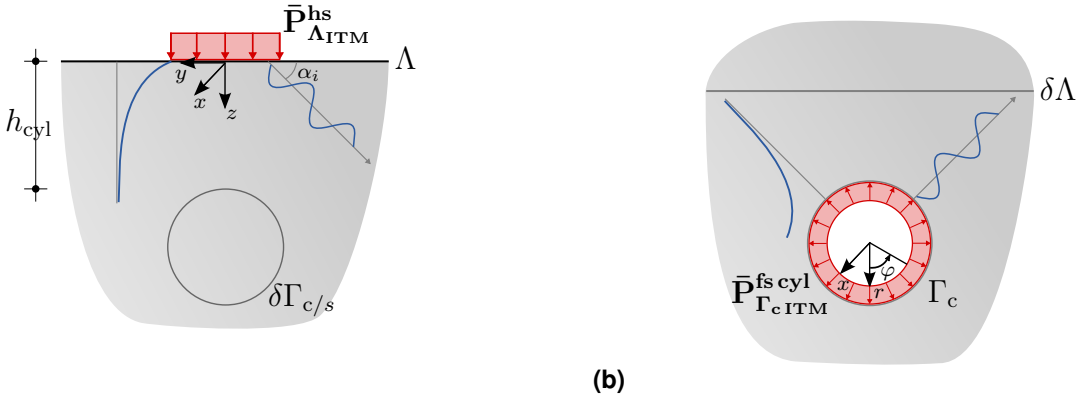

Figure 3.8: Illustration of the different wave propagation characteristics in (a) homogeneous halfspace and (b) fullspace with cylindrical cavity.

Homogeneous halfspace

In the homogeneous halfspace the propagation behaviour of the waves perpendicular to the halfspace surface depends for $\omega < 0$ on the exponential functions $\mathrm{e}^{-\lambda_1 z}$ and $\mathrm{e}^{-\lambda_2 z}$ (cp. Eqs. (2.16)). If the wavenumbers $k_L^2 = k_x^2 + k_y^2$ of the unit stresses on the halfspace surface Λ are larger than the compressional or the shear wavenumber k_p resp. k_s, the exponents λ_1 resp. λ_2 become real, resulting in evanescent waves attenuating with increasing depth z (cp. Fig. 3.8a). In contrast for $k_x^2 + k_y^2 < k_p^2$ resp. k_s^2 the exponents are imaginary and

the solution describes spatially propagating waves. Thereby the radiation angles w.r.t. the ground surface are given by $\sin\alpha_i = \left(c_i\sqrt{k_x^2+k_y^2}\right)/\omega$ with $i = p, s$.

For the superposition procedure only combinations $o\Delta k_x^2 + s\Delta k_y^2$ for which the solution has a considerable influence on the virtual surfaces $\delta\Gamma_\mathrm{c}$ resp. $\delta\Gamma_\mathrm{s}$ need to be included. Therefore, all series members for which the unit stress states on Λ lead to stresses $|\hat{\sigma}(k_x,k_y,z = h_\mathrm{cyl},\omega)|$ at the virtual cylindrical or spherical surface with an amplitude below a certain threshold ϵ can be excluded from the superposition. This finally leads to the following truncation criterion

$$\frac{\mathrm{e}^{-\lambda_1 h_\mathrm{cyl}}}{\mathrm{e}^{-\lambda_1 0}} < \epsilon \quad \text{resp.} \quad \frac{\mathrm{e}^{-\lambda_2 h_\mathrm{cyl}}}{\mathrm{e}^{-\lambda_2 0}} < \epsilon \tag{3.44}$$

where h_cyl is the height of the soil cover over the virtual surface.

Furthermore, since the halfspace solution exhibits a singularity for the Rayleigh wave with the wavenumber k_r in the undamped case, which leads to very large amplitudes of the stresses and displacements, in general all wavenumber combinations with $k_L < 1.3 \cdot k_r$ are considered for the superposition to ensure, that the influence of the Rayleigh wave on the virtual surfaces is included [160].

Fullspace with cylindrical cavity

In case of the fullspace with cylindrical cavity, the propagation characteristics of the waves in radial direction depend for $\omega < 0$ on the Hankel functions of first kind $H_n^{(1)}$ (cp. Eqs. (2.37)). If the wavenumber $k_x = k_L$ of the unit stress states on the cylindrical cavity surface is smaller than k_p resp. k_s, the argument of the Hankel functions $k_1 r$ and $k_2 r$ become real, resulting in spatially propagating waves in the radial direction r (cp. Fig. 3.8b). In contrast for $k_x > k_p$ resp. k_s, the arguments get imaginary and describe waves strongly decaying with increasing distance from the surface Γ_c.

For the superposition procedure only the series members (k_x,n) need to be considered, for which the unit stress states on the cavity surface have a significant impact on the stresses on the virtual halfspace surface. Therefore, all series members for which the amplitude of the stresses $|\hat{\sigma}(k_x,r = R + h_\mathrm{cyl},n,\omega)|$ on $\delta\Lambda$ is smaller than the threshold ϵ, chosen as 10^{-6} within the implementation, can be neglected. This leads to the following truncation criterion [230]

$$\frac{H_n^{(1)}(k_1 \cdot (R + h_\mathrm{cyl}))}{H_n^{(1)}(k_1 \cdot R)} < \epsilon \quad \text{resp.} \quad \frac{H_n^{(1)}(k_2 \cdot (R + h_\mathrm{cyl}))}{H_n^{(1)}(k_2 \cdot R)} < \epsilon \tag{3.45}$$

Furthermore, for the system with two parallel tunnels all series members n_1 of the unit stresses on Γ_{c_1}, which lead to significant stresses on the virtual second cavity surface $\delta\Gamma_{c_2}$ and vice versa need to be considered. In this case the truncation criterion yields

$$\frac{H_n^{(1)}(k_1 \cdot \mathrm{d}_{\mathrm{T}_{1-2}})}{H_n^{(1)}(k_1 \cdot R_1)} < \epsilon \quad \text{resp.} \quad \frac{H_n^{(1)}(k_2 \cdot \mathrm{d}_{\mathrm{T}_{1-2}})}{H_n^{(1)}(k_2 \cdot R_1)} < \epsilon \tag{3.46}$$

Fullspace with spherical cavity

For the fullspace with a spherical cavity, only waves propagating spatially in the radial direction, that are described by the spherical Hankel functions $h_m^{(1)}$, occur in the undamped case, while no evanescent waves arise. Since the energy brought into the system by the load on the spherical surface is spread over a larger area as in case of the cylinder, corresponding to a larger geometrical damping, the introduced waves are attenuating rather fast. Therefore, within the superposition procedure the series members (m,l), for which the unit stresses on the spherical cavity lead to stresses $|\hat{\sigma}(r = R + h_{\mathrm{sph}},m,l,\omega)|$ on the virtual halfspace surface smaller than the threshold ϵ can be excluded [160]. This leads to the following truncation criterion

$$\frac{h_m^{(1)}(|k_p| \cdot (R + h_{\mathrm{sph}}))}{h_m^{(1)}(|k_p| \cdot R_1)} < \epsilon \quad \text{resp.} \quad \frac{h_m^{(1)}(|k_s| \cdot (R + h_{\mathrm{sph}}))}{h_m^{(1)}(|k_s| \cdot R_2)} < \epsilon \tag{3.47}$$

3.5.3 Error measures and similarity assessment

In order to enable a quantitative comparison of the numerical values of two arrays, a variety of different proximity measures like the Dice coefficient, the Manhattan or City Block Metric, the Pearson correlation coefficient etc. are available in literature [255–257]. Within this thesis, the Tanimoto coefficient, as introduced in [257], is used to asses the similarity between two discrete vectors $\mathbf{x}$ and $\mathbf{y}$ with each n elements defined as

$$\mathrm{Tan} = \frac{\sum_{i=1}^{n} x_i y_i}{\sum_{i=1}^{n} x_i^2 + \sum_{i=1}^{n} y_i^2 - \sum_{i=1}^{n} x_i y_i} \tag{3.48}$$

Thereby Tan is equal to one, if the vectors are exactly identical. The more the entries of $\mathbf{x}$ and $\mathbf{y}$ differ, the more the Tanimoto coefficient deviates from 1 towards lower values [258]. As shown in [259], the Tanimoto coefficient is an appropriate measure to evaluate the similarity between results obtained by a numerical computation and the samples of a corresponding analytical solution by a single valued quantity. Hence, it will be used later on to asses the quality of the solutions computed with the numerical approaches presented in this work, compared to either analytical solutions or reference solutions from literature.

Furthermore, to cover also the deviations in the peak values, in some cases also the relative and the absolute error of the maximum values of the considered quantities defined as

$$\mathrm{err}_{\max} = |x_{\mathrm{ref,max}} - x_{\max}| \qquad \text{and} \qquad \mathrm{err}_{\mathrm{rel}} = \left| \frac{x_{\mathrm{ref,max}} - x_{\max}}{x_{\mathrm{ref,max}}} \right| \cdot 100\% \tag{3.49}$$

are given, where $x_{\mathrm{ref,max}}$ is the maximum value of a reference solution, to which the maximum value $x_{\max}$ of the approximate solution is compared.

3.5.4 Parallel computing and code acceleration

The general idea of parallel computing is to separate the overall problem into many independent smaller problems which can be dispersed and solved on several processing elements simultaneously. Therefore, parallel computing enables the activation of distributed resources, either within one central processing unit (CPU) through its multiple cores or on several different CPUs within a cluster leading to drastically reduced computation times.

Speed up

However, the reduction of CPU time is always limited, as the total calculation time T is composed of a sequential part $t_s = \alpha T$ and a part that can be parallelized $t_p = (1-\alpha)T$. Thus T is given by [260]

$$T = t_s + t_p = \alpha T + (1-\alpha)T \tag{3.50}$$

The sequential part thereby comprises amongst others the reading of input files, defining geometry, setting up system matrices, writing the results as well as additional tasks necessary for the communication between the single processors. The parallelizable part are tasks which are independent from each other and can be solved separately. The speed up is defined as the quotient of the computation time T for a pure serial implementation ($\alpha = 1$) and the total computation time in case of a parallel computation [77]

$$\eta_s = \frac{T_{\alpha=1}}{t_s + \frac{t_p}{n_p}} \leq \lim_{n_p \to \infty} \frac{T_{\alpha=1}}{t_s + \frac{t_p}{n_p}} = \frac{T_{\alpha=1}}{t_s} \tag{3.51}$$

wherein the parallel part t_p is divided by the number of available processing units n_p. This relation is also known as Amdahl's law and states, that the speed up is limited by the sequential part and the computation time T cannot be reduced below a certain threshold, regardless the number of available processing elements.

Parallel implementation for ITM substructures

The division into a sequential and a parallelizable part described above also applies to the computational processes for the fundamental solutions of Ch. 2, the superposed systems of Ch. 3 as well as some of the coupled systems that will be presented in Ch. 5. Therefore, the applicability of a parallelisation for these solutions is illustrated below and an overview on the parallel implementation within the developed code using the Matlab® Parallel Computing Toolbox is given which allows to run independent iterations in parallel on multicore CPUs, GPUs and computer clusters.

For the fundamental system homogeneous halfspace, the Lamé equation was decoupled via the Helmholtz approach and transformed in the wavenumber frequency domain, in which the solution of the resulting ordinary differential equations (Eqs. (2.11) and (2.12)) can be computed independently for each combination (k_x, k_y, ω). In order to be able to synthesize the separate contributions to the total response in the original domain, the analytical solution needs to be evaluated for all wavenumbers and frequencies necessary to describe the system sufficiently. Instead of determining the solutions sequentially by means of nested loops, due to the independence of the single problems, the computation can be parallelized w.r.t. to any of the independent parameters k_x, k_y or ω.

A parallelization of the problem is generally meaningful, if either a large number of iterations has to be performed or if there are only a few iterations which require a high computational effort. In the first case the amount of iterations should be so large, that the distribution of the tasks onto the separate CPUs does not need more time than the solution processes on them. In other words, the communication overhead should be small compared to the actual computation time. Within the thesis, harmonic analyses are performed for single frequencies as well as the transfer functions are determined for a larger frequency range. Since the acceleration of the code by the parallelization is to be applied in all cases, it is implemented in dependence of the wavenumbers k_x, whose amount is in any case large enough to ensure a reasonable speed up. In Matlab, this is accomplished by the use of parallel loops, dividing the iterations in groups and executing the single iterations in a nondeterministic order on a parallel pool of workers using the multiple cores of the CPU [261]. A pseudocode of the parallel implementation for the homogenous halfspace is illustrated in Alg. 1. Therein procedures 1, 3 and 4 can directly be assigned to the sequential part, whereas in procedure 2 only the loop over the frequencies is performed consecutively. All tasks within the parfor loop are distributed and executed in parallel.

Analogously, it is possible to implement the parallelization for the halfspace with cylindrical cavity w.r.t. the wavenumber k_x, as the solutions of both involved fundamental systems, the

halfspace and the fullspace with cylindrical cavity, can be determined independently for each combination of (k_x, ω). In Ch. 4 and 5 it will be shown that also the finite element subsystem, used to model structures inside the cylindrical cavity, can be described by a 2.5D approach and thus in dependence on the longitudinal wavenumber and the frequency. Consequently, the system of equations, representing the entire coupled ITM-FEM model, can be set up independently for each combination (k_x, ω) and be solved in parallel. More details for this case are given in Sec. 5.1.2.

In the case of the halfspace with spherical cavity, the solutions of the fundamental systems involved in the superposition procedure do not have a joint wavenumber. Since the halfspace is solved in dependence of k_x, k_y and ω and the fullspace with spherical cavity in dependence of the radius r, the spherical harmonics m,l and ω, a parallelisation is only possible w.r.t. the common parameter, which is the frequency ω. Therefore, only a parallel computation of the system transfer functions is possible, whereas a harmonic analysis for a single frequency cannot be parallelized. This also holds for the halfspace including a FEM substructure with spherical boundary presented in Sec. 5.2.

Algorithm 1 Parallel implementation of ITM approach for homogeneous halfspace within the developed Matlab® code

procedure 1 SET UP SYSTEM AND LOADING( )
  Initialization and input parameters
  Discretization, material and geometry
  External loading $\hat{\mathbf{P}}^{\mathbf{hs}}_{\mathbf{\Lambda_{ITM}}}(k_x,k_y,z,\omega)$

procedure 2 DETERMINE DISPLACEMENTS $\hat{\mathbf{u}}^{\mathbf{hs}}_{\mathbf{\Lambda_{ITM}}}$ (k_x,k_y,ω)
  for all ω **do**
    parfor all k_x **do**
      for all k_y **do**
        Determine $\hat{\mathbf{K}}^{\mathbf{hs}}_{\mathbf{ITM}}$ w.r.t. (k_x,k_y,ω) on Λ
        Solve total system of equations $\hat{\mathbf{u}}^{\mathbf{hs}}_{\mathbf{\Lambda_{ITM}}} = \hat{\mathbf{K}}^{\mathbf{hs}\,-\mathbf{1}}_{\mathbf{ITM}}\,\hat{\mathbf{P}}^{\mathbf{hs}}_{\mathbf{\Lambda_{ITM}}}$

procedure 3 INVERSE FOURIER TRANSFORM( )
  IFFT of $\hat{\mathbf{u}}^{\mathbf{hs}}_{\mathbf{\Lambda_{ITM}}}$ to $\bar{\mathbf{u}}^{\mathbf{hs}}_{\mathbf{\Lambda_{ITM}}}$ (x,y,z,ω)

procedure 4 POSTPROCESSING AND PLOTS( )
  Plot displacements
  Export results

Further measures for code acceleration

The key competence of Matlab® is to work efficiently with potentially large vectors and matrices. Therefore, first and foremost all calculations should, if it is feasible, be vectorized.

However, there are cases when this is not possible, cumbersome or time consuming so that the use of loops is unavoidable. Since Matlab® originally is an interpreted language, meaning that every line is translated into machine code when executed, it is very beneficial in terms of performance to use already compiled functions within a loop, especially if a huge amount of iterations is necessary. Within the software this can easily be accomplished, as compiled C/C^{++} code can be created from existing Matlab® code automatically. The resulting MEX files, can then directly be run using the same input as for the original Matlab® functions. Hence, execution times of functions within loops can be reduced significantly leading to a considerable speed up. Within this thesis, MEX files are used for several functions such as the computation of the element stiffness matrices or the element stresses of the 2.5D FEM substructure (cp. Sec. 4.1).

4 Finite Element Method substructures

The Finite Element Method (FEM) is able to represent geometrically complex, finite objects consisting of various materials by means of a discrete mathematical description. Therefore, the FEM is used to model structures and a part of the surrounding soil which are then coupled into the cylindrical or spherical cavity within the ITM substructure and consequently need to match the shape of the resp. cavity surfaces Γ_c and Γ_s. In order to enable a direct stiffness coupling of the ITM and the FEM, as presented in Ch. 5, the dynamic stiffness matrices of FEM meshes with a cylindrical and a spherical outer boundary must be computed first.

The dynamic stiffness of the halfspace with cylindrical cavity was derived in the wavenumber frequency domain in dependency of k_x and ω. Exploiting the length invariance of the system, the 2.5D approach makes it possible to reduce the originally three dimensional calculation to a series of two dimensional, quasi static calculations for each combination (k_x,ω) [176]. It is thus favourable to introduce also a 2.5D FEM description which allows to represent the 3D response on a two dimensional mesh [262]. Accordingly, plane quadrilateral finite elements with linear shape functions can be used to discretize the cross section of the FEM substructure, including additional degrees of freedom in lengthwise direction. However, the FEM formulation has to be adopted to the wavenumber frequency domain as presented in [162, 263] and briefly summarized in Sec. 4.1.1.

Since the spherical FEM structure to be coupled to the halfspace with spherical cavity (Sec. 3.3) is spatially limited and exhibits no invariance in any direction, usual three dimensional solid elements can be used. Therefore, the dynamic stiffness matrix is computed in the frequency domain w.r.t. Cartesian coordinates (x,y,z,ω) as presented in Sec. 4.2.1.

The Finite Element Method can also be applied for the modelling of structures above the ground surface, which are subsequently coupled to the soil via the compatibility conditions at the soil structure interface (cp. Sec. 5.3). The element formulations used to model the foundations and the multi storey frame in Sec. 6.5 are briefly introduced within this chapter in Sec. 4.2.2.

4.1 2.5D Finite Element Method

4.1.1 Element stiffness matrix

The common procedure to derive the stiffness matrix for a finite element is based on the principle of virtual work. Hereinafter, the latter is applied to deduce a 4-node quadrilateral element with three degrees of freedom at each node (Fig. 4.1b) from a common three dimensional, isoparametric volume element (Fig. 4.1a) with local coordinates (x,η,ζ). Thereby the additional third degree of freedom is introduced in order to describe the displacements w.r.t. the $x-$coordinate, corresponding to the out of plane direction.

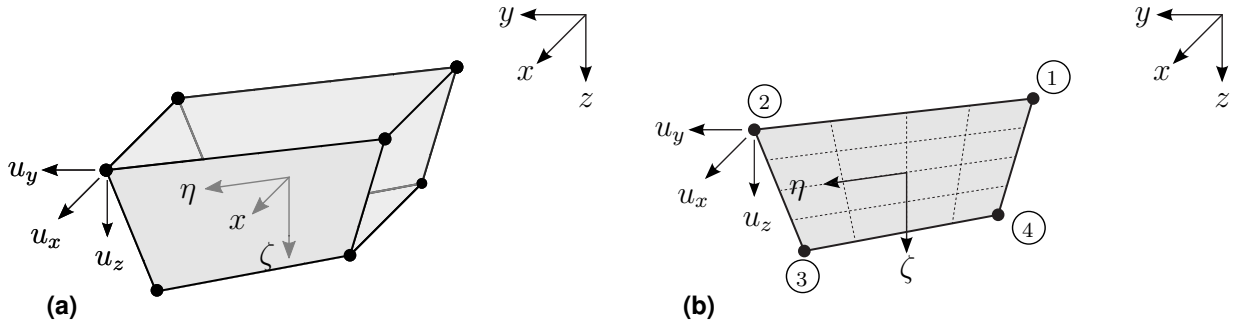

Figure 4.1: (a) Three dimensional 8-node solid element and (b) 2.5 dimensional 4-node element.

The weak form of the internal virtual work of the solid element, with $\delta\boldsymbol{\varepsilon}$ as the vector containing the virtual strains and $\boldsymbol{\sigma}$ as the vector of the real stress components, yields

$$\delta W_i = -\int\limits_{(V)} \delta\boldsymbol{\varepsilon}(x,\eta,\zeta)\ \boldsymbol{\sigma}(x,\eta,\zeta)\ \mathrm{d}V \tag{4.1}$$

Due to the length invariance of the system in $x-$direction, the integral over the volume is substituted by an integral over the cross sectional area A and an integral from $-\infty$ to ∞ w.r.t. x. Moreover, a transformation into the wavenumber domain $x \rightarrow k_x$ according to Parseval's identity [264], is performed resulting in

$$\delta W_i = -\int\limits_{-\infty}^{\infty}\int\limits_{(A)} \delta\boldsymbol{\varepsilon}(x,\eta,\zeta)\ \boldsymbol{\sigma}(x,\eta,\zeta)\ \mathrm{d}A\ \mathrm{d}x = -\frac{1}{2\pi}\int\limits_{-\infty}^{\infty}\int\limits_{(A)} \delta\bar{\boldsymbol{\varepsilon}}^{*}(k_x,\eta,\zeta)\ \bar{\boldsymbol{\sigma}}(k_x,\eta,\zeta)\ \mathrm{d}A\ \mathrm{d}k_x \tag{4.2}$$

where * signifies the conjugate complex of a parameter.

To enable a numerical computation, the integration of k_x is replaced by a summation over all discrete wavenumbers k_{x_n} leading to the following equation

$$\delta W_i = -\frac{1}{N_x} \sum_{n=1}^{N_x} \int_{(A)} \delta\tilde{\boldsymbol{\varepsilon}}^{T*}(k_{x_n},\eta,\zeta)\, \tilde{\boldsymbol{\sigma}}(k_{x_n},\eta,\zeta)\, \mathrm{d}A \tag{4.3}$$

The external virtual work and the virtual work of the inertia forces can be adapted analogously, so that the total virtual work $\delta W = \delta W_i + \delta W_e + \delta W_I$ results as

$$\begin{aligned} \delta W = \frac{1}{N_x} \sum_{n=1}^{N_x} \int_{(A)} & -\delta\tilde{\boldsymbol{\varepsilon}}^{H}(k_{x_n},\eta,\zeta)\, \tilde{\boldsymbol{\sigma}}(k_{x_n},\eta,\zeta) + \delta\tilde{\mathbf{u}}^{H}(k_{x_n},\eta,\zeta)\, \tilde{\mathbf{p}}(k_{x_n},\eta,\zeta) \\ & - \delta\tilde{\mathbf{u}}^{H}(k_{x_n},\eta,\zeta)\, \rho\, \omega^2 \tilde{\mathbf{u}}(k_{x_n},\eta,\zeta)\, \mathrm{d}A = 0 \end{aligned} \tag{4.4}$$

with the superscript H denoting the conjugate complex transpose. The virtual work performed by the internal and inertia forces is defined negative, since it is associated with restoring forces, whereas the external virtual work is defined positive, since energy is introduced into the system.

Eq. (4.4) is especially satisfied if $\delta W = 0$ holds for each combination of wavenumber and frequency (k_x,ω). The initial integration over the volume could be replaced by an integration over the cross sectional area A of the element for all virtual work contributions. Thus, the original 3D element with infinite extension in x is substituted by a 2D element, that contains the information about the deformation in longitudinal direction in terms of k_x. [162]

Applying the linear shape functions w.r.t. the natural coordinates (η,ζ)

$$\begin{aligned} N_1(\eta,\zeta) &= \frac{1}{4}(1-\eta)(1-\zeta) \qquad & N_2(\eta,\zeta) &= \frac{1}{4}(1-\eta)(1+\zeta) \\ N_3(\eta,\zeta) &= \frac{1}{4}(1+\eta)(1+\zeta) \qquad & N_4(\eta,\zeta) &= \frac{1}{4}(1+\eta)(1-\zeta) \end{aligned} \tag{4.5}$$

and using an isoparametric approach, the displacement field $\tilde{\mathbf{u}}(x,\eta,\zeta) = \mathbf{N}\tilde{\mathbf{u}}_\mathbf{n}$ can be described in dependency of the displacements $\tilde{\mathbf{u}}_\mathbf{n}$ at the element nodes. Assuming linear elastic material behaviour $\tilde{\boldsymbol{\sigma}} = \mathbf{D}\tilde{\boldsymbol{\varepsilon}}$ and replacing the derivatives of the shape functions within $\mathbf{B}$ in $x-$direction, according to the rules of the Fourier transform, by a multiplication with $\mathrm{i}k_x$, so that $\tilde{\boldsymbol{\varepsilon}} = \bar{\mathbf{B}}\tilde{\mathbf{u}}_\mathbf{n}$, the virtual work for one combination (k_x,ω), results as

$$-\delta\tilde{\mathbf{u}}_\mathbf{n}^H \underbrace{\left(\int_{(A)} \bar{\mathbf{B}}^H \mathbf{D}\bar{\mathbf{B}}\, \mathrm{d}A\right)}_{\bar{\mathbf{K}}} \tilde{\mathbf{u}}_\mathbf{n} + \delta\tilde{\mathbf{u}}_\mathbf{n}^H \underbrace{\left(\int_{(A)} \mathbf{N}^H \tilde{\mathbf{p}} \mathrm{d}A\right)}_{\tilde{\mathbf{p}}_\mathbf{n}} + \delta\tilde{\mathbf{u}}_\mathbf{n}^H \omega^2 \underbrace{\left(\int_{(A)} \rho\mathbf{N}^H \mathbf{N} \mathrm{d}A\right)}_{\mathbf{M}} \tilde{\mathbf{u}}_\mathbf{n} = 0 \tag{4.6}$$

with the elasticity matrix

$$\mathbf{D} = \begin{bmatrix} \lambda+2\mu & \lambda & \lambda & 0 & 0 & 0 \\ \lambda & \lambda+2\mu & \lambda & 0 & 0 & 0 \\ \lambda & \lambda & \lambda+2\mu & 0 & 0 & 0 \\ 0 & 0 & 0 & \mu & 0 & 0 \\ 0 & 0 & 0 & 0 & \mu & 0 \\ 0 & 0 & 0 & 0 & 0 & \mu \end{bmatrix} \tag{4.7}$$

the matrix of the shape functions

$$\mathbf{N} = \begin{bmatrix} N_1(\eta,\zeta) & 0 & 0 & N_2(\eta,\zeta) & 0 & 0 & \cdots \\ 0 & N_1(\eta,\zeta) & 0 & 0 & N_2(\eta,\zeta) & 0 & \cdots \\ 0 & 0 & N_1(\eta,\zeta) & 0 & 0 & N_2(\eta,\zeta) & \cdots \end{bmatrix} \tag{4.8}$$

and the matrix $\bar{\mathbf{B}}$ including the derivatives of the shape functions

$$\bar{\mathbf{B}} = \begin{bmatrix} \mathrm{i}k_x N_1(\eta,\zeta) & 0 & 0 & \mathrm{i}k_x N_2(\eta,\zeta) & 0 & \cdots \\ 0 & \frac{\partial N_1(\eta,\zeta)}{\partial y} & 0 & 0 & \frac{\partial N_2(\eta,\zeta)}{\partial y} & \cdots \\ 0 & 0 & \frac{\partial N_1(\eta,\zeta)}{\partial z} & 0 & 0 & \cdots \\ \frac{\partial N_1(\eta,\zeta)}{\partial y} & \mathrm{i}k_x N_1(\eta,\zeta) & 0 & \frac{\partial N_2(\eta,\zeta)}{\partial y} & \mathrm{i}k_x N_2(\eta,\zeta) & \cdots \\ 0 & \frac{\partial N_1(\eta,\zeta)}{\partial z} & \frac{\partial N_1(\eta,\zeta)}{\partial y} & 0 & \frac{\partial N_2(\eta,\zeta)}{\partial z} & \cdots \\ \frac{\partial N_1(\eta,\zeta)}{\partial z} & 0 & \mathrm{i}k_x N_1(\eta,\zeta) & \frac{\partial N_2(\eta,\zeta)}{\partial z} & 0 & \cdots \end{bmatrix} \tag{4.9}$$

Finally the system of equations can be written as

$$\bar{\mathbf{K}}\tilde{\mathbf{u}}_\mathbf{n} - \omega^2\mathbf{M}\tilde{\mathbf{u}}_\mathbf{n} = \left(\bar{\mathbf{K}} - \omega^2\mathbf{M}\right)\tilde{\mathbf{u}}_\mathbf{n} = \tilde{\mathbf{p}}_\mathbf{n} \tag{4.10}$$

The integral over the element area A for the stiffness matrix $\bar{\mathbf{K}}$, the mass matrix $\mathbf{M}$ as well as the nodal load vector $\tilde{\mathbf{p}}_\mathbf{n}$ in Eq. (4.6) is carried out numerically by means of a Gauß integration with four Gauß points (GP) at the coordinates η_k and ζ_l and using the weighting factors w_k and w_l given in [265]

$$\bar{\mathbf{K}} = \sum_{k=1}^{n_\mathrm{GP}} \sum_{l=1}^{n_\mathrm{GP}} \bar{\mathbf{B}}^H(k_x,\eta_k,\zeta_l)\,\mathbf{D}\,\bar{\mathbf{B}}(k_x,\eta_k,\zeta_l)\det(\mathbf{J})\,w_k\,w_l \tag{4.11}$$

$$\mathbf{M} = \sum_{k=1}^{n_\mathrm{GP}} \sum_{l=1}^{n_\mathrm{GP}} \rho\mathbf{N}^H(\eta_k,\zeta_l)\,\mathbf{N}(\eta_k,\zeta_l)\;\det(\mathbf{J})\,w_k\,w_l \tag{4.12}$$

with $\mathbf{J}$ being the Jacobian matrix, relating the global and the local coordinates.

4.1.2 Dynamic stiffness for cylindrical substructure

In order to be coupled to the halfspace with cylindrical cavity, the overall FEM substructure must exhibit a cylindrical outer boundary. Therefore, the nodes on the cylindrical coupling surface Γ_c are distributed equally over the circumference in order to match with the discretization points of the ITM substructure, leading to a constant distance $\mathrm{d}s$ between the nodes, as depicted in Fig. 4.2. [176] Inside the FEM domain Ω_c, the nodes can in principle be arranged arbitrarily. Nevertheless, the element size should be so small that the predominant waves at a certain frequency are represented sufficiently. For this purpose, a number of about five to ten elements per wavelength is often stated in literature [266–268].

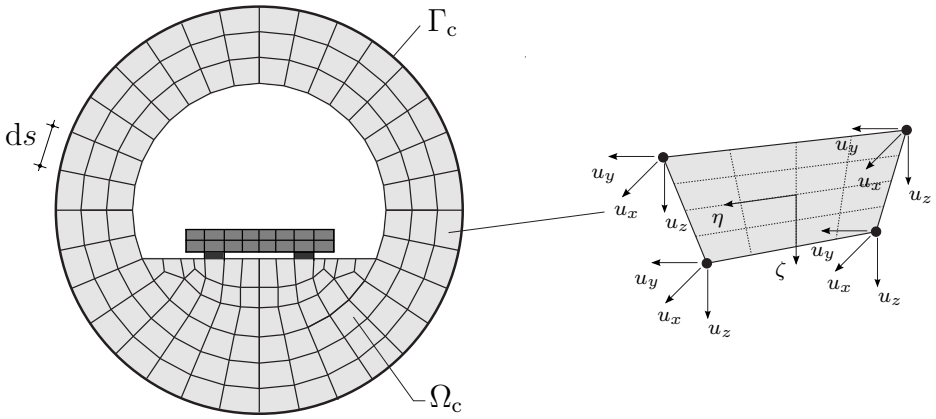

Figure 4.2: Cylindrical FEM substructure consisting of 2.5D elements.

With Eqs. (4.11) and (4.12) it is possible to compute the dynamic stiffness matrix for each element of the FEM substructure as

$$\tilde{\mathbf{K}}(k_x,\omega) = \bar{\mathbf{K}}(k_x) - \omega^2\mathbf{M} \tag{4.13}$$

Assembling all element stiffness matrices into a global stiffness matrix and sorting them w.r.t. the degrees of freedom at the cylindrical coupling surface Γ_c and inside the FEM substructure Ω_c the total system of equations, relating the nodal forces and the nodal displacements, results as

$$\underbrace{\begin{bmatrix} \tilde{\mathbf{K}}^{\mathbf{hs\ cyl}}_{\mathbf{\Gamma_c\Gamma_c\ FE}} & \tilde{\mathbf{K}}^{\mathbf{hs\ cyl}}_{\mathbf{\Gamma_c\Omega_c\ FE}} \\ \tilde{\mathbf{K}}^{\mathbf{hs\ cyl}}_{\mathbf{\Omega_c\Gamma_c\ FE}} & \tilde{\mathbf{K}}^{\mathbf{hs\ cyl}}_{\mathbf{\Omega_c\Omega_c\ FE}} \end{bmatrix}}_{\tilde{\mathbf{K}}^{\mathbf{hs\ cyl}}_{\mathbf{FE}}} \underbrace{\begin{pmatrix} \tilde{\mathbf{u}}^{\mathbf{hs\ cyl}}_{\mathbf{\Gamma_c\ FE}} \\ \tilde{\mathbf{u}}^{\mathbf{hs\ cyl}}_{\mathbf{\Omega_c\ FE}} \end{pmatrix}}_{\tilde{\mathbf{u}}^{\mathbf{hs\ cyl}}_{\mathbf{FE}}} = \underbrace{\begin{pmatrix} \tilde{\mathbf{P}}^{\mathbf{hs\ cyl}}_{\mathbf{\Gamma_c\ FE}} \\ \tilde{\mathbf{P}}^{\mathbf{hs\ cyl}}_{\mathbf{\Omega_c\ FE}} \end{pmatrix}}_{\tilde{\mathbf{P}}^{\mathbf{hs\ cyl}}_{\mathbf{FE}}} \tag{4.14}$$

4.1.3 Element stresses for 2.5D formulation

After the computation of the nodal displacements $\tilde{\mathbf{u}}_{\mathbf{FE}}^{\mathbf{hs\,cyl}}$ by solving Eq. (4.14), the element stresses can be computed in a postprocessing step. Therefore, firstly the nodal displacements of a certain element $\tilde{\mathbf{u}}_{\mathbf{n}}$ are extracted from the global displacement vector. From them, the elemental stresses are determined as

$$\tilde{\boldsymbol{\sigma}}_{\mathbf{k}}(k_x,\eta_k,\zeta_k,\omega) = \mathbf{D}\,\bar{\mathbf{B}}(k_x,\eta_k,\zeta_k)\,\tilde{\mathbf{u}}_{\mathbf{n}}(k_x,\omega) \tag{4.15}$$

Usually the stresses are evaluated at the Gauß points initially, as there the results are most exact, and then extrapolated to the element nodes using the shape functions. As the displacements, the stresses are evaluated for all discrete wavenumbers k_x and negative frequencies ω. After adding the complex conjugate counter part of the stresses for positive frequencies, the stresses $\bar{\boldsymbol{\sigma}}_{\mathbf{n}}(x,y,z,\omega)$ in the frequency or $\boldsymbol{\sigma}_{\mathbf{n}}(x,y,z,t)$ in the time domain are obtained performing the corresponding discrete inverse Fourier transforms.

In case of the cylindrical finite element substructure the mesh is created using the Ansys® APDL, whereas the computation of the element and global stiffness matrices, due to the adaptions, necessary for the 2.5D approach, is preformed in Matlab®. Therefore, one has to take care that the definition of the Gauß points and the corresponding element nodes matches within both software applications [269].

4.2 3D Finite Element Method

4.2.1 Dynamic stiffness for spherical substructure

The Finite Element substructure to be coupled to the halfspace with spherical cavity must exhibit its boundary nodes on a spherical outer surface with the same radius as specified by the ITM substructure. On this spherical surface Γ_s, both substructures are coupled applying the continuity of displacements and the equilibrium of forces. Since the spherical inclusion, modelled with the FEM, is a finite structure, for the purpose of a harmonic analysis it can be described with Cartesian coordinates in the frequency domain (x,y,z,ω).

Prerequisites for FEM mesh

The stresses and displacements of the halfspace with spherical cavity on Γ_s are defined in the (r,m,l,ω) domain, which is chosen as common basis for the coupling. Thus, the stiffness of the

FEM substructure, associated with the DOFs on Γ_s, is transformed in spherical coordinates and developed in series of spherical harmonics. To be able to apply the same transformation procedures for the FEM as derived for the ITM substructure (cp. Sec. 3.5.1), the stiffness of the FEM model must be available at the same discrete points that are used for the numerical evaluation of the stiffness of the ITM substructure. Therefore, the arrangement of the FEM nodes on the spherical boundary is chosen such, that they coincide with the intersection points of the N_ϑ latitudes and the N_φ longitudes, as depicted in Fig. 4.3.

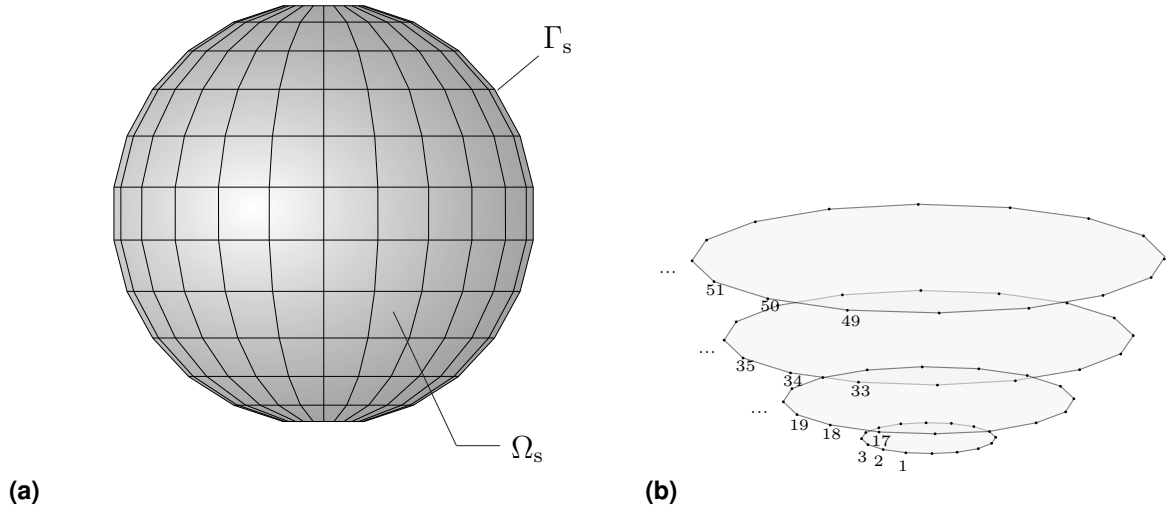

Figure 4.3: (a) 3D finite element mesh with spherical boundary and (b) numbering of nodes.

The z-coordinates of the latitudes are chosen on the N_ϑ Gauß points that are distributed on the z-axis along the diameter of the sphere, in order to allow a numerical integration of the associated Legendre polynomials, used for the expansion of the parameters on the spherical boundary Γ_s into series of spherical harmonics. The longitudes are spaced equally over the circumference, leading to a constant distance of the nodes $\mathrm{d}s_\varphi = 2\pi/(N_\varphi - 1)$ on one latitude. [84]

Restrictions and modelling approach

The freedom in the design of the finite element mesh in total features a couple of restrictions as the prescribed boundary coupling nodes must be hit. The decreasing distance of the Gauß points when approaching the poles, enforces the element lengths $\mathrm{d}s_\vartheta$ between the latitudes to diminish as well. Therefore, the element size in the interior is predetermined by the coupling nodes to a large degree and results in some limitations in the ability to model arbitrary structures within the FEM subsystem.

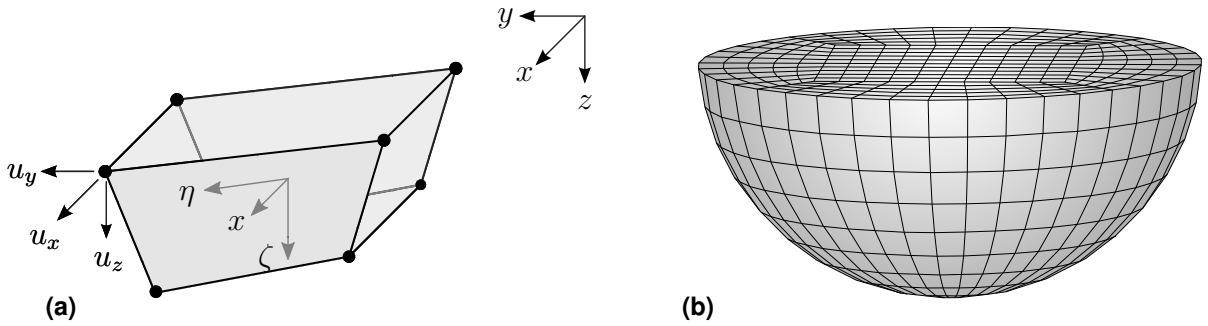

Figure 4.4: (a) Three dimensional 8-node solid element and (b) corresponding FEM mesh for coupling to halfspace with spherical indentation.

In order to comply with the given boundary conditions, the obvious choice are eight node solid elements with linear shape functions which allow a coupling of each node of an element with a coupling node on Γ_s. The structural configuration of the FE mesh using this element type is exemplarily depicted in Fig. 4.4. The quadratic core enables to model surface or embedded foundations with or without elastic bedding as well as a rectangular excavation inside the soil rather easily. Examples for these cases will be presented later on in Secs. 6.2.3 and 6.2.5.

Higher order rectangular elements are in contrast not easily applicable, since they exhibit further nodes on their edges which then do not match with the coupling nodes and thus violate the transition conditions to the surrounding soil.

Alternative meshes and coupling procedures

As an alternative, three dimensional, four node tetrahedron elements could be used to model the FEM substructure with spherical boundary. This element type permits the generation of a FE mesh, in which all coupling nodes are hit and simultaneously a refinement of the mesh towards the interior of the sphere is possible. This allows a more detailed and free modelling of structures inside. However, the size of the elements connecting to Γ_s is still strictly given by the coupling nodes. The arrangement of the FEM mesh is exemplarily illustrated in Fig. 4.5 and results for tetrahedral elements compared to hexahedral elements are shown in Sec. 6.1.3.

A further possibility to enable a completely free modelling of structures inside the spherical boundary, is to approximate the overall solution by coupling only a limited number of the spherical harmonics, describing the stresses and displacements on the interaction surface of the ITM and the FEM substructures. However this approach was not implemented within the scope of this thesis. In this case different algorithms could be used for the development

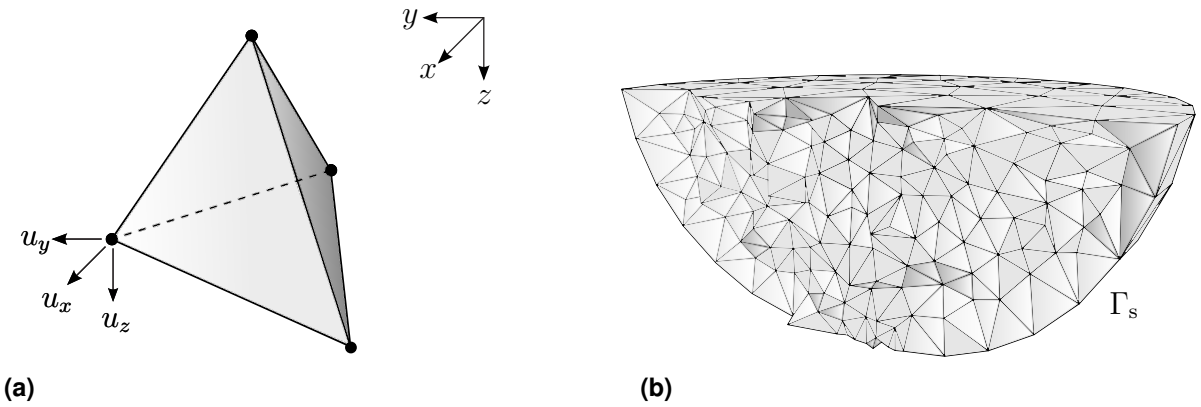

Figure 4.5: (a) Three dimensional 4-node tetrahedron element and (b) corresponding FEM mesh for coupling to halfspace with spherical indentation.

of the quantities on Γ_s in series of spherical harmonics for the two substructures. As presented in [252, 254] algorithms exist, which allow the numerical evaluation of the associated Legendre transforms on arbitrary grids. Since therewith neither the number or location of the boundary nodes nor the element size is predefined by the ITM, an arbitrary distribution of the FEM nodes on the spherical boundary is possible and a free meshing of any structure can be performed using standard FEM tools. Developing the stresses and displacements of the FEM substructure on Γ_s into series of spherical harmonics, the amount of boundary nodes and thus also the number of series members m, l obtained is not necessarily equal for both substructures. For the coupling therefore the upper limit of the spherical harmonics taken into account is given by the maximum of series members reached by either the ITM or the FEM substructure. This maximum should be, however, chosen such that all physical phenomena as reflection, transmission, refraction and scattering of the waves at the spherical boundary are sufficiently represented.

Another approach would be to use so called Mortar methods [270–272], which enable a coupling of non conform discretizations on non overlapping subdomains by not satisfying the continuity conditions at the interface point wise, but reformulating it in a weak variational manner. In this case again the Finite Element substructure can be meshed arbitrarily, as the FEM nodes do not have to match with the ITM nodes on Γ_s. To perform the coupling of the ITM and the FEM applying the Mortar concept, the stresses and displacements need to be evaluated for both substructures on their respective discretization points on Γ_s w.r.t. to a common reference frame chosen as (x,y,z,ω). By introducing interface fields for the quantities on Γ_s with additional degrees of freedom in form of Lagrange multipliers, the continuity conditions are enforced via conservation of energy at the coupling surface in a weak form. An application for this kind of indirect coupling of the FEM to a solution using analytical solution approaches, i.e. the Wave Based Method (WBM), which could similarly

be applied to the ITM-FEM coupling can be found in [273, 274].

Dynamic stiffness of the FEM substructure

Within this thesis, the approach to use the ITM discretization points as boundary nodes for the FEM substructure is used, and the coupling is finally performed in the (r,m,l,ω) domain after the respective transformations. To discretize the volume within Γ_s, either hexahedra with 8 nodes or tetrahedra with 4 nodes are used and arranged such that their nodes coincide with the discretization points of the ITM on the spherical surface. Since no further modifications on the elements are necessary, as it was the case for the 2.5D elements, the generation of the mesh as well as the computation of the mass, stiffness and damping matrices is directly done within a commercial FEM software. The Ansys® Mechanical APDL is used, as it allows to set up a structured mesh including the given prerequisites very precisely and also offers enhanced formulations for the employed elements.

For the computation of $\bar{\mathbf{K}}$, $\bar{\mathbf{C}}$ and $\mathbf{M}$, a substructure analysis is used in Ansys®, wherein a matrix reduction technique is applied to reduce the system matrices to a smaller set of DOFs, representing a collection of previously assembled elements as one single super element. Thereby the DOFs of the interface nodes, necessary for the coupling, as well as the DOFs of nodes at which the results shall be evaluated after solving the system have to be retained [275]. Since the reduction technique is implemented and executed automatically within the commercial FEM software and requires only little calculation capacity, it is very beneficial to apply the substructure analysis regarding the computational effort for the total solution procedure. Due to the reduced number of nodes and DOFs, the effort for both, the export of $\bar{\mathbf{K}}$, $\bar{\mathbf{C}}$ and $\mathbf{M}$ from Ansys® and the import into the developed Matlab® program, inside which the coupling of the ITM and the FEM substructures as well as the overall solution are performed, can be reduced significantly. Furthermore, the amount of sorting and renumbering operations, due to the necessity to distinguish between nodes on Γ_s, needed for the coupling and the interior nodes within Ω_s, is minimized. Last but not least, also the size of the total system of equations describing the coupled ITM-FEM system and thus the time necessary to solve it decreases considerably.

In Ansys® as standard procedure a Guyan reduction is applied, corresponding to an elimination of the DOFs not needed for the further analysis [276]. Therefore, the degrees of freedom in the general structural equation

$$\left(-\omega^2\mathbf{M} + \mathrm{i}\,\omega\,\mathrm{sign}(\omega)\,\bar{\mathbf{C}} + \bar{\mathbf{K}}\right)\bar{\mathbf{u}} = \bar{\mathbf{P}} \tag{4.16}$$

are partitioned in master DOFs $\bar{\mathbf{u}}_m$, which are retained, and slave DOFs $\bar{\mathbf{u}}_s$, which are eliminated [277]. For the static case ($\omega = 0$) the reorganized system of equations yields

$$\underbrace{\begin{bmatrix} \bar{\mathbf{K}}_{mm} & \bar{\mathbf{K}}_{ms} \\ \bar{\mathbf{K}}_{sm} & \bar{\mathbf{K}}_{ss} \end{bmatrix}}_{\bar{\mathbf{K}}_{\text{full}}} \underbrace{\begin{bmatrix} \bar{\mathbf{u}}_m \\ \bar{\mathbf{u}}_s \end{bmatrix}}_{\bar{\mathbf{u}}_{\text{full}}} = \underbrace{\begin{bmatrix} \bar{\mathbf{P}}_m \\ \bar{\mathbf{P}}_s \end{bmatrix}}_{\bar{\mathbf{P}}_{\text{full}}} \tag{4.17}$$

Solving the bottom equation of (4.17), substituting the result in top equation and setting the forces at all interior degrees of freedom $\bar{\mathbf{P}}_s$ to zero it follows

$$\underbrace{\left[\, \bar{\mathbf{K}}_{mm} - \bar{\mathbf{K}}_{ms}\bar{\mathbf{K}}_{ss}^{-1}\bar{\mathbf{K}}_{sm} \,\right]}_{\bar{\mathbf{K}}_{\text{red}}} \underbrace{\left[\, \bar{\mathbf{u}}_m \,\right]}_{\bar{\mathbf{u}}_{\text{red}}} = \underbrace{\left[\, \bar{\mathbf{P}}_m - \bar{\mathbf{K}}_{ms}\bar{\mathbf{K}}_{ss}^{-1}\bar{\mathbf{P}}_s \,\right]}_{\bar{\mathbf{P}}_{\text{red}}} \tag{4.18}$$

The foregoing is equivalent to a coordinate transform [276]

$$\begin{bmatrix} \bar{\mathbf{u}}_m \\ \bar{\mathbf{u}}_s \end{bmatrix} = \begin{bmatrix} \mathbf{I} \\ \bar{\mathbf{G}}_{sm} \end{bmatrix} \bar{\mathbf{u}}_m = \mathbf{T}\, \bar{\mathbf{u}}_m \tag{4.19}$$

where $\mathbf{I}$ is the identity matrix and $\bar{\mathbf{G}}_{sm} = \bar{\mathbf{K}}_{ss}^{-1}\bar{\mathbf{K}}_{sm}$ contains the constraint modes that are mode shapes induced to the interior DOFs by applying successive unit displacements on one interface DOF, while all other interface DOFs are held fix [278].

Applying the above transformations to the structural potential and kinetic energies, the reduced stiffness matrix $\bar{\mathbf{K}}_{\text{red}} = \mathbf{T}^T\bar{\mathbf{K}}_{\text{full}}\mathbf{T}$, mass matrix $\bar{\mathbf{M}}_{\text{red}} = \mathbf{T}^T\bar{\mathbf{M}}_{\text{full}}\mathbf{T}$ and damping matrix $\bar{\mathbf{C}}_{\text{red}} = \mathbf{T}^T\bar{\mathbf{C}}_{\text{full}}\mathbf{T}$ for the dynamic case can be obtained according to [276], finally leading to

$$\bar{\mathbf{K}}_{\text{red}} = \bar{\mathbf{K}}_{mm} - \bar{\mathbf{K}}_{ms}\bar{\mathbf{K}}_{ss}^{-1}\bar{\mathbf{K}}_{sm} \tag{4.20a}$$

$$\mathbf{M}_{\text{red}} = \bar{\mathbf{M}}_{mm} + \bar{\mathbf{M}}_{ms}\bar{\mathbf{G}}_{sm} + \bar{\mathbf{G}}_{ms}\left(\bar{\mathbf{M}}_{sm} + \bar{\mathbf{M}}_{ss}\bar{\mathbf{G}}_{sm}\right) \tag{4.20b}$$

$$\bar{\mathbf{C}}_{\text{red}} = \bar{\mathbf{C}}_{mm} + \bar{\mathbf{C}}_{ms}\bar{\mathbf{G}}_{sm} + \bar{\mathbf{G}}_{ms}\left(\bar{\mathbf{C}}_{sm} + \bar{\mathbf{C}}_{ss}\bar{\mathbf{G}}_{sm}\right) \tag{4.20c}$$

It is important to point out that in case of the stiffness matrix the reduction leads to no loss of information and complexity, since all elements of the original stiffness matrix contribute [276]. For the reduced mass matrix, both stiffness and mass elements are used in the computation, which results in the eigenvalue problem not being preserved exactly in the reduced system. This can lead to smaller deviations at higher frequencies, compared to using the complete system matrices for the analysis. Alternatively to the Guyan reduction,

a Component Mode Synthesis (CMS) could be used to obtain eigenvalue preserving reduced system matrices. Furthermore, it should be mentioned that, since the master DOFs for the reduction must always include all degrees of freedom connected to the second substructure, it is not simply possible to create a freely meshed FEM model and condense all nodes on Γ_s that do not match with the ITM coupling nodes, although this might seem like an easy to handle solution at the first glance.

Since the global, assembled, reduced system matrices are symmetric, for the export it is sufficient to write the lower triangular part into the export file (Harvel Boeing format) in order to save writing time. After the import of the matrices into Matlab® the upper part is supplemented, before the FEM nodes are split in interior nodes and nodes on the spherical surface. The latter are reordered such that they coincide with the order of the ITM nodes which are numbered clock wise within one latitude, starting with the bottommost latitude and then consecutively up to the one next to the upper pole (Fig. 4.3b). With the nodes, also the DOFs and thus the reduced system matrices in Eqs. (4.20) need to be resorted, so that they eventually end up in a system of equation with the following form

$$\underbrace{\begin{bmatrix} \bar{\mathbf{K}}^{\mathbf{hs\,sph}}_{\mathbf{\Gamma_s \Gamma_s\,FE}} & \bar{\mathbf{K}}^{\mathbf{hs\,sph}}_{\mathbf{\Gamma_s \Omega_s\,FE}} \\ \bar{\mathbf{K}}^{\mathbf{hs\,sph}}_{\mathbf{\Omega_s \Gamma_s\,FE}} & \bar{\mathbf{K}}^{\mathbf{hs\,sph}}_{\mathbf{\Omega_s \Omega_s\,FE}} \end{bmatrix}}_{\bar{\mathbf{K}}^{\mathbf{hs\,sph}}_{\mathbf{FE}}} \underbrace{\begin{pmatrix} \bar{\mathbf{u}}^{\mathbf{hs\,sph}}_{\mathbf{\Gamma_s\,FE}} \\ \bar{\mathbf{u}}^{\mathbf{hs\,sph}}_{\mathbf{\Omega_s\,FE}} \end{pmatrix}}_{\bar{\mathbf{u}}^{\mathbf{hs\,sph}}_{\mathbf{FE}}} = \underbrace{\begin{pmatrix} \bar{\mathbf{P}}^{\mathbf{hs\,sph}}_{\mathbf{\Gamma_s\,FE}} \\ \bar{\mathbf{P}}^{\mathbf{hs\,sph}}_{\mathbf{\Omega_s\,FE}} \end{pmatrix}}_{\bar{\mathbf{P}}^{\mathbf{hs\,sph}}_{\mathbf{FE}}} \tag{4.21}$$

whereby $\bar{\mathbf{K}}^{\mathbf{hs\,sph}}_{\mathbf{FE}} = \left(-\omega^2 \mathbf{M}_{\mathrm{red}} + \mathrm{i}\,\omega\,\mathrm{sign}(\omega)\,\bar{\mathbf{C}}_{\mathrm{red}} + \bar{\mathbf{K}}_{\mathrm{red}}\right)$ is the dynamic stiffness matrix of the system and $\bar{\mathbf{u}}^{\mathbf{hs\,sph}}_{\mathbf{FE}}$ and $\bar{\mathbf{P}}^{\mathbf{hs\,sph}}_{\mathbf{FE}}$ refer to the condensed degrees of freedom $\bar{\mathbf{u}}_m$.

4.2.2 Dynamic stiffness for structures on the ground surface

In order to model an arbitrary finite, three dimensional superstructure on the ground surface, generally usual 8-node solid elements with three translatory DOFs can be used. If a plate like structure is considered, the use of shell elements is favourable concerning computational efficiency. Therefore, a quadrilateral shell element with six DOFs per node (Fig. 4.6a) is used to model the foundation and the floor slabs of the multi-storey frame in the present work. Furthermore, the use of a shell element is advantageous with regard to the coupling with the 3D beam elements (Fig. 4.6b), used to model the frame columns, as then both, the translational and the rotational degrees of freedom can be coupled directly at the common nodes. The coupling to the underlying ground at the soil foundation interface via the con-

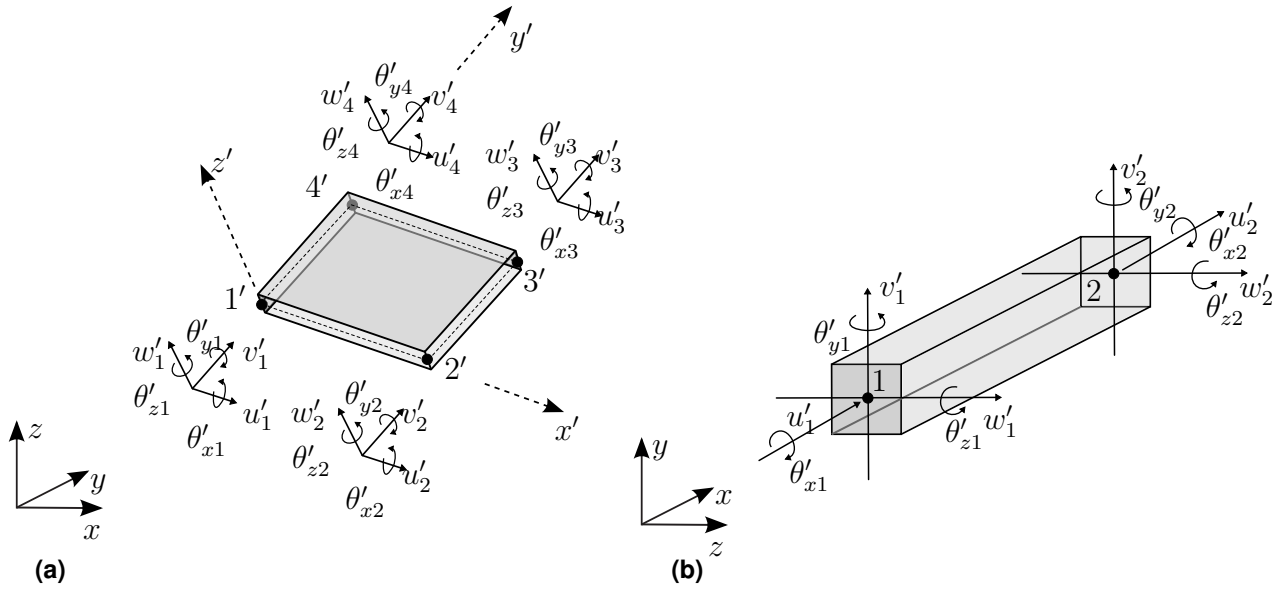

Figure 4.6: Local displacements and rotations of a (a) quadrilateral thin flat layered shell element (cp. [279]) and (b) spatial beam element with each 6 DOFs per node.

tinuity conditions (cp. Sec. 5.3) is carried out w.r.t. Cartesian coordinates in the frequency domain (x,y,z,ω).

Thus, also the stiffness and mass matrices of the element formulations presented hereinafter are derived in this domain applying a common displacement based finite element approach via the weak form of the equation of motion by means of the principle of virtual work

$$\delta W = \delta W_i + \delta W_I = \int\limits_{(V)} \delta\bar{\boldsymbol{\varepsilon}}^T \, \mathbf{D} \, \bar{\boldsymbol{\varepsilon}} \, \mathrm{d}V - \omega^2 \int\limits_{(V)} \delta\bar{\mathbf{u}}^T \, \rho \, \bar{\mathbf{u}} \, \mathrm{d}V \tag{4.22}$$

$$= \delta\bar{\mathbf{u}}^T \left(\int\limits_{(V)} \mathbf{B}^T \, \mathbf{D} \, \mathbf{B} \, \mathrm{d}V \right) \bar{\mathbf{u}} - \omega^2 \delta\bar{\mathbf{u}}^T \left(\int\limits_{(V)} \mathbf{N}^T \, \rho \, \mathbf{N} \, \mathrm{d}V \right) \bar{\mathbf{u}} \tag{4.23}$$

The numerical integration of the above integrals is carried out via the Gauß quadrature.

Quadrilateral thin flat layered shell element (QTFLS)

The implemented shell element was introduced in [279] as a superposition of a quadrilateral layered membrane element with drilling degrees of freedom, presented in [280], and the Discrete Kirchhoff Quadrilateral (DKQ) element, defined in [281]. This combination allows to incorporate the in-plane stretching and the out of plane bending behaviour within one 4-node quadrilateral thin flat layered shell element (QTFLS), that exhibits 6 DOFs (three translations and three rotations) per node.

In order to derive the element stiffness matrix, the membrane and bending kinematics are superposed, assuming a state of plane stress over the thickness and the Kirchhoff theory for the bending, thereby neglecting the strain due to shear. This finally leads to an extended local strain vector, separated for the local membrane strain $\bar{\boldsymbol{\varepsilon}}_m^{'}$ and the local curvature due to bending $\bar{\boldsymbol{\varepsilon}}_b^{'}$, defined in dependence of the nodal DOFs $\mathbf{u}'_{\mathrm{sh}}$

$$\underbrace{\begin{bmatrix} \bar{\boldsymbol{\varepsilon}}_m^{'} \\ \bar{\boldsymbol{\varepsilon}}_b^{'} \end{bmatrix}}_{\boldsymbol{\varepsilon}'_{\mathrm{sh}}} = \underbrace{\begin{bmatrix} \mathbf{B}'_m(x',y') & \mathbf{0} \\ \mathbf{0} & \mathbf{B}'_b(x',y') \end{bmatrix}}_{\mathbf{B}'_{\mathrm{sh}}} \underbrace{\begin{bmatrix} \bar{\mathbf{u}}'_m \\ \bar{\mathbf{u}}'_b \end{bmatrix}}_{\mathbf{u}'_{\mathrm{sh}}} \tag{4.24}$$

wherein $\mathbf{B}'_m(x',y')$ includes the kinematics for the membrane and $\mathbf{B}'_b(x',y')$ those for the bending element, as given in [279]. Also the nodal displacement vector is separated w.r.t. the membrane and the bending DOFs

$$\mathbf{u}'_m = [u'_1,\, v'_1,\, \theta'_{z1}, ..., u'_4,\, v'_4,\, \theta'_{z4}]^T \quad \text{and} \quad \mathbf{u}'_b = \left[w'_1,\, \theta'_{x1},\, \theta'_{y1}, ..., w'_4,\, \theta'_{x4},\, \theta'_{y4}\right]^T \tag{4.25}$$

Therewith, the local tangent stiffness matrix of the shell element can be derived as [279]

$$\mathbf{K}'_{\mathrm{sh}} = \int\limits_{(A')} \mathbf{B}'^T_{\mathrm{sh}}\, \mathbf{D}'_{\mathrm{sh}}\, \mathbf{B}'_{\mathrm{sh}} \mathrm{d}A' = \sum_{k=1}^{n_{\mathrm{GP}}} \sum_{l=1}^{n_{\mathrm{GP}}} \mathbf{B}'^T_{\mathrm{sh}}(x'_k,y'_l)\, \mathbf{D}'_{\mathrm{sh}}\, \mathbf{B}'_{\mathrm{sh}}(x'_k,y'_l)\, \det(\mathbf{J})\, w_k\, w_l \tag{4.26}$$

where $\mathbf{D}'_{\mathrm{sh}}$ is the section tangent matrix including the contributions of the membrane and the bending relating the corresponding stresses and the strains.

An usual consistent mass matrix formulation is used to deduce

$$\mathbf{M}'_{\mathrm{sh}} = \int\limits_{(A')} \mathbf{N}'^T_{\mathrm{sh}}\, \boldsymbol{\rho}_{\mathrm{sh}}\, \mathbf{N}'_{\mathrm{sh}} \mathrm{d}A' = \sum_{k=1}^{n_{\mathrm{GP}}} \sum_{l=1}^{n_{\mathrm{GP}}} \mathbf{N}'^T_{\mathrm{sh}}(x'_k,y'_l)\, \boldsymbol{\rho}_{\mathrm{sh}}\, \mathbf{N}'_{\mathrm{sh}}(x'_k,y'_l)\, \det(\mathbf{J})\, w_k\, w_l \tag{4.27}$$

with $\mathbf{N}'_{\mathrm{sh}}$ being the matrix including the usual shape functions for a quadrilateral element in local coordinates (cp. Eq. (4.5)) and $\boldsymbol{\rho}_{\mathrm{sh}}$ including the mass density per area and the rotational inertia on its main diagonal. Structural damping is not included in the current implementation of the shell element.

3D spatial beam element

The implemented 3D beam element exhibits also three translations and three rotations at each of its two nodes. A local coordinate system with origin in the center of gravity and shear of the uniform cross section is used, with axis being equal to the principal axis of the element. Assuming the Euler Bernoulli beam theory and isotropic material behaviour,

the axial, bending and torsional effects decouple and can be considered independently. The internal virtual work used to derive the element stiffness matrix thus results as [282]

$$\delta W_i = \int\limits_{(L)} \delta \boldsymbol{\varepsilon}'^{T}_{\text{beam}} \mathbf{D}_{\text{beam}} \boldsymbol{\varepsilon}'_{\text{beam}} \mathrm{d}x' = \int\limits_{(L')} \left(EA u'^{2}_{,x'} + EI_y \theta'^{2}_{y',x'} + EI_z \theta'^{2}_{z',x'} + GI_T \theta'^{2}_{x',x'} \right) \mathrm{d}x' \tag{4.28}$$

with the comma subscript denoting the derivative w.r.t. a certain coordinate. Eq. (4.28) can be reformulated in dependency of the nodal displacements and rotations

$$\bar{\mathbf{u}}'_{\text{beam}} = \left[u'_1, v'_1, w'_1, \theta'_{x1}, \theta'_{y1}, \theta'_{z1}, u'_2, v'_2, w'_2, \theta'_{x2}, \theta'_{y2}, \theta'_{z2} \right]^T \tag{4.29}$$

assuming linear interpolation functions for the axial and the torsional deformation and cubic Hermite polynomials for the bending deflection finally leading to

$$\mathbf{K}'_{\text{beam}} = \int\limits_{(L')} \mathbf{B}'^{T}_{\text{beam}} \mathbf{D}'_{\text{beam}} \mathbf{B}'_{\text{beam}} \mathrm{d}L' = \sum_{k=1}^{n_{\text{GP}}} \mathbf{B}'^{T}_{\text{beam}}(x'_k) \mathbf{D}'_{\text{beam}} \mathbf{B}'_{\text{beam}}(x'_k) \det(\mathbf{J}) \, w_k \tag{4.30}$$

given in Appx. A.6.1 and $\mathbf{D}'_{\text{beam}}$ being the isotropic material matrix for the Euler Bernoulli beam.

For the consistent mass matrix, different shape functions $\mathbf{N}'_{\text{beam}}$ are used in order to be able to consider also the effects of rotational inertia, but neglecting the shear deformation effects as presented in [283]. This leads eventually to the mass matrix

$$\mathbf{M}'_{\text{beam}} = \int\limits_{(L')} \mathbf{N}'^{T}_{\text{beam}} \rho \, \mathbf{N}'_{\text{beam}} \mathrm{d}L' = \sum_{k=1}^{n_{\text{GP}}} \mathbf{N}'^{T}_{\text{beam}}(x'_k) \rho \, \mathbf{N}'_{\text{beam}}(x'_k) \det(\mathbf{J}) \, w_k \tag{4.31}$$

whereby ρ is the mass density and L the length of the beam element. The mass matrix is given in Appx. A.6.2.

To include damping, a common Rayleigh damping approach was implemented

$$\mathbf{C}'_{\text{beam}} = \alpha \mathbf{M}'_{\text{beam}} + \beta \mathbf{K}'_{\text{beam}} \tag{4.32}$$

For the coupling with the ITM soil substructure, of course the element stiffness and mass matrices need to be transformed to a common global reference frame and assembled into a global stiffness matrix.

5 Coupling of substructures

In this chapter the previously derived ITM and FEM substructures are coupled, applying the compatibility conditions at the common interface. In Sec. 5.1 length invariant structures, either fully or partially embedded in the soil and modelled with the 2.5D FEM approach, are coupled to the halfspace with cylindrical cavity or indentation. Finite 3D structures embedded in a portion of soil exhibiting a spherical outer boundary, modelled with the FEM, are coupled to the halfspace with spherical cavity or indentation in Sec. 5.2. To enable the investigation of the dynamic interaction of above-ground structures with the underlying soil, in Sec. 5.3 firstly a procedure to compute the dynamic stiffness matrix at the surface of an arbitrary soil subsystem, described by the ITM or a coupled ITM-FEM approach, is introduced. Subsequently, the methodology for the coupling of three dimensional structures to the underlying ground at the soil foundation interface is presented. In the Sec. 5.4, a postprocessing procedure is outlined to calculate the stress and displacement distributions in the subgrade due to the dynamic soil structure interaction. Finally, it is shown how the power input at the soil foundation interface due to the SSI contact stresses can be determined and how the radiation directivity of the induced waves can be accounted for by the power flow through a control volume within the linear elastic homogenous or layered soil.

5.1 Coupling on the cylindrical interaction surface

For the coupling of the ITM and the FEM substructures at the cylindrical interaction surface, the equilibrium of forces and the compatibility of displacements are used as transition conditions [162]. In order to apply these equations, the quantities on Γ_c (cp. Fig. 5.1) have to be described in terms of a common reference frame, for which the ITM basis is chosen. Within the system of equations (3.8), which describes the halfspace with cylindrical cavity or indentation, the degrees of freedom are sorted separately according to those on the halfspace surface and the cylindrical coupling surface. The dynamic stiffnesses, displacements and the loads on Γ_c are described in the threefold Fourier transformed (k_x,r,n,ω) domain in

cylindrical coordinates. The same holds also for the halfspace with two cylindrical tunnels or indentations described by Eqs. (3.18) as well as for the multilayered halfspace with cylindrical cavity in Eqs. (3.29). Analogously, for the 2.5D FEM substructure, represented by Eqs. (4.14), it is distinguished between the DOFs on Γ_c and in the interior Ω_c. The quantities on the cylindrical surface are described in the wavenumber frequency domain w.r.t. Cartesian coordinates (k_x,y,z,ω) and are transformed into the basis of the ITM system for the coupling. The necessary transformation matrices are exemplarily derived for the displacements hereinafter.

5.1.1 Dynamic stiffness matrix

First, a transformation from Cartesian coordinates (y, z) into polar coordinates (r, φ) is performed using the transformation matrix $\mathbf{T_{c1}}$.

$$\begin{pmatrix} u_x(y_1,z_1) \\ u_y(y_1,z_1) \\ u_z(y_1,z_1) \\ u_x(y_2,z_2) \\ \vdots \end{pmatrix} = \underbrace{\begin{bmatrix} 1 & 0 & 0 & 0 & 0 & 0 & \cdots \\ 0 & -\sin(\varphi_1) & -\cos(\varphi_1) & 0 & 0 & 0 & \cdots \\ 0 & \cos(\varphi_1) & -\sin(\varphi_1) & 0 & 0 & 0 & \cdots \\ 0 & 0 & 0 & 1 & 0 & 0 & \cdots \\ 0 & 0 & 0 & 0 & -\sin(\varphi_2) & -\cos(\varphi_2) & \cdots \\ 0 & 0 & 0 & 0 & \cos(\varphi_2) & -\sin(\varphi_2) & \cdots \\ \vdots & \vdots & \vdots & \vdots & \vdots & \vdots & \ddots \end{bmatrix}}_{\mathbf{T_{c1}}} \begin{pmatrix} u_x(r_1,\varphi_1) \\ u_r(r_1,\varphi_1) \\ u_\varphi(r_1,\varphi_1) \\ u_x(r_2,\varphi_2) \\ \vdots \end{pmatrix} \tag{5.1}$$

In a second step, the parameters on the cylindrical surface ($r_1 = r_2 = ... = R$) are developed into a Fourier series along the circumferential direction, which is expressed in matrix notation by the transformation matrix $\mathbf{T_{c2}}$. [176]

$$\begin{pmatrix} u_x(R,\varphi_1) \\ u_r(R,\varphi_1) \\ u_\varphi(R,\varphi_1) \\ u_x(R,\varphi_2) \\ \vdots \end{pmatrix} = \underbrace{\begin{bmatrix} \mathrm{e}^{\mathrm{i}n_1\varphi_1} & 0 & 0 & \mathrm{e}^{\mathrm{i}n_2\varphi_1} & 0 & 0 & \mathrm{e}^{\mathrm{i}n_3\varphi_1} & \cdots \\ 0 & \mathrm{e}^{\mathrm{i}n_1\varphi_1} & 0 & 0 & \mathrm{e}^{\mathrm{i}n_2\varphi_1} & 0 & 0 & \cdots \\ 0 & 0 & \mathrm{e}^{\mathrm{i}n_1\varphi_1} & 0 & 0 & \mathrm{e}^{\mathrm{i}n_2\varphi_1} & 0 & \cdots \\ \mathrm{e}^{\mathrm{i}n_1\varphi_2} & 0 & 0 & \mathrm{e}^{\mathrm{i}n_2\varphi_2} & 0 & 0 & \mathrm{e}^{\mathrm{i}n_3\varphi_2} & \cdots \\ 0 & \mathrm{e}^{\mathrm{i}n_1\varphi_2} & 0 & 0 & \mathrm{e}^{\mathrm{i}n_2\varphi_2} & 0 & 0 & \cdots \\ \vdots & \vdots & \vdots & \vdots & \vdots & \vdots & \vdots & \ddots \end{bmatrix}}_{\mathbf{T_{c2}}} \begin{pmatrix} u_x(R,n_1) \\ u_r(R,n_1) \\ u_\varphi(R,n_1) \\ u_x(R,n_2) \\ \vdots \end{pmatrix} \tag{5.2}$$

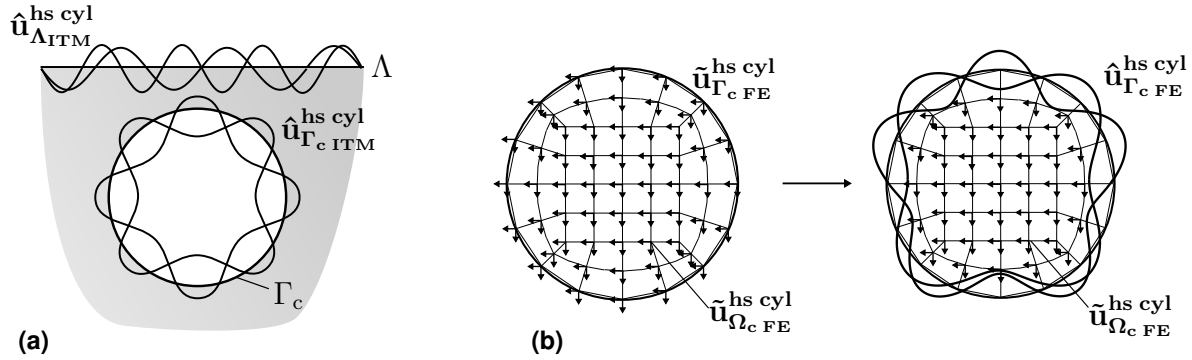

Figure 5.1: (a) Displacements of the ITM substructure in the Fourier transformed domain and (b) transformation of the displacements of the FEM substructure on Γ_c from the (k_x,y,z,ω) to the (k_x,r,n,ω) domain.

Combining Eqs. (5.1) and (5.2), the displacements on Γ_c originally defined in the (k_x, y, z, ω) domain and denoted with the ˜ symbol are expressed by the parameters in the threefold transformed domain (k_x, r, n, ω), as depicted in Fig. 5.1b. [176]

$$\tilde{\mathbf{u}}^{\mathbf{hs\ cyl}}_{\mathbf{\Gamma_c\ FE}} = \mathbf{T_{c1}}\mathbf{T_{c2}}\,\hat{\mathbf{u}}^{\mathbf{hs\ cyl}}_{\mathbf{\Gamma_c\ FE}} = \mathbf{T_c}\,\hat{\mathbf{u}}^{\mathbf{hs\ cyl}}_{\mathbf{\Gamma_c\ FE}} \tag{5.3}$$

The nodal load vector is transformed analogously

$$\tilde{\mathbf{P}}^{\mathbf{hs\ cyl}}_{\mathbf{\Gamma_c\ FE}} = \mathbf{T_{c1}}\mathbf{T_{c2}}\,\hat{\mathbf{P}}^{\mathbf{hs\ cyl}}_{\mathbf{\Gamma_c\ FE}} = \mathbf{T_c}\,\hat{\mathbf{P}}^{\mathbf{hs\ cyl}}_{\mathbf{\Gamma_c\ FE}} \tag{5.4}$$

leading to the transition conditions for the displacements and the equilibrium of forces on the cylindrical coupling surface w.r.t. (k_x, r, n, ω)

$$\hat{\mathbf{u}}^{\mathbf{hs\ cyl}}_{\mathbf{\Gamma_c\ ITM}} = \hat{\mathbf{u}}^{\mathbf{hs\ cyl}}_{\mathbf{\Gamma_c\ FE}} = \hat{\mathbf{u}}^{\mathbf{hs\ cyl}}_{\mathbf{\Gamma_c}} \tag{5.5}$$

$$\hat{\mathbf{P}}^{\mathbf{hs\ cyl}}_{\mathbf{\Gamma_c\ ITM}} + \frac{1}{\mathrm{d}s}\hat{\mathbf{P}}^{\mathbf{hs\ cyl}}_{\mathbf{\Gamma_c\ FE}} = \hat{\mathbf{P}}^{\mathbf{hs\ cyl}}_{\mathbf{\Gamma_c}} \tag{5.6}$$

The factor ds is the element length of a finite element along the circumference of the cylinder as illustrated in Fig. 4.2 and is used to transform the nodal loads of the FEM into the continuous stresses of the ITM. As also visible in this figure, the cylindrical outer boundary is only approximated by the quadrilateral elements. However, the error caused by this is relatively small (cp. Sec. 6.1.2) and can be reduced by increasing the number of discretisation points resp. Fourier series members on Γ_c. [162]

Using the transformation matrix $\mathbf{T_c}$ and the continuity conditions (5.5) and (5.6), the ITM substructure represented by Eq. (3.8) and the 2.5D FEM substructure with cylindrical outer boundary described by Eq. (4.14) are coupled, yielding the following system of equations

describing a halfspace with a cylindrical FEM inclusion [176]

$$\underbrace{\begin{bmatrix} \hat{\mathbf{K}}^{\text{hs cyl}}_{\mathbf{\Lambda\Lambda_{ITM}}} & \hat{\mathbf{K}}^{\text{hs cyl}}_{\mathbf{\Lambda\Gamma_{c\,ITM}}} & \mathbf{0} \\ \hat{\mathbf{K}}^{\text{hs cyl}}_{\mathbf{\Gamma_c\Lambda_{ITM}}} & \hat{\mathbf{K}}^{\text{hs cyl}}_{\mathbf{\Gamma_c\Gamma_{c\,ITM}}} + \frac{1}{\mathrm{d}s}\mathbf{T_c}^{-1}\tilde{\mathbf{K}}^{\text{hs cyl}}_{\mathbf{\Gamma_c\Gamma_{c\,FE}}}\mathbf{T_c} & \frac{1}{\mathrm{d}s}\mathbf{T_c}^{-1}\tilde{\mathbf{K}}^{\text{hs cyl}}_{\mathbf{\Gamma_c\Omega_{c\,FE}}} \\ \mathbf{0} & \tilde{\mathbf{K}}^{\text{hs cyl}}_{\mathbf{\Omega_c\Gamma_{c\,FE}}}\mathbf{T_c} & \tilde{\mathbf{K}}^{\text{hs cyl}}_{\mathbf{\Omega_c\Omega_{c\,FE}}} \end{bmatrix}}_{\hat{\mathbf{K}}^{\text{hs cyl}}_{\mathbf{ITM\,FE}}} \underbrace{\begin{pmatrix} \hat{\mathbf{u}}^{\text{hs cyl}}_{\mathbf{\Lambda_{ITM}}} \\ \hat{\mathbf{u}}^{\text{hs cyl}}_{\mathbf{\Gamma_c}} \\ \tilde{\mathbf{u}}^{\text{hs cyl}}_{\mathbf{\Omega_{c\,FE}}} \end{pmatrix}}_{\hat{\mathbf{u}}^{\text{hs cyl}}_{\mathbf{ITM\,FE}}} = \underbrace{\begin{pmatrix} \hat{\mathbf{P}}^{\text{hs cyl}}_{\mathbf{\Lambda_{ITM}}} \\ \hat{\mathbf{P}}^{\text{hs cyl}}_{\mathbf{\Gamma_c}} \\ \tilde{\mathbf{P}}^{\text{hs cyl}}_{\mathbf{\Omega_{c\,FE}}} \end{pmatrix}}_{\hat{\mathbf{P}}^{\text{hs cyl}}_{\mathbf{ITM\,FE}}} \tag{5.7}$$

The above presented methodology can analogously be applied for the coupling of FEM structures to a halfspace with two cylindrical cavities. Thereby the cavities can have varying radii and different structures can be modelled by the FEM in the interior domains Ω_{c_1} and Ω_{c_2}. Of course the quantities on both coupling surfaces Γ_{c_1} and Γ_{c_2} need to be transformed into the respective ITM basis. Thus also the transformation matrix $\mathbf{T_c}$ must be evaluated separately for both FEM substructures due to the different coordinates and sizes.

In case of the cylindrical indentation, the 2.5D FEM substructure to be included, initially only exhibits nodes on the fraction of Γ_{c} located inside the soil, where a physical coupling to the surrounding soil takes place. However, the previously derived coupling procedure enforces the continuity conditions in the basis of the ITM substructure (k_x,r,n,ω) for each Fourier series member n along Γ_{c}. To ensure a full coupling, retroactively additional nodes are introduced along the total cylindrical interaction surface, so that the quantities of the FEM substructure can be developed into the same number of Fourier series members n on Γ_{c}, as in case of the halfspace with indentation [269]. The FEM nodes are sorted separately according to those within Ω_{c} and on Γ_{c}, which are arranged consecutively with increasing anti-clockwise angle φ in order to match with the ITM node alignment. Due to the insertion of the additional degrees of freedom, associated with the auxiliary nodes, a renumbering and reorganisation of $\tilde{\mathbf{K}}^{\text{hs cyl}}_{\mathbf{FE}}$, $\tilde{\mathbf{u}}^{\text{hs cyl}}_{\mathbf{FE}}$ and $\tilde{\mathbf{P}}^{\text{hs cyl}}_{\mathbf{FE}}$ is necessary before applying the transformation matrix $\mathbf{T_c}$ and the assembling into the total system of equations (5.7). The auxiliary DOFs and the resulting adjusted arrangement of the system matrices must also be taken into account, when finally extracting the results after the solution and the inverse Fourier transform.

Furthermore, a FEM substructure can be coupled into a cylindrical cavity embedded in a multilayered halfspace using the methodology outlined above. The coupling of ITM and FEM remains unaffected by the incorporation of additional top soil layers, as these are only fixed to the surface of the homogeneous halfspace via continuity conditions, as shown in Sec. 3.4, and do not contribute to the stiffness at the cylindrical cavity. The same applies to the multilayered halfspace with two FEM inclusions, depicted in Fig. 5.2b, for which the

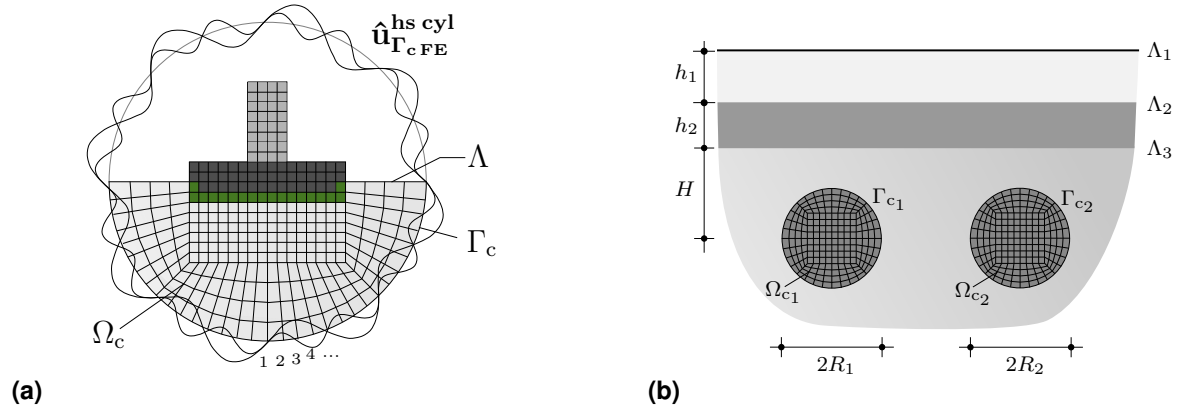

Figure 5.2: (a) Displacements of the FEM substructure on Γ_c w.r.t. (k_x,r,n,ω) for the coupling to the halfspace with cylindrical indentation and (b) multilayered halfspace with two FEM inclusions.

total system of equations is exemplarily given here below

$$\hat{\mathbf{K}}^{\mathbf{hs\ cyl\,L\,tw}}_{\mathbf{ITM\,FE}}\ \hat{\mathbf{u}}^{\mathbf{hs\ cyl\,L\,tw}}_{\mathbf{ITM\,FE}} = \hat{\mathbf{P}}^{\mathbf{hs\ cyl\,L\,tw}}_{\mathbf{ITM\,FE}} \tag{5.8}$$

with

$$\hat{\mathbf{K}}^{\mathbf{hs\ cyl\,L\,tw}}_{\mathbf{ITM\,FE}} = \begin{bmatrix}
\hat{\mathbf{K}}^{\mathbf{L}}_{\mathbf{\Lambda_1\Lambda_{1\,ITM}}} & \hat{\mathbf{K}}^{\mathbf{L}}_{\mathbf{\Lambda_1\Lambda_{3\,ITM}}} & \mathbf{0} & \mathbf{0} & \mathbf{0} & \mathbf{0} \\
\hat{\mathbf{K}}^{\mathbf{L}}_{\mathbf{\Lambda_3\Lambda_{1\,ITM}}} & \begin{pmatrix}\hat{\mathbf{K}}^{\mathbf{L}}_{\mathbf{\Lambda_3\Lambda_{3\,ITM}}} \\ +\hat{\mathbf{K}}^{\mathbf{hs\ cyl\,tw}}_{\mathbf{\Lambda_3\Lambda_{3\,ITM}}}\end{pmatrix} & \hat{\mathbf{K}}^{\mathbf{hs\ cyl\,tw}}_{\mathbf{\Lambda_3\Gamma_{c_1\,ITM}}} & \mathbf{0} & \hat{\mathbf{K}}^{\mathbf{hs\ cyl\,tw}}_{\mathbf{\Lambda_3\Gamma_{c_2\,ITM}}} & \mathbf{0} \\
\mathbf{0} & \hat{\mathbf{K}}^{\mathbf{hs\ cyl\,tw}}_{\mathbf{\Gamma_{c_1}\Lambda_{3\,ITM}}} & \begin{pmatrix}\hat{\mathbf{K}}^{\mathbf{hs\ cyl\,tw}}_{\mathbf{\Gamma_{c_1}\Gamma_{c_1\,ITM}}} \\ +\hat{\mathbf{K}}^{\mathbf{hs\ cyl\,tw}}_{\mathbf{\Gamma_{c_1}\Gamma_{c_1\,FE}}}\end{pmatrix} & \hat{\mathbf{K}}^{\mathbf{hs\ cyl\,tw}}_{\mathbf{\Gamma_{c_1}\Omega_{c_1\,FE}}} & \hat{\mathbf{K}}^{\mathbf{hs\ cyl\,tw}}_{\mathbf{\Gamma_{c_1}\Gamma_{c_2\,ITM}}} & \mathbf{0} \\
\mathbf{0} & \mathbf{0} & \hat{\mathbf{K}}^{\mathbf{hs\ cyl\,tw}}_{\mathbf{\Omega_{c_1}\Gamma_{c_1\,FE}}} & \hat{\mathbf{K}}^{\mathbf{hs\ cyl\,tw}}_{\mathbf{\Omega_{c_1}\Omega_{c_1\,FE}}} & \mathbf{0} & \mathbf{0} \\
\mathbf{0} & \hat{\mathbf{K}}^{\mathbf{hs\ cyl\,tw}}_{\mathbf{\Gamma_{c_2}\Lambda_{3\,ITM}}} & \hat{\mathbf{K}}^{\mathbf{hs\ cyl\,tw}}_{\mathbf{\Gamma_{c_2}\Gamma_{c_1\,ITM}}} & \mathbf{0} & \begin{pmatrix}\hat{\mathbf{K}}^{\mathbf{hs\ cyl\,tw}}_{\mathbf{\Gamma_{c_2}\Gamma_{c_2\,ITM}}} \\ +\hat{\mathbf{K}}^{\mathbf{hs\ cyl\,tw}}_{\mathbf{\Gamma_{c_2}\Gamma_{c_2\,FE}}}\end{pmatrix} & \hat{\mathbf{K}}^{\mathbf{hs\ cyl\,tw}}_{\mathbf{\Gamma_{c_2}\Omega_{c_2\,FE}}} \\
\mathbf{0} & \mathbf{0} & \mathbf{0} & \mathbf{0} & \hat{\mathbf{K}}^{\mathbf{hs\ cyl\,tw}}_{\mathbf{\Omega_{c_2}\Gamma_{c_2\,FE}}} & \tilde{\mathbf{K}}^{\mathbf{hs\ cyl\,tw}}_{\mathbf{\Omega_{c_2}\Omega_{c_2\,FE}}}
\end{bmatrix} \tag{5.9}$$

$$\hat{\mathbf{u}}^{\mathbf{hs\ cyl\,L\,tw}}_{\mathbf{ITM\,FE}} = \left(\begin{array}{cccccc} \hat{\mathbf{u}}^{\mathbf{hs\ cyl\,L\,tw}}_{\mathbf{\Lambda_{1\,ITM}}} & \hat{\mathbf{u}}^{\mathbf{hs\ cyl\,L\,tw}}_{\mathbf{\Lambda_{3\,ITM}}} & \hat{\mathbf{u}}^{\mathbf{hs\ cyl\,L\,tw}}_{\mathbf{\Gamma_{c_1}}} & \tilde{\mathbf{u}}^{\mathbf{hs\ cyl\,L\,tw}}_{\mathbf{\Omega_{c_1\,FE}}} & \hat{\mathbf{u}}^{\mathbf{hs\ cyl\,L\,tw}}_{\mathbf{\Gamma_{c_2}}} & \tilde{\mathbf{u}}^{\mathbf{hs\ cyl\,L\,tw}}_{\mathbf{\Omega_{c_2\,FE}}} \end{array} \right)^T \tag{5.10}$$

$$\hat{\mathbf{P}}^{\mathbf{hs\ cyl\,L\,tw}}_{\mathbf{ITM\,FE}} = \left(\begin{array}{cccccc} \hat{\mathbf{P}}^{\mathbf{hs\ cyl\,L\,tw}}_{\mathbf{\Lambda_{1\,ITM}}} & \hat{\mathbf{P}}^{\mathbf{hs\ cyl\,L\,tw}}_{\mathbf{\Lambda_{3\,ITM}}} & \hat{\mathbf{P}}^{\mathbf{hs\ cyl\,L\,tw}}_{\mathbf{\Gamma_{c_1}}} & \tilde{\mathbf{P}}^{\mathbf{hs\ cyl\,L\,tw}}_{\mathbf{\Omega_{c_1\,FE}}} & \hat{\mathbf{P}}^{\mathbf{hs\ cyl\,L\,tw}}_{\mathbf{\Gamma_{c_2}}} & \tilde{\mathbf{P}}^{\mathbf{hs\ cyl\,L\,tw}}_{\mathbf{\Omega_{c_2\,FE}}} \end{array} \right)^T \tag{5.11}$$

Herein, the transformation of the stiffnesses, displacements and nodal loads on Γ_{c_1} and Γ_{c_2} is already included and the corr. matrices in the (k_x,r,n,ω) domain are indicated with a $\hat{}$.

With the system of equations (5.8) it is possible to directly compute the displacements on Λ_1, Λ_2, Γ_{c_1}, Γ_{c_2}, Ω_{c_1} and Ω_{c_2} due to an external load applied on resp. in one, several or all of these surfaces resp. domains. Thereby, the displacements and the loads on the ground surface and the transition surface from the stratification to the homogeneous halfspace are

described in terms of (k_x,k_y,z,ω), while on the cylindrical ITM-FEM coupling surfaces they are defined in the (k_x,r,n,ω) domain. Both quantities are described w.r.t. (k_x,y,z,ω) in the interior of the FEM substructures. Therefore, the external loads to be applied on the coupled system firstly need to be transformed into the respective domain, before solving the overall system of equations. It must be noted that in the case of the ITM substructure, stresses are applied as external loads, whereas nodal loads are imposed within the FEM structure. The results for the entire three dimensional system in Cartesian coordinates (x,y,z), either in the frequency or the time domain, can eventually be obtained via the corresponding Fourier syntheses resp. inverse Fourier transforms.

5.1.2 Parallel implementation

In the following, some relevant features of the system matrices and their effects on the parallel computation of the halfspace with cylindrical FEM inclusion are outlined. The pseudocode of the parallel implementation is illustrated in Alg. 2. Therein, all tasks within the parallel loop are distributed on several CPUs and executed in parallel for all k_x, whereas procedures 1, 3 and 4 and the loop over the frequencies ω in procedure 2 are performed sequentially. However, in Matlab® functions such as the fast Fourier transform algorithm are parallelised internally by default.

Since the transformation matrix $\mathbf{T_c}$ is independent of the longitudinal wavenumber and frequency, it can be calculated in advance and then be applied to the dynamic stiffness matrix $\tilde{\mathbf{K}}_{\mathbf{FE}}^{\mathbf{hs\,cyl}}(k_x,\omega)$ for any combination (k_x,ω). The mass matrix $\mathbf{M}_{\mathbf{FE}}^{\mathbf{hs\,cyl}}$ is also independent of k_x and ω and the stiffness matrix $\bar{\mathbf{K}}_{\mathbf{FE}}^{\mathbf{hs\,cyl}}(k_x)$ just depends on k_x, so they also could be computed outside the frequency loop and only be combined to $\tilde{\mathbf{K}}_{\mathbf{FE}}^{\mathbf{hs\,cyl}}(k_x,\omega) = \bar{\mathbf{K}}_{\mathbf{FE}}^{\mathbf{hs\,cyl}}(k_x) - \omega^2\mathbf{M}_{\mathbf{FE}}^{\mathbf{hs\,cyl}}$ within each iteration. However, $\tilde{\mathbf{K}}_{\mathbf{FE}}^{\mathbf{hs\,cyl}}(k_x,\omega)$ must be assembled into the overall stiffness matrix $\hat{\mathbf{K}}_{\mathbf{ITM\,FE}}^{\mathbf{hs\,cyl}}(k_x,\omega)$ together with the dynamic stiffness of the ITM substructure $\hat{\mathbf{K}}_{\mathbf{ITM}}^{\mathbf{hs\,cyl}}(k_x,\omega)$, which is directly dependent on k_x and ω and must be computed separately for each of this combinations before solving the coupled system. Saving, distributing and reloading the FEM mass and stiffness matrices for the corresponding (k_x,ω) thereby affords more computational effort than directly computing them newly within the parallel k_x loop. This holds at least for common meshes that do not have a conspicuously large number of elements, since then the effort for calculating the element stiffness matrices is greater than that for the determination of the dynamic stiffness of the ITM substructure. However, by using more sophisticated programming languages and parallelisation tools, where the implementation of nested parallel loops is possible and one has greater influence on the distribution of tasks as well as memory allocation, the above outlined properties could be used to further speed up the computation.

Algorithm 2 Parallel 2.5D ITM-FEM approach for halfspace with cylindrical inclusion

procedure 1 SET UP SYSTEM AND LOADING( )
Initialize and input parameter
Discretization, material and geometry
Finite Element mesh with Ansys® → nodes, elements
External loading $\hat{\mathbf{P}}^{\mathbf{hs\,cyl}}_{\mathbf{\Lambda_{ITM}}}(k_x,k_y,z,\omega)$ and/or $\tilde{\mathbf{P}}^{\mathbf{hs\,cyl}}_{\mathbf{\Omega_{FE}}}(k_x,y,z,\omega)$

procedure 2 DETERMINE DISPLACEMENTS $\hat{\mathbf{u}}^{\mathbf{hs\,cyl}}_{\mathbf{ITM\,FE}}(k_x,\omega)$
Precompute transformation matrix $\mathbf{T_c}$
for all ω **do**
parfor all k_x **do**
Compute element matrices $\bar{\mathbf{K}}^{\mathbf{hs\,cyl}}_{\mathbf{FE}}(k_x,y,z)$ and $\mathbf{M}^{\mathbf{hs\,cyl}}_{\mathbf{FE}}(y,z)$
Assemble dynamic FEM stiffness $\tilde{\mathbf{K}}^{\mathbf{hs\,cyl}}_{\mathbf{FE}}(k_x,y,z,\omega)$
Transform $\hat{\mathbf{K}}^{\mathbf{hs\,cyl}}_{\mathbf{FE}}$ on Γ_c to (k_x,r,n,ω) for coupling
for all k_y and n **do**
Determine $\hat{\mathbf{K}}^{\mathbf{hs\,cyl}}_{\mathbf{ITM}}$ w.r.t. (k_x,k_y,z,ω) on Λ and (k_x,r,n,ω) on Γ_c
Assembling global stiffness $\hat{\mathbf{K}}^{\mathbf{hs\,cyl}}_{\mathbf{ITM\,FE}}$ and load vector $\hat{\mathbf{P}}^{\mathbf{hs\,cyl}}_{\mathbf{ITM\,FE}}$
Solve total system of equations $\hat{\mathbf{u}}^{\mathbf{hs\,cyl}}_{\mathbf{ITM\,FE}} = \hat{\mathbf{K}}^{\mathbf{hs\,cyl}\,-1}_{\mathbf{ITM\,FE}}\,\hat{\mathbf{P}}^{\mathbf{hs\,cyl}}_{\mathbf{ITM\,FE}}$

procedure 3 INVERSE FOURIER TRANSFORM( )
IFFT of $\hat{\mathbf{u}}^{\mathbf{hs\,cyl}}_{\mathbf{\Lambda_{ITM}}}(k_x,k_y,z,\omega)$ to $\bar{\mathbf{u}}^{\mathbf{hs\,cyl}}_{\mathbf{\Lambda_{ITM}}}(x,y,z,\omega)$ resp. $\mathbf{u}^{\mathbf{hs\,cyl}}_{\mathbf{\Lambda_{ITM}}}(x,y,z,t)$
IFFT of $\hat{\mathbf{u}}^{\mathbf{hs\,cyl}}_{\mathbf{\Gamma_c}}(k_x,r,n,\omega)$ to $\bar{\mathbf{u}}^{\mathbf{hs\,cyl}}_{\mathbf{\Gamma_c}}(x,y,z,\omega)$ resp. $\mathbf{u}^{\mathbf{hs\,cyl}}_{\mathbf{\Lambda_{ITM}}}(x,y,z,t)$
IFFT of $\hat{\mathbf{u}}^{\mathbf{hs\,cyl}}_{\mathbf{\Omega_c\,FE}}(k_x,y,z,\omega)$ to $\bar{\mathbf{u}}^{\mathbf{hs\,cyl}}_{\mathbf{\Omega_c\,FE}}(x,y,z,\omega)$ resp. $\mathbf{u}^{\mathbf{hs\,cyl}}_{\mathbf{\Lambda_{ITM}}}(x,y,z,t)$

procedure 4 POSTPROCESSING AND PLOTS( )
Compute $\hat{\boldsymbol{\sigma}}^{\mathbf{hs\,cyl}}_{\mathbf{\Omega_c\,ITM\,FE}}$
Plot stresses and displacements
Export results

The parallel computation of the harmonic response of a halfspace with cylindrical FEM inclusion (cp. Fig. 5.3) for one single frequency applying Alg. 2 on a workstation equipped with an Intel® Xeon® W-2245 3.90GHz with 8 cores and 64 GB RAM takes in total 140.02 s. In contrast the completely serial computation of the same system, with the code developed in Hackenberg [162], requires 288.43 s and thus more than twice as long.

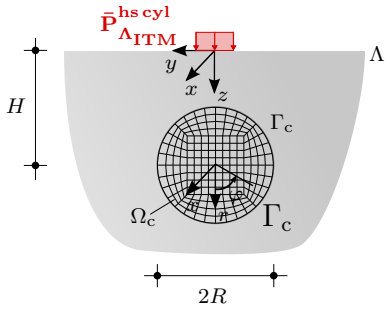

Dimensions		Sampling	
$B_x = B_y$	128 m	$N_x = N_y$	2^8
H	2.1 m	N_φ	2^5
R	2.0 m	N_f	1

Figure 5.3: Setup and system parameters for comparison of parallel and serial computation times.

5.2 Coupling on the spherical interaction surface

For the coupling of a three dimensional FEM substructure into a halfspace with spherical cavity, modelled by the ITM as depicted in Fig. 5.4b, the continuity conditions are applied on the spherical interaction surface. In the governing equations for the ITM and the FEM substructure, it is again distinguished between the degrees of freedom on the halfspace surface Λ, the spherical surface Γ_s and within the FEM inclusion Ω_s. The stresses and displacements of the homogenous or layered halfspace with spherical cavity on Γ_s in Eqs. (3.26) resp. (3.30) are described in terms of spherical harmonics and the frequency in the (r,m,l,ω) domain, whereas the displacements and the nodal forces of the FEM substructure on Γ_s in Eqs. (4.21) are defined in Cartesian coordinates in the (x,y,z,ω) domain. As before the parameters of the FEM substructure on Γ_s are transformed into the ITM basis (cp. Fig. 5.4a), which is chosen as common reference frame for the coupling. The transformations are again performed by means of matrix multiplications and are exemplarily presented for the displacements hereinafter. [84]

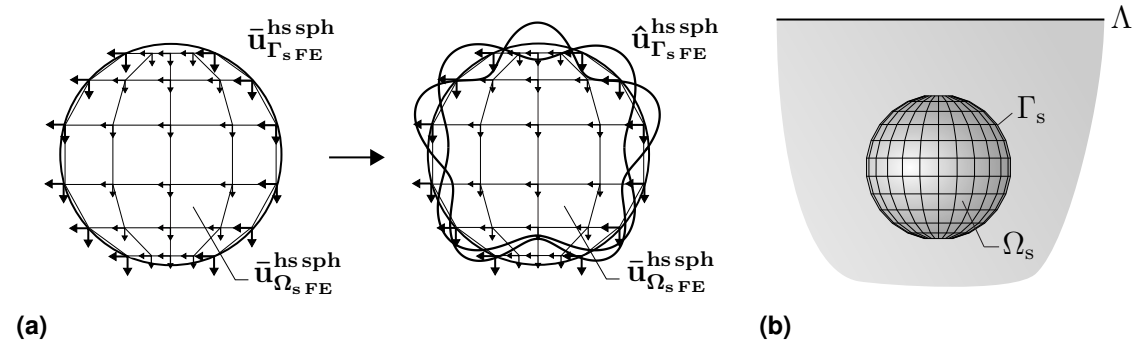

Figure 5.4: (a) Transformation of displacements of the FEM substructure on Γ_s from (x,y,z,ω) to the (r,m,l,ω) domain and (b) halfspace with spherical FEM inclusion.

In a first step, the nodal displacements on Γ_s are transformed from Cartesian into spherical coordinates using the relation between the two reference frames given by $\mathbf{T_{s1}}$

$$\begin{pmatrix} u_x(x_1,y_1,z_1) \\ u_y(x_1,y_1,z_1) \\ u_z(x_1,y_1,z_1) \\ u_x(x_2,y_2,z_2) \\ u_y(x_2,y_2,z_2) \\ u_z(x_2,y_2,z_2) \\ \vdots \end{pmatrix} = \underbrace{\begin{bmatrix} \sin(\vartheta_1)\cos(\varphi_1) & \cos(\vartheta_1)\cos(\varphi_1) & -\sin(\varphi_1) & 0 & \cdots \\ \sin(\vartheta_1)\sin(\varphi_1) & \cos(\vartheta_1)\sin(\varphi_1) & \cos(\varphi_1) & 0 & \cdots \\ \cos(\vartheta_1) & -\sin(\vartheta_1) & 0 & 0 & \cdots \\ 0 & 0 & 0 & \sin(\vartheta_2)\cos(\varphi_2) & \cdots \\ 0 & 0 & 0 & \sin(\vartheta_2)\sin(\varphi_2) & \cdots \\ 0 & 0 & 0 & \cos(\vartheta_2) & \cdots \\ \vdots & \vdots & \vdots & \vdots & \end{bmatrix}}_{\mathbf{T_{s1}}} \begin{pmatrix} u_r(r_1,\vartheta_1,\varphi_1) \\ u_\vartheta(r_1,\vartheta_1,\varphi_1) \\ u_\varphi(r_1,\vartheta_1,\varphi_1) \\ u_r(r_2,\vartheta_2,\varphi_2) \\ u_\vartheta(r_2,\vartheta_2,\varphi_2) \\ u_\varphi(r_2,\vartheta_2,\varphi_2) \\ \vdots \end{pmatrix} \tag{5.12}$$

The second transformation matrix $\mathbf{T_{s2}}$ contains the development of the degrees of freedom on Γ_s with $r_1 = r_2 = ... = R$ into spherical harmonics [84]

$$\begin{pmatrix} u_r(R,\vartheta_1,\varphi_1) \\ u_\vartheta(R,\vartheta_1,\varphi_1) \\ u_\varphi(R,\vartheta_1,\varphi_1) \\ u_r(R,\vartheta_2,\varphi_2) \\ u_\vartheta(R,\vartheta_2,\varphi_2) \\ u_\varphi(R,\vartheta_2,\varphi_2) \\ \vdots \end{pmatrix} = \underbrace{\begin{bmatrix} Y_{m_1}^{l_1}(\vartheta_1,\varphi_1) & 0 & 0 & Y_{m_2}^{l_2}(\vartheta_1,\varphi_1) & \cdots \\ 0 & Y_{m_1}^{l_1}(\vartheta_1,\varphi_1) & 0 & 0 & \cdots \\ 0 & 0 & Y_{m_1}^{l_1}(\vartheta_1,\varphi_1) & 0 & \cdots \\ Y_{m_1}^{l_1}(\vartheta_2,\varphi_2) & 0 & 0 & Y_{m_2}^{l_2}(\vartheta_2,\varphi_2) & \cdots \\ 0 & Y_{m_1}^{l_1}(\vartheta_2,\varphi_2) & 0 & 0 & \cdots \\ \vdots & \vdots & \vdots & \vdots & \ddots \end{bmatrix}}_{\mathbf{T_{s2}}} \begin{pmatrix} u_r(R,m_1,l_1) \\ u_\vartheta(R,m_1,l_1) \\ u_\varphi(R,m_1,l_1) \\ u_r(R,m_2,l_2) \\ u_\vartheta(R,m_2,l_2) \\ u_\varphi(R,m_2,l_2) \\ \vdots \end{pmatrix} \tag{5.13}$$

with the degrees m_i and orders l_i arranged as summarized in Tab. 5.1.

After the transformation of the displacements and the nodal loads

$$\bar{\mathbf{u}}_{\mathbf{\Gamma_s\,FE}}^{\mathbf{hs\,sph}} = \mathbf{T_{s1}}\mathbf{T_{s2}}\,\hat{\mathbf{u}}_{\mathbf{\Gamma_s\,FE}}^{\mathbf{hs\,sph}} = \mathbf{T_s}\hat{\mathbf{u}}_{\mathbf{\Gamma_s\,FE}}^{\mathbf{hs\,sph}} \tag{5.14}$$

$$\bar{\mathbf{P}}_{\mathbf{\Gamma_s\,FE}}^{\mathbf{hs\,sph}} = \mathbf{T_{s1}}\mathbf{T_{s2}}\,\hat{\mathbf{P}}_{\mathbf{\Gamma_s\,FE}}^{\mathbf{hs\,sph}} = \mathbf{T_s}\hat{\mathbf{P}}_{\mathbf{\Gamma_s\,FE}}^{\mathbf{hs\,sph}} \tag{5.15}$$

the coupling conditions can be formulated as [84]

$$\hat{\mathbf{u}}_{\mathbf{\Gamma_s\,ITM}}^{\mathbf{hs\,sph}} = \hat{\mathbf{u}}_{\mathbf{\Gamma_s\,FE}}^{\mathbf{hs\,sph}} = \hat{\mathbf{u}}_{\mathbf{\Gamma_s}}^{\mathbf{hs\,sph}} \tag{5.16}$$

$$\hat{\mathbf{P}}_{\mathbf{\Gamma_s\,ITM}}^{\mathbf{hs\,sph}} + \frac{1}{\mathrm{d}s_\vartheta \mathrm{d}s_\varphi}\hat{\mathbf{P}}_{\mathbf{\Gamma_s\,FE}}^{\mathbf{hs\,sph}} = \hat{\mathbf{P}}_{\mathbf{\Gamma_s}}^{\mathbf{hs\,sph}} \tag{5.17}$$

with the elements lengths $\mathrm{d}s_\vartheta$ and $\mathrm{d}s_\varphi$ of the finite elements on Γ_s in the directions of the longitudes and the latitudes. They are introduced in order to express the nodal loads of the FEM domain by the distributed loads of the ITM substructure.

With the Eqs. (5.16) and (5.17), the stiffness matrices can be coupled in general. However, in contrast to a Fourier series development, the number of parameters is changed by the development into spherical harmonics, so $\mathbf{T_{s2}}$ is not square. Therefore, the inversion of $\mathbf{T_s}$

	$i=1$	$i=2$	$i=3$	$i=4$	$i=5$	$i=6$	$i=7$	$i=8$	$i=9$	...
m_i	0	1	1	1	2	2	2	2	2	...
l_i	0	-1	0	1	-2	-1	0	1	2	...

Table 5.1: Degree and order of the spherical harmonics.

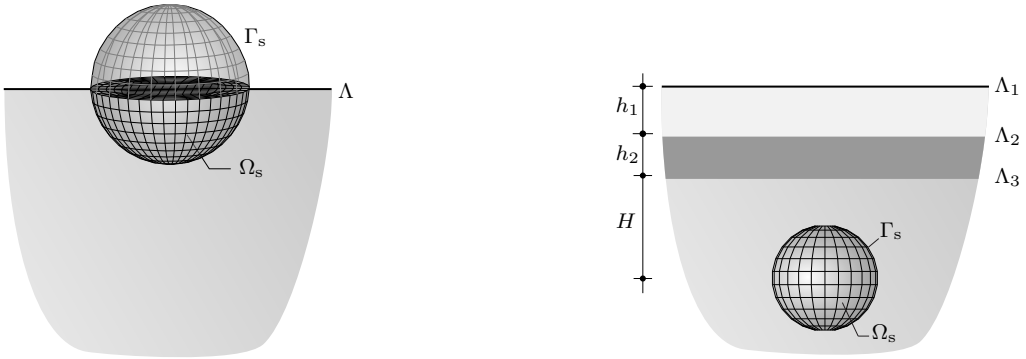

Figure 5.5: (a) Additional nodes above ground surface for coupling of FEM substructure to the halfspace with spherical indentation and (b) layered halfspace with spherical FEM inclusion.

that is necessary for the transformation of the system of equations is not easily possible. However, as $\mathbf{T_{s2}}$ consists of more rows than columns (which are linearly independent), a left multiplication of $\mathbf{T_{s2}}$ with its Moore-Penrose pseudoinverse $\mathbf{T_{s2}^{+}}$ leads to the identity matrix $\mathbf{T_{s2}^{+}T_{s2}} = \mathbf{I}$. Therefore, the inverse of $\mathbf{T_s}$ results as $\mathbf{T_s}^{+} = \mathbf{T_{s2}}^{+}\,\mathbf{T_{s1}}^{-1}$. [84]

Introducing the transformation matrices and applying the transition conditions leads to the coupled system of equations for a halfspace with spherical FEM inclusion. [84]

$$\underbrace{\begin{bmatrix} \hat{\mathbf{K}}^{\mathbf{hs\,sph}}_{\mathbf{\Lambda\Lambda_{ITM}}} & \hat{\mathbf{K}}^{\mathbf{hs\,sph}}_{\mathbf{\Lambda\Gamma_{s\,ITM}}} & \mathbf{0} \\ \hat{\mathbf{K}}^{\mathbf{hs\,sph}}_{\mathbf{\Gamma_s\Lambda_{ITM}}} & \hat{\mathbf{K}}^{\mathbf{hs\,sph}}_{\mathbf{\Gamma_s\Gamma_{s\,ITM}}} + \frac{1}{\mathrm{d}s_\vartheta \mathrm{d}s_\varphi}\mathbf{T_s}^{+}\bar{\mathbf{K}}^{\mathbf{hs\,sph}}_{\mathbf{\Gamma_s\Gamma_{s\,FE}}}\mathbf{T_s} & \frac{1}{\mathrm{d}s_\vartheta \mathrm{d}s_\varphi}\mathbf{T_s}^{+}\bar{\mathbf{K}}^{\mathbf{hs\,sph}}_{\mathbf{\Gamma_s\Omega_{s\,FE}}} \\ \mathbf{0} & \bar{\mathbf{K}}^{\mathbf{hs\,sph}}_{\mathbf{\Omega_s\Gamma_{s\,FE}}}\mathbf{T_s} & \bar{\mathbf{K}}^{\mathbf{hs\,sph}}_{\mathbf{\Omega_s\Omega_{s\,FE}}} \end{bmatrix}}_{\hat{\mathbf{K}}^{\mathbf{hs\,sph}}_{\mathbf{ITM\,FE}}} \underbrace{\begin{pmatrix} \hat{\mathbf{u}}^{\mathbf{hs\,sph}}_{\mathbf{\Lambda_{ITM}}} \\ \hat{\mathbf{u}}^{\mathbf{hs\,sph}}_{\mathbf{\Gamma_s}} \\ \bar{\mathbf{u}}^{\mathbf{hs\,sph}}_{\mathbf{\Omega_{s\,FE}}} \end{pmatrix}}_{\hat{\mathbf{u}}^{\mathbf{hs\,sph}}_{\mathbf{ITM\,FE}}} = \underbrace{\begin{pmatrix} \hat{\mathbf{P}}^{\mathbf{hs\,sph}}_{\mathbf{\Lambda_{ITM}}} \\ \hat{\mathbf{P}}^{\mathbf{hs\,sph}}_{\mathbf{\Gamma_s}} \\ \bar{\mathbf{P}}^{\mathbf{hs\,sph}}_{\mathbf{\Omega_{s\,FE}}} \end{pmatrix}}_{\hat{\mathbf{P}}^{\mathbf{hs\,sph}}_{\mathbf{ITM\,FE}}} \tag{5.18}$$

In case of a halfspace with spherical indentation, besides the desired 3D structure only the part of the surrounding soil matching with the spherical cavity located below the ground surface needs to be modelled by the FEM. Therefore, the FEM substructure initially only exhibits nodes on the intersections of the latitudes and longitudes on Γ_s of a theoretically complete sphere, which are located inside the soil. It should be noted, that due to the distribution of the latitudes on the positions ϑ_i, prescribed by the Gauss-Legendre integration points, there is no latitude on the equator of the sphere that would bisect it. Consequently, the FEM substructure must be modelled and located such that the largest existing latitude below the equator aligns with the halfspace surface $z = 0$. For a direct full coupling of the two substructures on the common spherical interaction surface, the parameters of the FEM model on Γ_s need to be developed into the same number of spherical harmonics m,l used in the

ITM solution, since the continuity conditions are applied in the basis of the latter. For this reason, additional nodes assigned with an unit stiffness, which is orders of magnitude smaller than the stiffness of the FEM nodes for $z > 0$, are introduced in the FEM substructure on the spherical surface Γ_s above the ground surface, as shown in Fig. 5.5a. The nodes are located on the intersections of the longitudes and latitudes coinciding with those of the ITM substructure, in order to be able to use the numerical procedures for the evaluation of the spherical harmonics outlined in Sec. 3.5.1. As for the halfspace with cylindrical indentation, the insertion of these auxiliary nodes and the corr. additional DOFs requires a renumbering and reorganisation of $\hat{\mathbf{K}}^{\mathbf{hs\,sph}}_{\mathbf{FE}}$, $\hat{\mathbf{u}}^{\mathbf{hs\,sph}}_{\mathbf{FE}}$ and $\hat{\mathbf{P}}^{\mathbf{hs\,sph}}_{\mathbf{FE}}$, before applying the transformation matrix $\mathbf{T_s}$ and assembling them into the total system of equations (5.18).

The coupling procedure presented above can be applied analogously to a layered halfspace with spherical FEM inclusion depicted in Fig. 5.5b. The additional upper soil layers have no influence on the stiffness members associated with the cavity surface Γ_s. Thus, they can be added over the halfspace with the embedded spherical FEM inclusion by enforcing the continuity conditions on Λ_3, without affecting the ITM-FEM coupling at the spherical interaction surface.

$$\underbrace{\begin{bmatrix} \hat{\mathbf{K}}^{\mathbf{L}}_{\mathbf{\Lambda_1\Lambda_1}\,\mathbf{ITM}} & \hat{\mathbf{K}}^{\mathbf{L}}_{\mathbf{\Lambda_1\Lambda_3}\,\mathbf{ITM}} & \mathbf{0} & \mathbf{0} \\ \hat{\mathbf{K}}^{\mathbf{L}}_{\mathbf{\Lambda_3\Lambda_1}\,\mathbf{ITM}} & \begin{pmatrix} \hat{\mathbf{K}}^{\mathbf{L}}_{\mathbf{\Lambda_3\Lambda_3}\,\mathbf{ITM}} \\ \hat{\mathbf{K}}^{\mathbf{hs\,sph}}_{\mathbf{\Lambda_3\Lambda_3}\,\mathbf{ITM}} \end{pmatrix}^{+} & \hat{\mathbf{K}}^{\mathbf{hs\,sph}}_{\mathbf{\Lambda_3\Gamma_s}\,\mathbf{ITM}} & \mathbf{0} \\ \mathbf{0} & \hat{\mathbf{K}}^{\mathbf{hs\,sph}}_{\mathbf{\Gamma_s\Lambda_3}\,\mathbf{ITM}} & \begin{pmatrix} \hat{\mathbf{K}}^{\mathbf{hs\,sph}}_{\mathbf{\Gamma_s\Gamma_s}\,\mathbf{ITM}} \\ \hat{\mathbf{K}}^{\mathbf{hs\,sph}}_{\mathbf{\Gamma_s\Gamma_s}\mathbf{FE}} \end{pmatrix}^{+} & \hat{\mathbf{K}}^{\mathbf{hs\,sph}}_{\mathbf{\Gamma_s\Omega_s}\mathbf{FE}} \\ \mathbf{0} & \mathbf{0} & \hat{\mathbf{K}}^{\mathbf{hs\,sph}}_{\mathbf{\Omega_s\Gamma_s}\mathbf{FE}} & \bar{\mathbf{K}}^{\mathbf{hs\,sph}}_{\mathbf{\Omega_s\Omega_s}\mathbf{FE}} \end{bmatrix}}_{\hat{\mathbf{K}}^{\mathbf{hs\,sph\,L}}_{\mathbf{ITM\,FE}}} \underbrace{\begin{pmatrix} \hat{\mathbf{u}}^{\mathbf{hs\,sph\,L}}_{\mathbf{\Lambda_1}\,\mathbf{ITM}} \\ \hat{\mathbf{u}}^{\mathbf{hs\,sph\,L}}_{\mathbf{\Lambda_3}\,\mathbf{ITM}} \\ \hat{\mathbf{u}}^{\mathbf{hs\,sph\,L}}_{\mathbf{\Gamma_s}} \\ \bar{\mathbf{u}}^{\mathbf{hs\,sph\,L}}_{\mathbf{\Omega_s}\,\mathbf{FE}} \end{pmatrix}}_{\hat{\mathbf{u}}^{\mathbf{hs\,sph\,L}}_{\mathbf{ITM\,FE}}} = \underbrace{\begin{pmatrix} \hat{\mathbf{P}}^{\mathbf{hs\,sph\,L}}_{\mathbf{\Lambda_1}\,\mathbf{ITM}} \\ \hat{\mathbf{P}}^{\mathbf{hs\,sph\,L}}_{\mathbf{\Lambda_3}\,\mathbf{ITM}} \\ \hat{\mathbf{P}}^{\mathbf{hs\,sph\,L}}_{\mathbf{\Gamma_s}} \\ \bar{\mathbf{P}}^{\mathbf{hs\,sph\,L}}_{\mathbf{\Omega_s}\,\mathbf{FE}} \end{pmatrix}}_{\hat{\mathbf{P}}^{\mathbf{hs\,sph\,L}}_{\mathbf{ITM\,FE}}} \tag{5.19}$$

5.3 Coupling on soil foundation interaction surface

5.3.1 Dynamic soil flexibility and stiffness

For the coupling of a foundation to the soil substructure, the soil displacements due to the transmitted contact stresses need to coincide with the structural displacements at the ground surface. Furthermore, the equilibrium of forces must be satisfied at the common interface. Outside the foundation, a traction free surface is assumed, on which the displacements can

adjust themselves freely. A direct coupling of the foundation stiffness to the soil stiffness in the wavenumber frequency domain as for the soil stratification, featuring the same extension as the underlying halfspace, is not directly possible due to the finite size of the foundation. Therefore, in this case the continuity conditions cannot be enforced over the entire interaction surface, but a mixed boundary value problem needs to be solved.

Dynamic flexibility at the ground surface

For this purpose, a relation between the concentrated harmonic forces $\bar{P}_n^j$ in direction n acting at discretization points j and the corresponding displacements $\bar{u}_m^i$ in direction m at the discretization points i on Λ needs to be established, which can be formulated by means of the dynamic flexibilities $\bar{F}_{mn}^{ij}$ with $m,n = x,y,z$ [51, 100]

$$\underbrace{\begin{pmatrix} \bar{u}_x^i \\ \bar{u}_y^i \\ \bar{u}_z^i \end{pmatrix}}_{\bar{\mathbf{u}}_\mathbf{s}^i} = \underbrace{\begin{pmatrix} \bar{F}_{xx}^{ij} & \bar{F}_{xy}^{ij} & \bar{F}_{xz}^{ij} \\ \bar{F}_{yx}^{ij} & \bar{F}_{yy}^{ij} & \bar{F}_{yz}^{ij} \\ \bar{F}_{zx}^{ij} & \bar{F}_{zy}^{ij} & \bar{F}_{zz}^{ij} \end{pmatrix}}_{\bar{\mathbf{F}}_\mathbf{s}^{ij}} \underbrace{\begin{pmatrix} \bar{P}_x^j \\ \bar{P}_y^j \\ \bar{P}_z^j \end{pmatrix}}_{\bar{\mathbf{P}}_\mathbf{s}^j} \overset{\text{relaxed BC}}{=} \underbrace{\begin{pmatrix} \bar{F}_{xx}^{ij} & \bar{F}_{xy}^{ij} & 0 \\ \bar{F}_{yx}^{ij} & \bar{F}_{yy}^{ij} & 0 \\ 0 & 0 & \bar{F}_{zz}^{ij} \end{pmatrix}}_{\bar{\mathbf{F}}_\mathbf{s}^{ij}} \underbrace{\begin{pmatrix} \bar{P}_x^j \\ \bar{P}_y^j \\ \bar{P}_z^j \end{pmatrix}}_{\bar{\mathbf{P}}_\mathbf{s}^j} \tag{5.20}$$

Since the dynamic load and the resulting displacements are usually out of phase, the dynamic flexibility matrix takes complex values. Thereby the real part represents the stiffness and inertia of the soil, whereas the imaginary part is attributed to the radiation and material damping. In general, the dynamic flexibility matrix $\bar{\mathbf{F}}_\mathbf{s}^{ij}$ for a pair of discretization points i and j is fully populated, since a load in one direction n causes displacements in all three spatial directions m. However, as the coupling of horizontal and vertical soil displacements is relatively weak, for many applications relaxed boundary conditions (frictionless contact between soil and foundation) can be assumed. [51] Therefore the system of equations (5.20) can be partly decoupled, leading to a significant reduction of computation time [52, 68].

The dynamic flexibilities $\bar{F}_{mn}^{ij}$ need to be known at the interaction areas of the foundations with the ground surface, as the nodal contact forces and displacements of both substructures must coincide there. For the solution of the soil substructure, the ground surface has been subdivided into a grid of equidistant discretization points with Cartesian coordinates given by $x = o\Delta x$ and $y = s\Delta y$, where $\Delta x, \Delta y$ are the incremental distances between the nodes. The FEM model of the foundations thus must be designed such that the nodes inside the mutual contact areas match with the discretization points of the soil, at which the flexibilities are known. As the members $\bar{F}_{mn}^{ij}$ of the dynamic soil flexibility matrix correspond to the displacements $\bar{u}_m^i$ due to a concentrated unit load $\bar{P}_n^j$, all previously derived stiffness formulations for the ITM and ITM-FEM systems, giving a direct relation between a load on

the ground surface and the corresponding displacements, can be used to determine $\bar{\mathbf{F}}_{\mathbf{s}}^{ij}$ for the respective soil substructure.

The contributions of the unit concentrated loads at all $n_{\mathrm{f_{tot}}}$ discretization points within the coupling surfaces are assembled into the overall soil flexibility matrix $\bar{\mathbf{F}}_{\mathbf{s}}$, which features a total size of $[3n_{\mathrm{f_{tot}}} \times 3n_{\mathrm{f_{tot}}}]$ and fully represents the reaction of the soil subsystem. To this end, the ground responses $\bar{\mathbf{u}}_{\mathbf{s}}^{i}$ have to be evaluated for all points $i = 1,...,n_{\mathrm{f_{tot}}}$ due to a harmonic excitation with the concentrated loads $\bar{\mathbf{P}}_{\mathbf{s}}^{j}$ in all spatial directions acting on each point $j = 1,...,n_{\mathrm{f_{tot}}}$ in turn. The total amount of discretization points $n_{\mathrm{f_{tot}}} = N_{\mathrm{f}}\, n_{\mathrm{f}}$ results from the number of foundations N_{f} and the number of nodes per foundation $n_{\mathrm{f}} = n_{\mathrm{f_x}} n_{\mathrm{f_y}}$, where $n_{\mathrm{f_x}}$ and $n_{\mathrm{f_y}}$ are the number of discretization points of a foundation in $x-$ and y-direction respectively. After assembling also the displacements and loads, the overall system of equations yields

$$\bar{\mathbf{u}}_{\mathbf{s}}(x,y,\omega) = \bar{\mathbf{F}}_{\mathbf{s}}(x,y,\omega)\, \bar{\mathbf{P}}_{\mathbf{s}}(x,y,\omega) \tag{5.21}$$

To allow a straightforward direct stiffness coupling with the finite element model of the foundation, defined w.r.t. a Cartesian reference frame in the frequency domain, it is beneficial to have the dynamic soil stiffness matrix $\bar{\mathbf{K}}_{\mathbf{s}}$ at the ground surface $z = 0$ also defined w.r.t. (x,y,ω). The latter is obtained by inverting the dynamic flexibility matrix $\bar{\mathbf{F}}_{\mathbf{s}}$

$$\bar{\mathbf{K}}_{\mathbf{s}}(x,y,\omega) = \bar{\mathbf{F}}_{\mathbf{s}}^{-1}(x,y,\omega) \tag{5.22}$$

However, the equations to determine the displacements at the surface of the soil substructures from Secs. 3 and 5 are defined in the (k_x,k_y,ω) domain. Consequently a twofold inverse Fourier transformation is necessary to obtain $\bar{\mathbf{u}}_{\mathbf{s}}(x,y,\omega)$, which is finally used to set up $\bar{\mathbf{K}}_{\mathbf{s}}(x,y,\omega)$. As calculations are carried out numerically, only a limited amount of discrete wavenumbers can be taken into account. By applying a load uniformly distributed over a small area with an unit resultant (in the following referred to as unit concentrated load) instead of an unit point load, the appearance of a singularity under the point of load application can be avoided. Furthermore, $\bar{\mathbf{P}}_{\mathbf{s}}(k_x,k_y,\omega)$ in this case decays towards zero at the limits of the considered wavenumber range in contrast to the constant wavenumber spectrum of a point load, which helps to minimize the numerical errors introduced by the truncation of the wavenumbers k_x and k_y. Therewith it can also be ensured that the displacements under the point of load application, being of particular importance since they form the main diagonal of $\bar{\mathbf{F}}_{\mathbf{s}}$, are not considerably affected by the discretization of the system. [51]

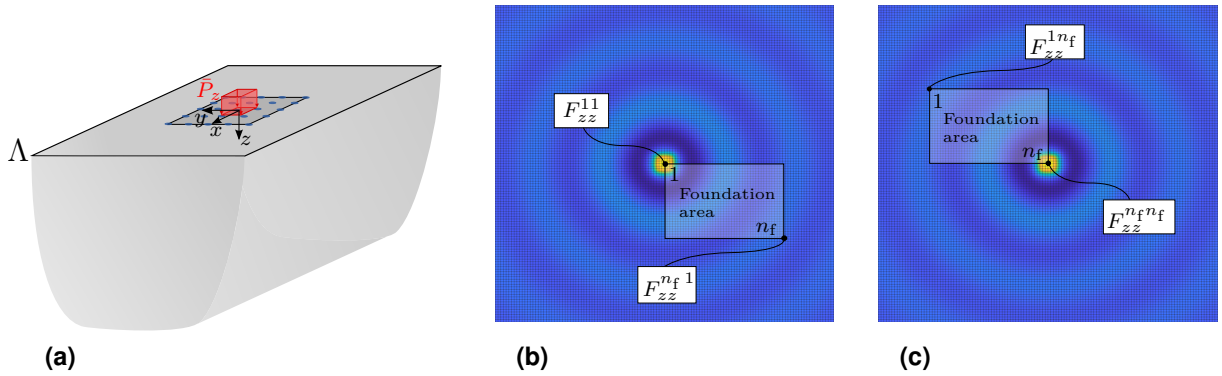

(a) (b) (c)

Figure 5.6: (a) Discretization points at soil foundation interface and unit concentrated load at center of the halfspace surface. (b) First and (c) last step of shifting procedure for the population of the flexibility matrix for a single foundation on homogeneous halfspace.

Shifting procedure for homogeneous and layered halfspace

The computational effort to determine the soil flexibility $\bar{\mathbf{F}}_\mathbf{s}$ of a single or a group of foundations resting on a homogeneous or layered halfspace can be reduced substantially by taking the symmetry conditions into account. Instead of applying the load at each of the $n_{\mathrm{f_{tot}}}$ interaction nodes and evaluating the corresponding displacements, the foundation areas can be shifted under the center of the concentrated load according to the discretization step size, such that every interaction node is positioned once under the unit concentrated load. [51, 100]

A prerequisite for the applicability of the shifting procedure is that the discretized surface area of the soil substructure is at least twice as large as the area enclosing all available foundations, so that for any shifting step the displacements at all foundation points can be evaluated. Apart from that, the dimensions of the discretized area are generally chosen such that the induced surface waves at the given frequency are mostly attenuated before reaching the domain boundaries, thus avoiding numerical errors due to the periodic repetition introduced by discrete calculation applying the FFT.

In case of the homogeneous or layered halfspace, due to the complete rotational symmetry of the systems, the position of the load on the surface is irrelevant and the displacement field only needs to be computed once for a vertical and once for one of the horizontal load directions [51]. Thereby, the necessary number of computations of the soil displacements $\bar{\mathbf{u}}_\mathbf{s}(x,y,\omega)$ is reduced from $3n_{\mathrm{f_{tot}}}$ to only two and all remaining displacements are supplemented by means of symmetry considerations. The first step of the shifting procedure for the population of the soil flexibility matrix in case of a single foundation resting on a homogenous halfspace is shown in Fig. 5.6b. Therein the discretization point at the left upper corner of the foundation is located at the position of the maximum displacement due to the

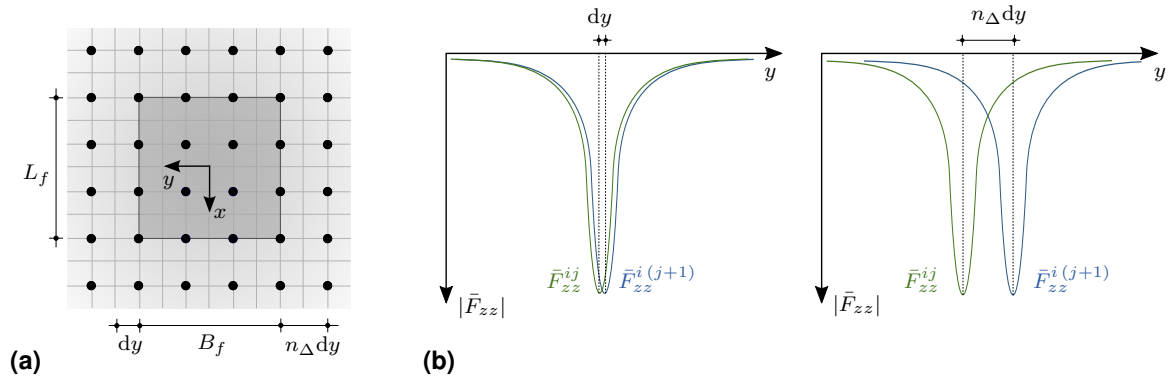

Figure 5.7: (a) Original fine and new coarse discretization for the determination of $\bar{\mathbf{F}}_\mathbf{s}$ within the foundation area. (b) Vertical flexibility $\bar{F}_{zz}^{ij}$ at a point i due to a concentrated unit load for two adjacent shifting steps j and $j+1$ (left) before and (right) after the introduction of the new discretization.

vertical unit concentrated load at the center of the ground surface, depicted in Fig. 5.6a. The corresponding displacements at all nodes of the soil foundation interface are sorted into the first column of the flexibility matrix. The same operation is repeated for each step of the shifting procedure, until the last foundation node n_f is located at the point of load application, as illustrated in Fig. 5.6c. Therefore, each column of the flexibility matrix comprises the displacements of all foundation nodes in x,y and z direction due to an unit load $\bar{P}_n^j$ at a specific position $j = 1,...,n_{\mathrm{f_{tot}}}$ in direction n, finally leading to the following structure of $\bar{\mathbf{F}}_\mathbf{s}$

$$\begin{pmatrix} \bar{u}_x^1 \\ \bar{u}_y^1 \\ \bar{u}_z^1 \\ \bar{u}_x^2 \\ \bar{u}_y^2 \\ \bar{u}_z^2 \\ \vdots \end{pmatrix} = \begin{pmatrix} \bar{F}_{xx}^{11} & \bar{F}_{xy}^{11} & \bar{F}_{xz}^{11} & \bar{F}_{xx}^{12} & \bar{F}_{xy}^{12} & \bar{F}_{xz}^{12} & \dots \\ \bar{F}_{yx}^{11} & \bar{F}_{yy}^{11} & \bar{F}_{yz}^{11} & \bar{F}_{yx}^{12} & \bar{F}_{yy}^{12} & \bar{F}_{yz}^{12} & \dots \\ \bar{F}_{zx}^{11} & \bar{F}_{zy}^{11} & \bar{F}_{zz}^{11} & \bar{F}_{zx}^{12} & \bar{F}_{zy}^{12} & \bar{F}_{zz}^{12} & \dots \\ \bar{F}_{xx}^{21} & \bar{F}_{xy}^{21} & \bar{F}_{xz}^{21} & \bar{F}_{xx}^{22} & \bar{F}_{xy}^{22} & \bar{F}_{xz}^{22} & \dots \\ \bar{F}_{yx}^{21} & \bar{F}_{yy}^{21} & \bar{F}_{yz}^{21} & \bar{F}_{yx}^{22} & \bar{F}_{yy}^{22} & \bar{F}_{yz}^{22} & \dots \\ \bar{F}_{zx}^{21} & \bar{F}_{zy}^{21} & \bar{F}_{zz}^{21} & \bar{F}_{zx}^{22} & \bar{F}_{zy}^{22} & \bar{F}_{zz}^{22} & \dots \\ \vdots & \vdots & \vdots & \vdots & \vdots & \vdots & \ddots \end{pmatrix} \begin{pmatrix} \bar{P}_x^1 \\ \bar{P}_y^1 \\ \bar{P}_z^1 \\ \bar{P}_x^2 \\ \bar{P}_y^2 \\ \bar{P}_z^2 \\ \vdots \end{pmatrix} \tag{5.23}$$

The use of the concentrated unit load, which occupies several nodes, in combination with a small discretization step size leads to numerical issues when applying the shifting procedure to populate $\bar{\mathbf{F}}_\mathbf{s}$. A shift of the load position by only one discretization point is not sufficient to achieve a significant change in the displacement field, so that the adjacent columns of the flexibility matrix contain very similar values (cp. Fig. 5.7b). Consequently, the determinant gets close to zero and $\bar{\mathbf{F}}_\mathbf{s}$ features a rather large condition number. This in turn leads to numerical instabilities and a reduced accuracy when inverting the flexibility matrix to $\bar{\mathbf{K}}_\mathbf{s}$, which is finally used to couple the soil substructure to the foundation substructure. To avoid this, the shifting procedure is performed on a coarser discretization as proposed by

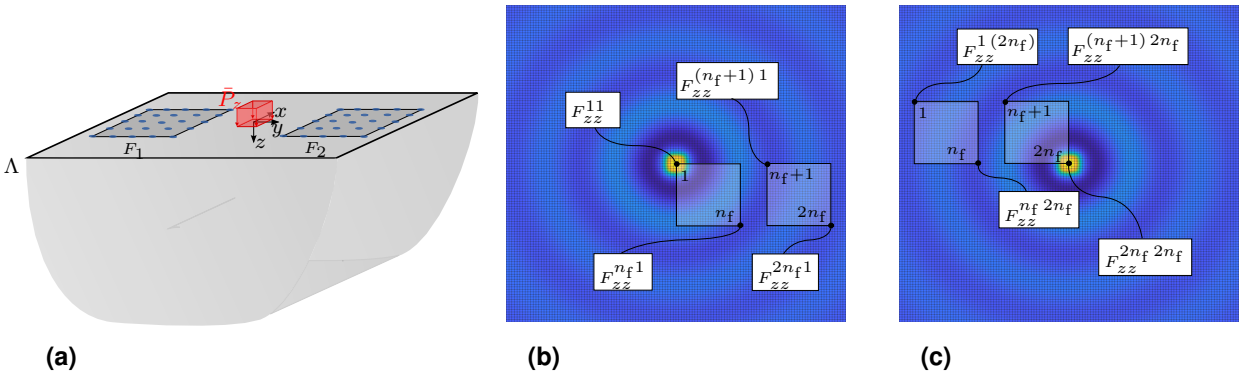

(a) **(b)** **(c)**

Figure 5.8: (a) Discretization points at soil foundation interface and vertical unit concentrated load at center of the halfspace surface. (b) First and (c) last step of the shifting procedure for the population of flexibility matrix for group of two foundation on homogeneous halfspace.

[85], ensuring larger differences of the displacement fields within a shifting step and thus a better conditioning of $\bar{\mathbf{F}}_\mathbf{s}$. The displacements on the new coarse mesh, shown in Fig. 5.7a, are determined as the mean value of all displacements w.r.t. the fine mesh within an area $A = n_\Delta \mathrm{d}x\, n_\Delta \mathrm{d}y$, whereby $\mathrm{d}x$,$\mathrm{d}y$ are the discretization step sizes of the fine mesh and n_Δ is the factor relating the old step size with the new one. To avoid that, due to the averaging, the displacement under the concentrated load no longer corresponds to the desired point flexibility, n_Δ should be chosen between one and three. Moreover, the discretization step sizes should be selected sufficiently small to represent the characteristic waves. [51]

In general the shifting procedure used for the single foundation is also applicable to set up $\bar{\mathbf{F}}_\mathbf{s}$ for a group of two or four foundations on a homogenous or layered halfspace. As illustrated in Fig. 5.8, again the foundation areas are shifted w.r.t. the discretization step size, such that each of the $n_{\mathrm{f_{tot}}}$ nodes is consecutively located under the center of the concentrated unit load once. Now, however, the displacements at the discretization points of all available foundations due one specific load position are sorted columnwise into the flexibility matrix. For this purpose, the coarse mesh with the averaged displacements is employed.

Within the implementation, the numbering of the foundation nodes is used for sorting the corr. displacements in $\bar{\mathbf{F}}_\mathbf{s}$ instead of their coordinates. Thereby, all nodes in x-direction of the foundation for the minimum y-coordinate are initially assigned consecutive numbers and then successively for all further y until the ultimate point at the outer edge of the last foundation is reached (cp. Fig 5.9a). This allows a straightforward filling up of the flexibility matrix for a single foundation or two foundations aligned in y-direction, as then all nodes of one foundation are numbered continuously. As a result, the desired structure of $\bar{\mathbf{F}}_\mathbf{s}$, with the contributions related to each foundation F_n arranged blockwise as $\bar{\mathbf{F}}_\mathbf{s}^{\mathbf{F_{ij}}}$, is obtained.

$$\begin{pmatrix} \bar{\mathbf{u}}_\mathbf{s}^{\mathbf{F_1}} \\ \bar{\mathbf{u}}_\mathbf{s}^{\mathbf{F_2}} \end{pmatrix} = \begin{pmatrix} \bar{\mathbf{F}}_\mathbf{s}^{\mathbf{F_{11}}} & \bar{\mathbf{F}}_\mathbf{s}^{\mathbf{F_{12}}} \\ \bar{\mathbf{F}}_\mathbf{s}^{\mathbf{F_{21}}} & \bar{\mathbf{F}}_\mathbf{s}^{\mathbf{F_{22}}} \end{pmatrix} \begin{pmatrix} \bar{\mathbf{P}}_\mathbf{s}^{\mathbf{F_1}} \\ \bar{\mathbf{P}}_\mathbf{s}^{\mathbf{F_2}} \end{pmatrix} \tag{5.24}$$

The matrices $\bar{\mathbf{F}}_{\mathbf{s}}^{\mathbf{F_{11}}}$ and $\bar{\mathbf{F}}_{\mathbf{s}}^{\mathbf{F_{22}}}$ each contain the flexibilities at the nodes of one foundation due to a load on the nodes belonging to the same foundation and thus after the coupling characterize the reaction of the soil-foundation system due to a load on the foundation itself. In contrast the matrices $\bar{\mathbf{F}}_{\mathbf{s}}^{\mathbf{F_{12}}}$ and $\bar{\mathbf{F}}_{\mathbf{s}}^{\mathbf{F_{21}}}$ contain the flexibilities on the nodes of foundation F_1 due to a load on the nodes of foundation F_2 and vice versa. They thus represent the through soil coupling of the two foundations and will later on be used to assess the SSSI. If both foundations exhibit the same size and flexural stiffness, it is only necessary to compute $\bar{\mathbf{F}}_{\mathbf{s}}^{\mathbf{F_{11}}}$ and $\bar{\mathbf{F}}_{\mathbf{s}}^{\mathbf{F_{12}}}$, since all other flexibilities can be supplemented from symmetry considerations. The shifting procedure then only needs to be applied for the nodes of foundation F_1.

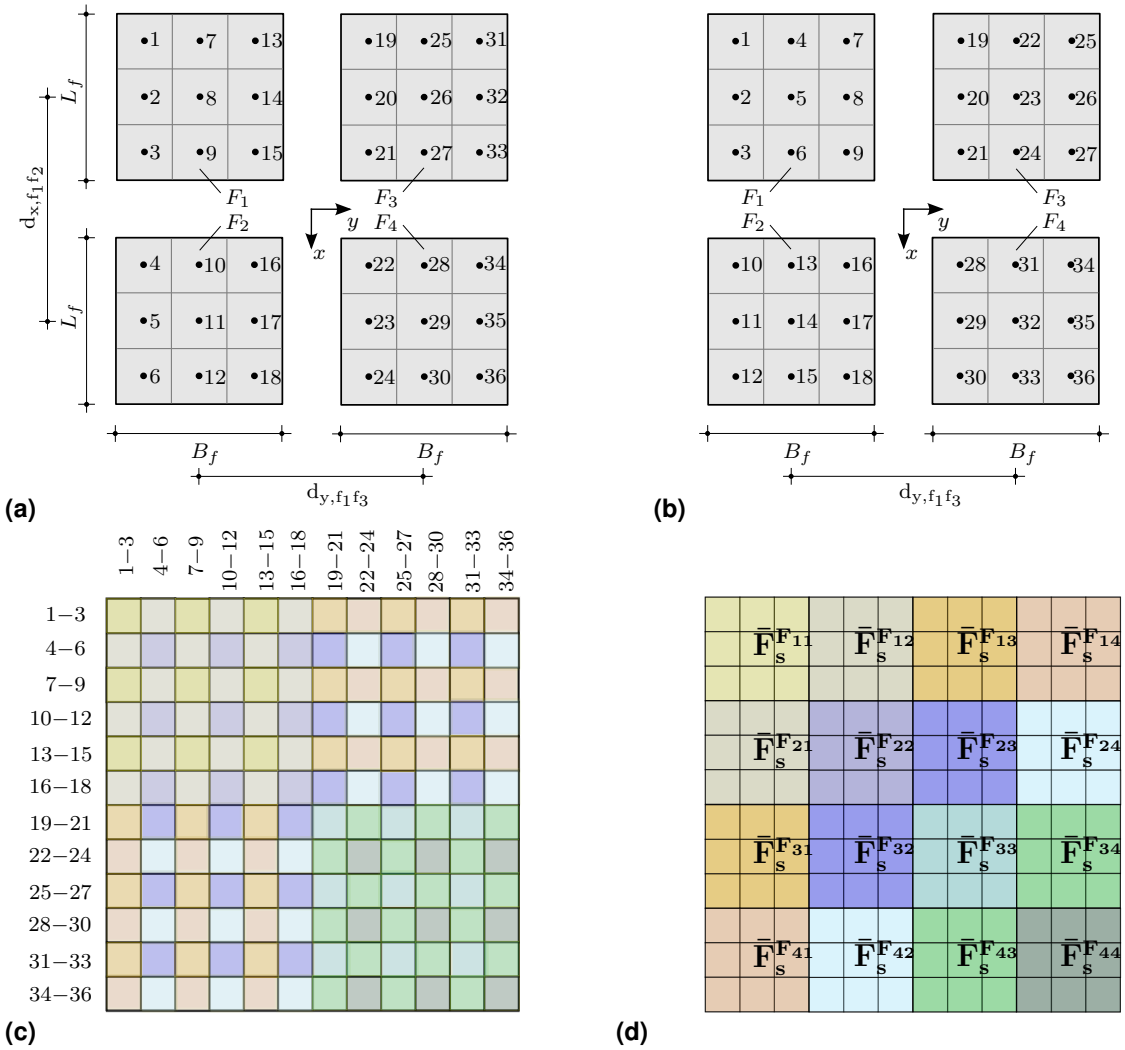

Figure 5.9: (a) Initial numbering of the nodes for a group of four foundations and (c) resulting structure of $\mathbf{F_s}$ after population applying the shifting procedure. (b) Continuous numbering of foundation nodes after reorganization and (d) corr. blockwise structure of the soil flexibility matrix. [284]

However, in case of two foundations aligned in x-direction, or a group of four foundations, due to the used numbering algorithm the nodes of one foundation are no more numbered continuously (cp. Fig 5.9a). This leads to an alternating arrangement of flexibility components belonging to different foundations when populating $\bar{\mathbf{F}}_\mathbf{s}$ as illustrated in Fig. 5.9c. Therefore, a retroactive reorganization of the flexibility matrix is necessary in order to obtain the common structure of $\bar{\mathbf{F}}_\mathbf{s}$ for the group of four adjacent foundations depicted in Fig. 5.9d, corresponding to a successive numbering of the nodes within each foundation shown in Fig 5.9b [284].

Shifting procedure for soil including a length invariant structure

In case of the halfspace with cylindrical inclusion, the assumption of rotational symmetry no longer applies, due to the inhomogeneity in the soil. Thus the position of the concentrated load on the soil surface is significant for the resulting displacement field. [100]

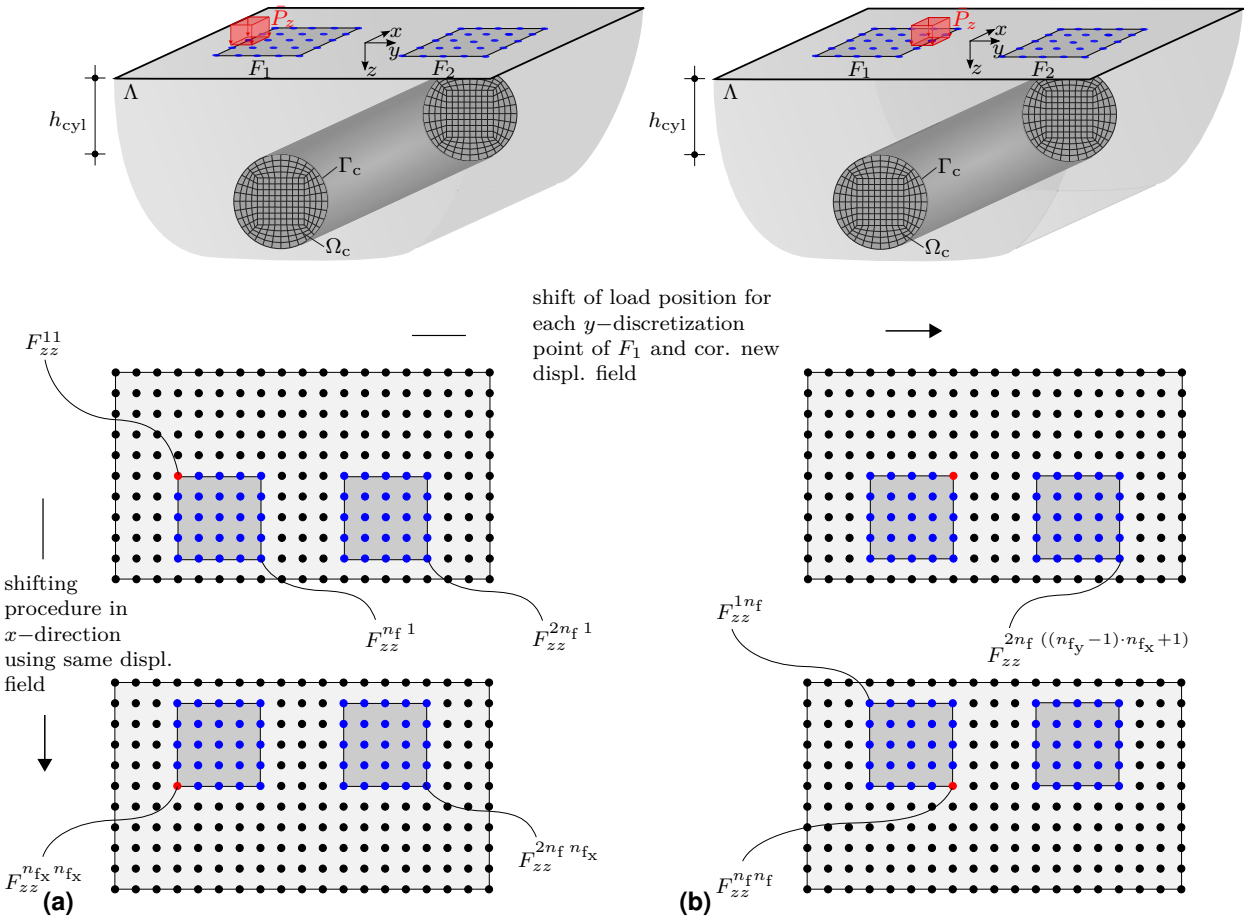

Figure 5.10: Modified shifting procedure for halfspace with cylindrical inclusion and selection of displacements for (a) concentrated load at first and (b) last load position on discretization points of soil foundation interface in y-direction of foundation F_1. [100]

However, as the system is length invariant only a different position in y-direction causes a different system response. Consequently the concentrated load needs to be placed once at each $y-$discretization point of the foundations. For two foundations located symmetrically w.r.t. the $x-$axis, it is even sufficient to only consider the $y-$discretization points of one foundation for the load positions, as the results for the second foundation again can be gained by symmetry considerations. Nevertheless, loads in the direction of all DOFs have to be considered. Fig. 5.10 illustrates the modified shifting procedure for the latter case. The load is positioned one after another on all $y-$discretization points of the first foundation F_1 and the response at all interaction points of both foundations with the soil surface Λ is evaluated. A new displacement field is determined for each of this load positions. For the discretization points of the foundations in $x-$direction the same system response is used and only the evaluation points are shifted under the point of load application. [100]

5.3.2 Soil foundation coupling

For the coupling of a finite 3D structure to the underlying ground at the soil foundation interface, the continuity conditions at the contact surface must be satisfied. Usually those structures and their foundations are modelled by the FEM and are thus discretized using the different elements introduced in Sec. 4.2.2. For structures with restricted deformation patterns, like rigid foundations, a simplified kinematic approach can be applied as outlined later on. Since the reaction of any linear structure supported by a foundation can be evaluated, once the frequency dependent response of the foundation in terms of its dynamic flexibility or stiffness is known [85], the focus of this work is on the investigation of the dynamic soil-foundation interaction. Furthermore, for any kind of building the interaction with the ground takes place via the foundation at the common contact surfaces. Therefore, the following explanations are limited to the coupling of one or several rigid and flexible foundations to different soil substructures at the ground surface. Nevertheless, results for more complex superstructures such as multi-storey frames will be presented later in the Sec. 6.5.

Flexible foundations

In case of a foundation with rather low flexural stiffness, the deformation of the foundation has a significant impact on the dynamic soil structure interaction. Therefore, a three dimensional FEM model is used to describe the foundation, as this allows to take the distribution of the nodal displacements and forces at the contact surface into account. Either solid or

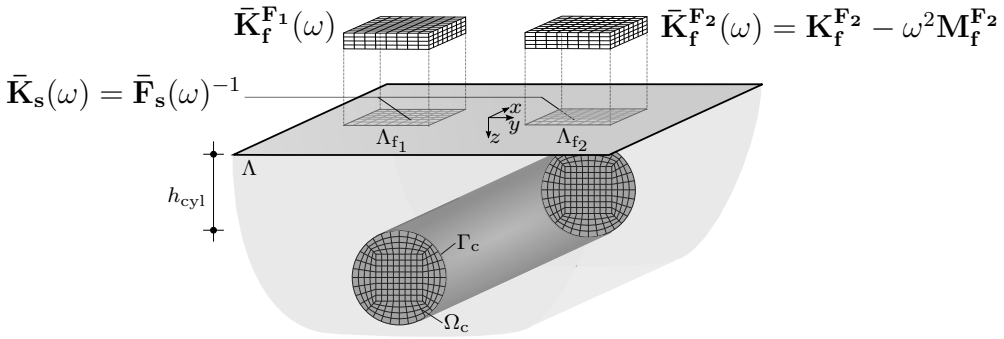

Figure 5.11: Coupling of foundations F_1 and F_2 modelled with 3D solid elements to the 2.5D ITM-FEM system halfspace with cylindrical inclusion at the contact areas Λ_{f_1} and Λ_{f_2}. [100]

shell elements are used, whereby with regard on the coupling in case of shell elements the rotational DOFs at the coupling interface have to be condensed out, as the discretization points of the soil substructure only posses the three translatory DOFs [51].

After assembling all elements, the equation of motion for the foundation F_n can be expressed in discretized form as

$$\left(\mathbf{K}_{\mathbf{f}}^{\mathbf{F_n}} - \omega^2\mathbf{M}_{\mathbf{f}}^{\mathbf{F_n}}\right)\bar{\mathbf{u}}_{\mathbf{f}}^{\mathbf{F_n}} = \bar{\mathbf{K}}_{\mathbf{f}}^{\mathbf{F_n}}(\omega)\,\bar{\mathbf{u}}_{\mathbf{f}}^{\mathbf{F_n}} = \bar{\mathbf{P}}_{\mathbf{f}}^{\mathbf{F_n}} \tag{5.25}$$

where $\mathbf{K}_{\mathbf{f}}^{\mathbf{F_n}}$ and $\mathbf{M}_{\mathbf{f}}^{\mathbf{F_n}}$ are the stiffness and the (lumped- or consistent) mass matrix of the respective foundation leading to the dynamic stiffness matrix $\bar{\mathbf{K}}_{\mathbf{f}}^{\mathbf{F_n}}$. $\bar{\mathbf{u}}_{\mathbf{f}}^{\mathbf{F_n}}$ is the nodal displacement vector and $\bar{\mathbf{P}}_{\mathbf{f}}^{\mathbf{F_n}}$ the nodal external force vector, all defined in the (x,y,ω) domain. The material properties of the linear elastic foundation are fully characterized by the Young's Modulus E_f, the Poisson ratio ν_f and the density ρ_f. Material damping can be introduced into the FEM model by replacing E_f by its complex counterpart. [51]

By placing each node of the FEM model to coincide with a discretization point at the interaction surface with the soil, one can combine the two substructures applying the compatibility conditions. These are enforced for all interaction nodes by assembling the dynamic stiffness matrix of the soil $\bar{\mathbf{K}}_{\mathbf{s}}$ at the appropriate positions into the total dynamic FEM stiffness matrices $\bar{\mathbf{K}}_{\mathbf{f}}^{\mathbf{F_n}}$ of the foundations resulting in the total system of equations [51]

$$\bar{\mathbf{K}}_{\text{sys}}\,\bar{\mathbf{u}}_{\text{sys}} = \bar{\mathbf{P}}_{\text{sys}} \qquad \text{resp.} \qquad \bar{\mathbf{u}}_{\text{sys}} = \bar{\mathbf{F}}_{\text{sys}}\bar{\mathbf{P}}_{\text{sys}} \tag{5.26}$$

whereby $\bar{\mathbf{u}}_{\mathbf{sys}}, \bar{\mathbf{P}}_{\mathbf{sys}}$ and $\bar{\mathbf{F}}_{\mathbf{sys}} = \bar{\mathbf{K}}_{\text{sys}}^{-1}$ are complex valued and comprise the DOFs at all nodes in the interior of the FEM substructures Ω_{f_n} as well as the interface nodes with the soil at the contact areas Λ_{f_n}. For two foundations being coupled to a halfspace with cylindrical inclusion Eq. (5.26) exemplarily results in the system of equations (5.27), which facilitates

the determination of the displacements of the coupled soil-foundation system due to an external load on one or both of the foundations fully considering the 3D SSSI.

$$\begin{pmatrix} \bar{\mathbf{K}}^{\mathbf{F_1 1}}_{\mathbf{s}\,\boldsymbol{\Lambda}_{\mathrm{f}_1}} + \bar{\mathbf{K}}^{\mathbf{F_1}}_{\mathbf{f}\,\boldsymbol{\Lambda}_{\mathrm{f}_1}\boldsymbol{\Lambda}_{\mathrm{f}_1}} & \bar{\mathbf{K}}^{\mathbf{F_1 2}}_{\mathbf{s}\,\boldsymbol{\Lambda}_{\mathrm{f}_2}} & \bar{\mathbf{K}}^{\mathbf{F_1}}_{\mathbf{f}\,\boldsymbol{\Lambda}_{\mathrm{f}_1}\boldsymbol{\Omega}_{\mathrm{f}_1}} & \mathbf{0} \\ \bar{\mathbf{K}}^{\mathbf{F_2 1}}_{\mathbf{s}\,\boldsymbol{\Lambda}_{\mathrm{f}_1}} & \bar{\mathbf{K}}^{\mathbf{F_2 2}}_{\mathbf{s}\,\boldsymbol{\Lambda}_{\mathrm{f}_2}} + \bar{\mathbf{K}}^{\mathbf{F_2}}_{\mathbf{f}\,\boldsymbol{\Lambda}_{\mathrm{f}_2}\boldsymbol{\Lambda}_{\mathrm{f}_2}} & \mathbf{0} & \bar{\mathbf{K}}^{\mathbf{F_2}}_{\mathbf{f}\,\boldsymbol{\Lambda}_{\mathrm{f}_2}\boldsymbol{\Omega}_{\mathrm{f}_2}} \\ \bar{\mathbf{K}}^{\mathbf{F_1}}_{\mathbf{f}\,\boldsymbol{\Omega}_{\mathrm{f}_1}\boldsymbol{\Lambda}_{\mathrm{f}_1}} & \mathbf{0} & \bar{\mathbf{K}}^{\mathbf{F_1}}_{\mathbf{f}\,\boldsymbol{\Omega}_{\mathrm{f}_1}\boldsymbol{\Omega}_{\mathrm{f}_1}} & \mathbf{0} \\ \mathbf{0} & \bar{\mathbf{K}}^{\mathbf{F_2}}_{\mathbf{f}\,\boldsymbol{\Omega}_{\mathrm{f}_2}\boldsymbol{\Lambda}_{\mathrm{f}_2}} & \mathbf{0} & \bar{\mathbf{K}}^{\mathbf{F_2}}_{\mathbf{f}\,\boldsymbol{\Omega}_{\mathrm{f}_2}\boldsymbol{\Omega}_{\mathrm{f}_2}} \end{pmatrix} \begin{pmatrix} \bar{\mathbf{u}}^{\mathbf{F_1}}_{\boldsymbol{\Lambda}_{\mathrm{f}_1}} \\ \bar{\mathbf{u}}^{\mathbf{F_2}}_{\boldsymbol{\Lambda}_{\mathrm{f}_2}} \\ \bar{\mathbf{u}}^{\mathbf{F_1}}_{\boldsymbol{\Omega}_{\mathrm{f}_1}} \\ \bar{\mathbf{u}}^{\mathbf{F_2}}_{\boldsymbol{\Omega}_{\mathrm{f}_2}} \end{pmatrix} = \begin{pmatrix} \bar{\mathbf{P}}^{\mathbf{F_1}}_{\boldsymbol{\Lambda}_{\mathrm{f}_1}} \\ \bar{\mathbf{P}}^{\mathbf{F_2}}_{\boldsymbol{\Lambda}_{\mathrm{f}_2}} \\ \bar{\mathbf{P}}^{\mathbf{F_1}}_{\boldsymbol{\Omega}_{\mathrm{f}_1}} \\ \bar{\mathbf{P}}^{\mathbf{F_2}}_{\boldsymbol{\Omega}_{\mathrm{f}_2}} \end{pmatrix} \tag{5.27}$$

Within the above outlined coupling approach the dynamic soil stiffness matrix $\bar{\mathbf{K}}_{\mathbf{s}}$ only needs to be computed once for a specific soil substructure and can be reused for various superstructures, provided that the discretization and the size of the contact areas do not change. The system of equations for a single or a group of four foundations can be set up analogously by adapting the respective system matrices. The inclusion of further elements as e.g. for the multi-storey frame, only leads to changes in the matrices associated with the DOFs in the interior of the FEM domains Ω_{f_1} and Ω_{f_2}. The DOFs of the interaction nodes on Λ_{f_1} and Λ_{f_2} and with that the coupling to the soil remain unaffected by these changes.

Rigid foundations

For the rigid foundation, two different modelling approaches are possible. First, a FEM model as outlined above can be used, with material and geometry adapted to achieve a reasonable flexural stiffness of the foundation. Here, the Young's modulus E_f and the height of the foundation slab H_f are the most important parameters. Second, the foundation can be considered as rigid body, for which the displacement field at the contact area to the soil can be expressed in terms of the amplitudes of the displacements and the rotations around the axis at the center of the respective foundation $\bar{\mathbf{u}}^{\mathbf{F_n}}_{\mathbf{f,r}} = (\bar{u}_{x,c}\,\bar{u}_{y,c}\,\bar{u}_{z,c}\,\bar{\varphi}_{x,c}\,\bar{\varphi}_{y,c}\,\bar{\varphi}_{z,c})^T$ as illustrated in Fig. 5.12a. The corresponding load vector including the amplitudes of the externally applied forces and moments on the rigid foundation F_n is defined as $\bar{\mathbf{P}}^{\mathbf{F_n}}_{\mathbf{f,r}} = \left(\bar{P}_{x,c}\,\bar{P}_{y,c}\,\bar{P}_{z,c}\,\bar{M}_{x,c}\,\bar{M}_{y,c}\,\bar{M}_{z,c}\right)^T$. Due to the compatibility conditions, the displacements $\bar{\mathbf{u}}^{\mathbf{F_n}}_{\mathbf{s}}$ at each of the discretization points $(x_i^{F_n}, y_i^{F_n})$ with $i = 1,...,n_{\mathrm{f}}$ of the soil subsystem at the interactions surface with the F_n^{th} foundation, must coincide with the rigid body motion of the respective foundation $\bar{\mathbf{u}}^{\mathbf{F_n}}_{\mathbf{f,r}}$ [285]

$$\bar{\mathbf{u}}^{\mathbf{F_n}}_{\mathbf{s}} = \bar{\mathbf{L}}^{\mathbf{F_n}}_{\mathbf{f,r}}\,\bar{\mathbf{u}}^{\mathbf{F_n}}_{\mathbf{f,r}} \qquad \text{with} \quad \bar{\mathbf{L}}^{\mathbf{F_n}}_{\mathbf{f,r}} = \left(\mathbf{a}^{\mathbf{F_n}}_{\mathbf{1}},...,\mathbf{a}^{\mathbf{F_n}}_{\mathbf{n_f}}\right)^T \tag{5.28}$$

Thereby $\bar{\mathbf{L}}^{\mathbf{F_n}}_{\mathbf{f,r}}$ is the assemblage of the n_{f} submatrices $\mathbf{a}^{\mathbf{F_n}}_{\mathbf{i}}$ with $i = 1,...,n_{\mathrm{f}}$ including the kinematic relation for each discretization point by means of its coordinates w.r.t. the center

of the resp. foundation [58]

$$\mathbf{a_i^{F_n}} = \begin{bmatrix} 1 & 0 & 0 & 0 & 0 & -y_i^{F_n} \\ 0 & 1 & 0 & 0 & 0 & x_i^{F_n} \\ 0 & 0 & 1 & y_i^{F_n} & -x_i^{F_n} & 0 \end{bmatrix} \tag{5.29}$$

Analogously, a relation between the external force vector $\bar{\mathbf{P}}_{\mathbf{f,r}}^{\mathbf{F_n}}$ and the nodal contact forces $\bar{\mathbf{P}}_{\mathbf{s}}^{\mathbf{F_n}}$ at the positions $(x_i^{F_n}, y_i^{F_n})$ can be established via the kinematic relations, such that the equilibrium of forces at $z = 0$ yields [63]

$$\bar{\mathbf{P}}_{\mathbf{f,r}}^{\mathbf{F_n}} = -\left[\bar{\mathbf{L}}_{\mathbf{f,r}}^{\mathbf{F_n}}\right]^T \bar{\mathbf{P}}_{\mathbf{s}}^{\mathbf{F_n}} = -\left[\bar{\mathbf{L}}_{\mathbf{f,r}}^{\mathbf{F_n}}\right]^T \mathbf{A}^{\mathbf{F_n}}\, \bar{\mathbf{P}}_{\mathbf{\Lambda}_{\mathrm{f_n}}}^{\mathbf{F_n}} \tag{5.30}$$

where $\mathbf{A}^{\mathbf{F_n}}$ is a diagonal matrix whose elements express the load influence area around the discretization points of a foundation F_n and $\bar{\mathbf{P}}_{\mathbf{\Lambda}_{\mathrm{f_n}}}^{\mathbf{F_n}}$ is the $3n_{\mathrm{f}} \times 1$ traction vector of the ITM or the ITM-FEM soil substructure at the contact surfaces $\Lambda_{\mathrm{f_n}}$.

Inserting Eqs. (5.28) and (5.30) into the force displacement relationship $\bar{\mathbf{K}}_{\mathbf{s}}^{\mathbf{F_n}}\, \bar{\mathbf{u}}_{\mathbf{s}}^{\mathbf{F_n}} = \bar{\mathbf{P}}_{\mathbf{s}}^{\mathbf{F_n}}$ and applying a left sided multiplication with $\left[\bar{\mathbf{L}}_{\mathbf{f,r}}^{\mathbf{F_n}}\right]^T$, a system of equations in terms of the external forces and the rigid body displacements results as

$$\bar{\mathbf{K}}_{\mathbf{f,r}}^{\mathbf{F_n}}\, \bar{\mathbf{u}}_{\mathbf{f,r}}^{\mathbf{F_n}} = \bar{\mathbf{P}}_{\mathbf{f,r}}^{\mathbf{F_n}} \qquad \text{with} \qquad \bar{\mathbf{K}}_{\mathbf{f,r}}^{\mathbf{F_n}} = -\left[\bar{\mathbf{L}}_{\mathbf{f,r}}^{\mathbf{F_n}}\right]^T \bar{\mathbf{K}}_{\mathbf{s}}^{\mathbf{F_n}} \left[\bar{\mathbf{L}}_{\mathbf{f,r}}^{\mathbf{F_n}}\right] \tag{5.31}$$

where $\bar{\mathbf{K}}_{\mathbf{f,r}}^{\mathbf{F_n}}$ is the 6×6 frequency dependent dynamic stiffness matrix of the rigid foundation coupled to the subsoil taking the following form

$$\bar{\mathbf{K}}_{\mathbf{f,r}}^{\mathbf{F_n}} = \begin{bmatrix} \bar{K}_{xx}^{F_n} & 0 & 0 & 0 & \bar{K}_{x,\varphi_y}^{F_n} & 0 \\ 0 & \bar{K}_{yy}^{F_n} & 0 & \bar{K}_{y,\varphi_x}^{F_n} & 0 & 0 \\ 0 & 0 & \bar{K}_{zz}^{F_n} & 0 & 0 & 0 \\ 0 & \bar{K}_{\varphi_x,y}^{F_n} & 0 & \bar{K}_{\varphi_x\varphi_x}^{F_n} & 0 & 0 \\ \bar{K}_{\varphi_y,x}^{F_n} & 0 & 0 & 0 & \bar{K}_{\varphi_y\varphi_y}^{F_n} & 0 \\ 0 & 0 & 0 & 0 & 0 & \bar{K}_{\varphi_z\varphi_z}^{F_n} \end{bmatrix} \tag{5.32}$$

Eq. (5.31) can also be written in the form

$$\bar{\mathbf{u}}_{\mathbf{f,r}}^{\mathbf{F_n}} = \bar{\mathbf{F}}_{\mathbf{f,r}}^{\mathbf{F_n}}\, \bar{\mathbf{P}}_{\mathbf{f,r}}^{\mathbf{F_n}} \tag{5.33}$$

where $\bar{\mathbf{F}}_{\mathbf{f,r}}^{\mathbf{F_n}}(\omega) = \bar{\mathbf{K}}_{\mathbf{f,r}}^{\mathbf{F_n}^{-1}}(\omega)$ is the 6×6 compliance matrix of the rigid surface foundation built up analogously to Eq. (5.32).

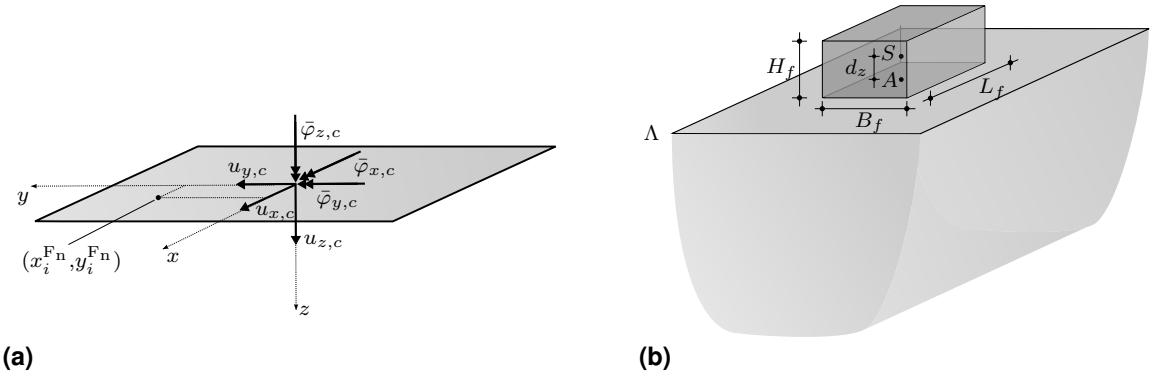

(a) **(b)**

Figure 5.12: (a) Kinematic relation of the discretization points $(x_i^{F_n}, y_i^{F_n})$ to the rigid body degrees of freedom $\bar{\mathbf{u}}_{\mathbf{f,r}}^{\mathbf{F_n}}$ at the center of the foundation F_n. (b) Dimensions and reference point A for the mass moments of inertia of a 3D surface foundation.

Furthermore, it is possible to consider the inertia effects due to the mass of the foundations and the superstructures by substituting the dynamic stiffness matrix with [107]

$$\bar{\mathbf{K}}_{\mathbf{f,rm}}^{\mathbf{F_n}} = \bar{\mathbf{K}}_{\mathbf{f,r}}^{\mathbf{F_n}} - \omega^2 \mathbf{M}_{\mathbf{f,r}}^{\mathbf{F_n}} \tag{5.34}$$

where $\mathbf{M}_{\mathbf{f,r}}^{\mathbf{F_n}}$ is the mass matrix including the total mass of the foundation $m_f = L_f B_f H_f \rho_f$ and the mass moments of inertia of the rigid foundation w.r.t. the center A of the foundation at the ground surface as depicted in Fig. 5.12b and given in [286]

$$\mathbf{M}_{\mathbf{f,r}}^{\mathbf{F_n}} = \begin{bmatrix} m_f & 0 & 0 & 0 & m_f d_z & 0 \\ 0 & m_f & 0 & -m_f d_z & 0 & 0 \\ 0 & 0 & m_f & 0 & 0 & 0 \\ 0 & -m_f d_z & 0 & I_x & 0 & 0 \\ m_f d_z & 0 & 0 & 0 & I_y & 0 \\ 0 & 0 & 0 & 0 & 0 & I_z \end{bmatrix} \quad \text{with} \quad \begin{aligned} I_x^A &= m_f \left(\frac{L_f^2 + H_f^2}{12} + d_z^2 \right) \\ I_y^A &= m_f \left(\frac{B_f^2 + H_f^2}{12} + d_z^2 \right) \\ I_z^A &= m_f \left(\frac{B_f^2 + L_f^2}{12} \right) \end{aligned} \tag{5.35}$$

The above relations for one foundation F_n can be straightforwardly extended to the interaction of several foundations with each other as well as with the underlying soil. Thus, the dimensions of the total dynamic stiffness and flexibility matrices of the rigid massless foundations $\bar{\mathbf{K}}_{\mathbf{f,r}}$ and $\bar{\mathbf{F}}_{\mathbf{f,r}}$ become $6N_f \times 6N_f$, where N_f is the number of foundations considered [104]. $\bar{\mathbf{K}}_{\mathbf{f,r}}$ is determined from the dynamic soil stiffness matrix $\bar{\mathbf{K}}_{\mathbf{s}}$ for a group of foundations applying the kinematic relations introduced above for each rigid foundation

$$\bar{\mathbf{K}}_{\mathbf{f,r}} = \bar{\mathbf{L}}_{\mathbf{f,r}}^T \bar{\mathbf{K}}_{\mathbf{s}} \bar{\mathbf{L}}_{\mathbf{f,r}} \tag{5.36}$$

where $\bar{\mathbf{L}}_{\mathbf{f,r}}$ is a block diagonal matrix with each of the blocks defined by $\bar{\mathbf{L}}_{\mathbf{f,r}}^{\mathbf{F_n}}$, as given in

Eqs. (5.28) and (5.29) [86]

$$\bar{\mathbf{L}}_{\mathbf{f,r}} = \begin{bmatrix} \bar{\mathbf{L}}_{\mathbf{f,r}}^{\mathbf{F_1}} & \mathbf{0} & \dots & \mathbf{0} \\ \mathbf{0} & \bar{\mathbf{L}}_{\mathbf{f,r}}^{\mathbf{F_2}} & \dots & \mathbf{0} \\ \vdots & \vdots & \ddots & \mathbf{0} \\ \mathbf{0} & \mathbf{0} & \ddots & \bar{\mathbf{L}}_{\mathbf{f,r}}^{\mathbf{F_{N_f}}} \end{bmatrix} \tag{5.37}$$

Thus the total dynamic stiffness $\bar{\mathbf{K}}_{\mathbf{f,r}}$ can be partitioned in the form

$$\bar{\mathbf{K}}_{\mathbf{f,r}} = \begin{bmatrix} \bar{\mathbf{K}}_{\mathbf{f,r}}^{\mathbf{F_{11}}} & \bar{\mathbf{K}}_{\mathbf{f,r}}^{\mathbf{F_{12}}} & \dots & \bar{\mathbf{K}}_{\mathbf{f,r}}^{\mathbf{F_{1N_f}}} \\ \bar{\mathbf{K}}_{\mathbf{f,r}}^{\mathbf{F_{21}}} & \bar{\mathbf{K}}_{\mathbf{f,r}}^{\mathbf{F_{22}}} & \dots & \bar{\mathbf{K}}_{\mathbf{f,r}}^{\mathbf{F_{2N_f}}} \\ \vdots & \vdots & \ddots & \vdots \\ \bar{\mathbf{K}}_{\mathbf{f,r}}^{\mathbf{F_{N_f1}}} & \bar{\mathbf{K}}_{\mathbf{f,r}}^{\mathbf{F_{N_f2}}} & \dots & \bar{\mathbf{K}}_{\mathbf{f,r}}^{\mathbf{F_{N_fN_f}}} \end{bmatrix} \tag{5.38}$$

in which the submatrices on the main diagonal represent the dynamic stiffness of each rigid foundation itself, whereas the off diagonal terms express the coupling between the respective foundations. Each of the submatrices exhibits the structure given in Eq. (5.32). The overall system of equations for the SSSI of several foundations in terms of the dynamic stiffness or flexibility results as

$$\bar{\mathbf{K}}_{\mathbf{f,r}}\, \bar{\mathbf{u}}_{\mathbf{f,r}} = \bar{\mathbf{P}}_{\mathbf{f,r}} \qquad \text{resp.} \qquad \bar{\mathbf{u}}_{\mathbf{f,r}} = \bar{\mathbf{F}}_{\mathbf{f,r}} \bar{\mathbf{P}}_{\mathbf{f,r}} \tag{5.39}$$

The total system equations including the effect of the massive foundation or superstructure can be derived analogously.

5.4 Postprocessing

5.4.1 Stresses and displacements from Soil Structure Interaction

In order to determine the stresses and displacements due to the SSI inside the complete soil domain, firstly the displacements $\bar{\mathbf{u}}_{\mathbf{c}}$ at the discretization points within the contact areas $\Lambda_{\mathrm{f_n}}$ resulting from an external load on the foundations have to be computed. If the foundations are modelled with the FEM, these can be obtained from solving Eq. (5.26) and extracting the displacements at the ground surface $\bar{\mathbf{u}}_{\mathbf{c}} = \bar{\mathbf{u}}_{\mathbf{sys}}(z = 0)$. In case of rigid foundations, considered via the kinematic boundary conditions, they can be computed as $\bar{\mathbf{u}}_{\mathbf{c}} = \bar{\mathbf{L}}_{\mathbf{f,r}}\, \bar{\mathbf{u}}_{\mathbf{f,r}}$ with the rigid body deformations $\bar{\mathbf{u}}_{\mathbf{f,r}}$ resulting from Eq. (5.39). The displacements $\bar{\mathbf{u}}_{\mathbf{c}}$

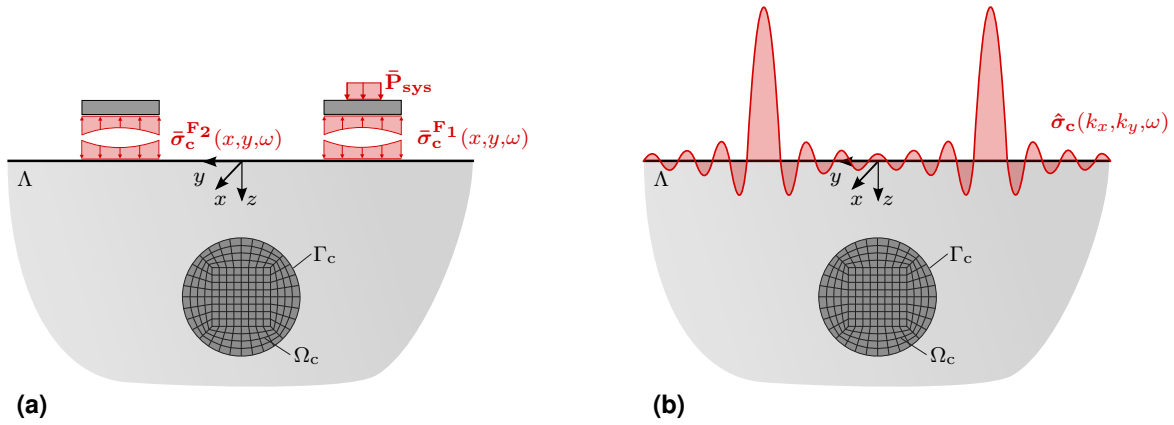

Figure 5.13: Postprocessing procedure: Application of the contact stresses $\bar{\boldsymbol{\sigma}}_{\mathbf{c}}$ at the soil foundation interfaces as external load on the surface of the 2.5D ITM-FEM system halfspace with cylindrical inclusion (a) in the original domain (x,y,z,ω) and (b) in the transformed domain (k_x,k_y,z,ω)

are further used to compute the nodal contact forces $\bar{\mathbf{P}}_{\mathbf{c}} = \bar{\mathbf{K}}_{\mathbf{s}}\,\bar{\mathbf{u}}_{\mathbf{c}}$ at the soil foundation interfaces in the (x,y,ω) domain. $\bar{\mathbf{P}}_{\mathbf{c}}(x,y,\omega)$ generally includes components in all spatial directions. However, in case of a vertical or rocking load on the foundations, the vertical displacements at $\Lambda_{\mathrm{f_n}}$ dominate the SSI response. If additionally relaxed boundary conditions are assumed, only the vertical contact forces are decisive for the stresses and displacements induced into the soil, so that the components in $x-$ and $y-$direction within $\bar{\mathbf{P}}_{\mathbf{c}}$ are neglected without introducing a considerable error. Within all equations describing the response of the different soil substructures, the external loads at the ground surface are applied in terms of stresses in the (k_x,k_y,ω) domain. Therefore, the nodal contact forces $\bar{\mathbf{P}}_{\mathbf{c}}(x,y,\omega)$ need to be divided by their respective load influence areas $\mathbf{A}^{\mathbf{F_n}}$ in a first step, to obtain the contact stresses $\bar{\boldsymbol{\sigma}}_{\mathbf{c}}(x,y,\omega)$. The latter are calculated w.r.t. the coarse discretization, as is the dynamic soil stiffness $\bar{\mathbf{K}}_{\mathbf{s}}$, and exist only at the contact surfaces of the foundations. However, the governing equations describing the soil substructure were originally calculated w.r.t. the fine discretization, so the contact stresses must be interpolated to provide a value at each of these points and are assumed to be zero at all discretization points outside the foundations. Eventually the contact stresses are transformed into the wavenumber frequency domain and $\hat{\boldsymbol{\sigma}}_{\mathbf{c}}(k_x,k_y,\omega)$ is applied to the soil substructure as boundary condition at the ground surface like illustrated in Fig. 5.13.

For a homogeneous or layered halfspace the wave amplitudes due to $\hat{\boldsymbol{\sigma}}_{\mathbf{c}}(k_x,k_y,\omega)$ at $z = 0$ and with them the stresses $\hat{\boldsymbol{\sigma}}(k_x,k_y,z,\omega)$ and displacements $\hat{\mathbf{u}}(k_x,k_y,z,\omega)$ in an arbitrary depth z inside the soil can be determined directly applying Eqs. (2.16) resp. (2.23) followed by (2.22). The results in the (x,y,z,ω) domain are obtained by a twofold inverse Fourier transform. In case of a halfspace with cylindrical inclusion, only the displacements at the ground surface Λ and inside the FEM domain due to the SSI contact stresses can be de-

termined directly. To compute the stresses and displacements for every possible position within the soil, a more elaborate postprocessing procedure is necessary. The displacements $\hat{\mathbf{u}}^{\mathbf{hs\ cyl}}_{\mathbf{ITM\,FE}}$ resp. $\hat{\mathbf{u}}^{\mathbf{hs\ cyl\,L}}_{\mathbf{ITM\,FE}}$ have to be applied as boundary conditions to the homogeneous or layered halfspace with cylindrical cavity excluding the coupling to the FEM. The superposition of all involved fundamental ITM systems has to satisfy these given displacement boundary conditions. Thus the wave amplitudes needed for the scaling of the displacements resulting from unit stress states can be computed for each fundamental system. Eventually, the stresses and displacements at any position of the overall system are determined out of the superposition of stresses and displacements of all fundamental systems, resulting from the unit stresses scaled with the calculated amplitudes, which are applied as external loads. All results are initially obtained in the wavenumber frequency domain and w.r.t. different reference systems referring to the corresponding fundamental systems. Therefore, different coordinate and inverse transformations are necessary in order to obtain the resulting stresses and displacements in Cartesian coordinates (x,y,z,ω). Further details on the postprocessing concerning the coupled ITM-FEM soil substructure can be found in [162]. [51]

5.4.2 Power flux through a control volume

In order to analyse the energy distribution inside the ground, the stresses $\bar{\boldsymbol{\sigma}}(x,y,z,\omega)$ and displacements $\bar{\mathbf{u}}(x,y,z,\omega)$ can further be used to compute the power flux through a defined control volume (CV), as illustrated in Fig. 5.14a. With that, it is possible to get a detailed insight into the wave propagation characteristics of the soil substructure. Moreover, conclusions about the radiation directivity as well as the attenuation behaviour can be drawn.

Power flux through a plane section

In a first step, the time averaged power input $\mathcal{P}_s(\omega)$ transmitted through one of the plane sections of the control volume within one period $T = 2\pi/\omega$ is considered. $\mathcal{P}_s(\omega)$ can be calculated from the integral of the intensity $\bar{\mathbf{I}}(x,y,\omega)$ over the area of the section A, given by the dot product of the stresses $\bar{\boldsymbol{\sigma}}$ and the velocities $\bar{\mathbf{v}}$. Since only negative frequencies are considered, the latter can be determined directly from the already known nodal displacements $\bar{\mathbf{v}} = \mathrm{i}\omega\bar{\mathbf{u}}$.

$$\mathcal{P}_s(\omega) = \frac{1}{T}\int_{(T)}\int_{(A)} \bar{\mathbf{I}}(x,y,\omega)\,\mathrm{d}A\mathrm{d}t = \frac{1}{T}\int_{(T)}\int_{(A)} \bar{\boldsymbol{\sigma}}(x,y,\omega)\cdot\bar{\mathbf{v}}(x,y,\omega)\,\mathrm{d}A\mathrm{d}t \tag{5.40}$$

For the power flux through a plane surface, only the normal and shear stresses in the section plane need to be considered along with the corresponding velocities w.r.t. a local Cartesian

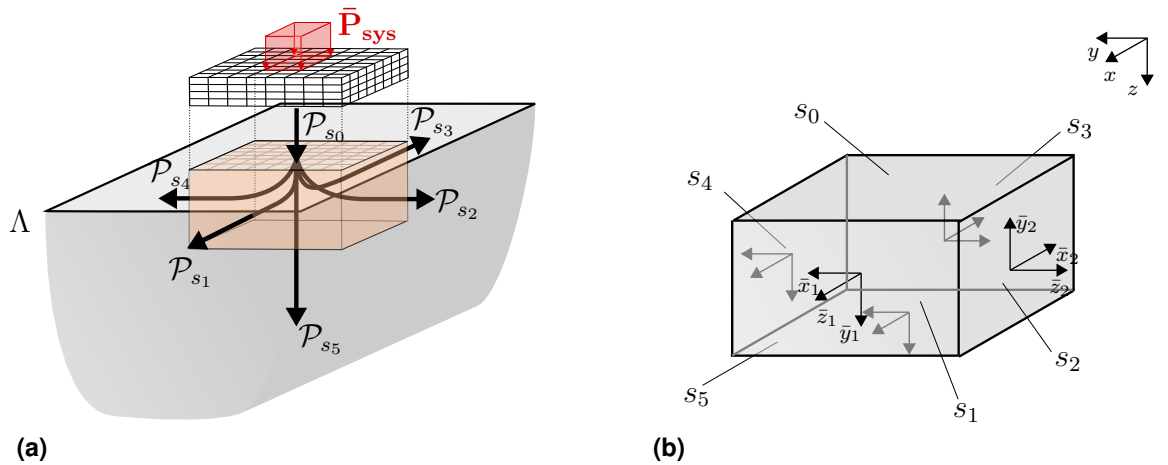

Figure 5.14: (a) Power flux through a defined control volume (CV) due to a power input at the soil foundation interface. (b) Numbering of CV surface areas and corr. local coordinate systems.

coordinate system, where $\bar{z}$ is defined as the out-of-plane direction and $\bar{x}, \bar{y}$ are defined as the in-plane directions, as shown in Fig. 5.14b.

$$\mathcal{P}_s(\omega) = \frac{1}{T}\int_{(T)}\int_{(A)} \bar{\boldsymbol{\sigma}}(x,y,\omega)\cdot\bar{\mathbf{v}}(x,y,\omega)\,\mathrm{d}A\mathrm{d}t = \frac{1}{T}\int_{(T)}\int_{(A)} (\bar{\sigma}_{\bar{z}\bar{z}}\bar{v}_{\bar{z}} + \bar{\sigma}_{\bar{z}\bar{x}}\bar{v}_{\bar{x}} + \bar{\sigma}_{\bar{z}\bar{y}}\bar{v}_{\bar{y}})\,\mathrm{d}A\mathrm{d}t \tag{5.41}$$

Since the integral over each of the summands in Eq. 5.41 can be evaluated separately, the time averaged power for one pair of the complex stress and displacement components

$$\sigma = \frac{1}{2}\left[\underbrace{(\sigma_R + \mathrm{i}\sigma_I)}_{\sigma_+}\mathrm{e}^{\mathrm{i}\omega t} + \underbrace{(\sigma_R - \mathrm{i}\sigma_I)}_{\sigma_-}\mathrm{e}^{-\mathrm{i}\omega t}\right] \tag{5.42}$$

$$v = \frac{1}{2}\left[\underbrace{(v_R + \mathrm{i}v_I)}_{v_+}\mathrm{e}^{\mathrm{i}\omega t} + \underbrace{(v_R - \mathrm{i}v_I)}_{v_-}\mathrm{e}^{-\mathrm{i}\omega t}\right] \tag{5.43}$$

can be computed as

$$\begin{aligned}\mathcal{P}_s(\omega) = \frac{1}{4T}\int_{(T)}\int_{(A)} \Big[&(\sigma_R + \mathrm{i}\sigma_I)(v_R + \mathrm{i}v_I)\,\mathrm{e}^{2\mathrm{i}\omega t} + (\sigma_R - \mathrm{i}\sigma_I)(v_R + \mathrm{i}v_I)\,\mathrm{e}^{0} + \\ &+ (\sigma_R + \mathrm{i}\sigma_I)(v_R - \mathrm{i}v_I)\,\mathrm{e}^{0} + (\sigma_R - \mathrm{i}\sigma_I)(v_R - \mathrm{i}v_I)\,\mathrm{e}^{-2\mathrm{i}\omega t}\Big]\,\mathrm{d}A\mathrm{d}t\end{aligned} \tag{5.44}$$

With the integrals $\int_0^T e^{\pm 2\mathrm{i}\omega t}\mathrm{d}t$ becoming zero, σ_- and v_- being the components associated with $-\omega$ and * denoting the conjugate complex of the corr. quantity it follows

$$\mathcal{P}_{s_i}(\omega) = \frac{1}{2}\int_{(A)} (\sigma_R v_R + \sigma_I v_I)\,\mathrm{d}A = \frac{1}{2}\,\mathrm{Re}\left(\int_{(\bar{x}_i)}\int_{(\bar{y}_i)} (\sigma_-\cdot v_-^*)\,\mathrm{d}\bar{y}_i\,\mathrm{d}\bar{x}_i\right) \tag{5.45}$$

Thus the overall power flux through the considered area finally results as

$$\begin{aligned}\mathcal{P}_{s_i}(\omega) &= \frac{1}{2}\,\mathrm{Re}\left(\int_{(\bar{x}_i)}\int_{(\bar{y}_i)} \bar{\sigma}_{\bar{z}_i\bar{z}_i}\bar{v}_{\bar{z}_i} + \bar{\sigma}_{\bar{z}_i\bar{x}_i}\bar{v}_{\bar{x}_i} + \bar{\sigma}_{\bar{z}_i\bar{y}_i}\bar{v}_{\bar{y}_i}\,\mathrm{d}\bar{y}_i\,\mathrm{d}\bar{x}_i\right) \\ &= \frac{1}{2}\mathrm{Re}\left(\int_{(\bar{x}_i)}\int_{(\bar{y}_i)} \bar{\boldsymbol{\sigma}}(\bar{x}_i,\bar{y}_i,\omega)\cdot\bar{\mathbf{v}}^*(\bar{x}_i,\bar{y}_i,\omega)\,\mathrm{d}\bar{y}_i\,\mathrm{d}\bar{x}_i\right)\end{aligned} \tag{5.46}$$

whereby the phase shift between the contact stresses and velocities is accounted for by the complex values of $\bar{\boldsymbol{\sigma}}$ and $\bar{\mathbf{v}}$. If these exhibit a phase shift of ninety degrees, the time averaged power $\mathcal{P}_s(\omega)$ becomes zero and no power is transmitted through the surface.

Numerical computation of the power flux

Due to the numerical computation, the stresses $\bar{\boldsymbol{\sigma}}(\bar{x}_i,\bar{y}_i,\bar{z}_i,\omega)$ and the velocities $\bar{\mathbf{v}}(\bar{x}_i,\bar{y}_i,\bar{z}_i,\omega)$ are only available at the equidistant discretization points located on a rectangular grid within the considered area s_i (cp. Fig. 5.15a). To determine $\mathcal{P}_s(\omega)$ in the (x,y,z,ω) domain, the surface integral in Eq. (5.46) must be solved. For this purpose, two different approaches are possible.

The first option is to assume a constant distribution of the stresses around each of the discretization points i within the resp. influence areas $\mathrm{d}A^i$, resulting from the product of the incremental distances $\mathrm{d}\bar{x}_i$ and $\mathrm{d}\bar{y}_i$ between the neighbouring points in the plane of the surface under consideration, as depicted in Fig. 5.15b. Therefrom, the equivalent nodal forces $\bar{P}^k_{\bar{n}}$ at the discretization point k in direction $\bar{n}$ are calculated as $\bar{P}^k_{\bar{n}} = \bar{\sigma}^k_{\bar{z}_i\bar{n}}\mathrm{d}A^i$. Subsequently $\mathcal{P}_{s_i}(\omega)$ can be computed as the component-wise sum of the nodal forces $\bar{\mathbf{P}}$ and the nodal velocities $\bar{\mathbf{v}}$ over all discretization points n of the considered area s_i

$$\mathcal{P}_{s_i}(\omega) \approxeq \frac{1}{2}\mathrm{Re}\left(\sum_n \bar{\mathbf{P}}(\bar{x}_i,\bar{y}_i,\omega)\,\cdot\,\bar{\mathbf{v}}^*(\bar{x}_i,\bar{y}_i,\omega)\right) = \frac{1}{2}\mathrm{Re}\left(\sum_{k=1}^{n} P^k_{\bar{x}_i}v^{*\,k}_{\bar{x}_i} + P^k_{\bar{y}_i}v^{*\,k}_{\bar{y}_i} + P^k_{\bar{z}_i}v^{*\,k}_{\bar{z}_i}\right) \tag{5.47}$$

Yet it must be noted, that for a rather coarse discretization this procedure only gives a relatively rough estimate for $\mathcal{P}_{s_i}(\omega)$ due to the assumption of the constant stresses. Furthermore, one has to take the different load influence areas at the edges and corners of the foundations into account when computing the nodal forces from the stresses.

A second option that resolves this problem and in addition allows a more accurate approximation of the power input is, to integrate the intensity distribution $\bar{\mathbf{I}}(\bar{x}_i,\bar{y}_i,\omega)$ directly. For this purpose, the values of the stresses $\bar{\boldsymbol{\sigma}}(\bar{x}_i,\bar{y}_i,\bar{z}_i,\omega)$ and the velocities $\bar{\mathbf{v}}(\bar{x}_i,\bar{y}_i,\bar{z}_i,\omega)$ at the

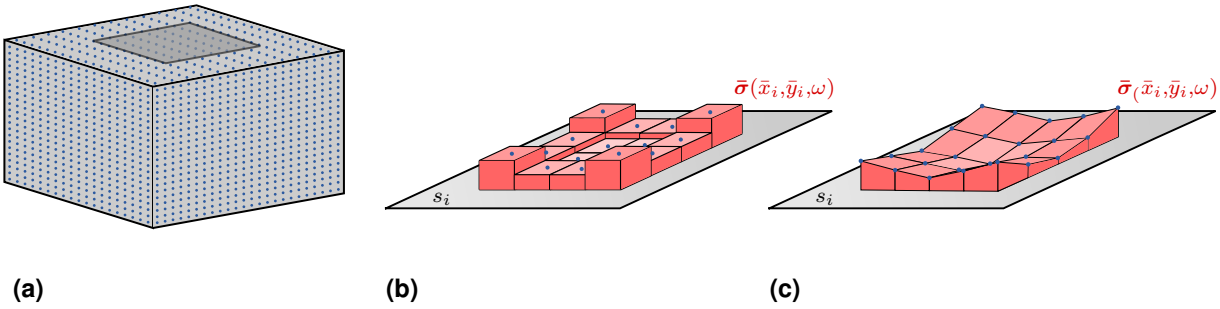

(a) **(b)** **(c)**

Figure 5.15: (a) Discretization points on the section planes of the control volume. (b) Constant distribution of the stresses around each discretization point and (c) approximation of the stress distribution over each element with linear shape functions in dependency of the nodal values.

discretization points k are assumed to be the nodal values σ_j^e and v_j^e of a four node quadrilateral element e and their distribution over the element area is approximated with the help of the linear shape functions from Eq. (4.5) as

$$\sigma^e(\eta,\zeta) = \sum_{j=1}^{4} \sigma_j^e \cdot N_i^e(\eta,\zeta) \qquad v^e(\eta,\zeta) = \sum_{j=1}^{4} v_j^e \cdot N_j^e(\eta,\zeta) \tag{5.48}$$

Applying an isoparametric approach, the geometry of the elements is described analogously

$$x^e(\eta,\zeta) = \sum_{j=1}^{4} x_j^e \cdot N_j^e(\eta,\zeta) \qquad y^e(\eta,\zeta) = \sum_{j=1}^{4} y_j^e \cdot N_j^e(\eta,\zeta) \tag{5.49}$$

As the shape functions are expressed in dependency of the natural coordinates of the element, the surface integral has to be evaluated also w.r.t. η,ζ instead of x,y

$$\int_{(\bar{x})}\int_{(\bar{y})} \bar{\mathbf{I}}(\bar{x},\bar{y})\,\mathrm{d}\bar{y}\,\mathrm{d}\bar{x} = \int_{(\eta)}\int_{(\zeta)} \bar{\mathbf{I}}(\eta,\zeta)\det\mathbf{J}\,\mathrm{d}\eta\,\mathrm{d}\zeta \quad \text{with} \quad \mathbf{J} = \begin{bmatrix} \dfrac{\partial\bar{x}}{\partial\eta} & \dfrac{\partial\bar{x}}{\partial\zeta} \\ \dfrac{\partial\bar{y}}{\partial\eta} & \dfrac{\partial\bar{y}}{\partial\zeta} \end{bmatrix} \tag{5.50}$$

The power flux through the considered area averaged over time and space finally results as

$$\mathcal{P}_{s_i}(\omega) = \sum_e \mathcal{P}_{s_i}^e(\omega) = \sum_e \frac{1}{2}\,\mathrm{Re}\left(\int_0^1\int_0^1 (\sigma_{\bar{z}_i\bar{z}_i}^e v_{\bar{z}_i}^{*e} + \sigma_{\bar{z}_i\bar{x}_i}^e v_{\bar{x}_i}^{*e} + \sigma_{\bar{z}_i\bar{y}_i}^e v_{\bar{y}_i}^{*e})\,\det\mathbf{J}\,\mathrm{d}\eta\,\mathrm{d}\zeta\right) \tag{5.51}$$

The integral over the element area in Eq. (5.51) can be solved analytically in advance and the resulting expression can be evaluated element-wise in dependency on the corresponding nodal values of the stresses and velocities.

The pseudocode of the implementation for the calculation of the power flow through a control volume for the two different approaches is given in Alg. 3.

Algorithm 3 Postprocessing: Power flux through control volume

procedure COMPUTE POWER FLUX CV
Compute contact forces $\bar{\mathbf{P}}_\mathbf{c}(x,y,\omega) = \bar{\mathbf{K}}_\mathbf{s}\bar{\mathbf{u}}_\mathbf{c}$ due to SSI
Determine contact stresses $\bar{\boldsymbol{\sigma}}_\mathbf{c}(x,y,\omega)$ at $z = 0$
Interpolate $\bar{\boldsymbol{\sigma}}_\mathbf{c}(x,y,\omega)$ to fine discretization
Supplement $\bar{\boldsymbol{\sigma}}_\mathbf{c}(x,y,\omega)$=0 outside contact areas
Fourier transform to $\hat{\boldsymbol{\sigma}}_\mathbf{c}(k_x,k_y,\omega)$

for all k_x, k_y, ω **do**
Determine $\hat{\mathbf{u}}(k_x,k_y,z,\omega)$ and $\hat{\boldsymbol{\sigma}}(k_x,k_y,z,\omega)$
at every position within the soil substructure

Inverse Fourier transform to $\bar{\mathbf{u}}(x,y,z,\omega)$ and $\bar{\boldsymbol{\sigma}}(x,y,z,\omega)$

function $\mathcal{P}_\text{in}$ AND $\mathcal{P}_\text{tot,cv}(\,)$ ▷ Via equivalent nodal forces
Define Control Volumes
Select all $\bar{\boldsymbol{\sigma}}(\bar{x}_i,\bar{y}_i,\bar{z}_i\omega)$ on nodes of CV surfaces
Calculate corresponding equivalent forces $\bar{\mathbf{P}}$
Select all $\bar{\mathbf{u}}(\bar{x}_i,\bar{y}_i,\bar{z}_i,\omega)$ on nodes of CV surfaces
Calculate $\bar{\mathbf{v}}(\bar{x}_i,\bar{y}_i,\bar{z}_i\omega) = i\omega\bar{\mathbf{u}}(\bar{x}_i,\bar{y}_i,\bar{z}_i\omega)$
Calculate power flux through CV surface wise
$\mathcal{P}_{s_i}(\omega) = \frac{1}{2}\mathrm{Re}\left(\sum_{k=1}^{n} P^k_{\bar{x}_i} v^{*\,k}_{\bar{x}_i} + P^k_{\bar{y}_i} v^{*\,k}_{\bar{y}_i} + P^k_{\bar{z}_i} v^{*\,k}_{\bar{z}_i}\right)$

function $\mathcal{P}_\text{in}$ AND $\mathcal{P}_\text{tot,cv}(\,)$ ▷ Via integration of intensity
Define Control Volumes
Select all $\bar{\boldsymbol{\sigma}}(\bar{x}_i,\bar{y}_i,\bar{z}_i\omega)$ on nodes of CV surfaces
Select all $\bar{\mathbf{u}}(\bar{x}_i,\bar{y}_i,\bar{z}_i\omega)$ on nodes of CV surfaces
Calculate $\bar{\mathbf{v}}(\bar{x}_i,\bar{y}_i,\bar{z}_i\omega) = i\omega\bar{\mathbf{u}}(\bar{x}_i,\bar{y}_i,\bar{z}_i\omega)$
Define coordinates and node numbers of discretization points
Create rectangular elements e on CV surfaces
Assign $\bar{\boldsymbol{\sigma}}(\bar{x}_i,\bar{y}_i,\bar{z}_i\omega)$ and $\bar{\mathbf{v}}(\bar{x}_i,\bar{y}_i,\bar{z}_i\omega)$ as nodal values of the elements
Compute power flux trough CV for all elements surface wise
$\mathcal{P}_{s_i}(\omega) = \sum_e \mathcal{P}^e_{s_i}(\omega) = \sum_e \frac{1}{2}\,\mathrm{Re}\left(\int_0^1\int_0^1 (\sigma^e_{\bar{z}_i\bar{z}_i} v^{*e}_{\bar{z}_i} + \sigma^e_{\bar{z}_i\bar{x}_i} v^{*e}_{\bar{x}_i} + \sigma^e_{\bar{z}_i\bar{y}_i} v^{*e}_{\bar{y}_i})\,\det\mathbf{J}\,\mathrm{d}\eta\,\mathrm{d}\zeta\right)$
Surface-wise summation of power contributions
Power input $\mathcal{P}_\text{in} = \mathcal{P}_{s_0}$ at soil foundation interface
Power transmission through all surfaces of CVs $\mathcal{P}_\text{tot,cv} = \sum_{i=1}^{5} \mathcal{P}_{s_i}$
Power ratios $\mathcal{P}_\text{tot,CV}/\mathcal{P}_\text{in}$, $\mathcal{P}_\text{sides}/\mathcal{P}_\text{tot,CV}$, $\mathcal{P}_\text{bottom}/\mathcal{P}_\text{tot,CV}$

Power flux through the control volume

By computing the power fluxes $\mathcal{P}_{s_i}(\omega)$ through all sectional planes s_i of the closed hexahedral control volume of Fig. 5.14 using the methodology outlined above, it is possible to investigate radiation patterns within a linearly elastic, homogeneous or layered soil. Since a stress free surface is assumed outside the soil-foundation interface, energy is introduced only by the contact stresses resulting from a harmonic loading of the foundation and performing work on the corr. displacements within the contact area.

In case of zero material damping, this energy is only dispersed throughout the soil by elastic waves so that with increasing distance from the source the energy is distributed over an enlarging area, resulting in a lower energy density. Yet no dissipation of energy takes place. Therefore, the power flux through a closed control volume needs to be equal to the sum of the power fluxes through the sectional planes of the CV inside the soil

$$\mathcal{P}_{\text{in}}(\omega) = \mathcal{P}_{s_0}(\omega) \stackrel{!}{=} \sum_{i=1}^{5} \mathcal{P}_{s_i}(\omega) = \mathcal{P}_{\text{tot,CV}}(\omega) \tag{5.52}$$

In contrast, if a displacement proportional, frequency independent, hysteretic material damping is applied via complex material parameters, a reduction of the power flux with increasing size of the CV occurs linked to the dissipated energy.

In order to be able to infer information on the directionality of the energy propagation within different soil subsystems from the power flow through the control volume, as presented in Sec. 6.3.1 and 6.3.2, the fluxes $\mathcal{P}_{s_i}(\omega)$ for different ensembles of the sectional planes are summarised and set in relation to each other

$$\begin{aligned} \mathcal{P}_{\text{in}}(\omega) &= \mathcal{P}_{s_0}(\omega) & \mathcal{P}_{\text{sides}}(\omega) &= \mathcal{P}_{s_{1-4}}(\omega) = \sum_{i=1}^{4} \mathcal{P}_{s_i}(\omega) \\ \mathcal{P}_{\text{bottom}}(\omega) &= \mathcal{P}_{s_5}(\omega) & \mathcal{P}_{\text{tot,CV}}(\omega) &= \mathcal{P}_{s_{1-5}}(\omega) = \sum_{i=1}^{5} \mathcal{P}_{s_i}(\omega) \end{aligned} \tag{5.53}$$

5.4.3 Power input at the soil foundation interface

With the energy flow analysis presented above, a deep insight into the dynamic response of the soil to the SSI loading is possible. However, this postprocessing requires a quite high computational effort, wherefore also only the power input at the soil foundation interface can be used as measure for the vibrational energy that is transmitted into the soil by the foundation. In the steady state, this power input is related to the energy which is dispersed

by elastic waves propagating in the soil (geometrical damping) as well as the energy expended by internal damping mechanisms, leading to an irreversible energy transfer from vibratory to thermal energy (material damping). Therefore, $\mathcal{P}_{\mathrm{in}}(\omega)$ characterizes the radiation ability of the foundation and thus allows to estimate the the potential of adjacent structures to be interfered by the induced vibrations by means of a single valued quantity. [51]

Since the nodal contact forces $\bar{\mathbf{P}}_{\mathbf{c}}(x,y,\omega) = \bar{\mathbf{K}}_{\mathbf{s}}(x,y,\omega)\bar{\mathbf{u}}_{\mathbf{c}}(x,y,\omega)$ and the corresponding velocities $\bar{\mathbf{v}}_{\mathbf{c}}(x,y,\omega)$ at the soil foundation interface are available as a direct result from the SSI analysis, it is favourable to use these immediately for the determination of the power input $\mathcal{P}_{\mathrm{in}}(\omega)$ at the contact surface, which thus results as

$$\mathcal{P}_{\mathrm{in}}(\omega) = \frac{1}{2}\mathrm{Re}\left(\int\limits_{(A)} \bar{\boldsymbol{\sigma}}_{\mathbf{c}}(x,y,\omega)\cdot\bar{\mathbf{v}}_{\mathbf{c}}^{*}(x,y,\omega)\,\mathrm{d}A\right) \approxeq \frac{1}{2}\mathrm{Re}\left(\sum_{n_{\mathrm{f}}} \bar{\mathbf{P}}_{\mathbf{c}}(x,y,\omega)\ \cdot\ \bar{\mathbf{v}}_{\mathbf{c}}^{*}(x,y,\omega)\right) \tag{5.54}$$

Furthermore, as the energy content of a signal in the original and the Fourier transformed domain can be represented in an analogous manner according to the Parseval-Plancherel identity [287], the power input of Eq. (5.54) can also be formulated as [51]

$$\begin{aligned}\mathcal{P}_{\mathrm{in}}(\omega) &= \frac{1}{8\pi^2}\,\mathrm{Re}\left(\int\limits_{-\infty}^{\infty}\int\limits_{-\infty}^{\infty} \hat{\boldsymbol{\sigma}}_{\mathbf{c}}(k_x,k_y,\omega)\cdot\hat{\mathbf{v}}_{\mathbf{c}}^{*}(k_x,k_y,\omega)\mathrm{d}k_x\mathrm{d}k_y\right)\\ &\approxeq \frac{1}{8\pi^2}\,\mathrm{Re}\left(\sum_{N_y}\sum_{N_x} \hat{\mathbf{P}}_{\mathbf{c}}(k_x,k_y,\omega)\ \cdot\ \hat{\mathbf{v}}_{\mathbf{c}}^{*}(k_x,k_y,\omega)\mathrm{d}k_x\mathrm{d}k_y\right)\end{aligned} \tag{5.55}$$

Since the quantities used for the determination of the power input in the wavenumber frequency domain were also computed numerically by means of the FFT, the integrals from $-\infty$ to ∞ are replaced by a summation over the number of considered series members N_x resp. N_y. The power for each combination of wavenumbers (k_x,k_y) at a given frequency thus yields [51]

$$\mathcal{P}_{\mathrm{in}}(k_x,k_y,\omega) = \frac{1}{2}\,\mathrm{Re}\left(\hat{\mathbf{P}}_{\mathbf{c}}(k_x,k_y,\omega)\cdot\hat{\mathbf{v}}_{\mathbf{c}}^{*}(k_x,k_y,\omega)\right) \tag{5.56}$$

Correlations between frequencies of high power input $\mathcal{P}_{\mathrm{in}}(\omega)$ and characteristic features of the dynamic soil response for different soil substructures are shown in detail later on. Moreover, the connection between the wavenumber spectra of the contact forces, the resulting displacements and the power input with the radiated elastic waves as well as their directivities will be illustrated in Sec. 6.3.

6 Dynamic response to stationary harmonic loads

In the upcoming chapter, the dynamic responses of multiple different systems, described by the previously introduced coupled 2.5D and 3D ITM-FEM approaches, due to stationary harmonic loads are presented. For this end, the system responses are evaluated separately for selected frequencies or the frequency range of interest for the considered problem and the results are given in the frequency domain. The main objectives herein are to verify the proposed approaches and procedures by comparing the obtained results with those of (semi-)analytical solutions or from the literature for different benchmark cases as well as to demonstrate the applicability and the suitability of the method for the assessment of practical issues.

Therefore, in Sec. 6.1, the semi-analytical solutions of the fundamental systems halfspace, layered halfspace and elastic stratum over rigid subsoil (cp. Sec. 2.2 and 2.3) are firstly validated by means of literature results. Subsequently, the coupling of ITM and FEM for different soil substructures with longitudinally invariant cylindrical inclusions (cp. Sec. 5.1) is verified by comparing the results with those of the previously validated fundamental systems. Both homogeneous and layered soils with one or two cylindrical inclusions or indentations are considered for different load scenarios and frequencies. The validation is then carried out analogously for the coupling of the halfspace with a spherical inclusion or indentation (cp. Sec. 5.2). Thereby, also results for different meshes of the FEM model of the spherical enclosure are presented.

Sec. 6.2 shows an application of the coupled ITM-FEM approach for the investigation of various vibration mitigation measures such as the installation of a heavy weight wall close to a railway track (Sec. 6.2.1), infilled or open infinite and finite trenches in the transmission path (Sec. 6.2.2, 6.2.3 and 6.2.4) or elastic building supports (Sec. 6.2.5). The method allows to predict the vibration reduction at the receiving position by means of numerical simulations and thus to assess the efficiency of a single measure or to compare the performance of

different ones. Furthermore, it makes the investigation of the physical mechanisms behind the mitigation measures possible and enables the identification of the most important design parameters due to the insights into the wave propagation characteristics obtained, among others, by the analysis in the wavenumber-frequency domain.

In Sec. 6.3 the coupling of three dimensional superstructures to the underlying ground, outlined in Sec. 5.3, is applied to determine the dynamic response of a single surface foundation for different subsoil and loading conditions. Initially, the main characteristic features of the frequency dependent foundation flexibilities and the power input at the soil foundation interface are illustrated for the rather simple support conditions of the homogeneous (Sec. 6.3.1) and the layered halfspace (Sec. 6.3.2). Thereby both, rigid and flexible massless or massive foundations are considered. Furthermore, wavenumber spectra of the displacements, contact forces and the power input resulting from the SSI are presented and correlations to the wave propagation characteristics are drawn. The deductions on the radiation directivity and the attenuation behaviour are further confirmed by the distributions of the displacements and the energy inside the soil obtained by the postprocessing procedure. The accuracy of the proposed methodology for the determination of the soil flexibility resp. stiffness matrix and the coupling is demonstrated by comparison of the obtained results to literature for standard benchmark cases. Finally, the behaviour of a foundation on more complex soil subsystems, including local inhomogeneities, is assessed (Sec. 6.3.3) by showing differences and similarities to the results presented before. [51]

The expansion of the proposed method for the SSSI of several adjacent foundations on the ground surface is outlined in Sec. 6.4. Thus, for validation purposes, the frequency dependent compliances of a group of rigid surface foundations on a homogeneous halfspace is first compared with literature results for standard cases (Sec. 6.4.1). Subsequently, the results for adjacent foundations resting on a halfspace with cylindrical inclusion, obtained by applying the modified shifting procedure to determine the soil stiffness matrix, are verified and a parametric study investigating the wave-impeding effect of a finite, stiff inclusion on the foundation compliances and the surface displacements is performed (Sec. 6.4.2). Parameters with a strong influence on the system response are identified and indications, under which circumstances the influence of the inclusion should necessarily be taken into account, are given.

In Sec. 6.5 the coupled ITM-FEM approach is applied to investigate the effect of the soil structure interaction on the dynamic response of spatial frame structures. The influence of different subsoil and founding conditions on the frequency response functions (FRFs) at characteristic points of the structure as well as the corr. modal behaviour is discussed.

Moreover, transfer functions relating the structural response due to a punctual loading of the soil in the vicinity of the building are presented, which can be used to asses the through soil coupling of a building and a nearby vibrational source.

Eventually, the effect of the dynamic interaction of two parallel tunnels is investigated in Sec. 6.6. Thereby, the significant influence on the vibration amplitudes at the ground surface due to the inclusion of the second tunnel into the model is illustrated by means of the insertion gains.

6.1 Verification examples

6.1.1 Homogeneous and layered halfspace

In the following, the dynamic responses of a linear elastic, isotropic, homogeneous and layered soil due to a harmonic load on the ground surface is determined by means of the fundamental ITM systems introduced in Secs. 2.2 and 2.3. The obtained results are compared with literature solutions, which have shown to be in good agreement with published measurement data, for validation purposes. The setup of the system which is investigated for different soil compositions and loading conditions as well as the associated dimensions are depicted in Fig. 6.1. The material parameters and the associated velocities of the compressional c_p, the shear c_s and the Rayleigh waves c_r for the different soil configurations considered are given in Tab. 6.1. The values were chosen on the basis of the measured soil properties of a particular British Rail site and therefore correspond to physically realistic values. They also match the material parameters chosen for the calculation of the surface displacements in [13, 16, 210], so that a direct comparison of the results is possible.

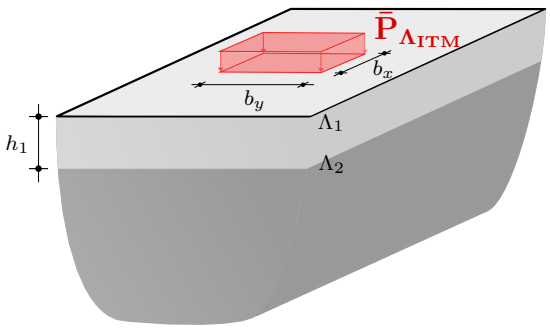

Figure 6.1: Setup and dimensions for validation of fundamental system layered halfspace.

	L_l	h_1 (m)	E_s (Nm^{-2})	ν_s (–)	ρ_s (kgm^{-3})	ζ_s (–)	c_p (ms^{-1})	c_s (ms^{-1})	c_r (ms^{-1})
Soil A	1	∞	$2.69 \cdot 10^8$	0.257	1550	0.05	460.00	263.07	242.32
Soil B	1	∞	$1.07 \cdot 10^9$	0.257	2000	0.05	809.92	463.18	426.64
Soil C	1	7	$2.69 \cdot 10^8$	0.257	1550	0.05	460.00	263.07	
	2	∞	$1.07 \cdot 10^9$	0.257	2000	0.05	809.92	463.18	426.64
Soil D	1	7	$2.69 \cdot 10^8$	0.257	1550	0.05	460.00	263.07	
	2	∞	$1.00 \cdot 10^{11}$	0.000	10000	0.05	3166.20	2238.90	1947.80

Table 6.1: Soil properties and composition at the reference sites.

Soils A and B each describe a homogeneous halfspace consisting entirely of the resp. material, while Soil C represents a stratified soil with a moderate stiffness difference between the upper soil layer and the underlying elastic halfspace, expressed by the ratio of the shear wave velocities $c_{s2}/c_{s1} \approx 1.75$. Soil D, in contrast, represents an elastic stratum over a rigid substrate with an inflexible interface at $z_1 = h_1$ and thus a large ratio $c_{s2}/c_{s1} \approx 8.5$.

First, the steady state displacements at the surface of Soil A due to a vertical strip load with $b_y = 1.5$ m and $b_x = B_x$ and amplitude $|\bar{p}_{zz,\Lambda}(x,y,\omega)| = 2\pi/b_y$ applied in the center of the coordinate axis are determined and compared to the results obtained by Lefeuve-Mesgouez et al. [210]. Therein, an analytical solution of the differential equation for the given boundary conditions in the wavenumber frequency domain assuming plane strain conditions is evaluated for discrete samples and a numerical inverse Fourier transform is applied to retrieve the results in the spatial domain.

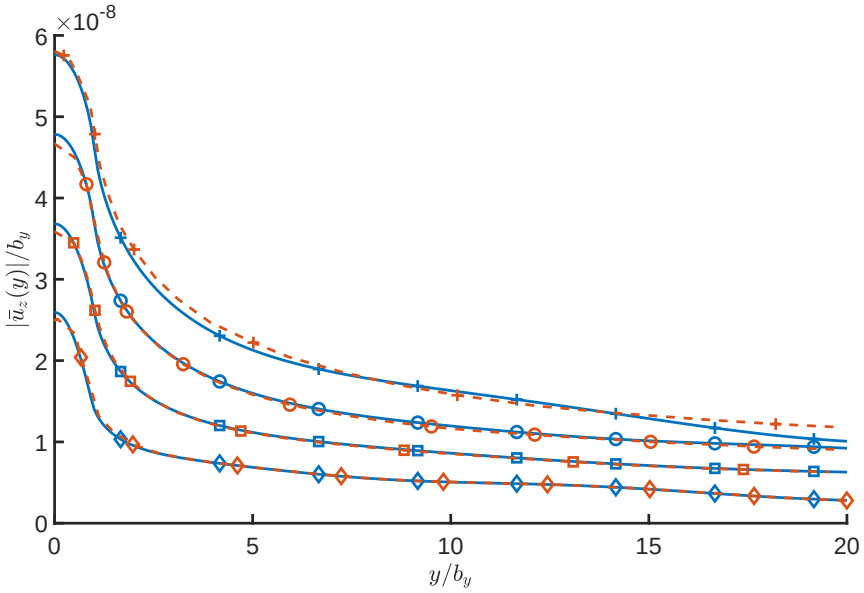

Figure 6.2: Comparison of $|\bar{u}_z(y)|/b_y$ at $x = 0$ on the ground surface of a homogeneous halfspace (Soil A) due to a vertical strip load for $f = 8$ Hz (+), $f = 16$ Hz (○), $f = 32$ Hz (□) and $f = 64$ Hz (◇) obtained with the ITM approach (—) to the results of Lefeuve-Mesgouez et al. [210] (– –).

Fig. 6.2 shows the absolute value $|\bar{u}_z(y)|$ of the vertical displacements normalized by the load width b_y at $x = 0$ for different frequencies, computed for a total discretized ITM domain size of $B_x = B_y = 256$ m with $N_x = N_y = 2^{12}$ sample points resp. Fourier series members. Since the displacement field is symmetric w.r.t. the load, only the values of $|\bar{u}_z(y)|$ for $y > 0$ are depicted. For these, a very good agreement between the both solutions regarding all considered frequencies can be observed.

Second, the response to a harmonic vertical block load for all soil compositions of Tab. 6.1 is computed applying the ITM approach and opposed to the results obtained by Jones et al. [16]. A square load with side length $b_x = b_y = 0.6$ m and amplitude $|\bar{p}_{zz,\Lambda}(x,y,\omega)| = 1/(b_x b_y)$, leading to an unit resultant, is applied at $z_1 = 0$. The rather high frequency of $f = 64$ Hz has been chosen, since therewith for the given ground parameters several propagating modes can occur within the upper 7 m thick soil layer for Soils C and D.

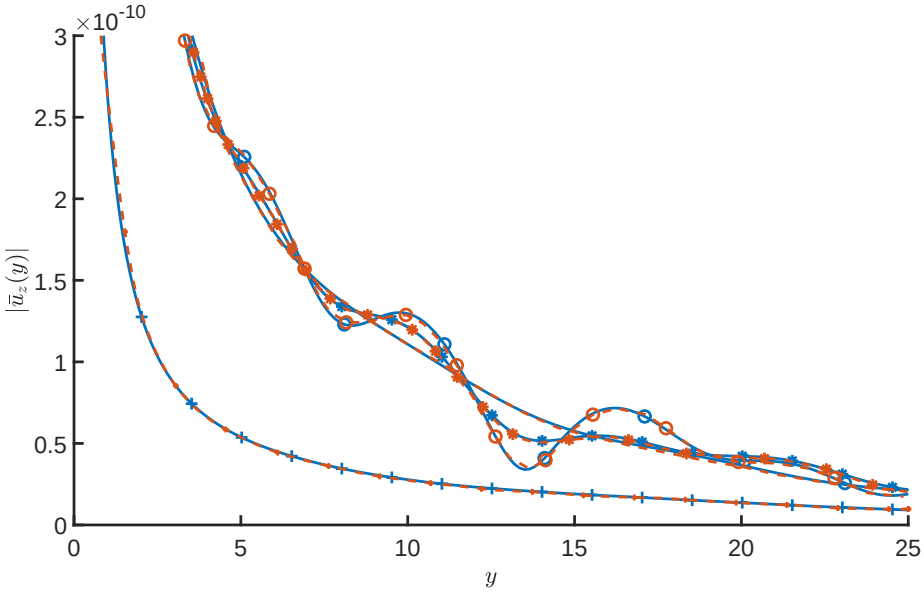

Figure 6.3: Comparison of $|\bar{u}_z(y)|$ at $x = 0$ on the ground surface of Soil A (−), Soil B (+), Soil C (∗) and Soil D (∘) due to a vertical rectangular block load with $f = 64$ Hz obtained with the ITM (—) approach to the results of Jones et al. [16] (—).

Fig. 6.3 shows the resulting vertical displacements $|\bar{u}_z(y)|$ along the y-axis up to 25 m from the load center, whereby the maximum at $y = 0$ has been cropped to better show the details of the variation of the displacement w.r.t. the y-direction for the different subsoil conditions. The responses for the homogeneous Soil A and the two layered Soils C and D are quite close to each other, since the underlying halfspace at the considered frequency only has little influence. This also agrees with the findings of Auersch [288], according to whom only the ground up to half the Rayleigh wavelength λ_r has an influence on the surface displacements. Due to its elastic interface at $z_1 = h_1$, Soil C represents an intermediate state between Soils A and D and leads to a less pronounced interference pattern of the modes propagating in

the layer than in the case of the rigid substrate. The difference between the three results would, however, be larger at the layer resonance frequencies [16]. The displacements for the stiffer homogeneous Soil B are much smaller and more concentrated, but like for Soil A show a strictly monotonic decrease with increasing distance from the load. The computed results for all different system setups show very good agreement with those presented in Jones et al. [16] and thus validate the proposed ITM approach for the fundamental systems halfspace and layered halfspace.

6.1.2 Halfspace with cylindrical inclusions

In order to verify the coupling of the ITM and the FEM at a cylindrical interaction surface as well as the coupling of a discrete soil stratification to an underlying soil substructure, both presented in Sec. 5.1, a selection of all possible system setups for different load scenarios is evaluated in the following and the results are compared to the previously validated semi-analytical solutions of the fundamental systems halfspace and layered halfspace.

For this purpose both, the cylindrical indentations or cavities are completely filled with finite elements that have the same material parameters as the surrounding Soil 1, given in Tab. 6.2. A layered halfspace, with identical material for the layer and the underlying infinite soil, is chosen as benchmark system for the validation of the embedded inclusions, since it allows to evaluate the displacements directly at a defined depth $z = H_{\mathrm{tot}}$ and compare them to those within the FEM domain of the coupled approach, additionally to the displacements on the ground surface. Furthermore, a load $\bar{\mathbf{P}}^{\mathbf{hs\,L}}_{\mathbf{\Lambda_2\,ITM}}$ can be applied as transition condition at the layer interface Λ_2 and therefore also a scenario with a load $\tilde{\mathbf{P}}_{\mathbf{\Omega_c\,FE}}$ inside the FEM domain of the coupled approach can be compared to the semi-analytical solution [84]. In case of the indentation, it is sufficient to use a homogeneous halfspace for the computation of the reference solution, since only the displacements at the ground surface are considered here.

In all following validation examples, a harmonic square block load with $f = 2, 30$ and 60 Hz and a width of $b_x = b_y = 2$ m is applied to both, the coupled approach and the reference system. For a load within the ITM domain, stresses $\bar{\mathbf{P}}_{\mathbf{\Lambda_1\,ITM}}$ resp. $\bar{\mathbf{P}}_{\mathbf{\Lambda_2\,ITM}}$ with unit amplitude 1 Nm^{-2} are used, while in case of a loading inside the FEM substructure equivalent nodal loads $\tilde{\mathbf{P}}_{\mathbf{\Omega_c\,FE}}$ are employed. Furthermore, unless explicitly stated differently, a total domain size of $B_x = B_y = 128$ m with $N_x = N_y = 2^9$ sampling points resp. wave numbers was chosen, resulting in an incremental step size on the ground surface for the ITM substructure of $\mathrm{d}x = \mathrm{d}y = 0.25$ m. This discretization allows an appropriate sampling of the propagating waves and ensures the attenuation of the displacement amplitudes under a certain threshold, before reaching the boundary of the discretized area, thus avoiding aliasing effects [84].

	E (Nm^{-2})	ν $(-)$	ρ (kgm^{-3})	ζ $(-)$	c_p (ms^{-1})	c_s (ms^{-1})	c_r (ms^{-1})
Soil 1	$2.60 \cdot 10^7$	0.3	2000	0.05	132.31	70.72	65.60
Soil 2	$5.00 \cdot 10^8$	0.3	2000	0.05	580.84	310.47	288.02
Foundation	$3.00 \cdot 10^{15}$	0.2	0	0.02	–	–	–

Table 6.2: Soil properties for verification of halfspace with cylindrical inclusion or indentation.

The cylindrical 2.5D FEM inclusion was discretized with $N_\varphi = 64$ equidistant nodes resp. Fourier series members along the circumference, leading to an element size of 0.125 m for the considered inclusion size of $R = 4$ m and thus approximately ten elements per shear wave length λ_s of the soil at the highest regarded frequency [100]. To decrease the computational effort, for the low frequency range also a coarser discretization can be chosen for both, the ITM and the FEM substructure, since the characteristic wave lengths are much larger and less sampling points are sufficient to cover the corr. waves. However, as the amount of discretization points on Γ_c also influences the geometric approximation of the cylindrical boundary by the FEM model, N_φ must not be reduced too strongly. To ensure that the influence on the wave propagation is taken into account when evaluating the displacement response, a rather large size of $R = 4$ m was chosen for the inclusion and the indentation. Therefore, even in the low-frequency range the dimension of the FEM substructure is sufficiently large compared to the wavelengths of the elastic waves. Furthermore, the selected total embedment depth H_{tot} of the inclusion guarantees that it is located within the influence region of the Rayleigh waves for large parts of the considered frequency spectrum $f = 2 - 60$ Hz.

Single inclusion in layered soil

As first validation example a stratified soil with a top layer of $h_1 = 2$ m and a single cylindrical inclusion with an overall embedment depth of $H_{\mathrm{tot}} = h_1 + H = 8$ m shifted from the center by $y_{\mathrm{Tc}} = 8$ m is considered, as illustrated in Fig. 6.4a.

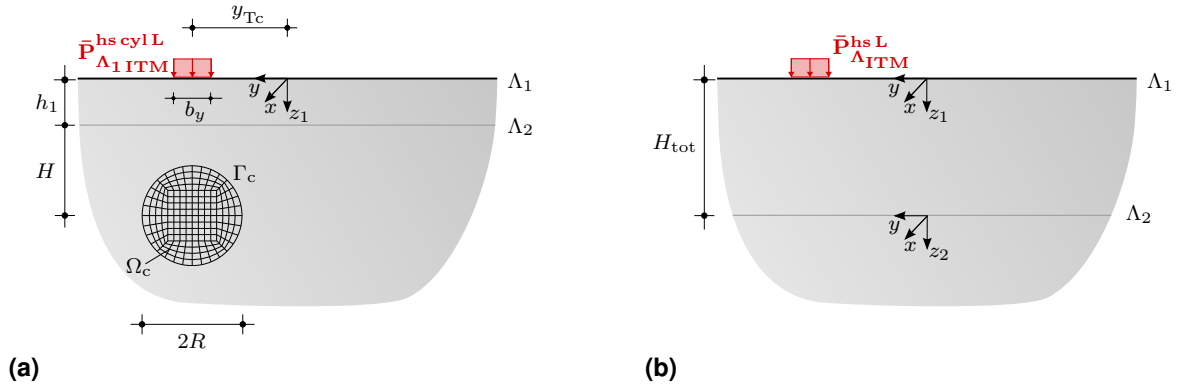

Figure 6.4: System setup for validation due to harmonic load at the soil surface: (a) Coupled ITM-FEM system layered halfspace with single cylindrical inclusion and (b) layered halfspace.

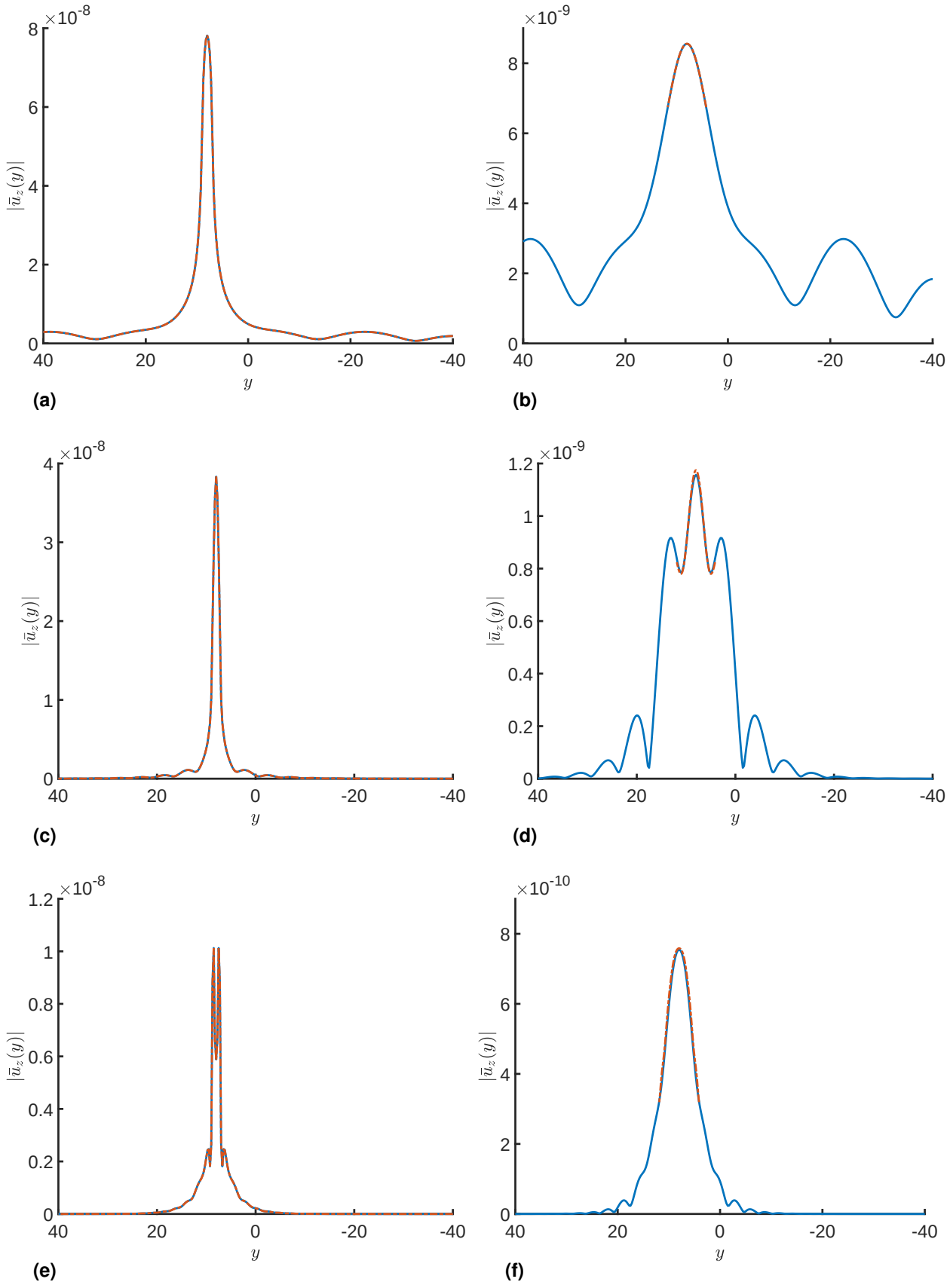

Figure 6.5: Vertical displacements $|\bar{u}_z(y)|$ at $x = 0$ for layered halfspace with inclusion (– –) and the layered halfspace (—) on the soil surface $z_1 = 0$ (left) and within the soil at $z_1 = H_{\text{tot}}$ (right) for (a),(b) $f = 2$ Hz, (c),(d) $f = 30$ Hz and (e),(f) $f = 60$ Hz for setup depicted in Fig. 6.4.

f (Hz)	z (m)	maximum value	maximum error	Tanimoto coefficient
2	0	$7.82 \cdot 10^{-8}$	$2.52 \cdot 10^{-11}$	1.00
2	H_{tot}	$8.55 \cdot 10^{-9}$	$4.56 \cdot 10^{-10}$	1.00
30	0	$3.83 \cdot 10^{-8}$	$3.39 \cdot 10^{-12}$	1.00
30	H_{tot}	$1.17 \cdot 10^{-9}$	$3.28 \cdot 10^{-12}$	1.00
60	0	$1.02 \cdot 10^{-8}$	$1.47 \cdot 10^{-11}$	0.99
60	H_{tot}	$7.58 \cdot 10^{-10}$	$1.07 \cdot 10^{-10}$	0.99

Table 6.3: Error measures for layered halfspace with single inclusion w.r.t. $|\bar{u}_z(y)|$.

Both systems of Fig. 6.4 are subjected to a square block load at the ground surface centred above the inclusion at $x = 0$. The corr. vertical displacements $|\bar{u}_z(y)|$ on the ground surface in the (x,y,ω) domain at $x = 0$ are presented in the left column of Fig. 6.5. Furthermore, the results within the soil at $z_1 = H_{\text{tot}}$ are depicted in the right column of Fig. 6.5, whereby for the layered halfspace with inclusion the results are only depicted along the center line of the FEM substructure. For all results a very good agreement between the coupled ITM-FEM approach and the semi-analytical solution of the layered halfspace can be observed. A quantitative comparison of the coupled approach and the layered halfspace at the ground surface and within the soil is presented in Tab. 6.3, where the maximum value, the maximum error as well as the Tanimoto coefficient refer to the absolute values $|\bar{u}_z(y)|$ at $x = 0$.

In addition, the results for both systems are compared due a square block load applied at depth H_{tot} inside the soil, as shown in Fig. 6.6. Embedment depth, layer thickness and inclusion size are chosen as before and the results for $|\bar{u}_z(y)|$ are presented analogously in Fig. 6.7. Also here a very good accordance between the proposed ITM-FEM approach and the reference solution can be stated.

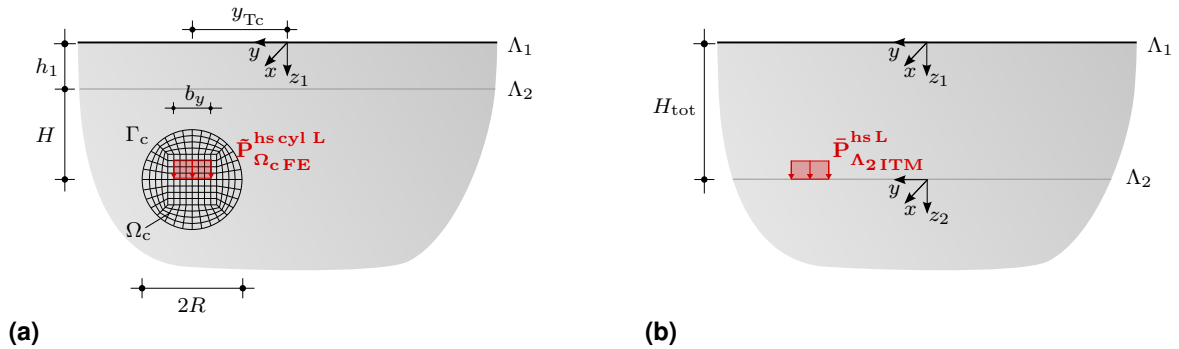

Figure 6.6: System setup for validation with harmonic excitation inside the soil: (a) Coupled ITM-FEM system layered halfspace with single cylindrical inclusion and (b) layered halfspace.

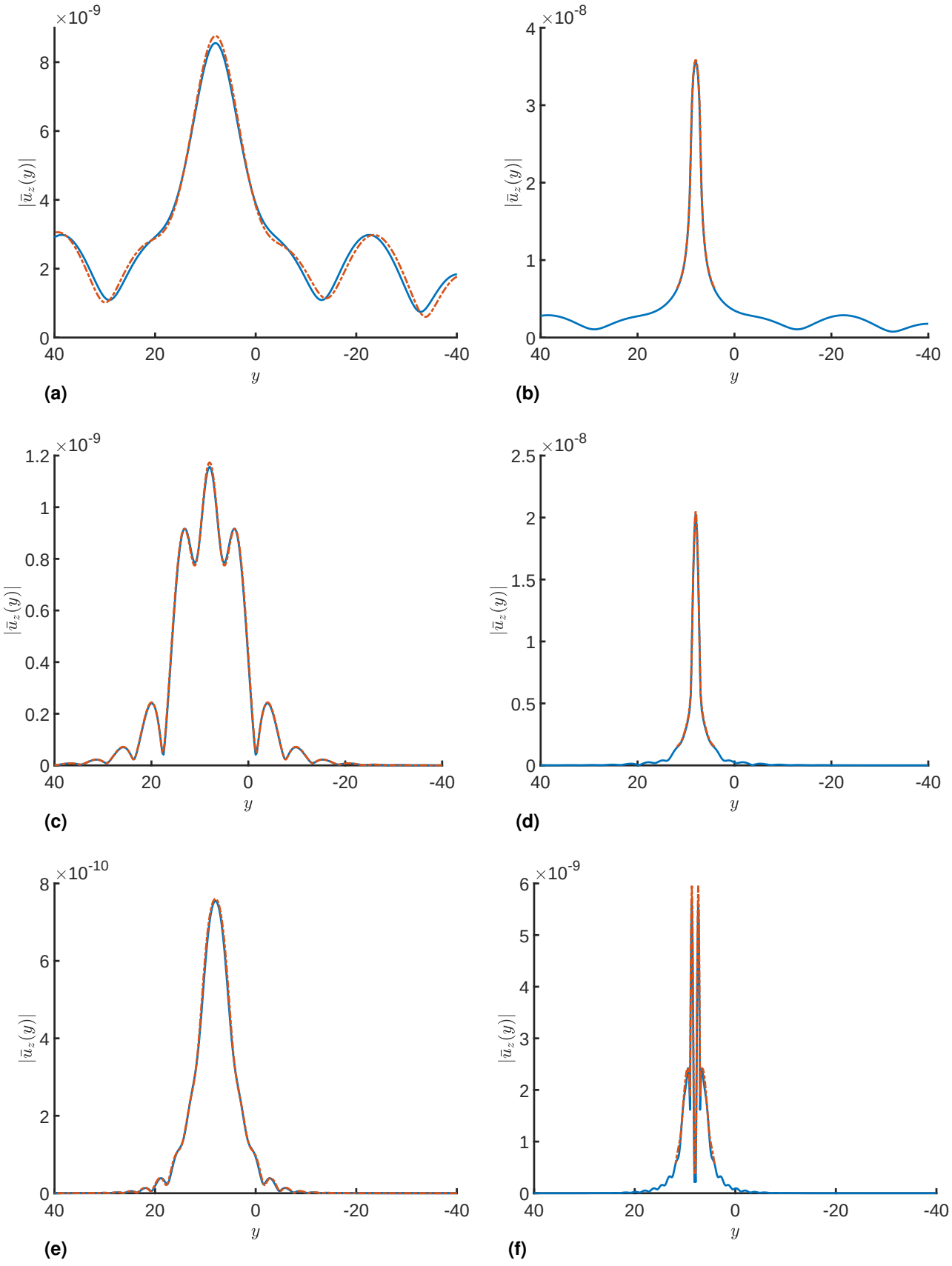

Figure 6.7: Vertical displacements $|\bar{u}_z(y)|$ at $x = 0$ for layered halfspace with inclusion (– –) and the layered halfspace (—) on the soil surface $z_1 = 0$ (left) and within the soil at $z_1 = H_{\text{tot}}$ (right) for (a),(b) $f = 2$ Hz, (c),(d) $f = 30$ Hz and (e),(f) $f = 60$ Hz for setup depicted in Fig. 6.6.

Two inclusions in homogeneous soil

Second, the dynamic response of a homogeneous halfspace with two parallel cylindrical inclusions, derived in Sec. 5.1 and depicted in Fig. 6.8a, is investigated. The inclusions are, with $y_{\mathrm{Tc}_1} = 8$ m and $y_{\mathrm{Tc}_2} = -8$ m, arranged symmetrically around the centre of the soil domain. The embedment depth is $H = 6$ m, so that a soil cover of $h_{\mathrm{cyl}} = 2$ m remains for an inclusion radius of $R = 4$ m.

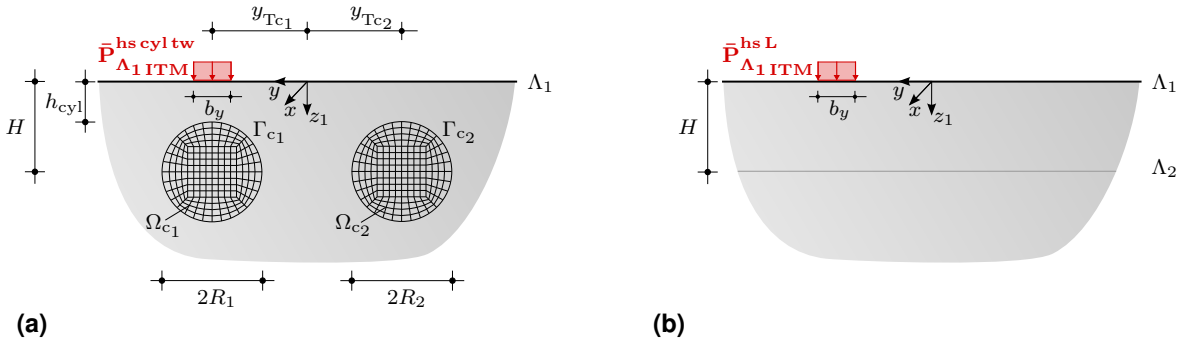

Figure 6.8: System setup for validation with harmonic load on the ground surface: (a) Coupled ITM-FEM system halfspace with two parallel cylindrical inclusions and (b) layered halfspace.

Analogous to the previous example, the vertical displacements $|\bar{u}_z(y)|$ along the $y-$axis at the surface and at depth $z = H$ inside the soil are evaluated due to the square block load at $z = 0$ centred over the inclusion T_1 at $y_{\mathrm{Tc}_1} = 8$ m and $x = 0$ and illustrated in Fig. 6.9. At $z = H$ the displacements of the coupled system are again only depicted on the center lines of the FEM domains Ω_{c_1} and Ω_{c_2}. The results of the ITM-FEM approach on the ground surface Λ_1 as well as inside the FEM substructures match nicely with the reference solution for all considered frequencies, proving that the interaction of the cavities through the soil works correctly and thus validating the superposition and coupling procedure for the halfspace with two cylindrical inclusions. The corresponding error measures are given in Tab. 6.4, showing a Tanimoto coefficient being almost consistently one.

f (Hz)	z (m)	maximum value	maximum error	Tanimoto coefficient
2	0	$7.82 \cdot 10^{-8}$	$2.63 \cdot 10^{-11}$	1.00
2	H	$1.20 \cdot 10^{-8}$	$3.21 \cdot 10^{-11}$	1.00
30	0	$3.84 \cdot 10^{-8}$	$2.44 \cdot 10^{-11}$	1.00
30	H	$2.50 \cdot 10^{-9}$	$3.84 \cdot 10^{-11}$	1.00
60	0	$1.01 \cdot 10^{-8}$	$2.71 \cdot 10^{-11}$	1.00
60	H	$1.37 \cdot 10^{-9}$	$5.91 \cdot 10^{-11}$	0.98

Table 6.4: Error measures for halfspace with two parallel inclusions w.r.t. $|\bar{u}_z(y)|$.

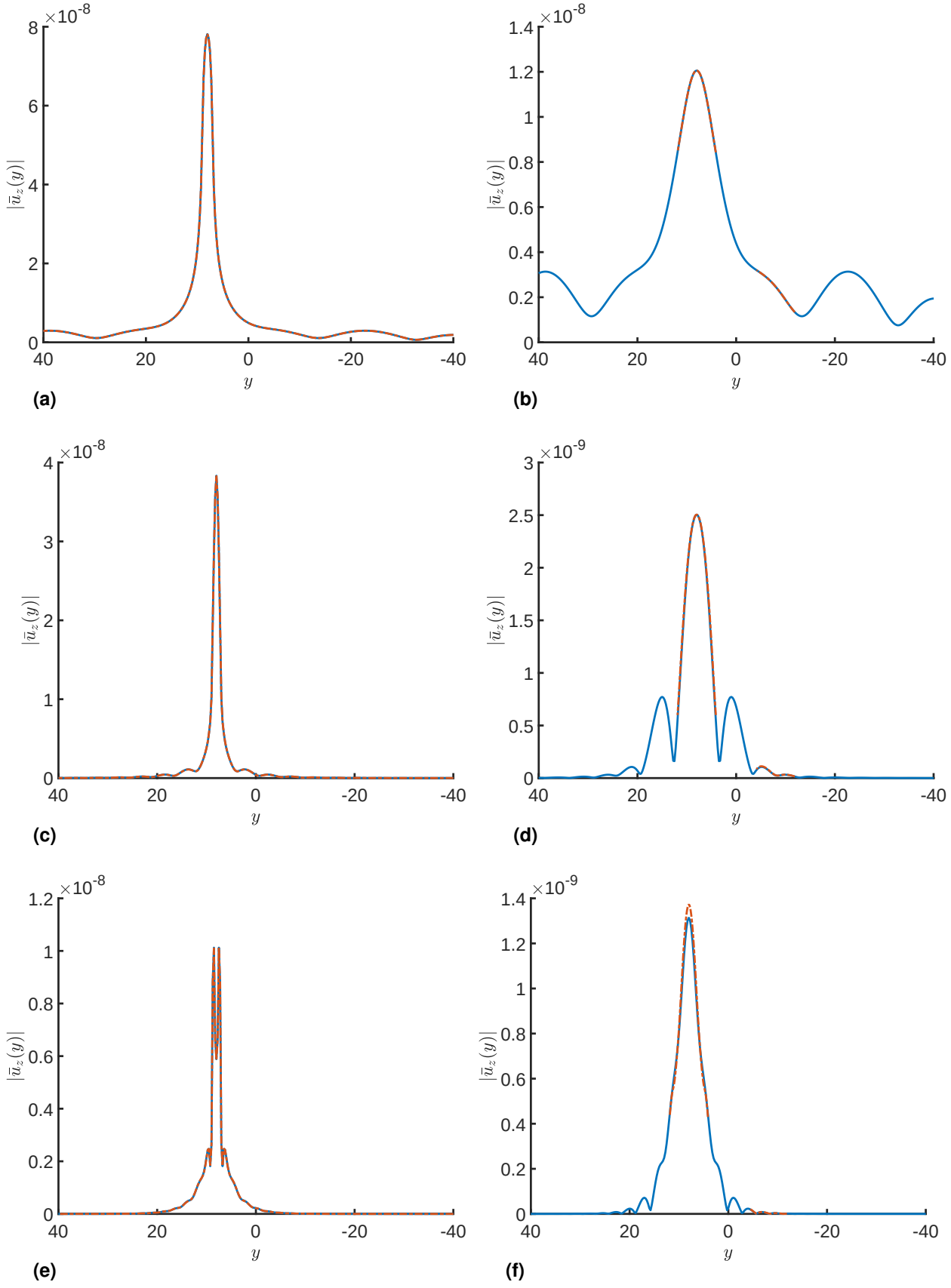

Figure 6.9: Vertical displacements $|\bar{u}_z(y)|$ at $x = 0$ for the halfspace with two parallel inclusions (– –) and the layered halfspace (—) on the soil surface $z_1 = 0$ (left) and within the soil at depth $z_1 = H_{\text{tot}}$ (right) at (a),(b) $f = 2$ Hz, (c),(d) $f = 30$ Hz and (e),(f) $f = 60$ Hz for setup depicted in Fig. 6.8.

Two indentations in homogenous soil

In order to validate the proposed approach also including the adaptations for the case of a halfspace with cylindrical indentations, described in Secs. 3.1 resp. 3.2 and 5.1, the system shown in Fig. 6.10a is investigated in the following.

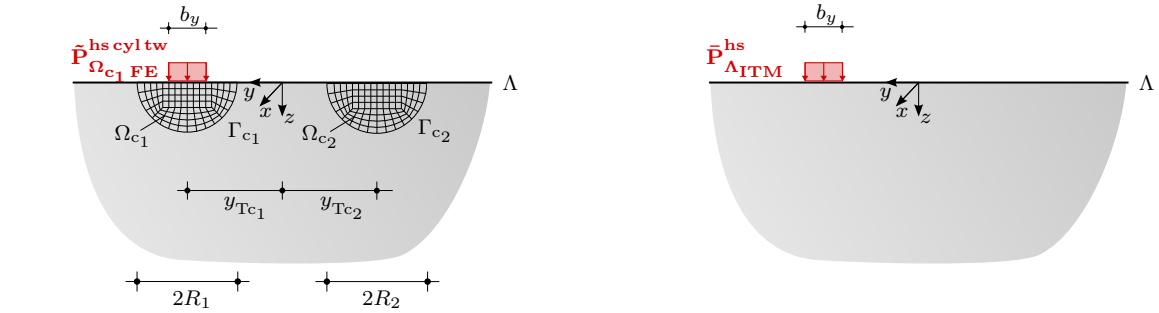

Figure 6.10: System setup for validation with harmonic load on the ground surface: (a) Coupled ITM-FEM system halfspace with two parallel cylindrical indentations and (b) layered halfspace.

The two parallel indentations have the same size R and are located at the same positions y_{Tc_1} and y_{Tc_2} as in the previous example, yet the embedment depth H is zero in the current case, so that exactly half of the cylinder lies within the soil. Again $N_\varphi = 64$ Fourier members along Γ_c are used, which now need to represent the discontinuity of stresses and displacements at the transition from below to above the ground surface in the series expansion along the complete cylindrical interaction surface necessary for the coupling. The total domain size $B_x = B_y$ is reduced to 64 m for $f = 60$ Hz, since due to the small wavelengths at higher frequencies the amplitudes decay much faster towards the edge. At the same time, this increases the discretization in the spatial domain and higher wavenumbers are taken into account (cp. Fig 3.7), contributing to a better representation of the shorter wavelengths.

The results for a square block load at the ground surface around the center of the FEM domain Ω_{c_1}, are illustrated in Fig. 6.11. Thereby, the left column shows $|\bar{u}_z(y)|$ on the ground surface along the $y-$axis at $x = 0$, while $|\bar{u}_z(x)|$ in the longitudinal direction of the cylinder at y_{Tc_1} is depicted in the right column. For $f = 2$ and 30 Hz, the results of the coupled system and the homogenous halfspace show very good accordance for both directions. This demonstrates clearly that the transmission of the vibrations from the FEM domain Ω_{c_1} into the ITM substructure and further into Ω_{c_2} is well represented in the model.

f (Hz)	z (m)	maximum value	maximum error	Tanimoto coefficient
2	0	$7.84 \cdot 10^{-8}$	$1.71 \cdot 10^{-9}$	0.99
30	0	$3.88 \cdot 10^{-8}$	$1.03 \cdot 10^{-10}$	0.99
60	0	$1.11 \cdot 10^{-8}$	$1.57 \cdot 10^{-9}$	0.85

Table 6.5: Error measures for halfspace with two parallel indentations w.r.t. $|\bar{u}_z(y)|$.

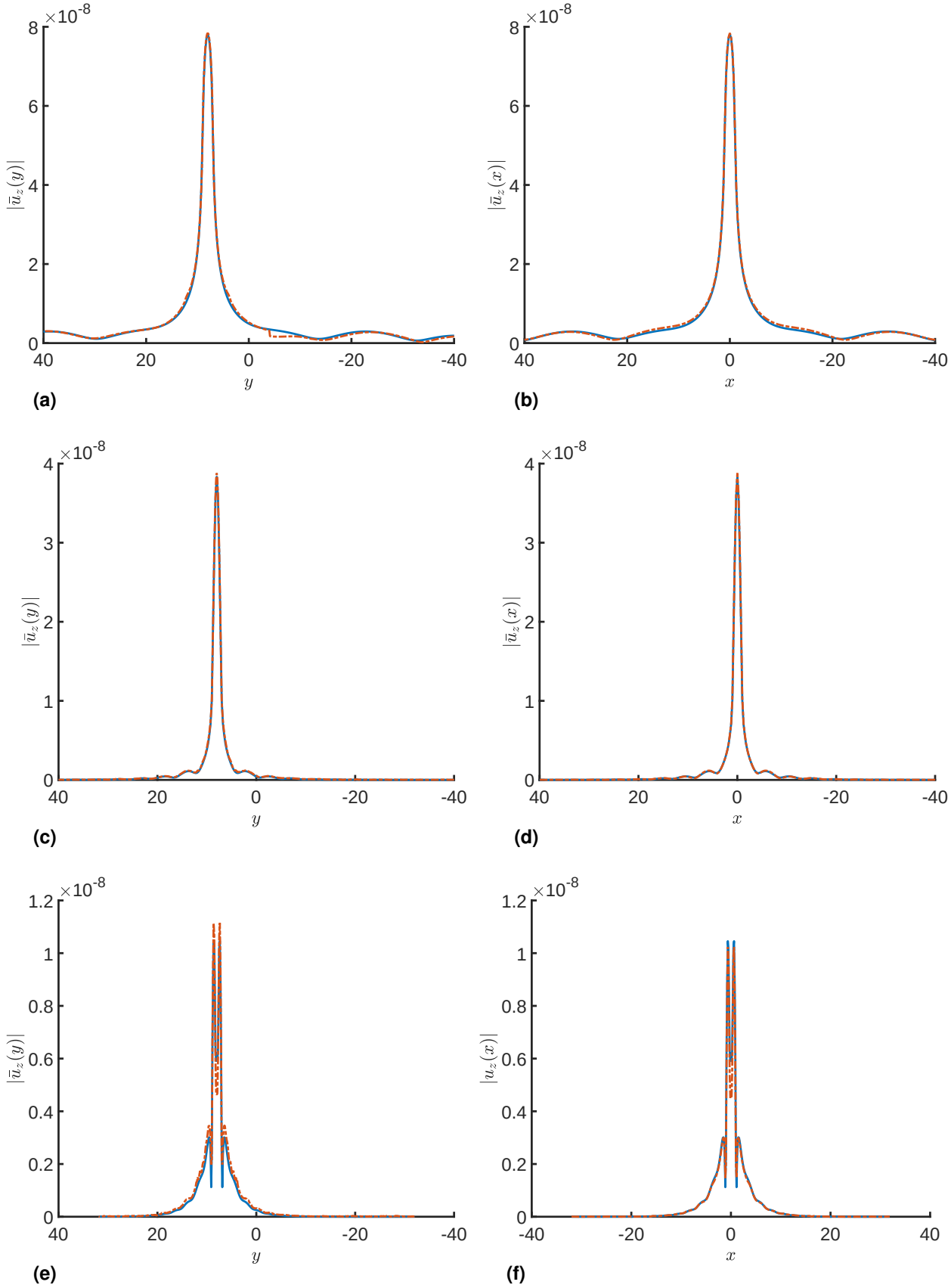

Figure 6.11: Vertical displacements $|\bar{u}_z(y)|$ at $x = 0$ (left) and $|\bar{u}_z(x)|$ at $y = y_{\mathrm{Tc}_1}$ (right) for the halfspace with parallel inclusions (– –) and the halfspace (—) on the soil surface at (a),(b) $f = 2$ Hz, (c),(d) $f = 30$ Hz and (e),(f) $f = 60$ Hz for the system setup depicted in Fig. 6.10.

For $f = 60$ Hz some deviations from the reference solution are visible, especially near the area of load application, indicating that the chosen discretization is not yet completely sufficient to maintain the high quality of the coupling and the solution. Thus, considering inclusions with large dimensions and investigating higher frequencies connected with small wavelengths, a refinement of the discretization is necessary. However, since this is always linked to a raising computational effort, a balance between computation time and an acceptable error needs to be found. Considering the Tanimoto coefficient for the computed solutions in Tab. 6.5, a quite good overall similarity of the results for the coupled approach and the semi-analytical reference solution can nevertheless be observed and thus the quality accepted as sufficient.

Response underneath a strip foundation

For the validation of the coupled ITM-FEM approach, also taking into account structures that extend over the soil surface and feature different material properties, a surface strip foundation depicted in Fig. 6.12 is investigated subsequently. The two limiting cases of a massless fully, flexible $E_f = 0$ and a massless, rigid foundation, represented by a very high Young's modulus $E_f = 3 \cdot 10^{15}$ Nm^{-2}, are considered. All other material parameters of the foundation are given in Tab. 6.2. The results are compared to those obtained in Radišić et al. [129], applying a coupled ITM-SEM approach. Therein the SSI problem is solved by coupling the mode shapes of a spectral Euler Bernoulli beam element with the modal dynamic stiffness of the soil applying the compatibility conditions at the soil foundation interface and carrying out a modal superposition approach.

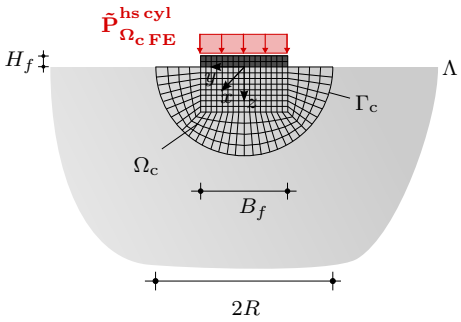

Figure 6.12: Strip foundation resting on a homogenous halfspace and subjected to uniform load.

A strip foundation with a width of $B_f = 1$ m and a height of $H_f = 0.2$ m, uniformly loaded with $|\tilde{\mathbf{P}}^{\mathbf{hs\,cyl}}_{\Omega_{\mathrm{c}}\,\mathrm{FE}}| = 10$ Nm^{-2} in the vertical direction and resting on a homogeneous halfspace, with the material of Soil 2 in Tab. 6.2 is considered. A total domain size of $B_x = B_y = 256$ m with $N_x = N_y = 2^{10}$ sample points resulting in an incremental distance of $\mathrm{d}x = \mathrm{d}y = 0.25$ m is chosen. The inclusion exhibits a radius of $R = 3$ m and $N_\varphi = 48$ sampling points are used

leading to nodal distance of $\mathrm{d}y_{\mathrm{FE}} = 0.125$ m and thus a sufficient refinement to properly model the elastic waves introduced at the load frequency of $f = 50$ Hz. The real and imaginary part of the vertical displacement $\bar{u}_z(y)$ for both limit cases are given in Fig. 6.13. The uniform displacement distribution under the rigid foundation turns out as expected, whereas no change in $\bar{u}_z(y)$ occurs compared to a direct loading of the soil for the flexible foundation. In general a very good agreement between the ITM-FEM and the ITM-SEM results can be observed.

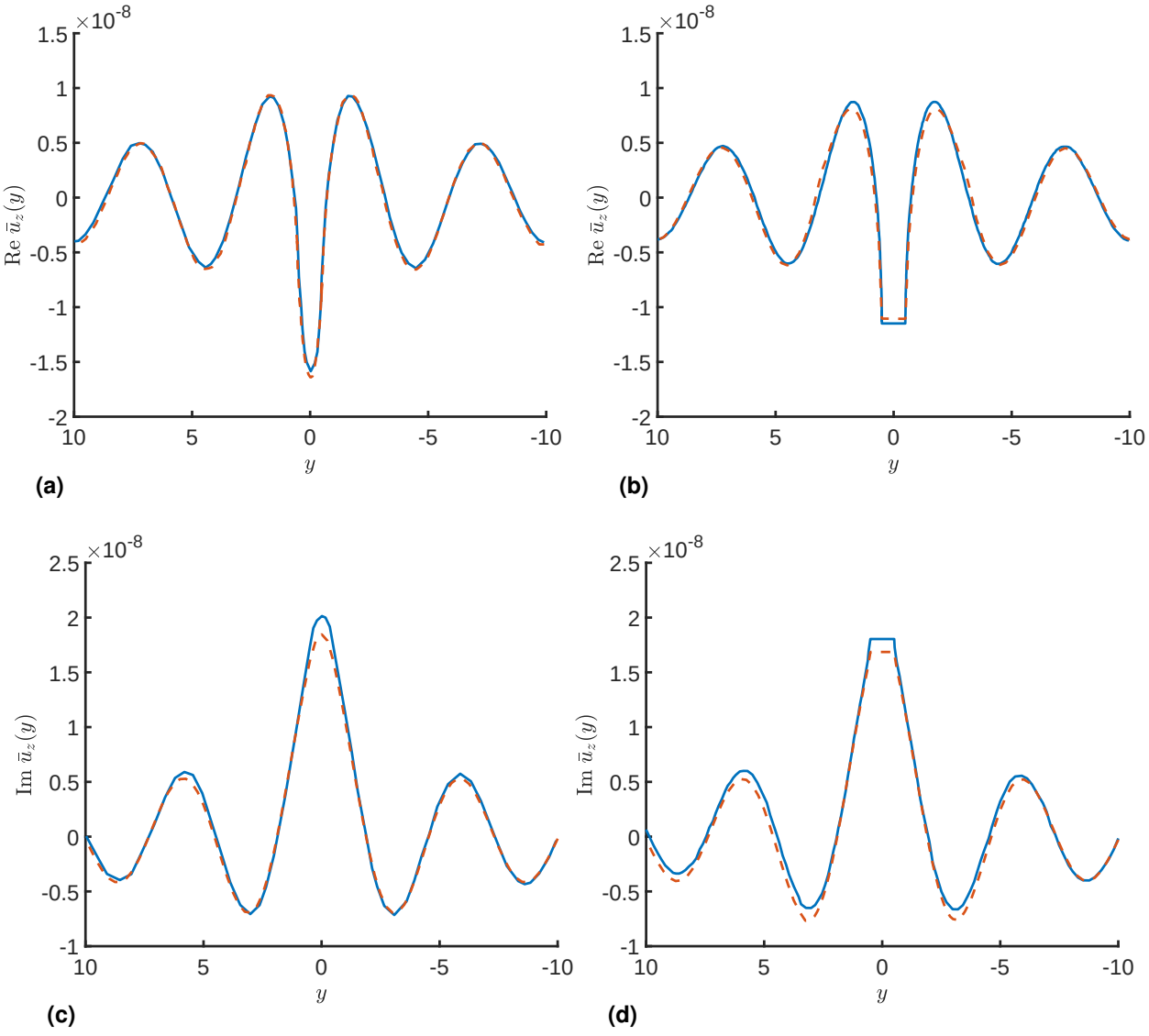

Figure 6.13: Real and imaginary part of $\bar{u}_z(y)$ at the surface of a homogenous halfspace due to the SSI of (a),(c) a completely flexible foundation and (b),(d) a rigid foundation for the ITM-FEM (– –) and the ITM-SEM approach (—).

6.1.3 Halfspace with spherical inclusion

Analogously to the halfspace with cylindrical inclusion, the superposition procedure for the halfspace with spherical cavity or indentation and the coupling of the latter with a matching FEM substructure is verified by comparison of the results to the semi-analytical solution of the homogeneous or layered halfspace. The material parameters of the soil, applied for the ITM and the FEM substructures, are given in Tab. 6.6.

	E_s (Nm^{-2})	ν_s $(-)$	ρ_s (kgm^{-3})	ζ_s $(-)$	c_p (ms^{-1})	c_s (ms^{-1})	c_r (ms^{-1})
Soil	$2.60 \cdot 10^8$	0.3	1600	0.05	468.29	250.31	232.21

Table 6.6: Soil properties for verification of halfspace with spherical inclusion or indentation.

Spherical enclosure

First, a spherical inclusion with radius $R = 2$ m is considered, which is completely buried within the soil and has a embedment depth of $H = 3$ m. The thickness of the upper layer H_{lat} of the benchmark system is equal to the depth of the nodes inside the FEM structure, positioned on the first latitude below the equator. A vertical, harmonic square block load with edge lengths $b_x = b_y = 2$ m and amplitude $|\bar{\mathbf{P}}^{\mathbf{hs\,sph}}_{\mathbf{\Lambda_{ITM}}}| = 1\ \mathrm{N\,m}^{-2}$ is applied to both systems on the ground surface, symmetrically distributed around the origin $x = y = 0$ with excitation frequencies 2, 30 and 60 Hz. [84]

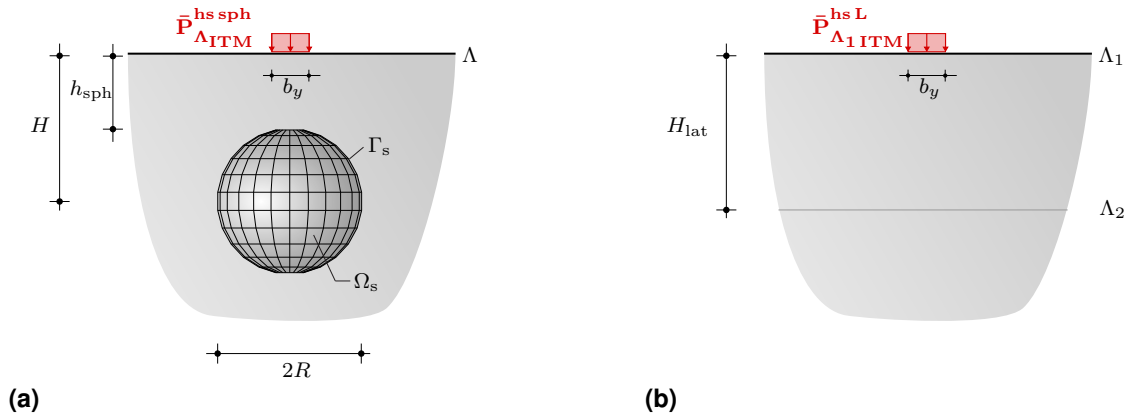

Figure 6.14: System setup for validation with harmonic load on the ground surface: (a) Coupled ITM-FEM system halfspace with spherical inclusion and (b) layered halfspace.

The dimensions B_x and B_y of the discretized domain and thus the increments $\mathrm{d}x$, $\mathrm{d}y$ in the ITM substructure were adapted to the Rayleigh wavelengths in dependency of the excitation frequencies as displayed in Tab. 6.7. Thereby an adequate representation of the elastic waves and the attenuation to the domain edges is guaranteed, while keeping the computational

f (Hz)	λ_p (m)	λ_s (m)	λ_r (m)	$B_x = B_y$ (m)	$N_x = N_y$	$\mathrm{d}x = \mathrm{d}y$ (m)
2	234.15	125.16	116.11	128	2^7	1.00
30	15.61	83.44	7.74	64	2^7	0.50
60	7.80	4.17	3.87	32	2^7	0.25

Table 6.7: Wave lengths and discretization parameters for given excitation frequencies.

effort solving the full 3D problem acceptable. The sphere was discretized using $N_\vartheta = 16$ latitudes and $N_\varphi = 32$ longitudes for all frequencies equally, leading to a maximum element size of $\mathrm{d}s_\vartheta = 0.48$ m and $\mathrm{d}s_\varphi = 0.39$ m in the FEM substructure. This correlates with approximately eight finite elements per Rayleigh wavelength λ_r along the center line of the sphere at the highest considered frequency $f = 60$ Hz. [84]

The results for the absolute value of the vertical displacement $|\bar{u}_z(y)|$ on the ground surface $z = 0$ and inside the soil at $z = H_{\mathrm{lat}}$ at $x = 0$ in the frequency domain (x,y,z,ω) are illustrated in Fig. 6.16 for both systems and show very good accordance. A quantitative comparison of $|\bar{u}_z(y)|$ on the ground surface is presented in Tab. 6.8.

f (Hz)	z (m)	maximum value	maximum error	Tanimoto coefficient
2	0	$5.88 \cdot 10^{-9}$	$6.78 \cdot 10^{-11}$	0.997
30	0	$4.54 \cdot 10^{-9}$	$1.24 \cdot 10^{-10}$	0.998
60	0	$3.79 \cdot 10^{-9}$	$1.26 \cdot 10^{-10}$	0.999

Table 6.8: Error measures for halfspace with spherical inclusion w.r.t. $|\bar{u}_z(y)|$ at $z = 0$.

In addition, the results of the coupled approach and the layered halfspace are compared for a load in the depth $z = H_{\mathrm{lat}}$ within the soil. Therefore, the ITM-FEM system is charged with nodal loads $\bar{\mathbf{P}}^{\mathbf{hs\,sph}}_{\boldsymbol{\Omega}_{\mathbf{s\,FE}}}$ inside the FEM domain. In the layered halfspace an equivalent load $\bar{\mathbf{P}}^{\mathbf{hs\,L}}_{\boldsymbol{\Lambda}_{\mathbf{2\,ITM}}}$ is applied at the layer interface as depicted in Fig. 6.15. Geometry, soil and load parameters are chosen analogously as before. The results for $|\bar{u}_z(y)|$ at $z = 0$ and $z = H_{\mathrm{lat}}$ are presented in Fig. 6.17, again exhibiting a very good agreement.

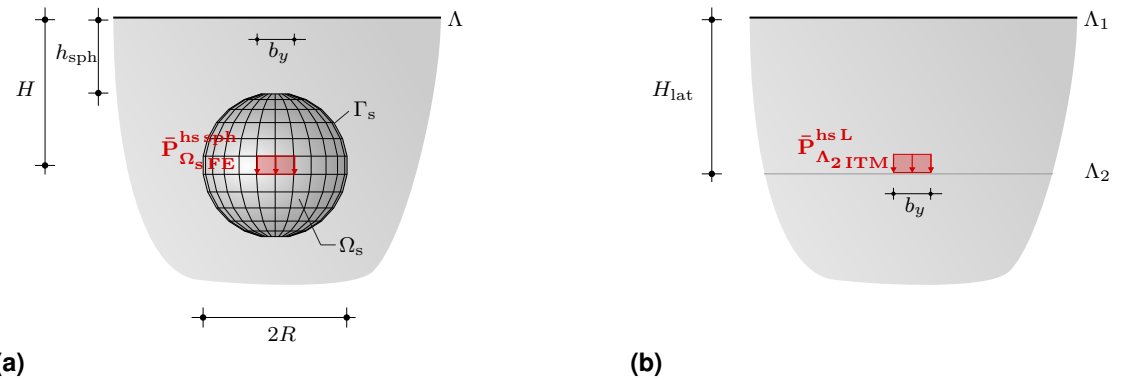

Figure 6.15: System setup for validation with harmonic load inside the ground: (a) Coupled ITM-FEM system halfspace with spherical inclusion and (b) layered halfspace.

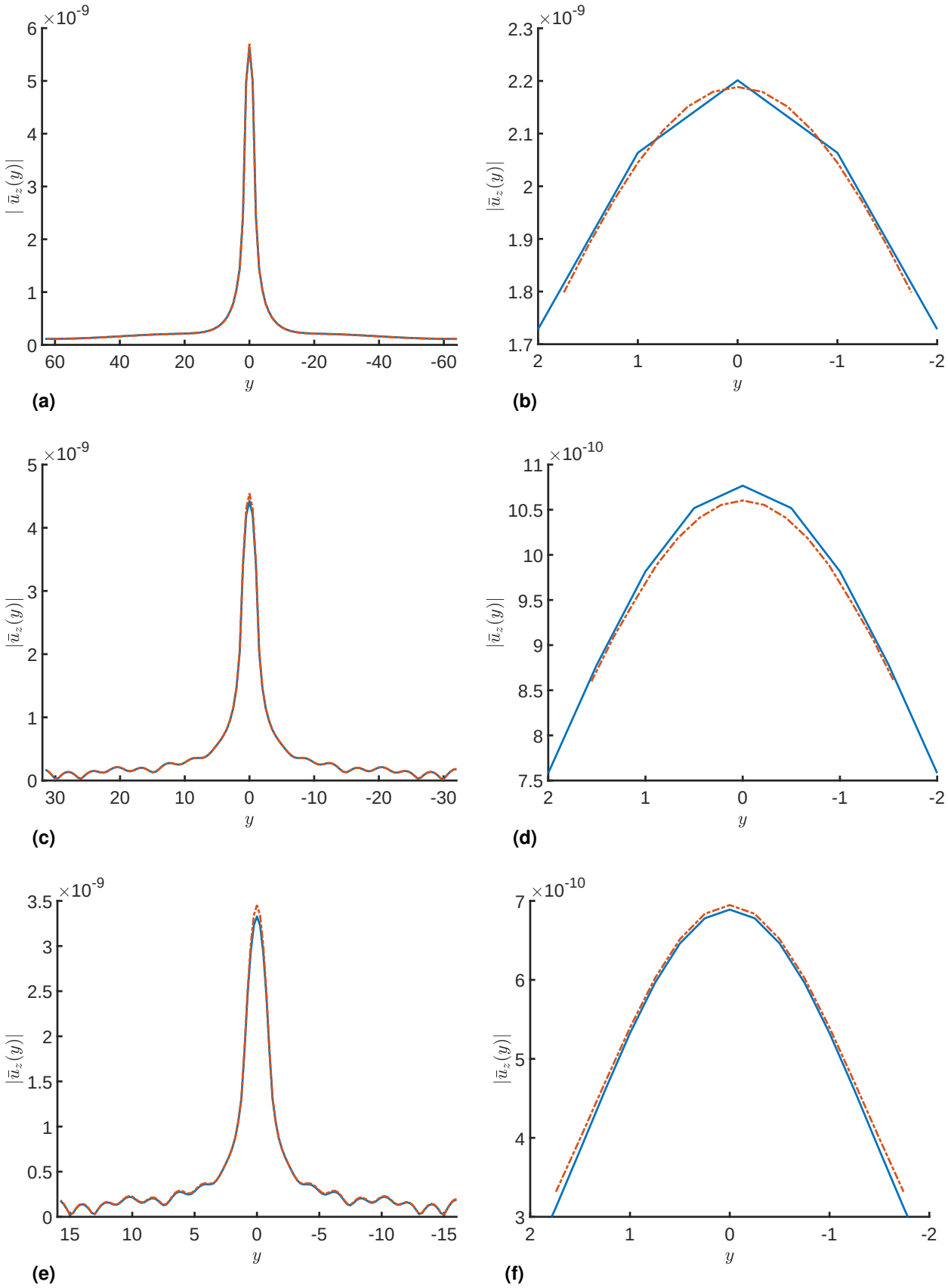

Figure 6.16: Vertical displacements $|\bar{u}_z(y)|$ at $x = 0$ for the halfspace with spherical inclusion (– –) and the layered halfspace (—) on the soil surface $z_1 = 0$ (left) and within the soil at $z_1 = H_{\text{lat}}$ (right) at (a),(b) $f = 2$ Hz, (c),(d) $f = 30$ Hz and (e),(f) $f = 60$ Hz for setup depicted in Fig. 6.14 with load on the ground surface.

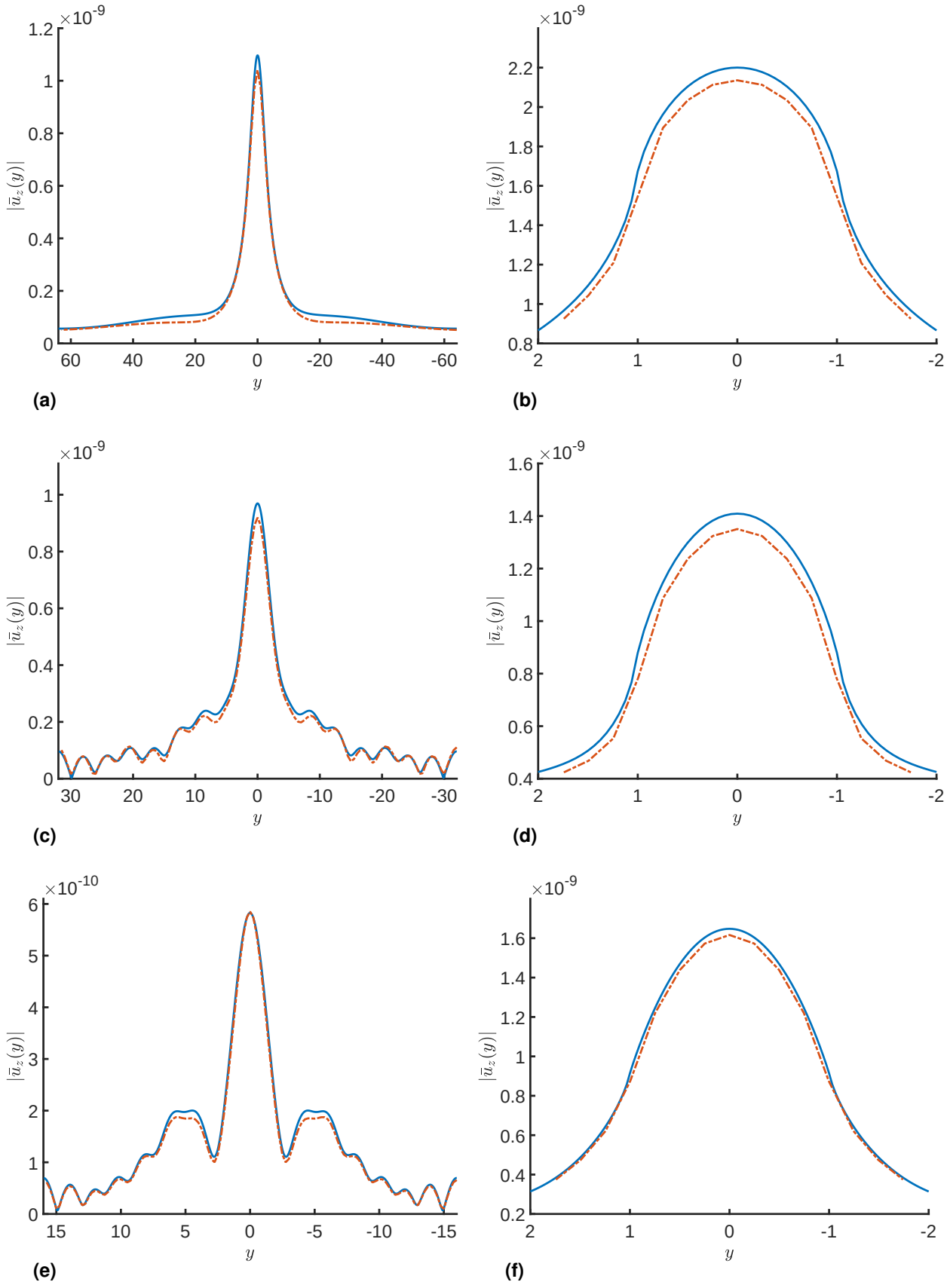

Figure 6.17: Vertical displacements $|\bar{u}_z(y)|$ at $x = 0$ for the halfspace with spherical inclusion (– –) and the layered halfspace (—) on the soil surface $z_1 = 0$ (left) and within the soil at $z_1 = H_{\text{lat}}$ (right) at (a),(b) $f = 2$ Hz, (c),(d) $f = 30$ Hz and (e),(f) $f = 60$ Hz for setup depicted in Fig. 6.15 with load inside the soil.

Spherical indentation

Hereinafter, the presented approach for the halfspace with spherical indentation (cp. Sec. 3.3.2 and 5.2) with a radius $R = 4$ m is validated by comparison of the results at the ground surface, with those of a corr. homogenous halfspace. Two load scenarios, depicted in Fig. 6.18, are considered with an unit square block load $b_x = b_y = 2$ m once with center at $(x,y) = (0, -10)$ besides the inclusion and once centred inside the inclusion Ω_s. The inclusion size and material are chosen as before. The FEM model is positioned such, that the largest latitude under the equator is aligned with the ground surface.

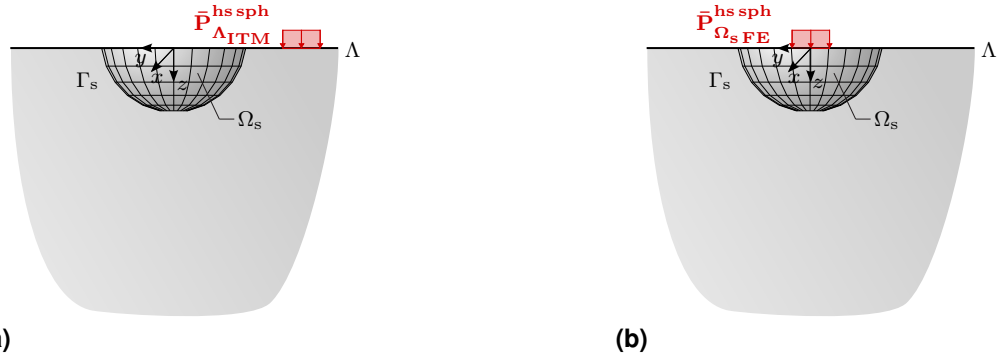

(a) **(b)**

Figure 6.18: Validation setup for the halfspace with spherical indentation, subjected to a harmonic load on the soil surface of (a) the ITM substructure and (b) the FEM substructure.

Firstly, a regular hexahedron mesh as illustrated in Fig. 6.20a and 6.20b is used. In order to represent the discontinuity in the distribution of the stresses and displacements along Γ_s at $z = 0$ sufficiently in the spherical harmonics expansion, which is needed for the superposition and the coupling, a higher number of series members is necessary for the indentation, as for the buried sphere, which shows a rather smooth distribution of the stresses and displacements over the complete spherical coupling surface.

Due to the non equidistant distribution of the Gauß points along the vertical axis of the sphere, required for the numerical integration of the spherical harmonics and getting denser when approaching to the poles, also the finite elements feature different size depending on their location. The elements close to the ground surface are also for high N_φ, N_ϑ rather large, whereas they get very small close to the lower pole. In the low frequency range this is not a problem and very good agreement can be achieved with the reference solution, as visible in Fig. 6.19a-d. However, at high frequencies, smaller element lengths are needed on the ground surface to cover the small wavelengths. This is due to the computational effort and the decreasing element quality close to the poles for increasing N_φ, N_ϑ not possible without limit and numerical errors occur, that manifest e.g. in the small ripples inside the area of the inclusion for $f = 60$ Hz in Fig. 6.19e. Therefore, the method provides good results, but its applicability is, for given inclusion size and soil material, limited to a certain frequency range. The maximum frequency to obtain rather accurate results can be estimated as $f_{\max} \approx c_s N_l/(32R)$ with $N_l \leq 48$ due to computational effort and element quality.

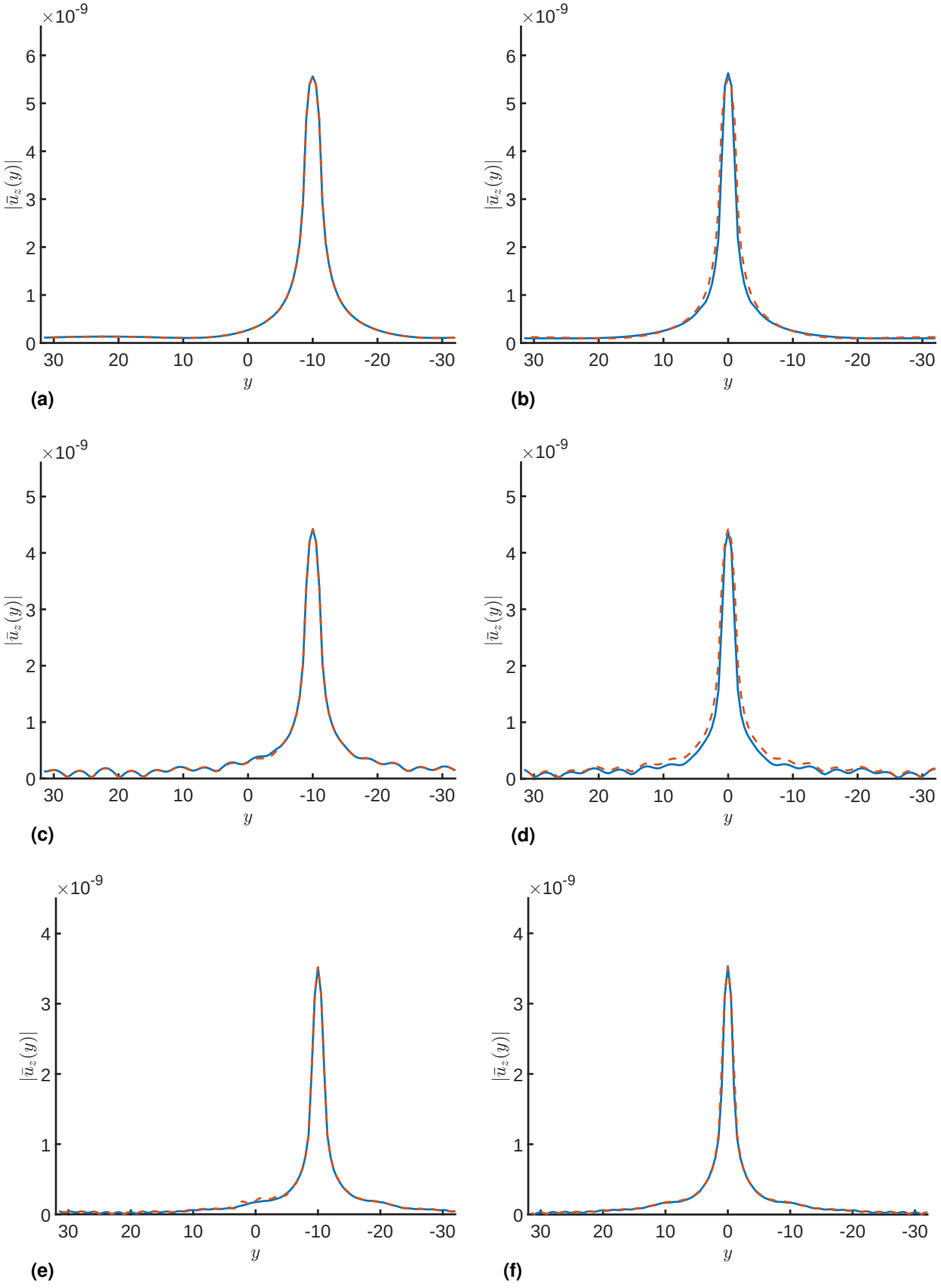

Figure 6.19: Vertical displacements $|\bar{u}_z(y)|$ at $x = 0$ for the halfspace with spherical indentation (– –) and the homogeneous halfspace (—) on the ground surface due to a load $\bar{\mathbf{P}}^{\mathbf{hs\,sph}}_{\mathbf{\Lambda_{ITM}}}$ at $y = -10$ m (left) and a load $\bar{\mathbf{P}}^{\mathbf{hs\,sph}}_{\mathbf{\Omega_{s\,FE}}}$ in the FEM domain (right) at (a),(b) $f = 2$ Hz, (c),(d) $f = 30$ Hz and (e),(f) $f = 60$ Hz for setup depicted in Fig. 6.18.

Response for different finite element meshes

As outlined in Sec. 4.2.1, alternatively to the regular FEM mesh, a free tetrahedron mesh depicted in Figs. 6.20c and 6.20d can be used. However, since the elements still have to match the discretization points on Γ_s, predefined by the ITM solution, the element size in the boundary layer is not free and the elements are rather large compared to the center of the indentation, also for high N_φ, N_ϑ. Thus the results of the fine free mesh do not show a considerable improvement compared to those for the coarse free mesh in Fig. 6.21. The agreement with the reference solution is worse than for the regular mesh. However, it has to be noted, that only a few points are directly located on the y-axis in case of the free mesh, which leads to a not entirely fair representation of the result quality when comparing $|\bar{u}_z(y)|$.

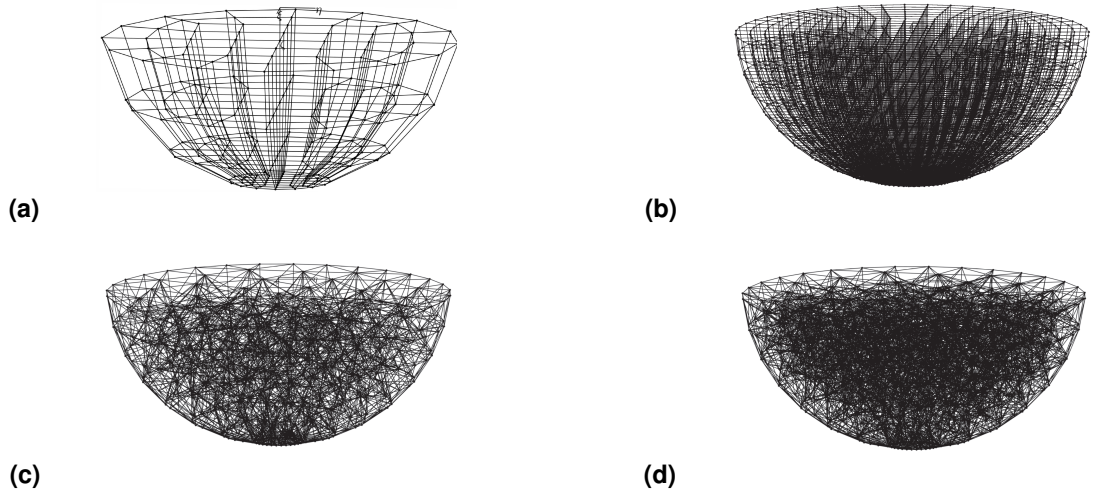

Figure 6.20: Finite element mesh of the spherical indentation with structured hexahedron elements with (a) four latitudes corr. to $N_\varphi = 16$ and (b) twelve latitudes corr. to $N_\varphi = 48$ as well as (c) coarse and (d) fine tetrahedron elements.

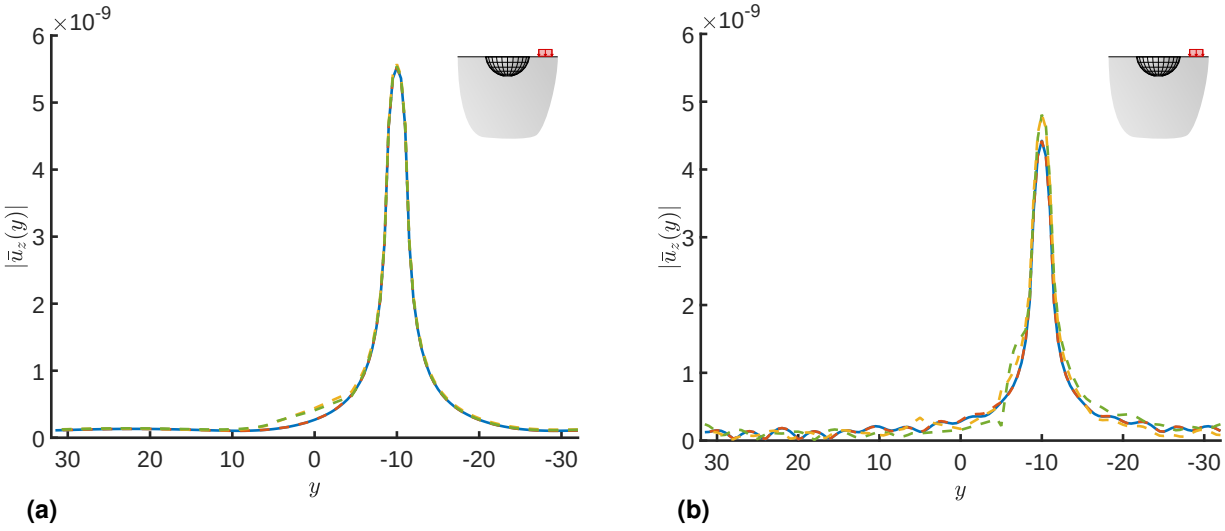

Figure 6.21: $|\bar{u}_z(y)|$ at $x = 0$ on the ground surface for a halfspace with spherical indentation with fine regular hexahedron FEM mesh (– –), free coarse (– –) and fine (– –) tetrahedron FEM mesh and homogeneous halfspace (—) at (a) $f = 2$ Hz and (b) $f = 30$ Hz for setup in Fig. 6.18a.

6.2 Vibration mitigation measures

In this section, the coupled ITM-FEM approach for the halfspace with cylindrical or spherical inclusions is applied to investigate the effectivity of different vibration mitigation measures by means of numerical simulations. For this purpose, the absolute values of the vertical displacements for a reference case $|\bar{u}_z^{\mathrm{ref}}|$ without the measure and the system including the measure $|\bar{u}_z|$ are set in relation by means of the amplitude reduction factor (A_r)

$$A_r(x,y,z,\omega) = \frac{|\bar{u}_z(x,y,z,\omega)|}{|\bar{u}_z^{\mathrm{ref}}(x,y,z,\omega)|} \tag{6.1}$$

or the insertion loss $\overline{\mathrm{IL}}_{\mathrm{z}}$ defined as

$$\overline{\mathrm{IL}}_z(x,y,z,\omega) = 20\log_{10}\frac{|\bar{u}_z^{\mathrm{ref}}(x,y,z,\omega)|}{|\bar{u}_z(x,y,z,\omega)|} \tag{6.2}$$

Thereby, for the amplitude reduction factor values of $A_r < 1$ correspond to a reduction of the vibrations compared to the reference case of $(1.0 - A_r) \cdot 100$ percent, whereas in case of the insertion loss, this is indicated by positive values of $\overline{\mathrm{IL}}_z$. The obtained results are compared to literature results for similar applications to underline the validity and accuracy of the proposed method.

6.2.1 Heavy masses next to the track

Firstly, the effectivity of heavy masses next to the track as mitigation measure in the transmission path to reduce railway induced ground vibrations is investigated. Therefore, a wall-like structure is erected in the immediate vicinity parallel to the track, which usually consist either of gabions or concrete blocks seamlessly lined up. In contrast to trenches, infilled barriers or wave impeding blocks, walls can additionally act as noise barrier and are beneficial since they require no modifications of the track.

The setup of the investigated problem as well as the dimensions are given in Fig. 6.22. The wall is placed on the ground surface at a distance $d_{\mathrm{gab}} = 4.0$ m from the centre of the track, which is located at $y = -2.5$ m. Within the 2.5D ITM-FEM approach, the gabions are modelled as a continuous wall with height h_{gab} and width b_{gab} using equivalent elastic parameters. Therefore, although in practise the gabions are usually only placed next to each other and thus are just loosely connected, within the coupled approach the longitudinal stiffness of the wall is considered fully and a wave propagation within the wall in lengthwise direction is possible. Gabion walls usually act mainly as an additional mass on the ground surface as their rigidity is in the same order of magnitude as typical soils. For comparably stiff

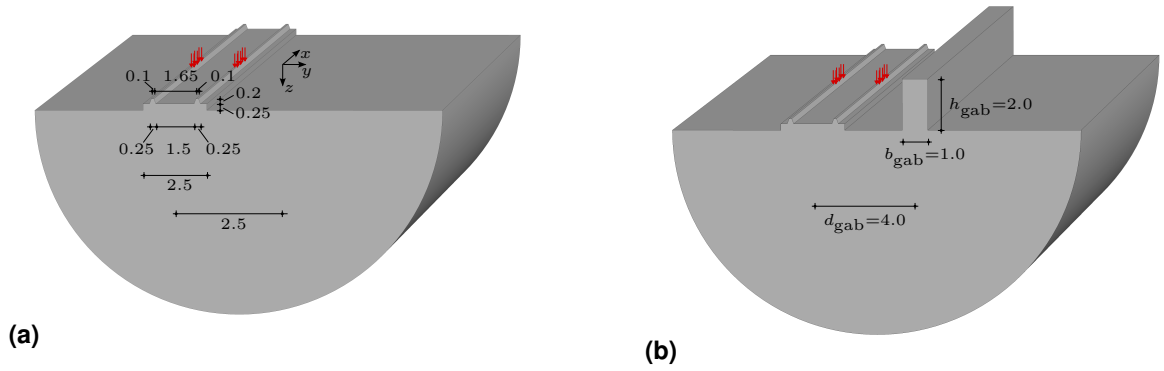

Figure 6.22: (a) Reference system and (b) system with gabion wall for the assessment of the effectiveness of heavy masses next to the track as vibration mitigation measure (all dimensions in m).

walls also the dimensions play an important role for the vibration mitigation. In the model, the rails are also monolithically connected to the track bed as well as designed continuously over the entire length and not connected segmentally or mounted elastically on the track bed, as it is often the case in practice. The material parameters for the soil, the track and the gabion are given in Tab. 6.9.

	E_s (Nm^{-2})	ν_s $(-)$	ρ_s (kgm^{-3})	ζ_s $(-)$	c_p (ms^{-1})	c_s (ms^{-1})	c_r (ms^{-1})
Soil	$2.60 \cdot 10^8$	0.30	2000	0.050	418.85	223.89	207.70
Sleeper	$3.70 \cdot 10^{10}$	0.20	2500	0.020	4056.00	2483.80	
Rail	$2.10 \cdot 10^{11}$	0.20	7850	0.001	6001.00	3207.70	
Gabion	$3.67 \cdot 10^8$	0.20	1700	0.020	490.00	300.06	

Table 6.9: Material properties for heavy masses next to the track.

Both systems in Fig. 6.22 are subjected to harmonic point loads on the top nodes of the rail over a length $b_x = 1$ m arranged symmetrically around $x = 0$. The system response is computed for load frequencies between $f = 2$ and 100 Hz in steps of $\Delta f = 2$ Hz. A total domain size of $B_x = B_y = 128$ m with $N_x = N_y = 2^9$ sample points is chosen for the lower frequency range, to hold the aliasing error small. For frequencies above $f = 30$ Hz, the total domain size is reduced to $B_x = B_y = 64$ m to ensure a sufficient resolution of the elastic waves. The inclusion size is chosen to $R = 8$ m with $N_\varphi = 64$ discretization points along Γ_c for all f, as $\mathrm{d}y_\mathrm{FE} = 0.25$ m leads to approx. ten elements per λ_r, also at the highest considered frequency.

Fig. 6.23 shows the insertion loss of the vertical displacements at two different locations $y = 5.5$ m and 13.5 m at $x = 0$ behind the wall over the frequency. In order to avoid that local variations in the insertion loss are overestimated, when evaluating $\overline{\mathrm{IL}}_z$ at a single position over f, the average of the levels within a range of 2 m around the evaluation point is computed. Below 30 Hz the gabion wall has only a very little effect on the transmission of the vibrations, except the peak in the insertion loss at 12 Hz, which can be attributed to

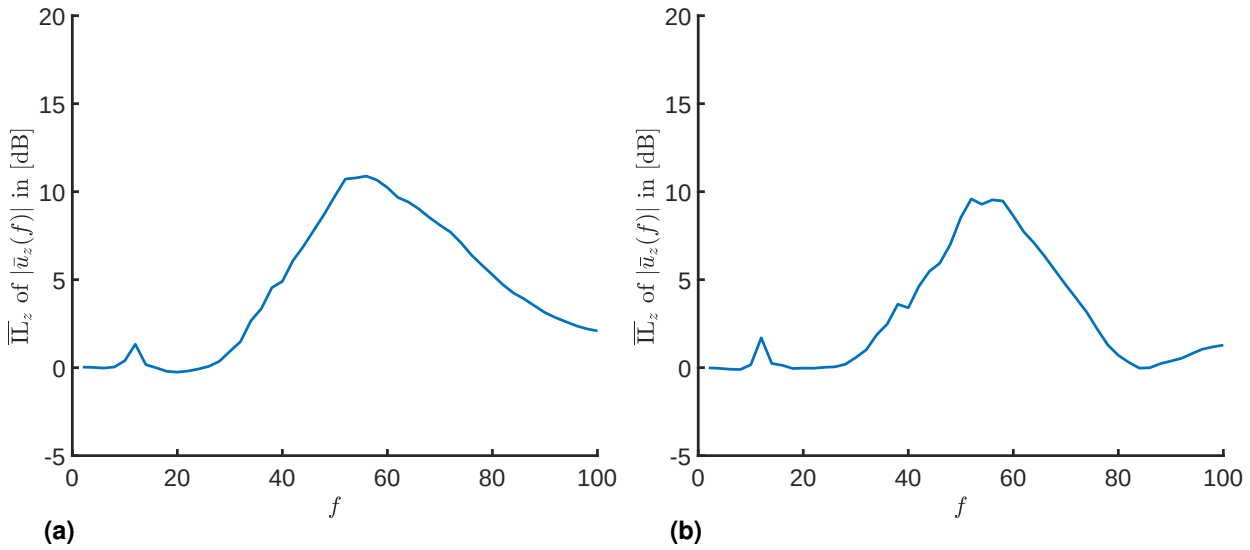

Figure 6.23: Averaged insertion loss of vertical displacements on ground surface due to the gabion wall for (a) $y = 5.5$ m and (b) $y = 13.5$ m at $x = 0$ over frequency.

the rocking mode of the wall as given in [183]

$$\omega_{0,\varphi_x} = \sqrt{\bar{K}^s_{\varphi_x\varphi_x}(\omega)/I_{\varphi_x}} \quad \text{with} \quad I_{0,\varphi_x} = \rho_{\mathrm{gab}} \left(\frac{\bar{u}_z h^3_{\mathrm{gab}}}{3} - \frac{h_{\mathrm{gab}} \bar{u}^3_z}{12} \right) \tag{6.3}$$

whereby $\bar{K}^s_{\varphi_x\varphi_x}$ is the rotational dynamic stiffness of the soil under a rigid structure and I_{0,φ_x} the mass moment of inertia of the rigid wall around the central axis at the ground surface. The peak value of $\overline{\mathrm{IL}}_z$ is observed around 60 Hz with 11 dB, whereas for higher frequencies the insertion loss decreases again. Furthermore, the insertion loss turns out to be rather independent of the distance behind the wall. The results at $y = 5.5$ m and 13.5 m show good qualitative agreement with the those obtained by Dijckmans et al. [183] for a similar system setup, however, with slightly different soil parameters and without the track model.

The distribution of the insertion loss over the soil surface for a case, in which the wall has almost no influence on the vibration propagation and the case of a maximum effect of the gabion wall are shown in Fig. 6.24. The gabion wall starts to act as an effective measure above the mass spring resonance frequency

$$\omega_{0,z} = \sqrt{\bar{K}^s_{zz}(\omega)/m_{\mathrm{gab}}} \tag{6.4}$$

resulting from the vertical dynamic stiffness of the soil under the wall $\bar{K}^s_{zz}(\omega)$, estimated from a rigid strip foundation, and its mass m_{gab} [289]. If the gabion wall is considered as a pure line mass with $m_{\mathrm{gab}} = 3400\ \mathrm{kg\,m^{-1}}$, the resonance frequency would result to ca. 30 Hz

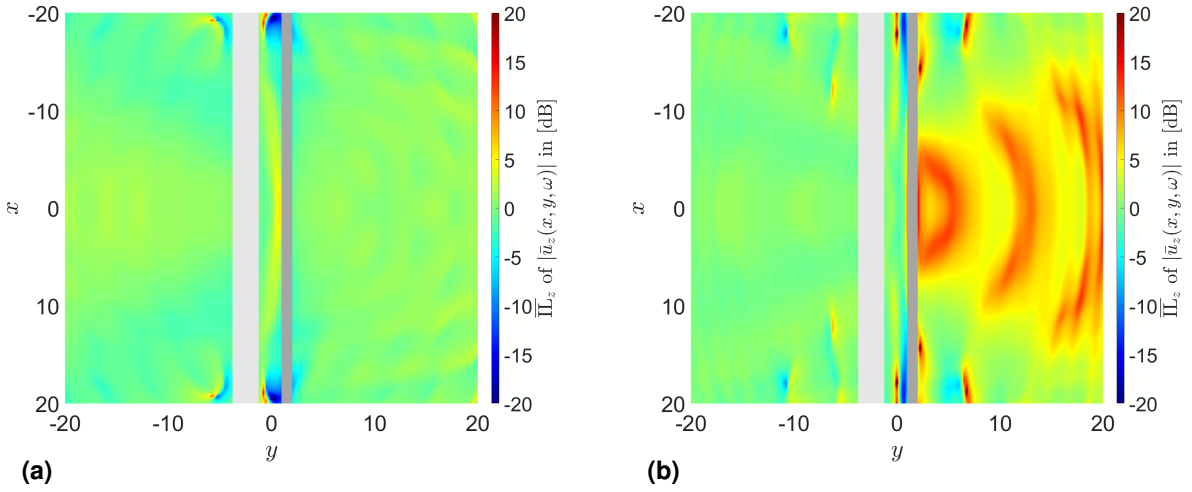

Figure 6.24: Insertion loss $\overline{\mathrm{IL}}_z$ of $|u_z(x,y,\omega)|$ due to the gabion wall at (a) $f = 30$ Hz and (b) $f = 60$ Hz.

[183]. Due to the reflection and scattering of the incident waves at the gabion wall, as well as its relative motion with respect to the soil, destructive interference occurs between the direct and secondary wave fields when these are out of phase, resulting in reduced vibration levels behind the wall around the resonance frequency [184, 290].

Since the considered gabion wall has finite dimensions, which cannot be neglected over the entire frequency range, the resonance frequency in Fig. 6.23 is shifted towards higher frequencies compared to the line mass model. Furthermore, the resonance peak is less pronounced due to the higher radiation damping, resulting from the broader footprint. A considerable insertion loss can also be observed at frequencies above the resonance, which can be attributed to the restriction of the ground surface movement and the impediment of the Rayleigh wave propagation, in case the footprint is large compared to λ_r and the stiffness of the wall is sufficiently high [184]. This effect is clearly visible in Figs. 6.25 and 6.26, comparing the real part of vertical surface displacements for both cases at $f = 60$ Hz.

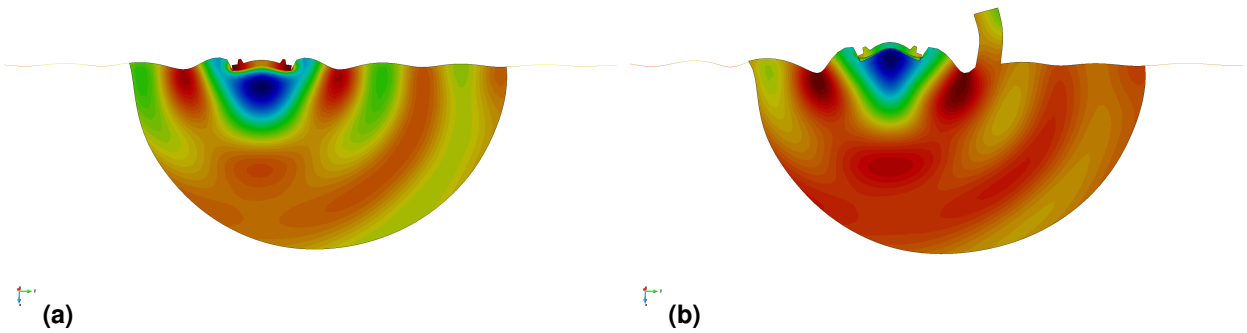

Figure 6.25: Real part of the vertical displacements in a cross section at $x = 0$ due to a harmonic load with $f = 60$ Hz for (a) the reference system and (b) the system with the gabion wall.

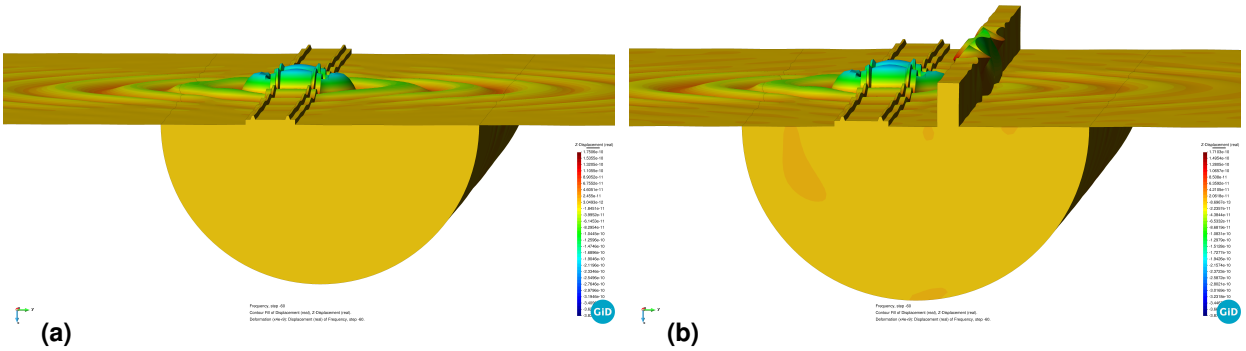

Figure 6.26: Real part of the vertical displacements of the three-dimensional system due to a harmonic load with $f = 60$ Hz for (a) the reference system and (b) the system with the gabion wall.

Further investigations by means of a parametric study presented in [291] underline that in order to achieve a good performance of the wall, especially at higher frequencies, rather heavy and stiff walls with a large footprint should be used. Moreover, in general better effectiveness is reached if the stiffness contrast between the wall and the soil is large. In this case also the longitudinal stiffness of the wall leads to an additional wave impeding effect, since then the wall acts as a stiff wave barrier, hindering the transmission of Rayleigh waves above the critical frequency, when the bending wave length in the wall is equal to the Rayleigh wave length in the soil (cp. Sec. 6.2.2) [179, 183].

6.2.2 Infilled barriers and open trench

In the following section, numerical results for length invariant open trenches and infilled barriers are shown, as presented in Freisinger and Müller [176]: "Coupled ITM-FEM approach for the assessment of the mitigation efficiency of finite and infinite open". Firstly the results gained with the proposed methodology for a concrete filled trench are compared with those available in published literature. Second, the effect of subgrade stiffening as a wave impeding barrier is shown, followed by a comparison of the mitigation efficiency and the operating mechanism of open trenches and soft or stiff barriers.

Concrete filled trench

In this example the Rayleigh wave diffraction by a rectangular trench in the transmission path, infilled with concrete and depicted in Fig. 6.27a, is investigated. The results are compared with those obtained by Haupt [171], applying the finite element method, and Beskos et al. [173] with a constant element based BEM implementation. As the literature

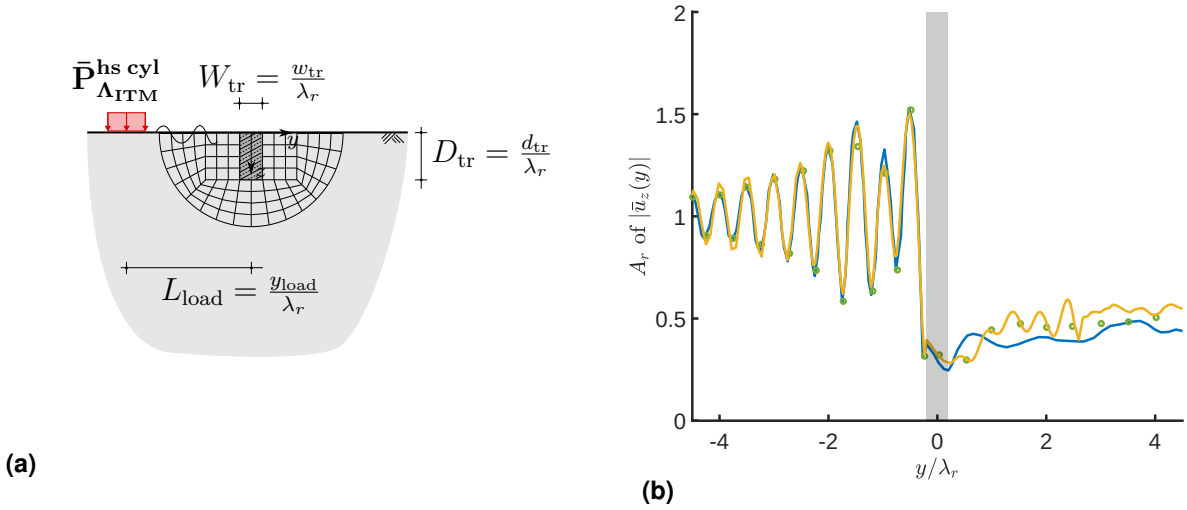

Figure 6.27: (a) ITM-FEM model for concrete filled trench in transmission path. (b) Comparison of ITM-FEM results (—) for amplitude reduction factor A_r of the vertical displacement $|\bar{u}_z|$ with BEM solution of Beskos et al. [173] (—) and FEM solution of Haupt [171] (○). [176]

results were calculated for a 2D case, the ITM-FEM solution is computed only for the wavenumber $k_x = 0$, which means constant conditions in the longitudinal direction x. [176]

A vertical harmonic load with amplitude $|\bar{\mathbf{P}}^{\text{hs cyl}}_{\mathbf{\Lambda}_{\text{ITM}}}| = 1\ \text{N m}^{-2}$ and a width of $b_y = 2$ m is applied at a distance of $y_{\text{load}} = -16$ m from the trench with a frequency of $f = 30$ Hz resulting in a Rayleigh wavelength of $\lambda_r = 3.18$ m. The width and depth of the barrier were chosen to $w_{\text{tr}} = 1.25$ m and $d_{\text{tr}} = 3.25$ m, prescribed by the FE discretization. Therefore the normalized dimensions result to $W_{\text{tr}} = 0.39$, $D_{\text{tr}} = 1.02$ and $L_{\text{load}} = 5.03$, which almost coincide with the dimensions used in [171, 173]. The further discretization and geometry parameters are given in Tab. 6.10 as well as the material parameters of the soil (Soil B) and the concrete filling (Infill A) in Table 6.11. [176]

	$N_x = N_y$	$B_x = B_y$	N_φ	R	$\text{d}x = \text{d}y = \text{d}x_{\text{FE}}$	$\text{d}y_{\text{FE}}$
Concrete filled trench	2^9	128	128	8	0.25	0.125
Subgrade stiffening	2^9	128	96	8	0.25	0.333
Comp. soft-stiff-open	2^8	64	192	8	0.25	0.166

Table 6.10: Discretization and geometry parameter for coupled ITM-FEM approach.

In Fig. 6.27b the amplitude reduction factor A_r for the absolute value of the vertical displacement $|\bar{u}_z(y)|$ in the (x,y,z,ω) domain on the halfspace surface is shown at $x = 0$ over the dimensionless distance y/λ_r. Significant amplifications are observed in front of the trench, caused by the constructive or destructive interference of the incident and reflected Rayleigh

	E $(\mathrm{Nm^{-2}})$	ν $(-)$	ρ $(\mathrm{kgm^{-3}})$	ζ $(-)$	c_p $(\mathrm{ms^{-1}})$	c_s $(\mathrm{ms^{-1}})$	c_r $(\mathrm{ms^{-1}})$
Soil A	$26.00 \cdot 10^6$	0.30	2000	0.05	132.5	70.8	65.7
Soil B	$46.12 \cdot 10^6$	0.25	1720	0.03	179.5	103.6	95.3
Soil C	$21.60 \cdot 10^7$	0.33	2000	0.05	400.5	201.7	188.0
Infill A	$15.81 \cdot 10^8$	0.25	2356	0.05	914.6	528.1	
Infill B	$15.12 \cdot 10^8$	0.248	2000	0.025	950.7	550.3	
Infill C	$30.00 \cdot 10^9$	0.2	2600	0.01	3580.5	2192.6	
Infill D	$25.00 \cdot 10^4$	0.4	700	0.05	27.6	11.3	

Table 6.11: Material parameters of different soils and infill materials

waves due to their phase difference [175], which is indicated by the peak distances being very close to $\lambda_r/2$. On the load remote site, a substantial amplitude reduction due to the concrete barrier of $50 - 70\%$ is achieved. A very good agreement between the literature results and the ITM-FEM approach can be stated. [176]

Subgrade stiffening as wave impeding barrier

In the following, the coupled approach is used to investigate the efficiency of subgrade stiffening as mitigation measure for ground borne vibrations in the transmission path. A block of stiffened soil (Infill B) with a width and depth of $w_{\mathrm{tr}} = d_{\mathrm{tr}} = 2$ m, located within a homogeneous halfspace (Soil C), is investigated as illustrated in Fig. 6.28a. The discretization parameters are given in Tab. 6.10, whereas the material parameters for the surrounding and the stiffened soil are presented in Tab. 6.11. A quadratic, harmonic block load with $|\bar{\mathbf{P}}^{\mathbf{hs\ cyl}}_{\mathbf{\Lambda_{ITM}}}| = 1\ \mathrm{N\,m^{-2}}$ and a width of $b_x = b_y = 1$ m is applied at a distance of $y_{\mathrm{load}} = -6$ m from the barrier. The insertion loss $\overline{\mathrm{IL}}_z$ and the vertical displacements over the total surface are evaluated for the reference case $|\bar{u}_z^{\mathrm{ref}}|$ without and the situation in presence of subgrade stiffening $|\bar{u}_z|$. [176]

Coulier et al. [179] showed by an investigation of the insertion loss due to subgrade stiffening next to a railway track in the wavenumber-frequency domain by means of a 2.5D FEM-BEM methodology, that the block of stiffened soil can act as a wave impeding barrier. Considering the stiffened block as an infinitely long beam, it was demonstrated that the wave impeding effect depends strongly on the trace wavelength of the Rayleigh wave in the soil in longitudinal direction λ_x and the free bending wave length in the beam λ_b. [176]

Fig. 6.28b shows a schematic sketch of the insertion loss $\overline{\mathrm{IL}}_z(\bar{k}_x, y, z = 0, \omega)$ over the dimensionless wavenumber $\bar{k}_x = k_x c_s/\omega$ and the frequency f as presented in [179]. A high insertion loss for the free field response behind the barrier is obtained for wavenumbers $\bar{k}_x$ smaller than

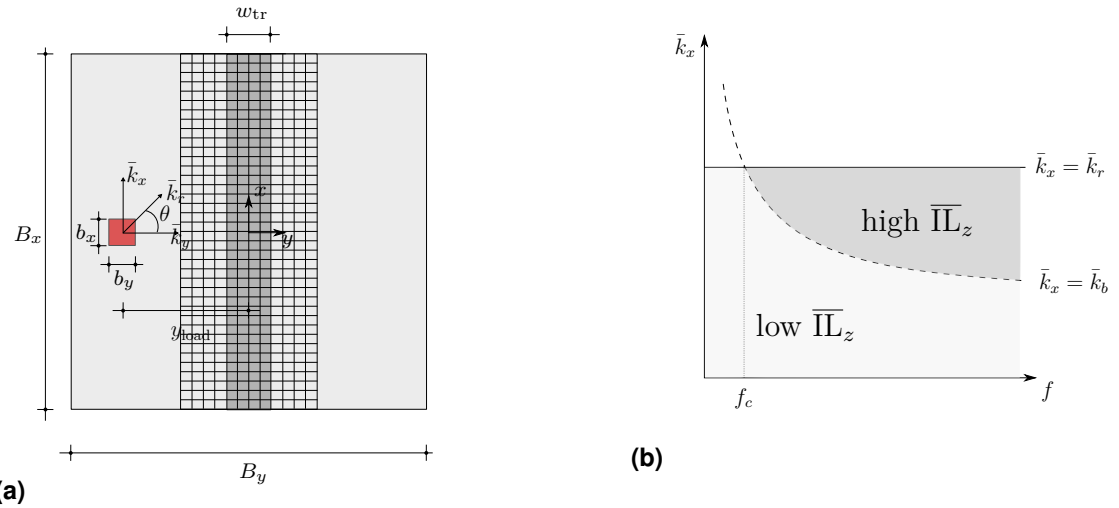

Figure 6.28: (a) Topview of setup for comparison of coupled ITM-FEM system with 2.5D FEM-BEM model of Coulier et al. [179]. (b) Schematic sketch insertion loss of free field response behind barrier and dispersion curves of the free bending wave in a Timoschenko beam and the Rayleigh wave in a homogeneous halfspace. [176]

the dimensionless Rayleigh wavenumber $\bar{k}_x = \bar{k}_r = c_s/c_r$ and bigger than the free bending wavenumber $\bar{k}_b$. The transmission of plane waves in the soil with $\lambda_x < \lambda_b$ resp. $\bar{k}_b < \bar{k}_x < \bar{k}_r$ is impeded for $f > f_c$, as the response of the beam is then dominated by its bending stiffness and the amplitude decreases proportionally to k_y^{-4} for a given frequency.

The contribution of wavenumbers $\bar{k}_x > \bar{k}_r$ to the total response and especially the response in the lateral direction is quite limited. This is because if one considers the Rayleigh wave, which contributes most to the overall response, the wavenumber $\bar{k}_y = \pm\sqrt{\bar{k}_r^2 - \bar{k}_x^2}$ becomes imaginary and the wave component in the y-direction thus becomes evanescent. Furthermore one can explain this by the rather low values of the transfer function of a homogeneous halfspace for $k_x^2 + k_y^2 > k_r^2$, which quickly decreases with increasing wavenumbers $\bar{k}_x > \bar{k}_r$.

The propagation direction of the elastic waves in the $x-y-$plane is in general given by $\theta = \tan^{-1}(\bar{k}_x/\bar{k}_y)$. In case of the Rayleigh wave the radiation angle can also be determined as $\theta_r = \sin^{-1}(\bar{k}_x/\bar{k}_r)$. The trace wavelength λ_x becomes infinite for plane waves propagating perpendicular to the barrier and is equal to λ_r for Rayleigh waves travelling along the barrier. The ratio of the trace wavelength λ_x and the bending wave length in the barrier λ_b thus depends strongly on the propagation direction θ_r. Beyond a critical angle of $\theta_c = \sin^{-1}(\bar{k}_b/\bar{k}_r)$ and assuming $f > f_c$, the wavenumbers $\bar{k}_x$ are larger than $\bar{k}_b$ and thus $\lambda_x < \lambda_b$ holds. Therefore, the impinging plane waves with $\theta > \theta_c$ are impeded by the barrier. Below this angle $\lambda_x > \lambda_b$ resp. $\bar{k}_x < \bar{k}_b$ holds. Therefore, large amplitudes of the bending waves occur in the beam and the Rayleigh wave is able to propagate through the stiffened block with low

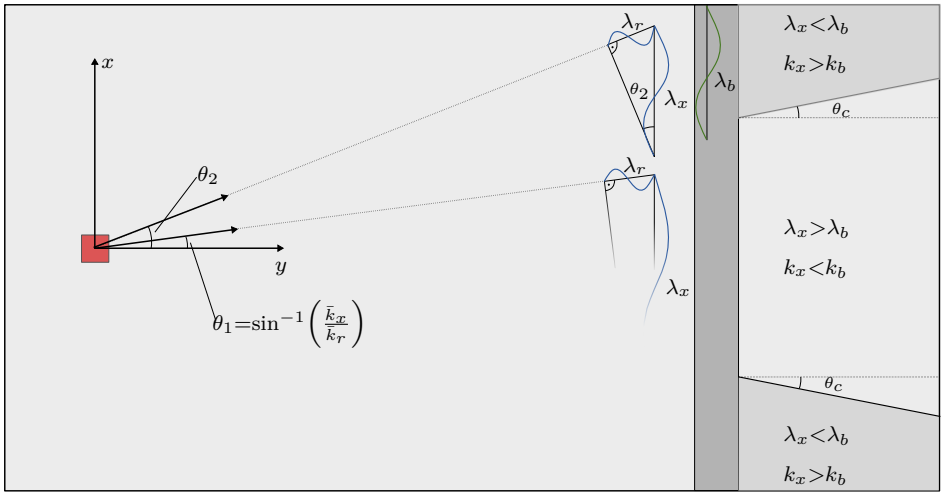

Figure 6.29: Schematic sketch of wave impeding behaviour of a stiff barrier and illustration of the trace wave length, critical angle as well as areas of high resp. low wave impeding effect.

transmission loss. The critical angle in dependency of the frequency yields [176, 179]

$$\theta_c(f) = \arcsin\left(c_r\sqrt{\rho\left(E+\mu\kappa \pm \sqrt{(E-\mu\kappa)^2+\frac{4E(\mu\kappa)^2A}{\rho I(\omega/2\pi)^2}}\right)(2E\mu\kappa)^{-1}}\right) \tag{6.5}$$

As visible in Fig. 6.28b the mitigation measure becomes effective only above a critical frequency f_c which can be determined by the intersection of the Rayleigh wave and the free bending wave dispersion curves either using the Euler-Bernoulli beam equation

$$f_c = \frac{c_r^2}{2\pi\, d_{\mathrm{tr}}}\sqrt{\frac{12\rho}{E}} \tag{6.6}$$

or the Timoschenko beam equation, additionally considering the shear deformation and the rotational inertia of the stiffened block of soil

$$f_c = \frac{c_r^2}{2\pi}\sqrt{\frac{\rho A}{EI}}\sqrt{\frac{E\mu\kappa}{(E-\rho c_r^2)(\mu\kappa-\rho c_r^2)}} \tag{6.7}$$

where E is the Young's modulus, μ the shear modulus, ρ the density, A the cross sectional area and I the moment of inertia of the beam. κ is the shear coefficient and can be set to $\kappa = 5/6$ for rectangular cross sections. c_r is the Rayleigh wave velocity in the soil. This critical frequency strongly depends on the stiffness contrast between the soil and the block of stiffened soil. Thus subgrade stiffening is more effective in soft soils. For the given material parameters the critical frequency results to $f_c = 12.37$ Hz. [176]

Fig. 6.30a and 6.30c show the real part of the vertical displacement $\bar{u}_z(x,y,z=0,\omega)$ due to a harmonic load with $f = 5$ Hz $< f_c$ below the critical frequency for the reference case and in case of subgrade stiffening. The Rayleigh wave length λ_r is much larger than the depth of the barrier and thus a significant part of the Rayleigh wave is able to pass beneath. For all waves impinging at the stiffened block, $\bar{k}_x < \bar{k}_b$ holds and therefore they are not impeded. The wave field in both cases is very similar and the corresponding insertion loss $\overline{\mathrm{IL}}_z$ in Fig. 6.30e is almost zero over the whole surface. [176]

In the case of an excitation frequency of $f = 30$ Hz $> f_c$, the displacement distribution $\bar{u}_z(x,y,z=0,\omega)$ in the reference case, shown in Fig. 6.30b, shows cylindrically propagating wavefronts. In contrast, when subgrade stiffening is applied, the wave field is no longer rotationally symmetric due to the interaction between the barrier and the soil, as shown in Fig. 6.30d. All waves hitting the barrier at an angle greater than the critical angle θ_c are impeded, leading to a significant reduction of vibrations in the areas with $\theta > \theta_c$. Hence, large values of the insertion loss, partly exceeding 10 dB, are observed there. The critical angle, which results to $\theta_c = 43.26°$ at $f = 30$ Hz, is also sketched in Fig. 6.30f. [176]

However, below the critical angle the amplitude reduction is rather small due to the relatively shallow barrier (only $d_{\mathrm{tr}}/\lambda_r = 0.32$ at $f = 30$ Hz) and the not so pronounced stiffness contrast between the barrier and the soil. Nevertheless, lines of increased $\overline{\mathrm{IL}}_z$ can be observed in this area due to the partial destructive interference, caused by the phase shift of the waves passing below the barrier and the waves transmitted through the barrier with much higher wave velocity. Therefore, this effect appears mainly for thick barriers of lower depth [292]. For larger depth of the barrier and an increased stiffness contrast also for angles $\theta < \theta_c$ a significant reduction can be achieved, as more reflections occur at the left face of the barrier and less vibrations are transmitted. Furthermore, a smaller part of the Rayleigh wave passes below the barrier. In Fig. 6.30f areas with higher and lower vibration levels compared to the reference case can also be detected on the load facing side of the barrier and be traced back to constructive or destructive interference of the direct Rayleigh waves and those being reflected at the barrier due to the impedance difference of the soil and the barrier materials.

On account of the preceding results in the following section the mitigation efficiency for an open trench, a soft and a stiff barrier are compared, assuming adequate dimensions and a sufficient stiffness contrast. [176]

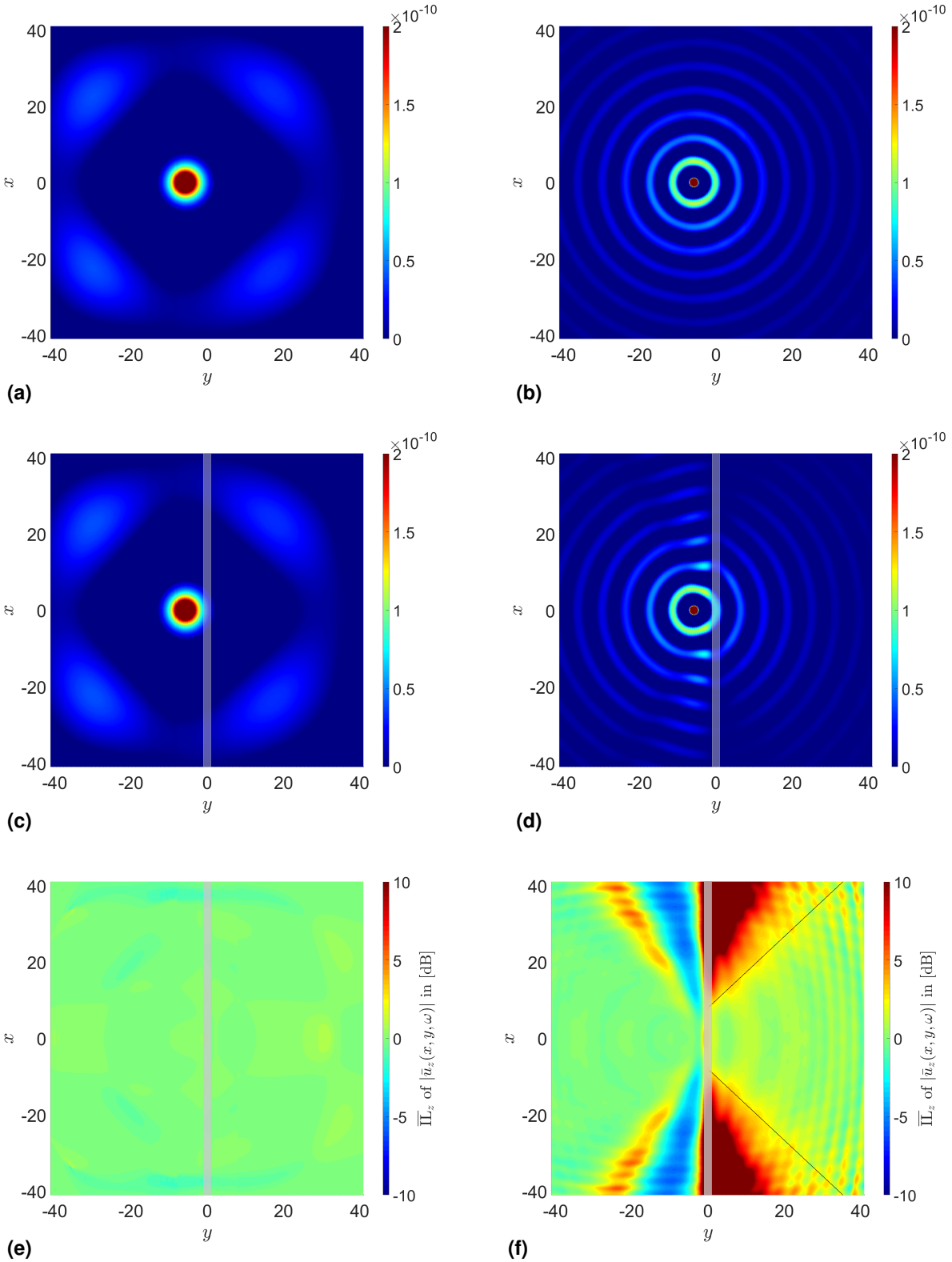

Figure 6.30: Real part of vertical displacement $\bar{u}_z(x,y,z=0,\omega)$ due to harmonic excitation with block load at $y = -6$ m in the reference case (a,b) and in case of subgrade stiffening (c,d) as well as the corr. insertion loss $\overline{\mathrm{IL}}_z(x,y,z=0,\omega)$ (e,f). Left column for $f_c > f = 5$ Hz and right column for $f_c < f = 30$ Hz. [176]

Stiff and soft barriers vs. open trench

The vibration screening efficiency of open trenches massively depends on the trench depth. A satisfactory screening efficiency of $A_r < 0.25$ can be achieved for depths d_{tr} greater than about $1.2\lambda_r$ of the soil [169]. Due to stability reasons the construction of ideal open trenches with vertical sides is limited to shallow depths. To this end, trenches are often filled with soft material that must be able to withstand the horizontal soil stresses, while still providing adequate insulation [180]. Open trenches achieve their vibration reduction effect mainly by the reflection of the incident Rayleigh waves. As no energy can be transferred across the open trench the vibration reduction usually is higher than for infilled trenches, where a part of the wave energy is transmitted through the barrier. If a very soft infill material is used, the behaviour of the filled trench resembles that of an open trench [145], which also yields for the mitigation efficiency. [176]

However, the physical mechanism, which is responsible for the vibration reduction changes, when it comes to stiff barriers. Additionally to the reflected and transmitted Rayleigh waves, the presence of the barrier gives rise to body (P- and S-) waves that are also reflected and transmitted [175]. Furthermore, body waves radiating downward the barrier occur, acting like a new wave source at the lower end of the stiff barrier, emitting body waves into the interior of the halfspace [292]. This transformation of Rayleigh waves into body waves is called mode conversion. The screening effect of a stiff barrier with adequate depth therefore is partly based on the reflection of the Rayleigh waves and partly on its transmission into the interior of the halfspace. For fixed dimensions, the decisive parameter for the vibration mitigation efficiency of a stiff barrier is the stiffness difference between soil and infilled trench [179]. The material damping of the infill material has no significant effect on the screening performance [293]. Therefore, very stiff barriers in relatively soft soils have a mitigation efficiency close to that obtained by an open trench [187]. [176]

Figure 6.31a shows the vertical displacement $|\bar{u}_z(x = 0,y,z = 0,\omega)|$ for an extremely stiff (Infill C) and a very soft (Infill D) barrier as well as an open trench and the reference case of a homogeneous halfspace (Soil A). The material properties of the barriers and the soil are given in Tab. 6.11, the used discretization in Tab. 6.10. Again a 1x1 m block load with $|\bar{\mathbf{P}}^{\mathbf{hs\ cyl}}_{\mathbf{\Lambda_{ITM}}}| = 1\ \mathrm{N\,m^{-2}}$ located at $y_{\mathrm{load}} = -4$ was chosen. For the excitation frequency of 20 Hz, λ_r results to 3.3 m and therefore the normalized dimensions of the trench resp. the barrier account for $D_{\mathrm{tr}} = 1.2$ and $W_{\mathrm{tr}} = 0.4$. The soft barrier and the open trench show large displacement amplitudes at the load sided edge, whereas in case of the stiff barrier the deformation is almost zero. This also reflects in the amplitude reduction factor depicted in Fig. 6.31b, exhibiting $A_r \ll 1$ for the open trench and the soft barrier. Due to the larger depth D_{tr} as well as the stiffer infill material (Infill C), A_r for the stiff barrier in Fig.6.31b also shows smaller values than in case of the concrete filled trench, investigated at the beginning

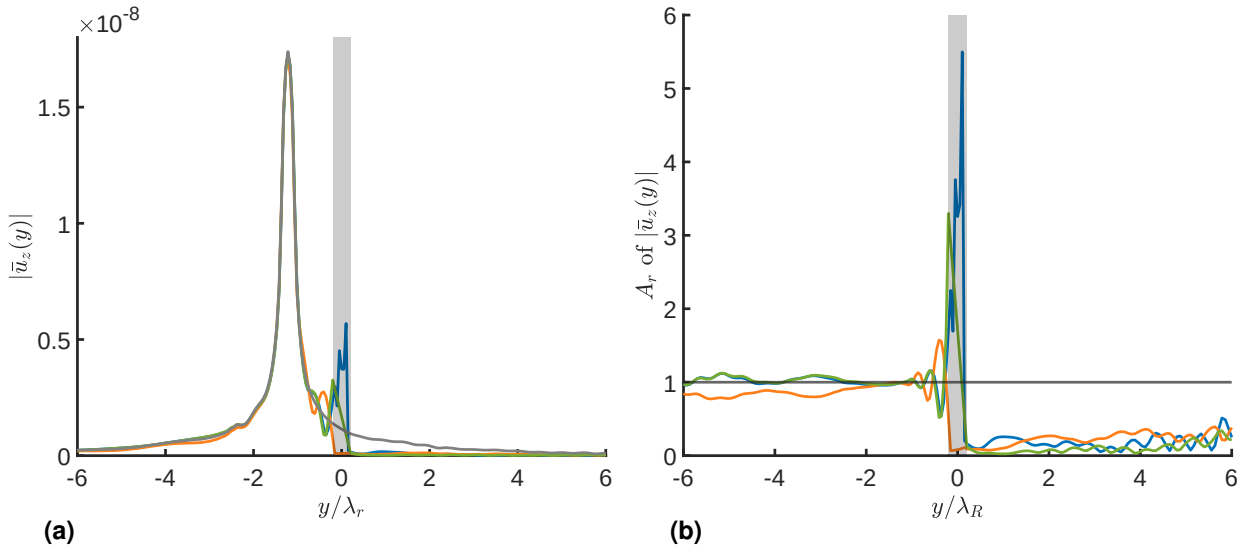

Figure 6.31: (a) $|\bar{u}_z(x=0,y,z=0,\omega)|$ at $f = 20$ Hz for soft barrier (—), stiff barrier (—), open trench (—), homogeneous halfspace (—) and (b) the corr. amplitude reduction factor A_r. The grey bar indicates the area enclosed by the open trench resp. the barrier. [176]

of Sec. 6.2.2. In general a significant reduction of vibrations is observed behind the trench for all three cases, albeit the open trench performs best over the largest part of the considered range [176].

This tendency is also visible in Figs. 6.32(a,c,e), where the amplitude reduction factor A_r over the surface with dimensions normalized by λ_r, is depicted. In the graphs, the area occupied by the barrier is marked by the white lines. The open trench shows the greatest reduction effect over the entire area on the load averted side. Nearly the same pattern of A_r develops on the load facing side for the open trench and the soft filled barrier, which can be explained by the similar physical mechanism for the vibration screening, relying almost solely on the reflection of the impinging Rayleigh waves. [176]

However, in case of the stiff barrier, due to the very different ratio of wave velocities in the soil and the barrier, compared to the soft infill material, as well as the larger amount of mode conversion, a very different interference pattern of the reflected waves occurs before the barrier. Moreover, in Figs. 6.32(b,d,f) the resultant of the displacements $\bar{\mathbf{u}}(x,y,z,\omega) = \sqrt{\bar{u}_x^2 + \bar{u}_y^2 + \bar{u}_z^2}$ within the FEM substructure is illustrated for all three cases in a section at $x = 0$. In the considered frequency range, the wave lengths in the soil are considerably larger than the barrier width and thus impose their displacements to the barrier quasi statically w.r.t. the $y-$direction [182]. It is clearly visible that with the soft filling material, large deformations occur at the edge and within the barrier, similar to the limit case of the reflection of the incident waves at the free end, as for an open trench. In contrast the stiff barrier shows no deformation at all and therefore almost acts as fixed boundary [177]. [176]

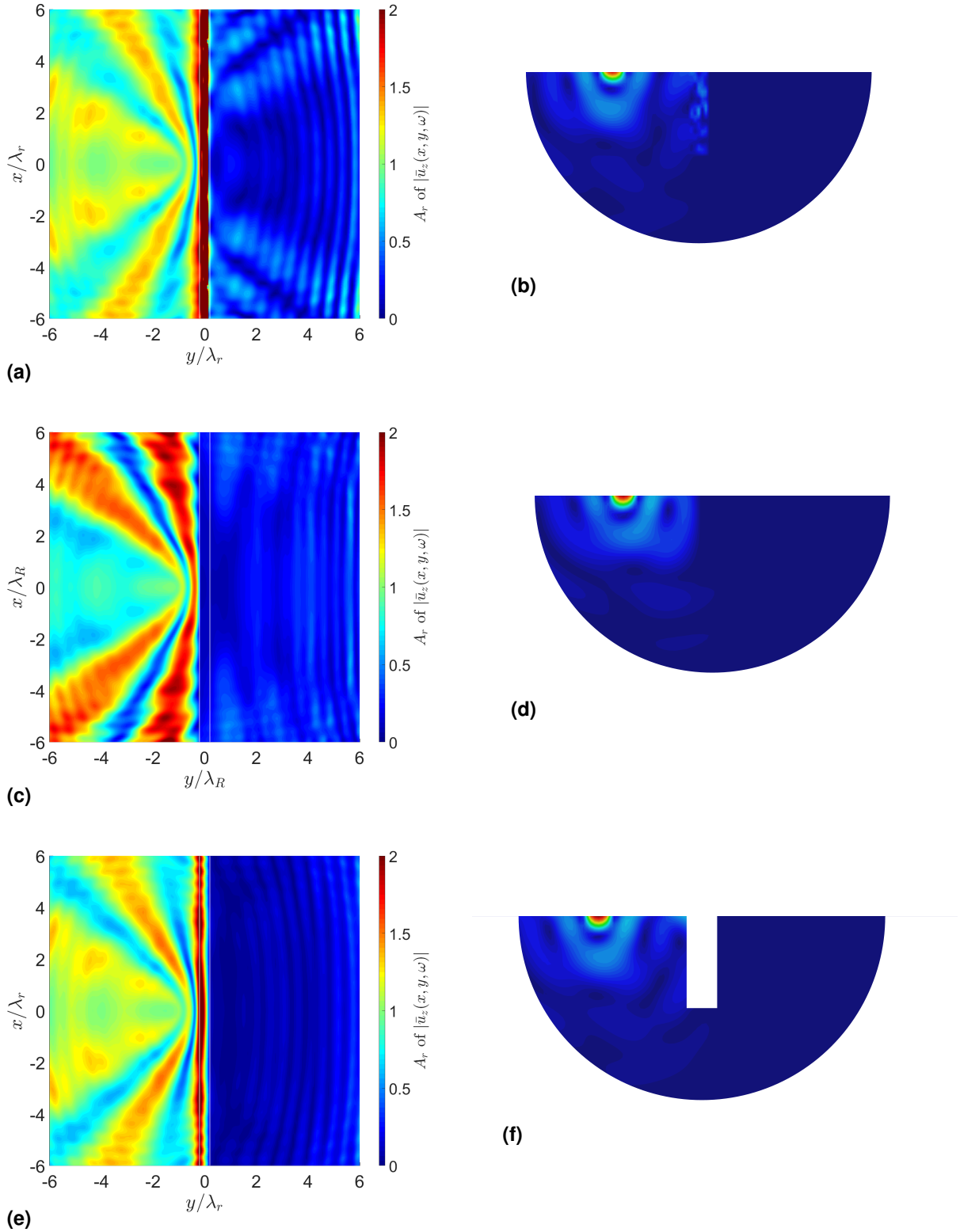

Figure 6.32: Amplitude reduction factor A_r (left) and resultant of displacements $|\bar{\mathbf{u}}(x,y,z,\omega)| = \sqrt{\bar{u}_x^2 + \bar{u}_y^2 + \bar{u}_z^2}$ (right) for (a,b) soft barrier, (c,d) stiff barrier and (e,f) open trench. [176]

6.2.3 Finite and infinite open trenches

Unlike the previously presented 2.5D approach, dealing with infinitely long mitigation measures in longitudinal direction, the 3D approach allows the investigation of spatially limited open trenches or barriers, closer to practical applications. For the length invariant structures, the energy transmission is restricted over the whole length, whereas in case of finite vibration shielding measures much more complex wave interference phenomena occur, as additionally to the lower trench end diffraction effects arise also at side edges [294]. Thus, regions on the ground surface with reduced or increased vibration amplitudes can clearly be observed in Figs. 6.35a and 6.35b. [176]

For the investigation of the finite open trench, the three dimensional ITM-FEM approach is applied, whereby the open trench is modelled within the half-spherically shaped FEM substructure, as displayed in Fig. 6.33. A radius of $R = 6$ m was chosen for the sphere and an open trench with $d_{\mathrm{tr}} = 3.8$ m, $w_{\mathrm{tr}} = 1.2$ m and $l_{\mathrm{tr}} = 4.8$ m included. A total region of $B_x = B_y = 64$ m was investigated using $N_x = N_y = 2^7$ Fourier series members on the halfspace surface as well as $N_\varphi = 40$ longitudes and $N_\vartheta = 20$ latitudes for the discretization of the sphere, leading to a finite element size of $\mathrm{d}x_{\mathrm{FE}} = \mathrm{d}y_{\mathrm{FE}} = 0.6$ m along the surface. The material properties of Soil A, given in Tab. 6.11, were used for the calculations. [176]

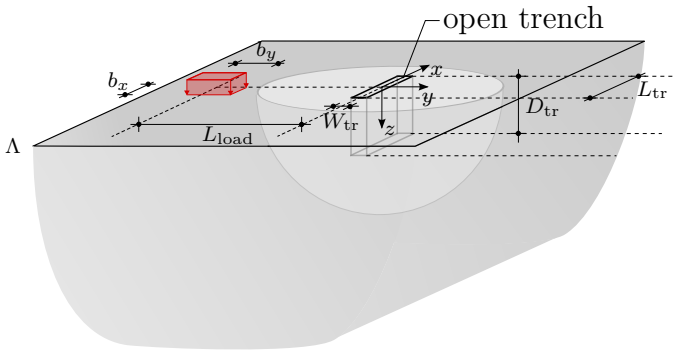

Figure 6.33: Setup of 3D ITM-FEM system for the vibration isolation by an finite open trench.

In the FEM subsystem solid elements with linear shape functions were used, which in general are not as accurate as higher order elements, if it comes to stress concentrations or detailed results for the displacement amplitude in the near field around the load are of interest. However, for the assessment of the vibration mitigation efficiency, the response behind the trench is more important than the deformation of the trench itself or the stress concentrations around it [294]. Therefore satisfactory precision is reached for the investigated problem, using the ITM-FEM approach.

In the following, the influence of the trench length and depth as well as the distance of the load from the trench is investigated and finally compared to results obtained for the infinite trench. [176]

Variation of the excitation frequency

Fig. 6.34a shows the absolute value of the vertical displacements at $x = 0$ over y due to a harmonic concentrated load located at $y_{\text{load}} = -8$ m with excitation frequencies of 12 Hz and 22 Hz. The corresponding amplitude reduction factor A_r is depicted in Fig. 6.34b. As the frequency changes, also the Rayleigh wavelength and therefore the relative dimensions of the open trench vary. At $f = 12$ Hz, λ_r results in 5.5 m and thus $D_{\text{tr}} = 0.69$, $W_{\text{tr}} = 0.22$ and $L_{\text{tr}} = 0.87$, whereas for $f = 22$ Hz the Rayleigh wave length is $\lambda_r = 2.9$ m and thereby $D_{\text{tr}} = 1.31$, $W_{\text{tr}} = 0.41$ and $L_{\text{tr}} = 1.65$. The amplitude reduction for 12 Hz, depicted in Fig. 6.35c, is rather limited as a significant part of energy passes below the open trench. With increasing frequency the penetration depth of the Rayleigh wave reduces and therefore the mitigation efficiency rises, as can be seen in Fig. 6.35d, showing A_r for an excitation frequency of 22 Hz. Amplifications of the displacement amplitudes can be observed in front of the trench and at the sides as well as a reduction behind the trench. For small ratios l_{tr}/λ_r amplifications occur also directly behind the open trench, a phenomenon which was also observed in Dasgupta et al. [294]. Due to the small trench length, especially for lower frequencies, the waves travel around the trench, thereby causing the amplifications visible in Fig. 6.34b. With increasing dimensionless length and depth, the mitigation efficiency rises and thus the shadow zone gets more defined. [176]

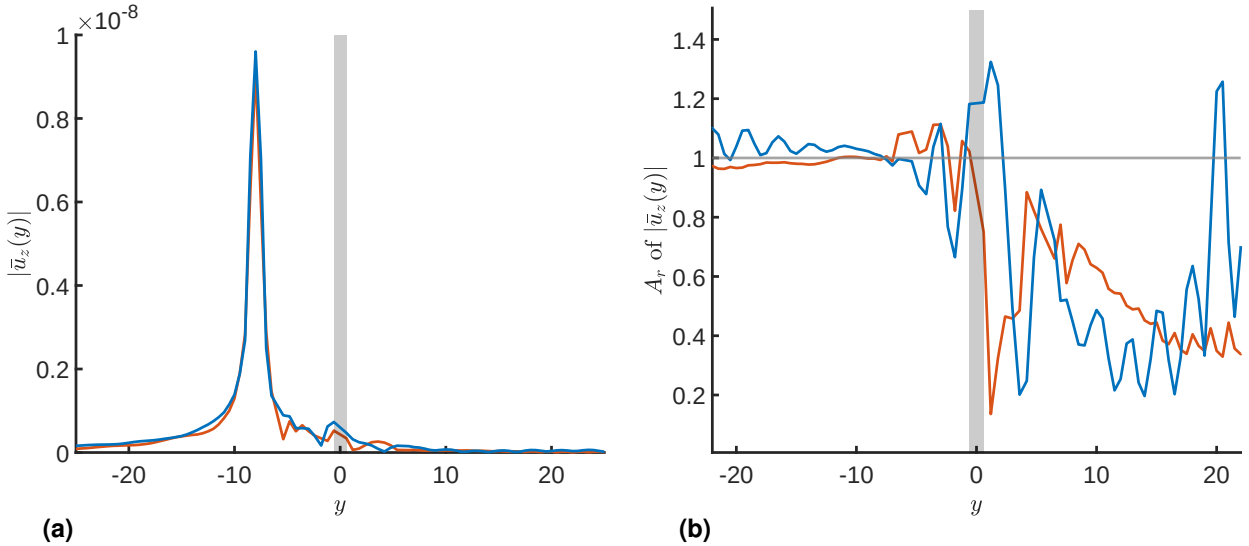

Figure 6.34: (a) Absolute value $|\bar{u}_z(x = 0,y,z = 0,\omega)|$ and (b) corresponding A_r for finite open trench due to a concentrated load at $y_{\text{load}} = -8$ m with $f = 12$ Hz (—) and $f = 22$ Hz (—). [176]

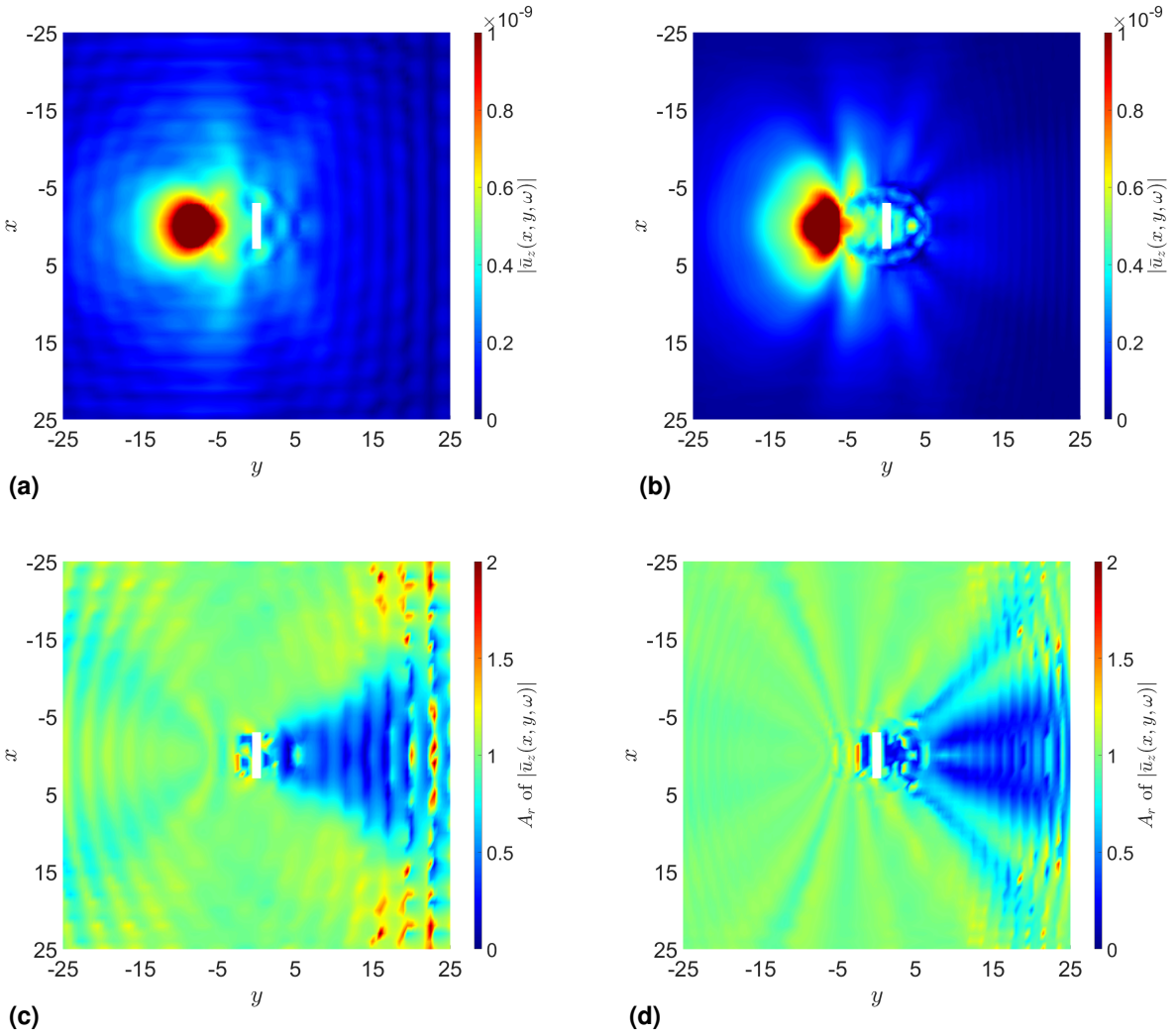

Figure 6.35: (a,b) Absolute value $|\bar{u}_z(x,y,z=0,\omega)|$ and (c,d) corresponding A_r for finite open trench due to block load at $y_{\text{load}} = -3$ m with $f = 12$ Hz (left) and $f = 22$ Hz (right). [176]

Variation of load position

Dolling [168] showed, that above a certain trench length the shielding effect no longer changes significantly and concluded that a radiation angle of $45° - 56°$ leads to an effective vibration reduction. Also Woods [169] found that larger trenches are required at greater distance from the source to achieve a certain amplitude reduction. Therefore, in this section the variation of the load position with a fixed open trench length, depth and width is investigated, as depicted in Figure 6.36a. This leads to a variation of the radiation angle [176]

$$\alpha = \tan^{-1}\left(\frac{L_{\text{tr}}/2}{L_{\text{load}} - W_{\text{tr}}/2}\right) \tag{6.8}$$

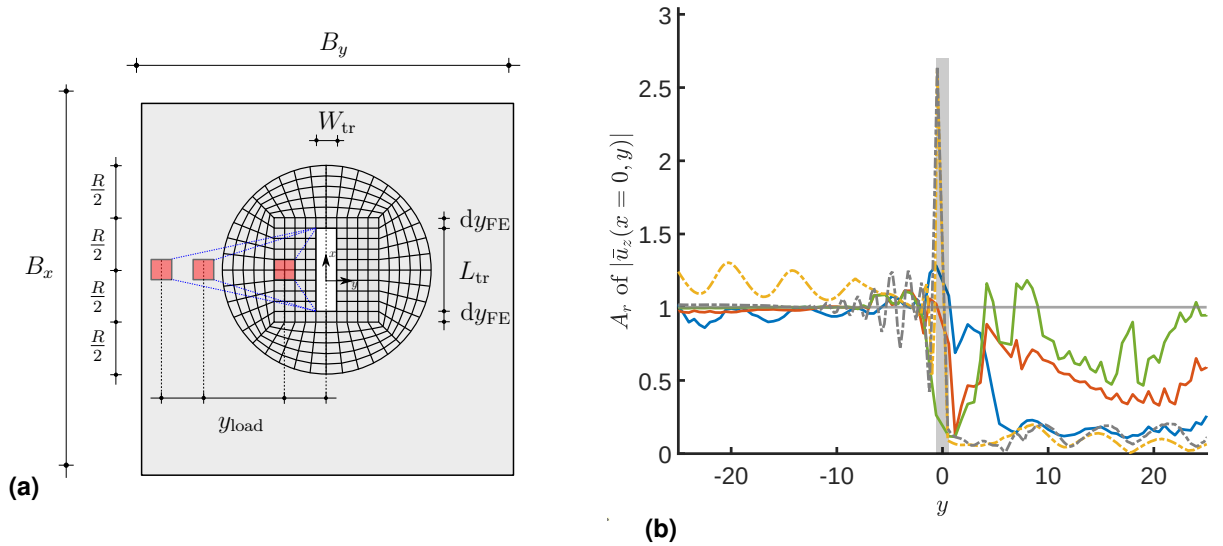

Figure 6.36: (a) Setup for variation of load position and radiation angle (blue lines). (b) Amplitude reduction factor A_r of $|\bar{u}_z(x=0,y,z=0,\omega)|$ for $y_{\mathrm{load}} = -3\mathrm{m}$ (—), $-8\mathrm{m}$ (—), $-14\mathrm{m}$ (—) for the finite and $y_{\mathrm{load}} = -3\mathrm{m}$ (– –), $-14\mathrm{m}$ (– –) for the infinite open trench at $f = 22$ Hz. [176]

of the waves on the open trench of 45° for $y_{\mathrm{load}} = -3$ to 10° for $y_{\mathrm{load}} = -14$ m and therefore a different shielding zone and mitigation efficiency. Figure 6.36b shows the amplitude reduction factor $A_r(x = 0,y,z = 0,\omega)$ for load positions $y_{\mathrm{load}} = -3, -8, -14$ m due to an excitation with $f = 22$ Hz. With increasing y_{load} the amplitude reduction at some distance behind the trench decreases substantially, which fits well to Woods's [169] statement, that the screening efficiency is larger if the trench is positioned close to the source. [176]

This is further confirmed, when the amplitude reduction factors for different load positions, considering the infinitely long trench are opposed to the ones obtained for the finite open trench, as depicted in Fig. 6.36b as well. The variation of A_r due to different load positions is very small for the length invariant open trench, because the radiation angle is not relevant in this case, as there is no possibility for the waves to travel around open trench. A more exposed peak in front of the trench can be observed in the 2.5D case, because a bigger part of the incoming waves is reflected, leading to a lower A_r over the whole length behind the trench as for the finite open trench. [176]

Summing up, the normalized depth of the barrier and the stiffness contrast between infill material and soil are found to be the most important parameters for the performance of the screening measure. More shallow barriers with less pronounced stiffness contrast, as in case of subgrade stiffening, act as wave impeding barrier up from a critical frequency and provide a significant insertion loss within an area delimited by a critical angle. For deeper stiff or soft filled barriers with distinct stiffness contrast, the performance is similar to an open trench. In

case of spatially limited open trenches also the dimensionless lengths play an important role. As diffraction occurs at the sides of the trench additionally to the bottom, more complex wave interference patterns occur. The radiation angle and therefore the distance of the source from the trench has fundamental impact on the mitigation efficiency, which is not the case for length invariant trenches. [176]

6.2.4 Two parallel infinite open trenches

Within this section, the vibration reduction due to one or two infinite open trenches is investigated (cp. Fig. 6.37). The system is subjected to an unit harmonic, square block load with $b_x = b_y = 1.0$ m, located at the center of the ground surface besides resp. between the two trenches positioned at $y_{\mathrm{Tc}} = \pm 6$ m. The radius of the cylindrical inclusions was chosen to $R = 4$ m, thus exhibiting a depth of the open trench of $d_{\mathrm{tr}} = 2$ m. A total domain size of $B_x = B_y = 64$ m with $N_x = N_y = 2^9$ and $N_\varphi = 64$ discretization points was chosen and material parameters of Soil A in Tab. 6.11 were used.

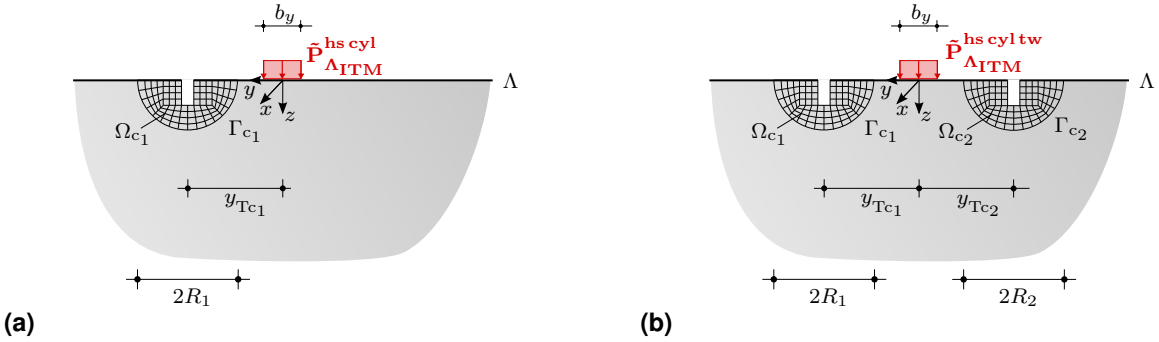

Figure 6.37: Setup for comparison of surface vibrations due to one and two infinite open trenches.

Fig. 6.38 shows a comparison of $|\bar{u}_z(y)|$ at $x = 0$ for a homogeneous halfspace and a halfspace with either one or two open trenches. At $f = 30$ Hz the trench depth w.r.t. the Rayleigh wave length yields $D_{\mathrm{tr}} = 0.91$ which leads to a strong reduction of the surface displacements on the load averted side(s) of the trench(es). The reduction at the left trench $y_{\mathrm{Tc}_1} = 6$m is quasi equal for the situation with one and two trenches and the amplitude of the displacements under the load are nearly unchanged. For the halfspace with two open trenches of course an additional reduction occurs for $y < y_{\mathrm{Tc}_2} = -6$ m. However, this only leads to increasing oscillations in the immediate vicinity of the open trench and has little influence on the distribution of $|\bar{u}_z(y)|$ between the trenches elsewhere. At $f = 60$ Hz, due to the relatively small wavelengths, the induced waves are largely attenuated by material and geometric damping before reaching the open trench(es), so that only a small difference is visible in the progressions of $|\bar{u}_z(y)|$ in Fig. 6.38b.

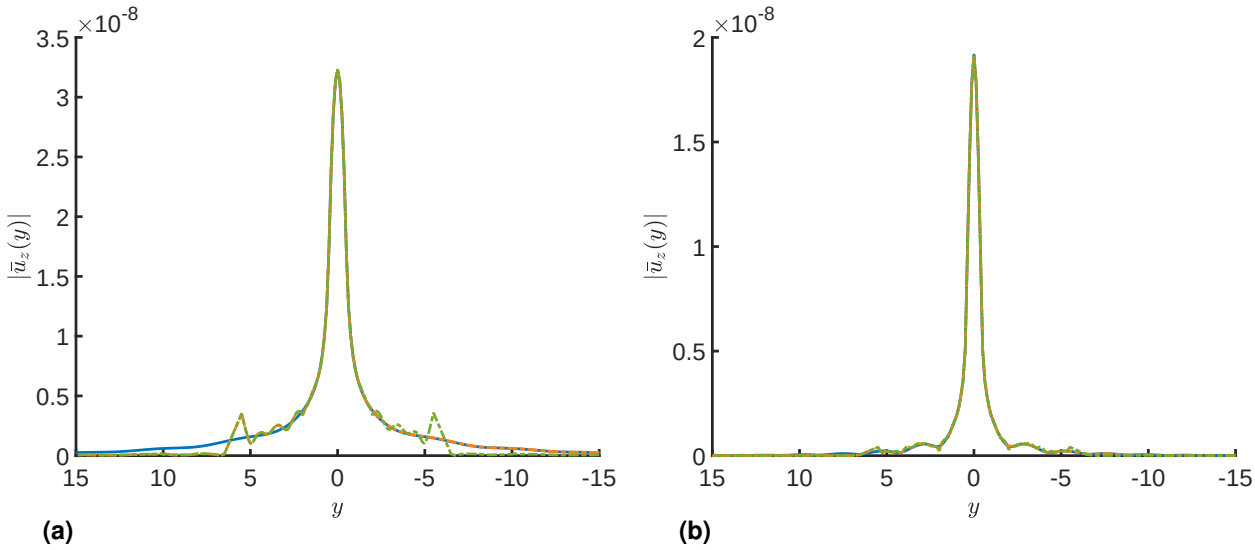

Figure 6.38: Comparison $|\bar{u}_z(y)|$ for homogeneous halfspace (—), halfspace with one (– –) or two (– –) open trenches for (a) $f = 30$ and (b) $f = 60$ Hz with setup cp. Fig. 6.37.

These observations are confirmed by the results in Fig. 6.39a, showing nearly no difference of the vertical displacements along the longitudinal $x-$direction at $y = 0$ for all three situations. In contrast, $|\bar{u}_z(x)|$ at the edge of the open trench at $y = -5.5$ m in Fig. 6.39b is considerably larger for the system with two open trenches. For the homogeneous halfspace and the system with one open trench, $|\bar{u}_z(x)|$ on the opposite side to the opening is quasi equal.

For a system with two infinite open trenches enclosing the load, the energy is prevented from dispersing uniformly in all directions. The reduction effect for the surface vibrations outside the trench(es) can be clearly seen in the Fig. 6.40 and Fig 6.41a, in which the insertion loss for the system with two trenches is given with reference to the homogenous halfspace.

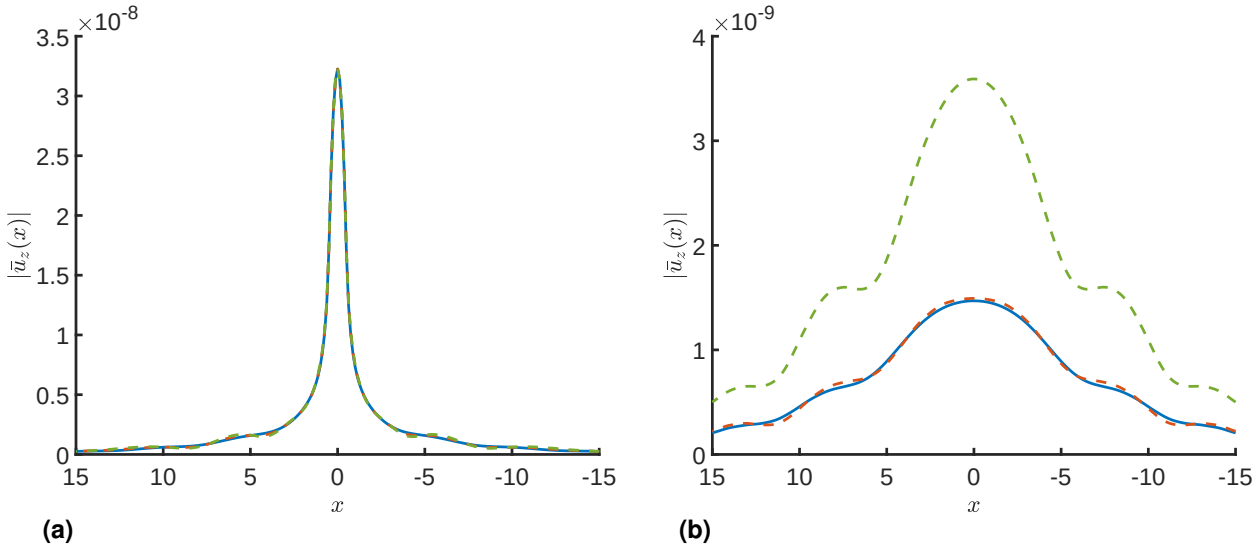

Figure 6.39: Comparison $|\bar{u}_z(x)|$ for homogeneous halfspace (—), halfspace with one (– –) or two (– –) open trenches for $f = 30$ Hz at (a) $y = 0$ m and (b) $y = -5.5$ m at the edge of the open trench as shown in Fig. 6.37b.

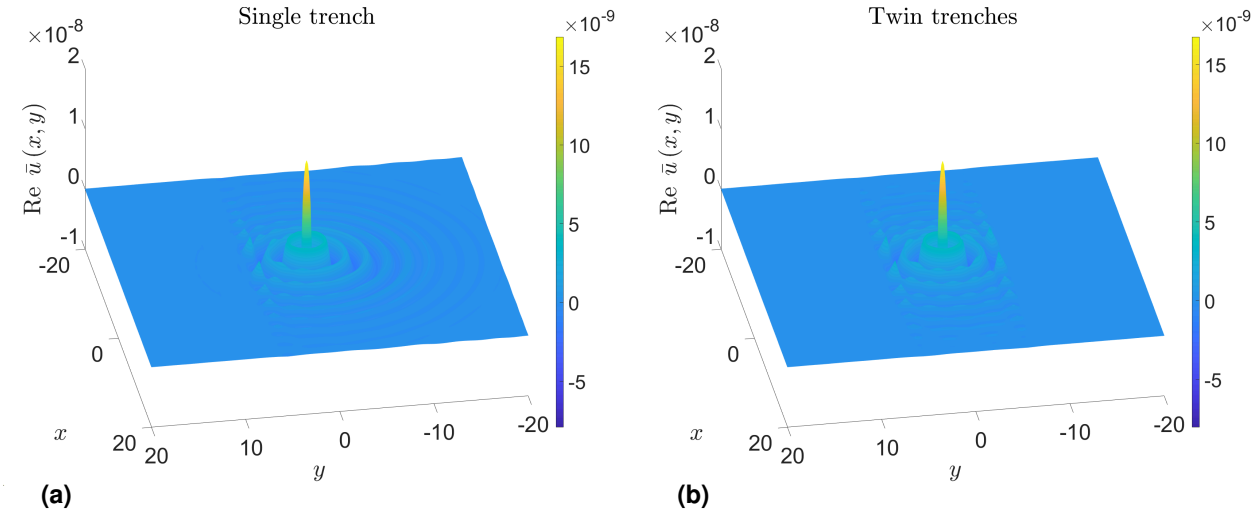

Figure 6.40: Real part of surface displacements $\mathrm{Re}\ \bar{u}_z(x,y)$ at $f = 30$ Hz for (a) one and (b) two open trenches with setup cp. Fig. 6.37.

Furthermore, it is apparent that there is a concentration of vibrations within the trenches, leading to increased amplitudes mainly in the region immediately adjacent to the openings, where due to the free edge condition, considerable deformations occur over the entire length of the trench. This is also reflected in the high levels of insertion gain

$$\overline{\mathrm{IG}}_z = 20 \log_{10} \frac{|\bar{u}_z^{\mathrm{Tc}_2}(x,y,f)|}{|\bar{u}_z^{\mathrm{Tc}_1}(x,y,f)|} \tag{6.9}$$

along the trench at $y_{\mathrm{Tc}_2} = -5.5$ m in Fig.6.41b, which denotes the increase in amplitudes when inserting two instead of only one trench. The outliers at the edge of the considered area result from the division of very similar small numerical values at a greater distance from the load, which leads to very high values of $\overline{\mathrm{IG}}_z$.

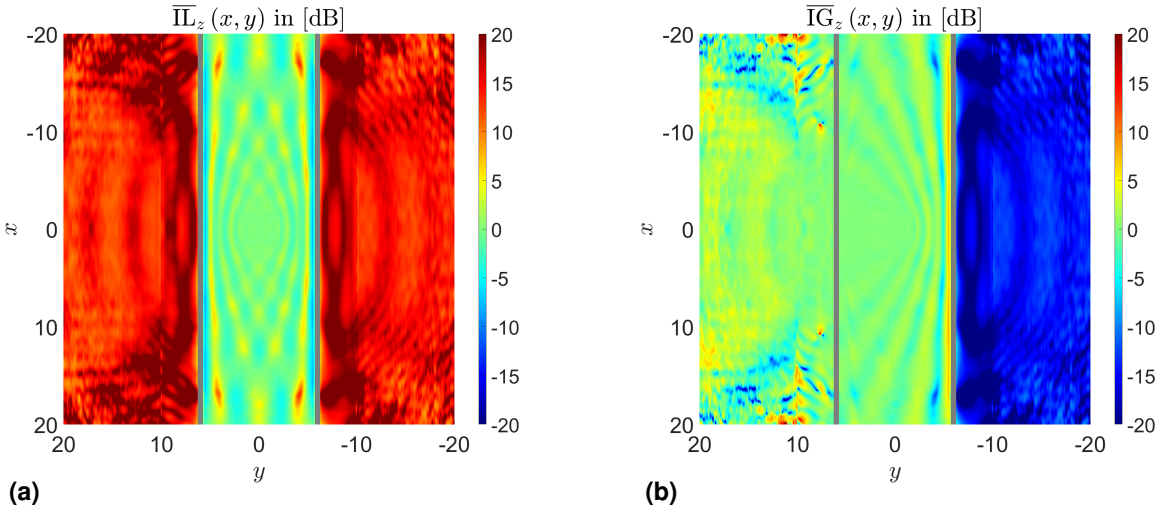

Figure 6.41: Distribution of (a) insertion loss $\overline{\mathrm{IL}}_z(x,y,f)$ for two infinite open trenches compared to homogeneous halfspace and (b) insertion gain $\overline{\mathrm{IG}}_z(x,y,f)$ for two trenches compared to situation with only one trench at $f = 30$ Hz.

6.2.5 Insertion loss due to elastic bearing

In the following, the 3D-ITM-FEM approach for the halfspace with spherical indentation is used to model a foundation, possibly supported elastically and resting on the surface of a homogeneous halfspace, as illustrated in Fig. 6.42. In the numerical model a width of

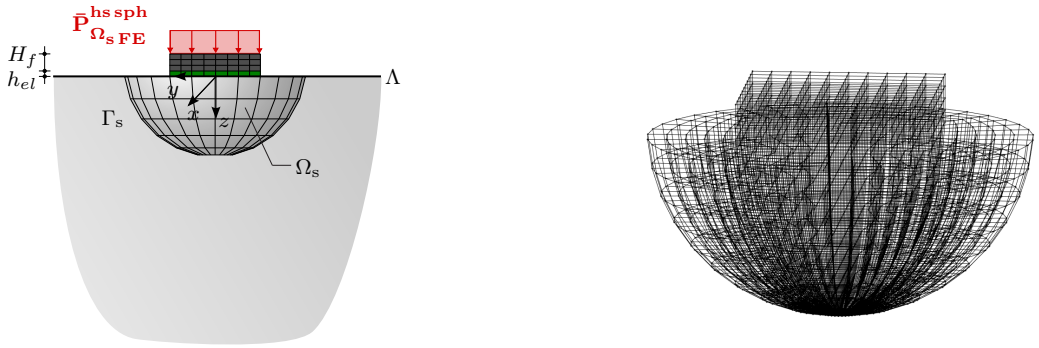

(a) **(b)**

Figure 6.42: (a) Setup for halfspace with spherical indentation and elastically mounted foundation and (b) FEM mesh for 3D inclusion.

$B_f = 4$ m and a height of $h_f = 1$ m is considered for the foundation, located inside the spherical inclusion with $R = 4$ m and discretized with $N_\vartheta = 20$ latitudes and $N_\varphi = 40$ longitudes. The inclusion is embedded in a soil with total domain size $B_x = B_y = 64$ m and $N_x = N_y = 2^7$ sample points for all frequencies within $f = 2 - 30$ Hz. A uniform load with $|\bar{\mathbf{P}}^{\mathbf{hs\,sph}}_{\Omega_{\mathbf{s}}\,\mathbf{FE}}| = 1$ Nm^{-2} is applied over the entire foundation surface in all cases. The material parameters for the subsoil, the foundation and the elastic mounting are given in Tab. 6.12.

	E (Nm^{-2})	ν (–)	ρ (kgm^{-3})	ζ (–)	c_p (ms^{-1})	c_s (ms^{-1})	c_r (ms^{-1})
Soil	$2.60 \cdot 10^{\,7}$	0.30	2000	0.05	132.5	70.8	65.7
Elastic layer	$5.50 \cdot 10^{\,5}$	0.36	620	0.10	38.66	18.08	
Foundation	$3.60 \cdot 10^{10}$	0.20	2400	0.05	$4.08 \cdot 10^3$	$2.50 \cdot 10^3$	

Table 6.12: Material parameters of soil, foundation and elastic mounting.

Firstly, a massless ($\rho_f = 0$) foundation without elastic mounting is considered. For the given parameters this results in a dimensionless stiffness and mass ratio as introduced by [60]

$$K = \frac{E_f H_f^3 (1 - \nu_s)}{12(1 - \nu_f^2)\mu_s B_f^3} \qquad \text{and} \qquad M = \frac{H_f \rho_f}{B_f \rho_s} \tag{6.10}$$

of $K = 4.44$ and $M = 0$. Thereby a stiffness ratio $K > 1$ can be considered to represent a rigid plate for practical applications. [51]

In order to be able to compare the obtained results for a rigid massless foundation with other methods or literature solutions, the dimensionless vertical displacements resp. compliances at the soil foundation interface are considered

$$\Delta^{ij}_{mm} = \frac{2}{(1-\nu_s)} C^{ij}_{mm} \quad \text{with} \quad C^{ij}_{mn} = \frac{\bar{u}^i_m \mu_s (B_f/2)}{\sum \bar{P}^j_{n\,\mathrm{sys}}} \tag{6.11}$$

where μ_s is the shear modulus of the soil, $\bar{u}^i_m$ is the displacement of the rigid foundation i in direction $m = x,y,z$ and $\sum \bar{P}^j_{n\,\mathrm{sys}}$ stands for the resultant of the external load applied on foundation j in direction n. In case of a flexible foundation, the position resp. the distribution of the load and the corr. compliances are mentioned explicitly, as they vary continuously over the foundation area. The compliance functions are evaluated over the dimensionless frequency $a_0 = \omega B_f / c_s$, whereby in case of a layered halfspace c_s refers to the shear wave velocity of the upper layer [51].

Fig. 6.43 shows the real and imaginary part of the dimensionless vertical compliance of a rigid massless foundation, obtained with the proposed coupled ITM-FEM approach as well as the results of Wong and Luco [53] and those computed with the FEM-BEM approach presented in Taddei [295]. In general, a good agreement between the results of all three methods can be stated. However, for low frequencies the ITM-FEM and the FEM-BEM approach behave slightly stiffer than the solution of Wong and Luco [53], converging towards the latter with increasing a_0. One reason for this lies the full coupling of all DOFs between foundation

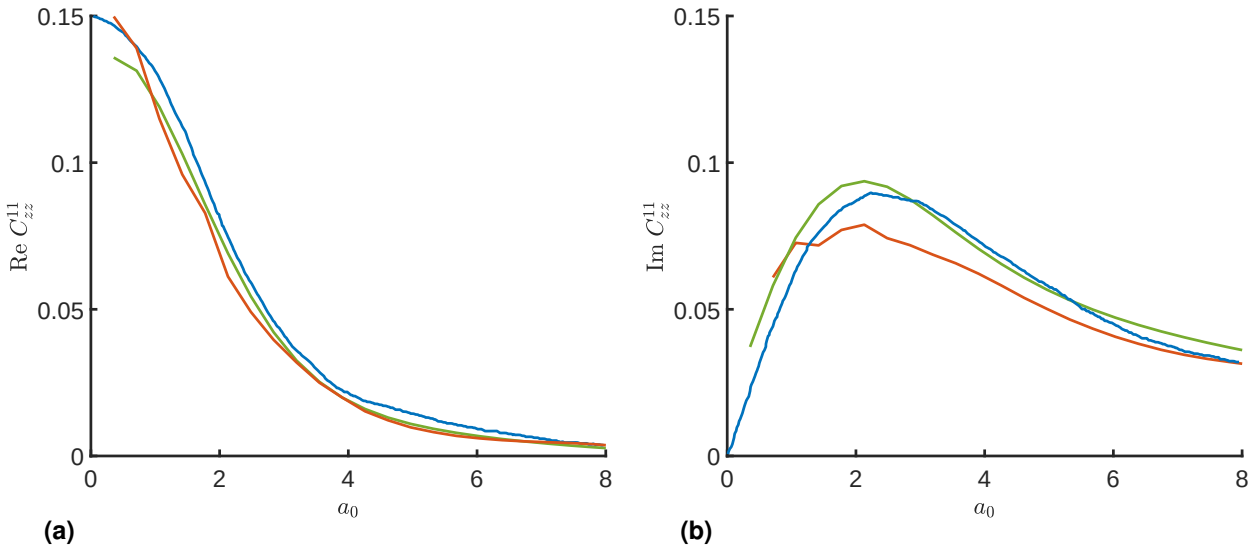

Figure 6.43: (a) Real and (b) imaginary part of the vertical compliance C^{11}_{zz} of a rigid, massless foundation on homogeneous halfspace at $x = y = z = 0$ over the dimensionless frequency a_0 obtained by Wong and Luco [53] (—), with the 3D ITM-FEM approach (—) and the FEM-BEM approach by Taddei [295] (—).

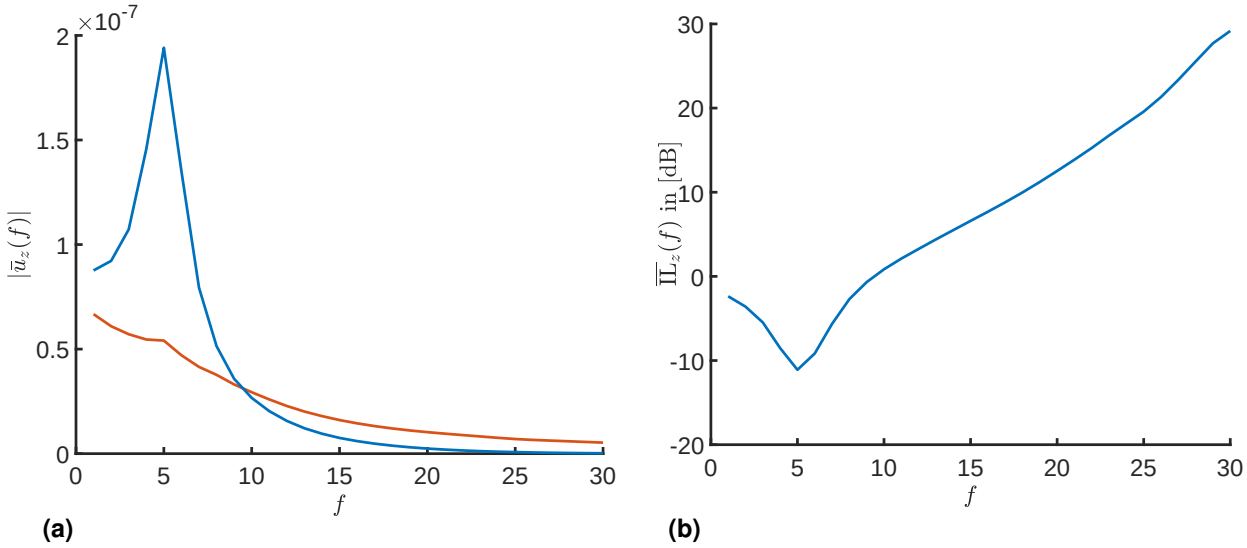

Figure 6.44: (a) $|\bar{u}_z(f)|$ at $x = y = 0$ and $z = -h_f$ for massive foundation without (—) and with elastic mounting (—). (b) Corresponding insertion loss $\overline{\mathrm{IL}}_z(f)$ (–+–) over frequency.

and soil in the ITM-FEM and the FEM-BEM approach, whereas Wong and Luco [53] used relaxed boundary conditions setting the shear stresses on the contact area to zero. [84]

The vertical displacements at the interface of a massive foundation, with $\rho_f = 2400\ \mathrm{kg\,m^{-3}}$ as given in Tab. 6.12, to the soil for the case with and without the elastic mounting are depicted in Fig. 6.44a. A clear resonance peak for the foundation mass oscillating on the elastic mounting can be observed, which also leads to the dip in the insertion loss curve in Fig. 6.44b at approx. 5 Hz. An equivalent Single Degree of Freedom (SDOF) model leads to a resonance frequency of

$$f_{\mathrm{res,el}} = \frac{1}{2\pi}\sqrt{\frac{E_{el}/h_{el}}{\rho_f H_f}} \approx 4.81\ \mathrm{Hz} \tag{6.12}$$

The slight deviations can be explained by the negligence of the 3D effects and the material damping of the elastic mounting in the SDOF model. Due to the restricted lateral strain, the full-surface elastic layer with $\nu_{el} \neq 0$ behaves stiffer than the equivalent spring model, leading to a raise in the resonance frequency compared to $f_{\mathrm{res,el}}$. Furthermore, the onset of a significant reduction of the vibrations, usually expected up from $\sqrt{2} f_{\mathrm{res,el}} \approx 6.80$ Hz [296], is shifted to higher frequencies, which is due to the elasticity of the underlying soil in contrast to a rigid support of the elastic layer, assumed typically.

6.3 Soil structure interaction for single surface foundation

The coupled ITM-FEM approach, presented in Sec. 5.3, is now applied to determine the dynamic response of 3D rigid and flexible surface foundations for different subsoil conditions, as depicted in Fig. 6.45. Thereby, the following section is largely based on Freisinger et al. [51], but extended by some noteworthy aspects and more detailed explanations. Initially, the main characteristic features of the frequency dependent foundation flexibilities and the power input at the soil foundation interface due to different load types (point load, uniform pressure, moment) are illustrated for the rather simple support conditions of the homogeneous (Sec. 6.3.1) and the layered halfspace (Sec. 6.3.2). The accuracy of the proposed method is demonstrated by comparison of the obtained results to literature for standard benchmark cases. Finally, the behaviour of foundations on more complex soil subsystems, including local inhomogeneities (models 3-5), is assessed (Sec. 6.3.3) by showing differences and similarities to the results presented before. [51]

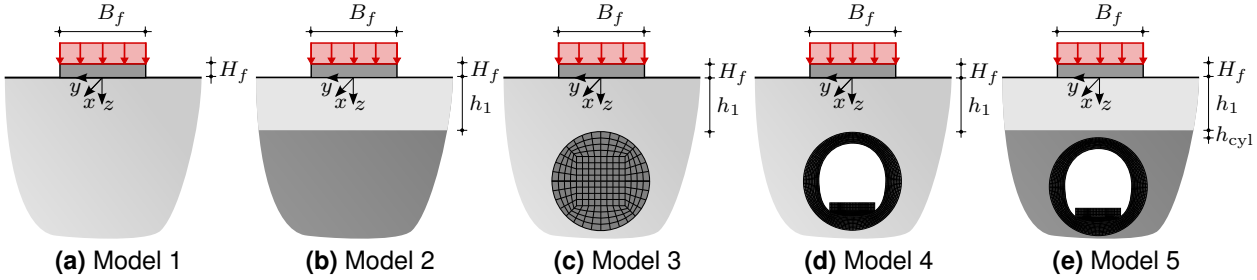

Figure 6.45: Investigation setup: (a) homogeneous and (b) layered halfspace, halfspace with (c) cyl. concrete inclusion and (d) cyl. tunnel as well as (e) layered halfspace with cyl. tunnel. [51]

For all calculations relaxed boundary conditions, a square foundation with $B_f = L_f = 2$ m, $H_f = 0.3$ m and $\nu_f = 0.3$ is chosen, while E_f and ρ_f are each adjusted to result in a desired dimensionless stiffness ratio K and mass ratio M, as defined in Eq. (6.10). The dimensions and discretization parameters of the soil were chosen to be identical for all calculations, unless explicitly stated different. A total domain size of $B_x = B_y = 128$ m was considered with $N_x = N_y = 2^{11}$ sampling points in each direction. Thus an original discretization length of $\mathrm{d}x = \mathrm{d}y = 0.0625$ m is used for the computation of the soil displacements due to an unit vertical concentrated load (cp. Sec. 5.3). This step size is enlarged by $n_\Delta = 2$ to avoid numerical errors when setting up the soil flexibility matrix $\bar{\mathbf{F}}_\mathbf{s}$. The material parameters for all considered soil conditions are given in Tab. 6.13. [51]

	E (Nm^{-2})	ν $(-)$	ρ (kgm^{-3})	ζ $(-)$	c_p (ms^{-1})	c_s (ms^{-1})	c_r (ms^{-1})
Soil A	$2.60 \cdot 10^7$	0.3	2000	0.020	132.31	70.72	65.60
Soil B	$1.06 \cdot 10^8$	0.3	2000	0.020	264.63	141.45	131.22
Soil C	$4.16 \cdot 10^8$	0.3	2000	0.020	529.26	282.90	262.44
Soil D	$4.68 \cdot 10^7$	0.3	1800	0.025	187.14	100.03	92.79

Table 6.13: Material parameters of different considered soils.

6.3.1 Foundation on homogeneous halfspace

Compliances of rigid massless foundations

Firstly, the response of a rigid ($K = 1000$), massless ($M = 0$) foundation resting on a homogeneous halfspace (Soil A) is investigated. A harmonic unit vertical point force ($|\bar{\mathbf{P}}_{\text{sys}}| = 1$) and an unit rocking moment ($|\bar{\mathbf{M}}_{\text{sys}}| = 1$) are applied as external load. The soil foundation interface is discretized with $16 \times 16 = 256$ shell elements, yielding an element size of $\mathrm{d}s = 0.125$ m w.r.t. the coarse mesh. [51]

Fig. 6.46a shows the real and imaginary parts of the vertical compliance functions at the soil foundation interface $z = 0$ at $(x,y) = (0,0)$, computed with the presented ITM-FEM approach. Very good agreement to the results obtained by Wong and Luco [53], Hirschauer [68] as well as Shahi and Noorzad [57] can be observed [51]. In case of the rocking compliance C_{φ_x}, depicted in Fig. 6.46b, the ITM-FEM approach returns slightly lower compliances presumably linked to the non-zero material damping unlike in the other methods. Due to a concentration of stresses and corresponding large displacement amplitudes within a rather small area close to the edges of the foundation, in case of a rocking motion the energy dissipated by the hysteretic material damping plays a bigger role as in case of uniformly distributed vertical vibrations, thus leading to smaller displacement amplitudes finally resulting in a decreased rotational flexibility.

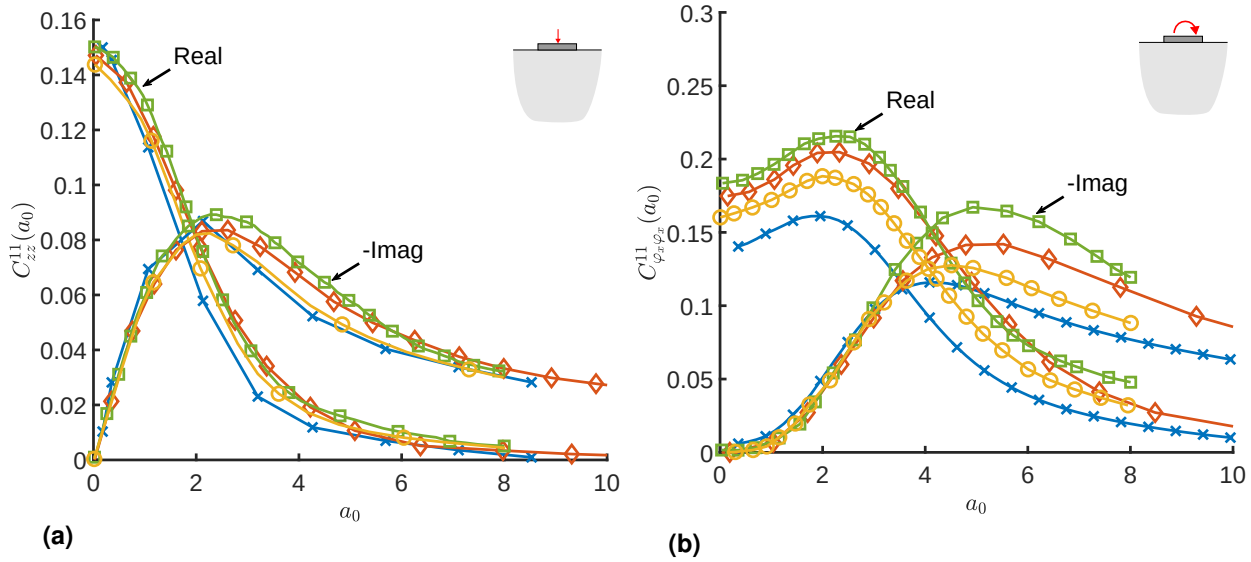

Figure 6.46: (a) Vertical and (b) rocking compliance of a rigid, massless square foundation on a homogeneous halfspace (Soil A) obtained with the presented ITM-FEM approach (–×–) and the results of Wong and Luco [53] (–□–), Hirschauer [68] (–◇–) and Shahi and Noorzad [57] (–○–).

Compliances of flexible massless foundations

Second, the dynamic behaviour of a flexible, massless foundation is studied. The foundation is subjected to both, a point load and an uniform pressure, since in case of a flexural plate the load distribution strongly influences the resulting distribution of displacements and stresses at the contact surface. The considered scope of foundation flexibilities ranges from $K = 0.0001$ to $K = 3.33$, corresponding to a very soft and a quasi-rigid plate respectively. [51]

Fig. 6.48 shows the dimensionless vertical displacement amplitude $|\Delta_{zz}^{11}(a_0)|$ for both load conditions and different values of K, evaluated at the center, the midside point and the corner of the plate at the soil foundation interface. The displacement in the center is generally larger for the flexible plate than for the stiff plate, while it behaves reverse at the corner. In case of the uniform load this leads to the typical dishing deformation that is clearly visible in Fig. 6.49a, which illustrates the real part of $\Delta_{zz}^{11}(y)$ along the half length of the center line of the foundation at $x = 0$ for $a_0 = 0$. The total displacement consists of a rigid body indentation and the bending deformation of the flexible plate, which provides a larger contribution to the total deflection with increasing frequency, whereas the proportion of the rigid body indentation decreases. Both diminish when approaching higher frequencies $a_0 > 2\pi$, where the total deflections are generally lower [60].

In case of the point load, the displacement distribution depends significantly on the stiffness of the plate (especially for soft foundations) and is very much concentrated under the point of load application as can be seen in Figs. 6.49b,d,f. This is furthermore illustrated in Fig. 6.47, where the real part of the vertical displacements on the ground surface $z = 0$ for a flexible foundation with $K = 0.004$ subjected to a uniform pressure and a point load are depicted. The displacements are much larger directly under the point load and decrease relatively fast with increasing distance from it, whereas for the uniform pressure the amplitudes of the radiated surface waves are of similar amplitude as those directly under the foundation.

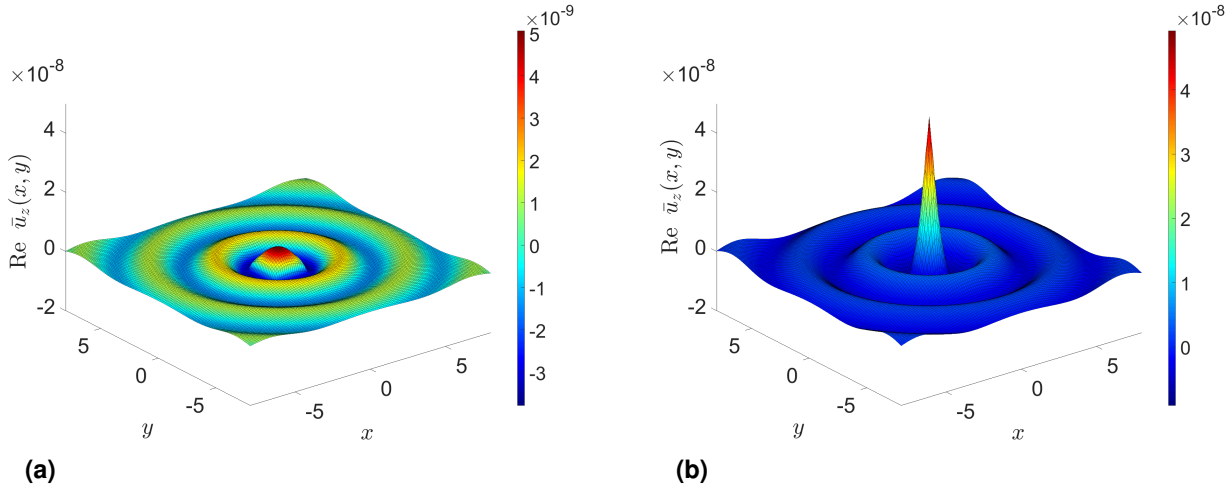

Figure 6.47: Real part of $\bar{u}_z(x,y)$ at $z = 0$ under flexible foundation ($K = 0.004$) subjected to (a) uniform pressure and (b) point load with $f = 18$ Hz located on homogeneous halfspace (Soil A).

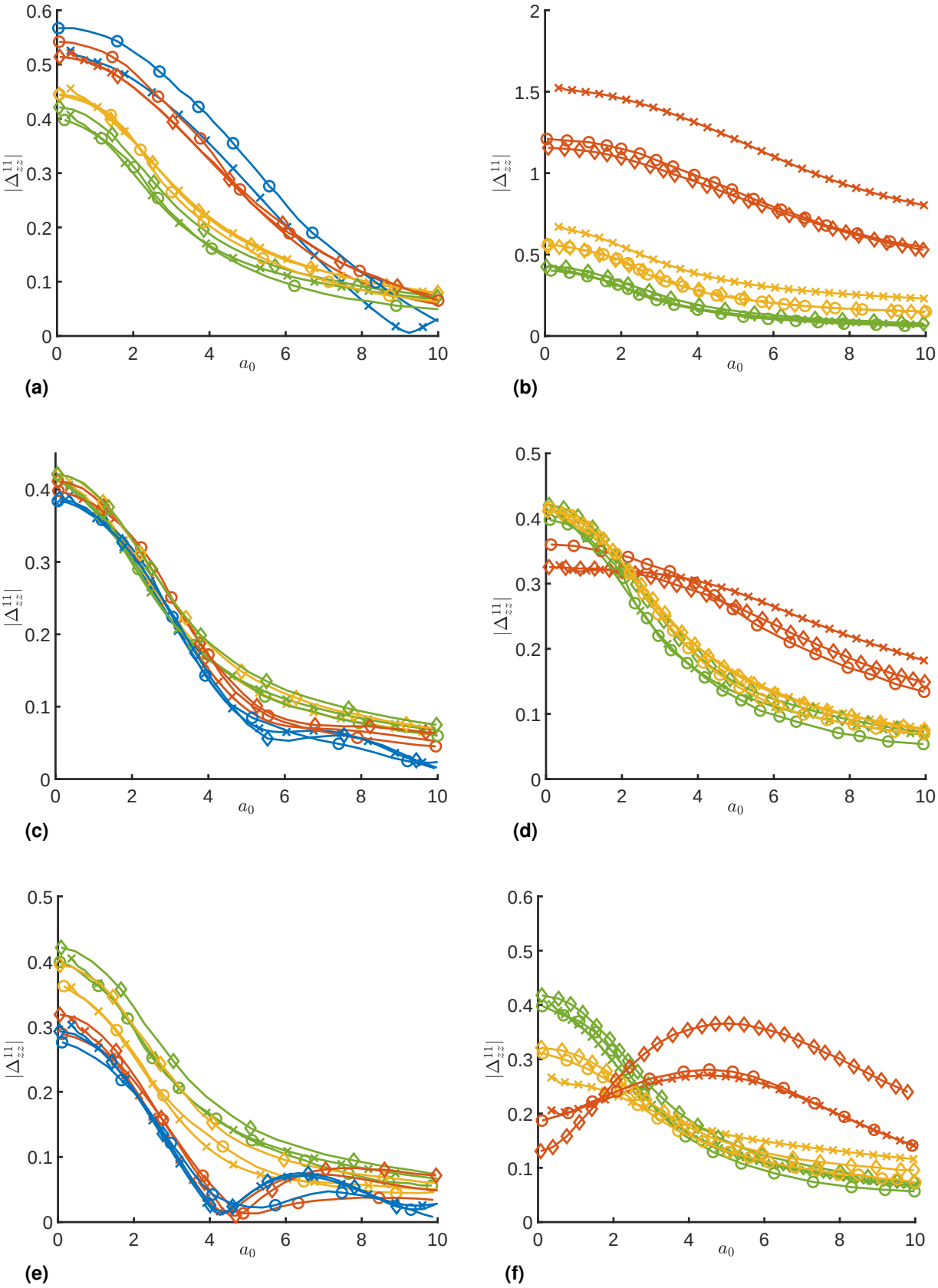

Figure 6.48: $|\Delta_{zz}(a_0)|$ of a flexible, massless square foundation subjected to a uniform load (left) and point load (right) evaluated at the (a),(b) center, (c),(d) edge and (e),(f) corner for the stiffness ratios $K = 0.001$ (—), $K = 0.004$ (—), $K = 0.06$ (—) and $K = 3.33$ (—) obtained with the ITM-FEM approach (X) and the results of Hirschauer [68] (◊) and Whittaker and Christiano [60] (○).

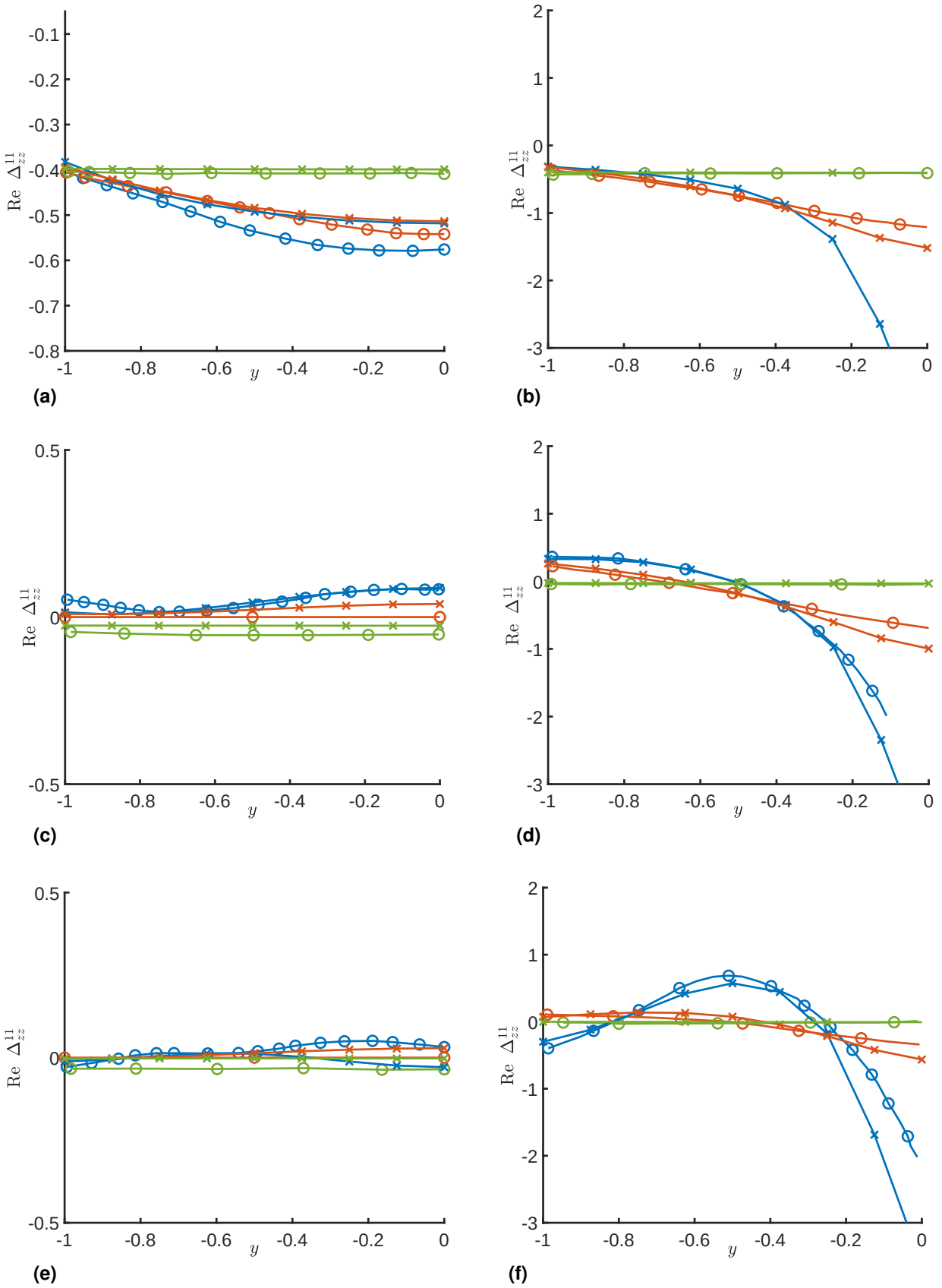

Figure 6.49: $|\Delta_{zz}(y)|$ at $x = 0$ of a flexible, massless square foundation subjected to a uniform load (left) and point load (right) evaluated for (a),(b) $a_0 = 0$, (c),(d) $a_0 = 5$ and (e),(f) $a_0 = 10$ for the stiffness ratios $K \approx 0.00$ (—), $K = 0.004$ (—) and $K = 3.33$ (—) obtained with the ITM-FEM approach (X) and the results of Whittaker and Christiano [60] (○).

A rather large stiffness is needed to avoid displacement and stress concentration under the load point and to distribute the contact stresses over the soil foundation interface. Thus, for very stiff foundations the displacement distribution for point and uniform load are almost equal, as can be seen in Fig. 6.49e,f. For both, the frequency responses in Fig. 6.48 and the displacement distributions in Fig. 6.49, the results obtained with the coupled ITM-FEM approach are in very good accordance to the results reported by Whittaker and Christiano [60] and Hirschauer [68].

Compliances of rigid foundations with mass

The effect of adding mass to a rigid foundation subjected to uniform pressure and resting on a halfspace (Soil D) is shown in Fig. 6.50. The vertical compliance at the soil-foundation interface $z = 0$ was calculated for varying mass ratios M (Eq. (6.10)) and loss factors η_s, characterising the material damping of the soil, using three different approaches.

Within the coupled FEM-BEM approach developed in Taddei [295] it is possible to use Greens functions based on the TLM with and without material damping for the fundamental solution of the soil subsystem, thereby allowing a direct comparison to the ITM-FEM results, for which the incorporation of material damping is indispensable due to numerical reasons. Additionally, an equivalent SDOF model based on Vrettos [297] was implemented which uses the dimensionless, frequency dependent stiffness and damping coefficients k_{zz} and c_{zz} for a rigid, massless rectangular foundation on homogeneous soil as presented e.g. in Gazetas [123] or Sarfeld [66]. Since the damping values c_{zz} only include the geometrical/radiation damping due to the energy dispersion linked with the expansion of the elastic waves in the halfspace, material damping is incorporated by means of the correspondence principle introducing a complex shear modulus G_s, finally leading to the complex stiffness

$$\bar{S}_{zz} = \frac{\bar{P}_z}{\bar{u}_z} = K_{0,zz}\left[k_{zz}(a_0') + \mathrm{i}a_0'\, c_{zz}(a_0')\right](1 + 2\mathrm{i}\,\mathrm{sign}(\omega)\,\zeta) \tag{6.13}$$

with $a_0' = a_0/(1 + \mathrm{i}\zeta)$ for $\zeta \ll 1$, the absolute value of the external load $|\bar{\mathbf{P}}_{\mathrm{sys}}| = \bar{P}_z$ and the static stiffness of a rigid rectangular foundation according to Pais and Kausel [298]

$$K_{0,zz} = \frac{\mathrm{Re}\, G_s\,(L_f/2)}{1-\nu_s}\left[3.1\,(B_f/L_f)^{0.75} + 1.6\right] \tag{6.14}$$

Therewith, the complex displacement of the foundation $\bar{u}_z$ can be computed as

$$\bar{u}_z = \frac{\bar{P}_z}{\mathrm{Re}\,\bar{S}_{zz} + \mathrm{i}\,\mathrm{Im}\,\bar{S}_{zz} - m_f\omega^2}$$

For all results depicted in Fig. 6.50, the typical shift of the resonance peak towards lower frequencies with simultaneously increasing amplitude $|C_{zz}^{11}|$ is clearly observed as well as the dominating effect of the inertia at limiting high frequencies. However, especially for the peak values rather large deviations exhibit between the results for $\eta_s = 0$ and $\eta_s = 0.05$, showing the strong influence of the hysteretic material damping on the system response at the resonance frequency of the foundation on the underlying soil. Furthermore, a very good agreement of the FEM-BEM solution, the equivalent SDOF model and the ITM-FEM approach for $\eta_s = 0.05$ is evident, thus ensuring an accurate representation of the mass and inertia properties of the foundation in the presented method.

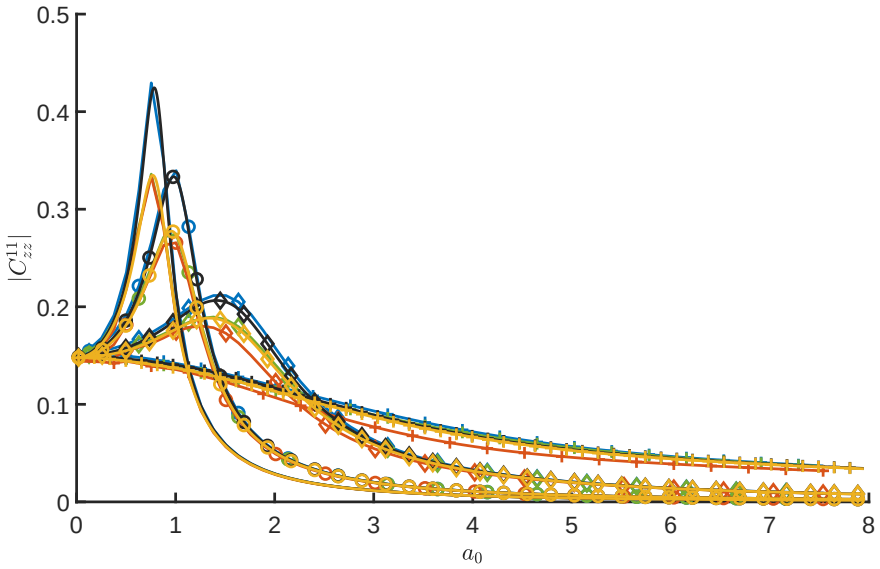

Figure 6.50: Compliance $|C_{zz}^{11}(a_0)|$ for rigid plate on homogenous halfspace (Soil D) computed with FEM-BEM approach of Taddei [295] for $\eta_s = 0$ (—) and $\eta_s = 0.05$ (—), the equivalent SDOF system corr. to Vrettos [297] for $\eta_s = 0$ (—) and $\eta_s = 0.05$ (—) and the ITM-FEM approach (—) with $\eta_s = 0.05$ for mass ratios $M = 0$ (+), $M = 1$ (⋄), $M = 3$ (∘) and $M = 5$ (−).

Power input and radiation characteristics

Next, an investigation of the frequency dependent power transmission $\mathcal{P}_{\text{in}}(\omega)$ at the contact area of a rigid or flexible massless foundation to the soil, as introduced in Sec. 5.4.3, is presented. The introduced power is calculated from the nodal velocities $\bar{\mathbf{v}}_\mathbf{c}$ and forces $\bar{\mathbf{P}}_\mathbf{c}$ at the interface (Eq. (5.54)) due to an unit harmonic uniform pressure, point load or rocking moment on the foundation. As relaxed boundary conditions are assumed, no in plane contact forces occur and only the vertical velocities need to be taken into account for the calculation of the transmitted power. Since with increasing frequency, the dimensions of the foundation get large compared to the wavelengths of the elastic waves in the soil, a strong directivity

in the excited wave field occurs. If a rigid plate is excited at high frequencies, the particles cannot elude sideways and the particle velocity in the elastic medium has to be equal to the velocity of the plate even outside the immediate vicinity of the radiating surface [287]. In the limit case of a plate with infinite extent only compressional waves perpendicular to the surface are radiated and the radiated power can be calculated as [287]

$$\mathcal{P}_{c_p} = \frac{1}{2}\rho_s c_p \bar{v}_{zz,0}^2 A = \frac{1}{2}\frac{\bar{p}_{zz,0}^2}{\rho_s c_p} A \tag{6.15}$$

The power transmission at the contact surface of the finite foundation to the soil $\mathcal{P}_{\text{in}}$ is therefore normalized by the power input $\mathcal{P}_{c_p}$ obtained for an uniformly loaded halfspace within an area $A = B_f^2$ due to a pressure with amplitude $\bar{p}_{zz,0} = 1/A$ or the resulting velocities $\bar{v}_{zz,0}$.

In Fig. 6.51 the total normalized power input converges to $\mathcal{P}_{\text{in}}/\mathcal{P}_{c_p} = 0.9$ relatively fast for the stiff foundations ($K = 0.06, 1000$), indicating that a large part of the introduced energy is radiated into the soil by plane waves propagating mainly in vertical direction. Due to the finite dimensions of the plate, additionally surface waves are excited in any case as well as plane waves with non vertical direction are introduced at the edges of the plate.

The reasonability of the asymptotic approximation of the power input at the soil foundation interface for rigid foundations, resulting from the ITM-FEM approach, can also be confirmed

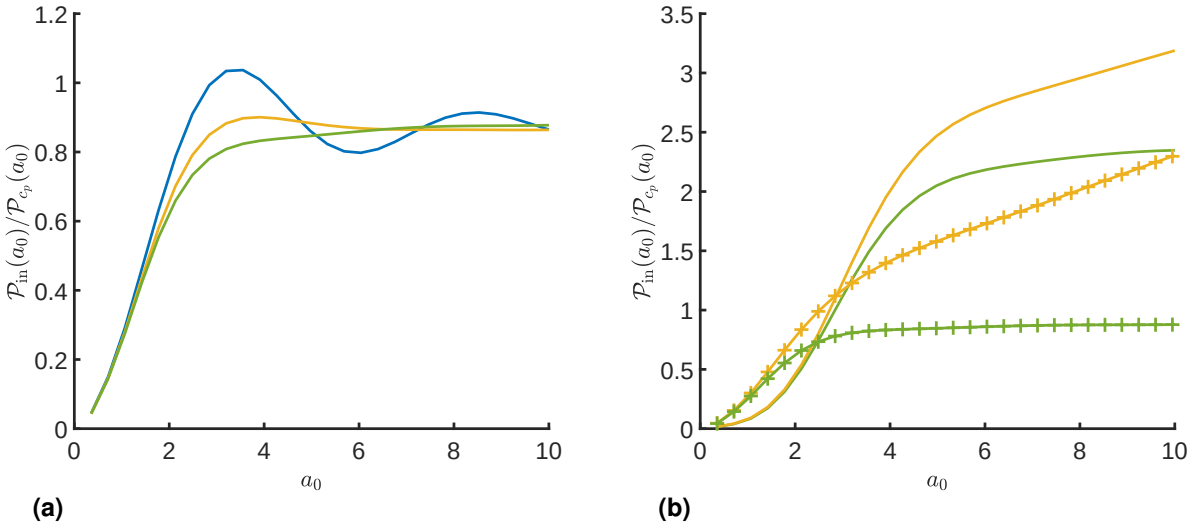

Figure 6.51: Normalized power input at the soil foundation interface $\mathcal{P}_{\text{in}}(a_0)/\mathcal{P}_{c_p}(a_0)$ for massless foundation with $K = 0.0001$ (—), $K = 0.06$ (—) and $K = 1000$ (—) on homogeneous halfspace (Soil A) subjected to (a) uniform pressure, (b) point load (+) and rocking moment (−).

by a theoretical consideration using the soil impedances of Gazetas [299]

$$\bar{Z}_{zz}(\omega) = \frac{\bar{P}_z}{\bar{v}_z} = K_{0,zz}\left(\frac{k_{zz}}{\mathrm{i}\omega} + \frac{B_f}{c_s}c_{zz}\right)(1 + 2\mathrm{i}\zeta) \tag{6.16}$$

which can be derived from Eq. (6.13) replacing $\bar{u}_z$ by the velocity $\bar{v}_z = \mathrm{i}\omega\bar{u}_z$. The stiffness related term in Eq. (6.16) converges to zero for high frequencies, whereas c_{zz} remains nearly constant and thus dominates the impedance. Therefore, assuming a constant external force $|\bar{\mathbf{P}}_{\mathrm{sys}}| = \bar{P}_z$, the velocity $\bar{v}_z$ approaches a constant value, too. Since, for the rigid foundation it yields $\sum_i |\bar{P}_{c,i}| = |\bar{P}_z|$ with $i = 1...n_f$ and $\bar{\mathbf{v}}_\mathbf{c}$ is constant over the area of the foundation, also the power $\mathcal{P}_{\mathrm{in}} \sim \bar{\mathbf{P}}_\mathbf{c} \cdot \bar{\mathbf{v}}_\mathbf{c}^*$ needs to tend to a constant value at high frequencies.

For the flexible plate ($K = 0.0001$) in Fig. 6.51a some oscillations in $\mathcal{P}_{\mathrm{in}}(a_0)$ occur, which nevertheless approaches to a constant value for high frequencies. The oscillations can be attributed to different bending deflection distributions at the contact surface having a different ability to excite elastic waves and thus to radiate energy into the soil. In case of a point load on a rigid foundation, the power input is equal as for the uniform pressure due to the load distribution effect of the plate. Since a relatively high stiffness is required to achieve this effect, for less stiff plates a concentration of the displacements under the point of load application can be observed, which then dominates the system response under the foundation. This, in combination with an only small increase of the soil resistance for a localized load, leads to velocities and a power input increasing with frequency (Fig. 6.51b) The rocking moment is applied as a couple of point forces pointing in opposite direction and located on the plate mid-axis at $x = 0$, resulting in an moment with unit amplitude. Therefore, the same general characteristics can be observed as in case of the point load (Fig. 6.51b). For the point load and the rocking moment only $K = 0.06$ and $K = 1000$ are evaluated, since for soft plates the singularity in the displacement response under the point load leads to no reasonable results for the power transmission.

The above presented results are also consistent with the results of the more detailed analysis of the wave fields in the ground as well as the wavenumber spectra of the surface displacements and the power input, gained from the computationally rather expensive postprocessing procedure. Therein the displacements on the ground surface and within the complete soil domain are determined in the wavenumber frequency domain and thus their wavenumber spectra can be used to deduce characteristic features of the system response that will confirm the findings stated before. For this purpose, a flexible foundation ($K = 0.0001$) resting on a homogeneous halfspace (Soil A) was excited harmonically with an uniform pressure at $f = 18, 34, 58$ Hz, corr. to the first maximum and the two following minima of the power

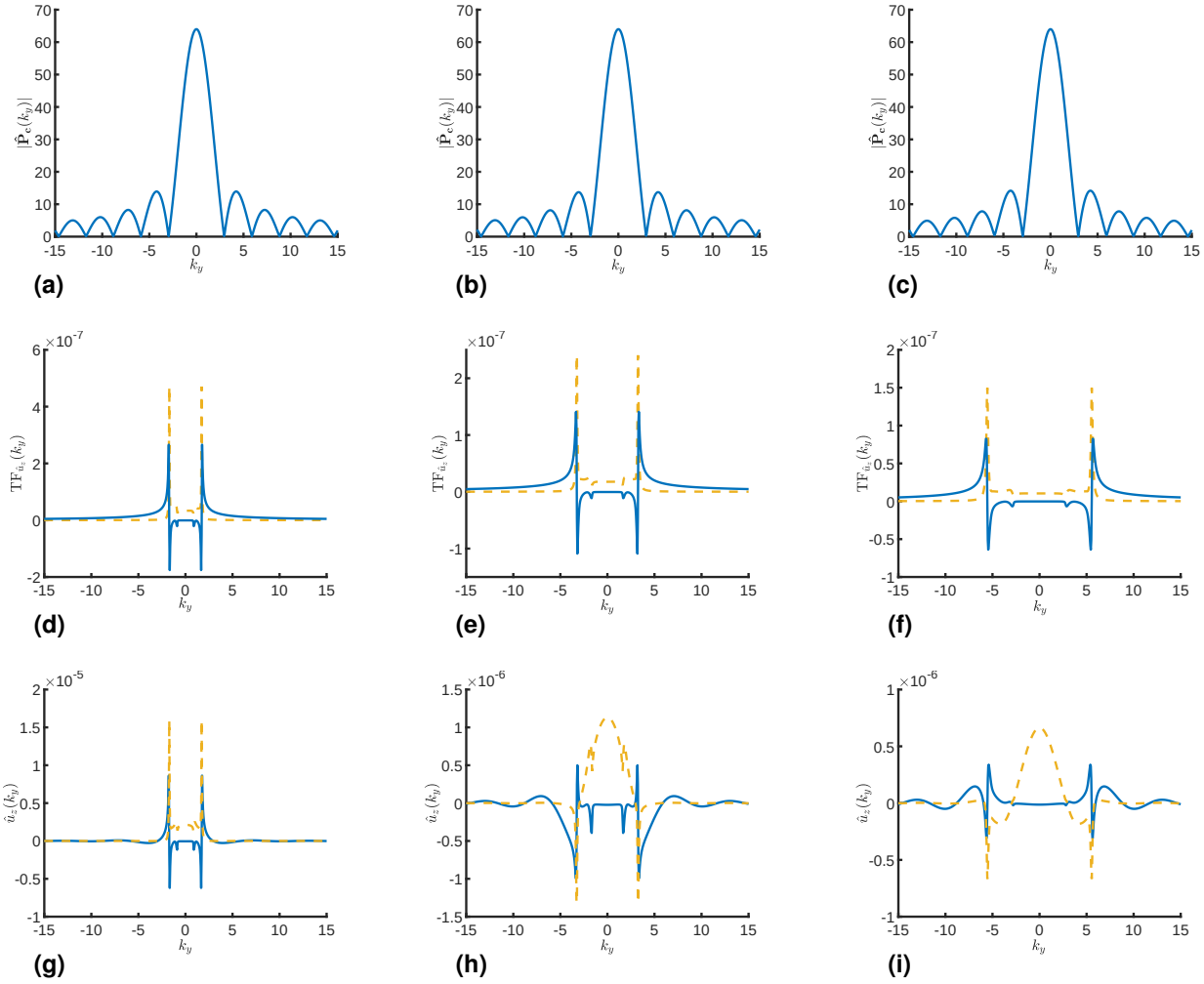

Figure 6.52: Wavenumber spectrum of (a)-(c) the contact forces $|\hat{\mathbf{P}}_\mathbf{c}(k_y)|$, real (—) and imaginary part (– –) of (d)-(f) the transfer function $\mathrm{TF}_{\hat{u}_z}(k_y)$ (g)-(i) vertical displacements $\hat{u}_z(k_y)$ at the ground surface $z = 0$ for a soft foundation $(K = 0.0001)$ subjected to uniform pressure resting on homogeneous halfspace (Soil A) for $f = 18$ Hz (left column), $f = 34$ Hz (middle colum) and $f = 58$ Hz (right column).

input in Fig. 6.51a. Due to the finite dimension of the foundation, the wavenumber spectra of the contact forces $|\hat{\mathbf{P}}_\mathbf{c}(k_y)|$ at $k_x = 0$, shown in Figs. 6.52a-c, do not show a single non-zero value at $k_y = 0$, as it would be the case for an infinite plate, but exhibit side lobes along with the main peak around $k_y = 0$. The ground substructure is therefore excited over the entire wavenumber range.

Scaling the transfer functions $\mathrm{TF}_{\hat{u}_z}(k_y)$ in Figs. 6.52d-f, defined as the system response due to a unit load over all k_x and k_y, with the amplitudes of the contact forces $|\hat{\mathbf{P}}_\mathbf{c}(k_y)|$, one obtains the wavenumber spectra of vertical displacements $\hat{u}_z(k_y)$ at the ground surface, illustrated in Figs. 6.52g-i. The wavenumber axis are not normalized with respect to e.g. the shear wavenumber k_s, to illustrate the frequency dependent behaviour of $\mathrm{TF}_{\hat{u}_z}(k_y)$. For all cases

k (rad m^{-1})	$f = 18$ (Hz)	$f = 34$ (Hz)	$f = 58$ (Hz)
k_p	0.85	1.61	2.75
k_s	1.59	3.02	5.15
k_r	1.72	3.25	5.54

Table 6.14: Wavenumbers of P-, S- and R-wave in a halfspace (Soil A) for selected frequencies.

$\hat{u}_z(k_y)$ shows considerable peaks at $k_i = \omega/c_i$ (with $i = p,s,r$), which are listed in Tab. 6.14 and can be attributed to the P-, S- and the Rayleigh wave (R-wave), shifting to higher k_y with increasing frequency. However, $|\hat{\mathbf{P}}_\mathbf{c}(k_y)|$ remains almost unchanged with frequency, so that in all cases the same wavenumber range is amplified by the major lobe of $|\hat{\mathbf{P}}_\mathbf{c}(k_y)|$, but the peaks in $\mathrm{TF}_{\hat{u}_z}(k_y)$ are scaled more or less strongly depending on the frequency considered. This results in rather large amplitudes of $\hat{u}_z(k_y)$ at $k_y = \pm k_r$ at $f = 18$ Hz in Fig. 6.52g, indicating a significant contribution of the Rayleigh wave to the overall response. In contrast, at $f = 34$ Hz and $f = 58$ Hz the smaller wavenumbers $k < k_r$ are more strongly amplified by the main peak of $|\hat{\mathbf{P}}_\mathbf{c}(k_y)|$ leading to a increasing share of the long wave components, while the Rayleigh wave provides a smaller relative contribution. This is accompanied by an ever stronger radiation of plane elastic waves perpendicular to the foundation surface, as the radiation angle w.r.t. the ground surface is given by $\sin\alpha_i = c_i k/\omega$ (with $i = p,s,r$). The increase in the radiation directivity is clearly visible in Fig. 6.53, showing the real part of the vertical displacements over the depth. However, due to the finite dimension of the foundation all wavenumbers are excited in any case and thus also plane elastic waves with different angles $\alpha \neq 0°$. Furthermore, considerable oscillations at the ground surface can be observed, which can be attributed to the waves belonging to $k \geq k_r$ in the wavenumber spectra $\hat{u}_z(k_y)$ in Fig. 6.52g-i.

The observations made for $\hat{u}_z(k_y)$ also apply for the wavenumber spectrum of the power

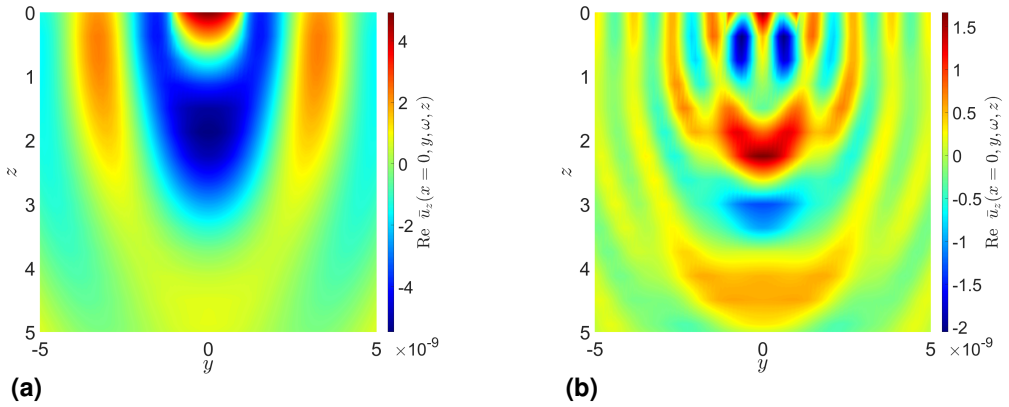

Figure 6.53: Vertical displacement $\bar{u}_z(x = 0,y,z,\omega)$ over depth for a soft foundation $(K = 0.0001)$ subjected to uniform pressure resting on homogeneous halfspace (Soil A) for (a) $f = 18$ Hz and (b) $f = 58$ Hz. [51]

input $\mathcal{P}_{\text{in}}(k_y)$ for a soft foundation ($K = 0.0001$) subjected to uniform pressure, depicted in Fig. 6.54. At $f = 18$ Hz significant peaks occur at $\pm k_r = \pm\omega/c_r$, implying a large contribution of the Rayleigh wave to the total power input. For $f = 34$ and 58 Hz only smaller peaks are observed for $\mathcal{P}_{\text{in}}(k_y = \pm k_r)$, whereas with increasing frequency the wave number spectrum with the major power input becomes increasingly narrow-banded. Thus the involvement of the long wave components with small radiation angles w.r.t. the ground surface increases, whereas the Rayleigh wave provides a smaller relative contribution. In general only very small values of $\mathcal{P}_{\text{in}}(k_y)$ appear for $|k| > |k_r|$, resulting in a negligible proportion of the total power input from the short wave surface wave components corresponding to high wave numbers. [51]

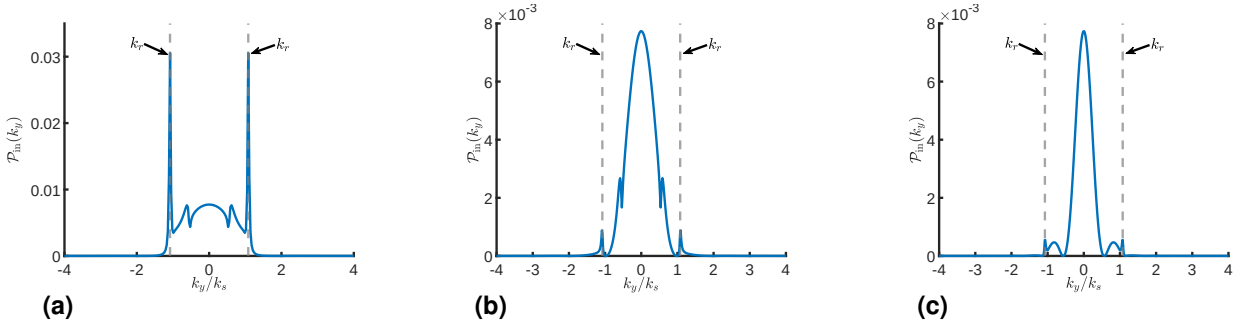

Figure 6.54: Power input at soil foundation interface $\mathcal{P}_{\text{in}}(k_y)$ at $k_x = 0$ for soft foundation ($K = 0.0001$) subjected to uniform pressure resting on homogeneous halfspace (Soil A) for (a) $f = 18$ Hz, (b) $f = 34$ Hz and (c) $f = 58$ Hz. [51]

Energy distribution under surface foundations of different size

In the previous section, the radiation directivity as well as the contributions of the body and the surface waves to the total response were shown to depend mainly on the considered frequency and the dimension of the foundation w.r.t. the wave lengths in the soil. The conclusions drawn from the investigation of the wavenumber spectra of the surface displacements and power input at the soil foundation interface can be confirmed and interpreted in more detail by analysing the power flow through a control volume (cp. Sec. 5.4.2). However, it has to be noted that, since the ratios of the power fluxes depend on the choice of the control volume, the results only give an insight into the power distribution for the chosen CV. Nevertheless, the procedure offers a good possibility to get an idea of the energy distribution inside the ground and the radiation characteristics.

For this purpose two rigid ($K = 1000$) massless ($M = 0$) foundations with different width $B_f = 2$ m and $B_f = 8$ m subjected to an unit uniform pressure and resting on a homogenous halfspace (Soil A) but with $\zeta_s = 0.01$ are considered. The halfspace was discretized with $N_x = N_y = 2^{10}$ and $N_z = 2^6$ sample points up to $B_z = 8$ m with $\mathrm{d}z = 0.125$ m. For the power flux analysis a control volume with $l_{\text{cv}} = b_{\text{cv}} = 8$ m and $h_{\text{cv}} = 2$ m was defined equally for both foundations as depicted in Fig. 6.55.

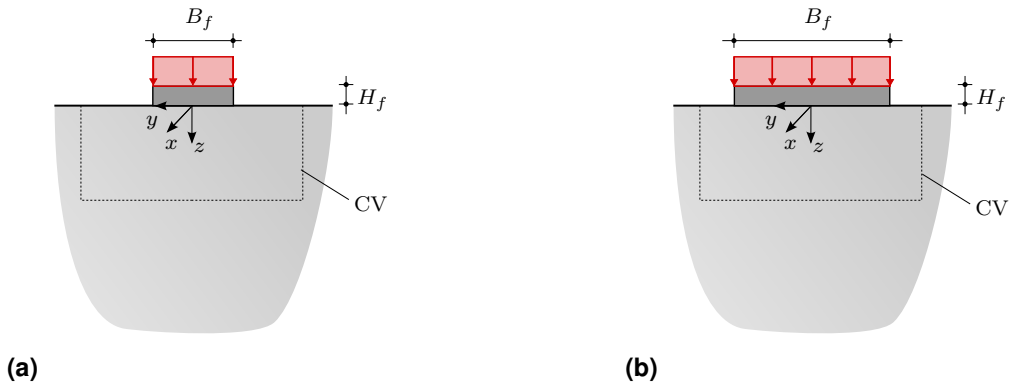

Figure 6.55: Setup for power flux analysis of rigid foundations with different size.

Fig. 6.56 shows the ratio of the power flows through all side areas $\mathcal{P}_{s_{1-4}}$ resp. the bottom surface $\mathcal{P}_{s_5}$ and the total power flow through the control volume $\mathcal{P}_{\text{tot,CV}}$ as defined in Eqs. (5.53) for both foundation sizes at selected frequencies. Furthermore, the portions of the power flows corresponding to the normal as well as horizontal and vertical shear stresses at the respective surfaces are given in Fig. 6.57. In case of the large foundation with $B_f = 8$ m the overall power flow in the control volume is dominated by the power passing through the bottom surface already in the low frequency range, indicating that a large portion of the introduced energy is radiated into the soil via plane elastic waves propagating in vertical direction. Moreover, Fig. 6.57b shows, that the largest part of $\mathcal{P}_{s_5}$ can be attributed to the power through the bottom surface due to normal stresses $\mathcal{P}_{s_5,n}$, which further increases with rising frequency and converges to a constant value of approx. 90%. In contrast the portion of the power due to the in plane shear stresses $\mathcal{P}_{s_5,sh}$ is very low over the entire frequency range. The dominating radiation of compressional waves propagating perpendicular to the

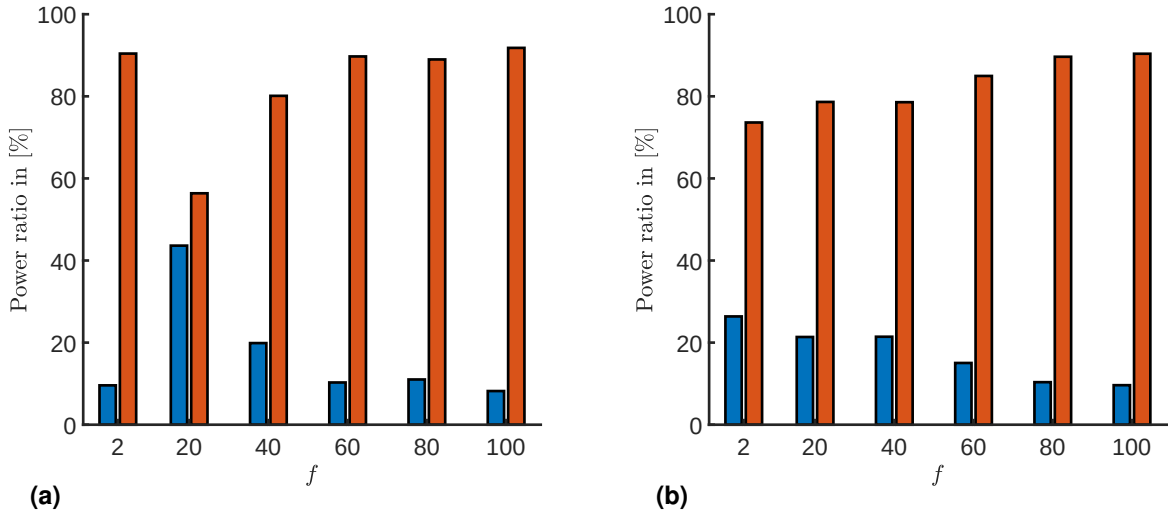

Figure 6.56: Power flow through side areas $\mathcal{P}_{s_{1-4}}$ (—) and bottom surface $\mathcal{P}_{s_5}$ (—) in relation to the power flow through the total control volume $\mathcal{P}_{\text{tot,CV}}$ for the foundation with $B_f = 2$ m (left) and $B_f = 8$ m (right).

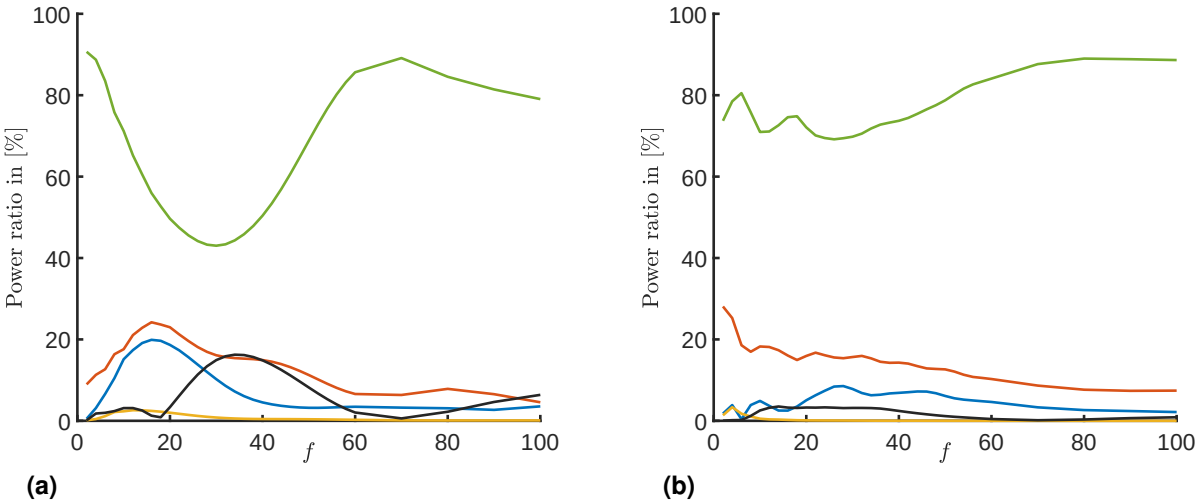

Figure 6.57: Ratios of power flux due to normal stresses $\mathcal{P}_{s_{1-4},n}$ (—), vertical $\mathcal{P}_{s_{1-4},sv}$ (—) and horizontal $\mathcal{P}_{s_{1-4},sh}$(—) shear stresses at the side areas as well as normal stresses $\mathcal{P}_{s_5,n}$ (—) and in plane shear stresses $\mathcal{P}_{s_5,sh}$ at the bottom surface (—) to the total power flux $\mathcal{P}_{\mathrm{tot,CV}}$ through the control volume for $B_f = 2$ m (left) and $B_f = 8$ m (right).

foundation and mainly causing normal stresses is also clearly visible in Fig. 6.58b, illustrating the distribution of the vertical displacements within the soil at $f = 80$ Hz.

For the smaller foundation with $B_f = 2$ m a considerable power flow through the side areas can be observed in the lower frequency range. Thereby the increase of $\mathcal{P}_{s_{1-4}}$ between 2 and 40 Hz in Fig. 6.56a correlates with the increase of the portion of the power flow through the side areas due to normal and vertical shear stresses $\mathcal{P}_{s_{1-4},n}$ resp. $\mathcal{P}_{s_{1-4},sv}$ as well as the decrease of $\mathcal{P}_{s_5,n}$ as depicted in Fig. 6.57a. This indicates that a larger share of the introduced power $\mathcal{P}_{\mathrm{in}}$ is radiated horizontally in this frequency range, fitting to the more uniform energy distribution for small ratios of B_f compared to the λ_i in the soil. The opposite yields for the high frequency range $f = 60 - 100$ Hz, where $\mathcal{P}_{s_{1-4},n}$ and $\mathcal{P}_{s_{1-4},sv}$ decrease and $\mathcal{P}_{s_5,n}$ generally increases. This also matches with the total power fluxes through the side and bottom surfaces in Fig. 6.56a. However, also for higher frequencies approximately 10% of the total power flux $\mathcal{P}_{\mathrm{tot,CV}}$ remain with $\mathcal{P}_{s_{1-4},n}$ and $\mathcal{P}_{s_{1-4},sv}$, which can be attributed to Rayleigh surface waves, which are almost always excited and are composed of a particular combination of P and SV waves fulfilling the boundary conditions of the free surface. The largest contribution of $\mathcal{P}_{\mathrm{tot,CV}}$ nevertheless comes from $\mathcal{P}_{s_5,n}$ with ca. 80% corresponding the vertically propagating P-waves (cp. Fig. 6.58a). The power flow associated with the horizontal shear stresses at the side areas $\mathcal{P}_{s_{1-4},sh}$ provides only a very small share over the whole frequency range independent of the foundation size, which is because of the vertical excitation and would change fundamentally in case of a horizontal loading of the foundation.

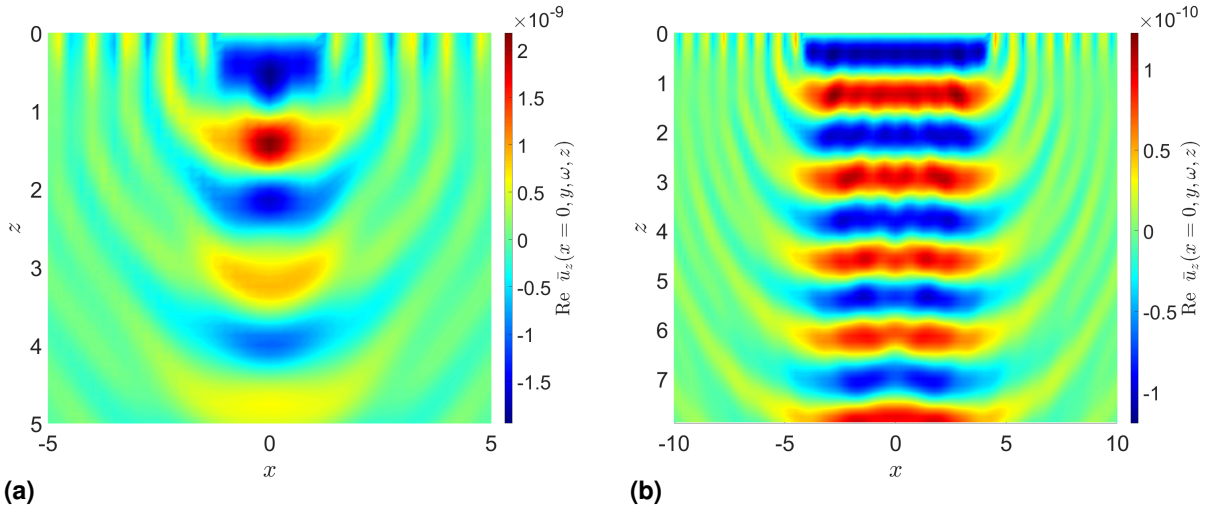

Figure 6.58: Real part of $\bar{u}_z(x = 0, y, z, \omega)$ in a homogenous halfspace under a rigid massless surface foundation with $B_f = 2$ m (left) and $B_f = 8$ m (right) excited uniformly with $f = 80$ Hz.

Intensity reduction with source distance

The power flow analysis can also be applied in order to assess the reduction of the energy density inside the soil with increasing distance or depth as well as to estimate the energy dissipated by the hysteretic material damping. For this purpose, a vertically oscillating energy source, modelled by a spot footing with $B_f = 0.5$ m, on the surface of an elastic halfspace with material parameters of Soil A but very low material damping $\zeta_s = 0.002$ is investigated. Thereby an area of $B_x = B_y = 256$ m and a depth of $B_z = 4$ m has been discretized with $N_x = N_y = 2^{11}$ and $N_z = 2^5$ sample points.

The dispersion of the energy, introduced into the soil by a single radiator at the surface, by means of compressional, shear and surface waves as well as the distribution of energy among the different wave types was analysed in detail by Miller and Pursey [300]. Both, the main wave propagation characteristics and the geometrical damping law for a purely elastic halfspace ($\zeta_s = 0$) are summarized in Fig. 6.59a and Tab. 6.15. P- and S-waves propagate radially into the halfspace outward from the source with wavefronts passing through continuously increasing spherical surfaces, whereas the Rayleigh waves radiate outward on a

Wave type	Energy portion	Energy decay	Amplitude decay	wave velocity
P-wave	7%	$1/r^2$	$1/r$	$c_p = \sqrt{\left(\frac{(2G\cdot\nu)}{(1-2\nu)}+2\cdot G\right)/\rho}$
S-wave	26%	$1/r^2$	$1/r$	$c_s = \sqrt{G/\rho}$
R-wave	67%	$1/r$	$1/\sqrt{r}$	$c_r = c_s(0.87 + 1.12\nu)/(1 + \nu)$

Table 6.15: Energy portions and geometrical damping of elastic waves and corr. wave velocities.

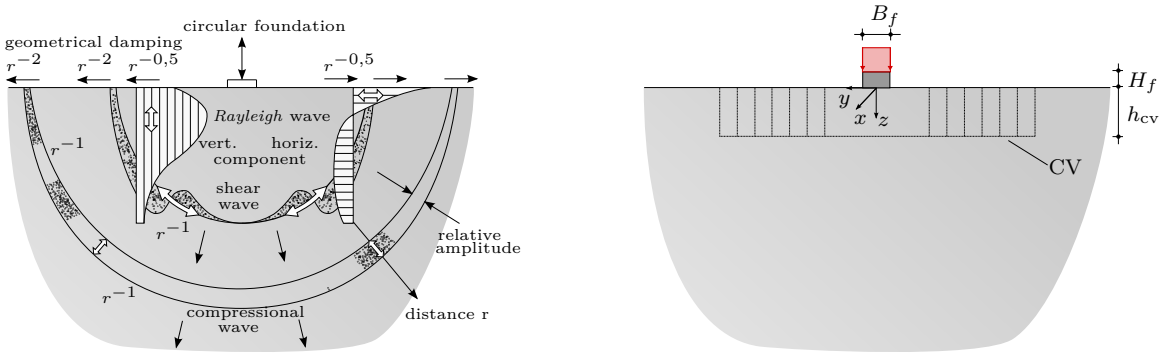

Figure 6.59: (a) Distribution of body and surface waves in the elastic halfspace due to vertical excitation cp. [169]. (b) ITM-FEM model for assessment of intensity decay with power flux analysis.

cylindrical wavefront within a layer of limited thickness of approximately $1.0\lambda_r - 1.5\lambda_r$ [297]. The amplitude of the body waves generally decay with distance by $1/r$, while those of the Rayleigh waves decay with $1/\sqrt{r}$, where r is the distance from the source. However, in the vicinity of the surface the body waves decay stronger $(1/r^2)$, wherefore up from a sufficient distance the vibrations close to the surface are dominated by the Rayleigh waves [169]. Since the energy in a wave is proportional to the square of the amplitude and the radiated energy is constant for $\zeta_s = 0$, the intensity decay (as energy per area) yields $\mathcal{I}(r) = \mathcal{I}_0(r_0) \cdot (r_0/r)$.

This theoretical decay of the intensity is in very good agreement with the intensity reduction $\mathcal{I}(r) = \mathcal{P}_{s_{1-4}}/A_{\mathrm{cv}}(r)$ computed numerically with the ITM-FEM approach as depicted in Fig. 6.60a. Therefore, the power flux through the side areas of several control volumes with constant height $h_{\mathrm{cv}} = \lambda_r \approx 2$ m and varying width $l_{\mathrm{cv}} = b_{\mathrm{cv}} = n_{\mathrm{cv}} \cdot 10\mathrm{m}$ was evaluated at $f = 34$ Hz as depicted in Fig. 6.59b. Integer numbers $n_{\mathrm{cv}} = 1,2,...,10$ where chosen for the control volume (CV) size and $A_{\mathrm{cv}}(r)$ is the total area of the side surfaces of the CV at a specific distance r. The slight deviations in $\mathcal{I}(r)$ are due to the non cylindrical surface of the rectangular control volumes as well as the non zero material damping in the ITM-FEM model. The influence of the material damping is shown in Fig. 6.60b, illustrating the ratio of the total power flow through the control volume to the introduced power at the soil foundation interface. Due to the very small damping ratio $\zeta_s = 0.002$ for CV_1 with $l_{\mathrm{cv}} = b_{\mathrm{cv}} = 10$ m the ratio $\mathcal{P}_{\mathrm{tot,CV}}/\mathcal{P}_{\mathrm{in}}$ results to $\approx 99\%$ meaning that nearly no energy is taken out of the system due to material damping. However, for the large CV_8 with $l_{\mathrm{cv}} = b_{\mathrm{cv}} = 80$ m the ratio only yields $\approx 77\%$ and thus nearly 23% of the introduced energy is dissipated.

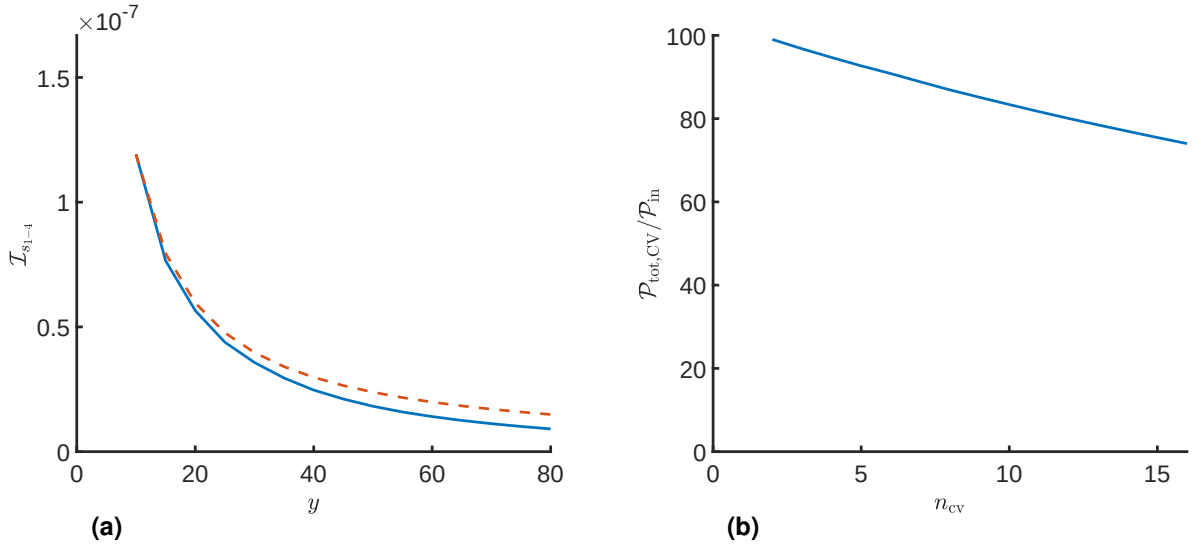

Figure 6.60: (a) Intensity decay $\mathcal{I}(r) = \mathcal{P}_{s_{1-4}}/A_{\mathrm{cv}}(r)$ resulting from ITM-FEM model for CVs with increasing width and constant depth $h_{\mathrm{cv}} = \lambda_r$ (—) and theoretical decay $I(r) = I_0 \cdot \frac{r_0}{r}$ (– –). (b) Ratio of total power flux through CV to input power $\mathcal{P}_{\mathrm{tot,CV}}/\mathcal{P}_{\mathrm{in}}$.

The power flux analysis can further be used to asses the energy distribution inside the soil with increasing depth and thus allows e.g. to estimate the effectivity of vibration mitigation measures in the transmission path. In order to confirm the accuracy of the method, it is applied in the following to estimate the energy reduction due to an completely reflective wave barrier of varying depth d_{tr} and the results are compared to those obtained by Dolling [168] analytically for an open trench (cp. Fig. 6.61a). Therefore, the power flow through the side areas $\mathcal{P}_{s_{1-4}}$ of a control volume with $l_{\mathrm{cv}} = b_{\mathrm{cv}} = 48$ m and $h_{\mathrm{cv}} = n_{\mathrm{cv}} \cdot 0.25$ m inside a halfspace with $B_x = B_y = 64$ m was computed up to depth of $B_z = 8$ m, whereby $N_x = N_y = 2^{10}$ and $N_z = 2^6$ sampling points were used. The material parameters of Soil A were used, however with $\nu = 0.33$ and $\eta = 0.01$ to be able to compare the results with [168].

Dolling [168] assumed for his analytical approach that the open trench is located at great distance from the source so that body waves are negligible and only the Rayleigh surface wave needs to be considered. Therefore, also the CV was chosen sufficiently large to satisfy this assumption, although with the power flux analysis also the energy of the body waves could easily be included in the investigation. The ITM-FEM model was evaluated for a vertically loaded foundation with $B_f = 0.25$ m resembling a point source for $f = 33$ Hz, resulting in a penetration depth of the Rayleigh wave of $\lambda_r \approx 2$ m. Analogously to [168], the energy decay over the depth z normalized by λ_r within one period was computed using control volumes with different heights h_{cv}, resembling different depth of the open trench (cp. Fig. 6.61b), as $E_r = \mathcal{P}_{s_{1-4}}(h_{\mathrm{cv}} = d_{\mathrm{tr}})/\mathcal{P}_{s_{1-4}}(h_{\mathrm{cv}} = 3\lambda_r)$. Thereby it is assumed that in a depth of $h_{\mathrm{cv}} = 3\lambda_r$ the energy of the Rayleigh wave is negligible and thus $\mathcal{P}_{s_{1-4}}(h_{\mathrm{cv}} = 3\lambda_r)$ includes the total energy of the surface waves.

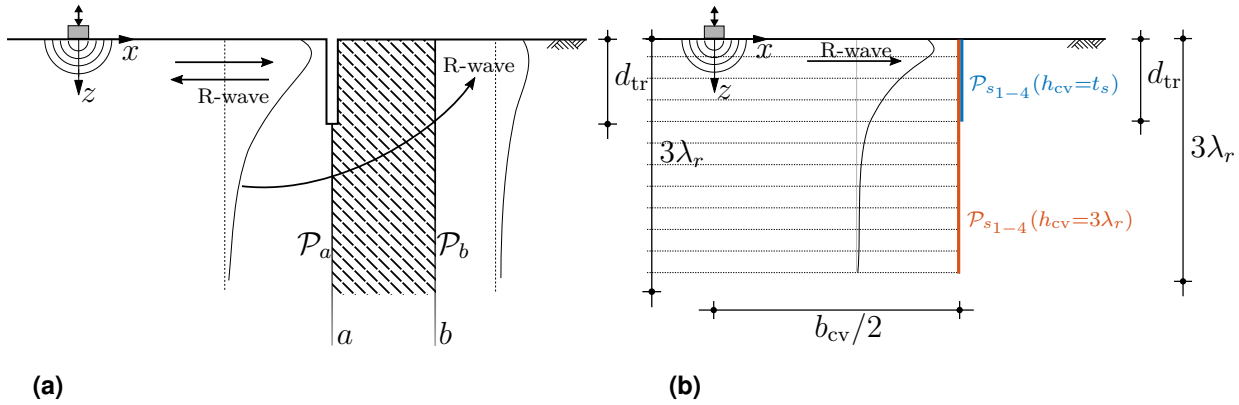

Figure 6.61: (a) Model for estimation vibration mitigation by an open trench in the transmission path in Dolling [168]. (b) Setup for assessment of energy distribution over depth by means of the power flux analysis with ITM-FEM approach.

The energy decay E_r depicted in Fig. 6.62a shows good agreement with the results of Dolling [168]. The slightly smaller E_r obtained with the ITM-FEM approach for larger depth d_{tr} is most likely due to the assumption of $\mathcal{P}_{s_{1-4}}(h_{\mathrm{cv}} = 3\lambda_r)$ as reference value, whereas Dolling [168] uses the integral over the intensity from the soil surface up to infinity for this. Fig. 6.62b shows the energy portions of the surface wave in steps of $\Delta h_{\mathrm{cv}} = 0.25$ m in relation to the total energy of the surface wave, thereby confirming the statement of Dolling [168] that the main part of the energy is contained up to a depth of $h_{\mathrm{cv}} \approx \lambda_r$.

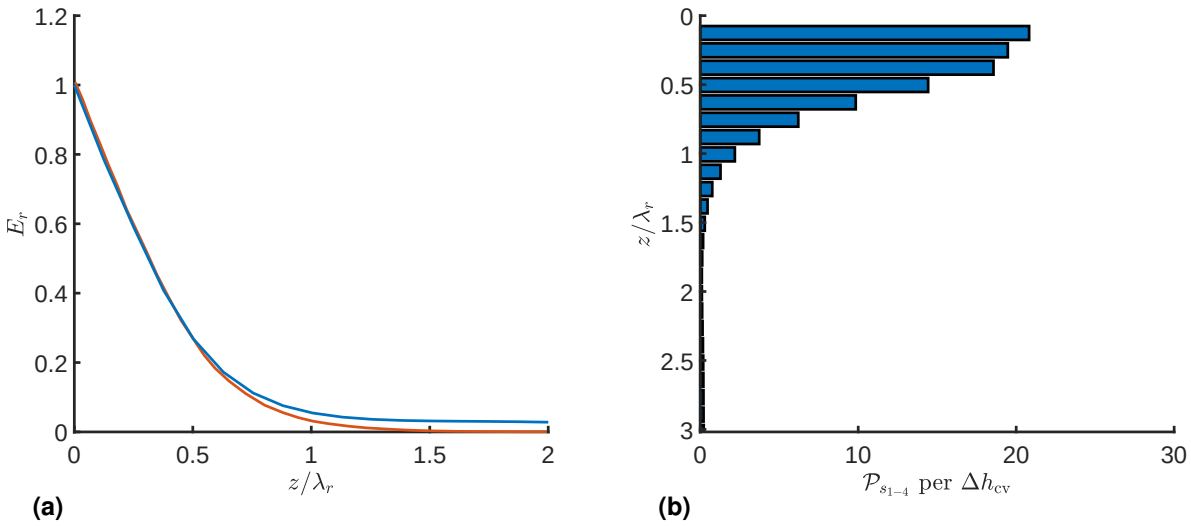

Figure 6.62: (a) Comparison of energy decay E_r for ITM-FEM approach (—) and Dolling [168] (—). (b) Portions of power flow through side areas per $\Delta h_{\mathrm{cv}} = 0.25$ m w.r.t. $\mathcal{P}_{s_{1-4}}(h_{\mathrm{cv}} = 3\lambda_r)$.

6.3.2 Foundation on a layered halfspace

Hereinafter, the characteristic effects of a soil layering on the dynamic foundation response are described. Therein the main influencing parameters are given by the ratio of the elastic properties of the layer and the underlying halfspace as well as the relation between the layer thickness and the foundation width h_1/B_f [26]. [51]

Foundation compliances

In Fig. 6.63 the absolute value of $C_{zz}^{11}(a_0)$ for a rigid, massless foundation resting on a stratified soil with different ratios h_1/B_f is depicted. For $h_1/B_f = 0$, corresponding to a homogeneous halfspace of Soil B, and $h_1/B_f = \infty$, corresponding to a halfspace of Soil A, the vertical compliance decreases monotonically with increasing a_0. In contrast for the layered halfspace, fluctuations with significant peaks occur in C_{zz}^{11} over the frequency. These can be associated with propagating surface waves and layer resonances, occurring due to interference effects of the waves reflected at the interface of the two different materials and the primary waves. The resonance frequencies of the considered layered halfspace with $c_{s1}/c_{s2} = 0.5$ are rather close to the eigenfrequencies of an elastic soil layer over bedrock. According to Kobori et al. [301], the latter are equal to the vertical and horizontal natural frequencies of

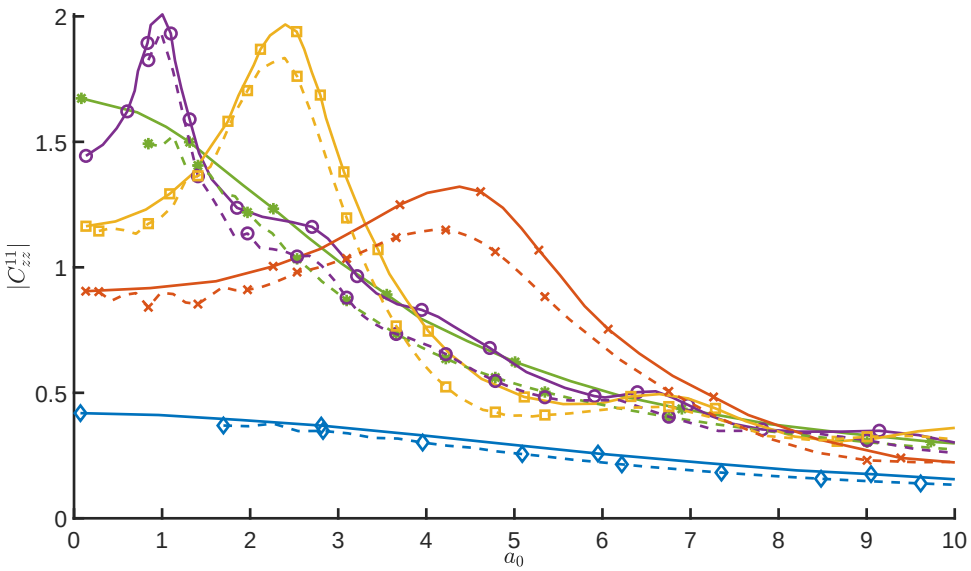

Figure 6.63: Vertical compliance of rigid, massless foundation resting on layered halfspace ($c_{s1}/c_{s2} = 0.5$) for different ratios $h_1/B_f = 0$ (–◇–), $h_1/B_f = 0.5$ (–×–), $h_1/B_f = 1$ (–□–), $h_1/B_f = 2.5$ (– ○ –) and $h_1/B_f = \infty$ (– ∗ –) obtained with ITM-FEM approach (– –) and the results of Hirschauer (—) [51].

an undamped one-dimensional rod of length h_1 and are given as in [51]

$$f_{\text{res,v}} = \frac{2m+1}{4h_1}\sqrt{\frac{(1-\nu_s)E_s}{\rho(1+\nu_s)(1-2\nu_s)}} \quad \text{and} \quad f_{\text{res,h}} = \frac{2m+1}{4h_1}\sqrt{\frac{\mu_s}{\rho}} \quad \text{with } m = 0,1,2,... \tag{6.17}$$

For the material parameters of the upper soil layer (Soil A) and $h_1/B_f = 1$ the first two resonance frequencies result in $f_{\text{res,v}} = 16.54$ and 49.62 Hz resp. $a_{0\,\text{res,v}} = 2.93$ and 8.81 for the vertical and $f_{\text{res,h}} = 8.83$ and 26.51 Hz resp. $a_{0\,\text{res,h}} = 1.57$ and 4.71 for the horizontal ones. The decrease in $f_{\text{res,v}}$ with increasing layer thickness h_1 can also clearly be observed in Fig. 6.63. Furthermore, comparing the results of the present approach with those of Hirschauer [68], a very good agreement can be found. [51]

Power input and radiation characteristics

As observed for the foundation flexibilities, the frequency dependent power input at the soil foundation interface, depicted in Fig. 6.64, also exhibits pronounced maxima in case of the stratified soil. These peaks can again be linked to the layer specific resonance phenomena, since at resonance the amplitudes get maximal and the phase shift between the excitation and the resulting velocities tends to zero resulting in a maximum power input. Due to the dissipative character of the medium and the non rigid boundary at $z = h_1$, the resonance amplitudes remain finite and f_{res} are shifted towards lower frequencies compared to Eq. (6.17). However, the maxima get more distinct and exhibit higher amplitudes if the stiffness of the underlying halfspace is increased. [51]

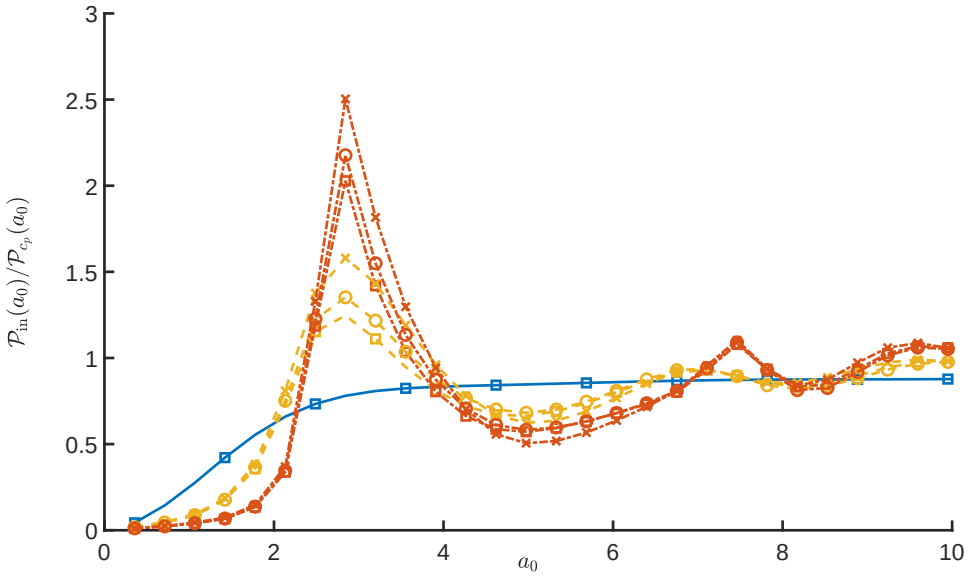

Figure 6.64: Power input $\mathcal{P}_{\text{in}}/\mathcal{P}_{c_p}$ at contact surface of massless foundation under uniform pressure with $K = 0.0001$ (X), $K = 0.06$ (○) and $K = 1000$ (□) on homogeneous halfspace (Soil A) (—) and layered halfspaces with $c_{s1}/c_{s2} = 0.5$ (– –) or $c_{s1}/c_{s2} = 0.25$ (–·–) for $h_1/B_f = 1$. [51]

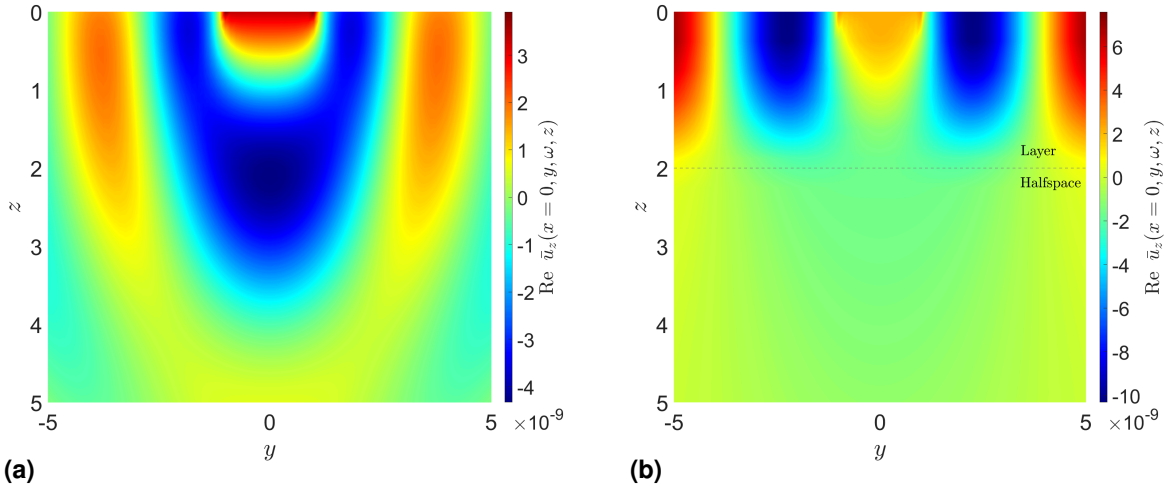

Figure 6.65: Distribution of real part of vertical displacement over depth z at $x = 0$ under a rigid, massless foundation ($K = 1000$) subjected to uniform pressure with $f = 16$ Hz $\approx f_{\mathrm{res,v1}}$ resting on a (a) homogeneous halfspace (Soil A) and (b) soft layer (Soil A) over stiffer halfspace with $c_{s1}/c_{s2} = 0.25$. [51]

Furthermore, Fig. 6.64 shows that the power transmission at the contact area is mainly dependent on the layer resonances and only marginally affected by a change in the foundation stiffness. Consequently, regardless of the stiffness ratio K, for a small difference between the material properties of layer and underlying halfspace, the power input resembles very much that of a homogeneous soil. However, for a large stiffness contrast only a small amount of energy is radiated into the halfspace, since most incoming waves are reflected at the transition surface. This in turn leads to a strong localization of the displacements within the upper layer. The dispersion of energy thus is mainly possible via horizontally propagating surface waves, corresponding to a 2D cylindrical energy radiation [301]. In contrast, the radiated energy in case of the homogeneous halfspace for low frequencies is distributed over a hemispherical volume. This behaviour is clearly visible in Fig. 6.65, which depicts the real part of the displacements $\bar{u}_z(x = 0,y,z,\omega)$ within the soil, obtained with the postprocessing procedure outlined in Sec. 5.4. Moreover, significantly larger amplitudes of the radiated surface waves can be observed in Fig. 6.65b compared to the homogeneous halfspace in Fig. 6.65a. This can be explained by the considerable reduction of the imaginary part of the impedance function associated with the damping for ratios $c_{s1}/c_{s2} < 0.6$ and intermediate values of the ratio $1 < h_1/B_f < 5$, as already outlined by Luco [26]. [51]

Fig. 6.66 shows the setup for the power flux analysis as well as the ratio $\mathcal{P}_{\mathrm{tot,CV}}/\mathcal{P}_{\mathrm{in}}$ of a rigid massless foundation with $B_f = 2$ m subjected to uniform pressure and resting on a layered halfspace with $c_{s1}/c_{s2} = 0.125$ and $h_1/B_f = 2$. The size of the control volume varies in width and depth as $l_{\mathrm{cv}} = b_{\mathrm{cv}} = n_{\mathrm{cv}} \cdot 2$ m and $h_{\mathrm{cv}} = n_{\mathrm{cv}} \cdot 1$ m with $n_{\mathrm{cv}} = 1, 2, \ldots 6$. The vertical layer resonance frequencies for the chosen system configuration can be approximated by those of an

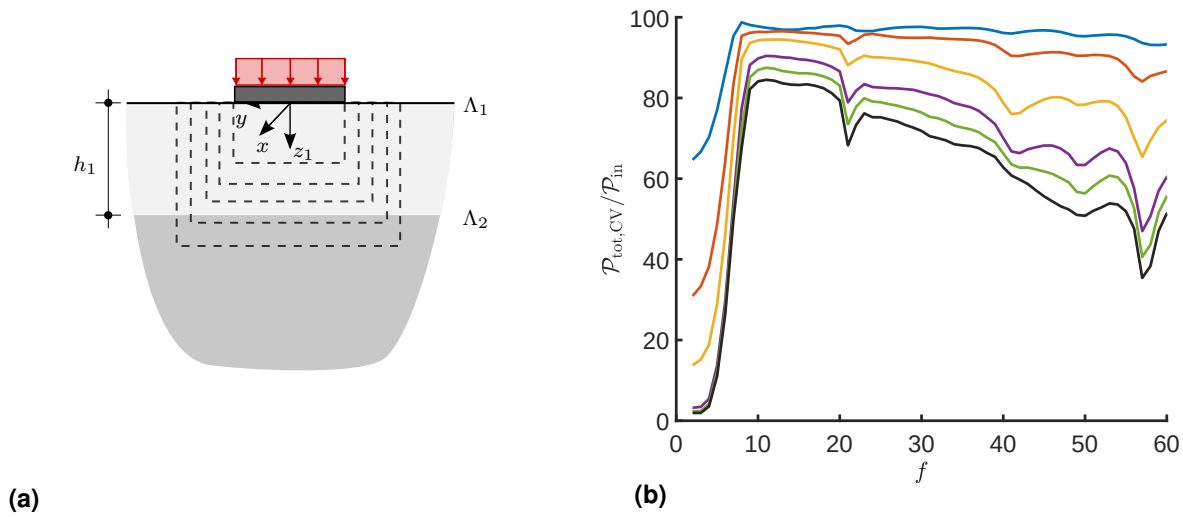

Figure 6.66: (a) Setup for power flux analysis of layered halfspace and (b) ratio $\mathcal{P}_{\mathrm{tot,CV}}/\mathcal{P}_{\mathrm{in}}$ over frequency for CV1 (—), CV2 (—), CV3 (—), CV4 (—), CV5 (—), CV6 (—).

elastic stratum over rigid bedrock with same dimensions resulting as $f_{\mathrm{res,v}} = 8.3$, 24.8, 41.3 and 57.9 Hz. Below $f_{\mathrm{res,v1}}$ no power is introduced into the soil as also stated by Chouw et al. [112] and explained in more detail later on (cp. Sec. 6.3.3). Furthermore, considerable dips are observed in Fig. 6.66b around the layer resonance frequencies. This is due to the rather large displacement amplitudes occurring at resonance in turn leading to a larger energy dissipation within the control volume due the displacement proportional hysteretic material damping.

In summary, the large values of $P_{\mathrm{in}}(a_0)$ at the resonant frequencies of the layered ground indicate a significant immission of energy into the soil. This, in combination with only a smaller possibility of energy dispersion in the layered soil compared to the homogeneous halfspace, leads to a significant transmission of vibrations within the upper soil layer, which can be highly relevant for the assessment of disturbances in neighbouring structures. The power input $P_{\mathrm{in}}(a_0)$ thus represents a suitable tool to infer the radiation capacity of the foundation and the wave propagation characteristics in the soil and to assess them on the basis of a single numerical value. [51]

6.3.3 Foundation on layered halfspace with inclusion

In this section, finally the presented coupled ITM-FEM approach is applied to investigate the influence of longitudinally invariant inclusions on the dynamic response of the foundation on the ground surface. Therefore, a stiff cylindrical concrete inclusion and a tunnel, located

within a homogeneous or layered halfspace, are considered (Fig. 6.45). For model 3 and 4, the inclusion within Soil A has a burial depth of $h_1 = h_{\mathrm{cyl}} = 2$ m, equal to the thickness of the soft layer in model 2, so that the ratio of foundation width to layer thickness results as $h_1/B_f = 1$. The tunnel in model 5 is additionally embedded by $h_{\mathrm{cyl}} = 2$ m in the stiffer halfspace (Soil B) w.r.t. the interface with the soft layer (Soil A). The material parameters of the concrete were chosen equally for the concrete inclusion and the tunnel shell, which has a thickness of $t_{\mathrm{sh}} = 0.4$ m, as $E_{\mathrm{concr}} = 3.4 \cdot 10^{10}$ Nm^{-2}, $\nu_{\mathrm{concr}} = 0.2$, $\rho_{\mathrm{concr}} = 2600$ kgm^{-3} and $\zeta_{\mathrm{concr}} = 0.05$. [51]

Fig. 6.67 presents the frequency dependent behaviour of $|\bar{u}_z|$, $|\bar{v}_z|$ and $\mathcal{P}_{\mathrm{in}}/\mathcal{P}_{c_p}$ of a rigid, massless square foundation subjected to uniform pressure for all models depicted in Fig. 6.45. Hereby the radius of the cylindrical structure was chosen as $R = 4.5$ m in all cases. Compared to the layered halfspace with $c_{s1}/c_{s2} = 0.5$ (model 2), the stiff cylindrical concrete inclusion (model 3) shows a larger peak in displacement, velocity and power input, slightly shifted to higher frequencies. This is owed to the rather large stiffness of the concrete structure and the (with a diameter of 9 m) fairly large dimensions compared to the foundation width of $B_f = 2$ m. On the contrary, for the tunnel in the homogeneous halfspace (model 4), which has a significantly lower stiffness, the main peak occurs at a lower frequency as in case of the layered halfspace and with smaller amplitude compared to the concrete inclusion. For both cases the main maxima in the power input can be attributed to vertical resonances of the soil stratum over the inclusion. [51]

The same features of the dynamic response are visible in Fig. 6.68, which shows the real and imaginary part of C_{zz}^{11} for all models. A very high similarity of the vertical flexibilities for the concrete inclusion (model 3) and the layered halfspace with $c_{s1}/c_{s2} = 0.25$ (model 2)

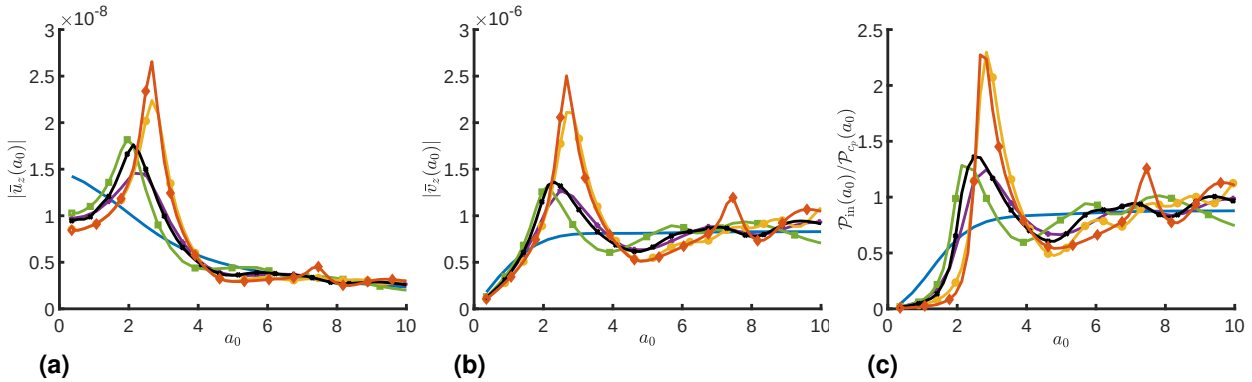

Figure 6.67: Amplitude of vertical (a) displacement, (b) velocity at $x = y = 0$ and (c) normalized total power input at $z = 0$ for a rigid, massless foundation subjected to uniform pressure for model 1 (—), model 2 with $c_{s1}/c_{s2} = 0.5$ (–+–) resp. $c_{s1}/c_{s2} = 0.25$ (–◇–), model 3 (–○–), model 4 (–□–) and model 5 with $c_{s1}/c_{s2} = 0.5$ (–×–) each with $R = 4.5$ m. [51]

is observed. The same yields for the tunnel within the layered halfspace (model 5) and the layered halfspace (model 2) with $c_{s1}/c_{s2} = 0.5$ in the frequency range $a_0 \gtrsim 3.5$, while for low a_0 the presence of the tunnel leads to deviations in the compliances. [51]

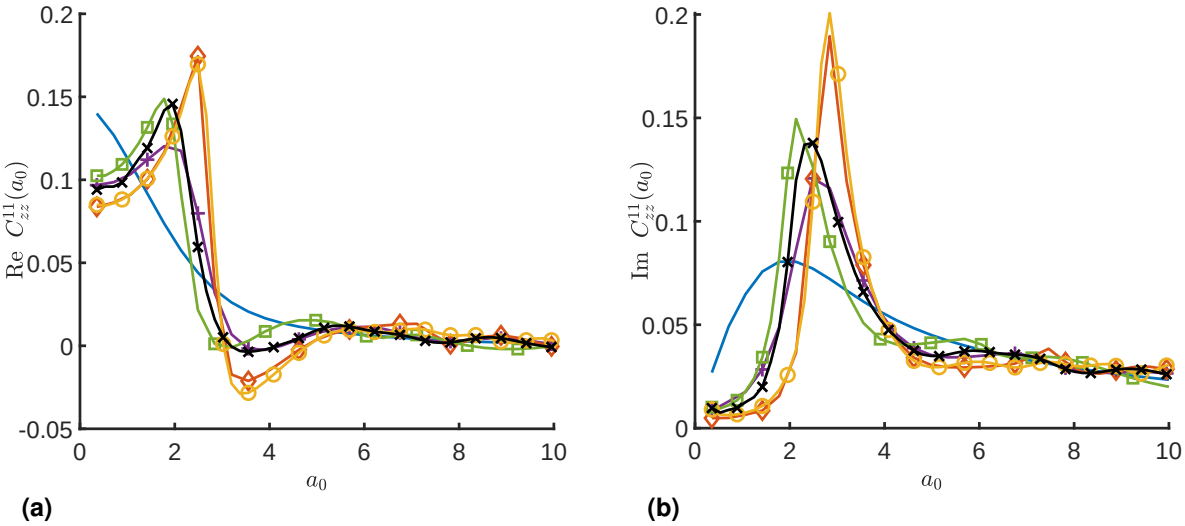

Figure 6.68: Real and imaginary part of compliance $C_{zz}^{11}(a_0)$ at soil foundation interface for rigid, massless foundation subjected to uniform pressure for model 1 (—), model 2 with $c_{s1}/c_{s2} = 0.5$ (–+–) resp. $c_{s1}/c_{s2} = 0.25$ (–◇–), model 3 (–○–), model 4 (–□–), and model 5 with $c_{s1}/c_{s2} = 0.5$ (–×–) each with $R = 4.5$ m. [51]

Furthermore, the very low values of the imaginary part of C_{zz}^{11} (Fig. 6.68b) and the power input (Fig. 6.67c) for $f < f_{\mathrm{res,v,1}}$ are noticeable. According to [301] and [112], in a perfectly elastic soil layer over bedrock ($\zeta_s = 0$), energy attenuation is possible only by free waves propagating in the radial direction away from the source, since no downward radiation of the induced body waves is possible due to the perfect reflections at the boundary. As for frequencies below the first layer resonance frequency $f_{\mathrm{res,1}}$ any propagation of free waves is impossible, no energy attenuation occurs in this frequency range. This leads to an imaginary part of the soil flexibility associated with damping of zero. In the case of a viscoelastic stratum ($\zeta_s \neq 0$), no explicit separation of dissipative and radiative energy attenuation is possible. Although in this case numerous modes of propagating free waves exist even for $f < f_{\mathrm{res,1}}$, each of them is highly damped, so that the energy attenuation caused by wave radiation is extremely small and the dissipative one dominates. However, there is a sudden increase in the imaginary part of C_{zz}^{11} and thus the energy attenuation from $f_{\mathrm{res,v,1}}$, which can be associated with the appearance of freely propagating waves that carry off energy to infinity. This is also accompanied by a significant increase in the power input $\mathcal{P}_{\mathrm{in}}$ at $z = 0$ in Fig 6.67c. With increasing frequency, layer thickness or embedment depth of the inclusion respectively, the elastic waves induced by the foundation almost attenuate before they reach

the layer boundary or buried structure. Consequently, for large ratios h_1/λ, the reflected waves only scarcely affect the behaviour of the foundation and C_{zz}^{11} converges towards that of the homogeneous halfspace for all models. [51]

This behaviour is also evident in Fig. 6.69, where the effect of varying embedment depth $h_1 = h_{\mathrm{cyl}}$ of the concrete inclusion of Fig. 6.45c with $R = 3$ m on the compliances C_{xx}^{11}, C_{yy}^{11} and C_{zz}^{11} is shown. The distinct peaks in the compliances can be linked to the horizontal and vertical resonance frequencies of the soil layer over the inclusion depicted in Fig. 6.69 by the vertical lines. The rather large inclusion diameter leads to a similar behaviour of $|C_{xx}^{11}|$ and $|C_{yy}^{11}|$. Nonetheless, $|C_{xx}^{11}|$ shows, due to the length invariance of the system in $x-$direction, slightly larger amplitudes and exhibits more peaked maxima which match better to $f_{\mathrm{res,h}}$ of the soil stratum. Because of the finite extend of the embedded structure and its cylindrical shape, which inevitably lead to a more complex wave field as in case of a horizontal material transition surface, the peaks of $|C_{zz}^{11}|$ only approximately coincide with the vertical layer resonance frequencies. [51]

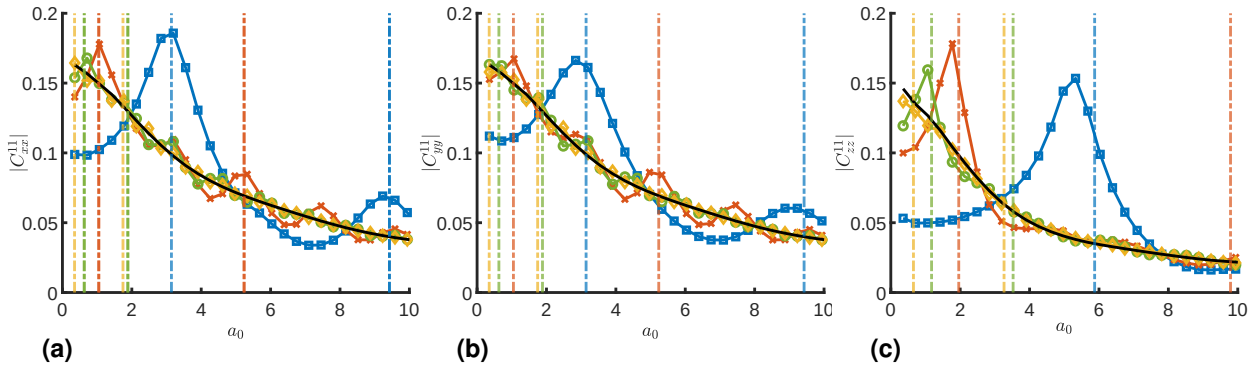

Figure 6.69: Absolute value of compliances (a) $|C_{xx}^{11}|$, (b) $|C_{yy}^{11}|$ and (c) $|C_{zz}^{11}|$ of a rigid, massless square foundation with $B_f = 2$ m on a halfspace with cylindrical concrete inclusion ($R = 3$ m) and varying embedment depth $h_{\mathrm{cyl}} = 1$ m (–□–), $h_{\mathrm{cyl}} = 3$ m (–×–), $h_{\mathrm{cyl}} = 5$ m (–○–), $h_{\mathrm{cyl}} = 9$ m (–◇–) and on a homogeneous halfspace (—). [51]

Fig. 6.70 shows the real part of $\bar{u}_z(x, y, z = 0, \omega)$ for both, a foundation resting on a homogeneous halfspace (Soil A) and one with a stiff concrete inclusion (model 3). The wave impeding effect of the inclusion for $f = 6$ Hz $< f_{\mathrm{res,v,1}}$ can clearly be observed in Fig. 6.70b, where nearly no surface vibrations occur. For $f = 16$ Hz $\approx f_{\mathrm{res,v,1}}$ in Fig. 6.70d larger vibration amplitudes appear on the soil surface due to waves propagating perpendicular to the cylindrical inclusion, whereas nearly no oscillations crop up along the inclusion. In contrast for the homogeneous halfspace at $f = 6$ and 16 Hz, an omnidirectional wave field with considerable amplitudes of the surface waves arises (Figs. 6.70a,c). [51]

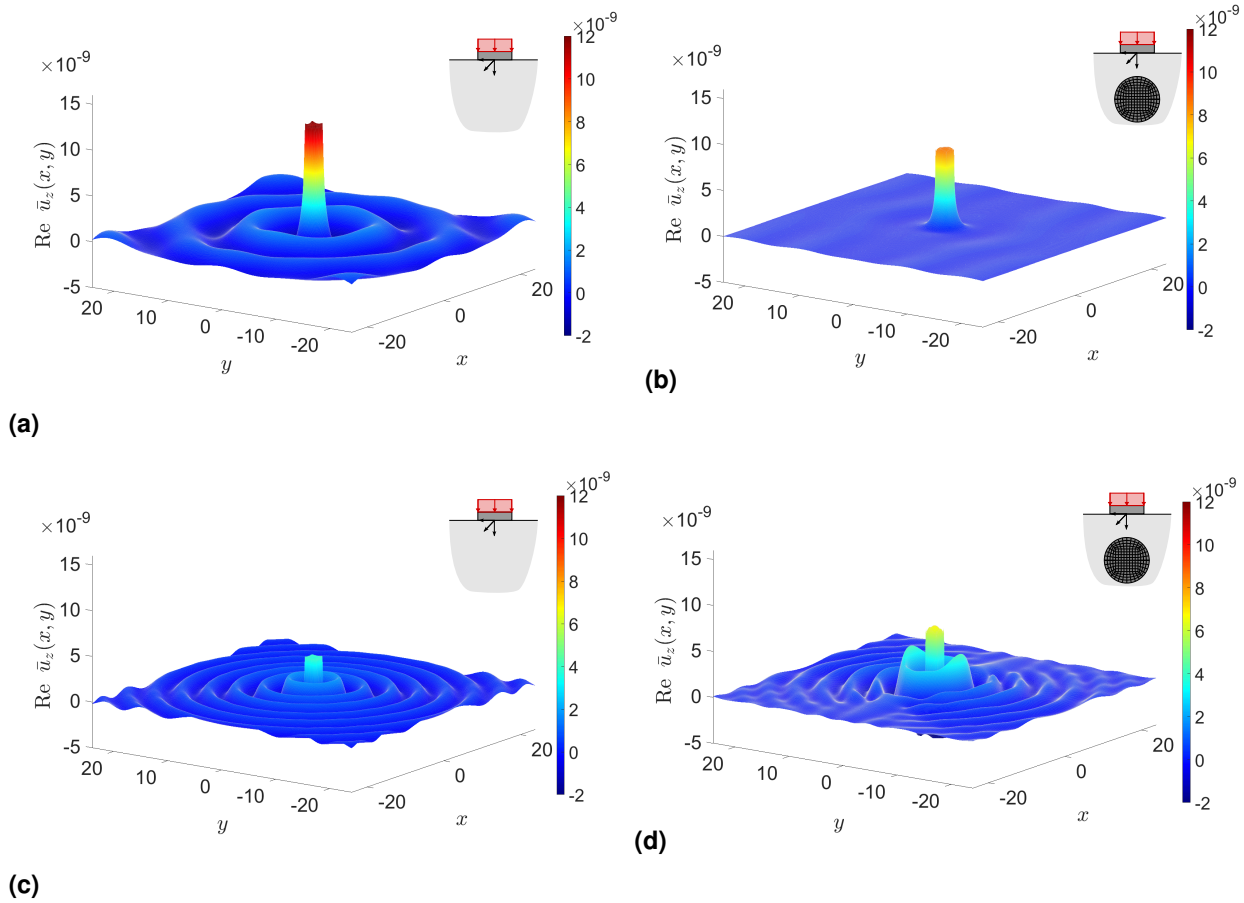

Figure 6.70: Real part of $\bar{u}_z(x,y,z=0,\omega)$ for rigid foundation under uniform pressure with (a),(b) $f = 6$ Hz and (c),(d) $f = 16$ Hz resting on (a),(c) homogeneous soil (model 1) and (b),(d) halfspace with concrete inclusion of $R = 4.5$ m (model 3). [51]

6.4 Soil structure interaction of several adjacent surface foundations

6.4.1 Adjacent foundations on homogeneous halfspace

Following, the coupled ITM-FEM approach for the dynamic interaction of a group of four rigid massless surface foundations resting on a homogeneous halfspace (cp. Sec. 5.3) is validated by comparison of the obtained frequency dependent foundation flexibilities with literature results. The investigated system setup is depicted in Fig. 6.71 and the material parameters of the soil and the foundations are given in Tab. 6.16. A total domain size of $B_x = B_y = 128$ m with $N_x = N_y = 2^{11}$ sample points and a factor $n_\Delta = 2$ is chosen. The square foundations, featuring a width $B_f = 1$ m, a height $H_f = 0.3$ m and a midpoint distance $\mathrm{d_{x,f_1f_2}} = 2$ m resp. $\mathrm{d_{y,f_1f_3}} = 2$ m, are modelled with shell elements and full coupling

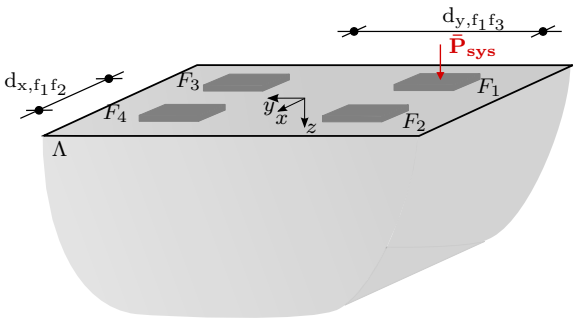

Figure 6.71: Setup for the validation of the ITM-FEM approach for the SSSI of a group of four adjacent surface foundations on homogeneous halfspace.

of all DOFs between soil and foundations is assumed. Fig. 6.72 shows the real and imaginary part of the vertical compliance of the second C_{zz}^{21} and the fourth C_{zz}^{41} foundation due to an unit harmonic point load on foundation F_1. Thereby foundation F_2 exhibits larger amplitudes than F_4 because of the lower distance to the loaded footing. The compliance C_{zz}^{31} (not shown here) is equal to C_{zz}^{21} due to symmetry. A very good agreement with the results presented in Radišić et al. [86] can be observed for all foundations.

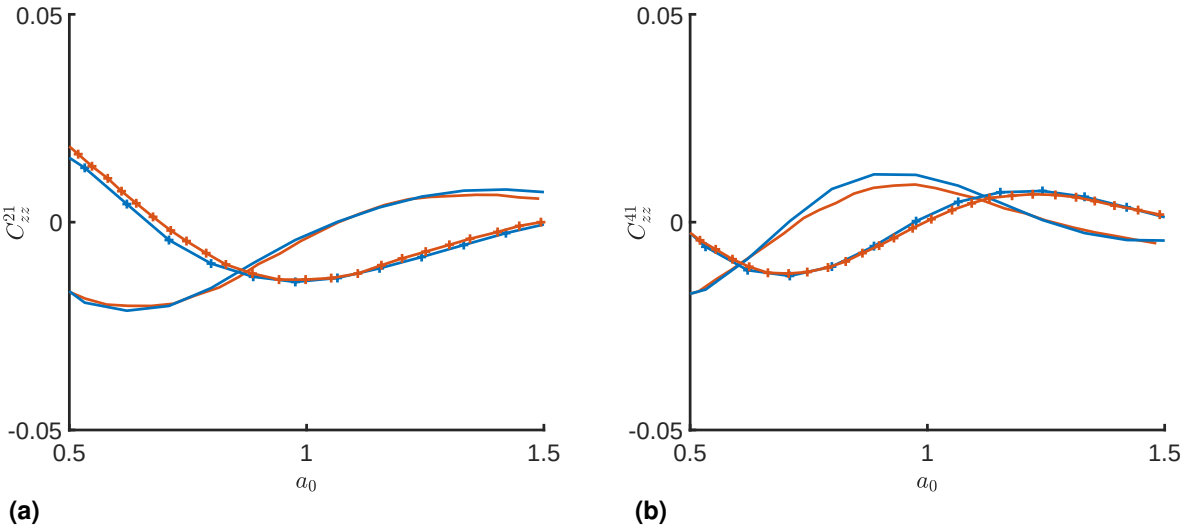

Figure 6.72: Real (−) and imaginary (+) part of vertical compliance for a group of four adjacent surface foundations resting on a homogeneous halfspace obtained with the ITM-FEM approach (—) and the results of Radišić et al. [86] (—).

6.4.2 Adjacent foundations on a halfspace with inclusion

In the following section, strongly based on Freisinger and Müller [100], the SSSI of two adjacent rigid, massless square foundations, resting on a soil with a stiff embedded, length invariant, cylindrical inhomogeneity, is investigated (cp. Fig. 6.73) in order to assess the effect

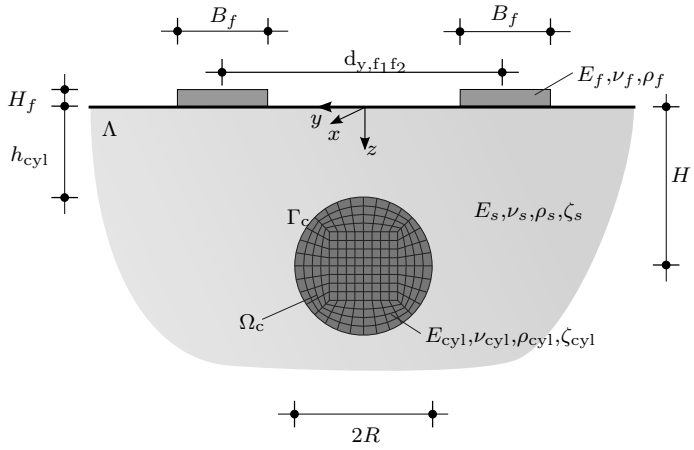

Figure 6.73: ITM-FEM model for halfspace with cylindrical inclusion with two surface foundations. [100]

of the inclusion on the dynamic response of the foundations taking into account the through soil coupling. However, the proposed method is also applicable for more complicated SSSI and FSFI problems, including flexible and massive structures with rectangular contact area to the soil as well as more complex inclusion geometries inside the 2.5D FEM substructure with cylindrical outer boundary. [100]

Due to the higher computational effort when considering also an inclusion, the total domain size is chosen as $B_x = B_y = 64$ m with only $N_x = N_y = 2^9$ sample points. The cylindrical 2.5D FEM inclusion was discretized with $N_\varphi = 32$ equidistant nodes along the circumference, leading to an element size between 0.25 and 0.375 m for the considered inclusion sizes R and thus approx. four elements per shear wave length of the soil at the highest regarded frequency. The material properties of the foundations, soil and inclusion are given in Tab. 6.16. [100]

Verification example

In order to validate the modified shifting procedure for the computation of the soil flexibility matrix of several foundations resting on a halfspace including a length invariant structure (cp. Sec. 5.3), firstly the foundation compliances of two adjacent surface foundations with $B_f = 2$ m and a midpoint distance $d_{y,f_1f_2} = 4$ m are computed. Thereby the material parameters of the inclusion are chosen to be identical to those of the surrounding soil to reproduce a homogeneous halfspace. The absolute value of the vertical compliance of the active $|C_{zz}^{11}|$ and the passive $|C_{zz}^{21}|$ foundation, due to an unit harmonic point load on foundation F_1, are depicted in Fig. 6.74. A perfect match of the presented 2.5D ITM-FEM approach applying shell elements with the ITM approach with the kinematic condition for the rigid foundation can be observed. Furthermore, the results show good agreement with those obtained by Radisic [85] and Karabalis and Mohammadi [104], who obtained larger compliances in the lower

	E (Nm^{-2})	ν $(-)$	ρ (kgm^{-3})	ζ $(-)$	c_p (ms^{-1})	c_s (ms^{-1})	c_r (ms^{-1})
Soil	$26.00 \cdot 10^6$	0.30	2000	0.05	132.5	70.8	
Infill A	$96.00 \cdot 10^6$	0.20	2000	0.04	231.0	141.5	
Infill B	$38.40 \cdot 10^7$	0.20	2000	0.04	461.9	282.9	
Infill C	$15.40 \cdot 10^8$	0.20	2000	0.04	925.2	566.5	
Infill D	$34.00 \cdot 10^9$	0.20	2000	0.04	4347.0	2661.9	
Foundation	$34.00 \cdot 10^{11}$	0.20	1	0.00	$2.142 \cdot 10^6$	$1.145 \cdot 10^6$	-

Table 6.16: Material parameters of soil, foundation and different inclusion infill materials.

frequency range due to zero material damping. At higher frequencies, where mainly the geometrical damping dominates the system response, the deviations diminish. [100] The rather high value of $|C_{zz}^{21}|$ at the lowest considered frequency as well as the oscillations in the results of Radisic [85] can be traced back to spatial aliasing, which can be remedied by increasing the total domain size and the number of sample points. Furthermore, a finer discretization leads to more precise results and thus a better agreement with literature (cp. Fig. 6.74). However, this is connected with an considerable increase of the computational effort.

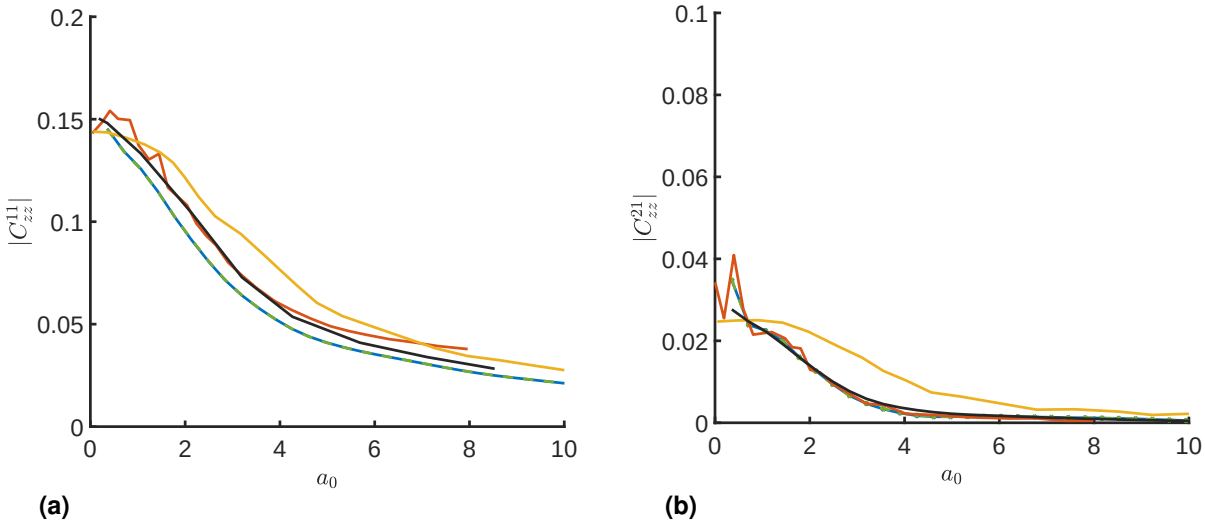

Figure 6.74: Comparison of $|C_{zz}^{ij}(a_0)|$ for (a) loaded and (b) unloaded of two adjacent rigid foundations with $B_f = 2$ m and distance $\mathrm{d_{y,f_1f_2}} = 4$ m on a halfspace with cylindrical inclusion (Soil) with $R = 3$ m and embedment depth $H = 4$ m obtained with presented 2.5D ITM-FEM approach with $N_x = N_y = 2^9$ (—) and $N_x = N_y = 2^{11}$ (—) applying shell elements and enforcing the kinematic of a rigid plate as displacement boundary condition (- -) to the results of Radisic [85] (—) and Karabalis and Mohammadi [104] (—). [100]

Overall the comparison with literature results shows, that the proposed method delivers valid results and can further be applied to determine compliance functions of adjacent foundations resting on soils with embedded structures or inhomogeneities. [100]

Parametric study on design parameters

Thus in the following, the influence of the embedment depth, size and stiffness of the inclusion is investigated for different configurations of the surface foundations. The frequency dependent dimensionless compliance functions at the soil-foundation interface are presented for the different system designs and compared with the results for equivalent foundations resting on a homogeneous halfspace to illustrate the influence of the inclusion. Furthermore, the impact of a stiff, length invariant cylindrical confinement on the displacement distribution over the entire ground surface as a result of a simultaneous harmonic excitation of both foundations, determined by the postprocessing procedure, is presented. [100]

Variation of embedment depth Firstly the compliance functions of two adjacent surface foundations with $B_f = 2$ m and a midpoint distance $\mathrm{d_{y,f_1f_2}} = 8$ m, resting on a halfspace with a stiff cylindrical inclusion (Infill D) of radius $R = 3$ m and varying embedment depth H are considered. In the horizontal compliance $|C_{xx}^{11}|$ of the loaded foundation in Fig. 6.75a only relatively small deviations from those obtained for the homogeneous halfspace are visible, because the loaded foundation is located besides the stiff inclusion. The largest deviations are observed for the smallest embedment depths and in the low frequency range. The amplifications occurring in that case can be traced back to the effect of waves reflected at the inclusion. With increasing H and a_0, $|C_{xx}^{11}|$ converges to that for the homogeneous halfspace. [100]

The compliance of the passive foundation $|C_{xx}^{21}|$ is very small for small H, as the main excitation takes place in the direction of the length invariant inclusion and a propagation of the elastic waves from the excited foundation F_1 to the unloaded foundation F_2 is disturbed by the cylindrical inclusion in the transmission path. Furthermore, in the soil layer over the inclusion propagating waves can occur mainly above the first (here horizontal) layer resonance frequency, which can e.g. be observed by the increase of $|C_{xx}^{21}|$ for $H = 4$ m at excitation frequencies $a_0 > 3.14$. With increasing H the amplitude of $|C_{xx}^{21}|$ in the low frequency range increases due to a smaller shielding effect of the cylindrical inclusion. For intermediate values of H, $|C_{xx}^{21}|$ shows to be larger than in case of a homogeneous halfspace, probably due to reflected waves at the top of the inclusion, amplifying the response at F_2. In case of large H and with increasing frequencies, the compliance again converges to that obtained for the homogeneous halfspace, as with increasing ratio of the soil layer thickness to the elastic wave lengths the influence of the inclusion diminishes. [100]

Comparing the results for the compliances in $x-$ and $y-$direction, it can be stated that $|C_{yy}^{11}|$ in Fig. 6.75 converges to the halfspace solution at higher frequencies as $|C_{xx}^{11}|$ and the deviations are larger, since the direction of excitation here directly points towards the inclusion located in the transmission path. Thus a bigger portion of elastic waves is reflected as for the excitation in $x-$direction. [100]

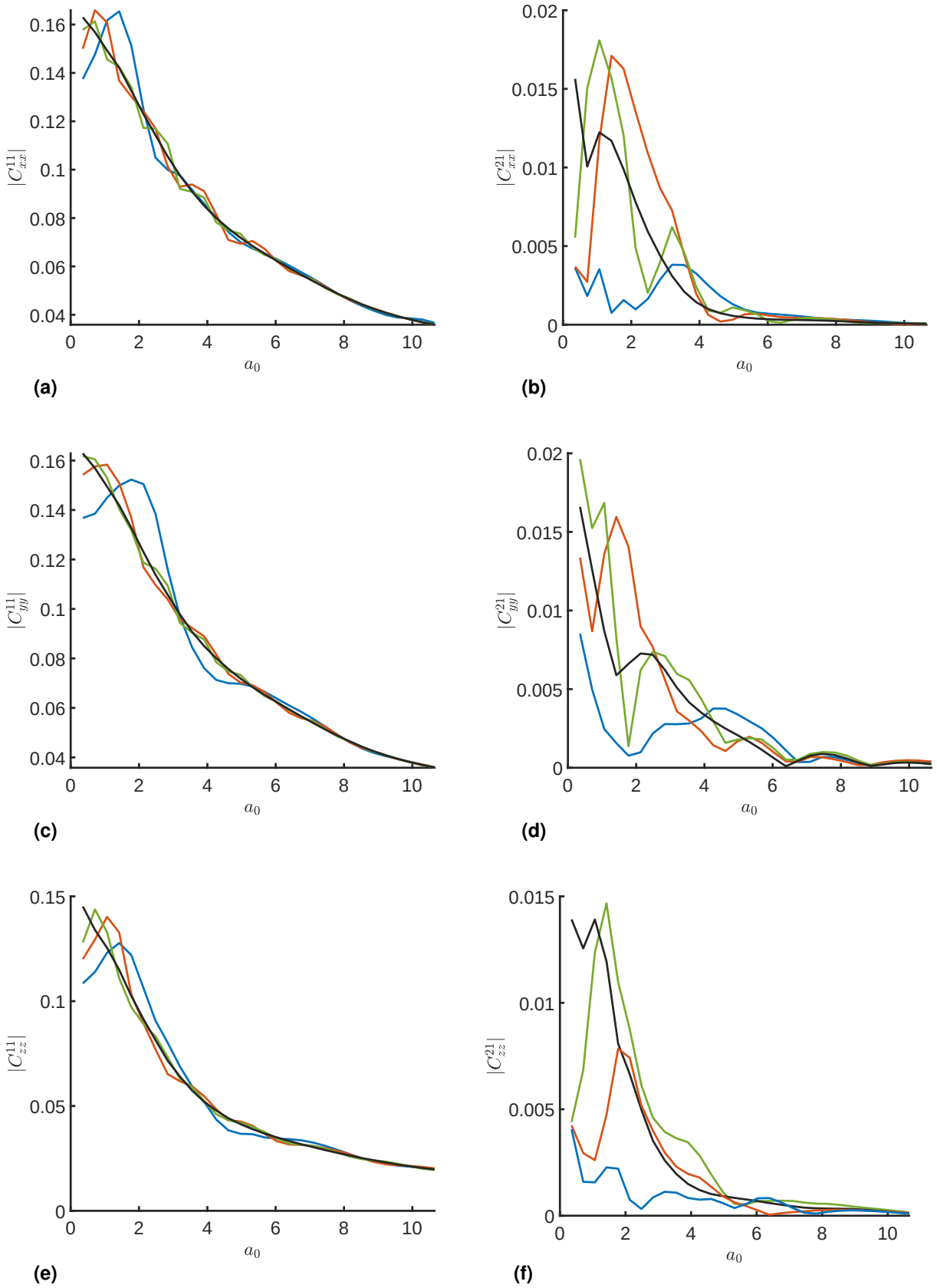

Figure 6.75: Compliance functions $|C^{ij}_{mn}(a_0)|$ for loaded (left column) and unloaded (right column) foundation with $B_f = 2$ m and distance $\mathrm{d_{y,f_1f_2}} = 8$ m on a halfspace with cylindrical inclusion (Infill D) with $R = 3$ m for varying embedment depth $H = 4$ m (—), $H = 6$ m (—), $H = 8$ m (—) and on a homogeneous halfspace (—). [100]

Concerning the vertical compliances $|C_{zz}^{11}|$ of the active foundation in Fig. 6.75, only small deviations occur as the foundation is located besides the inclusion and only a little part of the induced elastic waves interacts with it. In general small compliances $|C_{zz}^{21}|$ are observed over the whole frequency range for small H. However, above the first vertical resonance frequency of the soil layer over the inclusion at $a_0 = 5.87$ for $H = 4$ m a slight increase of $|C_{zz}^{21}|$ can be observed. The overall trend of the compliances tending to those obtained for the homogeneous halfspace for increasing H and a_0 is also found here. [100]

Variation of the inclusion radius Next, the embedment depth $H = 4$ m, the foundation width $B_f = 2$ m and midpoint distance $\mathrm{d_{y,f_1f_2}} = 8$ m are fixed and only the inclusion size R is varied. Fig. 6.76 shows, that the vertical compliances of the loaded foundation on the soil with inclusion are very close to $|C_{zz}^{11}|$ of a homogeneous soil for small inclusion size R. Also for the largest considered radius $R = 3$ m, only small deviations occur, as the foundation is located besides the inclusion and the share of waves travelling downwards or to the inclusion averted side (thus not affected by it) is quite large. The compliances $|C_{zz}^{21}|$ of the passive foundation show low amplitudes for large R and converge, due to the effects already pointed out earlier, to those for the homogeneous halfspace with decreasing inclusion size. [100]

For the system configuration with the maximum inclusion size of $R = 3$, the displacements on the whole ground surface have been determined with the postprocessing procedure. The left column of Fig. 6.77 shows the results for the real part of the vertical displacements, obtained for a harmonic excitation with $f = 6$ Hz of both resp. only one foundation, resting on a

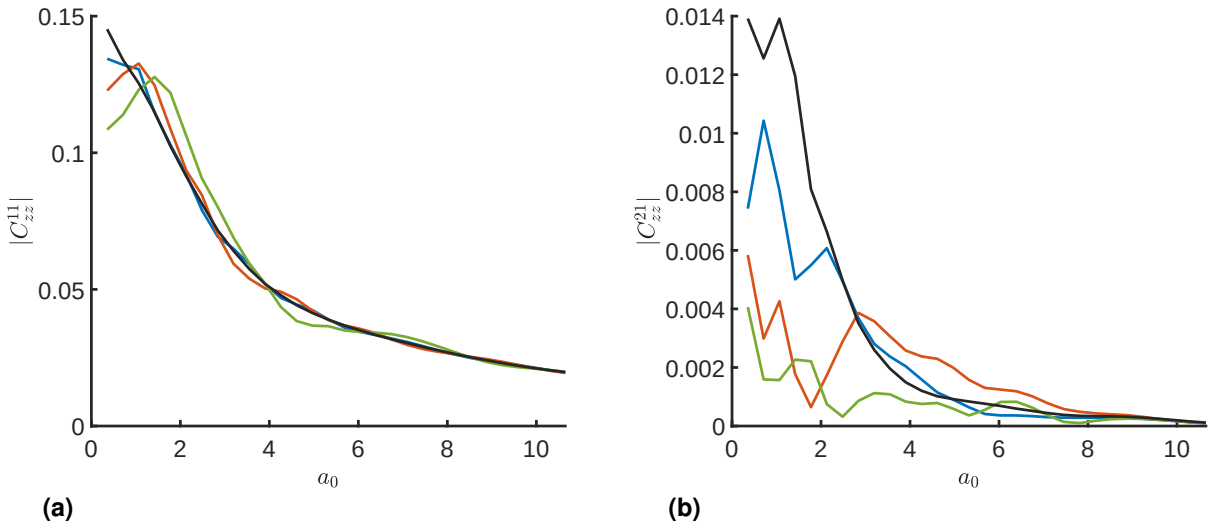

Figure 6.76: Absolute vertical compliance $|C_{zz}^{ij}(a_0)|$ for (a) first (loaded) and (b) second (unloaded) of two adjacent rigid, massless square foundations with $B_f = 2$ m and distance $\mathrm{d_{y,f_1f_2}} = 8$ m on a halfspace with cylindrical inclusion (Infill D) with embedment depth $H = 4$ m for varying radius $R = 1$ m (—), $R = 2$ m (—), $R = 3$ m (—) and a homogeneous halfspace (—). [100]

homogeneous halfspace. In Fig 6.77a, a wave propagation concentrated on the direction of the foundation alignment and perpendicular to it can be observed, whereas Fig 6.77c shows a nearly omnidirectional propagation of the surface waves. The second, unloaded foundation only hardly influences the displacement field on the ground surface, except the area directly under it, where a linear displacement distribution arises due to the rigidity of the foundation plate. In case of a massive foundation the inertia effects would lead to a much higher influence of the unloaded foundation on the system response. The right column of Fig. 6.77 shows the results for same foundation and load configuration, but on a halfspace with stiff inclusion. Fig. 6.77b shows a significant reduction of $\bar{u}_z(x,y,z=0,\omega)$ in a limited area along the entire length of the stiff inclusion compared to the case of the homogeneous halfspace, in turn leading to an increase in amplitudes in the direction perpendicular to the inclusion on both sides. Furthermore, the behaviour of the stiff inclusion as wave barrier can clearly be observed in Fig. 6.77d, where a considerable reduction of $\bar{u}_z(x,y,z=0,\omega)$ occurs on the load averted side of the inclusion. These effects get even more obvious, when comparing the displacements $\bar{u}_z(y)$ for $x=0$ for both cases in Fig. 6.78. [100]

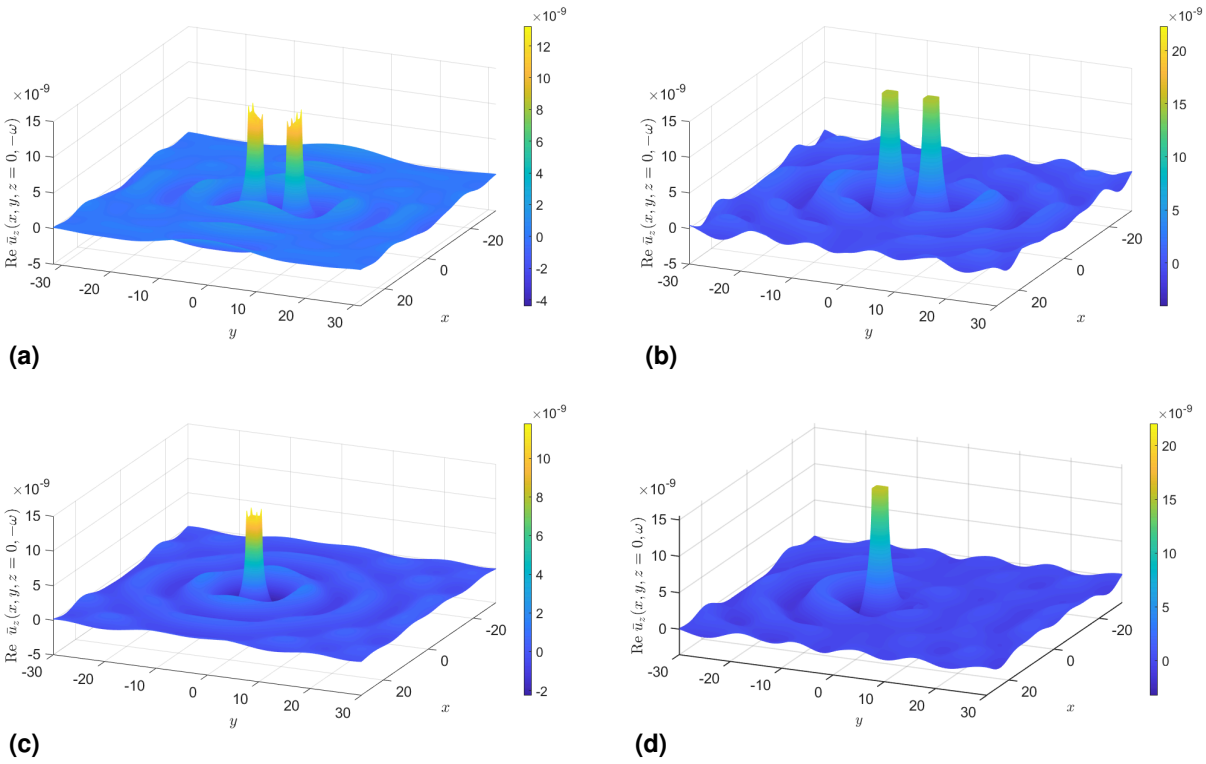

Figure 6.77: Real part of vertical displacement $\bar{u}_z(x,y,z=0,\omega)$ on whole ground surface due to harmonic loading ($f=6$ Hz) on (a),(b) both and (c),(d) only one of the adjacent rigid, massless foundations with $B_f=2$ m and $\mathrm{d_{y,f_1f_2}}=8$ m resting on the surface of a (a),(c) homogeneous halfspace and (b),(d) halfspace with a stiff cylindrical inclusion (Infill D) with $H=4$ m and $R=3$ m, obtained with the postprocessing procedure. [100]

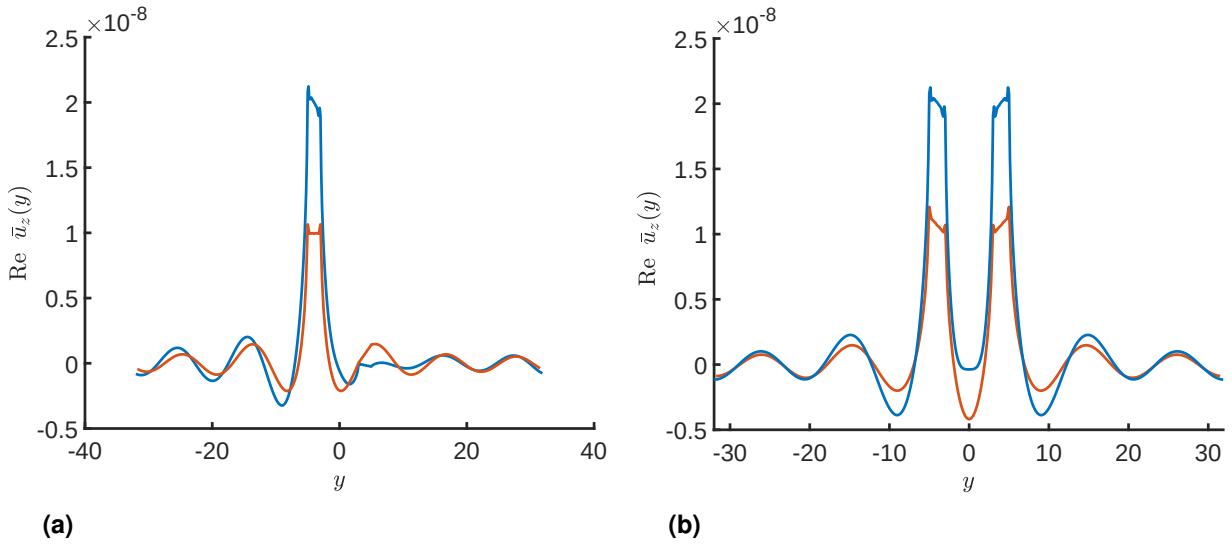

Figure 6.78: Real part of vertical displacement $\bar{u}_z(x = 0,y,z = 0,\omega)$ along $y-$direction for $x = 0$ due to harmonic loading with $f = 6$ Hz on (a) only one and (b) both of the adjacent rigid, massless foundations with $B_f = 2$ m and $\mathrm{d}_{\mathrm{y,f_1f_2}} = 8$ m resting on the surface of a homogeneous halfspace (—) and a halfspace with a stiff cylindrical inclusion (Infill D) (—) with $H = 4$ m and $R = 3$ m, obtained with the postprocessing procedure. [100]

Variation of foundation distance The variation of the midpoint distance $\mathrm{d}_{\mathrm{y,f_1f_2}}$ in Fig. 6.79 for a constant foundation width, inclusion size, location and material shows that the cross interaction between the foundations decreases with increasing distance regardless the underlying soil. For a homogeneous halfspace, $|C_{zz}^{11}|$ of the loaded foundation is equal for all $\mathrm{d}_{\mathrm{y,f_1f_2}}$, whereas the influence of the inclusion is clearly visible for small distances of the foundations and decreases with increasing $\mathrm{d}_{\mathrm{y,f_1f_2}}$, thereby converging to the halfspace solution. In general larger $|C_{zz}^{21}|$ are observed for the homogeneous halfspace, which also decrease with increasing $\mathrm{d}_{\mathrm{y,f_1f_2}}$ and a_0. Due to the rather large inclusion located closely to the halfspace surface, only very low compliance values $|C_{zz}^{21}|$ show up for larger foundations distances. For the likewise nearby foundations with $\mathrm{d}_{\mathrm{y,f_1f_2}} = 4$ m, an increase of the compliance amplitude above the first horizontal resonance frequency of the soil layer at $a_0 = 3.14$ can be observed and attributed to the in this case possible propagation of surface waves, passing through the soil over the inclusion and impinging at the second foundation. [100]

Variation of inclusion stiffness Finally, the effect of a varying stiffness of the inclusion is investigated. Therefore the Young's modulus E_{cyl} is adapted such that the ratio of the shear wave velocity of the infill material and the soil $c_{\mathrm{s,cyl}}/c_s$ takes values between 2 and 8, additionally to the very stiff inclusion with $c_{\mathrm{s,cyl}}/c_s = 37.6$, investigated previously.

The vertical compliance of the active foundation $|C_{zz}^{11}|$ in Fig. 6.80a generally differs only slightly from the results for the homogeneous halfspace. However, an increase of the smooth peak in the low frequency range and a rising waviness in the compliances is observed for a

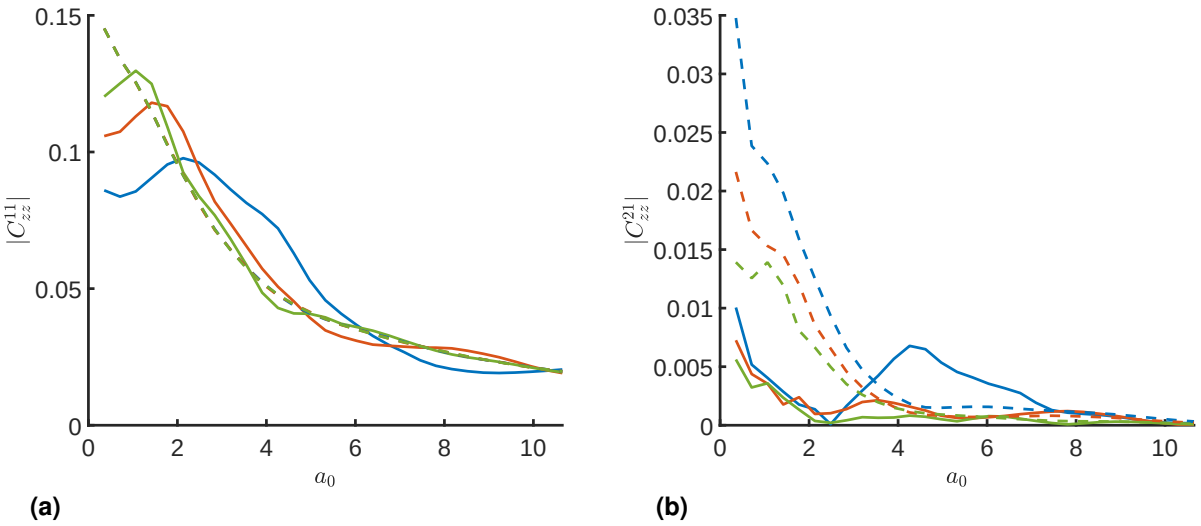

Figure 6.79: Absolute vertical compliance functions $|C_{zz}^{ij}(a_0)|$ for (a) first (loaded) and (b) second (unloaded) of two adjacent rigid, massless square foundations with $B_f = 2$ m on halfspace with cylindrical inclusion (Infill D) with embedment depth $H = 3$ m and radius $R = 2$ m (solid lines) and on a homogeneous halfspace (dashed lines) for varying distance $\mathrm{d_{y,f_1f_2}} = 4$ m (—), $\mathrm{d_{y,f_1f_2}} = 6$ m (—) and $\mathrm{d_{y,f_1f_2}} = 8$ m (—).

higher stiffness of the inclusion. The compliance of the passive foundation $|C_{zz}^{21}|$ in Fig. 6.80b drastically reduces with increasing stiffness E_{cyl}. The oscillations in $|C_{zz}^{21}|$ imply, that in dependency of the frequency and with that the corresponding wavelengths, the elastic waves interact differently with the inclusion and the wave field resulting from the direct and reflected waves at the inclusion shows amplification and attenuation effects compared to the nearly monotonous decay of the compliance $|C_{zz}^{21}|$ in case of the homogeneous halfspace.[100]

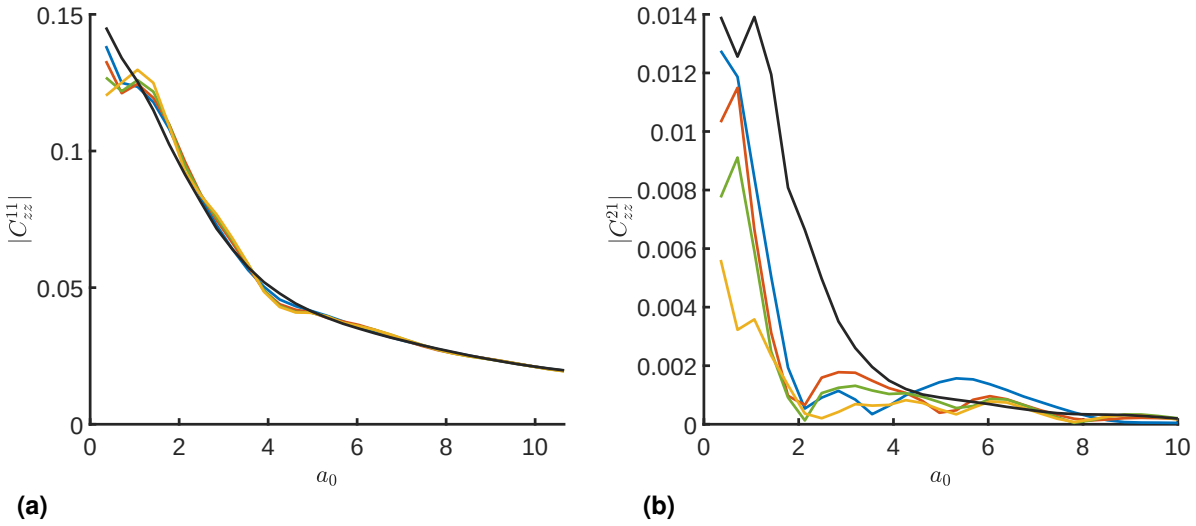

Figure 6.80: $|C_{zz}^{ij}(a_0)|$ for (a) loaded and (b) unloaded foundation with $B_f = 2$ m and $\mathrm{d_{y,f_1f_2}} = 8$ m on halfspace with cylindrical inclusion with $H = 3$ m and radius $R = 2$ m for varying stiffness E_{cyl}: Infill A $c_{\mathrm{s,cyl}} = 141.4$ ms^{-1} (—), Infill B $c_{\mathrm{s,cyl}} = 282.8$ ms^{-1} (—), Infill C $c_{\mathrm{s,cyl}} = 565.68$ ms^{-1} (—), Infill D $c_{\mathrm{s,cyl}} = 2661.45$ ms^{-1} (—) and on a homogeneous halfspace (—).

In summary, it is of particular importance to take the structure soil structure interaction into account if inclusions are located closely to the halfspace surface and if the dimensions of the embedded structure are large, especially in comparison with the size of the foundation area of the surface structure. Moreover, structures buried deeper in the soil may have a significant impact on the foundation flexibility if an excitation in the low frequency range is considered. In this case both, stiff and soft inclusions influence the total dynamic response of the system, whereby the stiffness contrast between the inclusion and the surrounding soil together with the size play the most important role. [51]

6.5 Soil structure interaction of frame structures

6.5.1 Dynamic response of a space frame

In the first part of the current section, the soil structure interaction of a three dimensional frame, which is coupled to the soil by means of different types of surface foundations, is investigated. For this purpose, the two setups depicted in Fig. 6.81, with a frame resting on one single large foundation or four small punctual foundations, are considered. Further research, including the influence of different subsoil conditions on the dynamic behaviour of multi-storey frames, can be found in [284].

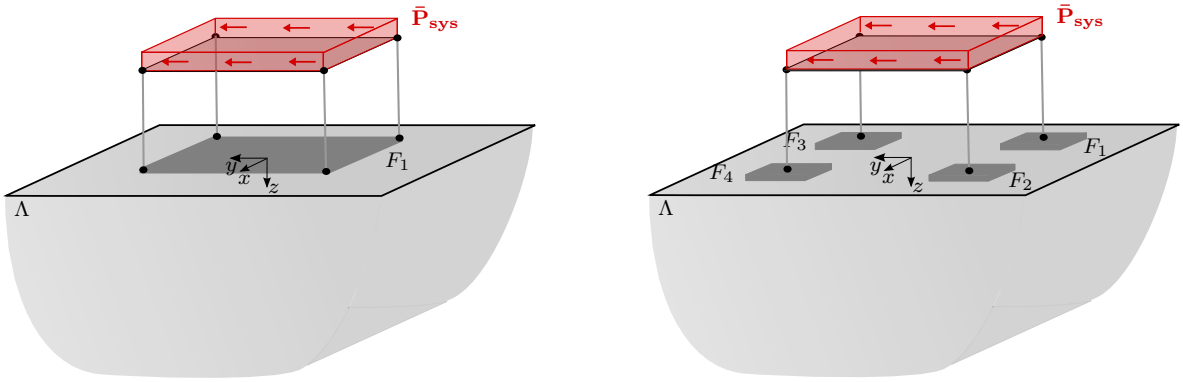

Figure 6.81: Setup for investigation of the SSI of space frame structures with different footing conditions.

The frame and the foundations are modelled using the FEM and are coupled to the underlying ground at the soil foundation contact surface via their dynamic stiffness applying the compatibility conditions. Shell elements are used for the foundations and the ceiling panel, while 3D beam elements are employed for the vertical columns (cp. Sec. 4.2.2). Since both elements feature 6 DOFs per node, all displacements and rotations are coupled at the common nodes. The geometry of the frame is chosen to be the same for both considered setups.

	E $(\mathrm{Nm^{-2}})$	ν $(-)$	ρ $(\mathrm{kgm^{-3}})$	ζ $(-)$	c_p $(\mathrm{ms^{-1}})$	c_s $(\mathrm{ms^{-1}})$	c_r $(\mathrm{ms^{-1}})$
Soil A	$2.60 \cdot 10^7$	0.30	2000	0.05	132.5	70.8	65.7
Soil B	$4.16 \cdot 10^8$	0.30	2000	0.05	529.26	282.9	262.4
Concrete	$3.00 \cdot 10^{10}$	0.20	2500	0.00	$3.65 \cdot 10^3$	$2.23 \cdot 10^3$	

Table 6.17: Material parameters of soil, foundation and frame structure.

Thereby the columns, supporting the 4×4 m ceiling slab with $h_{\mathrm{ceil}} = 0.3$ m, have a square cross section with $l_{\mathrm{col}} = b_{\mathrm{col}} = 0.3$ m and a height of $h_{\mathrm{col}} = 4$ m. The single foundation has a size of $L_f = B_f = 4$ m equal to that of the ceiling. The punctual foundations have a side length of 1 m and are each arranged with a midpoint distance of 4 m symmetrically to the origin, such that the columns are connected to them at their midpoints. The discretization of the foundations and the ceiling panel is equal to that of the soil surface, for which a total domain size of $B_x = B_y = 64$ m with $N_x = N_y = 2^{10}$ sample points and $n_\Delta = 2$ was chosen. Furthermore, the thickness of the foundations is given as $H_f = 0.4$ m in all cases.

Fig. 6.82a shows the absolute values $|\bar{u}_y(f)|$ at the midpoint of the ceiling due to an uniform harmonic loading over the latter in y-direction w.r.t. frequency. To check the validity of the model in a first step the response of a frame with rigid, massive ceiling and massless columns clamped at the bottom was computed and compared to the eigenfrequency of an equivalent SDOF system $f_{\mathrm{res}} = \sqrt{k_{\mathrm{eq}}/m_{\mathrm{ceil}}}/(2\pi)$ with $k_{\mathrm{eq}} = 4 \cdot 12EI_y/h_{\mathrm{col}}^3$ and m_{ceil} as the total mass of the ceiling. For this case, a clear peak in $|\bar{u}_y(f)|$ very close to $f_{\mathrm{res}} = 5.66$ Hz can be observed, while at higher frequencies the response decreases monotonously due to the inertia of the ceiling slab. This also matches with the first eigenfrequency at 5.61 Hz, corr. to a horizontal mode (cp. Fig. 6.82b) of the ceiling, obtained by a modal analysis of the system. Since in the current implementation only a linear eigenvalue solver is implemented, instead of using the non-linearly frequency dependent soil stiffness matrix $\bar{\mathbf{K}}_{\mathbf{s}}(\omega)$, the latter was approximated as $\bar{\mathbf{K}}_{\mathbf{s}}(\omega = 2\pi\, 20 \text{ rad s}^{-1})$ for the solution of the eigenvalue problem

$$\left(-\omega^2 \bar{\mathbf{M}}_{\mathbf{FE}} + \mathrm{i}\,\mathrm{sign}(\omega)\bar{\mathbf{C}}_{\mathbf{FE}} + \bar{\mathbf{K}}_{\mathbf{FE}} + \bar{\mathbf{K}}_{\mathbf{s}}(\omega)\right)\boldsymbol{\lambda} = 0 \tag{6.18}$$

Thereby it could be shown that the lower eigenmodes of the system behave quite robust for different frequencies of $\bar{\mathbf{K}}_{\mathbf{s}}(\omega)$, which is not the case for the higher modes [284].

Moreover, the results for the space frame with massive columns as well as massive, flexible foundation and ceiling slabs, consisting completely out of concrete and resting on a homogeneous halfspace of Soil A (material parameters cp. Tab. 6.17) are shown in Fig. 6.82a. To highlight the influence of the SSI and the different founding conditions, also the response of the frame if the bottom nodes of the columns are fully clamped is depicted as reference solution. A shift of the horizontal mode peak to lower frequencies can be observed, when the mass of the columns is taken into account and the footing conditions becomes softer.

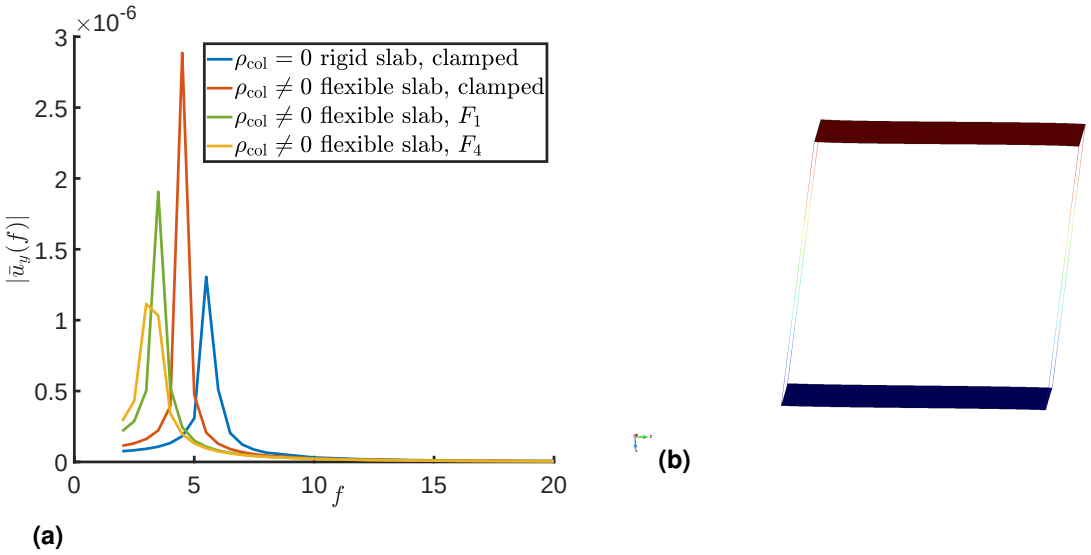

Figure 6.82: (a) Horizontal displacement $|\bar{u}_y(f)|$ at midpoint of the ceiling due to uniform horizontal loading in $y-$direction for different footing conditions and (b) first horizontal mode at $f = 5.61$ Hz of the frame for single massive flexible foundation and slab as well as massive columns.

6.5.2 Transfer functions soil-frame

Furthermore, the coupled ITM-FEM approach can be used to determine the transfer functions between a specific location on the soil surface and selected points of the frame structure. For this purpose, the dynamic soil stiffness is calculated for the nodes on the soil surface as in case of the coupling of two foundations. However, the foundation with the attached frame structure is coupled only to the interaction nodes required for this purpose and the remaining calculated potential coupling points are retained for the application of an external harmonic load, as illustrated in Fig. 6.83. Therewith the dynamic response of the frame structure due to a load applied directly on the soil surface, taking into account the SSI, can be computed.

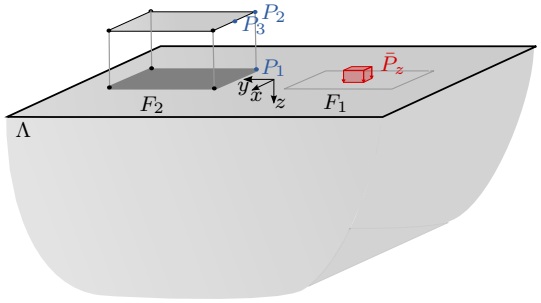

Figure 6.83: Setup for determination of the soil-frame frequency response functions.

Fig. 6.84 shows the frequency response of the horizontal and the vertical displacements for the points P_1 to P_3 in Fig. 6.83, considering a soft and a stiff soil with material parameters of Soil A resp. B in Tab. 6.17, due to an unit vertical block load with $b_x = b_y = 0.25$ m applied at $(x,y) = (0, -8)$ in steps of $\Delta f = 1$ Hz. For the foundation and the frame the same material,

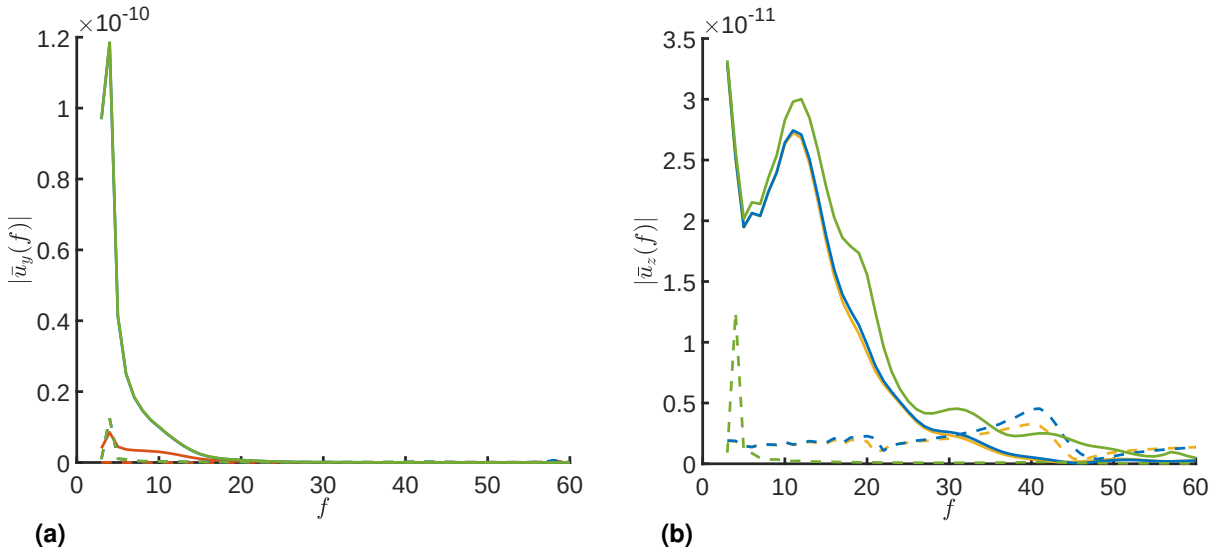

Figure 6.84: (a) Horizontal and (b) vertical displacement of points P_1 (—), P_2 (—) and P_3 (—) of the frame structure resting on a homogeneous halfspace of Soil A (straight) and Soil B (dashed).

discretization and geometry were used as in the previous example. However, the center point of the single foundation was chosen to be located at $(x,y) = (0,8)$. Strong peaks in $|\bar{u}_y|$ around 4 Hz are visible for points P_2 and P_3, situated on the ceiling plate, and can be assigned to the first horizontal mode of the frame. Also here the horizontal displacements decrease because of the inertia of the ceiling with increasing frequency, while generally rather small $|\bar{u}_y|$ are observed at P_1. For low frequencies, a considerable vertical displacement emerges for all considered points in case of the soft soil and $|\bar{u}_z|$ is significantly smaller for the stiff soil. In contrast to $|\bar{u}_y|$, for $|\bar{u}_z|$ several further peaks of different magnitudes appear especially for the point P_3 at the midpoint of the ceiling edge, which can be linked to different higher modes of the frame structure that are excited by the introduced elastic waves, propagating through the soil and finally impinging at the foundation.

6.6 Dynamic interaction of twin tunnels

In this section, the dynamic interaction of twin tunnels embedded in a homogenous halfspace is investigated applying the 2.5D coupled ITM-FEM approach. In order to highlight the effect of the second tunnel on the dynamic system response, the model is evaluated for both, a single tunnel and two parallel tunnels, as depicted in Fig. 6.85.

	E $(\mathrm{Nm^{-2}})$	ν $(-)$	ρ $(\mathrm{kgm^{-3}})$	ζ $(-)$	c_p $(\mathrm{ms^{-1}})$	c_s $(\mathrm{ms^{-1}})$	c_r $(\mathrm{ms^{-1}})$
Soil	$2.60 \cdot 10^7$	0.30	2000	0.05	132.5	70.8	65.7
Concrete	$3.40 \cdot 10^{10}$	0.20	2000	0.02	4347.0	2662.0	

Table 6.18: Material parameters of soil and tunnel.

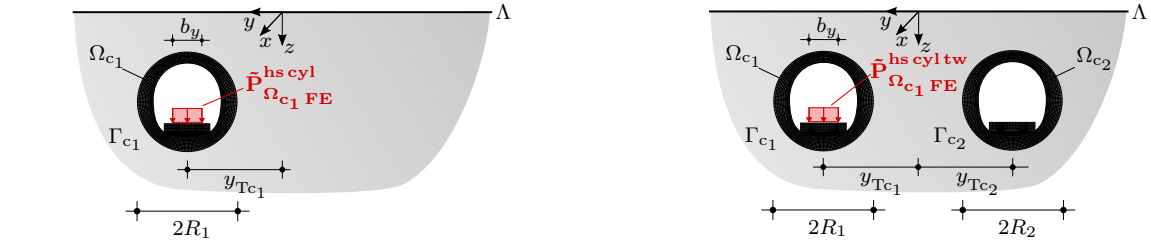

Figure 6.85: ITM-FEM model of (a) single and (b) twin tunnel system within a homogeneous soil cp. [244].

The resulting displacements on the ground surface due to the waves radiated from the harmonically excited tunnel are compared and the change caused by the inclusion of the second tunnel is quantified by means of the insertion gain $\overline{\text{IG}}_z$, given in Eq. (6.9). [244]

For this purpose one resp. two identical subway tunnels are modelled within the cylindrical inclusion featuring a radius of $R = 4.5$ m, an embedment depth $H = 6$ m and a distance $|y_{\text{Tc}_1}| = |y_{\text{Tc}_2}| = 8$ m. The 0.2 m thick tunnel shell and the sleepers are connected monolithically and consist of concrete, whose material parameters are given in Tab. 6.18 together with the soil. In all cases only tunnel T_1 is loaded by an unit block load with $b_x = b_y = 1.0$ m arranged symmetrically to the $x-$axis. A total domain size of $B_x = B_y = 64$ m with $N_x = N_y = 2^9$ sample points was chosen and the cylindrical inclusion discretized with $N_\varphi = 64$ nodes along the circumference.

Figs. 6.86a-d show the absolute value of the vertical displacements on the ground surface for both systems exemplarily for $f = 30$ and 60 Hz. In case of the single tunnel system, the body waves induced by the harmonic load in the tunnel propagate undisturbed through the soil and lead to Rayleigh waves at the surface of the halfspace [244]. However, the resulting displacement field exhibits no cylindrical wave fronts emerging from the centre of excitation but, due to the stiffness of the longitudinally invariant tunnel, a displacement distribution symmetrical to the tunnel axis. For the twin tunnel system the symmetry is disrupted by the reflection, diffraction and scattering of the waves at the second tunnel, leading to regions of significantly increased surface displacements compared to the single tunnel system.

The insertion gains in Fig. 6.86e,f show amplifications up to 20 dB, which occur almost exclusively on the side facing towards the unloaded tunnel. For both frequencies considered, a pattern of strong changes in surface displacements can be seen along lines parallel to the tunnel axis. However, the distribution of areas with very high values of $\overline{\text{IG}}_z$ is strongly dependent on the frequency. At $f = 30$ Hz these tend to occur at a greater distance from the centre of load application with respect to the $y-$direction, whereas at $f = 60$ Hz the maximum values of the insertion gain occur much more localised around $x = 0$ and above the second tunnel. Furthermore, a certain shielding effect in larger distances behind the second tunnel, with a reduction of the vibration amplitudes also up to 20 dB, is visible in Fig. 6.86f.

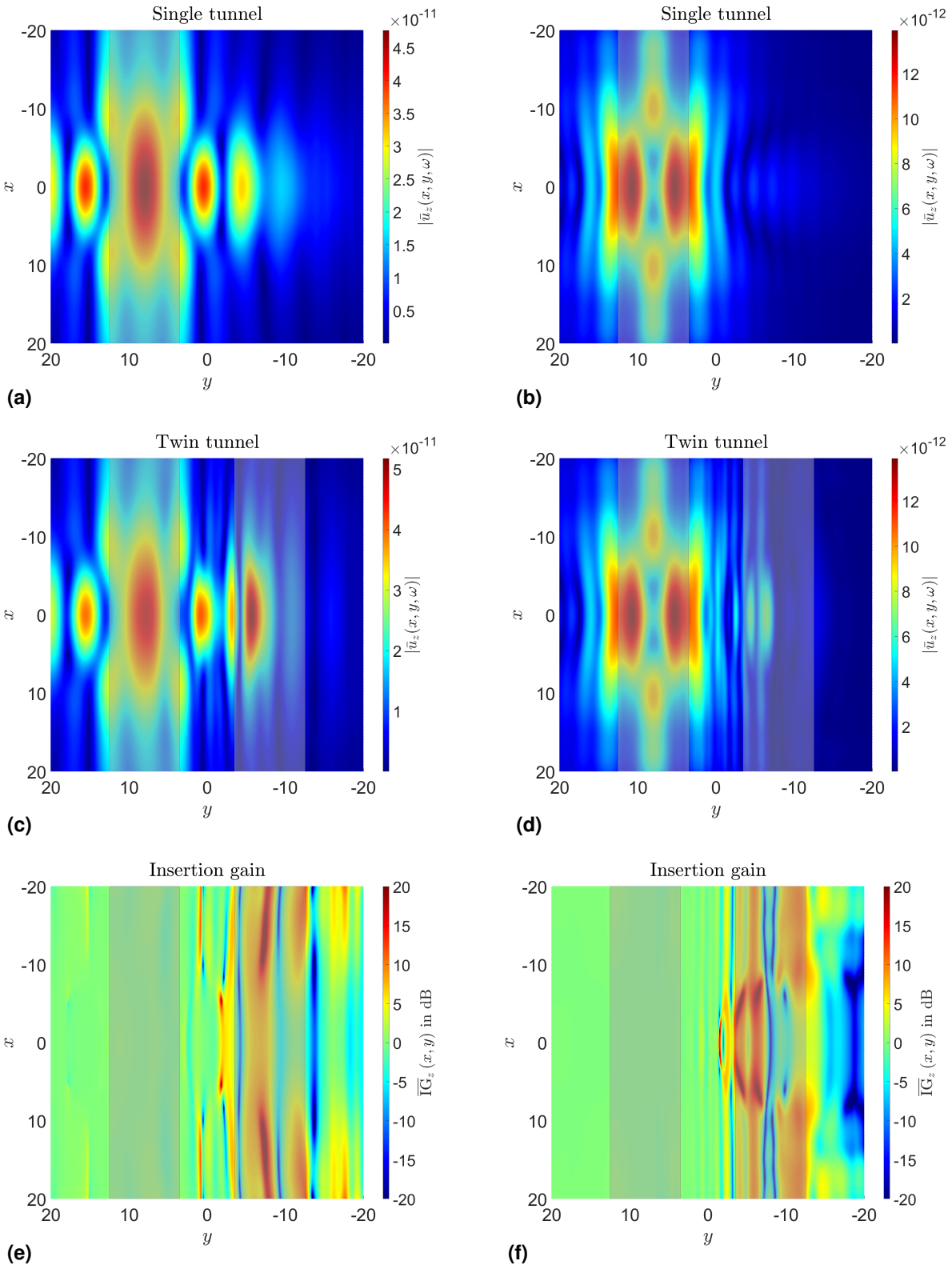

Figure 6.86: Absolute value of vertical displacements $|\bar{u}_z(x,y)|$ on the ground surface for (a),(b) single tunnel and (c),(d) twin tunnels due to a harmonic block load on the invert of tunnel T_1 at $f = 30\text{Hz}$ (left) and $f = 60\text{Hz}$ (right) as well as the corr. insertion gain $\overline{\text{IG}}_z$ according to the setup in Fig. 6.85 cp. [244].

7 Dynamic response to stationary transient loads

For many issues in soil dynamics and soil structure interaction, a frequency domain analysis provides a very good insight into the dynamic behaviour of the system and the wave propagation characteristics. However, as soon as non harmonic processes such as earthquake, impact or pulse loads shall be considered, an investigation in the time domain is beneficial. Therein the transient response usually is gained by the convolution of an appropriate impulse or step response function with the respective transient load.

An alternative approach is to solve the governing equations in the frequency domain first in order to determine the complex frequency response functions of the system. The methodology for calculating these response functions, hereafter referred to as transfer functions (TFs), in the context of the presented approach is described in Sec. 7.1. Following, in Sec. 7.2 two equivalent procedures for the determination of the time histories of the system response are outlined in more detail. Therein Sec. 7.2.1 deals with the Fourier synthesis approach, applying a IFFT to the discrete frequency spectrum of the system response, whereas Sec. 7.2.2 treats the discrete convolution of the impulse response functions (IRFs), obtained from an inverse transform of the TFs for a large frequency range, with the transient load in the time domain. The influence of the restriction of the amount of considered frequencies for the computation of the TFs due to limited computational capacities is discussed and a confidence measure quantifying the introduced error is defined. Subsequently, the transient response of a homogeneous halfspace to a superposition of harmonic loads with different frequencies is presented in Sec. 7.3.1, while Sec. 7.3.2 covers the response to a suddenly applied rectangular load on the soil surface, illustrating the time dependent displacements at different positions on the ground surface. Furthermore, the effects introduced by the numerical computation applying the FFT as well as the influence of the hysteretic material damping on the causality of the response are discussed. Sec. 7.4 addresses the transient response of rigid massless and massive surface foundations due to a Heaviside loading. The obtained dimensionless foundation flexibilities are compared to literature solutions for validation. Finally, in Sec. 7.5 the

transient response of a twin tunnel system, modelled with the 2.5D coupled ITM-FEM approach, due to a pulse load in one of the two tunnel tubes is investigated and displacements at the ground surface as well as in both tunnels are presented.

7.1 Frequency transfer functions (TFs)

The transfer function describes the dynamic behaviour of a system as a function of frequency and can thus be used to calculate the conversion of any input signal through the system and to determine the corresponding output signals. It thus describes the dynamic response of the system completely and independently of the respective frequency amplitude spectra of the input [302]. For the considered systems, the input is specified by a loading $\bar{\mathbf{P}}(x,y,z,\omega)$ at selected discretization points of either the ITM or the FEM substructure, while the corresponding output signals are given by the resulting displacements $\bar{\mathbf{u}}(x,y,z,\omega)$ at all points (x,y,z) of interest. Thus the TFs for a specific frequency are defined as

$$\overline{\mathbf{TF}}(x,y,z,\omega)\ \bar{\mathbf{P}}(x,y,z,\omega) = \bar{\mathbf{u}}(x,y,z,\omega) \tag{7.1}$$

In order to compute the transfer function matrix $\overline{\mathbf{TF}}(x,y,z,\omega)$ of a system, its steady state response due to a harmonic load with unit amplitude over a sufficiently large frequency range, whose limits depend on the resp. system characteristics (cp. Sec. 7.2.3), is determined. In this case the TFs correspond directly to the response $\bar{\mathbf{u}}(x,y,z,\omega)$, which thus can be used to populate $\overline{\mathbf{TF}}(x,y,z,\omega)$.

However, since the solution of the fundamental and coupled systems, presented in Chs. 2, 3 and 5, is performed in the wavenumber frequency domain for negative frequencies, also the transfer functions are firstly evaluated w.r.t. this domain. Eq. (7.2) exemplarily gives the rule for the computation of the transfer functions for the soil displacements in case of a homogeneous halfspace due to a given load distribution $|\bar{\mathbf{P}}^{\mathbf{hs}}_{\mathbf{\Lambda_{ITM}}}(x,y,z,\omega)| = 1$ with unit frequency spectrum on the ground surface Λ

$$\widehat{\overline{\mathbf{TF}}}(k_x,k_y,z,\omega \leq 0) = \hat{\mathbf{K}}^{\mathbf{hs}\ -1}_{\mathbf{ITM}}(k_x,k_y,z,\omega \leq 0)\ \hat{\mathbf{P}}^{\mathbf{hs}}_{\mathbf{\Lambda_{ITM}}}(k_x,k_y,z,\omega \leq 0) \tag{7.2}$$

Obviously, for the solution of the elastodynamic problem, the spatial distribution of the load firstly needs to be transformed into the wavenumber frequency domain, in which the dynamic stiffness matrix of the considered system is defined. Eq. (7.2) holds analogously for all ITM and ITM-FEM systems introduced in this thesis. Depending on the system under consideration, only the dynamic stiffness matrix needs to be exchanged and the load vector

adjusted accordingly. Furthermore, it has to be noted, that in case of the cylindrical FEM substructure embedded in the soil, also the differing reference system in the transformed domain (k_x,r,n,ω) has to be considered.

Before applying the respective coordinate and discrete inverse Fourier transforms, to obtain the transfer functions in the spatial domain w.r.t. frequency $\overline{\mathbf{TF}}(x,y,z,\omega)$, the results for the positive frequencies $\omega > 0$ are supplemented as the corresponding conjugate complex values of $\omega < 0$. Thereby the following relations between the complex transfer functions $\overline{\mathbf{TF}}$ and their conjugate complex counterparts $\overline{\mathbf{TF}}^*$, deduced in [162], need to be satisfied

$$\overline{\mathbf{TF}}(+k_x,+k_y,\omega) = \overline{\mathbf{TF}}^*(-k_x,-k_y,-\omega) \qquad \overline{\mathbf{TF}}(-k_x,+k_y,\omega) = \overline{\mathbf{TF}}^*(+k_x,-k_y,-\omega)$$
$$\overline{\mathbf{TF}}(+k_x,-k_y,\omega) = \overline{\mathbf{TF}}^*(-k_x,+k_y,-\omega) \qquad \overline{\mathbf{TF}}(-k_x,-k_y,\omega) = \overline{\mathbf{TF}}^*(+k_x,+k_y,-\omega)$$

With $\overline{\mathbf{TF}}(x,y,z,\omega)$, valid for the initially chosen load configuration and after the complex conjugate expansion available over the total frequency range from $-\omega_{\max}$ ... $\omega_{\max}$, the basis for the determination of the transient system response is given.

7.2 Time domain response

7.2.1 Fourier synthesis approach

The most straightforward approach to determine the transient system response is, to scale the previously computed transfer functions $\overline{\mathbf{TF}}(x,y,z,\omega)$ for each discretization point with the frequency spectrum $\bar{\mathbf{P}}(\omega)$ of the time history of the load $\mathbf{P}(t)$. Since $\bar{\mathbf{P}}(\omega)$ is applied to all discretization points equally, the spatial dependency is omitted. The system response for a given load configuration can thus be determined as $\bar{\mathbf{u}}(x,y,z,\omega) = \overline{\mathbf{TF}}(x,y,z,\omega)\ \bar{\mathbf{P}}(\omega)$ and further be transformed back into the time domain $\mathbf{u}(x,y,z,t)$ using the IFFT.

However, in order to obtain a sufficiently fine discretization $\Delta t = 2\pi/(2\omega_{\max})$ for the response $\mathbf{u}(x,y,z,t)$ in the time domain by simultaneously long observation times $T = N_t \Delta t$, the system has to be evaluated for a large number of frequencies $N_f = N_t$ to reach a sufficient $\omega_{\max} = N_f\,\Delta\omega$ with a small frequency step size $\Delta\omega$, leading to a high computational effort. Depending on the type of load, two approaches were followed in this work to reduce the necessary calculation costs. In case of a harmonic load consisting of a superposition of sine or cosine loads with different frequencies and amplitudes, the system response is calculated only for the load frequencies and sorted into a matrix containing the transfer functions $\overline{\mathbf{TF}}(x,y,z,\omega)$ with a corresponding fine frequency discretization reaching up to a large $\omega_{\max}$ (cp. Fig. 7.1a). In case of a transient loading, the transfer functions are evaluated for a predefined set of frequencies $|\omega_{\text{calc}}| \leq \omega_{\max}$ and the values of $\overline{\mathbf{TF}}(x,y,z,\omega)$ for the intermediate

frequencies, in order to reach the desired $\Delta\omega$, are interpolated using a modified Akima cubic Hermite interpolation inherent in Matlab (cp. Fig. 7.1b). Thereby "the interpolated value at a query point is based on a piecewise function of polynomials with degree at most three evaluated using the values of neighbouring grid points in each respective dimension" [303]. This procedure works very well for the smooth transfer functions in case of a homogenous soil. However, in case of a soft soil layer over a rather stiff underlying halfspace, exhibiting layer resonances linked to distinct peaks in the transfer functions, the calculated frequencies have to be carefully chosen with a generally small spacing $\Delta\omega$. In general, the interpolation could also be performed in the wavenumber domain (k_x,k_y,ω), however, it is much more unstable there due to the strong peaks at k_s and k_r. Thus, the integration over the wavenumbers and the application of the interpolation over the frequency in the spatial domain is advantageous for the quality of the transient system response.

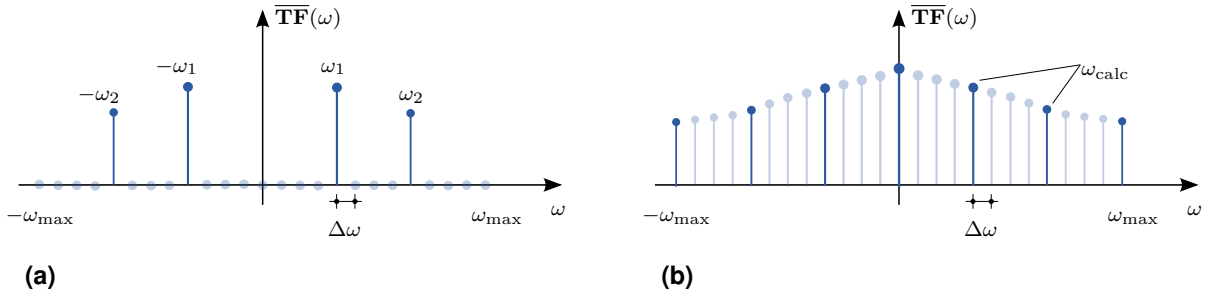

Figure 7.1: (a) Sorting of $\overline{\mathbf{TF}}(\omega_{\text{calc}})$ determined for the harmonic load frequencies ω_{calc} into a fine frequency vector and (b) interpolation of $\overline{\mathbf{TF}}(\omega)$ from ω_{calc} on finer frequency discretization, both exemplarily depicted for one single discretization point.

The same procedures are also applicable for the computation of the time histories of the flexibilities of rigid surface foundations $\mathbf{F_{f,r}}(t)$. In case an external load with unit amplitude, constant over the entire considered frequency range is chosen, the foundation flexibilities $\bar{\mathbf{F}}_{\mathbf{f,r}}(\omega)$, resulting from the frequency domain calculation, can simply be interpolated w.r.t. ω and then be scaled with the spectrum of the transient load $\bar{\mathbf{P}}_{\mathbf{sys}}(\omega)$ before applying the inverse Fourier transform.

The main steps of the procedure for the transient soil and rigid foundation response in case of a homogeneous or layered halfspace are exemplarily gathered in the pseudo code in Alg. 4.

7.2.2 Discrete convolution (Duhamel)

A different but equivalent approach to determine the transient system response is to use the Duhamel integral, which states that for linear systems the response $\mathbf{u}(t)$ to an arbitrary

Algorithm 4 Transient soil and foundation response for homog. and layered soil

procedure MAIN HS 1L FVAR
Initialize and input parameters
Material parameter
Discretization and geometry
Load for TF $\bar{\mathbf{P}}(x,y,z,\omega) \rightarrow \hat{\mathbf{P}}(k_x,k_y,z,\omega)$ with $|\hat{\mathbf{P}}(\omega)| = 1$

function DISPL ITM( )
$\widehat{\mathbf{TF}}(k_x,k_y,z,\omega \leq 0) = \hat{\mathbf{K}}^{-1}_{\mathbf{ITM}}(k_x,k_y,z,\omega \leq 0)\, \hat{\mathbf{P}}_{\mathbf{\Lambda_{ITM}}}(k_x,k_y,z,\omega \leq 0)$
via fundamental solution for each (k_x, k_y, ω)

Add conj. complex solution for $\omega > 0$
IFFT w.r.t. space: $\widehat{\mathbf{TF}}(k_x,k_y,z,\omega) \rightarrow \overline{\mathbf{TF}}(x,y,z,\omega)$
Load for time domain response $\mathbf{P}(t) \rightarrow \bar{\mathbf{P}}(\omega)$

function IFFT DISPL PT( )
Transient soil response $\bar{\mathbf{u}}(x,y,z,\omega) = \overline{\mathbf{TF}}(x,y,z,\omega)\, \bar{\mathbf{P}}(\omega)$
Inverse transform w.r.t. time: $\mathbf{u}(x,y,z,t) = \text{IFFT}\,(\,\bar{\mathbf{u}}(x,y,z,\omega))$

function STIFF FOUND RIGID( )
Soil flexibility at contact surface $\bar{\mathbf{F}}_{\mathbf{s}}(x,y,z,\omega)$
due to concentrated load with $|\bar{\mathbf{P}}(x,y,\omega)| = 1$
Transfer function of rigid foundation flexibility $\overline{\mathbf{TF}}_{\mathbf{F_{f,r}}}(\omega)$
via kinematic condition

function IFFT DISPL PT FOUND( )
Transient foundation response $\bar{\mathbf{F}}_{\mathbf{f,r}}(\omega) = \overline{\mathbf{TF}}_{\mathbf{F_{f,r}}}(\omega)\, \bar{\mathbf{P}}_{\mathbf{sys}}(\omega)$
Inverse transform w.r.t. time: $\mathbf{F}_{\mathbf{f,r}}(t) = \text{IFFT}\left(\bar{\mathbf{F}}_{\mathbf{f,r}}(\omega)\right)$
Postprocessing
Export and save

transient load $\mathbf{P}(t)$ can be calculated by superposing the responses $\mathbf{H}(t-\tau)$ to a sequence of infinitesimal impulses $\mathbf{P}(\tau)$ up to the considered time t

$$\mathbf{u}(t) = \int_{\tau=0}^{\tau=t} \mathbf{P}(\tau)\mathbf{H}(t-\tau)d\tau = \mathbf{P}(t) * \mathbf{H}(t)$$

This superposition is equal to a convolution of the time dependent load $\mathbf{P}(t)$ and the impulse response function (IRF) of the investigated system $\mathbf{H}(t)$. For the considered ITM and ITM-FEM systems, the IRFs are obtained from an inverse Fourier transform of the TFs for a large frequency range, approximating the spectrum of a temporal Dirac impulse $\delta(t = 0)$.

Since the TFs are calculated numerically and thus the impulse response is not available in analytical form, the convolution integral must also be computed discretely and is given by

$$\mathbf{u}(k) = \sum_j \mathbf{P}(j)\ \mathbf{H}(k-j+1) \tag{7.3}$$

with $j = \max(1,k+1-n) : 1 : \min(k,m)$, whereby m and n are the number of time samples of $\mathbf{P}(t)$ and $\mathbf{H}(t)$ [304].

As before, the discrete convolution can be applied equivalently to the computation of transient soil displacements as well as foundation flexibilities by using the respective impulse response functions $\mathbf{H}(t)$. The procedure for both possible approaches, the Fourier synthesis and the discrete convolution are exemplarily depicted in Fig. 7.2 for the computation of the time histories $\mathbf{F}^{\mathbf{F_{11}}}_{\mathbf{f,r}}(t)$ of a rigid massless surface foundation on a homogeneous halfspace.

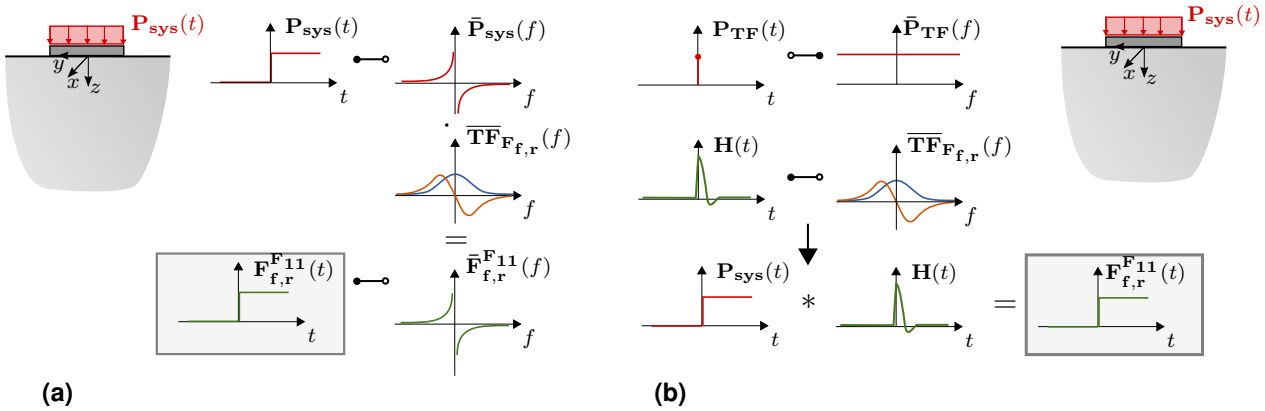

Figure 7.2: Procedure for the determination of the transient response of a rigid massless foundation with (a) the Fourier synthesis approach and (b) the discrete convolution.

7.2.3 Assessment of frequency band limitation

In the numerical evaluation of a system, only a limited number of discrete values can generally be processed due to computational limitations. Therefore, when dealing with transient system responses, which were originally obtained from frequency domain solutions, the following question immediately arises: Up to which maximum frequency $\omega_{\max}$ must the system response be calculated so that only a negligible error is introduced into the solution? This question applies to both, the determination of the time history of the system response from the frequency spectrum by means of Fourier synthesis and the determination of the impulse response function used for the discrete convolution. In order to enable a quantitative assessment of this question, a short excursion into system norms, as used in signal theory, is provided hereinafter.

Signal processing and energy considerations

In signal processing system norms, measuring the magnitude of the signals involved, are used to quantitatively estimate the performance of a system. To this end the L_2 norm resp. the root sum square (RSS) for a discrete signal is introduced as

$$||x(t)||_2 = \sqrt{\sum_{n=-\infty}^{\infty} |x[n]|^2} \tag{7.4}$$

with $x(t)\,\epsilon\,L_2$ and the L_2-space being a set of square integrable signals with $\int_{-\infty}^{\infty} |x(t)|^2\,\mathrm{d}t < \infty$. Therewith, the total energy of a signal E_{sig}, defined as the area under the squared magnitude of the signal can also be expressed as the square of the L_2 norm $||x(t)||_2^2$.

$$E_{\mathrm{sig}} = \sum_{n=-\infty}^{\infty} |x[n]|^2 \tag{7.5}$$

Furthermore, with the Plancherel theorem, stating that the energy content of a signal in the time and the frequency domain is equal, and Parseval's identity, relating the signal energy to the sum over the squares of its Fourier coefficients, it can be shown that the squares of the L_2 norms of a discrete signal with N samples in time and frequency domain are equal up to the constant factor N [305].

$$E_{\mathrm{sig}} \approx \sum_{n=0}^{N-1} |x[n]|^2 = \frac{1}{N} \sum_{k=0}^{N-1} |X[k]|^2 \tag{7.6}$$

Thereby $|X[k]|^2$ is proportional to the energy content of the signal at a specific frequency k and is further used to introduce an error measure for the frequency band limitation in terms of the signal energy in the frequency domain. However, it should be noted that the physical energy of a system, unlike the energy of a signal, is linked to the units of the respective physical quantities, which can be incorporated via a system related constant factor Z

$$E = \frac{1}{Z} E_{\mathrm{sig}} \tag{7.7}$$

The physical energy of a signal is proportional to the RSS of the signal as long as Z is constant over the frequency. Since the response of the system and thus the signal in case of the SSI analysis depends on the soil stiffness $\bar{\mathbf{K}}_{\mathbf{s}}(\omega)$, E is not directly proportional to E_{sig}. Nevertheless, the RSS still provides a good estimate of the contribution of the signal up to a certain frequency threshold value regarding its total energy content.

Confidence measure

For the definition of the confidence measure, it is assumed that all frequencies, providing a relevant contribution to the transient system response, are included up to a threshold $f_{\max}$ (following f instead of ω is used for convenience) and thus higher frequency components $f > f_{\max}$ are quasi negligible. Therefore, the RSS of the signal $\sqrt{\sum_{k=0}^{f_{\max}} |X[k]|^2}$ is defined as reference solution and the difference in the system response, if evaluated only up to a frequency f_{ev}, is quantified by

$$\text{conf} = \frac{\sqrt{\sum_{0}^{f_{\text{ev}}} |X[k]|^2}}{\sqrt{\sum_{0}^{f_{\max}} |X[k]|^2}} \tag{7.8}$$

Fig. 7.3a shows the dimensionless vertical foundation flexibilities $|C_{zz}^{11}(f)|$ of a rigid massless square foundation with $B_f = 2$ m resting on a homogeneous halfspace (Soil A), evaluated up to $f_{\max} = 200$ Hz for a total domain size of $B_x = B_y = 256$ m with $N_x = N_y = 2^{11}$ sample points and $n_\Delta = 2$. The corresponding confidence measure, as defined in Eq. (7.8), is illustrated in Fig. 7.3b for a maximum evaluation frequency $f_{\text{ev}} = 100$ Hz. The confidence measure increases rather strongly in the low frequency range, indicating a large contribution of these components to the total system response regarding their energy content. In the higher frequency range the gain of the confidence measure decreases significantly, indicating a smaller contribution of these components.

This behaviour can also be explained by the monotonous decaying foundation flexibilities, converging to zero with increasing f and thus leading to a finite value of the sum over $|C_{zz}^{11}(f)|^2$ for $f \to \infty$, corresponding to the system energy. Therefore, the evaluation of the

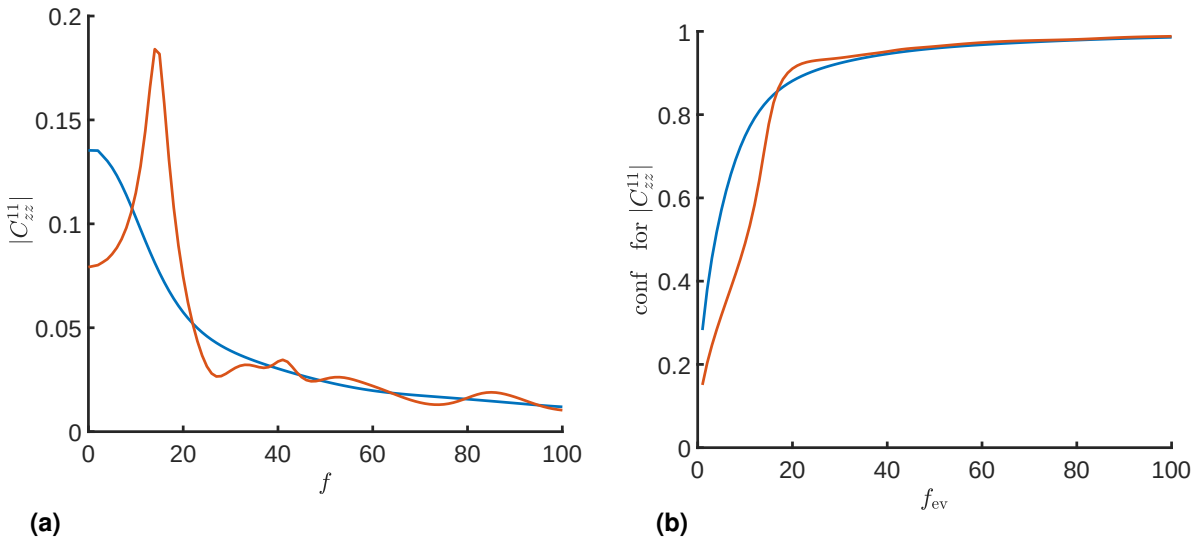

Figure 7.3: (a) Vertical dimensionless foundation flexibility $|C_{zz}^{11}|$ and (b) corr. confidence measure conf of rigid massless square foundation on homogeneous halfspace (—) and layered halfspace (—) with $B_f/h_1 = 1$ and $c_{s2}/c_{s1} = 3.16$.

foundation flexibilities up to conf(f_{ev}) until reaching a nearly horizontal slope is sufficient to obtain the transient system response with only a non significant error due to the frequency band limitation. The decrease of the slope of conf(f) and its approximation to a horizontal tangent would be even stronger in case of a massive footing, since $|C_{zz}^{11}(f)|$ tends to zero for considerably lower f, due to the mass inertia of the foundation.

In case of a layered ground with a soft layer (Soil A) of $h_1 = 2$ m over a stiffer halfspace (Soil B), a less monotonous decay of $|C_{zz}^{11}(f)|$ and clear peaks at the layer resonance frequencies are observed in Fig. 7.3a. However, the corresponding confidence measure conf(f), shown in Fig. 7.3b, converges to unity also here, since the peak amplitudes due to the large dimensions of h_1 compared to the wavelengths of the elastic waves in the ground diminish with increasing f and thus the behaviour approaches that of a homogeneous halfspace. Depending on the layer thickness and the stiffness contrast between layer and halfspace, the maximum evaluated frequency f_{ev} to reach conf ≈ 1 has to be adjusted accordingly.

7.3 Transient response of homogeneous halfspace

In the subsequent section, the transient response of a homogeneous halfspace (Soil A) due to a vertical, rectangular load on the ground surface $\mathbf{P}^{\mathbf{hs}}_{\mathbf{\Lambda_{ITM}}}(x,y,t)$ with a width of $b_x = b_y = 2$ m and different time histories $\mathbf{P}(t)$ is investigated, as depicted in Fig. 7.4. The material parameters of the soil are given in Tab. 7.1 and results are computed with a total domain size of $B_x = B_y = 128$ m with $N_x = N_y = 2^{11}$ samples.

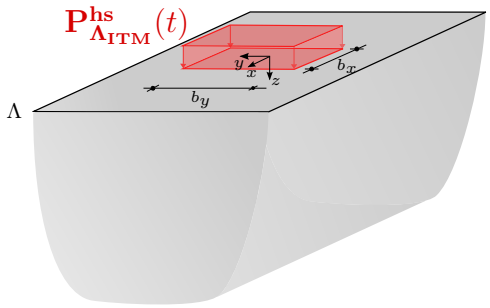

Figure 7.4: Setup for investigation of transient halfspace response.

7.3.1 Superposition of harmonic loads

Firstly, the soil response due to $|\mathbf{P}^{\mathbf{hs}}_{\mathbf{\Lambda_{ITM}}}(x,y)| = 1$ for a superposition of harmonic loads with $f_1 = 6$ Hz and $f_2 = 12$ Hz given by $\mathbf{P}(t) = P_{01}\cos(2\pi f_1 t) + P_{02}\cos(2\pi f_2 t)$ with $|P_{01}| = |P_{02}| = 2$ is analysed. This investigation is performed to test the implemented discrete procedure for the determination of the transient system response using the Fourier synthesis approach for a load case for which the time history of the displacements, after calculating the transfer function for the chosen frequencies, can be easily determined analytically for

	E (Nm^{-2})	ν $(-)$	ρ (kgm^{-3})	ζ $(-)$	c_p (ms^{-1})	c_s (ms^{-1})	c_r (ms^{-1})
Soil A	$2.60 \cdot 10^7$	0.30	2000	0.05	132.5	70.8	65.7
Soil B	$2.60 \cdot 10^8$	0.30	2000	0.05	418.8	223.9	207.7

Table 7.1: Material parameters of homogeneous and layered halfspace for transient analysis.

verification. The time history and the frequency spectrum $\bar{\mathbf{P}}(f) = \sum_i \delta(f - f_i) + \delta(f + f_i)$ of the load with $i = 1,2$ are depicted in Fig. 7.5a,b. The transfer function $\overline{\mathbf{TF}}$ of the vertical displacements $\bar{u}_z(f)$ at $(x,y,z) = (0,0,0)$ for the given load distribution $\mathbf{P}(x,y)$, shown in Fig. 7.5d, is further scaled with the load spectrum $\bar{\mathbf{P}}(f)$ to obtain the frequency response $\bar{u}_z(f)$, which in this case correspond directly to the values of $\overline{\mathbf{TF}}$ of $\bar{u}_z$ at $\pm f_1$ and $\pm f_2$.

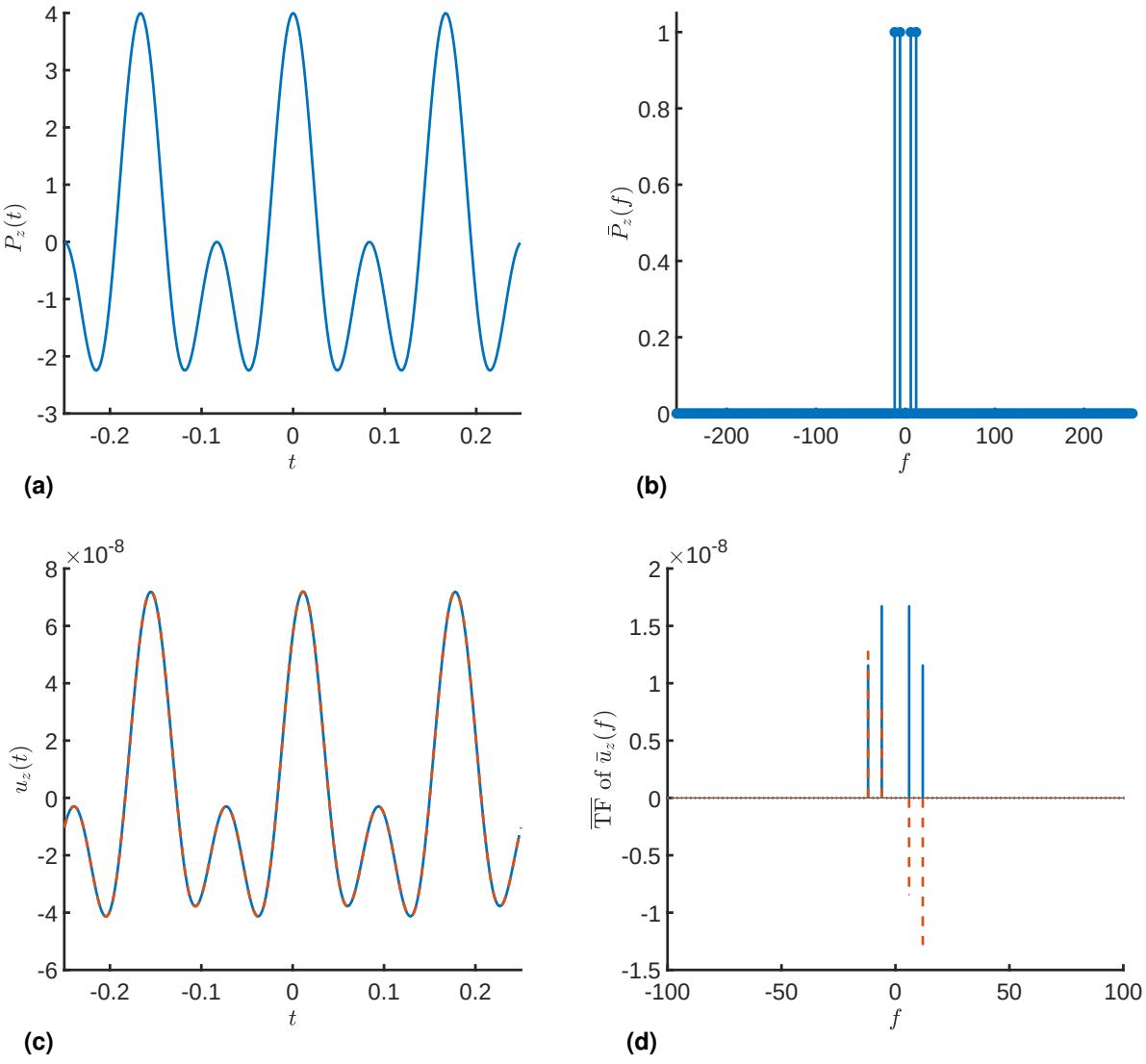

Figure 7.5: (a) Time history $P_z(t)$ and (b) frequency spectrum of the transient load $\bar{P}_z(f)$ as well as (d) real (—) and imaginary part (– –) of the transfer function of the soil displacements at $(x,y,z) = (0,0,0)$ for the given $\mathbf{P}(x,y)$ and (c) corr. transient soil displacements $u_z(x = 0, y = 0, z = 0, t)$ via numerical IFFT (—) and the analytical inverse transform (– –).

However, if a discrete inverse Fourier transform is applied, to achieve a sufficient time discretization for $u_z(t)$ the system response $\bar{u}_z(f)$ needs to be sorted into a finely discretized frequency vector with $|f_{\max}| = 256$ Hz in steps of $\Delta f = 1/T = 2$ Hz and thus $N_f = N_t = 2^8$ samples. The transient soil displacements, obtained from an IFFT of $\bar{u}_z(f)$ are illustrated in Fig. 7.5c for an observation time $T = 0.5$ s and a time step size of $\Delta t = T/N_t \approx 0.002$ s. Additionally to the numerical inverse transform via the IFFT, the analytical inverse Fourier transform was computed, using the values of $\bar{u}_z(f)$, at $\pm f_1$ and $\pm f_2$, which yields

$$u_z(t) = \sum_i \mathrm{Re}\left(\bar{u}_z(-f_i) + \bar{u}_z(f_i)\right)\cos(\omega_i t) + \sum_i \mathrm{Im}\left(\bar{u}_z(-f_i) - \bar{u}_z(f_i)\right)\sin(\omega_i t) \tag{7.9}$$

and is also depicted in Fig. 7.5c. Therein $u_z(t)$ at the center of the load $(x,y,z) = (0,0,0)$ on the ground surface shows a slight phase shift compared to the load $P_z(t)$ because of the soil damping. Otherwise the vertical soil displacements follow the progression of the load function rather accurately.

7.3.2 Suddenly applied loading

Soil response due to rectangular block load

Now the setup of Fig. 7.4 is investigated for a suddenly applied horizontal and vertical loading $|\mathbf{P}^{\mathbf{hs}}_{\mathbf{\Lambda_{ITM}}}(x,y)| = 1/(b_x\, b_y)$, with a time dependence given by the Heaviside step function (cp. App. A.5.3) and depicted in Fig. 7.6. The soil displacements are evaluated at $y = 0$ for different positions x_{ev} and presented w.r.t. to the dimensionless time $\tau = tc_s/x_{\mathrm{ev}}$ in Fig. 7.7. The results of the ITM approach were computed up to a maximum frequency $f_{\max} = 200$ Hz in steps of 2 Hz. To ensure a sufficient time discretization, the transfer function of the soil displacements was interpolated (cp. Sec. 7.2), finally providing $N_f = N_t = 3200$ frequency samples with $\Delta f = 0.125$ Hz leading to a time increment of

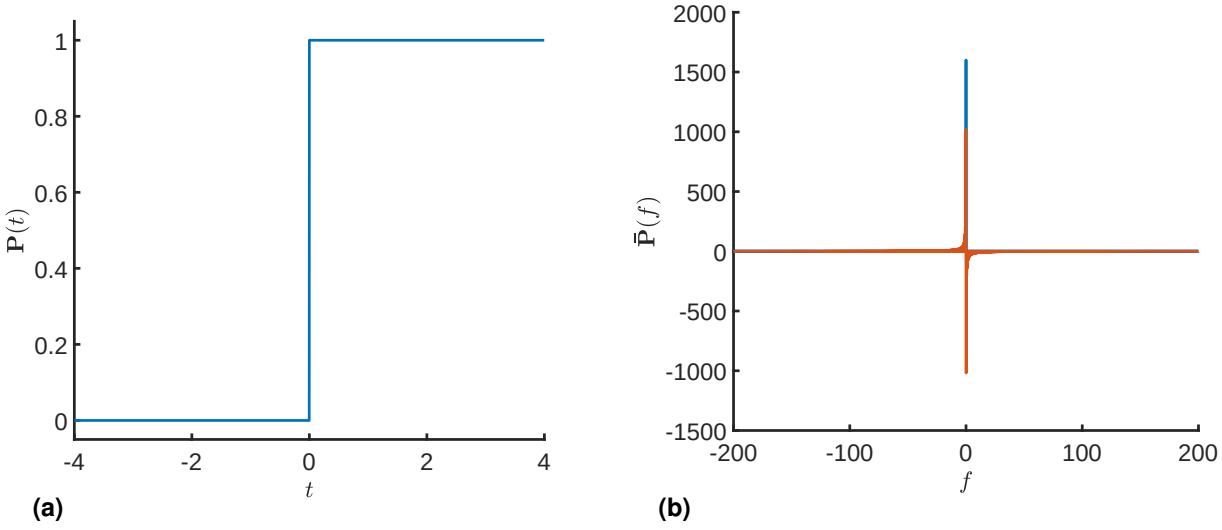

Figure 7.6: (a) Time history $\mathbf{P}(t)$ of the load with a time dependence given by the Heaviside step function and (b) real (—) and imaginary part (—) of the corr. frequency spectrum $\bar{\mathbf{P}}(f)$.

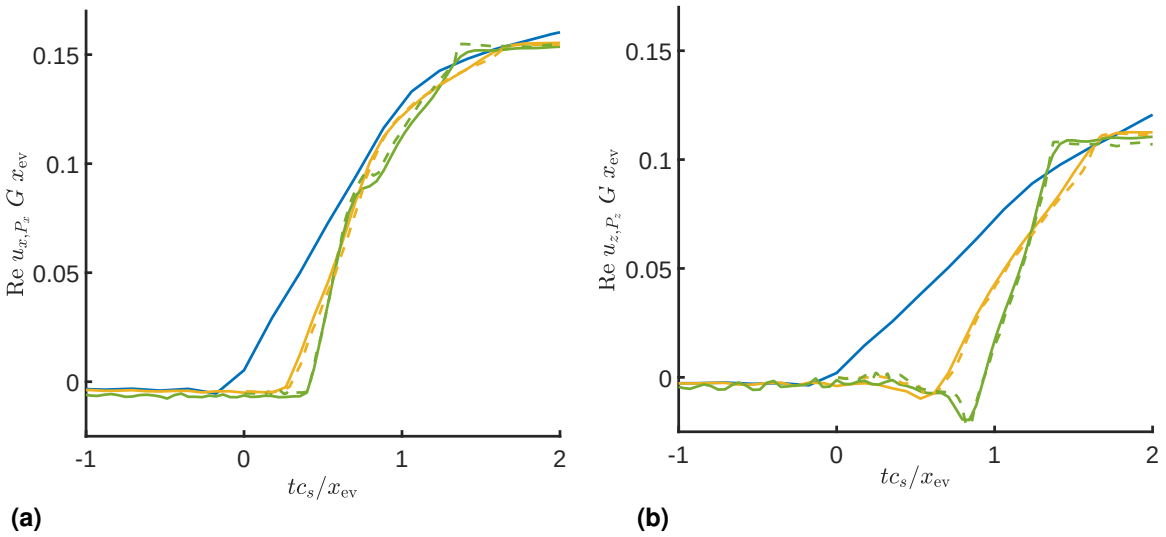

Figure 7.7: Dimensionless (a) horizontal $u_{x,P_x}(t)$ and (b) vertical $u_{z,P_z}(t)$ soil displacements due to a suddenly applied rectangular load (a) $P_x(t)$ and (b) $P_z(t)t$ evaluated at different positions $x_{ev} = b_x/2$ (—), $x_{ev} = b_x$ (—) and $x_{ev} = 2b_x$ (—) obtained with the ITM approach (straight) and by Guan and Novak [12] (dashed) w.r.t. dimensionless time $\tau = tc_s/x_{ev}$.

$\Delta t = 0.0025$ s for a total observation time of $T = 8$ s. For comparison the results presented in Guan and Novak [12], who derived a closed form solution for the considered problem by means of a Laplace transform w.r.t. time and Fourier transform w.r.t. space, are also included in Fig. 7.7. Since the solution in [12] was derived for an undamped soil and $\nu = 1/3$ the parameters of Soil A in Tab.7.1 were adapted to $\nu = 0.33$ and $\zeta = 0.02$.

In the histories of $u_{x,P_x}(t)$ and $u_{z,P_z}(t)$ due to a load $\mathbf{P}(x,y)$ in $x-$resp. $z-$direction, discontinuities arise at the arrival and during the passage of the Rayleigh waves, while these subsequently assume the values of the respective static deformation [12]. In addition, a more pronounced change in the displacements is observed as the distance of the receiving point increases, indicating a significant contribution of the Rayleigh wave due to its lower geometrical damping compared to the body waves. In general, a very good agreement between the ITM and the literature results is observed.

7.4 Transient response of a rigid foundation on homogeneous halfspace

7.4.1 Response of suddenly loaded massless or massive foundations

Within this section, firstly the response of a rigid massless ($M = 0$) and massive ($M = 1$) surface foundation with the dimensionless mass M given in Eq. (6.10), foundation width $B_f = 2$ m and height $H_f = 0.5$ m, resting on a homogenous halfspace (cp. Fig. 7.8), due to

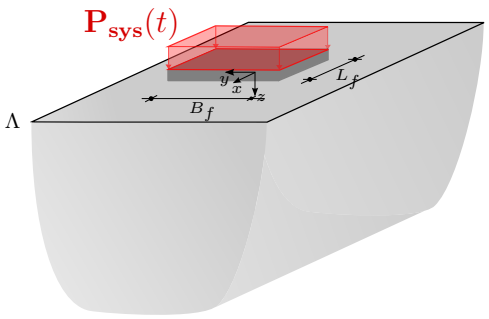

Figure 7.8: Setup for transient response of rigid surface foundation on homogeneous halfspace.

a Heaviside step load is investigated. For the soil, material parameters of Soil A in Tab. 7.1, however with $\zeta = 0.02$, were used in order to allow a better comparison with the literature solutions obtained for an undamped soil later on. The foundation can either be modelled via the kinematic condition or by a FEM model with large E_f (cp. Sec. 5.3.2), both leading to the same results (cp. Fig. 6.74). All calculations in this section were run with a total domain size of $B_x = B_y = 128$ m with $N_x = N_y = 2^{12}$ samples.

The transfer functions of the vertical flexibilities of the massless and the massive foundation were computed by means of a frequency domain analysis with $\Delta f = 2$ Hz up to $|f_{\max}| = 100$ Hz. The interpolated $\overline{\text{TF}}$s of $C_{zz}^{11}(f)$ with $N_f = 800$ are depicted in Fig. 7.9a, whereby in case of $M = 1$ the resonance peak of the vertical rigid body mode in the low frequency range is clearly visible as well as the much stronger decay of $|C_{zz}^{11}|$ towards zero with increasing frequency, due to the inertia of the foundation. Fig. 7.9b shows the time history of C_{zz}^{11}

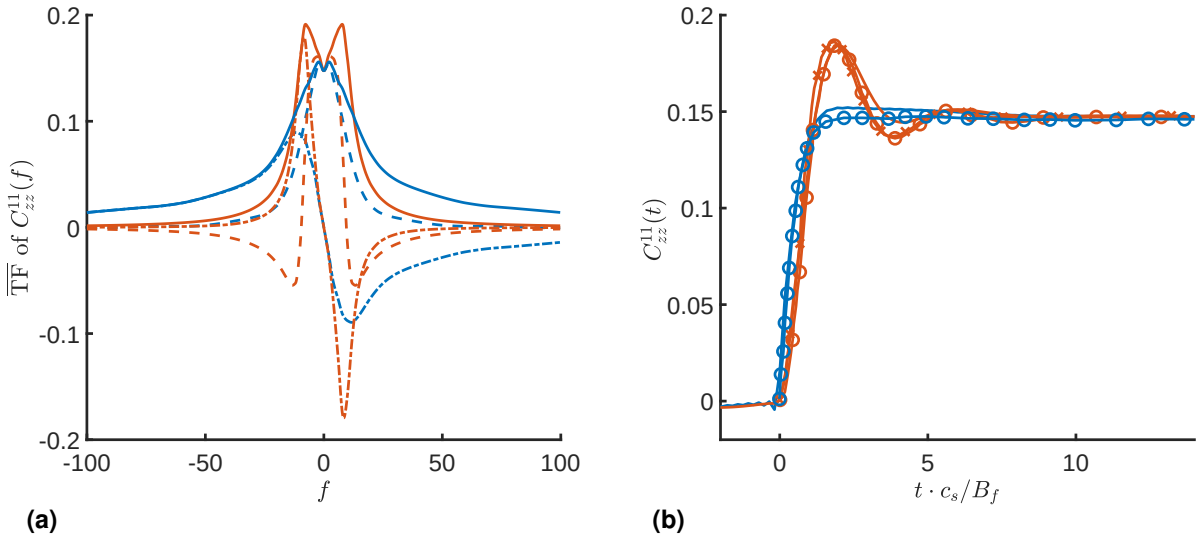

Figure 7.9: (a) Real (dash), imaginary (dash-dot) and absolute value (straight) of the frequency transfer function $\overline{\text{TF}}$ of C_{zz}^{11} of a rigid foundation on homogeneous soil for $M = 0$ (—) and $M = 1$ (—) and (b) transient flexibility $C_{zz}^{11}(t)$ due to Heaviside load $P_z(t)$ obtained with the ITM-FEM approach ($-$) as well as the results of Friedrich [286] ($\circ$) and Bode [67] ($\times$).

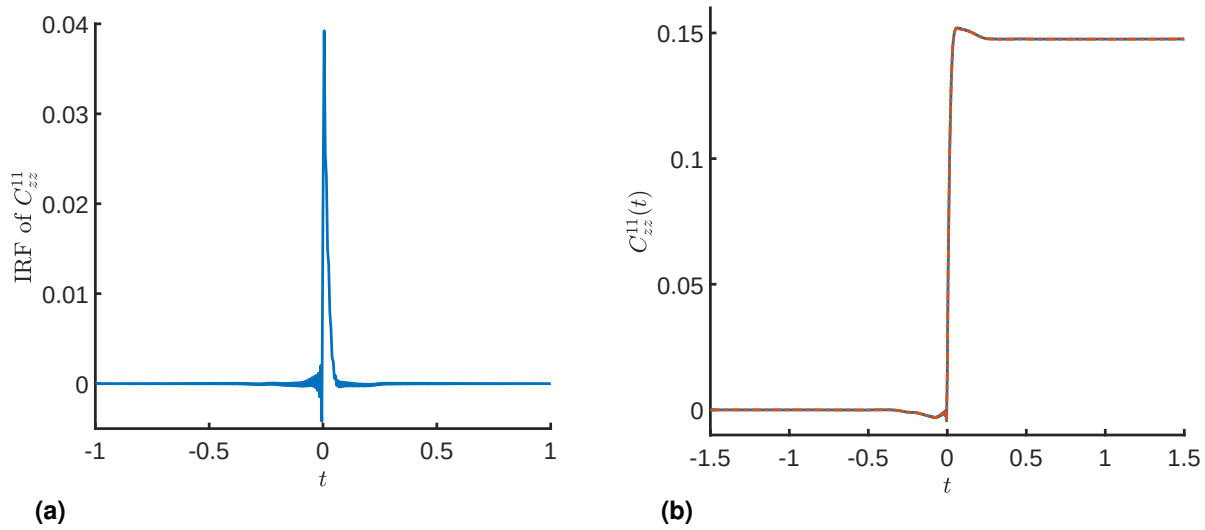

Figure 7.10: (a) Impulse response function IRF of C_{zz}^{11} of a rigid massless foundation on homogeneous soil and (b) corr. transient foundation flexibility $C_{zz}^{11}(t)$ obtained with the ITM-FEM approach applying the Fourier synthesis approach (—) and the discrete convolution (—).

computed with the ITM-FEM approach for $N_t = 800$ time samples, leading to a time step of $\Delta t = 0.005$ s for an observation time of $T = 4$ s. The static compliance remains unchanged regardless the foundation mass, yet the time to reach the static state differs considerably due to pronounced natural vibrations caused by the mass inertia. Tab. 7.2 summarises some normalised static compliance presented in literature and determined using different time and frequency domain methods, showing good agreement with the results gained from the ITM-FEM approach. Furthermore, the time histories of C_{zz}^{11} for $M = 0$ and $M = 1$ in Fig. 7.9b generally show good accordance with those in Bode [67] and Friedrich [286]. However, for $M = 1$, the ITM-FEM results converge to the static solution faster and show a small phase shift compared to the literature results, which is due to the hysteretic material damping required in the ITM and not included in [67, 286].

Fig. 7.10a shows the impulse response function for the vertical flexibility C_{zz}^{11} of a rigid massless foundation, computed from the interpolated transfer function of Fig. 7.9a. The

	$\lvert C_{zz}^{11}(f=0)\rvert$	mesh size
Friedrich [286]	0.1458	(5×5)
Mohammadi and Karabalis [58]	0.1437	(8×8)
Wong and Luco [285]	0.1475	(8×8)
Bode et al. [69]	0.1441	(20×20)
ITM-FEM approach	0.1463	(16×16)
ITM-FEM approach	0.1475	(32×32)

Table 7.2: Comparison of the normalized static flexibility $\lvert C_{zz}^{11}(f=0)\rvert$ for a rigid square foundation resting on a homogeneous soil ($\nu = 0.3$).

IRF exhibits a strong peak at $t = 0$, when the step load is applied, and then decays rather quickly due to the large damping effect of the soil. The corresponding time history $C_{zz}^{11}(t)$, obtained from the discrete convolution of the IRF with the transient load $\mathbf{P}(t)$ is depicted in Fig. 7.10b. A complete agreement of the results from the convolution and those determined by means of the IFFT from the frequency spectrum $C_{zz}^{11}(f)$ is observed.

7.4.2 Causality and FFT effects

Considering the time history of $C_{zz}^{11}(t)$ in Fig. 7.10b over a longer period of time t instead of the only very short section in Fig. 7.9b presented w.r.t. tc_s/B_f, a small deflection already before the onset of the load as well as an overshoot beyond the static flexibility is noticeable. These effects can be traced back to two phenomena that are inherent in the ITM-FEM approach and are elaborated in more detail hereafter.

Firstly, within the ITM-FEM approach a frequency independent hysteretic material damping was introduced via complex material parameters applying the correspondence principle. It was shown in Crandall [306] and is also reported by Veletsos and Verbic [307] and Kausel [308], that hysteretic oscillators do not rigorously satisfy causality, since when their motions "are transformed from the frequency domain into the time domain, small non-causal response precursors may precede the excitation" [308]. This effect is clearly visible in the time histories of the vertical displacement of a hysteretically damped SDOF system due to a Heaviside load, depicted in Fig. 7.11b for different ratios ζ. An increase of the precursor effect with increasing ζ is evident, whereas nearly no non-causal response occurs for low damping ratios. The corresponding transfer function in the frequency domain

$$\overline{\mathbf{TF}}(\omega) = \frac{1}{k\,(1 + \mathrm{i}\,\mathrm{sign}(\omega)2\zeta) - m\omega^2} \tag{7.10}$$

for $\zeta = 0.05$ is presented in Fig. 7.11a, showing a non vanishing imaginary part of $\overline{\mathbf{TF}}$ for $\omega \to 0$ related to the hysteretic damping and leading to a phase shift between excitation and response also for very low frequencies.

Secondly, the Heaviside load function exhibits a discontinuity at $t = 0$, which cannot be fully represented by a Fourier series expansion. An over- resp. undershoot up to 9% of the actual function values occurs at the jump discontinuity (Gibbs phenomenon) regardless the (finite) amount of considered Fourier members [309]. Since the frequency spectrum of the system response $C_{zz}^{11}(f)$ is obtained by multiplying the spectrum $\bar{\mathbf{P}}(f)$ of the Heaviside load with the transfer function $\overline{\mathbf{TF}}$, these overshoots also occur in the time history of the response $C_{zz}^{11}(t)$, obtained from a Fourier synthesis.

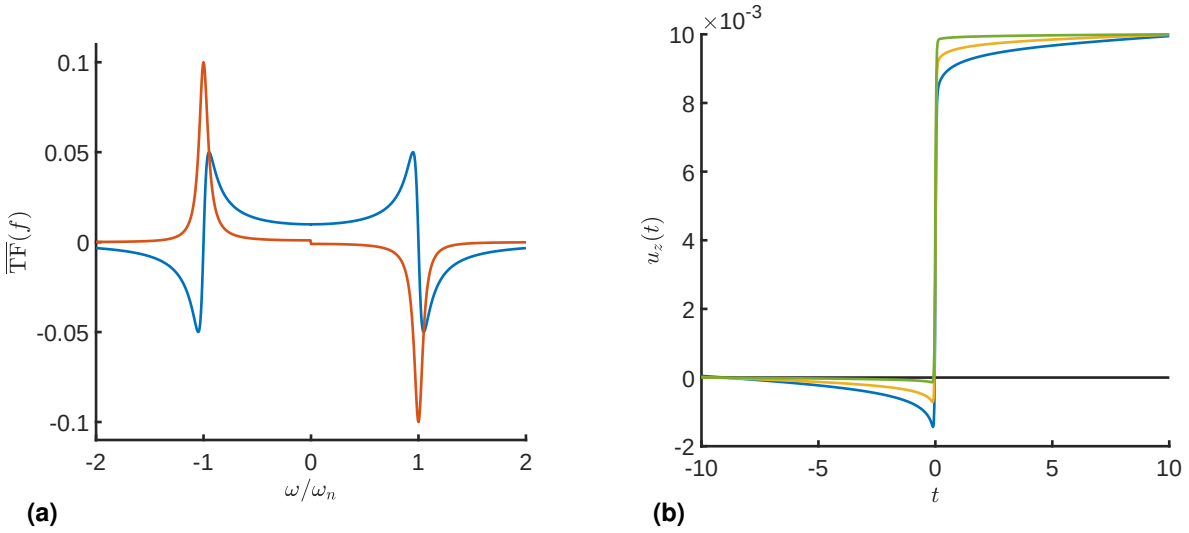

Figure 7.11: (a) Real (—) and imaginary part (—) of the frequency transfer function of the SDOF system for $\zeta = 0.05$ and $\omega_n = \sqrt{k/m}$. (b) Corresponding time history $u_z(t)$ due to a Heaviside load $\mathbf{P}(t)$ for $\zeta = 0.005$ (—), $\zeta = 0.025$ (—) and $\zeta = 0.05$ (—).

The combined effect of both phenomena leads to the time history of $C_{zz}^{11}(t)$, as it can be observed in Fig. 7.10b. One possibility to reduce the introduced numerical error due to Gibbs phenomenon is, to use a continuously defined load function without a jump such as the logistic function $\mathbf{P}(t) = (1 + \mathrm{e}^{-t})^{-1}$, which still exhibits a very steep slope at $t = 0$ but allows a much better approximation by a Fourier series expansion, thus significantly reducing the overshooting (cp. Fig. 7.12). Furthermore, a decrease of the hysteretic damping ratio ζ leads to a less pronounced non-causal effect. However, in order to minimize spatial aliasing and to guarantee a sufficient discretization of the small wavelengths at high frequencies in this case, large domain sizes B_x, B_y by simultaneously large sample numbers N_x, N_y need to be used, which leads to a significant increase in the computational effort.

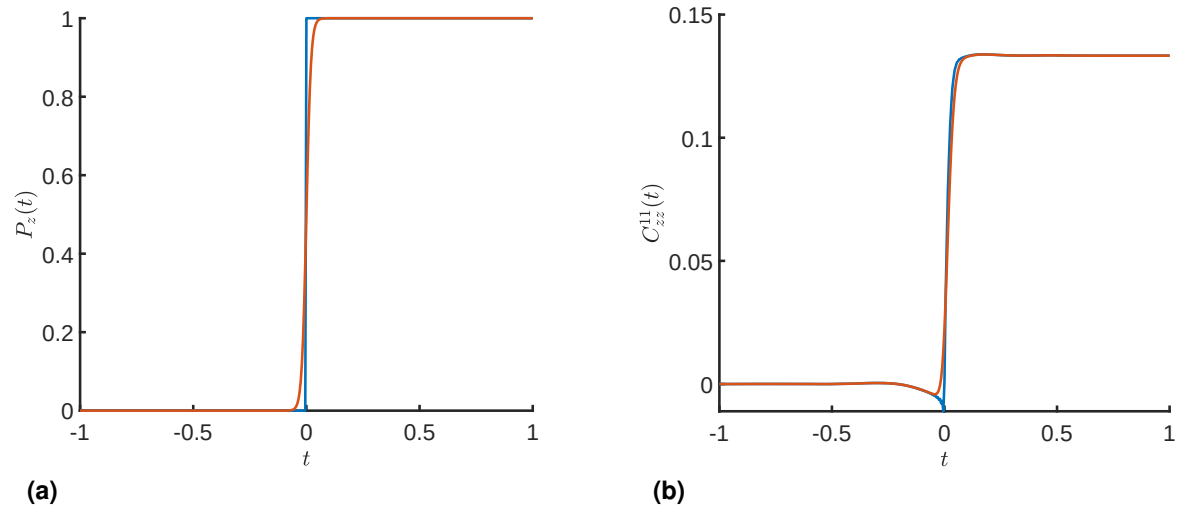

Figure 7.12: (a) Time history of load $P_z(t)$ for Heaviside (—) and logistic (—) load function. (b) Time history of corr. vertical flexibilities $C_{zz}^{11}(t)$ of rigid foundation with $B_f = 2$ m on homogenous halfspace (Soil A) for $\zeta = 0.05$ and $B_x = B_y = 128$ m, $N_x = N_y = 2^{10}$ with $f_{\max} = 100$ and $\Delta f = 2$ Hz resulting in $\Delta t = 0.005$ for $T = 4$ s.

7.4.3 Transient SSI contact stresses via postprocessing procedure

With the methodology outlined in this chapter, it is possible to determine the transient response of one or several foundations resting on a homogeneous or stratified soil as well as a soil with a length invariant inclusion. Thus, the transient contact stresses $\boldsymbol{\sigma}_{\mathbf{c}}(t)$ at the soil-foundation contact surface due to the SSI can also be calculated from the frequency spectrum $\bar{\boldsymbol{\sigma}}_{\mathbf{c}}(f)$ and used to predict the time dependent propagation of the elastic waves induced in the soil as well as the corr. deformation states, applying the postprocessing procedure outlined in Sec. 5.4.

7.5 Transient response of twin tunnels

Finally, the transient response of the twin tunnel system of Sec. 6.6, modelled with the coupled 2.5D ITM-FEM approach and depicted in Fig. 7.13, is investigated. Geometry, material and discretization parameter are chosen analogously as before, but instead of a harmonic load, a Gaussian-modulated sinusoidal pulse with $b_x = b_y = 1$ m is applied on the track within the tunnel T_1.

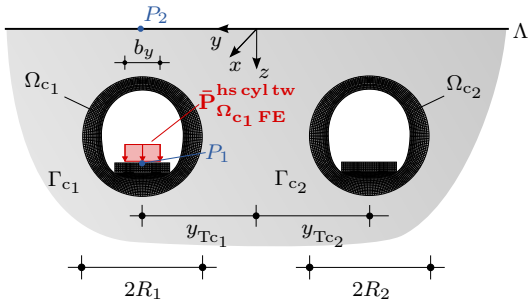

Figure 7.13: ITM-FEM model of a twin tunnel system embedded in homogeneous soil.

The time history as well as the frequency spectrum of the Gaussian-modulated sinusoidal pulse with a center frequency of $f_c = 10$ Hz and a bandwidth of 0.8 are shown in Fig. 7.14. The spectrum shows two major peaks around $\pm f_c$, while only small amplitudes occur for low frequencies. Moreover $\bar{\mathbf{P}}(f)$ tends to zero in the higher frequency range, i.e. $f \gtrapprox 20$ Hz. This characteristic is very beneficial for the application within the ITM-FEM approach for two reasons. Firstly, the system response only needs to be computed for a limited frequency range, since the transfer function is scaled with $\bar{\mathbf{P}}(f)$ and thus the spectrum of the system response also exhibits very small values for $f \gtrapprox 20$ Hz, as is clearly visible in Fig. 7.15a,c. Secondly, the rather small amplitudes of $\bar{\mathbf{P}}(f)$ for low frequencies lead to only a

small contribution of the response in this frequency range, for which the numerical solution is afflicted with larger numerical errors due to restrictions in the maximum possible size of the discretized domain, resulting from limited computational resources.

The transfer functions of the system response were originally calculated up to a maximum frequency $|f_{\max}| = 40$ Hz in steps of 1 Hz and interpolated subsequently, leading to $\overline{\mathbf{TF}}(f)$ discretized with $N_f = 320$ samples and $\Delta f = 0.25$ Hz. A total observation time of $T = 4$ s was chosen with $N_t = 320$ samples resulting in a time step of $\Delta t = 0.0125$ s. The corr. spectra $\bar{u}_z(f)$ and time histories $u_z(t)$ of the vertical displacements at the upper edge of the roadway in tunnel T_1 beneath the centre of the load as well as on the soil surface at $(x, y, z) = (0, 8, 0)$ directly over the tunnel T_1, indicated as P_1 and P_2 in Fig. 7.13, are presented in Fig. 7.15. As expected, the displacements at point P_1 follow the load progression very closely, while at point P_2 the influence of the wave propagation in the soil leads to a considerably altered spectrum as well as a slight temporal offset and a modified pulse shape in the time history of the displacements.

In addition, the deformation of the tunnels and the corr. distribution of the displacements on the ground surface are presented in Fig. 7.16 for different time steps t. Fig. 7.16a shows the first slight deformations in the left tunnel due to the onset of pulse loading, whereas no displacements occur yet at the surface and in the second tunnel. In the following, the disturbance propagates very quickly in longitudinal direction of the tunnel due to the high wave velocities in the concrete, whereas the propagation through the soil towards the second tunnel and the soil surface proceeds considerably slower. After h_{cyl}/c_i, the first shear and

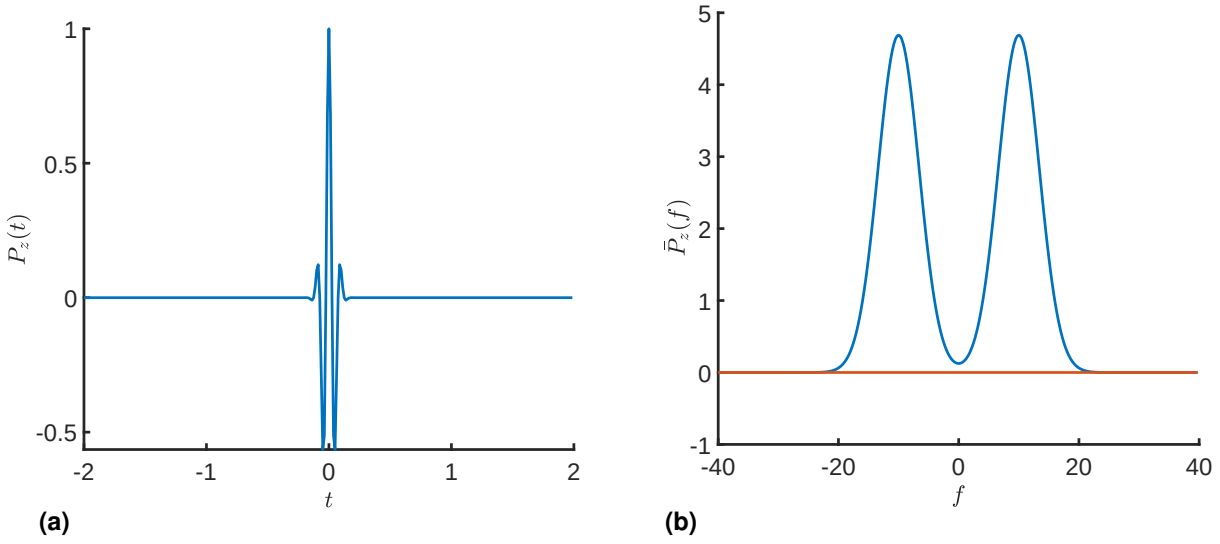

Figure 7.14: (a) Time history $P_z(t)$ and (b) real (—) and imaginary part (—) of frequency spectrum $\bar{P}_z(f)$ of the Gaussian-modulated sinusoidal pulse with $f_c = 10$ Hz and bandwidth of 0.8.

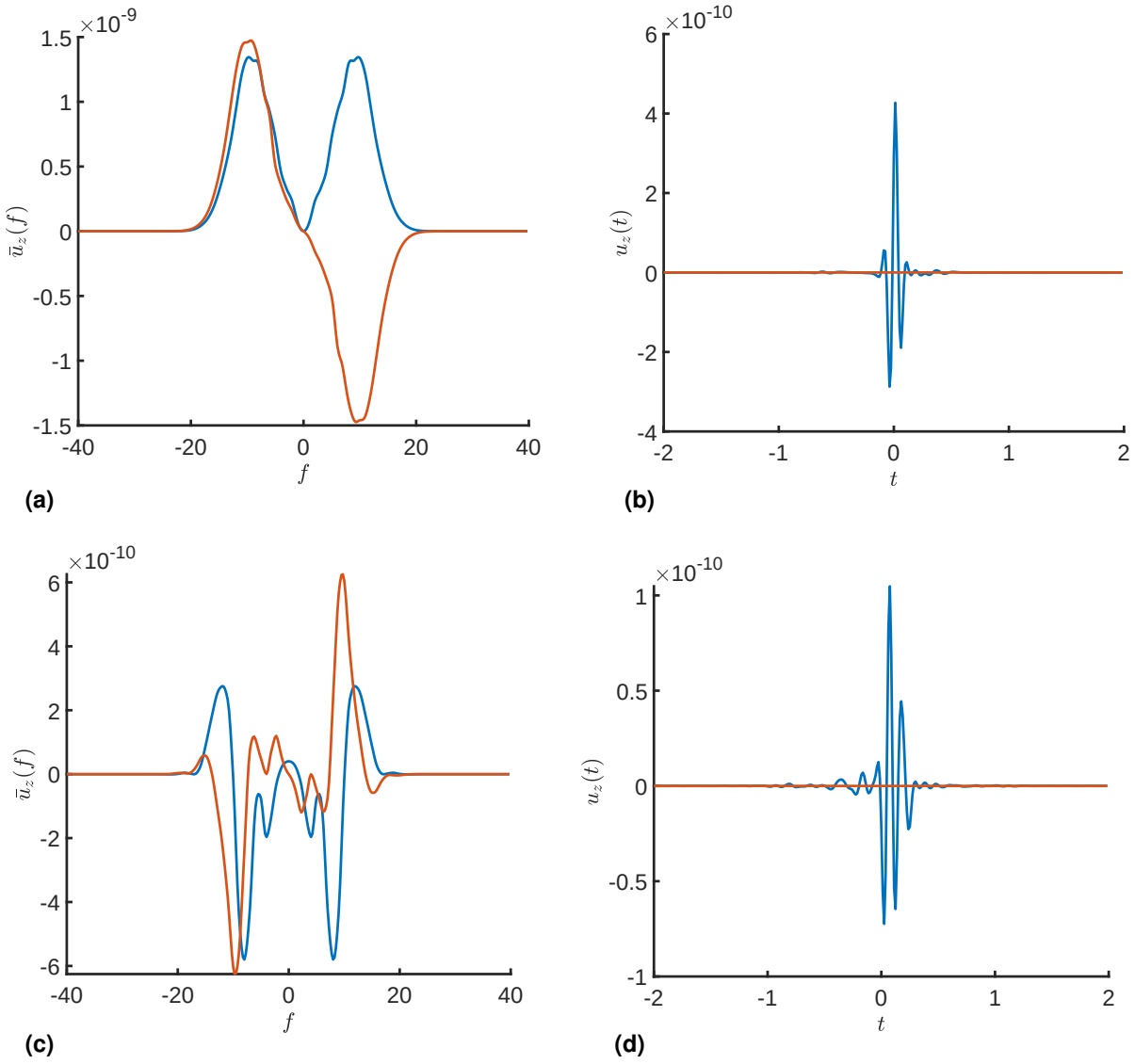

Figure 7.15: Real (—) and imaginary part (—) of $\bar{u}_z(f)$ (left) and $u_z(t)$ (right) due to the Gaussian-modulated sinusoidal pulse (a,b) at P_1 on the top of the slab within tunnel T_1 at $(x,y) = (0,8)$ and (c,d) P_2 on the soil surface $(x,y,z) = (0,8,0)$ directly above the loaded tunnel T_1.

Rayleigh waves, induced by $P_z(t)$ in T_1, reach the ground surface in Fig. 7.16c and propagate outwards from the source with wave fronts stretched in the x-direction, rather than cylindrically, due to the longitudinal stiffness of the tunnel. Moreover, in Figs. 7.16c,d first slight displacements are visibile at the second tunnel due to the arrival of the induced P-wave after $\mathrm{d}_{\mathrm{T}_{1-2}}/c_p$. First vertical shifts in T_2 appear in Figs. 7.16e,f when the S- and R- waves firstly impinge there. In Figs. 7.16h,i the further expansion of the waves within the soil and at the soil surface are depicted and the amplification of the displacement amplitudes at $y_{\mathrm{T}_{c2}} = -8$ m due to the superposition of the primary and the scattered waves at the second tunnel gets visible. At the same time, the displacements in the tunnel T_1 diminish after the end of the pulse loading $P_z(t)$ until it is at rest again.

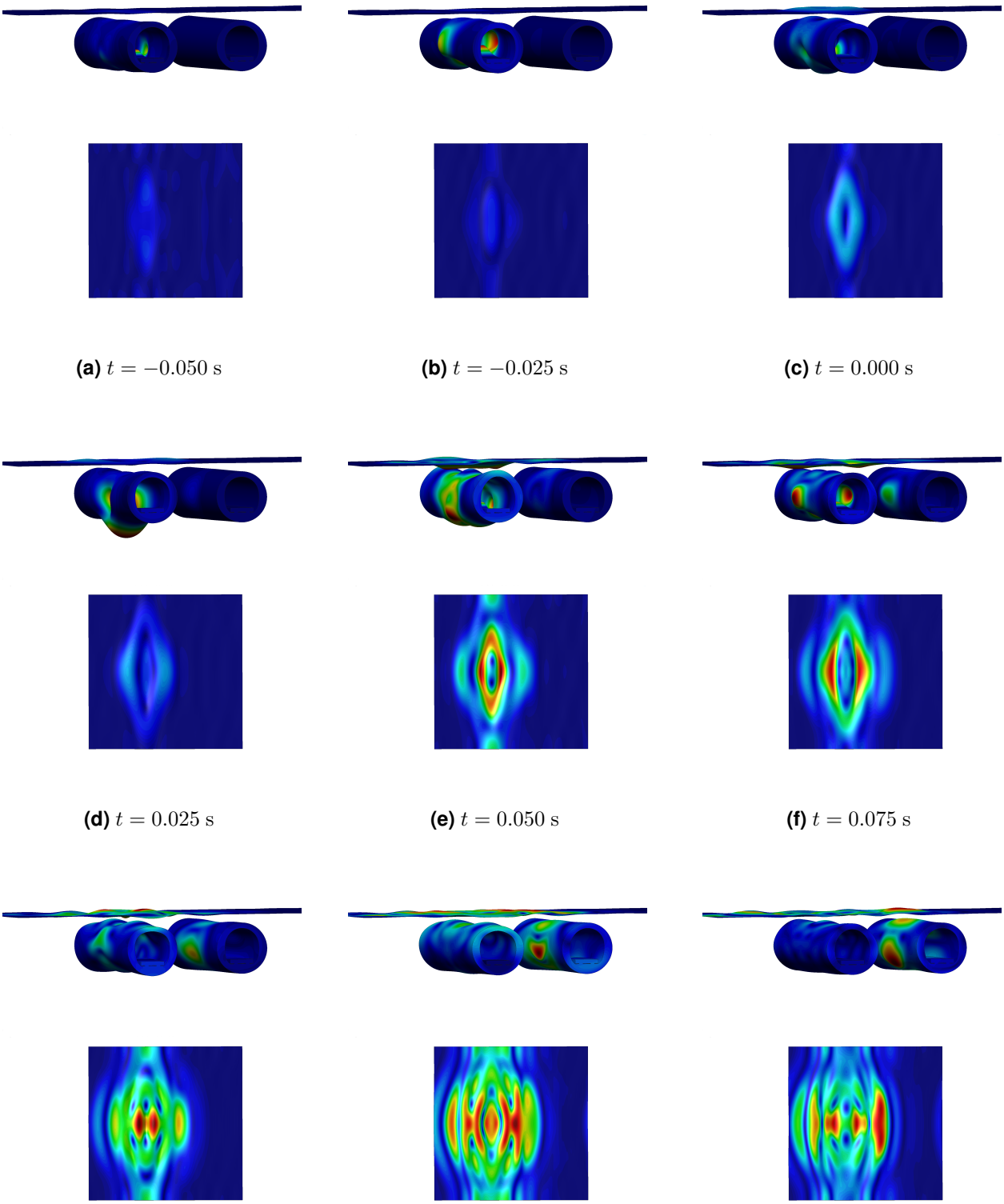

(a) $t = -0.050$ s **(b)** $t = -0.025$ s **(c)** $t = 0.000$ s

(d) $t = 0.025$ s **(e)** $t = 0.050$ s **(f)** $t = 0.075$ s

(g) $t = 0.100$ s **(h)** $t = 0.125$ s **(i)** $t = 0.150$ s

Figure 7.16: Time evolution of absolute value of total displacements for the entire twin tunnel system of Fig. 7.13 (upper subplot) and on the ground surface $z = 0$ (lower subplot) due to the Gaussian-modulated sinusoidal pulse of Fig. 7.14 for different time steps t (a-i).

8 Dynamic response to moving loads

After the investigation of the dynamic response of different fundamental and coupled systems due to stationary harmonic and transient loads, in the upcoming chapter the response to a constant or harmonically oscillating moving load is considered. For this purpose, firstly the general methodology for the incorporation of moving loads in the proposed ITM-FEM approach is derived in Sec. 8.1. Subsequently in Sec. 8.2, the implementation is validated by comparison of the results for a constant moving load on the homogeneous halfspace with literature results. Furthermore, the presented approach is applied in order to reproduce some typical physical phenomena such as the formation of shock waves for load speeds exceeding the wave velocities in the soil as well as the Doppler effect, occurring in case of an oscillating moving load, which is outlined in Sec. 8.3. Thereby relations of these effects to the corr. wavenumber spectra are drawn, highlighting the advantages of the analysis in the Fourier transformed domain for the interpretation of the wave propagation phenomena. Eventually, the moving load approach for coupled ITM-FEM systems is validated and a numerical example for a moving load within one tube of a twin tunnel system, modelled with the 2.5D ITM-FEM approach, is presented in Sec. 8.4.

8.1 Solution in the wavenumber frequency domain

The computation of the system response in the Fourier transformed domain offers the possibility to take into account dynamic loads moving on a straight line with a constant velocity very easily. Subsequently the procedure is exemplarily derived for a constant or harmonically oscillating load with arbitrary spatial distribution $\mathbf{P}_{\text{ITM}}(x,y)$ moving with constant velocity on the soil surface or within a layered soil. Thus the superscripts, indicating the resp. system, and the subscripts, indicating the surface on which the load is applied, are omitted. The procedure can analogously be adapted for moving loads inside a length invariant structure in case of the 2.5D ITM-FEM approach, whereby within the FEM substructure a Fourier transform is only necessary w.r.t. x and ω, while y remains untransformed.

A load $\mathbf{P_{mov}}(x,y,t)$ moving in $x-$direction and varying in time with $\mathbf{P}(t)$ is described by

$$\mathbf{P_{mov}}(x,y,t) = \mathbf{P_{ITM}}(x - vt,y) \cdot \mathbf{P}(t) \tag{8.1}$$

Applying a twofold Fourier transform from the spatial (x,y) into the wavenumber domain (k_x,k_y) and using the shifting theorem of the Fourier transform one obtains [160]

$$\tilde{\mathbf{P}}_{\mathbf{mov}}(k_x,k_y,t) = \int_{-\infty}^{\infty} \bar{\mathbf{P}}_{\mathbf{ITM}}(x - vt,k_y)\ \mathbf{P}(t)\ \mathrm{e}^{-\mathrm{i}\,k_x x}\ \mathrm{d}x = \tilde{\mathbf{P}}_{\mathbf{ITM}}(k_x,k_y)\ \mathrm{e}^{-\mathrm{i}\,vtk_x} \cdot \mathbf{P}(t) \tag{8.2}$$

A further Fourier transform into the frequency domain yields

$$\hat{\mathbf{P}}_{\mathbf{mov}}(k_x,k_y,\omega) = \tilde{\mathbf{P}}_{\mathbf{ITM}}(k_x,k_y) \int_{-\infty}^{\infty} \mathbf{P}(t)\ \mathrm{e}^{-\mathrm{i}\,vtk_x}\ \mathrm{e}^{-\mathrm{i}\,\omega t}\ \mathrm{d}t = \tilde{\mathbf{P}}_{\mathbf{ITM}}(k_x,k_y) \cdot \bar{\mathbf{P}}(\omega + vk_x) \tag{8.3}$$

Thus an axial movement of a load with velocity v oscillating with ω, leads to a wavenumber dependent frequency shift in the Fourier transformed domain $\bar{\omega} = \omega + vk_x$, whereas for a constant load with $\omega = 0$ simply a shifted frequency $\bar{\omega} = vk_x$ results.

In case of $\mathbf{P}(t) = \cos(\Omega t)$ the frequency spectrum yields $\bar{\mathbf{P}}(\omega) = \pi(\delta(\omega - \Omega) + \delta(\omega + \Omega))$ and therefore the moving load is given by

$$\hat{\mathbf{P}}_{\mathbf{mov}}(k_x,k_y,\omega) = \tilde{\mathbf{P}}_{\mathbf{ITM}}(k_x,k_y)\,\pi(\delta(\omega + vk_x - \Omega) + \delta(\omega + vk_x + \Omega)) \tag{8.4}$$

The resulting displacements $\hat{\mathbf{u}}_{\mathbf{ITM}}$ in the (k_x,k_y,z,ω) domain can be calculated using the fundamental solution $\hat{\mathbf{K}}^{-1}_{\mathbf{ITM}}$ for an unit load $|\hat{\mathbf{P}}_{\mathbf{ITM}}| = 1$ for each tuple (k_x,k_y,ω)

$$\begin{aligned}\hat{\mathbf{u}}_{\mathbf{ITM}}(k_x,k_y,\omega) &= \hat{\mathbf{K}}^{-1}_{\mathbf{ITM}}(k_x,k_y,\omega)\,\hat{\mathbf{P}}_{\mathbf{mov}}(k_x,k_y,\omega) \\ &= \hat{\mathbf{K}}^{-1}_{\mathbf{ITM}}(k_x,k_y,\omega)\,\tilde{\mathbf{P}}_{\mathbf{ITM}}(k_x,k_y) \cdot\ \pi\left(\delta(\omega + vk_x - \Omega) + \delta(\omega + vk_x + \Omega)\right)\end{aligned} \tag{8.5}$$

The displacements $\mathbf{u}_{\mathbf{ITM}}(x,y,t)$ in the original domain are obtained by means of a threefold inverse Fourier transform. Thereby the transformation into the time domain, applying the sifting property of the $\delta-$function $\int_{-\infty}^{\infty} f(x)\delta(x - x_0)\mathrm{d}x = f(x_0)$, yields

$$\begin{aligned}\tilde{\mathbf{u}}_{\mathbf{ITM}}(k_x,k_y,t) &= \frac{1}{2\pi} \int_{-\infty}^{\infty} \hat{\mathbf{u}}_{\mathbf{ITM}}(k_x,k_y,\omega)\,\mathrm{e}^{\mathrm{i}\omega t}\mathrm{d}\omega \\ &= \frac{1}{2}\tilde{\mathbf{P}}_{\mathbf{ITM}}(k_x,k_y)\left[\hat{\mathbf{K}}^{-1}_{\mathbf{ITM}}(k_x,k_y,+\Omega - vk_x)\mathrm{e}^{\mathrm{i}t(+\Omega - vk_x)}\right] \\ &+ \frac{1}{2}\tilde{\mathbf{P}}_{\mathbf{ITM}}(k_x,k_y)\left[\hat{\mathbf{K}}^{-1}_{\mathbf{ITM}}(k_x,k_y,-\Omega - vk_x)\mathrm{e}^{\mathrm{i}t(-\Omega - vk_x)}\right]\end{aligned} \tag{8.6}$$

A subsequent inverse transform from the wavenumber to the space domain results in

$$\begin{aligned}\mathbf{u}_{\mathbf{ITM}}(x,y,t) = \frac{1}{8\pi^2} \int_{-\infty}^{\infty}\int_{-\infty}^{\infty} \tilde{\mathbf{P}}_{\mathbf{ITM}}(k_x,k_y)\hat{\mathbf{K}}^{-1}_{\mathbf{ITM}}(k_x,k_y,+\Omega - vk_x)\mathrm{e}^{\mathrm{i}(t\Omega - tvk_x + yk_y + xk_x)}\mathrm{d}k_x\mathrm{d}k_y \\ + \frac{1}{8\pi^2} \int_{-\infty}^{\infty}\int_{-\infty}^{\infty} \tilde{\mathbf{P}}_{\mathbf{ITM}}(k_x,k_y)\hat{\mathbf{K}}^{-1}_{\mathbf{ITM}}(k_x,k_y,-\Omega - vk_x)\mathrm{e}^{\mathrm{i}(-t\Omega - tvk_x + yk_y + xk_x)}\mathrm{d}k_x\mathrm{d}k_y\end{aligned} \tag{8.7}$$

Introducing a moving coordinate system $\check{x} = x - vt$, which is equivalent to the evaluation of the displacement $\check{\mathbf{u}}(\check{x},y,z,t)$ at the current position of the load, the following relationship for the displacement with respect to the moving and a fixed coordinate system holds

$$\check{\mathbf{u}}_{\mathbf{ITM}}(\check{x},y,t) = \mathbf{u}_{\mathbf{ITM}}(x = \check{x} + vt,y,t) \tag{8.8}$$

Under application of the moving coordinate system and the shifting theorem one obtains

$$\begin{aligned}\check{\mathbf{u}}(\check{x},y,t) = \frac{\mathrm{e}^{\mathrm{i}\Omega t}}{8\pi^2} \int_{-\infty}^{\infty}\int_{-\infty}^{\infty} \tilde{\mathbf{P}}_{\mathbf{ITM}}(k_x,k_y)\hat{\mathbf{K}}^{-1}_{\mathbf{ITM}}(k_x,k_y,+\Omega - vk_x)\mathrm{e}^{\mathrm{i}(\check{x}k_x + yk_y)}\mathrm{d}k_y\mathrm{d}k_x \\ + \frac{\mathrm{e}^{-\mathrm{i}\Omega t}}{8\pi^2} \int_{-\infty}^{\infty}\int_{-\infty}^{\infty} \tilde{\mathbf{P}}_{\mathbf{ITM}}(k_x,k_y)\hat{\mathbf{K}}^{-1}_{\mathbf{ITM}}(k_x,k_y,-\Omega - vk_x)\mathrm{e}^{\mathrm{i}(\check{x}k_x + yk_y)}\mathrm{d}k_y\mathrm{d}k_x\end{aligned} \tag{8.9}$$

Because the resulting displacement $\check{\mathbf{u}}_{\mathbf{ITM}}(\check{x},y,z,t)$ in the original domain is a physical quantity, and therefore has to be real, the integrands in Eq. (8.9) must be conjugate complex. The two summands in (8.9) can thus be interpreted as pointers in the complex plane rotating in opposite direction. Hence, it is sufficient to determine only one of the two, as all necessary information (amplitude and phase) is comprised. To avoid the necessity of a case study, only the complex pointer related to the negative excitation frequency is taken into account [216]. The total real displacements in the moving coordinate system thus results as

$$\check{\mathbf{u}}(\check{x},y,t) = \frac{1}{4\pi^2}\,\mathrm{Re}\left(\mathrm{e}^{-\mathrm{i}\Omega t}\int_{-\infty}^{\infty}\int_{-\infty}^{\infty} \tilde{\mathbf{P}}_{\mathbf{ITM}}(k_x,k_y)\hat{\mathbf{K}}^{-1}_{\mathbf{ITM}}(k_x,k_y,-\Omega - vk_x)\mathrm{e}^{\mathrm{i}(\check{x}k_x + yk_y)}\mathrm{d}k_y\mathrm{d}k_x\right) \tag{8.10}$$

Therewith the displacements due to a moving load w.r.t. a moving coordinate system can be calculated using the spatially transformed load $\tilde{\mathbf{P}}_{\mathbf{ITM}}(k_x,k_y)$ and the soil stiffness, inserting a modified angular frequency $-\Omega - vk_x$. This wavenumber and velocity dependent frequency shift leads to a rotation in the $k_x - \omega-$spectrum of the system response exemplarily shown in Fig. 8.1.

Figure 8.1: Schematic sketch of the $k_x-\omega-$spectrum of the system response for (a) a stationary harmonic load and (b) a moving harmonic load.

The displacements w.r.t. a fixed coordinate system finally result as

$$\mathbf{u}(x,y,t) = \check{\mathbf{u}}(\check{x} = x - vt, y, t) \tag{8.11}$$

Thereby, due to the complexity of the integrals in equation (8.10), the inverse Fourier transform is not conducted analytically but evaluated numerically using the IFFT for a finite amount of wavenumbers k_x and k_y.

8.2 Constant moving load on homogenous halfspace

In this section, the response of a homogeneous halfspace due to a non-oscillating rectangular block load ($\mathbf{P}(t) = \text{const.}$) moving with constant velocity along the surface in positive $x-$direction (Fig. 8.2) is investigated. The steady state solution is considered, i.e. the disturbance due to the initial application of the load is not taken into account. Thereby three cases have to be considered, depending on the ratio of the load speed to the velocities of the elastic waves, expressed in terms of the *Mach* numbers $M_i = v/c_i$ with $i = p, s$ associated with the compressional resp. shear wave [200]: The subsonic case (M_p, $M_s < 1$), the transonic case ($M_p < 1$, $M_s > 1$) and the supersonic case (M_p,$M_s > 1$).

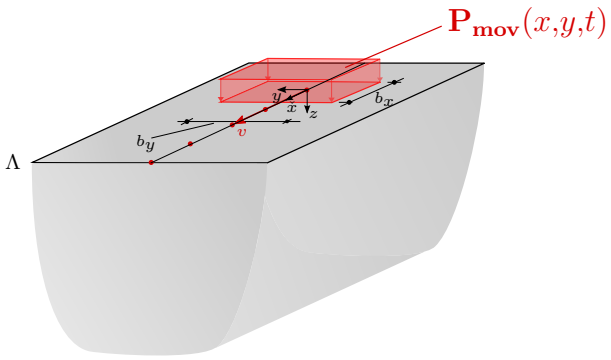

Figure 8.2: Halfspace with moving rectangular load on the soil surface.

8.2.1 Validation

Firstly, in order to validate the implementation of the ITM-FEM approach for moving loads, the results obtained for a subsonic load are compared to literature. Therefore, a constant rectangular block load with a width $b_x = b_y$ of approximately 2 m and unit total amplitude, moving with $v = 100$ ms^{-1} on the surface of a homogeneous halfspace with material parameters of Soil A in Tab. 8.1 is investigated.

	E (Nm^{-2})	ν $(-)$	ρ (kgm^{-3})	ζ $(-)$	c_p (ms^{-1})	c_s (ms^{-1})	c_r (ms^{-1})
Soil A	$1.88 \cdot 10^8$	0.30	1800	0.05	375.4	200.7	186.2
Soil B	$2.69 \cdot 10^8$	0.257	1550	0.05	460.0	263.1	242.3
Soil C	$2.60 \cdot 10^7$	0.30	2000	0.05	132.5	70.8	65.7

Table 8.1: Material parameters of the soil for moving load analysis.

A total domain size of $B_x = B_y = 100$ m with $N_x = N_y = 2^9$ sample points was chosen, leading to a maximum angular frequency of $|\omega_{\max}| = |-vk_x| = 1608.5$ rad s^{-1} with a step size of $\Delta\omega = 2\pi$. Thus in total $N_f = 2^9$ frequencies were considered for the Fourier synthesis, leading to the time history of the displacements $u_z(t)$ at $x = y = z = 0$ depicted in Fig. 8.3. The time history of $u_z(t)$ computed with the ITM-FEM approach shows a rather similar progression as those obtained by Bian and Chen [310], using an explicit time domain solution based on the TLM and the analytical solution given by Eason [201]. The differences in the results can be attributed to the slightly larger dimensions of the block load in the ITM-FEM approach, as well as the non-causal response due to the frequency-independent hysteretic damping. The load dimensions cannot be chosen completely arbitrarily, but are constrained to some extent by the implementation. The non-causality leads to a response, preceding the excitation, and thus a response prior to the actual passage of the load at the observation point. The combined effect results in the broader peak as in the literature solutions.

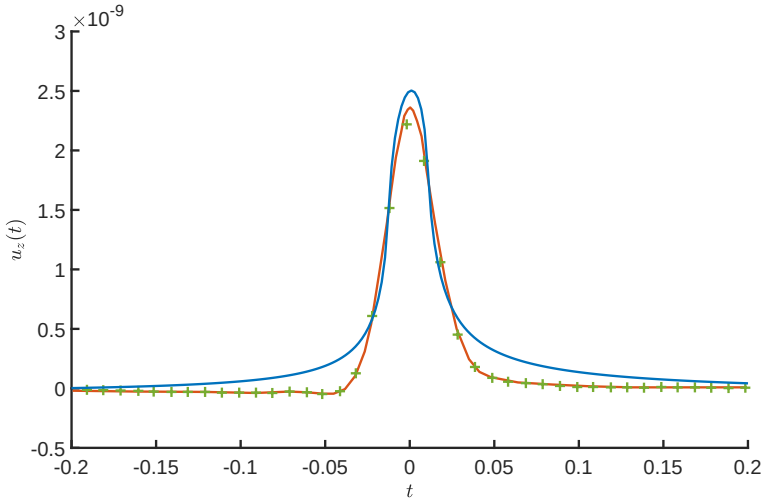

Figure 8.3: Vertical displacements $u_z(t)$ at $(x,y,z) = (0,0,0)$ due to moving rectangular block load on the surface of a homogeneous halfspace (Soil A) with $v = 100$ ms^{-1} obtained with ITM-FEM approach (—), Eason [201] in [310] (—) and Bian and Chen [310] (+).

8.2.2 Effect of varying load speed

Next, the effect of different velocities v of a non-oscillating block load with $b_x = b_y = 1$ m and $|\mathbf{P}^{\mathbf{hs}}_{\mathbf{\Lambda_{ITM}}}| = 1$ Nm^{-2} on the surface displacements of a homogeneous halfspace (Soil B in Tab. 8.1) is investigated. Within the computations, the total domain size ($B_x = B_y$) was adjusted in the corr. calculation depending on the load velocity in order to avoid spurious effects coming from the periodic repetition due to the FFT. However, in all cases $N_x = N_y = 2^9$ samples were considered and $N_f = 2^9$ frequency components up to $\omega_{\max} = -vk_x$ in steps of $\Delta\omega = 2\pi v/B_x$ Hz were taken into account.

The varying characteristics of the soil reaction in dependence of v become clearly visible in $u_z(x,y)$ on the ground surface for $t = 0$, when the load passes through the origin $(x,y) = (0,0)$. The resp. displacement distributions are shown in Fig. 8.4 and are subsequently discussed separately for the subsonic, the transonic and the supersonic regime.

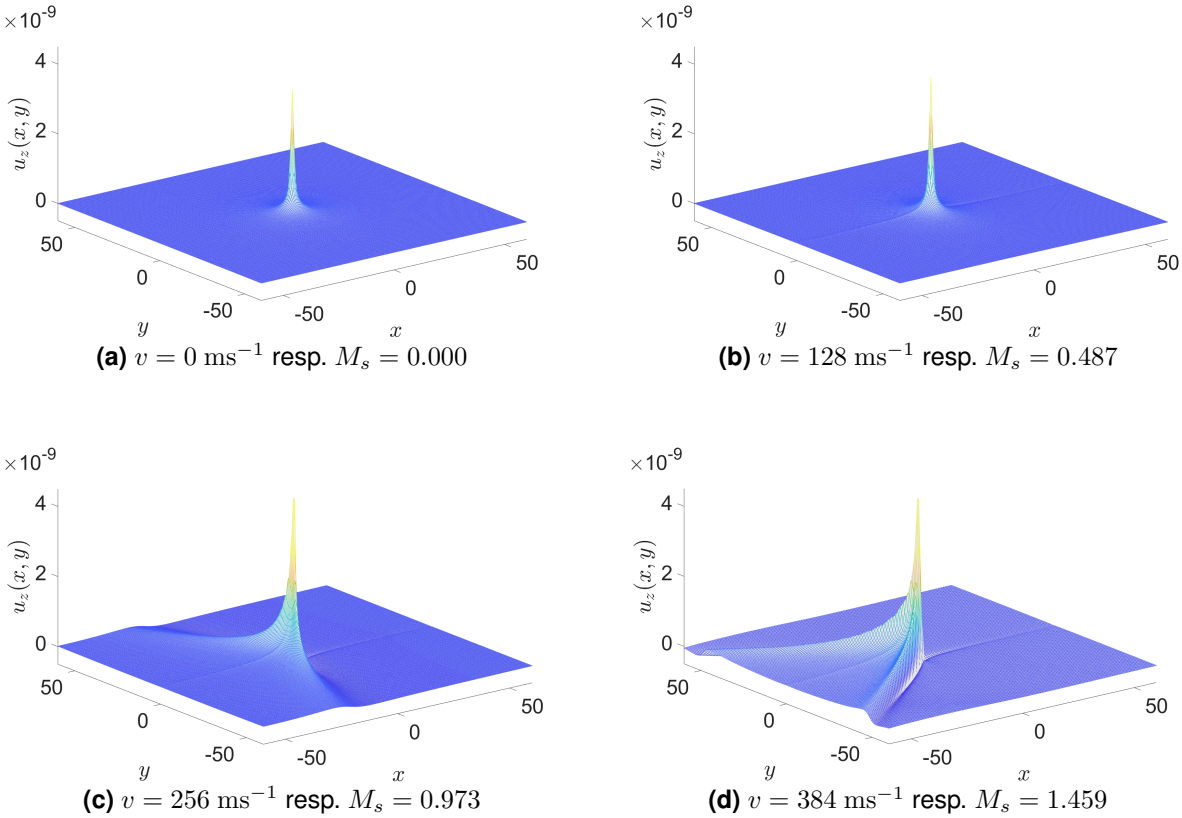

(a) $v = 0$ ms^{-1} resp. $M_s = 0.000$ **(b)** $v = 128$ ms^{-1} resp. $M_s = 0.487$

(c) $v = 256$ ms^{-1} resp. $M_s = 0.973$ **(d)** $v = 384$ ms^{-1} resp. $M_s = 1.459$

Figure 8.4: Vertical displacement $u_z(x,y)$ on the halfspace surface $z = 0$ for $t = 0$ due to a rectangular load with $f = 0$ moving along the x-axis with constant velocity v.

Subsonic load velocity

The vertical surface displacements in the subsonic regime $v < c_s < c_p$ are illustrated in Figs. 8.4a-c, wherein the first two load velocities are smaller than the Rayleigh wave velocity of the medium and the last one slightly exceeds c_r. A comparison of these figures shows, that the shape of the deflection for subsonic load velocities differs completely, depending on whether v is smaller or larger than the phase velocity of the surface waves c_r [209]. For $v < c_r$, the displacement $u_z(x,y)$ is quite similar to that of the static load, rather symmetric to both coordinate axes and travelling with the load. The displacements are confined to a region close to the current position of the load and no propagating waves are excited. As soon as v exceeds c_r, propagating waves are emitted by the moving load, leading to a sharp discontinuity along two lines, originating in the current load position, which can be associated with the Mach lines of the Rayleigh wave fronts [209]. As the load propagates faster than the displacements due to the excited surface waves, no deflection related to the Rayleigh wave occurs in front of the load.

A simple model to approximate the wave field caused by a concentrated moving load by placing a sequence of discrete pulses, radiating cylindrical waves, along the line passed by the load is shown in Fig. 8.5a. Therewith, the response at any point of the surface at a specific time t can be determined by the superposition of the responses to all impulses that have been applied previous to that time [203]. Within the time t the load covers a distance $x = v \cdot t$, but the disturbances due to the impulses have only propagated up to all points at a distance $c_i \cdot t$ by this time. Therefore, all disturbances are confined to the region that is bounded by the two Mach lines through the current position of the load with the angle φ_i

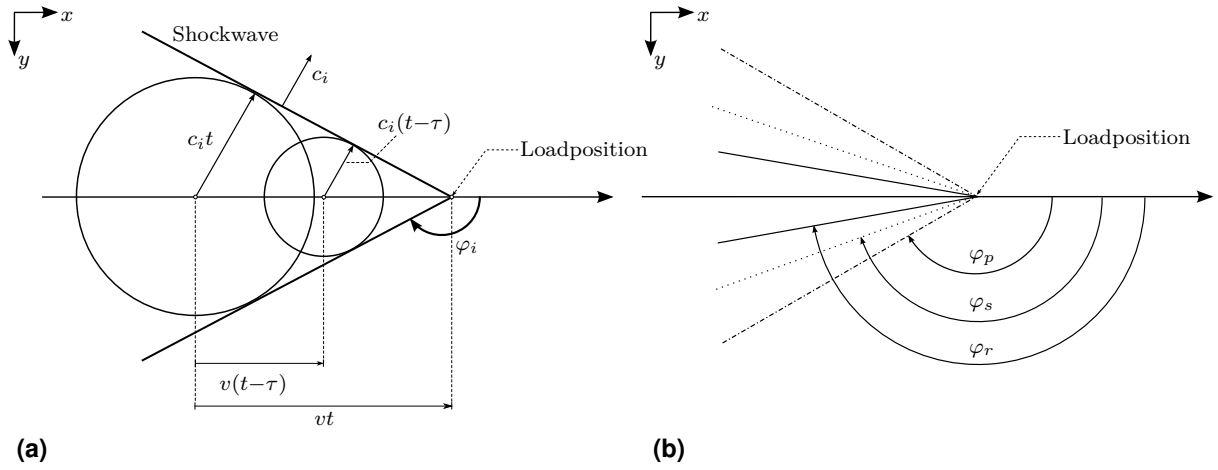

Figure 8.5: (a) Approximation of the response and shock wave formation due to a moving load by an impulse model cp. [18] and (b) Mach lines and corr. angles φ_i cp. [203].

to the x-axis depicted in Fig. 8.5b and given by

$$\varphi_i = \pm\left[\pi - \arcsin\left(\frac{c_i}{v}\right)\right] = \pm\left[\pi - \arcsin\left(\frac{1}{M_i}\right)\right] \tag{8.12}$$

with $\varphi_p < \varphi_s < \varphi_r$ and M_i the corresponding Mach numbers.

These lines are associated with a jump in the displacement and an impulse in the stress components, commonly known as shock waves [18]. The largest displacements occur along the Rayleigh Mach lines, since the Rayleigh wave dominates $u_z(x,y)$ on the surface.

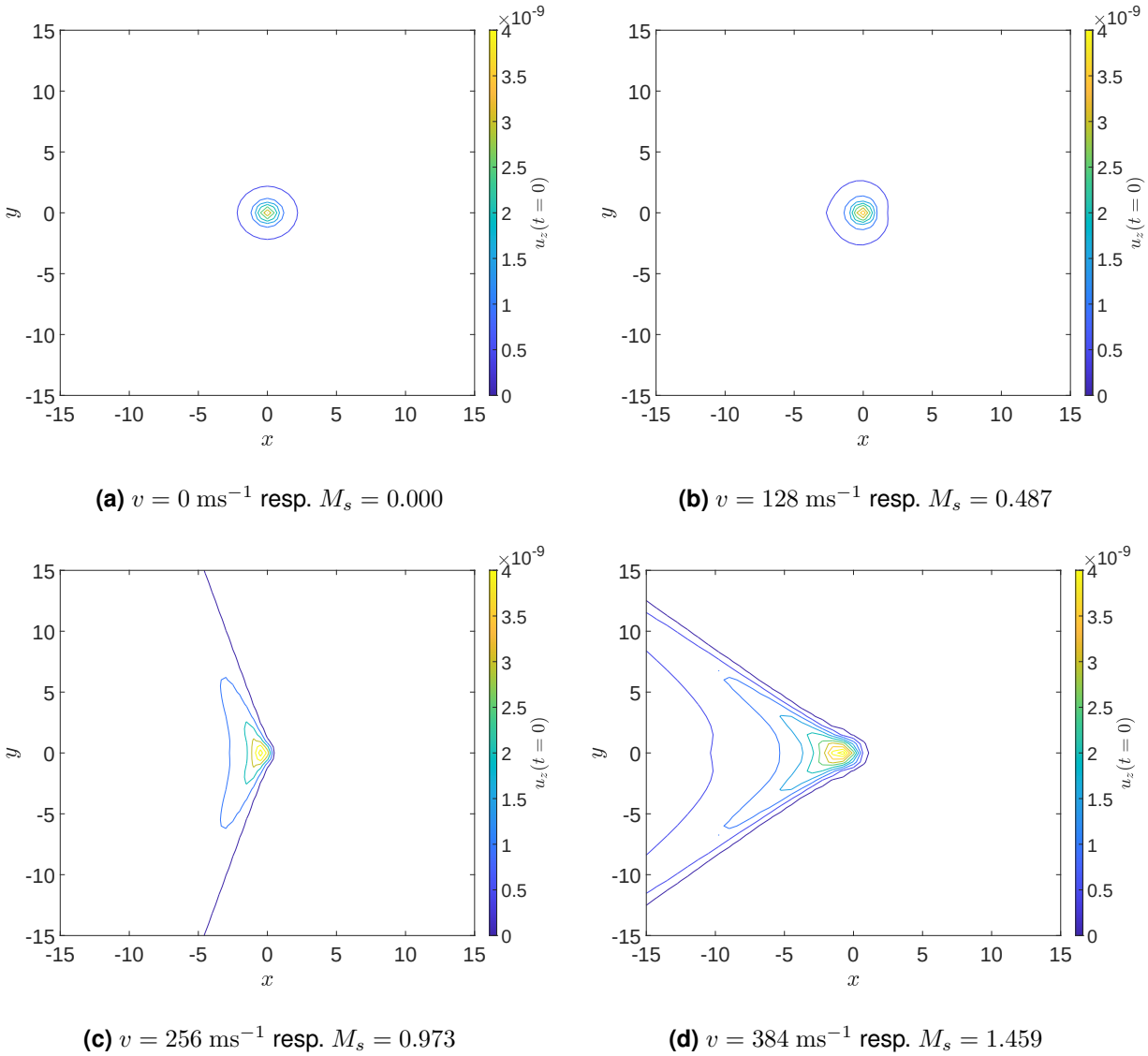

(a) $v = 0\ \mathrm{ms}^{-1}$ resp. $M_s = 0.000$

(b) $v = 128\ \mathrm{ms}^{-1}$ resp. $M_s = 0.487$

(c) $v = 256\ \mathrm{ms}^{-1}$ resp. $M_s = 0.973$

(d) $v = 384\ \mathrm{ms}^{-1}$ resp. $M_s = 1.459$

Figure 8.6: Contour line plots of $u_z(x,y)$ on the halfspace surface $z = 0$ for $t = 0$ due to a rectangular load with $f = 0$ moving along the x-axis with constant velocity v.

Fig. 8.6 shows the contour line plots corr. to the surface displacements in Fig. 8.4. Therein the formation of the Rayleigh Mach lines for the load velocities $v = 256\ \mathrm{ms}^{-1}$ and $v = 384\ \mathrm{ms}^{-1}$ is clearly visible as well as the increase of φ_r with raising velocity v. Furthermore, the resulting angles of the Mach lines $\varphi_r \approx 109°$ and $\varphi_r \approx 143°$ in Figs. 8.6c,d, are in very good accordance to the analytical solution for the Mach angles $\varphi_r = 108.80°$ and $\varphi_r = 140.88°$ due to a moving single load obtained by Lansing [203] and thus further validate the implementation of the moving load problem within the proposed ITM-FEM approach.

Transonic load velocity

If the velocity of the moving load exceeds the propagation velocity of the shear waves c_s, a second Mach line with $\varphi_s \approx 139°$ occurs in Fig. 8.6d. All displacements created by the R- and the S-waves are confined within the two Mach wedges on the halfspace surface. The maximum displacements are located on the Rayleigh Mach lines as before, while the displacements linked to the S-wave are comparably small and not so obviously visible, as they are rather close to the Rayleigh peak. In front of the load, some small undulations corresponding to the compressional wave can be observed.

Supersonic load velocity

In the supersonic case, not presented here, three Mach lines corr. to the compressional, the shear and the Rayleigh wave arise and the displacement field in front of the P-wave Mach line is zero, as the load position is always in front of all expanding waves.

8.3 Harmonic moving load on homogenous halfspace

Following the characteristic response of a halfspace (Soil B) due to the moving block load of Sec. 8.2.2 depicted in Fig. 8.2, but oscillating harmonically with a frequency $f = 64$ Hz, is considered and the results are computed using the same discretization as before. In contrast to a moving load with constant amplitude, which only generates propagating waves for $v > c_r$, a load with time varying amplitude induces propagating waves regardless of the load speed [222]. This is evident in the displacement field $u_z(x,y)$ on the halfspace surface in Fig. 8.7a, which results from a stationary load with $v = 0$ and causes cylindrical waves that propagate rotationally symmetric away from the point of load application.

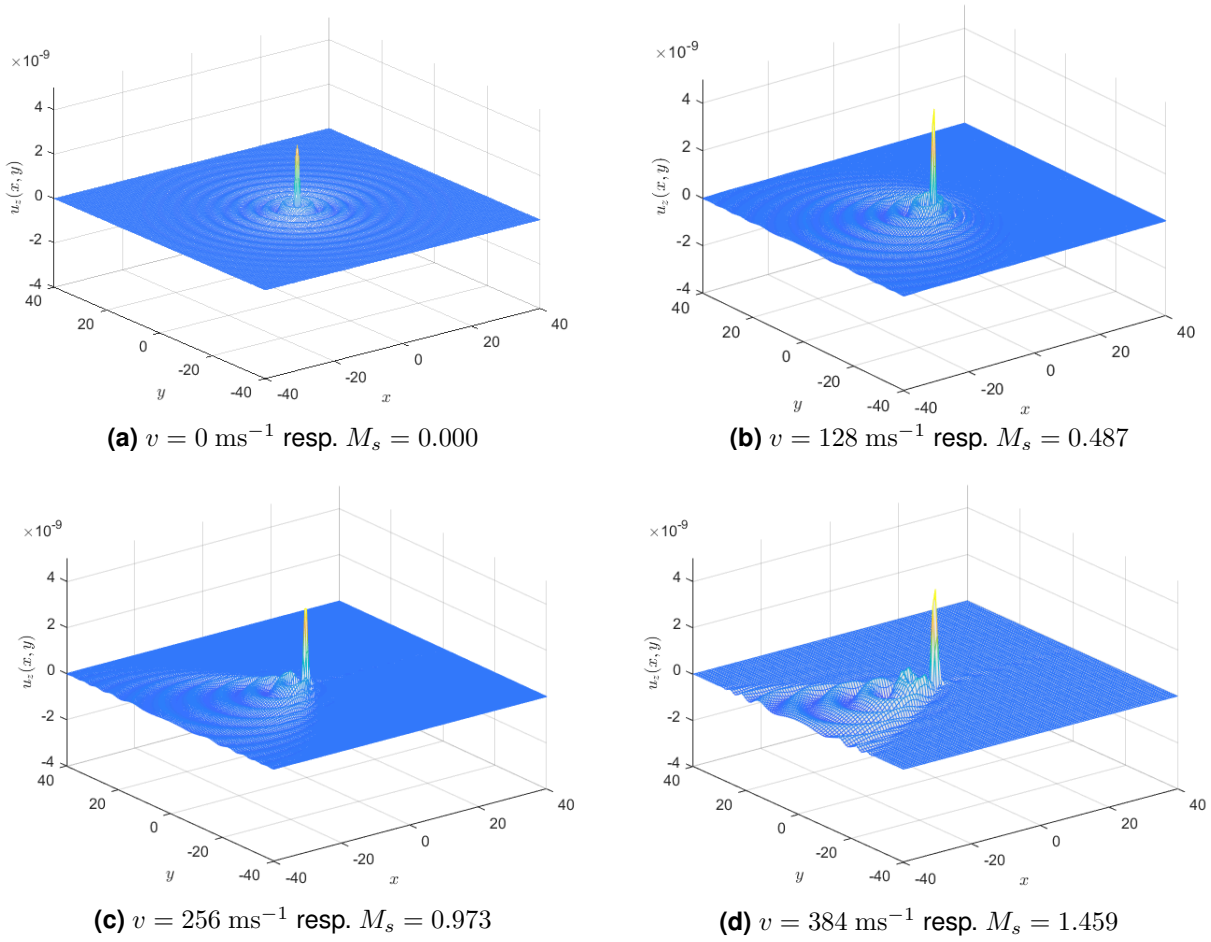

(a) $v = 0$ ms^{-1} resp. $M_s = 0.000$

(b) $v = 128$ ms^{-1} resp. $M_s = 0.487$

(c) $v = 256$ ms^{-1} resp. $M_s = 0.973$

(d) $v = 384$ ms^{-1} resp. $M_s = 1.459$

Figure 8.7: Vertical displacements $u_z(x,y)$ on the halfspace surface $z = 0$ for $t = 0$ due to a rectangular load with $f = 64$ Hz moving along the x-axis with constant velocity v.

8.3.1 Doppler effect

Moreover, in case of the moving harmonic load in Figs. 8.7b-d, the Doppler effect (cp. Fig. 8.8) gets clearly visible by the shorter wavelengths in front of the load linked to a higher frequency registered at a fixed observation point ahead of the source, while longer wavelengths appear behind the load, corr. to a lower frequency at a fixed position beyond the source [191].

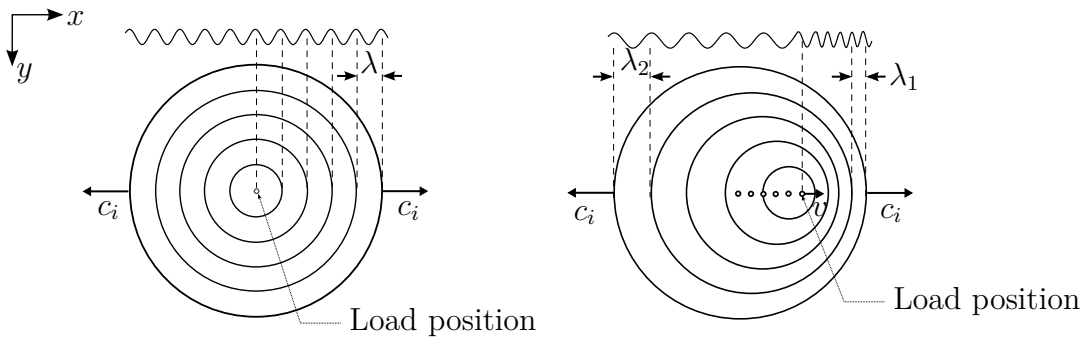

Figure 8.8: Doppler effect for moving load cp. [311].

As in case of the non-oscillating moving load, for load velocities exceeding c_r resp. c_s "the wave field displays a similar Mach cone, however, without the large amplification observed in the zero frequency case" [191].

8.3.2 Wavenumber characteristics

These features of the system response are also clearly observable in the Fourier transformed domain. For this purpose, firstly the response of a homogeneous halfspace due to an unit impulse w.r.t. space and time leading to a constant spectrum $|\hat{p}^{\mathrm{hs}}_{zz,\Lambda}(k_x,k_y,\omega)| = 1$ in the wavenumber frequency domain is considered. Therein, the combinations (k_x,k_y,ω) for which the largest amplitudes of the response occur, are located on the limiting lines of a double cone, as illustrated in Fig. 8.9 [217]. For a stationary time harmonic excitation with angular frequency Ω the solution in the transformed domain reduces to the two planes slicing the double cone at $\omega = \pm\Omega$. Within this plane the largest values of the system response are located on circles rotationally symmetric to the origin of the $k_x - k_y$ plane, which can be associated with the wavenumbers of the compressional, the shear and the Rayleigh wave k_p, k_s and k_r [217].

In case of a harmonic load moving along the $x-$axis, the cutting planes, intersecting with the double cone in Fig. 8.9, are inclined w.r.t k_x, whereby the angle depends on the load speed [217]. This tilt corresponds also to the wavenumber dependent frequency shift in the fundamental solution $\hat{\mathbf{K}}^{-1}_{\mathrm{ITM}}(k_x,k_y,-\Omega - vk_x)$ described in Sec. 8.1 and leads to a distortion

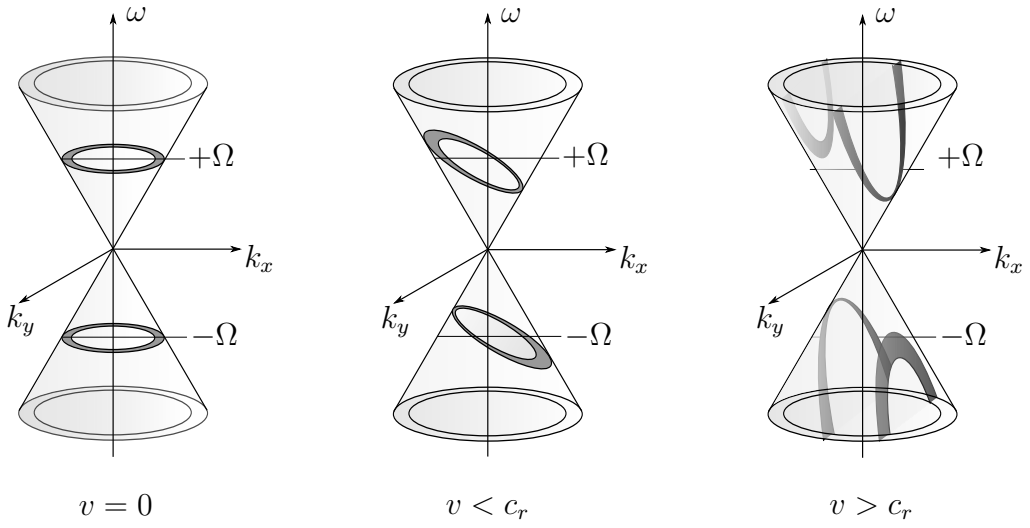

Figure 8.9: Illustration of the different response characteristics of a homogeneous halfspace in the (k_x,k_y,ω) domain due to an impulse load for different load velocities cp. [217].

of the locations of the maximum values on the cutting plane compared to the circle for $v = 0$. If e.g. the Rayleigh wave number k_r is considered, the following relationship holds

$$k_r^2 = k_{rx}^2 + k_{ry}^2 = \frac{(-\Omega - vk_{rx})^2}{c_r^2} \tag{8.13}$$

After a transformation to the normal form, the equation indicating the location of the considered wavenumber results as

$$(v^2 - c_r^2)k_{rx}^2 - \frac{1}{c_r^2}(v^2 - c_r^2)k_{ry}^2 + \Omega^2 = 0 \tag{8.14}$$

According to Eq. (8.14), the location of the largest amplitudes of $\hat{u}(k_x, k_y, \omega)$ is given by ellipses for $v < c_r$ and hyperbolas for $v > c_r$ [312]. These shapes are also observed in the sectional planes of the double cone in Fig. 8.9 as well as in the contour line plots of the displacements in the wavenumber frequency domain in Fig. 8.10, corresponding to the displacement $u_z(x,y,t)$ illustrated in Fig. 8.7. Furthermore, the distribution of the transformed displacements is in good agreement with the results presented in Jones et al. [313].

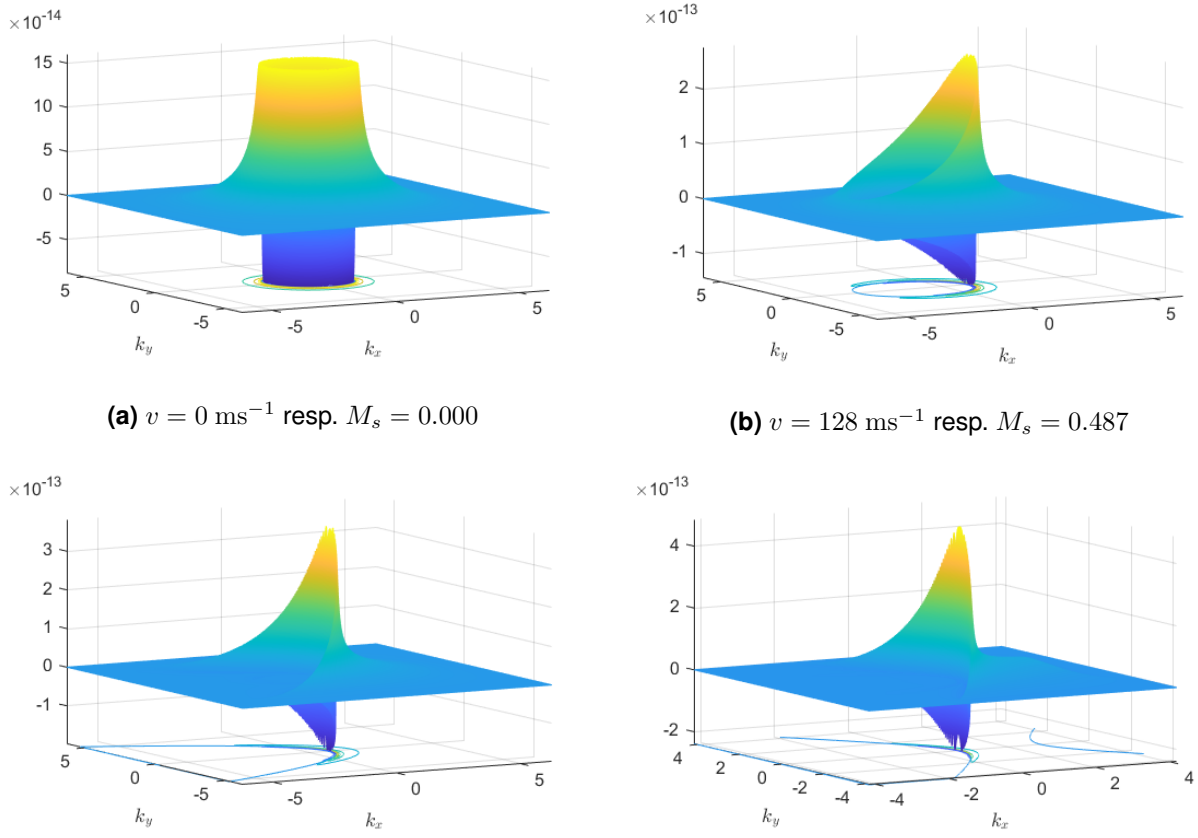

(a) $v = 0$ ms^{-1} resp. $M_s = 0.000$

(b) $v = 128$ ms^{-1} resp. $M_s = 0.487$

(c) $v = 256$ ms^{-1} resp. $M_s = 0.973$

(d) $v = 384$ ms^{-1} resp. $M_s = 1.459$

Figure 8.10: Real part of vertical displacement $\hat{u}_z(k_x,k_y,\omega)$ on the halfspace surface $z = 0$ due to a rectangular load with $f = 64$ Hz moving along the x-axis with constant velocity v.

The change of the transformed displacements in dependence of the wavenumber k_x for $k_y = 0$ with increasing load velocity v is shown in Fig. 8.11. For the stationary load, the main peaks are located at the wave numbers k_r, k_s and k_p. According to Müller [81], the contributions of $\hat{u}_z(k_x,k_y,\omega)$ for $\omega > 0$ and $k_x > 0$ can be associated with waves travelling in negative $x-$direction, while for $k_x < 0$ they travel in positive $x-$direction. In Fig. 8.11 the amplitude of the peaks in the negative wavenumber range decrease and move towards $-\infty$ when the load speed increases, indicating that their contribution to the waves propagating in front of the load are not significant. In contrast, the peaks in the positive range of k_x increase in

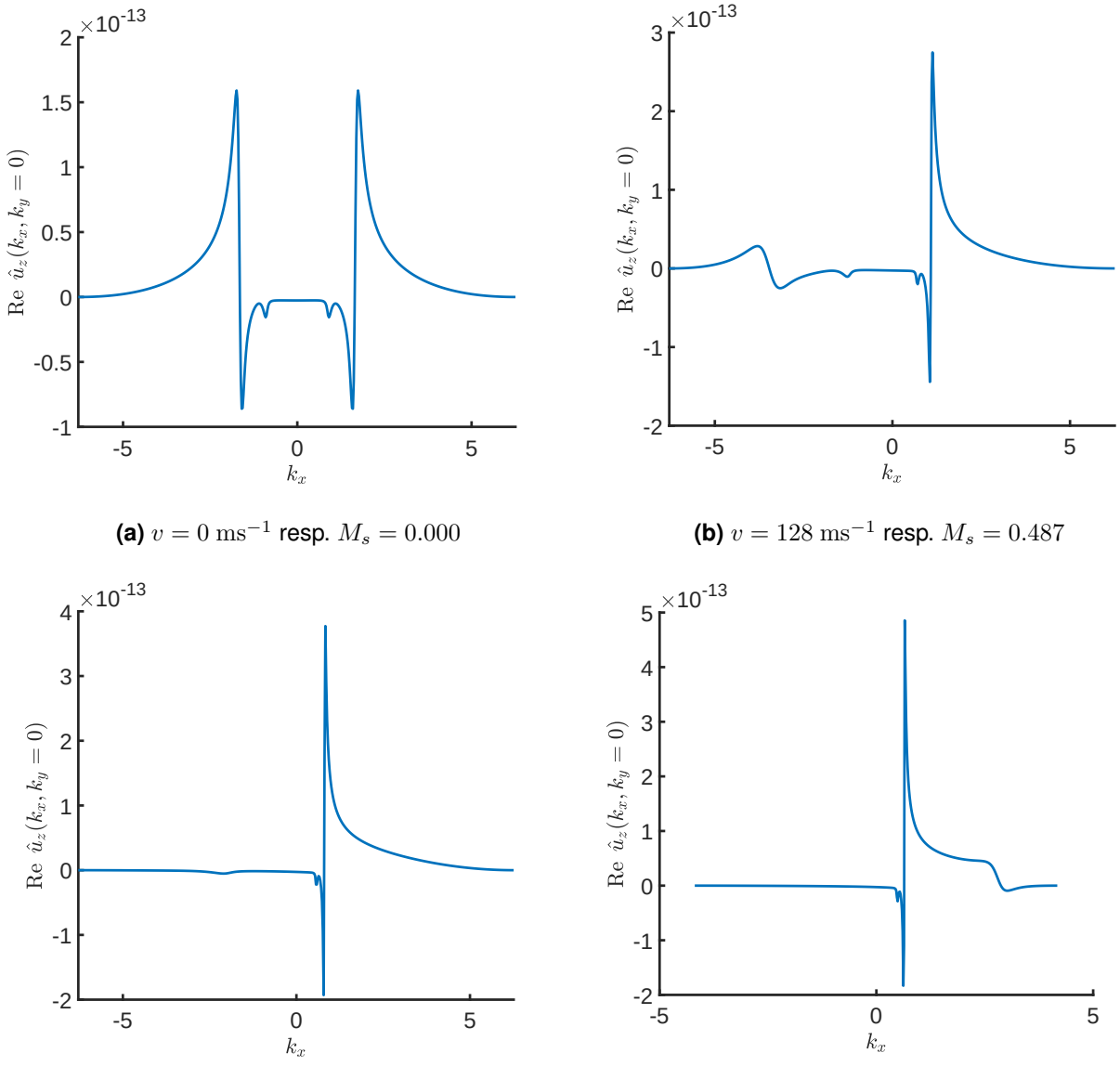

(a) $v = 0$ ms^{-1} resp. $M_s = 0.000$

(b) $v = 128$ ms^{-1} resp. $M_s = 0.487$

(c) $v = 256$ ms^{-1} resp. $M_s = 0.973$

(d) $v = 384$ ms^{-1} resp. $M_s = 1.459$

Figure 8.11: Real part of vertical displacement $\hat{u}_z(k_x,k_y = 0,+\omega)$ on the halfspace surface $z = 0$ due to a rectangular load with $f = 64$ Hz moving along the x-axis with constant velocity v.

amplitude and move towards zero [210]. Furthermore, when v exceeds c_r, the peak from the negative wavenumber range jumps to the positive one and approaches from $+\infty$ towards zero, reflecting the transition from the ellipse to the hyperbola (cp. Fig. 8.10), linked with the change of the velocity regime [314]. Thus for $v > c_s$ in Fig. 8.11d, non zero values of $\hat{u}_z(k_x,k_y,\omega)$ occur almost only in the positive k_x range, linked to backward running waves, and nearly no displacements emerge in front of the load (cp. Fig. 8.7d). The evolution of the transformed displacements, determined with the ITM-FEM approach thereby shows very good agreement with the results presented in Lefeuve-Mesgouez et al. [210].

8.4 Moving load on coupled systems

8.4.1 Verification

Firstly, in order to verify the implemented approach also for the application to the coupled ITM-FEM systems, the results obtained with the latter are compared to those of the fundamental system of the homogeneous halfspace presented before. For this purpose, the harmonically oscillating moving load of Sec. 8.3 is applied to the surface of a halfspace of Soil B, given in Tab. 8.1, with a cylindrical enclosure of radius $R = 4.5$ m, consisting of the same material. An embedment depth of $H = 6$ m was chosen and the inclusion was discretized with $N_\varphi = 64$ points along the circumference. For both systems in Fig. 8.12 a total domain size of $B_x = B_y = 128$ m with $N_x = N_y = 2^9$ sample points was considered and the response computed for $N_f = 2^9$ frequency components up to a maximum shifted frequency $|\omega_{\max}| = |-\Omega - vk_x| = 1206.4\ \mathrm{rad\,s^{-1}}$ corr. to $|f_{\max}| = 192$ Hz in steps of $\Delta f = 1$ Hz. The response for a load velocity of $v = 128\ \mathrm{ms^{-1}}$ and $f = 64$ Hz in the Fourier transformed and the original domain for both systems are depicted in Fig. 8.13 and show good agreement.

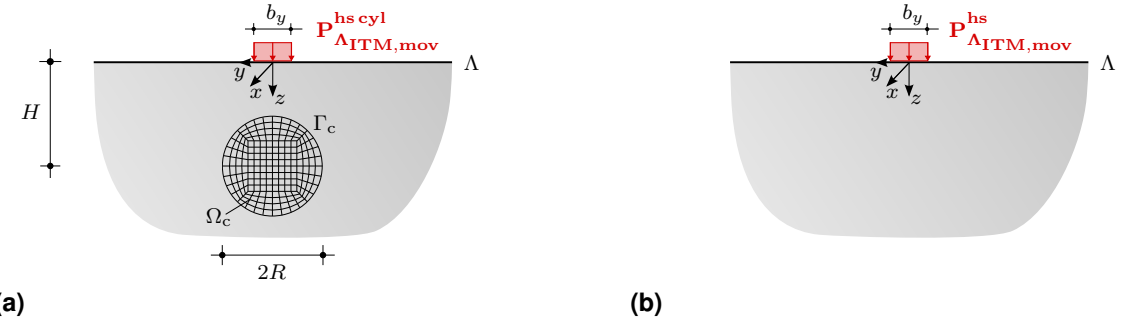

Figure 8.12: Setup for validation of coupled ITM-FEM approach for moving loads. (a) Halfspace with cylindrical inclusion of same material as surrounding soil and (b) homogeneous halfspace.

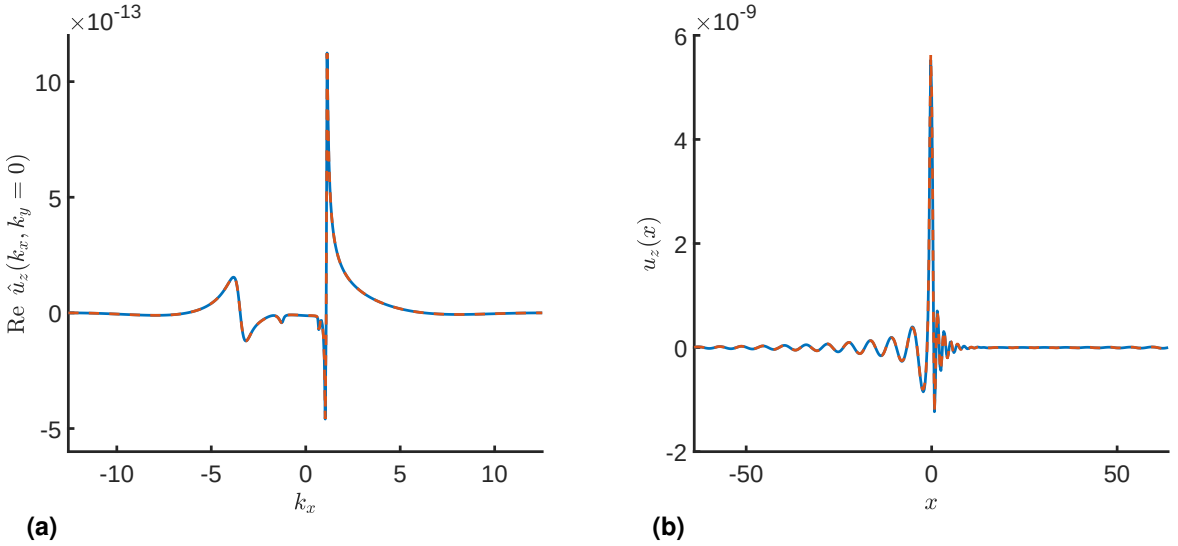

Figure 8.13: Real part of the vertical displacements on the ground surface of the halfspace with cylindrical inclusion (—) and the homogeneous halfspace (- -) due to a moving load with $v = 128\ \mathrm{ms}^{-1}$ and $f = 64$ Hz (a) in the transformed domain $\hat{u}_z(k_x)$ for $k_y = 0$ and (b) the original domain $u_z(x)$ at $y = 0$ and $t = 0$.

8.4.2 Moving load in twin tunnel system

Eventually, the response of the twin tunnel system of Secs. 6.6 and 7.5 due to a moving load with $b_x = b_y = 1$ m and $v = 128\ \mathrm{ms}^{-1}$ oscillating with $f = 64$ Hz within tunnel T_1, as illustrated in Fig. 8.14, is investigated. The material parameters of Soil C in Tab. 8.1 were used for the halfspace and the discretization was chosen analogously to Sec. 8.4.1.

The frequency spectrum of the resulting vertical displacements $\bar{u}_z(f)$ at points P_1 and P_2 at the top of the slab in tunnel T_1 and at the ground surface directly above the tunnel, both at $x = 0$ (cp. Fig. 8.14), is shown in Fig. 8.15a. Due to the velocity dependent frequency shift, $\bar{u}_z(f)$ shows a narrowband frequency spectrum around the excitation frequency $f = \pm 64$ Hz

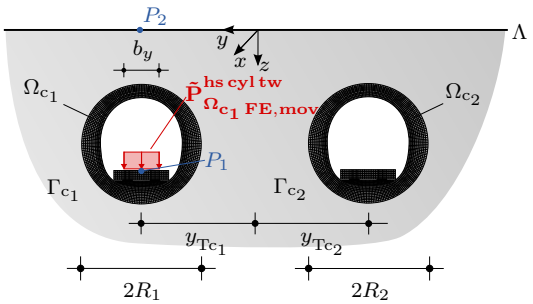

Figure 8.14: Harmonically oscillating moving load in a twin tunnel system.

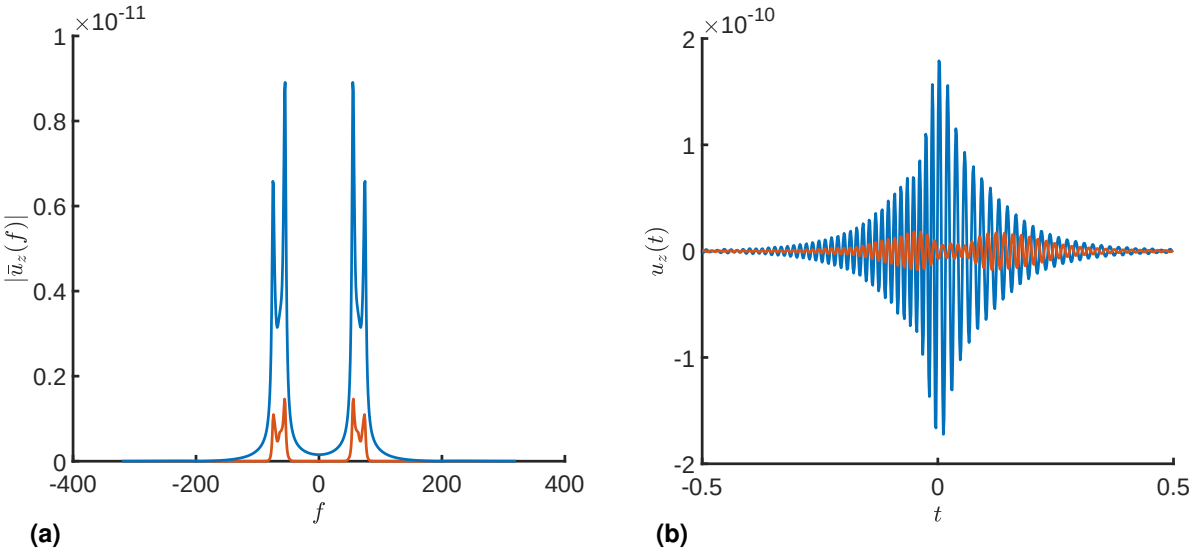

Figure 8.15: (a) $|\bar{u}_z(f)|$ and (b) $u_z(t)$ of the twin tunnel system due to a moving load in tunnel T_1 with $v = 128\ \mathrm{ms}^{-1}$ and $f = 64$ Hz at P_1 (—) and P_2 (—) as depicted in Fig. 8.14.

instead of a Dirac characteristic. Moreover, much higher amplitudes are observed on the tunnel slab than on the ground surface, which can also be seen in $u_z(t)$ in Fig. 8.15b. For P_1, the maximum amplitude of $u_z(t)$ is reached when the load passes the observation point, while for P_2 the largest displacements occur before and after the passage of the load.

In the contour plot of $\hat{u}_z(k_x,k_y,\omega)$ on the soil surface, depicted in Fig. 8.16a, the hyperbolic distribution in the wavenumber-frequency spectrum in case of a load velocity v larger than c_r of the soil is slightly visible. However, this characteristic is, due to the higher complexity of the system and the effects of the SSI, much less pronounced as in case the load is directly applied on the surface of a homogeneous halfspace. Nevertheless, some conclusions

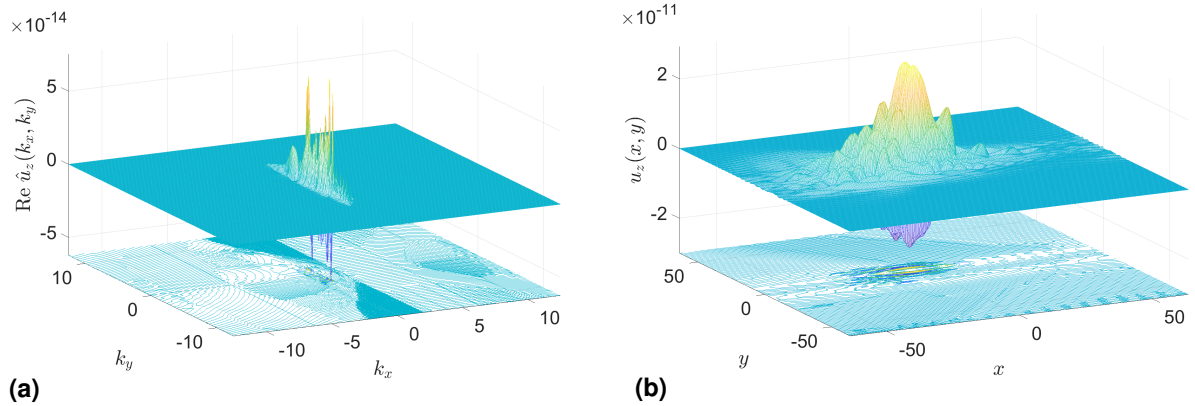

Figure 8.16: Real part of the vertical displacements (a) $\hat{u}_z(k_x,k_y)$ in the wavenumber-frequency domain and (b) $u_z(x,y)$ for $t = 0$ on the soil surface due to a moving load in tunnel T_1 with $v = 128\ \mathrm{ms}^{-1}$ and $f = 64$ Hz.

about the composition of the displacement response can be deduced from the wavenumber spectrum. The rather narrow band spectrum of $\hat{u}_z(k_x,k_y,\omega)$ w.r.t. k_x indicates a large contribution of long wave components associated with small wavenumbers finally leading to a displacement field $u_z(x,y)$ stretched in $x-$direction. The latter can also be explained by the stiffness of the tunnel in longitudinal direction. In contrast, a wider range of $\hat{u}_z(k_x,k_y,\omega)$ w.r.t. k_y, exhibiting considerable amplitudes, is observed, indicating a radiation of waves with smaller wavelengths in cross sectional direction. This can also be noted in Fig. 8.16b, showing the displacements $u_z(x,y)$ on the soil surface. In addition, some amplification of the surface displacements is observed over the second tunnel due to the effect of waves reflected or diffracted as a consequence of the impedance jump at the boundary Γ_{c2}. Finally, the progression of the load in positive $x-$direction with increasing t is shown in Fig. 8.17. It illustrates the displacements in the tunnel itself as well as the displacements on the surface and at the second tunnel, arising due to the Structure-Soil-Structure-Interaction. The latter occur mainly at the level of the load position and in a limited area before and after the moving, oscillating load. On the side of the second tunnel facing away from the load, almost no deformations occur, which is due to a certain shielding effect of the, in comparison to the surrounding soil, rather stiff tunnel T_2. An effect, which has also already been observed for the stationary and transient loads in sections 6.6 and 7.5. In Fig. 8.17f, the deformation of the stiff concrete roadway slab (although visualized strongly exaggerated) due to the load crossing is evident, which is then transmitted to the surrounding soil through the tunnel shell.

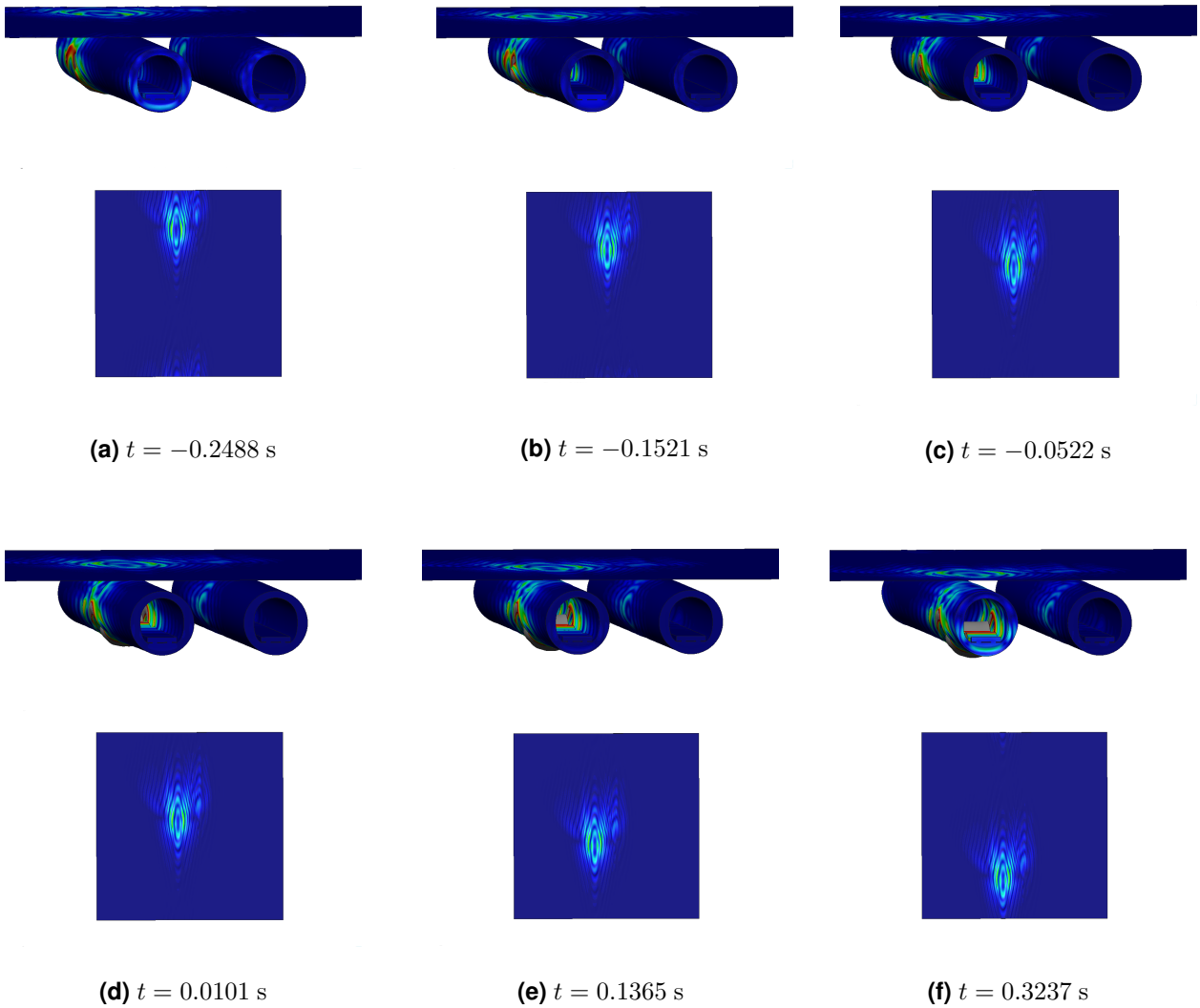

(a) $t = -0.2488$ s **(b)** $t = -0.1521$ s **(c)** $t = -0.0522$ s

(d) $t = 0.0101$ s **(e)** $t = 0.1365$ s **(f)** $t = 0.3237$ s

Figure 8.17: Time evolution of absolute value of total displacements for the twin tunnel system within a homogeneous halfspace (Soil C) due to a rectangular moving block load in tunnel T_1 with $v = 128$ ms^{-1} and $f = 64$ Hz (upper subplot) and on the ground surface $z = 0$ (lower subplot).

9 Summary and Outlook

9.1 Summary

In the present thesis a 2.5D and a 3D coupled ITM-FEM approach are developed, enabling the investigation of the dynamic interaction of a single surface or underground structure with the underlying or surrounding soil as well as the interaction of several adjacent surface and underground structures coupled through the soil. The proposed methodology allows to predict the dynamic response of a broad range of different systems due to stationary harmonic or transient loads as well as moving loads. In order to represent the real system behaviour as accurately as possible and thus allow a modelling on a very high level of complexity, a domain decomposition approach was employed, subdividing the overall system into substructures with different characteristics. This facilitates to use different methods to describe the subsystems and to exploit their respective advantages. Within this work the soil with its semi-infinite extension is described by the ITM, whereas the structures, exhibiting a complex geometry and material distribution, are accounted for by the FEM.

To this end, firstly analytical solutions for different fundamental systems are derived from the basic elastodynamic equations and then superposed and coupled to deduce closed form semi-analytical solutions for more complex systems with several boundary surfaces as e.g. a halfspace with one/two cylindrical cavities/indentations or a halfspace with spherical cavity/indentation. This eventually leads to wavenumber and frequency dependent dynamic stiffness matrices for the ITM substructures, providing a direct relation between the external stresses applied at the boundaries of the system and the resulting displacements. To enable a straightforward integration of the two involved methods to an overall model, the FEM substructures must exhibit a suitable outer boundary and the dynamic stiffness matrices need to be separated for the DOFs on the interaction surfaces and within the structures. In case of length-invariant structures, 2.5D quadrilateral elements are used, allowing the solve the 3D problem by a series of quasi-static 2D computations, while common 3D beam, shell or solid elements are used to describe the finite structures on or within the ground and a part of the surrounding soil.

The coupling between the ITM and the FEM is realized by imposing the compatibility conditions on the common interaction surfaces, leading to a total dynamic stiffness matrix

describing the overall system. In order to couple a FEM substructure to a cylindrical or spherical cavity or indentation within the soil, a complete coupling of all quantities along the entire bounding surface is performed. Since for this a common reference frame is necessary, the quantities of the FEM subsystem on the interaction surface are transformed into the respective ITM basis. For the coupling of finite surface structures to any soil substructure, being able to be modelled by an ITM or coupled ITM-FEM approach, the dynamic soil stiffness is computed at discrete points on the ground surface by evaluating the displacements due to a concentrated unit load and applying a special shifting procedure in combination with the introduction of a coarser discretization. Furthermore, a postprocessing procedure is introduced, which facilitates the computation of the stress and displacement distributions on the surface or within the soil, resulting from the dynamic soil structure interaction. Therewith, it is also possible to determine the power input at the soil foundation interface and the power flux through a defined control volume.

The proposed method is firstly applied to determine the frequency domain response due to stationary harmonic loads for different systems. Thereby the validity of the semi-analytical solutions for the basic ITM systems is demonstrated by comparison with literature results for certain benchmark cases, before these are used to confirm the accuracy of the results for different coupled 2.5D and 3D ITM-FEM systems. The latter are employed for the assessment of the vibration reduction efficiency of different finite and length invariant mitigation measures at the source or in the transmission path as well as the identification of the prevailing physical mechanisms, decisive design parameters and wave propagation characteristics. Thereby stiff gravity walls with a wide footprint are found to be particularly effective, especially at higher frequencies, whereas for trenches and infilled barriers the normalised depth and the impedance contrast between infill material and soil are the most important parameters. Shallow barriers with less pronounced stiffness contrast act as wave impeding barrier up from a critical frequency and provide a significant insertion loss within an area delimited by a critical angle. In case of finite trenches, due to diffraction phenomena also their length and the source distance have considerable influence on the performance. The insertion of a second open trench leads to an energy concentration between these, whereas no significant changes of the insertion loss occur on the trench averted sides.

A comparison of the compliance functions and displacement curves of rigid and flexible, massless and massive surface foundations resting on a homogeneous or stratified ground and subjected to different load types (uniform pressure, point load, rocking moment) with literature results shows very good agreement, demonstrating the reliability of the proposed method for the investigation of the dynamic soil structure interaction. Thus the method is subsequently applied to analyse the influence of different subsoil conditions on the radiation characteristics of the surface structures, the frequency dependent power transmission into the

soil as well as the resulting displacement distributions and properties of the wave dispersion within the ground. The wavenumber spectra of the SSI contact stresses and the surface displacements are inherently provided by the postprocessing procedure, giving insight into the contributions of the different wave types and the propagation directivity. By means of the power flux through a defined control volume, also the direction of the energy dispersion and the attenuation behaviour due to geometrical and material damping can be predicted. Since this procedure is computationally rather expensive, the power input at the soil-foundation interface is introduced as a single-valued quantity, that indicates the radiation ability of the foundation and characterises the amount of energy, that is introduced into the soil and has to be dispersed by the induced elastic waves.

For a single foundation on a homogeneous halfspace, at low frequencies the energy is radiated almost uniformly within the ground. In contrast an increasing proportion of plane elastic waves with small wavenumbers occurs, propagating increasingly in vertical direction as the frequency rises. Simultaneously the relative contribution of the Rayleigh waves decreases and the power input at the soil foundation interface approaches a constant value, close to the power input associated with a pure compressional wave radiation. In case of a soft soil layer resting on a rather stiff halfspace, a strong localisation of the energy within the upper stratum is observed, leading to a considerable radiation in the horizontal direction. Moreover, a significantly higher power input is observed at the layer resonance frequencies, whereas below the first layer resonance no propagating waves occur and the power input tends to zero. The presence of a length-invariant stiff inclusion or an underground tunnel shows to have a significant impact on the power input and the flexibilities of a single or several adjacent foundations. The influence is generally higher, when the inclusions are large, located closely to the ground surface and feature a distinct stiffness contrast to the soil. However, even structures with greater embedment depth show a considerable effect in the low frequency range due to the large wavelength, while with increasing frequency the short-wave elastic waves have usually sufficiently decreased before reaching the embedded structure. Thus the influence decreases and the flexibilities converge to those obtained for the homogeneous halfspace. Considering two foundations arranged symmetrically to an inclusion, the soil layer above the latter plays a decisive role, since below the cut off frequency no wave propagation through the stratum is possible, which leads in combination with the wave barrier effect to a very small reaction of the passive foundation. In addition, the effect of different footing conditions on the dynamic response of a space frame is studied and frequency transfer functions between a concentrated load on the soil surface close to a structure and characteristic locations on the latter are given for varying soil properties. Finally, the effect of the dynamic SSSI of a twin tunnel system, embedded in a homogeneous soil, is illustrated and quantified by means of the insertion gain of the ground surface displacements.

To enable the analysis of the dynamic systems response to stationary transient loads under full consideration of the SSI resp. the SSSI, the proposed 2.5D and 3D ITM-FEM approaches are applied to compute complex frequency transfer functions. With these, the time histories of the resulting vibrations can be obtained by either a Fourier synthesis approach or a discrete convolution of the transient load with the impulse response functions, resulting from a IFFT of the transfer functions for a large frequency range. Since both techniques are based on the solution in the frequency domain and require the validity of the superposition principle, the applicability is limited to linear problems. To ensure a sufficient time discretization by simultaneously large observation times, a procedure for the interpolation of the transfer functions is implemented. The influence of considering a restricted amount of frequencies on the quality of the results is reconsidered and quantified by means of an energy equivalent confidence measure. Due to the relatively strong decay of the transfer functions with increasing frequency, the calculation up to a moderately high frequency is sufficient to cause only a limited error. In case of layered media, the frequency spacing in the range of the layer resonances has to be selected carefully in order not to neglect components with a large contribution. Moreover, the hysteretic material damping leads to a non-causal system response, which evokes a reaction of the system already before the start of the load application. Therefore, low damping ratios combined with large discretized areas and high sampling densities, reducing spatial aliasing, are required in order to achieve an accurate solution. The transient response of a homogenous halfspace and the time dependent flexibilities of rigid massless or massive surface foundations due to a suddenly applied load are computed, whereby very good agreement with literature results is achieved. Furthermore, the transient response of a twin tunnel system, subjected to a Gaussian-modulated sinusoidal pulse within one tunnel tube is investigated, demonstrating the applicability of the ITM-FEM approach for the analysis of the transient SSSI of complex systems.

Eventually, a methodology for the incorporation of constant and oscillating moving loads within the fundamental and coupled ITM-FEM systems is derived and validated by comparison with other methods and reproducing typical physical phenomena. In case of constant moving loads, the formation of shock waves for load speeds exceeding the wave velocities in the soil is illustrated and the resulting Mach cones match well with those predicted by analytical models. Also for oscillating moving loads, the modified distribution of the surface displacements due to the Doppler effect and the changes in the wavenumber characteristics for different load speeds correspond well with the results reported in literature. The implementation for coupled ITM-FEM systems is validated by comparison with the semi-analytical solutions of the homogenous halfspace and subsequently applied to compute the response of twin tunnel system with a moving load inside one of the tunnel tubes.

9.2 Outlook and future work

A perspective continuation, expansion and optimisation of the present work is possible at several points, as outlined hereinafter. Within the presented approach, it is only possible to consider horizontal soil layers and the inclusion can only be located within the halfspace beneath the soil stratification. Therefore, an adaptation of the implementation by superposing further fundamental or coupled systems, allowing also cavities within a soil layer or even across a layer transition, would considerably extend the ability of the method to model practical issues. The same applies to the possibility of representing oblique layer boundaries in the model. Furthermore, while the method allows arbitrary external loads to be applied to the ground surface, the layer boundaries or cavity surfaces of the ITM substructure, or at any location within the FEM substructure, it is not yet possible to include a seismic wave excitation. However, this could be achieved by changing the non-local boundary conditions in the ITM formulation, allowing specified elastic waves to propagate from infinity towards the ground surface at defined angles of incidence.

Considering the finite element substructure coupled to the halfspace with spherical cavity or indentation, there are rather strict requirements for the FE model due to the chosen numerical integration scheme for the spherical harmonics, describing the quantities on the coupling surface. Therefore, an arbitrary modelling of 3D structures within the FEM domain is only possible to a limited extent and the frequency range in which the method is applicable is restricted due to the prescribed element sizes, increasing towards the equator. The implementation of a different algorithm for the numerical integration on the spherical surface, which allows a free distribution of the discretization points on it, would on the one hand considerably expand the modelling freedom and on the other hand extend the frequency range that can be covered, since the element sizes could be freely chosen within the entire FEM domain. Alternatively, a technique for the coupling of non-conforming meshes, as described in the context of the Mortar methods, could be used to enable a coupling of the ITM and FEM substructures with different discretizations on the spherical interaction surface and thus lead to the same enhancements.

As pointed out in the thesis, large dimensions for the discretized domain and a high number of sampling points should be chosen in order to obtain accurate results and minimise spatial aliasing, which, however, involves considerable computational effort. For this purpose, the wavenumber characteristic of the system response could be exploited to significantly reduce the number of calculations required. Since the contribution of the short-wave components, associated with wavenumbers significantly above the Rayleigh wavenumber, to the overall

system response is very small, as these are strongly damped and therefore attenuate rapidly, a fine sampling of the high wavenumber range is not necessary. For the accuracy of the results, in contrast, it would be more important to sample the low wavenumber range, in which significant peaks occur, delicately. The application of a non-uniform fast Fourier transform algorithm, enabling adaptive sampling in the wavenumber domain with non equidistant samples, could account for this issue, thereby reducing the number of operations for the inverse Fourier transform and thus the computational cost substantially.

Moreover, currently only finite elements with linear shape functions are employed for the FEM substructures coupled to the halfspace with cylindrical or spherical cavity, requiring a large number of elements especially in the higher frequency range in order to guarantee a sufficient representation of the resulting stresses and displacements. Therefore, the implementation of higher order elements would reduce the amount of elements necessary at the same time improving the result quality. However, it must be ensured that all nodes of the elements are coupled with discretization points of the ITM substructure on the common interaction surfaces, such that the compatibility is satisfied node wise.

In this work the solution of fundamental systems is only derived considering the homogeneous solution and solving the boundary value problem. However, it would also be possible to include the volume forces in the Lamé differential equation to compute the forced vibration response in order to deduce a solution for an excavated soil, which then can be filled with a FEM substructure again. This approach could be used as an alternative to the coupling of the FEM to a half-space with spherical indentation in order to investigate the SSI of finite three dimensional structures embedded in the soil. Finally, an adaptation of the underlying linear elastic, isotropic material law to anisotropic or porous materials as well as the introduction of a probabilistic description of the soil properties, to cover local varying ground conditions, would be conceivable.

A Appendix

A.1 System matrices for the halfspace

A.1.1 Dynamic case

The stresses $\hat{\boldsymbol{\sigma}}^{\mathbf{hs}}_{\mathbf{ITM}} = \left(\hat{\sigma}_{xx}\ \hat{\sigma}_{yy}\ \hat{\sigma}_{zz}\ \hat{\sigma}_{xy}\ \hat{\sigma}_{yz}\ \hat{\sigma}_{xz}\right)^T$ and displacements $\hat{\mathbf{u}}^{\mathbf{hs}}_{\mathbf{ITM}} = \left(\hat{u}_x\ \hat{u}_y\ \hat{u}_z\right)^T$ in a homogeneous, isotropic halfspace can be calculated for each combination (k_x, k_y, z, ω) as

$$\hat{\boldsymbol{\sigma}}^{\mathbf{hs}}_{\mathbf{ITM}} = \hat{\mathbf{S}}^{\mathbf{hs}}_{\mathbf{ITM}}\, \hat{\mathbf{C}}^{\mathbf{hs}}_{\mathbf{ITM}} \tag{A.1}$$

$$\hat{\mathbf{u}}^{\mathbf{hs}}_{\mathbf{ITM}} = \hat{\mathbf{U}}^{\mathbf{hs}}_{\mathbf{ITM}}\, \hat{\mathbf{C}}^{\mathbf{hs}}_{\mathbf{ITM}} \tag{A.2}$$

with

$$\hat{\mathbf{S}}^{\mathbf{hs}}_{\mathbf{ITM}} = \mu \begin{bmatrix} -2k_x^2 - \frac{\lambda}{\mu}k_p^2 & 0 & 2\mathrm{i}k_x\lambda_2 \\ -2k_y^2 - \frac{\lambda}{\mu}k_p^2 & -2\mathrm{i}k_y\lambda_2 & 0 \\ 2\lambda_1^2 - \frac{\lambda}{\mu}k_p^2 & 2\mathrm{i}k_y\lambda_2 & -2\mathrm{i}k_x\lambda_2 \\ -2k_xk_y & -\mathrm{i}k_x\lambda_2 & \mathrm{i}k_y\lambda_2 \\ -2\mathrm{i}k_y\lambda_1 & \lambda_2^2 + k_y^2 & -k_xk_y \\ -2\mathrm{i}k_x\lambda_1 & k_xk_y & -\lambda_2^2 - k_x^2 \end{bmatrix} \tag{A.3}$$

$$\hat{\mathbf{U}}^{\mathbf{hs}}_{\mathbf{ITM}} = \begin{bmatrix} \mathrm{i}k_x & 0 & \lambda_2 \\ \mathrm{i}k_y & -\lambda_2 & 0 \\ -\lambda_1 & -\mathrm{i}k_y & \mathrm{i}k_x \end{bmatrix} \tag{A.4}$$

The vector of the unknown coefficients $\hat{\mathbf{C}}^{\mathbf{hs}}_{\mathbf{ITM}}$ is given by

$$\hat{\mathbf{C}}^{\mathbf{hs}}_{\mathbf{ITM}} = \left(A_2\mathrm{e}^{-\lambda_1 z}\ \ B_{x2}\mathrm{e}^{-\lambda_2 z}\ \ B_{y2}\mathrm{e}^{-\lambda_2 z}\right)^T \tag{A.5}$$

A.1.2 Static case

The stresses $\hat{\boldsymbol{\sigma}}^{\mathbf{hs}}_{\mathbf{0_{ITM}}} = \left(\hat{\sigma}_{xx}\ \hat{\sigma}_{yy}\ \hat{\sigma}_{zz}\ \hat{\sigma}_{xy}\ \hat{\sigma}_{yz}\ \hat{\sigma}_{xz}\right)^T$ and displacements $\hat{\mathbf{u}}^{\mathbf{hs}}_{\mathbf{0_{ITM}}} = \left(\hat{u}_x\ \hat{u}_y\ \hat{u}_z\right)^T$ in a homogeneous, isotropic halfspace can be calculated for each combination (k_x, k_y, z, ω) as

$$\hat{\boldsymbol{\sigma}}^{\mathbf{hs}}_{\mathbf{0_{ITM}}} = \hat{\mathbf{S}}^{\mathbf{hs}}_{\mathbf{0_{ITM}}}\, \hat{\mathbf{C}}^{\mathbf{hs}}_{\mathbf{0_{ITM}}} \tag{A.6}$$

$$\hat{\mathbf{u}}^{\mathbf{hs}}_{\mathbf{0_{ITM}}} = \hat{\mathbf{U}}^{\mathbf{hs}}_{\mathbf{0_{ITM}}}\, \hat{\mathbf{C}}^{\mathbf{hs}}_{\mathbf{0_{ITM}}} \tag{A.7}$$

with

$$\hat{\mathbf{S}}^{\mathbf{hs}}_{\mathbf{0_{ITM}}} = \mu \begin{bmatrix} -2k_x^2 z + 2\frac{\lambda k_r}{\lambda+\mu} & 0 & 2\mathrm{i}k_x k_r \\ -2k_y^2 + 2\frac{\lambda k_r}{\lambda+\mu} & -2\mathrm{i}k_y k_r & 0 \\ 2k_r^2 z + 2\frac{(\lambda+2\mu)k_r}{\lambda+\mu} & 2\mathrm{i}k_y k_r & -2\mathrm{i}k_x k_r \\ -2k_x k_y z & -\mathrm{i}k_x k_r & \mathrm{i}k_y k_r \\ -2\mathrm{i}k_y\left(k_r z + \frac{\mu}{\lambda+\mu}\right) & k_r^2 + k_y^2 & -k_x k_y \\ -2\mathrm{i}k_x\left(k_r z + \frac{\mu}{\lambda+\mu}\right) & k_x k_y & -k_r^2 - k_x^2 \end{bmatrix} \tag{A.8}$$

$$\hat{\mathbf{U}}^{\mathbf{hs}}_{\mathbf{0_{ITM}}} = \begin{bmatrix} \mathrm{i}k_x z & 0 & k_r \\ \mathrm{i}k_y z & -k_r & 0 \\ -k_r z - \frac{\lambda+3\mu}{\lambda+\mu} & -\mathrm{i}k_y & \mathrm{i}k_x \end{bmatrix} \tag{A.9}$$

The vector of the unknown coefficients $\hat{\mathbf{C}}^{\mathbf{hs}}_{\mathbf{0_{ITM}}}$ is given by

$$\hat{\mathbf{C}}^{\mathbf{hs}}_{\mathbf{0_{ITM}}} = \left(A_{02}\mathrm{e}^{-k_r z}\ \ B_{0x2}\mathrm{e}^{-k_r z}\ \ B_{0y2}\mathrm{e}^{-k_r z}\right)^T \tag{A.10}$$

with $k_r = \sqrt{k_x^2 + k_y^2}$, for which in the static case $k_r = \lambda_1 = \lambda_2$ (cp. Eq.(2.15)) holds. The zero in the indices of the matrices indicate, that the are associated with the static solution.

A.2 System matrices for the layered halfspace

A.2.1 Dynamic case

The stresses $\hat{\boldsymbol{\sigma}}^{\mathbf{hs\ L}_l}_{\mathbf{ITM}} = \left(\hat{\sigma}_{xx}\ \hat{\sigma}_{yy}\ \hat{\sigma}_{zz}\ \hat{\sigma}_{xy}\ \hat{\sigma}_{yz}\ \hat{\sigma}_{xz}\right)^T$ and displacements $\hat{\mathbf{u}}^{\mathbf{hs\ L}_l}_{\mathbf{ITM}} = \left(\hat{u}_x\ \hat{u}_y\ \hat{u}_z\right)^T$ within one layer l of a layered soil can be calculated for each combination (k_x, k_y, z, ω) as

$$\hat{\boldsymbol{\sigma}}^{\mathbf{hs\ L}_l}_{\mathbf{ITM}} = \hat{\mathbf{S}}^{\mathbf{hs\ L}_l}_{\mathbf{ITM}}\, \hat{\mathbf{C}}^{\mathbf{hs\ L}_l}_{\mathbf{ITM}} \tag{A.11}$$

$$\hat{\mathbf{u}}^{\mathbf{hs\ L}_l}_{\mathbf{ITM}} = \hat{\mathbf{U}}^{\mathbf{hs\ L}_l}_{\mathbf{ITM}}\, \hat{\mathbf{C}}^{\mathbf{hs\ L}_l}_{\mathbf{ITM}} \tag{A.12}$$

with

$$\hat{\mathbf{S}}^{\mathbf{hs\ L}_l}_{\mathbf{ITM}} = \mu_l \begin{bmatrix} -2k_x^2 - \frac{\lambda_l}{\mu_l}k_{p_l}^2 & -2k_x^2 - \frac{\lambda_l}{\mu_l}k_{p_l}^2 & 0 & 0 & -2\mathrm{i}k_x\lambda_{2_l} & 2\mathrm{i}k_x\lambda_{2_l} \\ -2k_y^2 - \frac{\lambda_l}{\mu_l}k_{p_l}^2 & -2k_y^2 - \frac{\lambda_l}{\mu_l}k_{p_l}^2 & 2\mathrm{i}k_y\lambda_{2_l} & -2\mathrm{i}k_y\lambda_{2_l} & 0 & 0 \\ 2\lambda_{1_l}^2 - \frac{\lambda_l}{\mu_l}k_{p_l}^2 & 2\lambda_{1_l}^2 - \frac{\lambda_l}{\mu_l}k_{p_l}^2 & -2\mathrm{i}k_y\lambda_{2_l} & 2\mathrm{i}k_y\lambda_{2_l} & 2\mathrm{i}k_x\lambda_{2_l} & -2\mathrm{i}k_x\lambda_{2_l} \\ -2k_xk_y & -2k_xk_y & \mathrm{i}k_x\lambda_{2_l} & -\mathrm{i}k_x\lambda_{2_l} & -\mathrm{i}k_y\lambda_{2_l} & \mathrm{i}k_y\lambda_{2_l} \\ 2\mathrm{i}k_y\lambda_{1_l} & -2\mathrm{i}k_y\lambda_{1_l} & \lambda_{2_l}^2 + k_y^2 & \lambda_{2_l}^2 + k_y^2 & -k_xk_y & -k_xk_y \\ 2\mathrm{i}k_x\lambda_{1_l} & -2\mathrm{i}k_x\lambda_{1_l} & k_xk_y & k_xk_y & -\lambda_{2_l}^2 - k_x^2 & -\lambda_{2_l}^2 - k_x^2 \end{bmatrix} \tag{A.13}$$

$$\hat{\mathbf{U}}^{\mathbf{hs\ L}_l}_{\mathbf{ITM}} = \begin{bmatrix} \mathrm{i}k_x & \mathrm{i}k_x & 0 & 0 & -\lambda_{2_l} & \lambda_{2_l} \\ \mathrm{i}k_y & \mathrm{i}k_y & \lambda_{2_l} & -\lambda_{2_l} & 0 & 0 \\ \lambda_{1_l} & -\lambda_{1_l} & -\mathrm{i}k_y & -\mathrm{i}k_y & \mathrm{i}k_x & \mathrm{i}k_x \end{bmatrix} \tag{A.14}$$

The vector of the unknown coefficients $\hat{\mathbf{C}}^{\mathbf{hs\ L}_l}_{\mathbf{ITM}}$ is given by

$$\hat{\mathbf{C}}^{\mathbf{hs\ L}_l}_{\mathbf{ITM}} = \begin{bmatrix} \underline{A}_{1,L_l}\mathrm{e}^{\lambda_{1_l}(z_l - h_l)} \\ A_{2,L_l}\mathrm{e}^{-\lambda_{1_l}z_l} \\ \underline{B}_{x1,L_l}\mathrm{e}^{\lambda_{2_l}(z_l - h_l)} \\ B_{x2,L_l}\mathrm{e}^{-\lambda_{2_l}z_l} \\ \underline{B}_{y1,L_l}\mathrm{e}^{\lambda_{2_l}(z_l - h_l)} \\ B_{y2,L_l}\mathrm{e}^{-\lambda_{2_l}z_l} \end{bmatrix} \tag{A.15}$$

with $\lambda_{1_l} = \sqrt{{k_x}^2 + {k_y}^2 - {k_{p_l}}^2}$ and $\lambda_{2_l} = \sqrt{{k_x}^2 + {k_y}^2 - {k_{s_l}}^2}$, where $k_{p_l} = \omega/c_{p_l}$ and $k_{s_l} = \omega/c_{s_l}$ are the wavenumbers of the compressional resp. shear waves for a given frequency ω. The parameters z_l and h_l are the vertical coordinate and the height of each layer l. The material properties are given by the Lamé constants λ_l and μ_l of each layer.

A.2.2 Static case

The stresses $\hat{\boldsymbol{\sigma}}^{\mathbf{hs\ L}_l}_{\mathbf{0_{ITM}}} = \left(\hat{\sigma}_{xx}\ \hat{\sigma}_{yy}\ \hat{\sigma}_{zz}\ \hat{\sigma}_{xy}\ \hat{\sigma}_{yz}\ \hat{\sigma}_{xz}\right)^T$ and displacements $\hat{\mathbf{u}}^{\mathbf{hs\ L}_l}_{\mathbf{0_{ITM}}} = \left(\hat{u}_x\ \hat{u}_y\ \hat{u}_z\right)^T$ within one layer l of a layered soil can be calculated for each combination (k_x, k_y, z, ω) as

$$\hat{\boldsymbol{\sigma}}^{\mathbf{hs\ L}_l}_{\mathbf{0_{ITM}}} = \hat{\mathbf{S}}^{\mathbf{hs\ L}_l}_{\mathbf{0_{ITM}}}\, \hat{\mathbf{C}}^{\mathbf{hs\ L}_l}_{\mathbf{0_{ITM}}} \tag{A.16}$$

$$\hat{\mathbf{u}}^{\mathbf{hs\ L}_l}_{\mathbf{0_{ITM}}} = \hat{\mathbf{U}}^{\mathbf{hs\ L}_l}_{\mathbf{0_{ITM}}}\, \hat{\mathbf{C}}^{\mathbf{hs\ L}_l}_{\mathbf{0_{ITM}}} \tag{A.17}$$

with

$$\hat{\mathbf{S}}^{\mathbf{hs\ L}_l}_{\mathbf{0_{ITM}}} = \mu_l \begin{bmatrix} -2k_x^2 z - 2\frac{\lambda_l k_r}{\lambda_l+\mu_l} & -2k_x^2 z + 2\frac{\lambda_l k_r}{\lambda_l+\mu_l} & 0 & 0 & -2\mathrm{i}k_x k_r & 2\mathrm{i}k_x k_r \\ -2k_y^2 - 2\frac{\lambda_l k_r}{\lambda_l+\mu_l} & -2k_y^2 + 2\frac{\lambda_l k_r}{\lambda_l+\mu_l} & 2\mathrm{i}k_y k_r & -2\mathrm{i}k_y k_r & 0 & 0 \\ 2k_r^2 z - 2\frac{(\lambda_l+2\mu_l)k_r}{\lambda_l+\mu_l} & 2k_r^2 z + 2\frac{(\lambda_l+2\mu_l)k_r}{\lambda_l+\mu_l} & -2\mathrm{i}k_y k_r & 2\mathrm{i}k_y k_r & 2\mathrm{i}k_x k_r & -2\mathrm{i}k_x k_r \\ -2k_x k_y z & -2k_x k_y z & \mathrm{i}k_x k_r & -\mathrm{i}k_x k_r & -\mathrm{i}k_y k_r & \mathrm{i}k_y k_r \\ 2\mathrm{i}k_y\left(k_r z - \frac{\mu_l}{\lambda_l+\mu_l}\right) & -2\mathrm{i}k_y\left(k_r z + \frac{\mu_l}{\lambda_l+\mu_l}\right) & k_r^2 + k_y^2 & k_r^2 + k_y^2 & -k_x k_y & -k_x k_y \\ 2\mathrm{i}k_x\left(k_r z - \frac{\mu_l}{\lambda_l+\mu_l}\right) & -2\mathrm{i}k_x\left(k_r z + \frac{\mu_l}{\lambda_l+\mu_l}\right) & k_x k_y & k_x k_y & -k_r^2 - k_x^2 & -k_r^2 - k_x^2 \end{bmatrix} \tag{A.18}$$

$$\hat{\mathbf{U}}^{\mathbf{hs\ L}_l}_{\mathbf{0_{ITM}}} = \begin{bmatrix} \mathrm{i}k_x z & \mathrm{i}k_x z & 0 & 0 & -k_r & k_r \\ \mathrm{i}k_y z & \mathrm{i}k_y z & k_r & -k_r & 0 & 0 \\ k_r z - \frac{\lambda_l+3\mu_l}{\lambda_l+\mu_l} & -k_r z - \frac{\lambda_l+3\mu_l}{\lambda_l+\mu_l} & -\mathrm{i}k_y & -\mathrm{i}k_y & \mathrm{i}k_x & \mathrm{i}k_x \end{bmatrix} \tag{A.19}$$

The vector of the unknown coefficients $\hat{\mathbf{C}}^{\mathbf{hs\ L}_l}_{\mathbf{0,ITM}}$ is given by

$$\hat{\mathbf{C}}^{\mathbf{hs\ L}_l}_{\mathbf{0_{ITM}}} = \begin{bmatrix} \underline{A}_{01,L_l} \mathrm{e}^{k_r(z_l - h_l)} \\ A_{02,L_l} \mathrm{e}^{-k_r z_l} \\ \underline{B}_{0x1,L_l} \mathrm{e}^{k_r(z_l - h_l)} \\ B_{0x2,L_l} \mathrm{e}^{-k_r z_l} \\ \underline{B}_{0y1,L_l} \mathrm{e}^{k_r(z_l - h_l)} \\ B_{0y2,L_l} \mathrm{e}^{-k_r z_l} \end{bmatrix} \tag{A.20}$$

with $k_r = \sqrt{k_x^2 + k_y^2}$, for which in the static case $k_r = \lambda_1 = \lambda_2$ holds.

It must be noted, that for $k_x = k_y = 0$ the solution gets singular and cannot be determined via Eqs. (A.16) and (A.17). However, as this case corresponds to a constant loading of the whole domain, the corresponding displacement can be obtained from the simple analytical solution of a rod with equivalent axial rigidity.

A.3 System matrices for the fullspace with cylindrical cavity

The stresses $\hat{\boldsymbol{\sigma}}^{\mathbf{fs\,cyl}}_{\mathbf{ITM}} = \left(\hat{\sigma}_{xx}\ \hat{\sigma}_{rr}\ \hat{\sigma}_{\varphi\varphi}\ \hat{\sigma}_{xr}\ \hat{\sigma}_{\varphi r}\ \hat{\sigma}_{x\varphi}\right)^T$ and the displacements $\hat{\mathbf{u}}^{\mathbf{fs\,cyl}}_{\mathbf{ITM}} = \left(\hat{u}_x\ \hat{u}_r\ \hat{u}_\varphi\right)^T$ in a fullspace with cylindrical cavity can be calculated for each combination (k_x, r, n, ω) as

$$\hat{\boldsymbol{\sigma}}^{\mathbf{fs\,cyl}}_{\mathbf{ITM}} = \hat{\mathbf{S}}^{\mathbf{fs\,cyl}}_{\mathbf{ITM}}\,\hat{\mathbf{C}}^{\mathbf{fs\,cyl}}_{\mathbf{ITM}} \tag{A.21}$$

$$\hat{\mathbf{u}}^{\mathbf{fs\,cyl}}_{\mathbf{ITM}} = \hat{\mathbf{U}}^{\mathbf{fs\,cyl}}_{\mathbf{ITM}}\,\hat{\mathbf{C}}^{\mathbf{fs\,cyl}}_{\mathbf{ITM}} \tag{A.22}$$

with the vector of the unknowns $\hat{\mathbf{C}}^{\mathbf{fs\,cyl}}_{\mathbf{ITM}} = \left(C_{1n}\ C_{2n}\ C_{3n}\ C_{4n}\ C_{5n}\ C_{6n}\right)^T$.

Elements of the matrix $\hat{\mathbf{S}}^{\mathbf{fs\,cyl}}_{\mathbf{ITM}}$ for the computation of the stress component $\hat{\sigma}_{xx}$:

$$\hat{S}^{\text{fs cyl}}_{\text{ITM},11} = \left({k_1}^2 - \frac{1}{2}{k_s}^2\right) 2\mu\, H_n^{(1)}(k_1 r)$$

$$\hat{S}^{\text{fs cyl}}_{\text{ITM},12} = 0$$

$$\hat{S}^{\text{fs cyl}}_{\text{ITM},13} = \mathrm{i}\ k_x\, {k_2}^2\, 2\mu\, H_n^{(1)}(k_2 r)$$

$$\hat{S}^{\text{fs cyl}}_{\text{ITM},14} = \left({k_1}^2 - \frac{1}{2}{k_s}^2\right) 2\mu\, H_n^{(2)}(k_1 r)$$

$$\hat{S}^{\text{fs cyl}}_{\text{ITM},15} = 0$$

$$\hat{S}^{\text{fs cyl}}_{\text{ITM},16} = \mathrm{i}\ k_x\, {k_2}^2\, 2\mu\, H_n^{(2)}(k_2 r)$$

Elements of the matrix $\hat{\mathbf{S}}^{\mathbf{fs\,cyl}}_{\mathbf{ITM}}$ for the computation of the stress component $\hat{\sigma}_{rr}$:

$$\hat{S}^{\text{fs cyl}}_{\text{ITM},21} = \left(\frac{n^2-n}{r^2} + {k_x}^2 - \frac{1}{2}{k_s}^2\right) 2\mu\, H_n^{(1)}(k_1 r) + \frac{1}{r} k_1\, 2\mu\, H_{n+1}^{(1)}(k_1 r)$$

$$\hat{S}^{\text{fs cyl}}_{\text{ITM},22} = \mathrm{i}\ \frac{n^2-n}{r^2}\ 2\mu\, H_n^{(1)}(k_2 r) - \mathrm{i}\ \frac{n}{r} k_2\, 2\mu\, H_{n+1}^{(1)}(k_2 r)$$

$$\hat{S}^{\text{fs cyl}}_{\text{ITM},23} = \mathrm{i}\left(\frac{n^2-n}{r^2} - {k_2}^2\right) k_x\, 2\mu\, H_n^{(1)}(k_2 r) + \mathrm{i}\ \frac{1}{r} k_x\, k_2\, 2\mu\, H_{n+1}^{(1)}(k_2 r)$$

$$\hat{S}^{\text{fs cyl}}_{\text{ITM},24} = \left(\frac{n^2-n}{r^2} + {k_x}^2 - \frac{1}{2}{k_s}^2\right) 2\mu\, H_n^{(2)}(k_1 r) + \frac{1}{r} k_1\, 2\mu\, H_{n+1}^{(2)}(k_1 r)$$

$$\hat{S}^{\text{fs cyl}}_{\text{ITM},25} = \mathrm{i}\ \frac{n^2-n}{r^2}\ 2\mu\, H_n^{(2)}(k_2 r) - \mathrm{i}\ \frac{n}{r} k_2\, 2\mu\, H_{n+1}^{(2)}(k_2 r)$$

$$\hat{S}^{\text{fs cyl}}_{\text{ITM},26} = \mathrm{i}\left(\frac{n^2-n}{r^2} - {k_2}^2\right) k_x\, 2\mu\, H_n^{(2)}(k_2 r) + \mathrm{i}\ \frac{1}{r} k_x\, k_2\, 2\mu\, H_{n+1}^{(2)}(k_2 r)$$

Elements of the matrix $\hat{\mathbf{S}}^{\mathbf{fs\,cyl}}_{\mathbf{ITM}}$ for the computation of the stress component $\hat{\sigma}_{\varphi\varphi}$:

$$\hat{S}^{\text{fs cyl}}_{\text{ITM},31} = -\left(\frac{n^2-n}{r^2} + \frac{1}{2}{k_s}^2 - {k_1}^2 - k_x^2\right) 2\mu\, H_n^{(1)}(k_1 r) - \frac{1}{r} k_1\, 2\mu\, H_{n+1}^{(1)}(k_1 r)$$

$$\hat{S}^{\text{fs cyl}}_{\text{ITM},32} = -\mathrm{i}\,\frac{n^2-n}{r^2}\, 2\mu\, H_n^{(1)}(k_2 r) + \mathrm{i}\,\frac{n}{r} k_2\, 2\mu\, H_{n+1}^{(1)}(k_2 r)$$

$$\hat{S}^{\text{fs cyl}}_{\text{ITM},33} = -\mathrm{i}\,\frac{n^2-n}{r^2}\, k_x\, 2\mu\, H_n^{(1)}(k_2 r) - \mathrm{i}\,\frac{1}{r} k_x\, k_2\, 2\mu\, H_{n+1}^{(1)}(k_2 r)$$

$$\hat{S}^{\text{fs cyl}}_{\text{ITM},34} = -\left(\frac{n^2-n}{r^2} + \frac{1}{2}{k_s}^2 - {k_1}^2 - k_x^2\right) 2\mu\, H_n^{(2)}(k_1 r) - \frac{1}{r} k_1\, 2\mu\, H_{n+1}^{(2)}(k_1 r)$$

$$\hat{S}^{\text{fs cyl}}_{\text{ITM},35} = -\mathrm{i}\,\frac{n^2-n}{r^2}\, 2\mu\, H_n^{(2)}(k_2 r) + \mathrm{i}\,\frac{n}{r} k_2\, 2\mu\, H_{n+1}^{(2)}(k_2 r)$$

$$\hat{S}^{\text{fs cyl}}_{\text{ITM},36} = -\mathrm{i}\,\frac{n^2-n}{r^2}\, k_x\, 2\mu\, H_n^{(2)}(k_2 r) - \mathrm{i}\,\frac{1}{r} k_x\, k_2\, 2\mu\, H_{n+1}^{(2)}(k_2 r)$$

Elements of the matrix $\hat{\mathbf{S}}^{\mathbf{fs\,cyl}}_{\mathbf{ITM}}$ for the computation of the stress component $\hat{\sigma}_{xr}$:

$$\hat{S}^{\text{fs cyl}}_{\text{ITM},41} = \mathrm{i}\,\frac{n}{r} k_x\, 2\mu\, H_n^{(1)}(k_1 r) - \mathrm{i}\, k_x\, k_1\, 2\mu\, H_{n+1}^{(1)}(k_1 r)$$

$$\hat{S}^{\text{fs cyl}}_{\text{ITM},42} = -\frac{n}{2r} k_x\, 2\mu\, H_n^{(1)}(k_2 r)$$

$$\hat{S}^{\text{fs cyl}}_{\text{ITM},43} = \frac{n}{2r}\left({k_2}^2 - {k_x}^2\right) 2\mu\, H_n^{(1)}(k_2 r) + \frac{1}{2}\left({k_x}^2 k_2 - {k_2}^3\right) 2\mu\, H_{n+1}^{(1)}(k_2 r)$$

$$\hat{S}^{\text{fs cyl}}_{\text{ITM},44} = \mathrm{i}\,\frac{n}{r} k_x\, 2\mu\, H_n^{(2)}(k_1 r) - \mathrm{i}\, k_x\, k_1\, 2\mu\, H_{n+1}^{(2)}(k_1 r)$$

$$\hat{S}^{\text{fs cyl}}_{\text{ITM},45} = -\frac{n}{2r} k_x\, 2\mu\, H_n^{(2)}(k_2 r)$$

$$\hat{S}^{\text{fs cyl}}_{\text{ITM},46} = \frac{n}{2r}\left({k_2}^2 - {k_x}^2\right) 2\mu\, H_n^{(2)}(k_2 r) + \frac{1}{2}\left({k_x}^2 k_2 - {k_2}^3\right) 2\mu\, H_{n+1}^{(2)}(k_2 r)$$

Elements of the matrix $\hat{\mathbf{S}}^{\mathbf{fs\,cyl}}_{\mathbf{ITM}}$ for the computation of the stress component $\hat{\sigma}_{\varphi r}$:

$$\hat{S}^{\text{fs cyl}}_{\text{ITM},51} = \text{i}\ \frac{n^2-n}{r^2}\,2\mu\,H^{(1)}_n(k_1 r) - \text{i}\ \frac{n}{r}k_1\,2\mu\,H^{(1)}_{n+1}(k_1 r)$$

$$\hat{S}^{\text{fs cyl}}_{\text{ITM},52} = \left(-\frac{n^2-n}{r^2} + \frac{1}{2}{k_2}^2\right) 2\mu\,H^{(1)}_n(k_2 r) - \frac{1}{r}k_2\,2\mu\,H^{(1)}_{n+1}(k_2 r)$$

$$\hat{S}^{\text{fs cyl}}_{\text{ITM},53} = -\frac{n^2-n}{r^2}\,k_x\,2\mu\,H^{(1)}_n(k_2 r) + \frac{n}{r}k_x\,k_2\,2\mu\,H^{(1)}_{n+1}(k_2 r)$$

$$\hat{S}^{\text{fs cyl}}_{\text{ITM},54} = \text{i}\ \frac{n^2-n}{r^2}\,2\mu\,H^{(2)}_n(k_1 r) - \text{i}\ \frac{n}{r}k_1\,2\mu\,H^{(2)}_{n+1}(k_1 r)$$

$$\hat{S}^{\text{fs cyl}}_{\text{ITM},55} = \left(-\frac{n^2-n}{r^2} + \frac{1}{2}{k_2}^2\right) 2\mu\,H^{(2)}_n(k_2 r) - \frac{1}{r}k_2\,2\mu\,H^{(2)}_{n+1}(k_2 r)$$

$$\hat{S}^{\text{fs cyl}}_{\text{ITM},56} = -\frac{n^2-n}{r^2}\,k_x\,2\mu\,H^{(2)}_n(k_2 r) + \frac{n}{r}k_x\,k_2\,2\mu\,H^{(2)}_{n+1}(k_2 r)$$

Elements of the matrix $\hat{\mathbf{S}}^{\mathbf{fs\,cyl}}_{\mathbf{ITM}}$ for the computation of the stress component $\hat{\sigma}_{x\varphi}$:

$$\hat{S}^{\text{fs cyl}}_{\text{ITM},61} = -\frac{n}{r}k_x\,2\mu\,H^{(1)}_n(k_1 r)$$

$$\hat{S}^{\text{fs cyl}}_{\text{ITM},62} = -\text{i}\ \frac{n}{2r}k_x\,2\mu\,H^{(1)}_n(k_2 r) + \text{i}\ \frac{1}{2}k_x\,k_2\,2\mu\,H^{(1)}_{n+1}(k_2 r)$$

$$\hat{S}^{\text{fs cyl}}_{\text{ITM},63} = \text{i}\ \frac{n}{2r}\left({k_2}^2 - {k_x}^2\right) 2\mu\,H^{(1)}_n(k_2 r))$$

$$\hat{S}^{\text{fs cyl}}_{\text{ITM},64} = -\frac{n}{r}k_x\,2\mu\,H^{(2)}_n(k_1 r)$$

$$\hat{S}^{\text{fs cyl}}_{\text{ITM},65} = -\text{i}\ \frac{n}{2r}k_x\,2\mu\,H^{(2)}_n(k_2 r) + \text{i}\ \frac{1}{2}k_x\,k_2\,2\mu\,H^{(2)}_{n+1}(k_2 r)$$

$$\hat{S}^{\text{fs cyl}}_{\text{ITM},66} = \text{i}\ \frac{n}{2r}\left({k_2}^2 - {k_x}^2\right) 2\mu\,H^{(2)}_n(k_2 r))$$

Elements of the matrix $\hat{\mathbf{U}}^{\mathbf{fs\,cyl}}_{\mathbf{ITM}}$ for the computation of the displacement component $\hat{u}_x$:

$$\hat{U}^{\text{fs cyl}}_{\text{ITM},11} = \text{i}\ k_x\, H_n^{(1)}(k_1 r)$$
$$\hat{U}^{\text{fs cyl}}_{\text{ITM},12} = 0$$
$$\hat{U}^{\text{fs cyl}}_{\text{ITM},13} = {k_2}^2 H_n^{(1)}(k_2 r)$$
$$\hat{U}^{\text{fs cyl}}_{\text{ITM},14} = \text{i}\ k_x\, H_n^{(2)}(k_1 r)$$
$$\hat{U}^{\text{fs cyl}}_{\text{ITM},15} = 0$$
$$\hat{U}^{\text{fs cyl}}_{\text{ITM},16} = {k_2}^2 H_n^{(2)}(k_2 r)$$

Elements of the matrix $\hat{\mathbf{U}}^{\mathbf{fs\,cyl}}_{\mathbf{ITM}}$ for the computation of the displacement component $\hat{u}_r$:

$$\hat{U}^{\text{fs cyl}}_{\text{ITM},21} = \frac{n}{r} H_n^{(1)}(k_1 r) - k_1\, H_{n+1}^{(1)}(k_1 r)$$
$$\hat{U}^{\text{fs cyl}}_{\text{ITM},22} = \text{i}\ \frac{n}{r} H_n^{(1)}(k_2 r)$$
$$\hat{U}^{\text{fs cyl}}_{\text{ITM},23} = \text{i}\ \frac{n}{r} k_x\, H_n^{(1)}(k_2 r) - \text{i}\ k_x\, k_2\, H_{n+1}^{(1)}(k_2 r)$$
$$\hat{U}^{\text{fs cyl}}_{\text{ITM},24} = \frac{n}{r} H_n^{(2)}(k_1 r) - k_1\, H_{n+1}^{(2)}(k_1 r)$$
$$\hat{U}^{\text{fs cyl}}_{\text{ITM},25} = \text{i}\ \frac{n}{r} H_n^{(2)}(k_2 r)$$
$$\hat{U}^{\text{fs cyl}}_{\text{ITM},26} = \text{i}\ \frac{n}{r} k_x\, H_n^{(2)}(k_2 r) - \text{i}\ k_x\, k_2\, H_{n+1}^{(2)}(k_2 r)$$

Elements of the matrix $\hat{\mathbf{U}}^{\mathbf{fs\,cyl}}_{\mathbf{ITM}}$ for the computation of the displacement component $\hat{u}_\varphi$:

$$\hat{U}^{\text{fs cyl}}_{\text{ITM},31} = \text{i}\ \frac{n}{r} H_n^{(1)}(k_1 r)$$
$$\hat{U}^{\text{fs cyl}}_{\text{ITM},32} = -\frac{n}{r} H_n^{(1)}(k_2 r) + k_2\, H_{n+1}^{(1)}(k_2 r)$$
$$\hat{U}^{\text{fs cyl}}_{\text{ITM},33} = -\frac{n}{r} k_x\, H_n^{(1)}(k_2 r)$$
$$\hat{U}^{\text{fs cyl}}_{\text{ITM},34} = \text{i}\ \frac{n}{r} H_n^{(2)}(k_1 r)$$
$$\hat{U}^{\text{fs cyl}}_{\text{ITM},35} = -\frac{n}{r} H_n^{(2)}(k_2 r) + k_2\, H_{n+1}^{(2)}(k_2 r)$$
$$\hat{U}^{\text{fs cyl}}_{\text{ITM},36} = -\frac{n}{r} k_x\, H_n^{(2)}(k_2 r)$$

A.4 System matrices for the fullspace with spherical cavity

The stresses $\hat{\boldsymbol{\sigma}}^{\mathbf{fs\,sph}}_{\mathbf{ITM}} = \left(\hat{\sigma}_{rr}\ \hat{\sigma}_{\vartheta\vartheta}\ \hat{\sigma}_{\varphi\varphi}\ \hat{\sigma}_{r\vartheta}\ \hat{\sigma}_{r\varphi}\ \hat{\sigma}_{\vartheta\varphi}\right)^T$ and the displacements $\hat{\mathbf{u}}^{\mathbf{fs\,sph}}_{\mathbf{ITM}} = \left(\hat{u}_r\ \hat{u}_\vartheta\ \hat{u}_\varphi\right)^T$ in a fullspace with spherical cavity can be calculated for each combination (r, m, l, ω) as

$$\hat{\boldsymbol{\sigma}}^{\mathbf{fs\,sph}}_{\mathbf{ITM}} = \hat{\mathbf{S}}^{\mathbf{fs\,sph}}_{\mathbf{ITM}}\,\hat{\mathbf{C}}^{\mathbf{fs\,sph}}_{\mathbf{ITM}} \tag{A.23a}$$

$$\hat{\mathbf{u}}^{\mathbf{fs\,sph}}_{\mathbf{ITM}} = \hat{\mathbf{U}}^{\mathbf{fs\,sph}}_{\mathbf{ITM}}\,\hat{\mathbf{C}}^{\mathbf{fs\,sph}}_{\mathbf{ITM}} \tag{A.23b}$$

with the vector of the unknowns $\hat{\mathbf{C}}^{\mathbf{fs\,sph}}_{\mathbf{ITM}} = \left(C_{1lm}\ C_{2lm}\ C_{3lm}\ C_{4lm}\ C_{5lm}\ C_{6lm}\right)^T$.

Elements of the matrix $\hat{\mathbf{S}}^{\mathbf{fs\,sph}}_{\mathbf{ITM}}$ for the computation of the stress component $\hat{\sigma}_{rr}$:

$$\begin{aligned}
\hat{S}^{\mathrm{fs\,sph}}_{\mathrm{ITM},11} &= \left(\frac{m^2-m}{r^2} - \frac{1}{2}|k_s|^2\right) \check{P}^l_m(\cos\vartheta)\ \mathrm{e}^{\mathrm{i}l\varphi}\ 2\mu\ h^{(1)}_m(|k_p|r) \\
&\quad + \frac{2}{r}\ |k_p|\ \check{P}^l_m(\cos\vartheta)\ \mathrm{e}^{\mathrm{i}l\varphi}\ 2\mu\ h^{(1)}_{m+1}(|k_p|r) \\
\hat{S}^{\mathrm{fs\,sph}}_{\mathrm{ITM},12} &= 0 \\
\hat{S}^{\mathrm{fs\,sph}}_{\mathrm{ITM},13} &= \frac{m^3-m}{r^2}\ \check{P}^l_m(\cos\vartheta)\ \mathrm{e}^{\mathrm{i}l\varphi}\ 2\mu\ h^{(1)}_m(|k_s|r) \\
&\quad - \frac{m^2+m}{r}\ |k_s|\ \check{P}^l_m(\cos\vartheta)\ \mathrm{e}^{\mathrm{i}l\varphi}\ 2\mu\ h^{(1)}_{m+1}(|k_s|r) \\
\hat{S}^{\mathrm{fs\,sph}}_{\mathrm{ITM},14} &= \left(\frac{m^2-m}{r^2} - \frac{1}{2}|k_s|^2\right) \check{P}^l_m(\cos\vartheta)\ \mathrm{e}^{\mathrm{i}l\varphi}\ 2\mu\ h^{(2)}_m(|k_p|r) \\
&\quad + \frac{2}{r}\ |k_p|\ \check{P}^l_m(\cos\vartheta)\ \mathrm{e}^{\mathrm{i}l\varphi}\ 2\mu\ h^{(2)}_{m+1}(|k_p|r) \\
\hat{S}^{\mathrm{fs\,sph}}_{\mathrm{ITM},15} &= 0 \\
\hat{S}^{\mathrm{fs\,sph}}_{\mathrm{ITM},16} &= \frac{m^3-m}{r^2}\ \check{P}^l_m(\cos\vartheta)\ \mathrm{e}^{\mathrm{i}l\varphi}\ 2\mu\ h^{(2)}_m(|k_s|r) \\
&\quad - \frac{m^2+m}{r}\ |k_s|\ \check{P}^l_m(\cos\vartheta)\ \mathrm{e}^{\mathrm{i}l\varphi}\ 2\mu\ h^{(2)}_{m+1}(|k_s|r)
\end{aligned}$$

Elements of the matrix $\hat{\mathbf{S}}^{\mathbf{fs\,sph}}_{\mathbf{ITM}}$ for the computation of the stress component $\hat{\sigma}_{\vartheta\vartheta}$:

$$
\begin{aligned}
\hat{S}^{\mathrm{fs\,sph}}_{\mathrm{ITM},21} &= \Bigg[\left(-\frac{m^2}{r^2} - \frac{1}{2}|k_s|^2 + |k_p|^2 + \frac{l^2 - m\cos^2\vartheta}{r^2\sin^2\vartheta} \right) \check{P}^l_m(\cos\vartheta)\ \mathrm{e}^{\mathrm{i}l\varphi} \\
&\quad + \frac{(m+l)\cos\vartheta}{r^2\sin^2\vartheta}\ \check{P}^l_{m-1}(\cos\vartheta)\ \mathrm{e}^{\mathrm{i}l\varphi} \Bigg] 2\mu\ h^{(1)}_m(|k_p|r) - \\
&\quad - \frac{1}{r}\ |k_p|\ \check{P}^l_m(\cos\vartheta)\ \mathrm{e}^{\mathrm{i}l\varphi}\ 2\mu\ h^{(1)}_{m+1}(|k_p|r) \\
\hat{S}^{\mathrm{fs\,sph}}_{\mathrm{ITM},22} &= \left(\mathrm{i}\ \frac{l(m-1)\cos\vartheta}{r\sin^2\vartheta}\ \check{P}^l_m(\cos\vartheta)\ \mathrm{e}^{\mathrm{i}l\varphi} - \mathrm{i}\ \frac{l(l+m)}{r\sin^2\vartheta}\ \check{P}^l_{m-1}(\cos\vartheta)\ \mathrm{e}^{\mathrm{i}l\varphi} \right) 2\mu\ h^{(1)}_m(|k_s|r) \\
\hat{S}^{\mathrm{fs\,sph}}_{\mathrm{ITM},23} &= \Bigg[\left(-\frac{m^3+m^2}{r^2} + \frac{l^2 - m\cos^2\vartheta}{r^2\sin^2\vartheta}(m+1) \right) \check{P}^l_m(\cos\vartheta)\ \mathrm{e}^{\mathrm{i}l\varphi} \\
&\quad + \frac{(m+l)\cos\vartheta}{r^2\sin^2\vartheta}(m+1)\ \check{P}^l_{m-1}(\cos\vartheta)\ \mathrm{e}^{\mathrm{i}l\varphi} \Bigg] 2\mu\ h^{(1)}_m(|k_s|r) + \\
&\quad + \Bigg[\left(\frac{m^2+m}{r}\ |k_s| - \frac{l^2 - m\cos^2\vartheta}{r\sin^2\vartheta}\ |k_s| \right) \check{P}^l_m(\cos\vartheta)\ \mathrm{e}^{\mathrm{i}l\varphi} \\
&\quad - \frac{(m+l)\cos\vartheta}{r\sin^2\vartheta}\ |k_s|\ \check{P}^l_{m-1}(\cos\vartheta)\ \mathrm{e}^{\mathrm{i}l\varphi} \Bigg] 2\mu\ h^{(1)}_{m+1}(|k_s|r) \\
\hat{S}^{\mathrm{fs\,sph}}_{\mathrm{ITM},24} &= \Bigg[\left(-\frac{m^2}{r^2} - \frac{1}{2}|k_s|^2 + |k_p|^2 + \frac{l^2 - m\cos^2\vartheta}{r^2\sin^2\vartheta} \right) \check{P}^l_m(\cos\vartheta)\ \mathrm{e}^{\mathrm{i}l\varphi} + \\
&\quad + \frac{(m+l)\cos\vartheta}{r^2\sin^2\vartheta}\ \check{P}^l_{m-1}(\cos\vartheta)\ \mathrm{e}^{\mathrm{i}l\varphi} \Bigg] 2\mu\ h^{(2)}_m(|k_p|r) \\
&\quad - \frac{1}{r}\ |k_p|\ \check{P}^l_m(\cos\vartheta)\ \mathrm{e}^{\mathrm{i}l\varphi}\ 2\mu\ h^{(2)}_{m+1}(|k_p|r) \\
\hat{S}^{\mathrm{fs\,sph}}_{\mathrm{ITM},25} &= \left(\mathrm{i}\ \frac{l(m-1)\cos\vartheta}{r\sin^2\vartheta}\ \check{P}^l_m(\cos\vartheta)\ \mathrm{e}^{\mathrm{i}l\varphi} - \mathrm{i}\ \frac{l(l+m)}{r\sin^2\vartheta}\ \check{P}^l_{m-1}(\cos\vartheta)\ \mathrm{e}^{\mathrm{i}l\varphi} \right) 2\mu\ h^{(2)}_m(|k_s|r) \\
\hat{S}^{\mathrm{fs\,sph}}_{\mathrm{ITM},26} &= \Bigg[\left(-\frac{m^3+m^2}{r^2} + \frac{l^2 - m\cos^2\vartheta}{r^2\sin^2\vartheta}(m+1) \right) \check{P}^l_m(\cos\vartheta)\ \mathrm{e}^{\mathrm{i}l\varphi} \\
&\quad + \frac{(m+l)\cos\vartheta}{r^2\sin^2\vartheta}(m+1)\ \check{P}^l_{m-1}(\cos\vartheta)\ \mathrm{e}^{\mathrm{i}l\varphi} \Bigg] 2\mu\ h^{(2)}_m(|k_s|r) + \\
&\quad + \Bigg[\left(\frac{m^2+m}{r}\ |k_s| - \frac{l^2 - m\cos^2\vartheta}{r\sin^2\vartheta}\ |k_s| \right) \check{P}^l_m(\cos\vartheta)\ \mathrm{e}^{\mathrm{i}l\varphi} \\
&\quad - \frac{(m+l)\cos\vartheta}{r\sin^2\vartheta}\ |k_s|\ \check{P}^l_{m-1}(\cos\vartheta)\ \mathrm{e}^{\mathrm{i}l\varphi} \Bigg] 2\mu\ h^{(2)}_{m+1}(|k_s|r)
\end{aligned}
$$

Elements of the matrix $\hat{\mathbf{S}}^{\mathbf{fs\,sph}}_{\mathbf{ITM}}$ for the computation of the stress component $\hat{\sigma}_{\varphi\varphi}$:

$$
\begin{aligned}
\hat{S}^{\mathrm{fs\,sph}}_{\mathrm{ITM},31} &= \Bigg[\left(\frac{m}{r^2} - \frac{1}{2}|k_s|^2 + |k_p|^2 - \frac{l^2 - m\cos^2\vartheta}{r^2\sin^2\vartheta} \right) \check{P}^l_m(\cos\vartheta)\ \mathrm{e}^{\mathrm{i}l\varphi} \\
&\quad - \frac{(m+l)\cos\vartheta}{r^2\sin^2\vartheta}\ \check{P}^l_{m-1}(\cos\vartheta)\ \mathrm{e}^{\mathrm{i}l\varphi} \Bigg]\ 2\mu\ h^{(1)}_m(|k_p|r)\ - \\
&\quad - \frac{1}{r}\ |k_p|\ \check{P}^l_m(\cos\vartheta)\ \mathrm{e}^{\mathrm{i}l\varphi}\ 2\mu\ h^{(1)}_{m+1}(|k_p|r) \\
\hat{S}^{\mathrm{fs\,sph}}_{\mathrm{ITM},32} &= \left(-i\ \frac{l(m-1)\cos\vartheta}{r\sin^2\vartheta} \check{P}^l_m(\cos\vartheta)\ \mathrm{i} + \mathrm{i}\ \frac{l(l+m)}{r\sin^2\vartheta}\ \check{P}^l_{m-1}(\cos\vartheta)\ \mathrm{e}^{\mathrm{i}l\varphi} \right) 2\mu\ h^{(1)}_m(|k_s|r) \\
\hat{S}^{\mathrm{fs\,sph}}_{\mathrm{ITM},33} &= \Bigg[\left(\frac{m^2+m}{r^2} - \frac{l^2 - m\cos^2\vartheta}{r^2\sin^2\vartheta}(m+1) \right) \check{P}^l_m(\cos\vartheta)\ \mathrm{e}^{\mathrm{i}l\varphi} \\
&\quad - \frac{(m+l)\cos\vartheta}{r^2\sin^2\vartheta}(m+1)\ \check{P}^l_{m-1}(\cos\vartheta)\ \mathrm{e}^{\mathrm{i}l\varphi} \Bigg] 2\mu\ h^{(1)}_m(|k_s|r)\ + \\
&\quad + \Bigg(\frac{l^2 - m\cos^2\vartheta}{r\sin^2\vartheta}\ |k_s|\ \check{P}^l_m(\cos\vartheta)\ \mathrm{e}^{\mathrm{i}l\varphi} \\
&\quad + \frac{(m+l)\cos\vartheta}{r\sin^2\vartheta}\ |k_s|\ \check{P}^l_{m-1}(\cos\vartheta)\ \mathrm{e}^{\mathrm{i}l\varphi} \Bigg) 2\mu\ h^{(1)}_{m+1}(|k_s|r) \\
\hat{S}^{\mathrm{fs\,sph}}_{\mathrm{ITM},34} &= \Bigg[\left(\frac{m}{r^2} - \frac{1}{2}|k_s|^2 + |k_p|^2 - \frac{l^2 - m\cos^2\vartheta}{r^2\sin^2\vartheta} \right) \check{P}^l_m(\cos\vartheta)\ \mathrm{e}^{\mathrm{i}l\varphi} \\
&\quad - \frac{(m+l)\cos\vartheta}{r^2\sin^2\vartheta}\ \check{P}^l_{m-1}(\cos\vartheta)\ \mathrm{e}^{\mathrm{i}l\varphi} \Bigg]\ 2\mu\ h^{(2)}_m(|k_p|r)\ - \\
&\quad - \frac{1}{r}\ |k_p|\ \check{P}^l_m(\cos\vartheta)\ \mathrm{e}^{\mathrm{i}l\varphi}\ 2\mu\ h^{(2)}_{m+1}(|k_p|r) \\
\hat{S}^{\mathrm{fs\,sph}}_{\mathrm{ITM},35} &= \left(-\mathrm{i}\ \frac{l(m-1)\cos\vartheta}{r\sin^2\vartheta} \check{P}^l_m(\cos\vartheta)\ \mathrm{e}^{\mathrm{i}l\varphi} + \mathrm{i}\ \frac{l(l+m)}{r\sin^2\vartheta}\ \check{P}^l_{m-1}(\cos\vartheta)\ \mathrm{e}^{\mathrm{i}l\varphi} \right) 2\mu\ h^{(2)}_m(|k_s|r) \\
\hat{S}^{\mathrm{fs\,sph}}_{\mathrm{ITM},31} &= \Bigg[\left(\frac{m^2+m}{r^2} - \frac{l^2 - m\cos^2\vartheta}{r^2\sin^2\vartheta}(m+1) \right) \check{P}^l_m(\cos\vartheta)\ \mathrm{e}^{\mathrm{i}l\varphi} \\
&\quad - \frac{(m+l)\cos\vartheta}{r^2\sin^2\vartheta}(m+1)\ \check{P}^l_{m-1}(\cos\vartheta)\ \mathrm{e}^{\mathrm{i}l\varphi} \Bigg] 2\mu\ h^{(2)}_m(|k_s|r)\ + \\
&\quad + \Bigg(\frac{l^2 - m\cos^2\vartheta}{r\sin^2\vartheta}\ |k_s|\ \check{P}^l_m(\cos\vartheta)\ \mathrm{e}^{\mathrm{i}l\varphi} \\
&\quad + \frac{(m+l)\cos\vartheta}{r\sin^2\vartheta}\ |k_s|\ \check{P}^l_{m-1}(\cos\vartheta)\ \mathrm{e}^{\mathrm{i}l\varphi} \Bigg) 2\mu\ h^{(2)}_{m+1}(|k_s|r)
\end{aligned}
$$

Elements of the matrix $\hat{\mathbf{S}}^{\mathbf{fs\,sph}}_{\mathbf{ITM}}$ for the computation of the stress component $\hat{\sigma}_{r\vartheta}$:

$$
\begin{aligned}
\hat{S}^{\mathrm{fs\,sph}}_{\mathrm{ITM},41} &= \Bigg(\frac{m\cot\vartheta}{r^2}\ (m-1)\ \check{P}^l_m(\cos\vartheta)\ \mathrm{e}^{\mathrm{i}l\varphi} \\
&\quad - \frac{m+l}{r^2\sin\vartheta}\ (m-1)\ \check{P}^l_{m-1}(\cos\vartheta)\ \mathrm{e}^{\mathrm{i}l\varphi} \Bigg) 2\mu\ h^{(1)}_m(|k_p|r) + \\
&\quad + \left(-\frac{m\cot\vartheta}{r}\ |k_p|\ \check{P}^l_m(\cos\vartheta)\ \mathrm{e}^{\mathrm{i}l\varphi} + \frac{m+l}{r\sin\vartheta}\ |k_p|\ \check{P}^l_{m-1}(\cos\vartheta)\ \mathrm{e}^{\mathrm{i}l\varphi} \right) 2\mu\ h^{(1)}_{m+1}(|k_p|r) \\
\hat{S}^{\mathrm{fs\,sph}}_{\mathrm{ITM},42} &= \mathrm{i}\ \frac{l}{2r\sin\vartheta}\ (m-1)\ \check{P}^l_m(\cos\vartheta)\ \mathrm{e}^{\mathrm{i}l\varphi}\ 2\mu\ h^{(1)}_m(|k_s|r) \\
&\quad - \mathrm{i}\ \frac{l}{2\sin\vartheta}\ |k_s|\ \check{P}^l_m(\cos\vartheta)\ \mathrm{e}^{\mathrm{i}l\varphi}\ 2\mu\ h^{(1)}_{m+1}(|k_s|r) \\
\hat{S}^{\mathrm{fs\,sph}}_{\mathrm{ITM},431} &= \Bigg[m\cot\vartheta \left(\frac{m^2-1}{r^2} - \frac{1}{2}\ |k_s|^2 \right) \check{P}^l_m(\cos\vartheta)\ \mathrm{e}^{\mathrm{i}l\varphi} \\
&\quad - \frac{m+l}{\sin\vartheta} \left(\frac{m^2-1}{r^2} - \frac{1}{2}\ |k_s|^2 \right) \check{P}^l_{m-1}(\cos\vartheta)\ \mathrm{e}^{\mathrm{i}l\varphi} \Bigg] 2\mu\ h^{(1)}_m(|k_s|r) + \\
&\quad + \left(\frac{m\cot\vartheta}{r}\ |k_s|\ \check{P}^l_m(\cos\vartheta)\ \mathrm{e}^{\mathrm{i}l\varphi} - \frac{m+l}{r\sin\vartheta}\ |k_s|\ \check{P}^l_{m-1}(\cos\vartheta)\ \mathrm{e}^{\mathrm{i}l\varphi} \right) 2\mu\ h^{(1)}_{m+1}(|k_s|r) \\
\hat{S}^{\mathrm{fs\,sph}}_{\mathrm{ITM},44} &= \Bigg(\frac{m\cot\vartheta}{r^2}\ (m-1)\ \check{P}^l_m(\cos\vartheta)\ \mathrm{e}^{\mathrm{i}l\varphi} \\
&\quad - \frac{m+l}{r^2\sin\vartheta}\ (m-1)\ \check{P}^l_{m-1}(\cos\vartheta)\ \mathrm{e}^{\mathrm{i}l\varphi} \Bigg) 2\mu\ h^{(2)}_m(|k_p|r) + \\
&\quad + \left(-\frac{m\cot\vartheta}{r}\ |k_p|\ \check{P}^l_m(\cos\vartheta)\ \mathrm{e}^{\mathrm{i}l\varphi} + \frac{m+l}{r\sin\vartheta}\ |k_p|\ \check{P}^l_{m-1}(\cos\vartheta)\ \mathrm{e}^{\mathrm{i}l\varphi} \right) 2\mu\ h^{(2)}_{m+1}(|k_p|r) \\
\hat{S}^{\mathrm{fs\,sph}}_{\mathrm{ITM},45} &= \mathrm{i}\ \frac{l}{2r\sin\vartheta}\ (m-1)\ \check{P}^l_m(\cos\vartheta)\ \mathrm{e}^{\mathrm{i}l\varphi}\ 2\mu\ h^{(2)}_m(|k_s|r) \\
&\quad - \mathrm{i}\ \frac{l}{2\sin\vartheta}\ |k_s|\ \check{P}^l_m(\cos\vartheta)\ \mathrm{e}^{\mathrm{i}l\varphi}\ 2\mu\ h^{(2)}_{m+1}(|k_s|r) \\
\hat{S}^{\mathrm{fs\,sph}}_{\mathrm{ITM},46} &= \Bigg[m\cot\vartheta \left(\frac{m^2-1}{r^2} - \frac{1}{2}\ |k_s|^2 \right) \check{P}^l_m(\cos\vartheta)\ \mathrm{e}^{\mathrm{i}l\varphi} \\
&\quad - \frac{m+l}{\sin\vartheta} \left(\frac{m^2-1}{r^2} - \frac{1}{2}\ |k_s|^2 \right) \check{P}^l_{m-1}(\cos\vartheta)\ \mathrm{e}^{\mathrm{i}l\varphi} \Bigg] 2\mu\ h^{(2)}_m(|k_s|r) + \\
&\quad + \left(\frac{m\cot\vartheta}{r}\ |k_s|\ \check{P}^l_m(\cos\vartheta)\ \mathrm{e}^{\mathrm{i}l\varphi} - \frac{m+l}{r\sin\vartheta}\ |k_s|\ \check{P}^l_{m-1}(\cos\vartheta)\ \mathrm{e}^{\mathrm{i}l\varphi} \right) 2\mu\ h^{(2)}_{m+1}(|k_s|r)
\end{aligned}
$$

Elements of the matrix $\hat{\mathbf{S}}^{\mathbf{fs\,sph}}_{\mathbf{ITM}}$ for the computation of the stress component $\hat{\sigma}_{r\varphi}$:

$$
\begin{aligned}
\hat{S}^{\mathrm{fs\,sph}}_{\mathrm{ITM},51} &= \mathrm{i}\,\frac{l}{r^2\sin\vartheta}\,(m-1)\,\check{P}^l_m(\cos\vartheta)\,\mathrm{e}^{\mathrm{i}l\varphi}\,2\mu\,h^{(1)}_m(|k_p|r)\\
&\quad-\mathrm{i}\,\frac{l}{r\sin\vartheta}\,|k_p|\,\check{P}^l_m(\cos\vartheta)\,\mathrm{e}^{\mathrm{i}l\varphi}\,2\mu\,h^{(1)}_{m+1}(|k_p|r)\\
\hat{S}^{\mathrm{fs\,sph}}_{\mathrm{ITM},52} &= \Bigg(-\frac{m\cos\vartheta}{2r\sin\vartheta}\,(m-1)\,\check{P}^l_m(\cos\vartheta)\,\mathrm{e}^{\mathrm{i}l\varphi}\\
&\quad+\frac{m+l}{2r\sin\vartheta}\,(m-1)\,\check{P}^l_{m-1}(\cos\vartheta)\,\mathrm{e}^{\mathrm{i}l\varphi}\Bigg)2\mu\,h^{(1)}_m(|k_s|r)\,+\\
&\quad+\left(\frac{m\cos\vartheta}{2\sin\vartheta}\,|k_s|\,\check{P}^l_m(\cos\vartheta)\,\mathrm{e}^{\mathrm{i}l\varphi}-\frac{m+l}{2\sin\vartheta}\,|k_s|\,\check{P}^l_{m-1}(\cos\vartheta)\,\mathrm{e}^{\mathrm{i}l\varphi}\right)2\mu\,h^{(1)}_{m+1}(|k_s|r)\\
\hat{S}^{\mathrm{fs\,sph}}_{\mathrm{ITM},53} &= \mathrm{i}\,\frac{l}{\sin\vartheta}\left(\frac{m^2-1}{r^2}-\frac{1}{2}|k_s|^2\right)\check{P}^l_m(\cos\vartheta)\,\mathrm{e}^{\mathrm{i}l\varphi}\,2\mu\,h^{(1)}_m(|k_s|r)\\
&\quad+\mathrm{i}\,\frac{l}{r\sin\vartheta}\,|k_s|\,\check{P}^l_m(\cos\vartheta)\,\mathrm{e}^{\mathrm{i}l\varphi}\,2\mu\,h^{(1)}_{m+1}(|k_s|r)\\
\hat{S}^{\mathrm{fs\,sph}}_{\mathrm{ITM},54} &= \mathrm{i}\,\frac{l}{r^2\sin\vartheta}\,(m-1)\,\check{P}^l_m(\cos\vartheta)\,\mathrm{e}^{\mathrm{i}l\varphi}\,2\mu\,h^{(2)}_m(|k_p|r)\\
&\quad-\mathrm{i}\,\frac{l}{r\sin\vartheta}\,|k_p|\,\check{P}^l_m(\cos\vartheta)\,\mathrm{e}^{\mathrm{i}l\varphi}\,2\mu\,h^{(2)}_{m+1}(|k_p|r)\\
\hat{S}^{\mathrm{fs\,sph}}_{\mathrm{ITM},55} &= \Bigg(-\frac{m\cos\vartheta}{2r\sin\vartheta}\,(m-1)\,\check{P}^l_m(\cos\vartheta)\,\mathrm{e}^{\mathrm{i}l\varphi}\\
&\quad+\frac{m+l}{2r\sin\vartheta}\,(m-1)\,\check{P}^l_{m-1}(\cos\vartheta)\,\mathrm{e}^{\mathrm{i}l\varphi}\Bigg)2\mu\,h^{(2)}_m(|k_s|r)\,+\\
&\quad+\left(\frac{m\cos\vartheta}{2\sin\vartheta}\,|k_s|\,\check{P}^l_m(\cos\vartheta)\,\mathrm{e}^{\mathrm{i}l\varphi}-\frac{m+l}{2\sin\vartheta}\,|k_s|\,\check{P}^l_{m-1}(\cos\vartheta)\,\mathrm{e}^{\mathrm{i}l\varphi}\right)2\mu\,h^{(2)}_{m+1}(|k_s|r)\\
\hat{S}^{\mathrm{fs\,sph}}_{\mathrm{ITM},56} &= \mathrm{i}\,\frac{l}{\sin\vartheta}\left(\frac{m^2-1}{r^2}-\frac{1}{2}|k_s|^2\right)\check{P}^l_m(\cos\vartheta)\,\mathrm{e}^{\mathrm{i}l\varphi}\,2\mu\,h^{(2)}_m(|k_s|r)\\
&\quad+\mathrm{i}\,\frac{l}{r\sin\vartheta}\,|k_s|\,\check{P}^l_m(\cos\vartheta)\,\mathrm{e}^{\mathrm{i}l\varphi}\,2\mu\,h^{(2)}_{m+1}(|k_s|r)
\end{aligned}
$$

Elements of the matrix $\hat{\mathbf{S}}^{\mathbf{fs\,sph}}_{\mathbf{ITM}}$ for the computation of the stress component $\hat{\sigma}_{\vartheta\varphi}$:

$$\hat{S}^{\mathrm{fs\,sph}}_{\mathrm{ITM},61} = \left(\mathrm{i}\ \frac{l(m-1)\cos\vartheta}{r^2\sin^2\vartheta}\ \check{P}^l_m(\cos\vartheta)\ \mathrm{e}^{\mathrm{i}l\varphi} - \mathrm{i}\ \frac{l(m+l)}{r^2\sin^2\vartheta}\ \check{P}^l_{m-1}(\cos\vartheta)\ \mathrm{e}^{\mathrm{i}l\varphi} \right) 2\mu\ h^{(1)}_m(|k_p|r)$$

$$\hat{S}^{\mathrm{fs\,sph}}_{\mathrm{ITM},62} = \left[\left(\frac{m^2-m}{2r} + \frac{m-l^2}{r\sin^2\vartheta} \right) \check{P}^l_m(\cos\vartheta)\ \mathrm{e}^{\mathrm{i}l\varphi} - \right.$$
$$\left. - \frac{(m+l)\cos\vartheta}{r\sin^2\vartheta}\ \check{P}^l_{m-1}(\cos\vartheta)\ \mathrm{e}^{\mathrm{i}l\varphi} \right] 2\mu\ h^{(1)}_m(|k_s|r)$$

$$\hat{S}^{\mathrm{fs\,sph}}_{\mathrm{ITM},63} = \left(\mathrm{i}\ \frac{l(m-1)\cos\vartheta}{r^2\sin^2\vartheta}\ (m+1)\ \check{P}^l_m(\cos\vartheta)\ \mathrm{e}^{\mathrm{i}l\varphi} \right.$$
$$\left. - \mathrm{i}\ \frac{l(m+l)}{r^2\sin^2\vartheta}\ (m+1)\ \check{P}^l_{m-1}(\cos\vartheta)\ \mathrm{e}^{\mathrm{i}l\varphi} \right) 2\mu\ h^{(1)}_m(|k_s|r) +$$
$$+ \left(- \mathrm{i}\ \frac{l(m-1)\cos\vartheta}{r\sin^2\vartheta}\ |k_s|\ \check{P}^l_m(\cos\vartheta)\ \mathrm{e}^{\mathrm{i}l\varphi} \right.$$
$$\left. + \mathrm{i}\ \frac{l(m+l)}{r\sin^2\vartheta}\ |k_s|\ \check{P}^l_{m-1}(\cos\vartheta)\ \mathrm{e}^{\mathrm{i}l\varphi} \right) 2\mu\ h^{(1)}_{m+1}(|k_s|r)$$

$$\hat{S}^{\mathrm{fs\,sph}}_{\mathrm{ITM},64} = \left(\mathrm{i}\ \frac{l(m-1)\cos\vartheta}{r^2\sin^2\vartheta}\ \check{P}^l_m(\cos\vartheta)\ \mathrm{e}^{\mathrm{i}l\varphi} - \mathrm{i}\ \frac{l(m+l)}{r^2\sin^2\vartheta}\ \check{P}^l_{m-1}(\cos\vartheta)\ \mathrm{e}^{\mathrm{i}l\varphi} \right) 2\mu\ h^{(2)}_m(|k_p|r)$$

$$\hat{S}^{\mathrm{fs\,sph}}_{\mathrm{ITM},65} = \left[\left(\frac{m^2-m}{2r} + \frac{m-l^2}{r\sin^2\vartheta} \right) \check{P}^l_m(\cos\vartheta)\ \mathrm{e}^{\mathrm{i}l\varphi} - \frac{(m+l)\cos\vartheta}{r\sin^2\vartheta}\ \check{P}^l_{m-1}(\cos\vartheta)\ \mathrm{e}^{\mathrm{i}l\varphi} \right] 2\mu\ h^{(2)}_m(|k_s|r)$$

$$\hat{S}^{\mathrm{fs\,sph}}_{\mathrm{ITM},66} = \left(\mathrm{i}\ \frac{l(m-1)\cos\vartheta}{r^2\sin^2\vartheta}\ (m+1)\ \check{P}^l_m(\cos\vartheta)\ \mathrm{e}^{\mathrm{i}l\varphi} \right.$$
$$\left. - \mathrm{i}\ \frac{l(m+l)}{r^2\sin^2\vartheta}\ (m+1)\ \check{P}^l_{m-1}(\cos\vartheta)\ \mathrm{e}^{\mathrm{i}l\varphi} \right) 2\mu\ h^{(2)}_m(|k_s|r) +$$
$$+ \left(- \mathrm{i}\ \frac{l(m-1)\cos\vartheta}{r\sin^2\vartheta}\ |k_s|\ \check{P}^l_m(\cos\vartheta)\ \mathrm{e}^{\mathrm{i}l\varphi} \right.$$
$$\left. + \mathrm{i}\ \frac{l(m+l)}{r\sin^2\vartheta}\ |k_s|\ \check{P}^l_{m-1}(\cos\vartheta)\ \mathrm{e}^{\mathrm{i}l\varphi} \right) 2\mu\ h^{(2)}_{m+1}(|k_s|r)$$

Elements of the matrix $\hat{\mathbf{U}}^{\mathbf{fs\,sph}}_{\mathbf{ITM}}$ for the computation of the displacement component $\hat{u}_r$:

$$\hat{U}^{\text{fs sph}}_{\text{ITM},11} = \frac{m}{r}\ \check{P}^l_m(\cos\vartheta)\ \mathrm{e}^{\mathrm{i}l\varphi}\ h^{(1)}_m(|k_p|r) - |k_p|\ \check{P}^l_m(\cos\vartheta)\ \mathrm{e}^{\mathrm{i}l\varphi}\ h^{(1)}_{m+1}(|k_p|r)$$

$$\hat{U}^{\text{fs sph}}_{\text{ITM},12} = 0$$

$$\hat{U}^{\text{fs sph}}_{\text{ITM},13} = \frac{m^2+m}{r}\ \check{P}^l_m(\cos\vartheta)\ \mathrm{e}^{\mathrm{i}l\varphi}\ h^{(1)}_m(|k_s|r)$$

$$\hat{U}^{\text{fs sph}}_{\text{ITM},14} = \frac{m}{r}\ \check{P}^l_m(\cos\vartheta)\ \mathrm{e}^{\mathrm{i}l\varphi}\ h^{(2)}_m(|k_p|r) - |k_p|\ \check{P}^l_m(\cos\vartheta)\ \mathrm{e}^{\mathrm{i}l\varphi}\ h^{(2)}_{m+1}(|k_p|r)$$

$$\hat{U}^{\text{fs sph}}_{\text{ITM},15} = 0$$

$$\hat{U}^{\text{fs sph}}_{\text{ITM},16} = \frac{m^2+m}{r}\ \check{P}^l_m(\cos\vartheta)\ \mathrm{e}^{\mathrm{i}l\varphi}\ h^{(2)}_m(|k_s|r)$$

Elements of the matrix $\hat{\mathbf{U}}^{\mathbf{fs\,sph}}_{\mathbf{ITM}}$ for the computation of the displacement component $\hat{u}_\vartheta$:

$$\hat{U}^{\text{fs sph}}_{\text{ITM},21} = \left(\frac{m\cot\vartheta}{r}\ \check{P}^l_m(\cos\vartheta)\ \mathrm{e}^{\mathrm{i}l\varphi} - \frac{m+l}{r\sin\vartheta}\ P^l_{m-1}(\cos\vartheta)\ \mathrm{e}^{\mathrm{i}l\varphi}\right) h^{(1)}_m(|k_p|r)$$

$$\hat{U}^{\text{fs sph}}_{\text{ITM},22} = \mathrm{i}\ \frac{l}{r\sin\vartheta}\ \check{P}^l_m(\cos\vartheta)\ \mathrm{e}^{\mathrm{i}l\varphi}\ h^{(1)}_m(|k_s|r)$$

$$\begin{aligned}\hat{U}^{\text{fs sph}}_{\text{ITM},23} = &\left(\frac{(m^2+m)\cot\vartheta}{r}\ \check{P}^l_m(\cos\vartheta)\ \mathrm{e}^{\mathrm{i}l\varphi} - \frac{(m+1)(m+l)}{r\sin\vartheta}\ P^l_{m-1}(\cos\vartheta)\ \mathrm{e}^{\mathrm{i}l\varphi}\right) h^{(1)}_m(|k_s|r) + \\ &+ \left(-m\cot\vartheta\ |k_s|\ \check{P}^l_m(\cos\vartheta)\ \mathrm{e}^{\mathrm{i}l\varphi} + \frac{m+l}{\sin\vartheta}\ |k_s|\ P^l_{m-1}(\cos\vartheta)\ \mathrm{e}^{\mathrm{i}l\varphi}\right) h^{(1)}_{m+1}(|k_s|r)\end{aligned}$$

$$\hat{U}^{\text{fs sph}}_{\text{ITM},24} = \left(\frac{m\cot\vartheta}{r}\ \check{P}^l_m(\cos\vartheta)\ \mathrm{e}^{\mathrm{i}l\varphi} - \frac{m+l}{r\sin\vartheta}\ P^l_{m-1}(\cos\vartheta)\ \mathrm{e}^{\mathrm{i}l\varphi}\right) h^{(2)}_m(|k_p|r)$$

$$\hat{U}^{\text{fs sph}}_{\text{ITM},25} = \mathrm{i}\ \frac{l}{r\sin\vartheta}\ \check{P}^l_m(\cos\vartheta)\ \mathrm{e}^{\mathrm{i}l\varphi}\ h^{(2)}_m(|k_s|r)$$

$$\begin{aligned}\hat{U}^{\text{fs sph}}_{\text{ITM},26} = &\left(\frac{(m^2+m)\cot\vartheta}{r}\ \check{P}^l_m(\cos\vartheta)\ \mathrm{e}^{\mathrm{i}l\varphi} - \frac{(m+1)(m+l)}{r\sin\vartheta}\ P^l_{m-1}(\cos\vartheta)\ \mathrm{e}^{\mathrm{i}l\varphi}\right) h^{(2)}_m(|k_s|r) + \\ &+ \left(-m\cot\vartheta\ |k_s|\ \check{P}^l_m(\cos\vartheta)\ \mathrm{e}^{\mathrm{i}l\varphi} + \frac{m+l}{\sin\vartheta}\ |k_s|\ P^l_{m-1}(\cos\vartheta)\ \mathrm{e}^{\mathrm{i}l\varphi}\right) h^{(2)}_{m+1}(|k_s|r)\end{aligned}$$

Elements of the matrix $\hat{\mathbf{U}}^{\mathbf{fs\,sph}}_{\mathbf{ITM}}$ for the computation of the displacement component $\hat{u}_\varphi$:

$$\hat{U}^{\mathrm{fs\,sph}}_{\mathrm{ITM},31} = \mathrm{i}\ \frac{l}{r\sin\vartheta}\ \check{P}^l_m(\cos\vartheta)\ \mathrm{e}^{\mathrm{i}l\varphi}\ h^{(1)}_m(|k_p|r)$$

$$\hat{U}^{\mathrm{fs\,sph}}_{\mathrm{ITM},32} = \left(-m\cot\vartheta\ \check{P}^l_m(\cos\vartheta)\ \mathrm{e}^{\mathrm{i}l\varphi} + \frac{m+l}{\sin\vartheta}\ P^l_{m-1}(\cos\vartheta)\ \mathrm{e}^{\mathrm{i}l\varphi}\right) h^{(1)}_m(|k_s|r)$$

$$\hat{U}^{\mathrm{fs\,sph}}_{\mathrm{ITM},33} = \mathrm{i}\ \frac{l(m+1)}{r\sin\vartheta}\ \check{P}^l_m(\cos\vartheta)\ \mathrm{e}^{\mathrm{i}l\varphi}\ h^{(1)}_m(|k_s|r) - \mathrm{i}\ \frac{l}{\sin\vartheta}\ |k_s|\ \check{P}^l_m(\cos\vartheta)\ \mathrm{e}^{\mathrm{i}l\varphi}\ h^{(1)}_{m+1}(|k_s|r)$$

$$\hat{U}^{\mathrm{fs\,sph}}_{\mathrm{ITM},34} = \mathrm{i}\ \frac{l}{r\sin\vartheta}\ \check{P}^l_m(\cos\vartheta)\ \mathrm{e}^{\mathrm{i}l\varphi}\ h^{(2)}_m(|k_p|r)$$

$$\hat{U}^{\mathrm{fs\,sph}}_{\mathrm{ITM},35} = \left(-m\cot\vartheta\ \check{P}^l_m(\cos\vartheta)\ \mathrm{e}^{\mathrm{i}l\varphi} + \frac{m+l}{\sin\vartheta}\ P^l_{m-1}(\cos\vartheta)\ \mathrm{e}^{\mathrm{i}l\varphi}\right) h^{(2)}_m(|k_s|r)$$

$$\hat{U}^{\mathrm{fs\,sph}}_{\mathrm{ITM},36} = \mathrm{i}\ \frac{l(m+1)}{r\sin\vartheta}\ \check{P}^l_m(\cos\vartheta)\ \mathrm{e}^{\mathrm{i}l\varphi}\ h^{(2)}_m(|k_s|r) - \mathrm{i}\ \frac{l}{\sin\vartheta}\ |k_s|\ \check{P}^l_m(\cos\vartheta)\ \mathrm{e}^{\mathrm{i}l\varphi}\ h^{(2)}_{m+1}(|k_s|r)$$

A.5 Mathematical functions

A.5.1 Bessel functions of integer order

The Bessel differential equation of integer order is defined as [243]

$$z^2 \frac{\mathrm{d}^2 \mathrm{f}(z)}{\mathrm{d}z^2} + z \frac{\mathrm{df}(z)}{\mathrm{d}z} + \left(z^2 - n^2\right) \mathrm{f}(z) = 0 \tag{A.24}$$

The Bessel functions of first kind $J_n(z)$ and second kind $Y_n(z)$ form a fundamental set of solutions for the Bessel differential equation A.24

$$\mathrm{f}(z) = C_1 \, J_n(z) + C_2 \, Y_n(z) \tag{A.25}$$

with the arbitrary constants C_1 and C_2 and

$$J_n(z) = \sum_{k=0}^{\infty} \frac{(-1)^k \left(\frac{z}{2}\right)^{n+2k}}{k! \Gamma(n+k+1)} \tag{A.26}$$

$$Y_n(z) = \frac{J_n(z) \cos n\pi - J_{-n}(z)}{\sin n\pi} \tag{A.27}$$

where Γ is the Gamma function.

The Bessel functions of third kind, also called Hankel functions of the first and second kind, are defined by linear combinations of the Bessel functions [315]

$$H_n^{(1)}(z) = J_n(z) + \mathrm{i} \, Y_n(z) \tag{A.28}$$

$$H_n^{(2)}(z) = J_n(z) - \mathrm{i} \, Y_n(z) \tag{A.29}$$

Thus, a solution of Eq. (A.24) is also given by

$$\mathrm{f}(z) = C_1 \, H_n^{(1)}(z) + C_2 \, H_n^{(2)}(z) \tag{A.30}$$

A.5.2 Bessel functions of fractional order

The Bessel differential equation of fractional order is defined as [243]

$$z^2 \frac{\mathrm{d}^2 \mathrm{f}(z)}{\mathrm{d}z^2} + 2z \frac{\mathrm{df}(z)}{\mathrm{d}z} + \Big(z^2 - n(n+1)\Big)\,\mathrm{f}(z) = 0 \tag{A.31}$$

where n is a real constant.

The spherical Bessel functions of first kind $j_n(z)$ and second kind $y_n(z)$ form a fundamental set of solutions for the Bessel differential equation A.31

$$\mathrm{f}(z) = C_1\, j_n(z) + C_2\, y_n(z) \tag{A.32}$$

with the arbitrary constants C_1 and C_2 and

$$j_n(z) = \sqrt{\frac{\pi}{2z}} J_{n+\frac{1}{2}}(z) \tag{A.33}$$

$$y_n(z) = \sqrt{\frac{\pi}{2z}} Y_{n+\frac{1}{2}}(z) \tag{A.34}$$

The spherical Bessel functions of third kind, also called spherical Hankel functions of the first and second kind, are defined by linear combinations of the spherical Bessel functions

$$h_n^{(1)}(z) = j_n(z) + \mathrm{i}\, y_n(z) = \sqrt{\frac{\pi}{2z}} H_{n+\frac{1}{2}}^{(1)} \tag{A.35}$$

$$h_n^{(2)}(z) = j_n(z) - \mathrm{i}\, y_n(z) = \sqrt{\frac{\pi}{2z}} H_{n+\frac{1}{2}}^{(2)} \tag{A.36}$$

Thus, a solution of Eq. (A.31) is also given by

$$\mathrm{f}(z) = C_1\, h_n^{(1)}(z) + C_2\, h_n^{(1)}(z) \tag{A.37}$$

A.5.3 Heaviside function

The Heaviside function is defined as

$$\mathbf{H}(t) = \begin{cases} 0 & t < 0 \\ \frac{1}{2} & t = 0 \\ 1 & t > 0 \end{cases} \tag{A.38}$$

According to [316] its Fourier transform is given by:

$$\bar{\mathbf{H}}(\omega) = \pi\delta(\omega) + \frac{1}{\mathrm{i}\,\omega} \tag{A.39}$$

A.6 Finite Element matrices

The dynamic equation of motion in the frequency domain can be solved in a discretized form applying the Finite Element method

$$\left(\mathbf{K} - \omega^2 \mathbf{M}\right) \mathbf{u} = \mathbf{P} \tag{A.40}$$

A.6.1 Stiffness matrix for beam element

The element stiffness matrix for a 3D beam element with 2 nodes and 12 DOFs, three translations and three rotations per node, applying the Euler Bernoulli beam theory and using linear elastic isotropic material yields as given in [282, 317]

$$\mathbf{K}_{\text{beam}} = \begin{bmatrix}
\frac{EA}{L} & 0 & 0 & 0 & 0 & 0 & -\frac{EA}{L} & 0 & 0 & 0 & 0 & 0 \\
 & \frac{12EI_z}{L^3} & 0 & 0 & 0 & \frac{6EI_z}{L^2} & 0 & -\frac{12EI_z}{L^3} & 0 & 0 & 0 & \frac{6EI_z}{L^2} \\
 & & \frac{12EI_y}{L^3} & 0 & -\frac{6EI_y}{L^2} & 0 & 0 & 0 & -\frac{12EI_y}{L^3} & 0 & -\frac{6EI_y}{L^2} & 0 \\
 & & & \frac{GI_T}{L} & 0 & 0 & 0 & 0 & 0 & -\frac{GI_T}{L} & 0 & 0 \\
 & & & & \frac{4EI_y}{L} & 0 & 0 & 0 & \frac{6EI_y}{L^2} & 0 & \frac{2EI_y}{L} & 0 \\
 & & & & & \frac{4EI_z}{L} & 0 & -\frac{6EI_z}{L^2} & 0 & 0 & 0 & \frac{2EI_y}{L} \\
 & & & & & & \frac{EA}{L} & 0 & 0 & 0 & 0 & 0 \\
 & & & & & & & \frac{12EI_z}{L^3} & 0 & 0 & 0 & -\frac{6EI_z}{L^2} \\
 & & & \text{sym.} & & & & & \frac{12EI_y}{L^3} & 0 & \frac{6EI_y}{L^2} & 0 \\
 & & & & & & & & & \frac{GI_T}{L} & 0 & 0 \\
 & & & & & & & & & & \frac{4EI_y}{L} & 0 \\
 & & & & & & & & & & & \frac{4EI_y}{L}
\end{bmatrix} \tag{A.41}$$

with the local DOFs $\bar{\mathbf{u}}_{\text{beam}} = [u_1, v_1, w_1, \theta_{x1}, \theta_{y1}, \theta_{z1}, u_2, v_2, w_2, \theta_{x2}, \theta_{y2}, \theta_{z2}]^T$

A.6.2 Mass matrix for beam element

The corresponding mass matrix including the rotational inertia but neglecting the shear deformation effects as given in [283] yields

$$\mathbf{M}_{\text{beam}} = \begin{bmatrix} \mathbf{M}^{11}_{\text{beam}} & \mathbf{M}^{12}_{\text{beam}} \\ \mathbf{M}^{21}_{\text{beam}} & \mathbf{M}^{22}_{\text{beam}} \end{bmatrix} \tag{A.42}$$

with

$$\mathbf{M}^{11}_{\text{beam}} = \begin{bmatrix} \frac{m}{3} & 0 & 0 & 0 & 0 & 0 \\ & m\left(\frac{13}{35}+\frac{6I_z}{5AL^2}\right) & 0 & 0 & 0 & m\left(\frac{11L}{210}+\frac{I_z}{10AL}\right) \\ & & m\left(\frac{13}{35}+\frac{6I_y}{5AL^2}\right) & 0 & m\left(\frac{-11L}{210}-\frac{I_y}{5AL^2}\right) & 0 \\ & & & m\frac{I_T}{3A} & 0 & 0 \\ & \text{sym.} & & & m\left(\frac{L^2}{105}+\frac{2I_y}{15A}\right) & 0 \\ & & & & & m\left(\frac{L^2}{105}+\frac{2I_z}{15A}\right) \end{bmatrix} \tag{A.43}$$

$$\mathbf{M}^{12}_{\text{beam}} = \begin{bmatrix} \frac{m}{6} & 0 & 0 & 0 & 0 & 0 \\ 0 & m\left(\frac{9}{70}-\frac{6I_z}{5AL^2}\right) & 0 & 0 & 0 & m\left(\frac{-13L}{420}+\frac{I_z}{10AL}\right) \\ 0 & 0 & m\left(\frac{9}{70}-\frac{6I_y}{5AL^2}\right) & 0 & m\left(\frac{13L}{420}-\frac{I_y}{10AL}\right) & 0 \\ 0 & 0 & 0 & m\frac{I_T}{6A} & 0 & 0 \\ 0 & 0 & m\left(\frac{-13L}{420}+\frac{I_y}{10AL}\right) & 0 & m\left(\frac{-L^2}{140}-\frac{I_y}{30A}\right) & 0 \\ 0 & m\left(\frac{13L}{120}-\frac{I_z}{10AL}\right) & 0 & 0 & 0 & m\left(\frac{-L^2}{140}-\frac{I_z}{30A}\right) \end{bmatrix} \tag{A.44}$$

$$\mathbf{M}^{22}_{\text{beam}} = \begin{bmatrix} \frac{m}{3} & 0 & 0 & 0 & 0 & 0 \\ & m\left(\frac{13}{35}+\frac{6I_z}{5AL^2}\right) & 0 & 0 & 0 & -m\left(\frac{11L}{210}+\frac{I_z}{10AL}\right) \\ & & m\left(\frac{13}{35}+\frac{6I_y}{5AL^2}\right) & 0 & m\left(\frac{11L}{210}+\frac{I_y}{5AL^2}\right) & 0 \\ & & & m\frac{I_T}{3A} & 0 & 0 \\ & \text{sym.} & & & m\left(\frac{L^2}{105}+\frac{2I_y}{15A}\right) & 0 \\ & & & & & m\left(\frac{L^2}{105}+\frac{2I_y}{15A}\right) \end{bmatrix} \tag{A.45}$$

wherein $m = \rho AL$ with A being the cross sectional area and L the length of the beam. Furthermore it holds $\mathbf{M}^{21}_{\text{beam}} = \mathbf{M}^{12\ T}_{\text{beam}}$ as $\mathbf{M}_{\text{beam}}$ in total is symmetric.

Bibliography

[1] E. Kausel, Early history of soil-structure interaction, Soil Dynamics and Earthquake Engineering 30 (2010) 822–832.

[2] J. Boussinesq, Application des potentiels à l'étude de l'équilibre et du mouvement des solides élastiques: Principalement Au Calcul Des Déformations Et Des Pressions, Gauthier-Villars, Imprimeur-Libraire, 1885.

[3] V. Cerruti, Ricerche intorno all'equilibrio de' corpi elastici isotropi, Reale Accademia dei Lincei, Roma, 13 edition, 1882.

[4] G. G. Stokes (Ed.), On the dynamical theory of diffraction, Transactions of the Cambridge Philsophial Society, 1849.

[5] H. Lamb, On the propagation of tremors over the surface of an elastic solid, Philosophical Transactions of the Royal Society A: Mathematical, Physical and Engineering Sciences 203 (1904) 1–42.

[6] C. L. Pekeris, The seismic surface pulse, Proceedings of the National Academy of Sciences of the United States of America 41 (1955) 469–480.

[7] C.-C. Chao, Dynamical response of an elastic half-space to tangential surface loadings, Journal of Applied Mechanics 27 (1960) 559–567.

[8] G. Eason, The displacements produced in an elastic half-space by a suddenly applied surface force, IMA Journal of Applied Mathematics 2 (1966) 299–326.

[9] L. Cagniard, E. A. Flinn, C. Hewitt Dix, W. G. Mayer, Reflection and refraction of progressive seismic waves, Physics Today 16 (1963) 64.

[10] A. T. de Hoop, A modification of Cagniard's method for solving seismic pulse problems, Applied Scientific Research, Section B 8 (1960) 349–356.

[11] M. Mitra, Disturbance produced in an elastic half-space by impulsive normal pressure, Mathematical Proceedings of the Cambridge Philosophical Society 60 (1964) 683–696.

[12] F. Guan, M. Novak, Transient response of an elastic homogeneous half-space to suddenly applied rectangular loading, Journal of Applied Mechanics 61 (1994) 256–263.

[13] D. V. Jones, M. Petyt, Ground vibration in the vicinity of a strip load: A two-dimensional half-space model, Journal of Sound and Vibration 147 (1991) 155–166.

[14] D. V. Jones, M. Petyt, Ground vibration in the vicinity of a rectangular load on a half-space, Journal of Sound and Vibration 166 (1993) 141–159.

[15] D. V. Jones, M. Petyt, Ground vibration in the vicinity of a strip load: An elastic layer on an elastic half-space, Journal of Sound and Vibration 161 (1993) 1–18.

[16] D. V. Jones, D. Le Houedec, M. Petyt, Ground vibrations due to a rectangular harmonic load, Journal of Sound and Vibration 212 (1998) 61–74.

[17] E. Kausel, Fundamental solutions in elastodynamics: a compendium, Cambridge University Press, 2006.

[18] A. C. Eringen, E. S. Suhubi, Elstodynamics, Vol. II.(Linear Theory), Academic Press: New York, 1975.

[19] J. Achenbach, Wave Propagation in Elastic Solids, North-Holland Series in Applied Mathematics and Mechanics, Elsevier Science, Amsterdam, 1984.

[20] E. Reissner, Stationäre, axialsymmetrische, durch eine schüttelnde Masse erregte Schwingungen eines homogenen elastischen Halbraumes, Ingenieur-Archiv 7 (1936) 381–396.

[21] G. N. Bycroft, Forced vibrations of a rigid circular plate on a semi-infinite elastic space and on an elastic stratum, Philosophical Transactions of the Royal Society of London. Series A, Mathematical and Physical Sciences 248 (1956) 327–368.

[22] W. T. Thomson, T. Kobori, Dynamical compliance of rectangular foundations on an elastic half-space, Journal of Applied Mechanics 30 (1963) 579–584.

[23] A. S. Veletsos, Y. T. Wei, Lateral and rocking vibration of footings, Journal of the Soil Mechanics and Foundations Division 97 (1971) 1227–1248.

[24] J. E. Luco, R. A. Westmann, Dynamic response of circular footings, Journal of the Engineering Mechanics Division 97 (1971) 1381–1395.

[25] J. E. Luco, R. A. Westmann, Dynamic response of a rigid footing bonded to an elastic half space, Journal of Applied Mechanics 39 (1972) 527–534.

[26] J. E. Luco, Impedance functions for a rigid foundation on a layered medium, Nuclear Engineering and Design 31 (1974) 204–217.

[27] G. Gazetas, Dynamic stiffness functions of strip and rectangular footings on layered media, Ph.D. thesis, Massachusetts Institute of Technology, 1975.

[28] P. Bettess, Infinite elements, International Journal for Numerical Methods in Engineering 11 (1977) 53–64.

[29] K. S. Kazakov, Elastodynamic infinite elements based on modified Bessel shape functions, applicable in the finite element method, Structural Engineering and Mechanics 42 (2012) 353–362.

[30] O. C. Zienkiewicz, C. Emson, P. Bettess, A novel boundary infinite element, International Journal for Numerical Methods in Engineering 19 (1983) 393–404.

[31] Y. Yang, S. Kuo, H. Hung, Frequency-independent infinite elements for analysing semi-infinite problems, International Journal for Numerical Methods in Engineering 39 (1996) 3553–3569.

[32] B. Engquist, A. Majda, Absorbing boundary conditions for the numerical simulation of waves, Mathematics of Computation 31 (1977) 629–651.

[33] D. Givoli, Non-reflecting boundary conditions, Journal of Computational Physics 94 (1991) 1–29.

[34] F. Collino, et al., High order absorbing boundary conditions for wave propagation models: straight line boundary and corner cases, in: Second International Conference on Mathematical and Numerical Aspects of Wave Propagation (Newark, DE, 1993), pp. 161–171.

[35] D. Rabinovich, D. Givoli, J. Bielak, T. Hagstrom, A finite element scheme with a high order absorbing boundary condition for elastodynamics, Computer Methods in Applied Mechanics and Engineering 200 (2011) 2048–2066.

[36] D. Baffet, J. Bielak, D. Givoli, T. Hagstrom, D. Rabinovich, Long-time stable high-order absorbing boundary conditions for elastodynamics, Computer Methods in Applied Mechanics and Engineering 241-244 (2012) 20–37.

[37] J.-P. Berenger, A perfectly matched layer for the absorption of electromagnetic waves, Journal of computational physics 114 (1994) 185–200.

[38] U. Basu, A. K. Chopra, Perfectly matched layers for time-harmonic elastodynamics of unbounded domains: Theory and finite-element implementation, Computer Methods in Applied Mechanics and Engineering 192 (2003) 1337–1375.

[39] F. Rammerstorfer, Simulation von Wellenausbreitung unter Verwendung von Perfectly Matched Layers, Diplomarbeit, TU Graz, 2008.

[40] E. Kausel, J. M. de Oliveira Barbosa, PMLs: A direct approach, International Journal for Numerical Methods in Engineering 90 (2012) 343–352.

[41] A. Fathi, B. Poursartip, L. F. Kallivokas, Time-domain hybrid formulations for wave simulations in three-dimensional PML-truncated heterogeneous media, International Journal for Numerical Methods in Engineering 101 (2015) 165–198.

[42] M. Papadopoulos, S. François, G. Degrande, G. Lombaert, The influence of uncertain local subsoil conditions on the response of buildings to ground vibration, Journal of Sound and Vibration 418 (2018) 200–220.

[43] I.-K. Fontara, W. Schepers, S. Savidis, F. Rackwitz, Finite element implementation of efficient absorbing layers for time harmonic elastodynamics of unbounded domains, Soil Dynamics and Earthquake Engineering 114 (2018) 625–638.

[44] J. Lysmer, R. L. Kuhlemeyer, Finite dynamic model for infinite media, Journal of the Engineering Mechanics Division 95 (1969) 859–877.

[45] G. Waas, Earth Vibration Effects and Abatement for Military Facilities. Report 3. Analysis Method for Footing Vibrations through Layered Media, 1972.

[46] E. Kausel, R. Peek, Dynamic loads in the interior of a layered stratum: An explicit solution, International Journal of Rock Mechanics and Mining Sciences & Geomechanics Abstracts 20 (1983) A57–A58.

[47] E. Kausel, Thin-layer method: Formulation in the time domain, International Journal for Numerical Methods in Engineering 37 (1994) 927–941.

[48] J. Park, Wave motion in finite and infinite media using the thin-layer method, Phd thesis, Massachusetts Institute of Technology, Cambridge, 2002.

[49] W. Schepers, E. Kausel, A Method to Increase the Accuracy of the Green's Functions for Layered Media Obtained by Means of the Thin Layer Method, in: F. Rackwitz (Ed.), Entwicklungen in der Bodenmechanik, Bodendynamik und Geotechnik, volume 37, Springer-Verlag, Berlin/Heidelberg, 2006, pp. 161–172.

[50] J. M. de Oliveira Barbosa, J. Park, E. Kausel, Perfectly matched layers in the thin layer method, Computer Methods in Applied Mechanics and Engineering 217-220 (2012) 262–274.

[51] J. Freisinger, M. Radišić, F. Taddei, G. Müller, Dynamic response of three-dimensional rigid and flexible foundations on layered soils with local inhomogeneities, Soil Dynamics and Earthquake Engineering 153 (2022) 107007.

[52] H. L. Wong, Dynamic soil-structure interaction, Ph.d. thesis, 1975.

[53] H. L. Wong, J. E. Luco, Dynamic response of rigid foundations of arbitrary shape, Earthquake Engineering & Structural Dynamics 4 (1976) 579–587.

[54] H. R. Hamidzadeh-Eraghi, P. Grootenhuis, The dynamics of a rigid foundation on the surface of an elastic half-space, Earthquake Engineering & Structural Dynamics 9 (1981) 501–515.

[55] W. Rücker, Dynamic behaviour of rigid foundations of arbitrary shape on a halfspace, Earthquake Engineering & Structural Dynamics 10 (1982) 675–690.

[56] J. Dominguez, J. M. Roesset, Dynamic stiffness of rectangular foundations, 1978.

[57] R. Shahi, A. Noorzad, Dynamic response of rigid foundations of arbitrary shape using half-space Green's function, International Journal of Geomechanics 11 (2011) 391–398.

[58] M. Mohammadi, D. L. Karabalis, 3-D soil-structure interaction analysis by BEM: Comparison studies and computational aspects, Soil Dynamics and Earthquake Engineering 9 (1990) 96–108.

[59] S. A. Savidis, T. Richter, Dynamic response of elastic plates on the surface of the half-space, International Journal for Numerical and Analytical Methods in Geomechanics 3 (1979) 245–254.

[60] W. L. Whittaker, P. Christiano, Dynamic response of plate on elastic half-space, Journal of the Engineering Mechanics Division 108 (1982) 133–154.

[61] M. Iguchi, J. E. Luco, Dynamic response of flexible rectangular foundations on an elastic half-space, Earthquake Engineering & Structural Dynamics 9 (1981) 239–249.

[62] H. L. Wong, J. E. Luco, M. D. Trifunac, Contact stresses and ground motion generated by soil-structure interaction, Earthquake Engineering & Structural Dynamics 5 (1977) 67–79.

[63] D. L. Karabalis, D. E. Beskos, Dynamic response of 3-D rigid surface foundations by time domain boundary element method, Earthquake Engineering & Structural Dynamics 12 (1984) 73–93.

[64] D. L. Karabalis, C.-F. D. Huang, Inertial soil-foundation interaction by a direct time domain BEM, Mathematical and Computer Modelling 15 (1991) 215–228.

[65] S. Ahmad, P. K. Banerjee, Time-domain transient elastodynamic analysis of 3-D solids by BEM, International Journal for Numerical Methods in Engineering 26 (1988) 1709–1728.

[66] W. Sarfeld, Numerische Verfahren zur dynamischen Boden-Bauwerk Interaktion, Ph.D. thesis, TU Berlin, 1994.

[67] C. Bode, Numerisches Verfahren zur Berechnung von Baugrund-Bauwerk-Interaktionen im Zeitbereich mittels Greennscher Funktionen für den Halbraum, Ph.D. thesis, TU Berlin, 2000.

[68] R. Hirschauer, Kopplung von finiten Elementen mit Rand-Elementen zur Berechnung der dynamischen Baugrund-Bauwerk-Interaktion., Ph.D. thesis, TU Berlin, Berlin, 2001.

[69] C. Bode, R. Hirschauer, S. A. Savidis, Soil–structure interaction in the time domain using halfspace Green's functions, Soil Dynamics and Earthquake Engineering 22 (2002) 283–295.

[70] D. C. Rizos, Z. Wang, Coupled BEM–FEM solutions for direct time domain soil–structure interaction analysis, Engineering Analysis with Boundary Elements 26 (2002) 877–888.

[71] P. Galvín, A. Romero, A 3D time domain numerical model based on half-space Green's function for soil–structure interaction analysis, Computational Mechanics 53 (2014) 1073–1085.

[72] C. Song, J. P. Wolf, The scaled boundary finite-element method—alias consistent infinitesimal finite-element cell method—for elastodynamics, Computer Methods in Applied Mechanics and Engineering 147 (1997) 329–355.

[73] C. Song, J. P. Wolf, Consistent Infinitesimal Finite-Element Cell Method: Three-Dimensional Vector Wave Equation, International Journal for Numerical Methods in Engineering 39 (1996) 2189–2208.

[74] J. P. Wolf, C. Song, Finite-element modelling of unbounded media, Wiley, Chichester, reprinted. edition, 1997.

[75] D. Chen, C. Birk, C. Song, C. Du, A high-order approach for modelling transient wave propagation problems using the scaled boundary finite element method, International Journal for Numerical Methods in Engineering 97 (2014) 937–959.

[76] J. Yann, C. Zhang, F. Jin, A coupling procedure of FE and SBFE for soil–structure interaction in the time domain, International Journal for Numerical Methods in Engineering 59 (2004) 1453–1471.

[77] M. Schauer, J. E. Roman, E. S. Quintana-Ortí, S. Langer, Parallel Computation of 3-D Soil-Structure Interaction in Time Domain with a Coupled FEM/SBFEM Approach, Journal of Scientific Computing 52 (2012) 446–467.

[78] C. Birk, R. Behnke, A modified scaled boundary finite element method for three-dimensional dynamic soil-structure interaction in layered soil, International Journal for Numerical Methods in Engineering 89 (2012) 371–402.

[79] Z. Han, L. Yang, H. Fang, J. Zhang, Transient analysis of three–dimensional dynamic interaction between multilayered soil and rigid foundation, International Journal for Numerical Methods in Engineering 121 (2020) 4406–4434.

[80] M. Aslmand, I. M. Kani, C. Birk, H. Gravenkamp, F. Krome, M. Eskandari-Ghadi, Dynamic soil-structure interaction in a 3D layered medium treated by coupling a semi-analytical axisymmetric far field formulation and a 3D finite element model, Soil Dynamics and Earthquake Engineering 115 (2018) 531–544.

[81] G. Müller, Ein Verfahren zur Erfassung der Fundament-Boden Wechselwirkung unter Einwirkung periodischer Lasten, Dissertation, Technische Universität München, München, 1989.

[82] G. F. Zirwas, Ein hybrides Verfahren zur Behandlung der Bauwerk-Boden-wechselwirkung mit analytischen Integraltransformationen und numerischen Ansätzen, Disseration, Technische Universität München, München, 1996.

[83] J. I. Rastandi, Modelization of dynamic Soil-Structure Interaction using Integral Transform-Finite Element coupling, Dissertation, Technische Universität München, 2003.

[84] J. Freisinger, M. Hackenberg, G. Müller, A coupled Integral Transform Method - Finite Element Method approach to model the Soil Structure Interaction of finite (3D) and length invariant (2.5D) systems, Journal of Sound and Vibration 482 (2020) 115443.

[85] M. Radisic, ITM-based dynamic analysis of foundations resting on a layered halfspace, Ph.D. thesis, Universität Belgrad, Belgrad, 2018.

[86] M. Radišić, G. Müller, M. Petronijevic, Impedance matrix for four adjacent rigid surface foundation, in: Eurodyn 2014, Porto.

[87] M. Radišić, M. Petronijević, G. Müller, Vibrations of rectangular flexible foundation on halfspace, XI International Conference on Structural Dynamics 2020 (2020) 2857–2866.

[88] C. Vrettos, Einflussfunktionen für inhomogene Böden und ihre Anwendung bei der Boden-Bauwerk Interaktion, Ph.D. thesis, TU Berlin, Berlin, 1997.

[89] D. Chen, Flachgründungen auf Böden mit tiefenabhängiger Steifigkeit unter vertikaler dynamischer Belastung: Ergebnisse von numerischen Berechnungen im Frequenz- und Zeitbereich, Ph.D. thesis, TU Kaiserslautern, Kaiserslautern, 2014.

[90] A. Katebi, A. Selvadurai, A frictionless contact problem for a flexible circular plate and an incompressible non-homogeneous elastic halfspace, International Journal of Mechanical Sciences 90 (2015) 239–245.

[91] G. Lin, Z. Han, J. Li, Soil–structure interaction analysis on anisotropic stratified medium, Géotechnique 64 (2014) 570–580.

[92] E. Esmaeilzadeh Seylabi, C. Jeong, E. Taciroglu, On numerical computation of impedance functions for rigid soil-structure interfaces embedded in heterogeneous half-spaces, Computers and Geotechnics 72 (2016) 15–27.

[93] M. Papadopoulos, R. van Beeumen, S. François, G. Degrande, G. Lombaert, Modal characteristics of structures considering dynamic soil-structure interaction effects, Soil Dynamics and Earthquake Engineering 105 (2018) 114–118.

[94] A. Zangeneh, S. François, G. Lombaert, C. Pacoste, Modal analysis of coupled soil-structure systems, Soil Dynamics and Earthquake Engineering 144 (2021) 106645.

[95] G. B. Warburton, J. D. Richardson, J. J. Webster, Forced vibrations of two masses on an elastic half space, Journal of Applied Mechanics 38 (1971) 148–156.

[96] T. Kobori, R. Minai, K. Kusakabe, Dynamical characteristics of soil-structure cross-interaction system, I, Bulletin of the Disaster Prevention Research Institute (1973).

[97] H. L. Wong, J. E. Luco, Dynamic interaction between rigid foundations in a layered half-space, Soil Dynamics and Earthquake Engineering 5 (1986) 149–158.

[98] E. Kausel, J. M. Roesset, G. Waas, Dynamic analysis of footings on layered media, Journal of Engineering Mechanics 101 (1975).

[99] H.-T. Lin, J. M. Roesset, J. L. Tassoulas, Dynamic interaction between adjacent foundations, Earthquake Engineering & Structural Dynamics 15 (1987) 323–343.

[100] J. Freisinger, G. Müller, Three dimensional dynamic interaction of adjacent foundations on a halfspace with local inhomogeneity applying a coupled ITM-FEM approach, Proceedings of 8th International Conference on Computational Methods in Structural Dynamics and Earthquake Engineering (2021) 5039–5065.

[101] T. Triantafyllidis, B. Prange, Dynamic subsoil-coupling between rigid rectangular foundations, Soil Dynamics and Earthquake Engineering 6 (1987) 164–179.

[102] J. Qian, D. E. Beskos, Harmonic wave response of two 3-D rigid surface foundations, Soil Dynamics and Earthquake Engineering 15 (1996) 95–110.

[103] J. Qian, L. G. Tham, Y. K. Cheung, Dynamic analysis of rigid surface footings by boundary element method, Journal of Sound and Vibration 214 (1998) 747–759.

[104] D. L. Karabalis, M. Mohammadi, 3-D dynamic foundation-soil-foundation interaction on layered soil, Soil Dynamics and Earthquake Engineering 17 (1998) 139–152.

[105] D. L. Karabalis, C.-F. D. Huang, 3-D foundation-soil-foundation interaction, WIT Transactions on Modelling and Simulation 8 (1970).

[106] C.-F. D. Huang, Dynamic soil-foundation and foundation-soil-foundation interaction in three dimensions, Ph.D. thesis, University of South Carolina, 1993.

[107] M. Mohammadi, D. L. Karabalis, Dynamic 3-D soil–railway track interaction by BEM–FEM, Earthquake Engineering & Structural Dynamics 24 (1995) 1177–1193.

[108] H. D. Aji, F. Wuttke, P. Dineva, 3D structure-soil-structure interaction in an arbitrary layered half-space, Soil Dynamics and Earthquake Engineering 159 (2022) 107352.

[109] B. Sbartai, Dynamic interaction of two adjacent foundations embedded in a viscoelastic soil, International Journal of Structural Stability and Dynamics 16 (2016) 1450110.

[110] Z. Han, G. Lin, J. Li, Dynamic 3D Foundation–Soil–Foundation Interaction on Stratified Soil, International Journal of Structural Stability and Dynamics 17 (2017) 1750032.

[111] M. Bybordiani, Y. Arici, Structure–soil–structure interaction of adjacent buildings subjected to seismic loading, Earthquake Engineering & Structural Dynamics 48 (2019) 731–748.

[112] N. Chouw, R. Le, G. Schmid, Propagation of vibration in a soil layer over bedrock, Engineering Analysis with Boundary Elements 8 (1991) 125–131.

[113] N. Chouw, G. Schmid, Building isolation using the transmitting behaviour of a soil layer, in: Proceedings of the 10th world conference on signal engineering, Madrid (Spain), volume 4, pp. 2519–2524.

[114] H. Antes, O. von Estorff, Dynamic response of 2D and 3D block foundations on a halfspace with inclusions, Soil Dynamics and Earthquake Engineering 13 (1994) 305–311.

[115] H. Takemiya, Field vibration mitigation by honeycomb wib for pile foundations of a high-speed train viaduct, Soil Dynamics and Earthquake Engineering 24 (2004) 69–87.

[116] G. Gao, J. Chen, X. Gu, J. Song, S. Li, N. Li, Numerical study on the active vibration isolation by wave impeding block in saturated soils under vertical loading, Soil Dynamics and Earthquake Engineering 93 (2017) 99–112.

[117] D. Clouteau, R. Cottereau, G. Lombaert, Dynamics of structures coupled with elastic media—a review of numerical models and methods, Journal of Sound and Vibration 332 (2013) 2415–2436.

[118] G. C. Gazetas, J. M. Roesset, Forced vibrations of strip footings on layered soils, in: Methods of structural analysis, pp. 115–131.

[119] C. C. Spyrakos, D. E. Beskos, Dynamic response of rigid strip-foundations by a time-domain boundary element method, International Journal for Numerical Methods in Engineering 23 (1986) 1547–1565.

[120] H. Antes, O. von Estorff, Dynamic response analysis of rigid foundations and of elastic structures by boundary element procedures, Soil Dynamics and Earthquake Engineering 8 (1989) 68–74.

[121] O. von Estorff, E. Kausel, Coupling of boundary and finite elements for soil-structure interaction problems, Earthquake Engineering & Structural Dynamics 18 (1989) 1065–1075.

[122] O. von Estorff, M. J. Prabucki, Dynamic response in the time domain by coupled boundary and finite elements, Computational Mechanics 6 (1990) 35–46.

[123] G. Gazetas, Analysis of machine foundation vibrations: State of the art, International Journal of Soil Dynamics and Earthquake Engineering 2 (1983) 2–42.

[124] J.-G. Sieffert, F. Cevaer, Manuel des fonctions d'impédance: Fondations superficielles, Ouest Ed, Nantes, 1992.

[125] Y. Wang, R. K. N. D. Rajapakse, A. H. Shah, Dynamic interaction between flexible strip foundations, Earthquake Engineering & Structural Dynamics 20 (1991) 441–454.

[126] C. C. Spyrakos, C. Xu, Dynamic analysis of flexible massive strip–foundations embedded in layered soils by hybrid bem–fem, Computers & Structures 82 (2004) 2541–2550.

[127] X. Chen, C. Birk, C. Song, Transient analysis of wave propagation in layered soil by using the scaled boundary finite element method, Computers and Geotechnics 63 (2015) 1–12.

[128] M. C. Genes, Dynamic analysis of large-scale SSI systems for layered unbounded media via a parallelized coupled Finite-Element/Boundary-Element/Scaled Boundary Finite-Element Model, Engineering Analysis with Boundary Elements 36 (2012) 845–857.

[129] M. Radišić, M. Petronijević, G. Müller, Vibrations of flexible strip on viscoelastic halfspace, Procedia Engineering 199 (2017) 2420–2425.

[130] S. W. Liu, S. K. Datta, K. R. Khair, A. H. Shah, Three dimensional dynamics of pipelines buried in backfilled trenches due to oblique incidence of body waves, Soil Dynamics and Earthquake Engineering 10 (1991) 182–191.

[131] L. Andersen, C. Jones, Coupled boundary and finite element analysis of vibration from railway tunnels—a comparison of two- and three-dimensional models, Journal of Sound and Vibration 293 (2006) 611–625.

[132] A. A. Stamos, D. E. Beskos, Dynamic analysis of large 3-D underground structures by the BEM, Earthquake Engineering & Structural Dynamics 24 (1995) 917–934.

[133] C. He, S. Zhou, P. Guo, H. Di, X. Zhang, Analytical model for vibration prediction of two parallel tunnels in a full-space, Journal of Sound and Vibration 423 (2018) 306–321.

[134] D. Clouteau, M. L. Elhabre, D. Aubry, Periodic BEM and FEM-BEM coupling, Computational Mechanics 25 (2000) 567–577.

[135] D. Clouteau, M. Arnst, T. M. Al-Hussaini, G. Degrande, Freefield vibrations due to dynamic loading on a tunnel embedded in a stratified medium, Journal of Sound and Vibration 283 (2005) 173–199.

[136] G. Degrande, D. Clouteau, R. Othman, M. Arnst, H. Chebli, R. Klein, P. Chatterjee, B. Janssens, A numerical model for ground-borne vibrations from underground railway traffic based on a periodic finite element–boundary element formulation, Journal of Sound and Vibration 293 (2006) 645–666.

[137] S. Gupta, M. Hussein, G. Degrande, H. Hunt, D. Clouteau, A comparison of two numerical models for the prediction of vibrations from underground railway traffic, Soil Dynamics and Earthquake Engineering 27 (2007) 608–624.

[138] S. Gupta, Y. Stanus, G. Lombaert, G. Degrande, Influence of tunnel and soil parameters on vibrations from underground railways, Journal of Sound and Vibration 327 (2009) 70–91.

[139] S. Gupta, G. Degrande, Modelling of continuous and discontinuous floating slab tracks in a tunnel using a periodic approach, Journal of Sound and Vibration 329 (2010) 1101–1125.

[140] M. Germonpré, G. Degrande, G. Lombaert, A track model for the prediction of ground-borne vibrations due to parametric excitation, Procedia Engineering 199 (2017) 2663–2668.

[141] X. Sheng, C. Jones, D. J. Thompson, Modelling ground vibration from railways using wavenumber finite- and boundary-element methods, Proceedings of the Royal Society A: Mathematical, Physical and Engineering Sciences 461 (2005) 2043–2070.

[142] X. Sheng, C. Jones, D. J. Thompson, Prediction of ground vibration from trains using the wavenumber finite and boundary element methods, Journal of Sound and Vibration 293 (2006) 575–586.

[143] S. François, M. Schevenels, P. Galvín, G. Lombaert, G. Degrande, A 2.5D coupled FE–BE methodology for the dynamic interaction between longitudinally invariant structures and a layered halfspace, Computer Methods in Applied Mechanics and Engineering 199 (2010) 1536–1548.

[144] P. Galvín, S. François, M. Schevenels, E. Bongini, G. Degrande, G. Lombaert, A 2.5D coupled FE-BE model for the prediction of railway induced vibrations, Soil Dynamics and Earthquake Engineering 30 (2010) 1500–1512.

[145] P. Coulier, A. Dijckmans, S. François, G. Degrande, G. Lombaert, A spatial windowing technique to account for finite dimensions in 2.5D dynamic soil–structure interaction problems, Soil Dynamics and Earthquake Engineering 59 (2014) 51–67.

[146] Q. Jin, D. J. Thompson, D. E. Lurcock, M. G. Toward, E. Ntotsios, A 2.5D finite element and boundary element model for the ground vibration from trains in tunnels and validation using measurement data, Journal of Sound and Vibration 422 (2018) 373–389.

[147] K. A. Kuo, M. Papadopoulos, G. Lombaert, G. Degrande, The coupling loss of a building subject to railway induced vibrations: Numerical modelling and experimental measurements, Journal of Sound and Vibration 442 (2019) 459–481.

[148] K. A. Kuo, G. Lombaert, G. Degrande, Quantifying dynamic soil-structure interaction for railway induced vibrations, Procedia Engineering 199 (2017) 2372–2377.

[149] C. He, S. Zhou, H. Di, Y. Shan, A 2.5-D coupled FE–BE model for the dynamic interaction between saturated soil and longitudinally invariant structures, Computers and Geotechnics 82 (2017) 211–222.

[150] G. Lombaert, G. Degrande, D. Clouteau, Numerical modelling of free field traffic-induced vibrations, Soil Dynamics and Earthquake Engineering 19 (2000) 473–488.

[151] G. Lombaert, G. Degrande, The experimental validation of a numerical model for the prediction of the vibrations in the free field produced by road traffic, Journal of Sound and Vibration 262 (2003) 309–331.

[152] P. Galvín, D. Mendoza, D. P. Connolly, G. Degrande, G. Lombaert, A. Romero, Scoping assessment of free-field vibrations due to railway traffic, Soil Dynamics and Earthquake Engineering 114 (2018) 598–614.

[153] C. He, S. Zhou, H. Di, P. Guo, J. Xiao, Analytical method for calculation of ground vibration from a tunnel embedded in a multi-layered half-space, Computers and Geotechnics 99 (2018) 149–164.

[154] H. Liravi, R. Arcos, D. Ghangale, J. Romeu, A 2.5D coupled FEM-BEM-MFS methodology for longitudinally invariant soil-structure interaction problems, Proceedings of the International Conference on Structural Dynamic , Eurodyn 2 (2020).

[155] J. A. Forrest, H. Hunt, A three-dimensional tunnel model for calculation of train-induced ground vibration, Journal of Sound and Vibration 294 (2006) 678–705.

[156] J. A. Forrest, H. Hunt, Ground vibration generated by trains in underground tunnels, Journal of Sound and Vibration 294 (2006) 706–736.

[157] M. Hussein, S. Gupta, H. Hunt, G. Degrande, J. P. Talbot, An efficient model for calculating vibration from a railway tunnel buried in a half-space, in: Proceedings of the Thriteenth International Congress on Sound and Vibration, Vienna.

[158] M. F. M. Hussein, H. E. M. Hunt, L. Rikse, S. Gupta, G. Degrande, J. P. Talbot, S. François, M. Schevenels, Using the PiP Model for Fast Calculation of Vibration from a Railway Tunnel in a Multi-layered Half-Space, in: B. Schulte-Werning, D. Thompson, P.-E. Gautier, C. Hanson, B. Hemsworth, J. Nelson, T. Maeda, P. Vos (Eds.), Noise and Vibration Mitigation for Rail Transportation Systems, volume 99 of *Notes on Numerical Fluid Mechanics and Multidisciplinary Design*, Springer Berlin Heidelberg, Berlin, Heidelberg, 2008, pp. 136–142.

[159] K. Müller, Dreidimensionale dynamische Tunnel-Halbraum-Interaktion: Ein Verfahren auf der Grundlage einer Kopplung der Integraltransformationsmethode mit der Finite-Elemente-Methode, Dissertation, Technische Universität München, München, 2007.

[160] G. Frühe, G. Müller, Modelling of the dynamic interaction of tunnel- or longitudinal trench-structures in the half-space by the application of a set of various fundamental solutions, Proceedings of the Institute of Acoustics & Belgium Acoustical Society, Noise in the Built Environment (2010).

[161] K. Müller, H. Grundmann, S. Lenz, Nonlinear interaction between a moving vehicle and a plate elastically mounted on a tunnel, Journal of Sound and Vibration 310 (2008) 558–586.

[162] M. Hackenberg, A Coupled Integral Transform Method - Finite Element Method Approach to Model the Soil-Structure-Interaction, Dissertation, Technische Universität München, München, 2016.

[163] K. A. Kuo, H. Hunt, M. Hussein, The effect of a twin tunnel on the propagation of ground-borne vibration from an underground railway, Journal of Sound and Vibration 330 (2011) 6203–6222.

[164] M. Hussein, H. Hunt, A numerical model for calculating vibration from a railway tunnel embedded in a full-space, Journal of Sound and Vibration 305 (2007) 401–431.

[165] W. I. Hamad, H. E. Hunt, J. P. Talbot, M. F. Hussein, D. J. Thompson, THE DYNAMIC INTERACTION OF TWIN TUNNELS EMBEDDED IN a HOMOGENEOUS HALF-SPACE, in: Proceedings of the 5th International Conference on Computational Methods in Structural Dynamics and Earthquake Engineering (COMPDYN 2015), Institute of Structural Analysis and Antiseismic Research School of Civil Engineering National Technical University of Athens (NTUA) Greece, 2015.

[166] A. Romero, P. Galvín, J. António, J. Domínguez, A. Tadeu, Modelling of acoustic and elastic wave propagation from underground structures using a 2.5D BEM-FEM approach, Engineering Analysis with Boundary Elements 76 (2017) 26–39.

[167] C. He, S. Zhou, P. Guo, H. Di, X. Zhang, F. Yu, Theoretical modelling of the dynamic interaction between twin tunnels in a multi-layered half-space, Journal of Sound and Vibration 456 (2019) 65–85.

[168] H.-J. Dolling, Die Abschirmung von Erschütterungen durch Bodenschlitze, Disseration, TU Berlin, Berlin, 1969.

[169] R. D. Woods, Screening of surface waves in soils, Soil mechanics and foundations division (1968) 951–980.

[170] G. Segol, J. F. Abel, P. C. Y. Lee, Amplitude reduction of surface waves by trenches, Journal of the Engineering Mechanics Division 104 (1978) 621–641.

[171] W. A. Haupt, Surface-waves in non-homogeneous halfspace, Proc. Dyn. Meth. in Soil and Rock Mech. (1978) 335–367.

[172] K. Emad, G. D. Manolis, Shallow trenches and propagation of surface waves, Journal of Engineering Mechanics 111 (1985) 279–282.

[173] D. E. Beskos, B. Dasgupta, I. G. Vardoulakis, Vibration isolation using open or filled trenches, Computational Mechanics (1986) 43–63.

[174] K. L. Leung, D. E. Beskos, I. G. Vardoulakis, Vibration isolation using open or filled trenches, Computational Mechanics 7 (1990) 137–148.

[175] S. Ahmad, T. M. Al-Hussaini, Simplified design for vibration screening by open and in–filled trenches, Journal of Geotechnical Engineering 117 (1991) 67–88.

[176] J. Freisinger, G. Müller, Coupled ITM-FEM approach for the assessment of the mitigation efficiency of finite and infinite open trenches and infilled barriers, Proceedings of the International Conference on Structural Dynamic , EURODYN (2020).

[177] L. Andersen, S. Nielsen, Reduction of ground vibration by means of barriers or soil improvement along a railway track, Soil Dynamics and Earthquake Engineering 25 (2005) 701–716.

[178] M. Adam, O. von Estorff, Reduction of train-induced building vibrations by using open and filled trenches, Computers & Structures 83 (2005) 11–24.

[179] P. Coulier, S. François, G. Degrande, G. Lombaert, Subgrade stiffening next to the track as a wave impeding barrier for railway induced vibrations, Soil Dynamics and Earthquake Engineering 48 (2013) 119–131.

[180] D. J. Thompson, J. Jiang, M. Toward, M. Hussein, E. Ntotsios, A. Dijckmans, P. Coulier, G. Lombaert, G. Degrande, Reducing railway-induced ground-borne vibration by using open trenches and soft-filled barriers, Soil Dynamics and Earthquake Engineering 88 (2016) 45–59.

[181] P. Coulier, V. Cuéllar, G. Degrande, G. Lombaert, Experimental and numerical evaluation of the effectiveness of a stiff wave barrier in the soil, Soil Dynamics and Earthquake Engineering 77 (2015) 238–253.

[182] S. François, M. Schevenels, B. Thyssen, J. Borgions, G. Degrande, Design and efficiency of a composite vibration isolating screen in soil, Soil Dynamics and Earthquake Engineering 39 (2012) 113–127.

[183] A. Dijckmans, P. Coulier, J. Jiang, M. Toward, D. J. Thompson, G. Degrande, G. Lombaert, Mitigation of railway induced ground vibration by heavy masses next to the track, Soil Dynamics and Earthquake Engineering 75 (2015) 158–170.

[184] M. Mhanna, I. Shahrour, M. Sadek, P. Dunez, Efficiency of heavy mass technology in traffic vibration reduction: Experimental and numerical investigation, Computers and Geotechnics 55 (2014) 141–149.

[185] G. Lombaert, G. Degrande, B. Vanhauwere, B. Vandeborght, S. François, The control of ground-borne vibrations from railway traffic by means of continuous floating slabs, Journal of Sound and Vibration 297 (2006) 946–961.

[186] A. Dijckmans, A. Ekblad, A. Smekal, G. Degrande, G. Lombaert, Efficacy of a sheet pile wall as a wave barrier for railway induced ground vibration, Soil Dynamics and Earthquake Engineering 84 (2016) 55–69.

[187] S. François, M. Schevenels, G. Lombaert, G. Degrande, A two-and-a-half-dimensional displacement-based PML for elastodynamic wave propagation, International Journal for Numerical Methods in Engineering 90 (2012) 819–837.

[188] S. François, H. Goh, L. F. Kallivokas, Non-convolutional second-order complex-frequency-shifted perfectly matched layers for transient elastic wave propagation, Computer Methods in Applied Mechanics and Engineering 377 (2021) 113704.

[189] P. Coulier, G. Degrande, A. Dijckmans, J. Houbrechts, G. Lombaert, W. Rücker, L. Auersch, M. Plaza, V. Cuellar, D. Thompson, et al., Scope of the parametric study on mitigation measures on the transmission path, RIVAS project SCP0-GA-2010-265754, Deliverable D 4 (2011).

[190] G. Lombaert, G. Degrande, S. François, D. J. Thompson, Ground-Borne Vibration due to Railway Traffic: A Review of Excitation Mechanisms, Prediction Methods and Mitigation Measures, in: J. C. Nielsen, D. Anderson, P.-E. Gautier, M. Iida, J. T. Nelson, D. Thompson, T. Tielkes, D. A. Towers, P. de Vos (Eds.), Noise and Vibration Mitigation for Rail Transportation Systems, volume 126 of *Notes on Numerical Fluid Mechanics and Multidisciplinary Design*, Springer Berlin Heidelberg, Berlin, Heidelberg, 2015, pp. 253–287.

[191] D. J. Thompson, G. Kouroussis, E. Ntotsios, Modelling, simulation and evaluation of ground vibration caused by rail vehicles, Vehicle System Dynamics 57 (2019) 936–983.

[192] S. K. Datta, P. M. O'Leary, A. H. Shah, Three-dimensional dynamic response of buried pipelines to incident longitudinal and shear waves, Journal of Applied Mechanics 52 (1985) 919.

[193] H. L. Wong, J. E. Luco, Tables of impedance functions for square foundations on layered media, International Journal of Soil Dynamics and Earthquake Engineering 4 (1985) 64–81.

[194] J. E. Luco, F. C. P. de Barros, Seismic response of a cylindrical shell embedded in a layered viscoelastic half-space. i: Formulation, Earthquake Engineering & Structural Dynamics 23 (1994) 553–567.

[195] J. E. Luco, F. C. P. de Barros, Dynamic displacements and stresses in the vicinity of a cylindrical cavity embedded in a half-space, Earthquake Engineering & Structural Dynamics 23 (1994) 321–340.

[196] C. H. Lin, V. W. Lee, M. I. Todorovska, M. D. Trifunac, Zero-stress, cylindrical wave functions around a circular underground tunnel in a flat, elastic half-space: Incident P-waves, Soil Dynamics and Earthquake Engineering 30 (2010) 879–894.

[197] Q. Liu, M. Zhao, L. Wang, Scattering of plane P, SV or Rayleigh waves by a shallow lined tunnel in an elastic half space, Soil Dynamics and Earthquake Engineering 49 (2013) 52–63.

[198] M. Zhao, K. N. van Dalen, J. Barbosa, A. V. Metrikine, Semi-analytical solution for the dynamic response of a cylindrical structure embedded in a homogeneous half-space, in: X. Bian, Y. Chen, X. Ye (Eds.), Environmental Vibrations and Transportation Geodynamics, Springer Singapore, Singapore, 2018, pp. 369–388.

[199] I. N. Sneddon, The stress produced by a pulse of pressure moving along the surface of a semi-infinite solid, Rendiconti del Circolo Matematico di Palermo 1 (1952) 57–62.

[200] J. D. Cole, J. H. Huth, Stresses produced in a half-plane by moving loads, ASME Journal of Applied Mechanics (1958) 433–436.

[201] G. Eason, The stresses produced in a semi-infinite solid by a moving surface force, International Journal of Engineering Science 2 (1965) 581–609.

[202] R. G. Payton, An application of the dynamic Betti-Rayleigh reciprocal theorem to moving-point loads in elastic media, Quarterly of Applied Mathematics 21 (1964) 299–313.

[203] D. L. Lansing, The displacements in an elastic half-space due to a moving concentrated normal load (1966).

[204] D. C. Gakenheimer, J. Miklowitz, Transient excitation of an elastic half space by a point load traveling on the surface, Journal of Applied Mechanics 36 (1969) 505.

[205] A. T. de Hoop, The moving-load problem in soil dynamics—the vertical displacement approximation, Wave Motion 36 (2002) 335–346.

[206] L. Frýba, Vibration of solids and structures under moving loads, Springer Netherlands, Dordrecht, 1972.

[207] A. Verruijt, C. C. Córdova, Moving loads on an elastic half-plane with hysteretic damping, Wave Motion 68 (2001) 915.

[208] J. Kaplunov, D. A. Prikazchikov, B. Erbaş, O. Şahin, On a 3D moving load problem for an elastic half space, Wave Motion 50 (2013) 1229–1238.

[209] F. de Barros, J. E. Luco, Response of a layered viscoelastic half-space to a moving point load, Wave Motion 19 (1994) 189–210.

[210] G. Lefeuve-Mesgouez, D. Le Houédec, A. Peplow, Ground Vibration In The Vicinity Of A High-Speed Moving Harmonic Strip Load, Journal of Sound and Vibration 231 (2000) 1289–1309.

[211] F. de Barros, J. E. Luco, Stresses and displacements in a layered half-space for a moving line load, Applied Mathematics and Computation 67 (1995) 103–134.

[212] H. Grundmann, M. Lieb, E. Trommer, The response of a layered half-space to traffic loads moving along its surface, Archive of Applied Mechanics (Ingenieur Archiv) 69 (1999) 55–67.

[213] X. Bian, Y. Chen, An explicit time domain solution for ground stratum response to harmonic moving load, Acta Mechanica Sinica 22 (2006) 469–478.

[214] P. Galvín, J. Domínguez, Analysis of ground motion due to moving surface loads induced by high-speed trains, Engineering Analysis with Boundary Elements 31 (2007) 931–941.

[215] H. A. Dieterman, A. Metrikine, et al., The equivalent stiffness of a half-space interacting with a beam. Critical velocities of a moving load along the beam, European Journal of Mechanics Series A Solids 15 (1996) 67–90.

[216] J. Dinkel, Ein semi-analytischen Modell zur dynamischen Berechnung des gekoppelten Systems Fahrzeug-Fahrweg-Untergrund für das Oberbausystem Feste Fahrbahn, Ph.D. thesis, Technische Universität München, München, 2000.

[217] S. Lenz, Nichtlineare Interaktion zwischen Fahrzeug und Untergrund unter Zuhilfenahme von Integraltransformationen, Dissertation, Technische Universität München, München, 2003.

[218] H. Grundmann, S. Lenz, Vibration of the soil caused by a vehicle moving over the randomly uneven surface of a slab track, PAMM 3 (2003) 489–490.

[219] A. V. Metrikine, S. N. Verichev, J. Blaauwendraad, Stability of a two-mass oscillator moving on a beam supported by a visco-elastic half-space, International Journal of Solids and Structures 42 (2005) 1187–1207.

[220] C. Madshus, M. Kaynia, High-speed railway lines on soft ground: dynamic behaviour at critical train speed, Journal of Sound and Vibration 231 (2000) 689–701.

[221] X. Sheng, C. Jones, M. Petyt, Ground vibration generated by a harmonic load acting on a railway track, Journal of Sound and Vibration 225 (1999) 3–28.

[222] X. Sheng, C. Jones, M. Petyt, Ground vibration generated by a load moving along a railway track, Journal of Sound and Vibration 228 (1999) 129–156.

[223] H. Chebli, D. Clouteau, A. Modaressi, Three-dimensional periodic model for the simulation of vibrations induced by high speed trains, Ital Geotech J 38 (2004) 26–31.

[224] T. Lu, A. V. Metrikine, M. Steenbergen, The equivalent dynamic stiffness of a visco-elastic half-space in interaction with a periodically supported beam under a moving load, European Journal of Mechanics - A/Solids 84 (2020) 104065.

[225] S. Gupta, G. Degrande, G. Lombaert, Experimental validation of a numerical model for subway induced vibrations, Journal of Sound and Vibration 321 (2009) 786–812.

[226] Y. B. Yang, H. H. Hung, Soil vibrations caused by underground moving trains, Journal of Geotechnical and Geoenvironmental Engineering 134 (2008) 1633–1644.

[227] X. Bian, W. Jin, H. Jiang, Ground-borne vibrations due to dynamic loadings from moving trains in subway tunnels, J. Zhejiang Univ. Sci. A 13 (2012) 870–876.

[228] Z. Yuan, A. Boström, Y. Cai, Benchmark solution for vibrations from a moving point source in a tunnel embedded in a half-space, Journal of Sound and Vibration 387 (2017) 177–193.

[229] L. Ma, H. Ouyang, C. Sun, R. Zhao, Le Wang, A curved 2.5D model for simulating dynamic responses of coupled track-tunnel-soil system in curved section due to moving loads, Journal of Sound and Vibration 451 (2019) 1–31.

[230] G. Frühe, Überlagerung von Grundlösungen in der Elastodynamik zur Behandlung der dynamischen Tunnel-Boden-Bauwerk-Interaktion, Dissertation, Technische Universität München, München, 2010.

[231] J. A. Studer, J. Laue, M. Koller, Bodendynamik, Springer Berlin Heidelberg, Berlin, Heidelberg, 2008.

[232] A. Konrad, Der Zylinder, der zylindrische Hohlraum und die dickwandige Kreiszylinderschale unter beliebigen, ruhenden oder bewegten Lasten, Inst. für Bauingenieurwesen I, 1985.

[233] B. O. Hardin, V. P. Drnevich, Shear modulus and damping in soils: measurement and parameter effects, Journal of the Soil Mechanics and Foundations Division (1972) 603–624.

[234] J. P. Wolf, Dynamic Soil-Structure Interaction, Prentice Hall, 1985.

[235] C. F. Long, On the completeness of the Lamè potentials, Acta Mechanica 3 (1967) 371–375.

[236] A. Sommerfeld, Partial Differential Equations in Physics, volume 1 of *Pure and Applied Mathematics*, Academic Press, New York, 1949.

[237] H. Grundmann, G. Müller, Schwingungen infolge zeitlich veränderlicher, bewegter Lasten im Untergrund, in: Wunderlich, W., und Stein, E (Ed.), Finite-Elemente, Anwendung in der Baupraxis, Ernst & Sohn, 1988.

[238] P. F. Papkovich, Solution générale des équations differentielles fondamentales d'élasticité exprimée par trois fonctions harmoniques, Compt. Rend. Acad. Sci. Paris (1932) 513–515.

[239] H. Neuber, Ein neuer Ansatz zur Lösung räumlicher Probleme der Elastizitätstheorie. Der Hohlkegel unter Einzellast als Beispiel, ZAMM - Journal of Applied Mathematics and Mechanics / Zeitschrift für Angewandte Mathematik und Mechanik 14 (1934) 203–212.

[240] E. Heine, Handbuch der Kugelflächenfunktionen, Georg Reimer, Berlin, 1861.

[241] E. W. Hobson, The Theory of Spherical and Ellipsoidal Harmonics, University press, Cambridge, 1931.

[242] T. Arens, F. Hettlich, C. Karpfinger, U. Kockelkorn, K. Lichtenegger, H. Stachel, Mathematik, Springer Berlin Heidelberg, 2018.

[243] M. Abramowitz, I. A. Stegun, Handbook of mathematical function: with formulas, graphs and mathematical tables, Dover Publications, New York, 1965.

[244] J. Freisinger, G. Müller, 2.5D ITM-FEM approach for the prediction of ground-borne vibrations from two parallel underground railway tunnels, International Conference on Noise and Vibration Engineering (ISMA) (2022).

[245] Y. Li, Modelling of a half space with two parallel tunnels, Masterthesis, TU München, München, 2022.

[246] A. V. Oppenheim, R. W. Schafer, J. R. Buck, L. Lee, Discrete-time Signal Processing, Prentice Hall international editions, Prentice Hall, 1999.

[247] E. O. Brigham, FFT-Anwendungen, De Gruyter, 1997.

[248] B. Osgood, The Fourier transform and its applications, Lecture notes for EE 261 (2009) 20.

[249] D. Potts, G. Steidl, M. Tasche, Fast and stable algorithms for discrete spherical Fourier transforms, Linear Algebra and its Applications 275-276 (1998) 433–450. Proceedings of the Sixth Conference of the International Linear Algebra Society.

[250] C. Gruber, Kugelfunktionen und Analyse heterogener Schweredaten im Spektralbereich, Univ. Berlin, 2007.

[251] M. J. Mohlenkamp, A fast transform for spherical harmonics, The Journal of Fourier Analysis and Applications 5 (1999) 159–184.

[252] W. F. Spotz, P. N. Swarztrauber, A performance comparison of associated legendre projections, Journal of computational physics 168 (2001) 339–355.

[253] P. N. Swarztrauber, On the spectral approximation of discrete scalar and vector functions on the sphere, SIAM Journal on Numerical Analysis 16 (1979) 934–949.

[254] P. N. Swarztrauber, W. F. Spotz, Generalized discrete spherical harmonic transforms, Journal of computational physics 159 (2000) 213–230.

[255] K. Backhaus, B. Erichson, R. Weiber, Fortgeschrittene Multivariate Analysemethoden, Springer Berlin Heidelberg, Berlin, Heidelberg, 2015.

[256] W. P. Jones, G. W. Furnas, Pictures of relevance: A geometric analysis of similarity measures, Journal of the American Society for Information Science 38 (1987) 420–442.

[257] P. Willett, J. M. Barnard, G. M. Downs, Chemical similarity searching, Journal of Chemical Information and Computer Sciences 38 (1998) 983–996.

[258] J. Kreutz, Augmented Beam Elements Using Unit Deflection Shapes Together with a Finite Element Discretisation of the Cross Section, Dissertation, TU München, München, 2013.

[259] F. Schneider, Parameterstudie zur Analyse des Anwendungsbereichs eines gekoppelten Verfahrens der Finite-Elemente-Methode mit Integraltransformationsmethoden, Bacherlor thesis, Technische Universität München, München, 2014.

[260] M. Schauer, Ein effizienter gekoppelter FEM-SBFEM Ansatz zur Analyse von Boden-Bauwerk-Interaktionen im Zeitbereich, Dissertation, TU Braunschweig, Braunschweig, 2014.

[261] The MathWorks Inc, Matlab parallel computing toolbox r2021b, Natick, Massachusetts, United States (2022).

[262] A. J. B. Tadeu, E. Kausel, Green's functions for two-and-a-half-dimensional elastodynamic problems, Journal of Engineering Mechanics 126 (2000) 1093–1097.

[263] M. Hackenberg, M. Dengler, G. Müller, Implementation of the Finite Element Method in the Fourier-Transformed Domain and Coupling with Analytical Solutions, in: Cunha A., Caetano E., Ribeiro P., Müller G (Ed.), Eurodyn 2014.

[264] M. B. Priestley, Spectral analysis and time series, Probability and mathematical statistics, Elsevier, London, repr edition, 2004.

[265] I. N. Bronstein, K. A. Semendjajev, G. Musiol, H. Mühlig, Taschenbuch der Mathematik, Harri Deutsch, 2006.

[266] O. C. Zienkiewicz, R. L. Taylor, J. Zhu, The finite element method, volume 1, Elsevier Butterworth-Heinemann, Amsterdam, 6. ed., repr edition, 2010.

[267] K.-J. Bathe, Finite-Elemente-Methoden, Springer, Berlin and Heidelberg, 2. aufl. edition, 2002.

[268] P. Langer, M. Maeder, C. Guist, M. Krause, S. Marburg, More than six elements per wavelength: The practical use of structural finite element models and their accuracy in comparison with experimental results, Journal of Computational Acoustics 25 (2017) 1750025.

[269] L. Wagner, 2.5D ITM-FEM-Ansatz zur Modellierung eines Halbraums mit zylinderförmigem Graben mit variablen Einschlüssen und Aufbauten, Master thesis, Technische Universität München, München, 2019.

[270] Y. Maday, C. Mavriplis, A. Patera, Nonconforming mortar element methods: application to spectral discretizations, NASA Technical Report (1988).

[271] C. Bernardi, Y. Maday, A. T. Patera, Domain decomposition by the mortar element method, in: H. G. Kaper, M. Garbey, G. W. Pieper (Eds.), Asymptotic and Numerical Methods for Partial Differential Equations with Critical Parameters, Springer Netherlands, Dordrecht, 1993, pp. 269–286.

[272] B. I. Wohlmuth, A mortar finite element method using dual spaces for the lagrange multiplier, SIAM Journal on Numerical Analysis 38 (2001) 989–1012.

[273] B. van Hal, Automation and performance optimization of the wave based method for interior structural-acoustic problems, Phd thesis, KU Leuven, 2001.

[274] B. Pluymers, W. Desmet, D. Vandepitte, P. Sas, Wave based modelling methods for steady-state interior acoustics: an overview, in: Proceeding of ISMA, pp. 2303–2358.

[275] Ansys Inc, Ansys academic research mechanical apdl, substructuring analysis guide (2020).

[276] R. J. Guyan, Reduction of stiffness and mass matrices, AIAA Journal 3 (1965) 380.

[277] P. Brumund, T. Dehaeze, Multibody simulations with reduced order flexible bodies obtained by fea (2021).

[278] R. R. Craig, M. Bampton, Coupling of substructures for dynamic analyses, AIAA Journal 6 (1968) 1313–1319.

[279] F. Rojas, J. C. Anderson, L. M. Massone, A nonlinear quadrilateral thin flat layered shell element for the modeling of reinforced concrete wall structures, Bulletin of Earthquake Engineering 17 (2019) 6491–6513.

[280] F. Rojas, J. C. Anderson, L. M. Massone, A nonlinear quadrilateral layered membrane element with drilling degrees of freedom for the modeling of reinforced concrete walls, Engineering Structures 124 (2016) 521–538.

[281] J.-L. Batoz, M. B. Tahar, Evaluation of a new quadrilateral thin plate bending element, International Journal for Numerical Methods in Engineering 18 (1982) 1655–1677.

[282] R. de Frias Lopez, A 3D finite beam element for the modelling of composite wind turbine wings, Master thesis, KTH, Stockholm, 2013.

[283] H. P. Gavin, Structural Element Stiffness, Mass, and Damping Matrices, Lecture notes cee 541 structural dynamics, Duke University, 2020.

[284] T. Habermann, 3D-Boden-Bauwerk-Interaktion unter Berücksichtigung der Baugrundkopplung zwischen starren Rechteckfundamenten durch einen gekoppelten ITM-FEM-Ansatz, Master thesis, TU München, München, 2021.

[285] H. L. Wong, J. E. Luco, Dynamic response of rectangular foundations to obliquely incident seismic waves, Earthquake Engineering & Structural Dynamics 6 (1978) 3–16.

[286] K. Friedrich, Einfluss der Bauwerk-Baugrund-Wechselwirkung auf das dynamische Verhalten des Eisenbahnoberbaus, Dissertation, Ruhr-Universität Bochum, 2004.

[287] L. Cremer, M. Heckl, Structure-Borne Sound, Springer Berlin Heidelberg, Berlin, Heidelberg, 1988.

[288] L. Auersch, Wave propagation in layered soils: Theoretical solution in wavenumber domain and experimental results of hammer and railway traffic excitation, Journal of Sound and Vibration 173 (1994) 233–264.

[289] D. Clouteau, Modifications of the ground motion in dense urban areas, Journal of Computational Acoustics 9 (2001) 1659–1675.

[290] V. V. Krylov, Control of traffic-induced ground vibrations by placing heavy masses on the ground surface, Journal of Low Frequency Noise, Vibration and Active Control 26 (2007) 311–321.

[291] S. Deutrich, Untersuchung der Effizienz einer Gabionenwand als Schwingungsreduktionsmaßnahme mit Hilfe eines gekoppelten ITM-FEM-Ansatzes, Bachelor thesis, TU München, München, 2020.

[292] W. A. Haupt, Wave propagation in the ground and isolation measures, International Conferences on Recent Advances in Geotechnical Earthquake Engineering and Soil Dynamics (1995).

[293] T. Bose, D. Choudhury, J. Sprengel, M. Ziegler, Efficiency of open and infill trenches in mitigating ground-borne vibrations, Journal of Geotechnical and Geoenvironmental Engineering 144 (2018) 04018048.

[294] B. Dasgupta, D. E. Beskos, I. G. Vardoulakis, Vibration isolation using open or filled trenches part 2: 3-d homogeneous soil, Computational Mechanics 6 (1990) 129–142.

[295] F. Taddei, Numerical investigation of soil-structure interaction for onshore wind turbines grounded on a layered soil, Dissertation, RWTH Aachen, Aachen, 2015.

[296] P. Zeller, Handbuch Fahrzeugakustik: Grundlagen, Auslegung, Berechnung, Versuch, SpringerLink Bücher, Vieweg+Teubner Verlag, Wiesbaden, 2., überarbeitete auflage edition, 2012.

[297] C. Vrettos, Bodendynamik, in: K. J. Witt (Ed.), Grundbau-Taschenbuch, Wiley-VCH Verlag GmbH & Co. KGaA, Weinheim, Germany, 2008, pp. 451–500.

[298] A. Pais, E. Kausel, Approximate formulas for dynamic stiffnesses of rigid foundations, Soil Dynamics and Earthquake Engineering 7 (1988) 213–227.

[299] G. Gazetas, Formulas and charts for impedances of surface and embedded foundations, Journal of Geotechnical Engineering 117 (1991) 1363–1381.

[300] G. F. Miller, H. Pursey, On the partition of energy between elastic waves in a semi-infinite solid, Proceedings of the Royal Society of London. Series A. Mathematical and Physical Sciences 233 (1955) 55–69.

[301] T. Kobori, R. Minai, T. Suzuki, The dynamical ground compliance of a rectangular foundation on a viscoelastic stratum, Bulletin of the Disaster Prevention Research Institute (1971) 289–329.

[302] M. A. Laughton, D. F. Warne (Eds.), Electrical engineer's reference book, Newnes, Oxford England and Boston, 16th ed. edition, 2003.

[303] The MathWorks Inc, Interpolation for gridded data, Natick, Massachusetts, United States (2022).

[304] The MathWorks Inc, Discrete convolution, Natick, Massachusetts, United States (2022).

[305] Wikipedia contributors, Parseval's theorem, 2022. Accessed: 2022-08-06.

[306] S. H. Crandall, Dynamic response of systems with structural damping, Air, Space and Instruments, Draper anniversary volume (New York: McGraw-Hill) (1963) 183–193.

[307] A. S. Veletsos, B. Verbic, Basic response functions for elastic foundations, Journal of the Engineering Mechanics Division 100 (1974) 189–202.

[308] E. Kausel, Advanced Structural Dynamics, Cambridge University Press, 2017.

[309] E. W. Weisstein, Gibbs phenomenon, https://mathworld.wolfram.com/GibbsPhenomenon.html, 2022. Accessed: 2022-05-22.

[310] X. Bian, Y. Chen, Analysis of moving load induced ground vibrations based on thin-layer method, J. Zhejiang Univ. Sci. A 7 (2006) 309–314.

[311] H. Niedrig, M. Sternberg, B physik, in: H. Czichos, M. Hennecke (Eds.), HÜTTE - Das Ingenieurwissen, Springer Berlin Heidelberg, Berlin, Heidelberg, 2012, pp. 185–473.

[312] M. Lieb, Adaptive numerische Fouriertransformation in der Bodendynamik unter Verwendung einer Waveletzerlegung, Dissertation, Technische Universität München, München, 1997.

[313] D. Jones, D. Le Houedec, A. Peplow, M. Petyt, Ground vibration in the vicinity of a moving harmonic rectangular load on a half-space, European Journal of Mechanics - A/Solids 17 (1998) 153–166.

[314] G. Lefeuve-Mesgouez, A. Mesgouez, Ground vibration due to a high-speed moving harmonic rectangular load on a poroviscoelastic half-space, International Journal of Solids and Structures 45 (2008) 3353–3374.

[315] G. B. Arfken, H. J. Weber, F. E. Harris, Bessel functions, in: Mathematical Methods for Physicists, volume 2 vols, Elsevier, 2013, pp. 643–713.

[316] B. Burrows, D. Colwell, The fourier transform of the unit step function, International Journal of Mathematical Education in Science and Technology 21 (1990) 629–635.

[317] C. A. Felippa, Introduction to finite element methods, University of Colorado 885 (2004).